



**HAL**  
open science

# Searching for new physics with CMB precision cosmology

Guillermo Franco Abellan

► **To cite this version:**

Guillermo Franco Abellan. Searching for new physics with CMB precision cosmology. Astrophysics [astro-ph]. Université de Montpellier, 2022. English. NNT : 2022UMONS032 . tel-04217480

**HAL Id: tel-04217480**

**<https://theses.hal.science/tel-04217480>**

Submitted on 25 Sep 2023

**HAL** is a multi-disciplinary open access archive for the deposit and dissemination of scientific research documents, whether they are published or not. The documents may come from teaching and research institutions in France or abroad, or from public or private research centers.

L'archive ouverte pluridisciplinaire **HAL**, est destinée au dépôt et à la diffusion de documents scientifiques de niveau recherche, publiés ou non, émanant des établissements d'enseignement et de recherche français ou étrangers, des laboratoires publics ou privés.

**THÈSE POUR OBTENIR LE GRADE DE DOCTEUR  
DE L'UNIVERSITÉ DE MONTPELLIER**

**En Physique**

**École doctorale : Information, Structures, Systèmes**

**Unité de recherche : Laboratoire Univers et Particules de Montpellier**

**Searching for new physics  
with CMB precision cosmology**

**Présentée par Guillermo Franco Abellán**

**Le 18 Juillet, 2022**

**Sous la direction de Julien Lavalley et Vivian Poulin**

**Devant le jury composé de**

**Ruth Durrer, Directrice de recherche, Université de Genève**  
**Julien Lavalley, Directeur de recherche, LUPM Montpellier**  
**Vivian Poulin, Chargé de recherche, LUPM Montpellier**  
**Yacine Ali-Haïmoud, Assistant professor, New York University**  
**Kimberly Boddy, Assistant professor, University of Texas**  
**Julien Lesgourgues, Professor, RWTH Aachen**  
**Olga Mena Requejo, CSIC researcher, IFIC Valencia**  
**Licia Verde, Professor, ICREA Barcelona**

**Présidente**  
**Directeur de thèse**  
**Co-directeur de thèse**  
**Rapporteur**  
**Rapporteuse**  
**Examinateur**  
**Examinatrice**  
**Examinatrice**



**UNIVERSITÉ  
DE MONTPELLIER**



*“The Cosmos is all that is or was or ever will be. Our feeblest contemplations of the Cosmos stir us – there is a tingling in the spine, a catch in the voice, a faint sensation, as if a distant memory, of falling from a height. We know we are approaching the greatest of mysteries.”*

*Carl Sagan, Cosmos*





# Agradecimientos

Tout d'abord j'aimerais remercier à Julien Lavalle et Vivian Poulin, mes directeurs de thèse. Julien, je te remercie énormément pour m'avoir accueilli dans ton équipe, pour ton soutien et pour les conseils très précieux que tu m'as donné pendant ces dernières années. Vivian, un grand merci pour ton implication constante, ton suivi et ton aide dans le travail. Je suis aussi très reconnaissant de l'opportunité que tu m'as donné de voyager en Europe et aux États-Unis pour présenter mon travail (quand la pandémie l'a permis!) et de participer à des projets hyper-intéressantes avec des collaborateurs internationaux. Cela m'a permis de m'intégrer du mieux possible à la communauté et de contribuer activement à un domaine de recherche qui est vraiment ma passion. Sans oublier la bonne humeur et tous les bons moments passés en dehors du laboratoire. Je te garderai non seulement comme un guide *exceptionnel* et un modèle à suivre, mais aussi comme un bon ami. J'espère qu'on gardera le contact et on continuera à collaborer ensemble dans le futur.

I would like to thank all the wonderful people that I had the chance to meet during my stay at the LUPM: Mihael, a.k.a. the bicycle man; Rodrigo, official founder of the latino sub-group; Riki and Marco, my dearest sardinian (although not necessarily italian) friends; the ever smiling Casey (&Jabba); Théo, Alice, Hugo and Chadi, the most tenacious Wordle players that could possibly exist, and Eva, la meva compatriota catalana. Without all the karaoke nights, the barbecues or the cycling trips to the beach, these three years would have been substantially less fun. A special thanks to Gaétan (*monsieur le président*), my office mate for more than two years. I will never forget our intense physics discussions and all the patience you had for answering my numerous questions. I will also keep a fond memory of all the PhD students that I met during the unforgettable *Les Houches summer school 2021*, including Adriana (*Menki*), Gonzalo (=Rafa), JoaQUIM, Arman, Nudzein, Maxl, Dror... I hope our paths will cross again in the future. I would also like to address my thanks to my colleagues in the USA for the various discussions and lively meetings we had in the last years: Zackaria Chacko, Peizhi Du, Yuhsin Tsai and Abhish Dev. For the same reasons, I am very thankful to all the people at Aachen and Amsterdam with whom I had the pleasure to collaborate in the " $H_0$  Olympics": Nils Schöneberg, Andrea Pérez, Sam Witte and Julien Lesgourgues. Let me thank warmly the members of my thesis committee, for accepting to judge my work. Special thanks to the rapporteurs for accepting to review the manuscript.

Me gustaría pasar a agradecer a todas las personas que han estado a mi lado desde mucho antes de que empezase mis andaduras en el mundo de la investigación. Para empezar, quiero agradecer a mis amigos murcianos de toda la vida: Edu y Salva (a.k.a los pollaringas), Carlos linkin, Gubensiko, Dory, Marta Takian y Guille (no-lennon). Muchas gracias por los momentos de risas que he podido compartir con vosotros (a pesar de la distancia Montpellier-Murcia) y que me han permitido mantener una buena salud mental durante las épocas más duras de mi

doctorado. Como no agradecer a mis amigos de la carrera, en particular a todos los integrantes de *El bussón de Higgs* (Chino, Edu-cuña, Pablezno, Josexo...), con los que tantísimas buenas experiencias he tenido. Especial mención a Chema *la seña nostre* y Castelo/Pincelo, por contagiarme vuestra enorme pasión por la física, y por haberme hecho alguna visitilla durante mi estancia en Montpellier.

Por supuesto, quiero dar las gracias a MJ, mi pareja en la vida desde hace ya más de 7 años. Estas pocas líneas no me dan para expresar la enorme gratitud que siento por todo el enorme apoyo que me has dado, y tu inestimable compañía y ayuda en los momentos más difíciles de mi tesis. Si he llegado hasta aquí ha sido en parte gracias a ti. Estoy convencido de que en los próximos años podremos seguir compaginando nuestra relación con nuestra vocación de investigadores, porque como dice la canción, “*te quiero libre, y libre te quiero conmigo*”.

Por último, pero no menos importante, me gustaría agradecer a todos los miembros tan maravillosos de mi familia. En particular, quiero dar las gracias a mis primos Felipe y Antonio, que me han dado consejos muy valiosos sobre diversos aspectos de la carrera investigadora. Y como no, infinitas gracias mamá y papá por haber creído siempre en mí, por haberme educado tan bien, y por haberme apoyado incondicionalmente en todas las decisiones que he tomado en mi vida. Si he llegado hasta aquí también es en parte gracias a vosotros, y me llena de felicidad saber que estaréis orgullosos de mí. Gracias también a Ferni y Poté por ser los mejores hermanos que uno podría desear.



# Contents

<b>1</b>	<b>The era of precision cosmology</b>	<b>1</b>
1.1	Historical introduction	3
1.1.1	Evidences of an expanding universe	3
1.1.2	From the Big Bang theory to the first hints of dark matter	4
1.1.3	The universe is accelerating	6
1.2	Timeline of the cosmos	7
1.3	The smooth universe	9
1.3.1	Geometry of the expanding universe	10
1.3.2	Cosmo-dynamics	12
1.3.3	Distances in cosmology	15
1.4	A few words on inflation	20
1.5	In and out of equilibrium	22
1.5.1	The Boltzmann formalism	23
1.5.2	Relativistic degrees of freedom and entropy conservation	26
1.5.3	Neutrino decoupling and evolution	28
1.5.4	WIMP freeze-out	30
1.5.5	Big-Bang Nucleosynthesis	33
1.5.6	Hydrogen recombination	36
1.6	The linearly perturbed universe	42
1.6.1	The gauge problem	45
1.6.2	Perturbation equations	49
1.6.3	Initial conditions	59
1.6.4	Acoustic oscillations	63
1.6.5	The CMB power spectra	67
1.6.6	The matter power spectrum	79
1.7	Successes and challenges of the $\Lambda$ CDM paradigm	87
1.7.1	The nature of the dark sector	87
1.7.2	Cosmic discordance	91
1.8	Outline	96
<b>2</b>	<b>Early dark energy and the <math>H_0</math> tension</b>	<b>99</b>
2.1	Best-fit EDE cosmology solving the $H_0$ discrepancy	100
2.2	Guidelines to solve the $H_0$ tension	102
2.3	Formalism of Early dark energy	107
2.3.1	Basic equations	107
2.4	Cosmological constraints	109
2.4.1	Baseline analysis: anatomy of the 3-parameter EDE model	110
2.4.2	Towards a 1-parameter resolution to the $H_0$ tension	114
2.4.3	Confronting EDE to weak-lensing data	115
2.4.4	EDE and the $S_8$ tension in light of the $A_{\text{lens}}$ anomaly	123

2.5	EDE in the context of other proposed solutions . . . . .	127
2.5.1	Brief overview of competitors . . . . .	127
2.5.2	Statistical tests to quantify model success . . . . .	129
2.5.3	Results of the contest . . . . .	131
2.6	Summary and outline . . . . .	135
<b>3</b>	<b>Decaying dark matter and the <math>S_8</math> tension</b>	<b>139</b>
3.1	Unstable dark matter and cosmic tensions . . . . .	140
3.2	Formalism of the two-body Dark Matter decay . . . . .	141
3.2.1	Background equations . . . . .	144
3.2.2	Linear perturbation equations . . . . .	146
3.2.3	Fluid approximation for the warm component . . . . .	148
3.2.4	Dynamics of perturbations . . . . .	149
3.3	Observable effects of the Dark Matter decay . . . . .	151
3.3.1	Impact on the matter power spectrum . . . . .	151
3.3.2	Impact on the CMB anisotropy spectra . . . . .	153
3.4	Cosmological constraints . . . . .	155
3.4.1	General constraints: background vs. linear perturbations . . . . .	156
3.4.2	Implications for the $S_8$ tension . . . . .	158
3.4.3	Implications for other cosmic tensions and the Xenon1T anomaly . . . . .	163
3.4.4	Detecting DDM in the CMB: impact of current and future data . . . . .	165
3.5	Summary and outline . . . . .	171
<b>4</b>	<b>New cosmological limits on the neutrino mass and lifetime</b>	<b>175</b>
4.1	Constraints on neutrino mass and lifetime from cosmological data . . . . .	176
4.2	The neutrino mass conundrum . . . . .	178
4.3	Parameter space of decaying neutrinos . . . . .	181
4.4	Formalism of invisible non-relativistic neutrino decay . . . . .	184
4.4.1	Derivation of Boltzmann equations . . . . .	184
4.4.2	Impact of the non-relativistic neutrino decay on the CMB spectra . . . . .	188
4.4.3	Consistency of the implementation of the Boltzmann equations . . . . .	189
4.5	Cosmological constraints . . . . .	192
4.5.1	Details of the analysis . . . . .	192
4.5.2	Updated limits on the neutrino mass and lifetime . . . . .	193
4.5.3	Comparison with former results and impact of <i>Planck</i> 2018 data . . . . .	194
4.6	Summary and outline . . . . .	195
<b>5</b>	<b>Conclusions</b>	<b>199</b>
<b>A</b>	<b>Complements on linear perturbation theory</b>	<b>205</b>
A.1	The four velocity in a generic gauge . . . . .	205
A.2	Gauge transformations . . . . .	205
A.3	The 0 component of the geodesic equation . . . . .	206
A.4	Elements of perturbed stress-energy tensor . . . . .	208
A.5	Collision term for photons . . . . .	209
A.6	Conservation equations from the collisionless Boltzmann equation . . . . .	212
A.7	Perturbed Einstein equations . . . . .	214
A.8	Conservation of the comoving curvature perturbation . . . . .	217
<b>B</b>	<b>Complements on parameter inference</b>	<b>219</b>
B.1	Parameter extraction . . . . .	219

B.1.1	Bayes Theorem . . . . .	220
B.2	Monte Carlo Markov chains . . . . .	222
B.2.1	Metropolis-Hastings algorithm . . . . .	223
B.3	Model selection . . . . .	224
<b>C</b>	<b>Complements on Early Dark Energy</b>	<b>227</b>
C.1	$\chi^2$ Tables . . . . .	227
C.2	A closer look to $N$ -body simulations . . . . .	228
<b>D</b>	<b>Complements on decaying dark matter</b>	<b>233</b>
D.1	Boltzmann equation for decaying dark matter in the synchronous gauge	233
D.1.1	Geodesic equation . . . . .	234
D.1.2	Collision integrals . . . . .	235
D.2	Background continuity equation for the WDM species . . . . .	236
D.3	Linear fluid equations for the WDM species . . . . .	237
D.3.1	Continuity equation . . . . .	238
D.3.2	Euler equation . . . . .	238
D.3.3	Adiabatic sound speed . . . . .	238
D.3.4	Anisotropic stress . . . . .	239
D.3.5	Semi-analytic understanding of the WDM sound speed . . . . .	241
D.4	Numerical implementation and accuracy of the fluid approximation . . . . .	243
D.5	Best-fit $\chi^2$ per experiment . . . . .	246
D.6	Comparison with the <i>Planck</i> constraints from CLARK et al. (2021a) . . . . .	246
D.7	Results with a linear prior on $\Gamma$ and $\varepsilon$ . . . . .	247
D.8	Results with the neutrino mass free in the ADDM cosmology . . . . .	249
<b>E</b>	<b>Complements on decaying neutrinos</b>	<b>251</b>
E.1	Collision term for decaying neutrinos . . . . .	251
E.2	Collision term for dark radiation daughters . . . . .	252
E.3	Fluid equations for decaying neutrinos . . . . .	253
E.4	Excluding the relativistic decay regime from the MCMC analysis . . . . .	255
<b>F</b>	<b>Résumé détaillé en français</b>	<b>257</b>
F.1	L'ère de la cosmologie de précision . . . . .	257
F.2	Energie noire précoce et la tension $H_0$ . . . . .	258
F.3	Matière noire instable et la tension $S_8$ . . . . .	260
F.4	Nouvelles contraintes sur la masse et la durée de vie des neutrinos . . . . .	261







# I

---

## The era of precision cosmology

---

*“All we ever see of stars are their old photographs.”*

*Dr. Manhattan, Watchmen*

### Contents

---

1.1	Historical introduction . . . . .	<b>3</b>
1.1.1	Evidences of an expanding universe . . . . .	3
1.1.2	From the Big Bang theory to the first hints of dark matter . . . . .	4
1.1.3	The universe is accelerating . . . . .	6
1.2	Timeline of the cosmos . . . . .	<b>7</b>
1.3	The smooth universe . . . . .	<b>9</b>
1.3.1	Geometry of the expanding universe . . . . .	10
1.3.2	Cosmo-dynamics . . . . .	12
1.3.3	Distances in cosmology . . . . .	15
1.4	A few words on inflation . . . . .	<b>20</b>
1.5	In and out of equilibrium . . . . .	<b>22</b>
1.5.1	The Boltzmann formalism . . . . .	23
1.5.2	Relativistic degrees of freedom and entropy conservation . . . . .	26
1.5.3	Neutrino decoupling and evolution . . . . .	28
1.5.4	WIMP freeze-out . . . . .	30
1.5.5	Big-Bang Nucleosynthesis . . . . .	33
1.5.6	Hydrogen recombination . . . . .	36
1.6	The linearly perturbed universe . . . . .	<b>42</b>
1.6.1	The gauge problem . . . . .	45
1.6.2	Perturbation equations . . . . .	49
1.6.3	Initial conditions . . . . .	59
1.6.4	Acoustic oscillations . . . . .	63
1.6.5	The CMB power spectra . . . . .	67
1.6.6	The matter power spectrum . . . . .	79
1.7	Successes and challenges of the $\Lambda$ CDM paradigm . . . . .	<b>87</b>
1.7.1	The nature of the dark sector . . . . .	87
1.7.2	Cosmic discordance . . . . .	91
1.8	Outline . . . . .	<b>96</b>

---

Cosmology is the study of the evolution and the properties of the universe as a whole. This scientific discipline addresses questions which are as old as humanity itself (*i.e.* "has the universe as we know existed forever?" "what's the ultimate fate of the cosmos?"). However, it was not until the beginning of the 20<sup>th</sup> century that it became a predictive science, when the theory of General Relativity (GR) was established as a solid theoretical framework to describe the universe. Since then, the field of cosmology has been constantly evolving, thanks to the rapid increase in the amount and precision of observations. In the last couple of decades, the so-called  $\Lambda$  Cold Dark Matter ( $\Lambda$ CDM) model of cosmology has emerged as a successful paradigm to explain several independent probes with an astonishing degree of accuracy. This model assumes that the universe is well described by a flat Friedman-Lemaître-Robertson-Walker metric, and is primarily composed of around 5% ordinary matter, 26 % cold dark matter, and 69 % dark energy in the form of a cosmological constant  $\Lambda$ . Unfortunately, the nature of its main constituents, dark matter and dark energy, still remains a mystery. In addition, the increase in precision in cosmological data has recently led to the appearance of several experimental discrepancies between probes of the early and late universe. In particular, there is a  $5\sigma$  tension in the determination of the current expansion rate of the universe (the Hubble constant), and a  $2 - 3\sigma$  tension in the determination of the clustering strength in the universe (described through the  $S_8$  parameter). For these reasons, in recent years there has been a growing interest in exploring different extensions of the  $\Lambda$ CDM model, which could shed some light on the very mysterious dark components, and possibly offer an explanation for the aforementioned discrepancies. On the other hand, the discovery of neutrino oscillations provides firm evidence of the existence of tiny but non zero neutrino masses, a phenomenon that cannot be explained within the Standard Model of particle physics. Cosmology is currently the most powerful probe of neutrino masses, and it can offer very valuable clues about its properties.

In this thesis we will investigate in detail the cosmological implications of several extensions of the  $\Lambda$ CDM paradigm. In the first part we will study two models, early dark energy (EDE) and decaying dark matter (DDM), which are directly targeted at explaining the Hubble and  $S_8$  tensions, respectively. In the second part, we will analyze another exotic scenario motivated by the neutrino mass puzzle, decaying neutrinos, whose formalism is very similar to that of the DDM. We will argue how the very precise measurements of the cosmic microwave background (CMB) anisotropies always play a central role in setting new and robust constraints for each of these models. To make this work as much self-contained as possible, in this introductory chapter we outline the most relevant mathematical tools and observables in cosmology. We start with a short historical introduction in [Sect. 1.1](#) and a sketch of the history of the universe in [Sect. 1.2](#). Then we move on to recapitulate the formalism that is required in order to understand cosmological observables such as the CMB anisotropy and matter power spectra. We will start with the description of the smooth background in [Sect. 1.3](#), and say a few words about inflation in [Sect. 1.4](#). Later we proceed to study the departures from equilibrium by introducing the Boltzmann treatment in [Sect. 1.5](#). We continue with a presentation of the theory of linear perturbations in [Sect. 1.6](#). We end with [Sect. 1.7](#), where we discuss the most important challenges to the  $\Lambda$ CDM model: the nature of the dark sector and the cosmological tensions.

## 1.1 Historical introduction

In this section we describe the historical context of the principal milestones that made cosmology be the very rich field that we know today. These milestones are the metric expansion of the cosmos, the cosmic microwave background, and the discoveries of dark matter and dark energy. Here the purpose is just to give a global picture of the recent history of cosmology, for more details we refer the reader to [HELGE \(2013\)](#).

### 1.1.1 Evidences of an expanding universe

In 1915, Albert Einstein publishes his theory of General Relativity (GR), which provides the most precise description of gravity until the present date. In 1917, Einstein studied the cosmological implications of his theory and proposed his own model of the universe ([EINSTEIN 1917](#)), which he described as being static and closed. Einstein noticed that, in order to keep the mean matter density  $\rho_m$  constant in time, he was forced to introduce a new constant in his field equations (today known as the cosmological constant  $\Lambda$ ) and had to adjust it to a very concrete value,  $\Lambda = 4\pi G\rho_m/c^2$ , where  $G$  is Newton's gravitational constant and  $c$  is the speed of light. It is important to note that, at that time, the general consensus in the scientific community was that the universe was static and eternal.

On the other side, some indications about the cosmic expansion had already started to appear. In particular, the American astronomer Vesto Slipher reported in 1915 the first observations of shifts in the spectral lines of 15 galaxies <sup>1</sup> ([SLIPHER 1915](#)). Out of the 15 *nebulae* that Slipher observed, 11 were actually *receding* from us, since they were redshifted to longer wavelengths. This phenomenon is typically quantified through the redshift factor  $z$ , defined as

$$z \equiv \frac{\lambda_{\text{obs}} - \lambda_{\text{emit}}}{\lambda_{\text{emit}}}. \quad (1.1)$$

However, the majority of scientists at the epoch didn't agree on the physical origin of these redshifts. In 1927, the Belgian physicist Georges Lemaître proposed an explanation. Using GR as a main tool, he theorized the idea of an expanding universe, and used this fact to explain the extra-galactic redshifts observed by Slipher ([LEMAÎTRE 1927](#)). In reality, the metric expansion had already been found in 1922 by the Russian mathematician Alexander Friedmann, as one of the possible cosmological solutions of Einstein's field equations ([FRIEDMANN 1922](#)). However, Friedmann regarded this merely as a mathematical curiosity, and didn't try to make a connection with observations, as Lemaître did. It is known that Einstein read Lemaître's article, but refused roundly the idea of an expanding universe, even saying to him "*Your calculations are correct, but your physic is abominable*".

A big discovery was provided in 1929 by the American astronomer Edwin Hubble. At the Mount Wilson Observatory (which at the time had the most powerful telescope in the world), Hubble measured the redshifts (and thus, the recessional velocities  $v \simeq cz$ ), as well as the distances of 24 galaxies ([HUBBLE 1929](#)). By placing the velocities and distances on a diagram, he obtained what is shown in [Fig. 1.1](#). What this plot suggested is that there exists a *linear positive correlation* between those quantities,

<sup>1</sup>The existence of other galaxies beyond the Milky Way had not yet been established in 1914, so they were actually known by the name of *extra-galactic nebulae*.

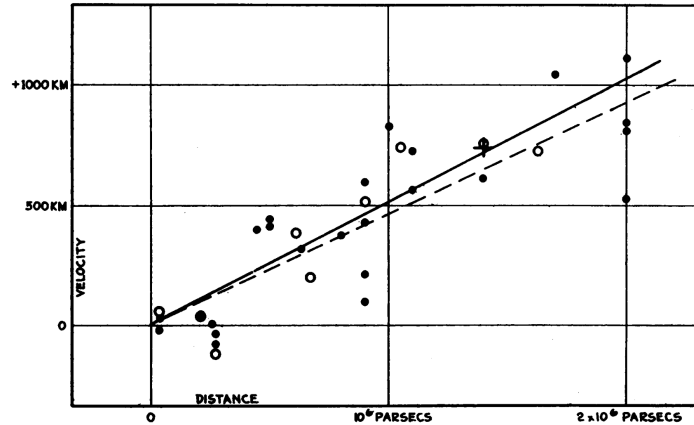


**Figure 1.1** – Velocity-Distance relation for the different *extra-galactic nebulae* observed by Hubble in 1929. The units on the X- and Y- axis are parsecs and km/s, respectively. Taken from HUBBLE (1929)

*i.e.* the further away the galaxies are, the faster they recede from us. This can be mathematically formulated in the following way

$$v = H_0 d, \quad (1.2)$$

where the factor of proportionality  $H_0$  is known as the Hubble's constant. This constant is typically expressed in units of km/s/Mpc, since velocities and distances to distant objects are commonly measured in units of km/s and Megaparsecs, respectively. The first measurements by Hubble yielded a value of around  $H_0 \simeq 500$  km/s/Mpc, which is significantly higher than the values accepted at present ( $H_0 \simeq 65 - 75$  km/s/Mpc, see Sect. 1.7.2), due to errors in the distance calibrations. The work of Hubble provided the first solid evidence of the expanding universe, although it is important to note that Hubble himself never associated his empirical law with the cosmic expansion. In 1930, the British astrophysicist Arthur Eddington reexamined the static universe model proposed by Einstein and proved that it was *unstable*, *i.e.* any tiny perturbation would lead to either an exponential contraction or expansion (EDDINGTON 1930). After that, Einstein definitely abandoned his idea of an static universe and a cosmological constant, which he regarded as "*the biggest blunder of his life.*"

### 1.1.2 From the Big Bang theory to the first hints of dark matter

The following decades after Hubble's big discovery were very fruitful in cosmology. In the 30s, scientists realized that the observed abundances of light elements such as hydrogen or helium could not have a stellar origin. In 1931, Lemaître suggested the existence of a very hot phase at the beginning of the universe, that he called *the primaeval atom*. During the 40s, the Russian physicist George Gamow expanded on the idea of Lemaître, and realized that densities and temperatures in the primordial universe were high enough to allow nucleosynthesis. The first computation of the relic abundances of light elements was carried out in 1948 by Alpher, Bethe and Gamow ALPHER et al. (1948). In the same year, Alpher and Hermann improved upon this calculation to account for the universe's expansion, and showed that at initial times the universe was dominated by radiation, rather than matter. They also predicted the existence of a blackbody radiation as a remnant of this hot early phase,

which today should have a temperature of a few K.

In those days the theory of the expanding universe still had many detractors. This is especially the case for the British astronomer Fred Hoyle, who coined the name *Big Bang* on BBC radio in 1949 to denigrate the model of the evolving universe, which had the serious issue of having a singularity at the origin. Another problem of this model was the *age paradox*. The age of the universe can in general be written as  $t_0 = F/H_0$ , where  $F$  is a dimensionless numerical factor depending on the cosmological model. In 1932, Albert Einstein and Willem de Sitter had proposed a model of an evolving flat universe, full of non-relativistic matter and with no cosmological constant, for which  $F = 2/3$  (EINSTEIN et al. 1932). With the estimations of  $H_0$  made during the 50s, this formula was giving an age of the universe *shorter than the age of the Earth*. The reality is that, even with the most recent estimates of  $H_0$ , this model leads to an age  $t_0 \simeq 9.3$  Gyrs, still shorter than the age of the oldest stars that have been observed (as we will discuss later, this problem is automatically solved when considering dark energy).

In 1965, the American physicists Arno Penzias and Robert Wilson discovered by accident a persistent radio noise coming from all directions, which could not be easily explained with terrestrial or known astronomical sources. It was soon realized that they had just detected the *cosmic microwave background* (CMB), a relic radiation coming from the primordial universe, for which they were awarded the Nobel prize in 1978. This discovery gave strong support to the Big Bang cosmological model. The spectrum of this radiation has been measured thanks to the FIRAS interferometer (onboard the COBE satellite) in 1996, revealing an almost perfect blackbody spectrum, with a mean temperature of  $T_0 = 2.7255 \pm 0.0006$  K and tiny anisotropic deviations at the level of  $10^{-5}$  (the latter measured by the COBE DMR instrument). For this breakthrough, the American physicists George F. Smoot and John C. Mather were awarded the Nobel prize in 2006. The anisotropies in the CMB radiation carry a wealth of information about the early universe, since they constitute the primordial seeds for the formation of galaxies. After COBE, these anisotropies have been subsequently measured with increasing angular resolution by the WMAP satellite in 2003 (SPERGEL et al. 2003) and the *Planck* satellite in 2013 (ADE et al. 2014).

As the 20<sup>th</sup> century advanced, many observations started to suggest that around 85 % of the total matter in the universe was in the form of a mysterious component called *dark matter*, whose effects have only been probed through gravity. The first convincing hint of dark matter came in 1933 by the Swiss physicist Fritz Zwicky. He observed a mismatch between the velocity dispersion measured in the Coma Cluster, and the one that was theoretically predicted from the luminous matter using the virial theorem (ZWICKY 1933). This led him to suggest the existence of large amounts of invisible matter in the Coma Cluster, that he called *dunkle Materie* (dark matter). However, Zwicky's proposal was not taken seriously by the scientific community until 1970, year in which the American astronomers Vera Rubin and Kent Ford carried out a pioneering work on galactic rotation curves (RUBIN et al. 1970). They observed that the velocities in spiral galaxies at large distances were significantly larger than the ones predicted from Newtonian gravity, considering only the luminous components (*i.e.* the stars and the neutral hydrogen gas). It was later understood that this excess velocity could be due to the presence of large spherical halos of dark matter, in which galaxies were immersed. Over the following years, many other probes have es-





**Figure 1.2** – Image of the galaxy cluster Abell 1689, taken with the Hubble Space Telescope. The galaxies and dark matter in the cluster act as a lens that warps the light of the background galaxies, leading to a plethora of arcs around the lens, as predicted by GR. This allows to reconstruct the mass distribution of dark matter, which is represented in purple. Taken from <https://esahubble.org/images/heic1014a/>

tablished the presence of dark matter on both galactic and cosmological scales, such as gravitational lensing (see Fig. 1.2), the CMB anisotropy spectra, or the distribution of large scale structure (for a review of the history of dark matter, see BERTONE et al. 2018). All these observations tell us that dark matter should be mostly cold (*i.e.* non-relativistic), collisionless, stable, and posses no (or very weak) non-gravitational interactions with the Standard Model (SM) particles <sup>2</sup>. However, its precise nature remains unknown until today.

### 1.1.3 The universe is accelerating

The last milestone in cosmology was set in 1998. That year, two independent groups (the Supernova Cosmology Project led by Saul Perlmutter, and the Supernova Search Team led by Adam Riess and Brian Schmidt) carried out the measurements of redshifts and distances to supernovae of type Ia (SNIa) (RIESS et al. 1998; PERLMUTTER et al. 1999). These objects have several advantages: they are believed to be good *standard candles* for measuring distances in the universe, their brightness is very intense and they are ubiquitous in the cosmos. This allowed the two teams to extend the Hubble diagram to much larger distances, where the distance-redshift relation becomes dependent on the cosmological model. Their analysis showed that the current cosmic expansion was *accelerating*, and that SNIa data favored a universe where vacuum energy (parameterized through the cosmological constant  $\Lambda$ ) dominated over matter <sup>3</sup> (see Fig. 1.3). This was reflected in the fact that SNIa appeared to be dimmer (due to the longer light-travel time) than what would have

<sup>2</sup>Current observations also allow to test small deviations from these hypotheses. Just to give an example, in Chapter 3 we put bounds on the lifetime of dark matter for a decay scenario happening entirely in the dark sector.

<sup>3</sup>It might appear contradictory that the cosmological constant that Einstein introduced to get a static universe has now been used to account for an accelerated expansion. However, one should bear in mind that Einstein had assumed a closed universe, and in addition he had cherry-picked the value of  $\Lambda$  to counteract the dynamics encoded in his theory.

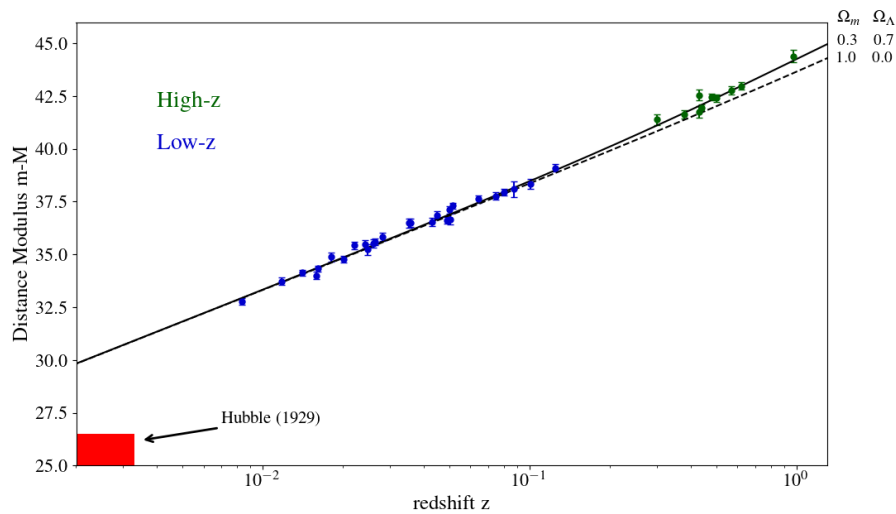


**Figure 1.3** – Hubble diagram for SNIa, showing the distance modulus (defined in Eq. (1.36)) vs. redshift. Data points are taken from Tabs. 5 and 10 in [RIESS et al. \(1998\)](#). The SNIa data at high- $z$  clearly select a universe dominated by a cosmological constant,  $\Omega_\Lambda > \Omega_m$ . The small red region in the lower left marks the maximum span of Hubble’s original diagram from 1929.

been expected in a decelerating universe full of matter. For this revolutionary finding, later corroborated by CMB and LSS data, Perlmutter, Riess and Schmidt received the Nobel prize in 2011.

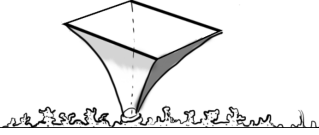
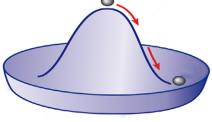
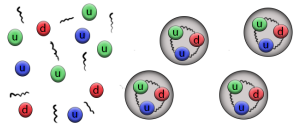
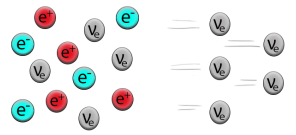
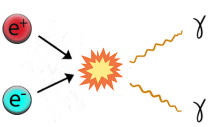
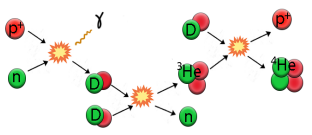
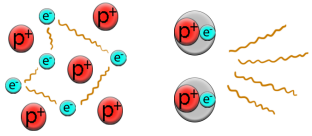
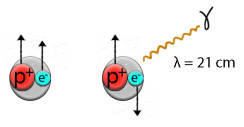
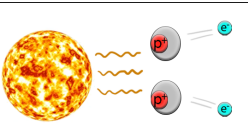
The cosmic acceleration can more generally be interpreted as a result of a dynamical substance with a negative pressure which dominates the energy content of the universe. Any component with these characteristics is typically referred to as *dark energy*. Another advantage of dark energy is that it allowed to solve the age paradox ([KRAUSS et al. 2003](#)). For an universe composed by around 31 % matter and 69 % dark energy in the form of a cosmological constant (as is now suggested by many different observations apart from SNIa), the age of the universe is predicted to be  $t_0 \simeq 13.8$  Gyrs (see end of [Sect. 1.3.2](#) for a derivation), which is consistent with the ages of all astronomical objects detected so far.

## 1.2 Timeline of the cosmos

Thanks to all the progress that was achieved in cosmology during the 20<sup>th</sup> century and in the recent decades, we have nowadays a clear picture of all the key events in the history of the universe, ranging from the complex interactions in the primordial soup to the formation of large scale structures at later times. In this section we give a brief summary of the key events in the history of the universe, with the aim of framing the relevant epochs for all the models and observables considered in this work. These events are listed in [Tab. \(1.1\)](#).

If the cosmic expansion is extrapolated back in time, one quickly realizes that at earlier times the universe must have been denser and also hotter. At some critical point, all the physical quantities (such as densities or temperatures) become infinite, signaling a breakdown of our theory. This is the so-called Big Bang (BB) singularity,



Event	Pictorial description	t	z	$T_{\text{CMB}}$
Inflation		?	?	?
EW transition		20 ps	$10^{15}$	100 GeV
QCD transition		$20 \mu\text{s}$	$10^{12}$	150 MeV
Neutrino decoupling		1 s	$6 \times 10^9$	1 MeV
electron-positron annihilation		6 s	$2 \times 10^9$	500 keV
Nucleosynthesis		3 min	$4 \times 10^8$	100 keV
Recombination		380 kyr	1100	0.27 eV
Dark ages		380 kyr – 400 Myr	30 – 1100	7 meV – 0.27 eV
Reionization		400 Myr – 1 Gyr	6 – 30	1.7 meV – 7 meV

**Table 1.1** – List of key events in the history of the universe.

which is conventionally defined as the origin of cosmic time. We remark that this is a fictitious instant, which in principle cannot be described without a complete theory of quantum gravity.

It is now commonly accepted that, at very early times, there was a phase of rapid accelerated expansion named *inflation*, which could have been sourced by a scalar field called the inflaton. After inflation ended, there was a period of *reheating*, during which the inflaton decayed into all the known SM elementary particles. This led

to the formation of a hot dense plasma where all particles were kept in thermal equilibrium due to the constant interactions between them. The densities of all these particles inherited the inhomogeneities that were created during inflation, when the quantum fluctuations in the inflaton were stretched to cosmic distances. Roughly 20 ps after the BB, when the temperature of the plasma decreased below the scale of electroweak (EW) symmetry breaking,  $T \lesssim 100$  GeV, the Higgs got trapped at the bottom of its potential, making all SM particles to acquire a mass. Later, when the temperature decreased below 150 MeV (approximately 20  $\mu$ s after the BB), the strong force between free quarks and gluons became significant, so that they could assemble to form the first hadrons. Only 1 s after the BB, the weak interactions between the neutrinos and the rest of particles became inefficient, and they decoupled from the thermal bath. Afterwards, at 6 s, electrons and positrons annihilated through the process  $e^+ + e^- \rightarrow \gamma + \gamma$ , leaving just a residual amount of non-relativistic electrons<sup>4</sup>. Then, a few minutes after the BB, the first nuclei of light elements, such as helium or lithium, were formed during a period called *Big Bang Nucleosynthesis* (BBN). Eventually, the energy density of non-relativistic matter started to dominate over the radiation one, point at which the inhomogeneities in the DM started to grow at a significant rate. When the universe was 380 kyr old, the bath temperature had decreased enough to allow the formation of the first hydrogen atoms at the *recombination* era, according to the process  $e^- + p^+ \rightarrow H + \gamma$ . This led to a sharp reduction in the free electron fraction, and the decoupling of photons from matter. The universe became transparent and photons started free-streaming through the universe. These photons constitute the CMB radiation that we observe today.

After recombination, the *dark ages* started, a period during which the only light in the universe came from the CMB photons and the 21 cm signal of neutral hydrogen. The first DM halos are believed to have formed during this era, due to the gravitational collapse of the large DM density fluctuations. The dark ages extended over a few hundred million years, until the first stars and galaxies were born and started emitting radiation that gradually reionized the hydrogen atoms in the intergalactic medium (IGM). The details of this *epoch of reionization* (EoR) are very poorly understood, but thanks to the measurements of Lyman- $\alpha$  absorption lines in quasar spectra, today we know the universe was nearly totally reionized around  $z \simeq 6$  (*i.e.*  $\simeq 1$  Gyr after the BB). Approximately 5 Gyr ago, dark energy began to dominate the energy budget of the universe, producing an accelerated expansion and impeding the formation of large scale structures to develop further.

### 1.3 The smooth universe

In this section we recapitulate the main tools required to describe the homogeneous and isotropic universe, starting with a discussion of the Friedmann equations and then moving to give several definitions of distances in cosmology. We use the  $(-+++)$  metric convention, and work in units where  $c = k_B = 1$ . As usual, latin indices indicate spatial components, *e.g.*  $i = 1, 2, 3$ , while greek indices are reserved for spacetime components, *e.g.*  $\mu = 0, 1, 2, 3$ . Einstein summation convention is assumed for greek indices. For this section and two subsequent ones we mainly follow

---

<sup>4</sup>This residual amount of electrons corresponds to an initial excess of matter over anti-matter, whose origin is still not understood. Models of baryogenesis try to predict the matter-antimatter asymmetry, and rely on physics beyond the SM.

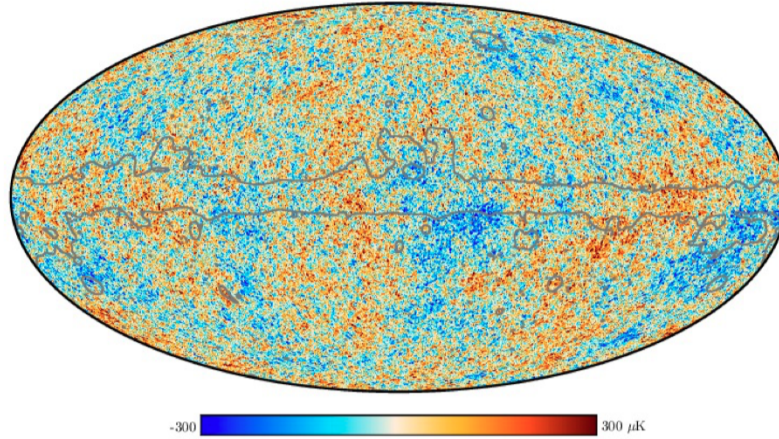


**Figure 1.4** – The CMB map of the temperature anisotropies, as seen by [AGHANIM et al. 2020b](#) – hereafter referred to as [Planck18](#). Colors label variations at the level of  $10^{-5}$  around a mean temperature of  $T_0 = 2.725 K$

[DODELSON \(2003\)](#), [BURGESS \(2016\)](#), [LESGOURGUES et al. \(2018\)](#), and [BAUMANN \(2021\)](#). For producing some of the plots shown in these sections, we use the public Boltzmann solver **CLASS** <sup>5</sup> ([BLAS et al. 2011](#)) .

### 1.3.1 Geometry of the expanding universe

Modern cosmology is built upon the idea that the universe is homogeneous and isotropic on sufficiently large scales (bigger than 100 Mpc). This simple but transcendental assumption is what we normally call *the cosmological principle*. There is plenty of observational data that confirm this hypothesis, such as the temperature map of the CMB (that we show in [Fig. 1.4](#)), exhibiting anisotropies only at the level of  $10^{-5}$ .

Homogeneity and isotropy, meaning ‘no preferred point in space’ and ‘no preferred direction’, impose a unique spacetime geometry of the universe. This geometry is described by the so-called *Friedmann-Lemaître-Robertson-Walker* (FLRW) metric  $g_{\mu\nu}$ , that we can read from the line element:

$$ds^2 = g_{\mu\nu} dx^\mu dx^\nu = -dt^2 + a(t)^2 \left( \frac{dr^2}{1 - kr^2} + r^2 (d\theta^2 + \sin^2(\theta)d\varphi^2) \right). \quad (1.3)$$

In the previous expression, we have introduced the cosmic time  $t$ , which is the time measured by observers who move with the cosmic expansion, and the comoving coordinates  $r$ ,  $\theta$  and  $\phi$ , which label the points in constant-time slices. The metric contains a single function of time, the *scale factor*  $a(t)$ , and a constant, the curvature parameter  $k$ . The scale factor relates physical distances  $d_{\text{phys}}$  with comoving distances  $d_{\text{com}}$  (that is, distances that do not change with the cosmic expansion),  $d_{\text{phys}} = a(t)d_{\text{com}}$ . The parameter  $k$  determines the three possibilities for the constant curvature of spatial slices:  $k = 0$  (euclidean),  $k = +1$  (spherical) and  $k = -1$  (hyperbolic).

We note that in [Eq. \(1.3\)](#) the scale factor  $a(t)$  has the dimension of a length, while  $r$  is dimensionless. Sometimes it is more convenient to make the scale factor dimen-

<sup>5</sup><http://class-code.net/>.

sionless and set it to unity today,  $a_0 \equiv a(t_0) = 1$ . This can be achieved by making use of the following rescaling symmetry:

$$a \rightarrow a/a_0, \quad r \rightarrow ra_0, \quad k \rightarrow k/a_0^2. \quad (1.4)$$

In this case,  $r$  now carries dimensions of length, and the curvature  $k$  is not normalized in general,  $|k| \neq 1$ . For convenience, we will often switch from cosmic time to conformal time  $\tau$ , defined by the relation  $d\tau = dt/a(t)$  <sup>6</sup>.

One of the ways to infer the cosmic expansion is by using the light we receive from distant objects. However, one must take into account that photons loose energy (or, equivalently, their wavelengths are stretched) due to the expansion. In order to understand this, we need to discuss first about the motion of particles. In a given spacetime, when no other forces apart from gravity are present, particles move along *geodesics*, which correspond to the shortest paths  $x^\mu(\sigma)$  in a curved geometry (here  $\sigma$  is an affine parameter that increases monotonically along the path of the particle). They satisfy the geodesic equation, which can be written in terms of their 4-momentum vector  $P^\mu \equiv \frac{dx^\mu}{d\sigma} = (P^0, P^i)$  as <sup>7</sup>

$$\frac{dP^\mu}{d\sigma} + \Gamma^\mu_{\alpha\beta} P^\alpha P^\beta = 0, \quad (1.5)$$

where  $\Gamma^\mu_{\alpha\beta}$  are the *Christoffel symbols*:

$$\Gamma^\mu_{\alpha\beta} = \frac{1}{2} g^{\mu\lambda} (\partial_\alpha g_{\beta\lambda} + \partial_\beta g_{\alpha\lambda} - \partial_\lambda g_{\alpha\beta}). \quad (1.6)$$

The only non-zero components of the FLRW metric in a spatially flat universe  $k = 0$  are:

$$\Gamma^j_{0i} = \frac{\dot{a}}{a} \delta^j_i, \quad \Gamma^0_{ij} = -\frac{\dot{a}}{a} g_{ij}. \quad (1.7)$$

Using the  $\mu = 0$  component of the geodesic equation in the FLRW geometry, one can show an important result: the amplitude  $p$  of the physical three-momentum, defined by  $p \equiv \sqrt{\sum_{ij} g_{ij} P^i P^j}$ , is inversely proportional to the scale factor

$$p \propto \frac{1}{a}, \quad (1.8)$$

where  $p = E$  and  $p = \sqrt{E^2 - m^2}$  for massless and massive particles, respectively. Since the wavelength of photons is inversely proportional to their momentum  $\lambda = h/p$ , then according to Eq. (1.8) the wavelength scales as  $a(t)$ . Photons emitted at time  $t$  with wavelength  $\lambda$  will arrive at  $t_0 > t$  with wavelength  $\lambda_0 = \frac{a_0}{a(t)} \lambda$ . This confirms that the wavelength of light is increased,  $\lambda_0 > \lambda$ , due to the expansion of spacetime,  $a_0 > a(t)$ . In terms of the redshift parameter introduced in Eq. (1.1), this fact implies the following relation

$$1 + z = \frac{a_0}{a(t)}. \quad (1.9)$$

<sup>6</sup>We will use a dot  $\dot{\phantom{x}}$  for derivatives with respect to cosmic time  $t$ , and a prime  $\prime$  for derivatives with respect to conformal time  $\tau$ .

<sup>7</sup>This definition is consistent with the 4-momentum that is typically introduced for particles with non-zero mass  $m$ ,  $P^\mu \equiv m \frac{dx^\mu}{d\sigma'}$ , since one can always make a parameter redefinition  $\sigma = \sigma'/m$ .

### 1.3.2 Cosmo-dynamics

All the discussion until now was purely kinematic, but in order to get the dynamical evolution of  $a(t)$ , we need to resort to Einstein field equations of GR. At the heart of this theory lie the *field equations*, which indicate how the matter and energy content (encoded in the stress-energy tensor  $T_{\mu\nu}$ ) curve space-time (encoded in the Einstein tensor  $G_{\mu\nu}$ )

$$G_{\mu\nu} \equiv R_{\mu\nu} - \frac{1}{2}g_{\mu\nu}R = 8\pi GT_{\mu\nu} - \Lambda g_{\mu\nu}. \quad (1.10)$$

Here  $G$  is Newton constant and  $\Lambda$  is the cosmological constant originally introduced by Einstein in 1917 (see Sect. 1.1). The quantities  $R_{\mu\nu}$  and  $R$  denote respectively the Ricci tensor and Ricci scalar, and they are constructed from the first and second derivatives of the metric

$$R_{\mu\nu} = \frac{\partial\Gamma^\sigma{}_{\mu\nu}}{\partial x^\sigma} - \frac{\partial\Gamma^\sigma{}_{\mu\sigma}}{\partial x^\nu} + \Gamma^\sigma{}_{\rho\sigma}\Gamma^\rho{}_{\mu\nu} - \Gamma^\sigma{}_{\rho\nu}\Gamma^\rho{}_{\mu\sigma}, \quad R = R_{\mu\nu}g^{\mu\nu}. \quad (1.11)$$

The symmetries of the FLRW metric enforce  $T^\mu{}_\nu$  to take the form of the stress-energy tensor corresponding to a *perfect fluid*

$$T^\mu{}_\nu = (\rho + P)U^\mu U_\nu + P\delta^\mu_\nu, \quad (1.12)$$

where  $U^\mu$  is the four-velocity of the fluid, which takes the simple form  $U^\mu = \delta_0^\mu$  if the fluid is at rest in the comoving frame. The fluid can be completely characterised by two functions, the mean density  $\rho$  and mean pressure  $P$ , which are the sum over the density and pressure of each single fluid species  $\rho = \sum_I \rho_I$  and  $P = \sum_I P_I$ . Any extra degrees of freedom, such as energy fluxes, momentum densities or anisotropic stresses, should be discarded as they would break the hypothesis of isotropy and homogeneity. Interestingly, the cosmological constant (typically assumed to be positive) can be absorbed as a contribution to the stress-energy tensor,  $T_{\mu\nu}^\Lambda = -\rho_\Lambda g_{\mu\nu}$ , with  $\rho_\Lambda \equiv \Lambda/8\pi G$ . By comparing with Eq. (1.12), we see that this corresponds to a fluid with constant density and a negative pressure given by  $P_\Lambda = -\rho_\Lambda$ .

Because of the Bianchi identities,  $\nabla_\mu G^{\mu\nu} = 0$ , the stress-energy tensor is conserved under the covariant derivative

$$\nabla_\mu T^{\mu\nu} \equiv \frac{\partial T^{\mu\nu}}{\partial x^\mu} + \Gamma^\nu{}_{\mu\rho}T^{\rho\mu} + \Gamma^\mu{}_{\mu\rho}T^{\rho\nu} = 0. \quad (1.13)$$

The previous equation is valid for the sum of all species present in the cosmic fluid, and also for each species separately *if those are non-interacting*. In the FLRW spacetime, the 0 component of Eq. (1.13) leads to the following continuity equation

$$\dot{\rho} + 3H(\rho + P) = 0, \quad (1.14)$$

where  $H \equiv \frac{\dot{a}}{a}$  is the so-called *Hubble parameter* (in a similar fashion, the conformal Hubble parameter is defined as  $\mathcal{H} \equiv \frac{a'}{a} = aH$ ). The term with  $H$  accounts for the expansion of the universe, and adds friction to the conservation equations. Because of the cosmological principle, only two Einstein equations are independent (00 and  $ij$  trace components), and they lead to the *Friedmann equations* for the evolution of the scale factor

$$H^2 = \frac{8\pi G}{3}\rho - \frac{k}{a^2}, \quad (1.15)$$

$$\frac{\ddot{a}}{a} = -\frac{4\pi G}{3}(\rho + 3P). \quad (1.16)$$

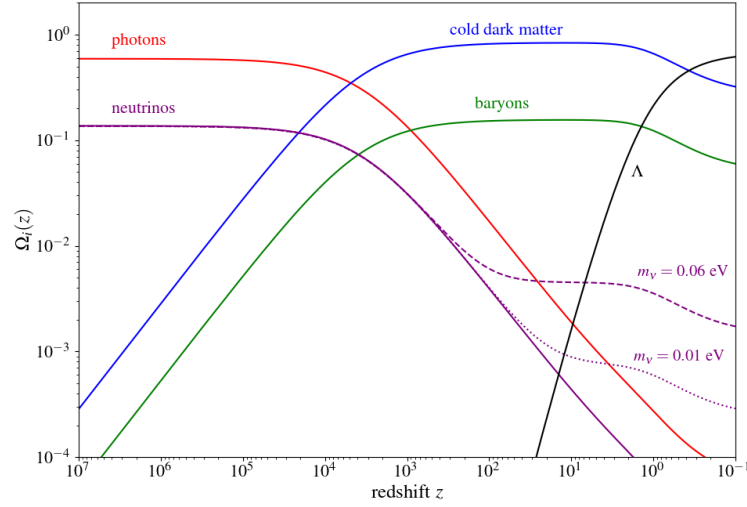


**Figure 1.5** – Evolution of the fractional energy densities of photons, baryons, three neutrino species (one massless and two massive, 0.06 and 0.01 eV) and a cosmological constant  $\Lambda$ .

By combining the time derivative of Eq. (1.15) with Eq. (1.16), one can arrive again at Eq. (1.14). This shows that the continuity equation is not adding any new information with respect to the Friedmann eqs., which is to be expected since the stress-energy conservation is a direct consequence of the Bianchi identities. However, Eq. (1.14) is useful to directly solve for the mean densities, once an equation of state is specified. In many cases of interest, fluids can be simply described with a parameter that relate pressure and density in a linear way,  $w_i = P_i/\rho_i$ . In the case of a constant  $w_i$ , the solution of Eq. (1.14) for each non-interacting fluid species reads

$$\rho_i(a) = \rho_i(a_0) \left( \frac{a}{a_0} \right)^{-3(1+w_i)}. \quad (1.17)$$

It is useful to classify the different species that populate the universe according to their Equation of State (EoS) parameter  $w_i$  :

- **Non-relativistic matter or dust.** This refers to any component for which the pressure is much smaller than the density,  $w_m \simeq 0$ . Baryons<sup>8</sup> and cold dark matter fall into this category. As we will show in Sect. 1.5, for a non-relativistic fluid the EoS is indeed of order  $w_m \sim \langle p^2 \rangle / m^2 \ll 1$ , where  $\langle p^2 \rangle$  denotes an average momentum squared. In this case, Eq. (1.17) gives  $\rho_m \propto a^{-3}$ . This dilution of energy density is simply reflecting the fact that the number of particles is conserved in a growing volume  $V \propto a^3$ .
- **Relativistic matter or radiation.** This corresponds to any substance for which pressure makes a significant contribution, of about one third of the density,  $w_r \simeq 1/3$ . This is the case of CMB photons or massless neutrinos. According to Eq. (1.17), this yields  $\rho_r \propto a^{-4}$ , because the dilution is now including the effect of an increasing wavelength  $E \propto \lambda^{-1} \propto a^{-1}$ .

<sup>8</sup>After hydrogen recombination, the only non-relativistic SM particles with a non-negligible cosmic abundance are neutral hydrogen, neutral helium, and some residual amount of free electrons and protons. They form a single fluid, whose energy density is dominated by the baryons. For this reason, cosmologists often refer to the electron-baryon fluid simply as baryons.



- **Dark energy.** This alludes to some kind of exotic substance responsible for the recent accelerated expansion of the universe. From Eq. (1.16), we see that any dominating species satisfying  $w < -1/3$  can lead to cosmic acceleration,  $\ddot{a} > 0$ . The cosmological constant is the simplest model, corresponding to  $w_\Lambda = -1$ .
- **Massive neutrinos.** As we will discuss in more detail in Sect. 1.5.3, massive neutrinos have a more complicated evolution, that cannot be captured by a constant EoS. In particular, they transition from being relativistic to non-relativistic, meaning that their EoS evolves from  $w_\nu = 1/3$  in the early universe to  $w_\nu = 0$  at late times. The transition time is fixed by the value of their mass. However, once the detailed evolution of  $w_\nu(a)$  is known, it is always possible to split their energy density into a relativistic contribution,  $\rho_{\nu,r} = 3w_\nu\rho_\nu$ , and a non-relativistic one,  $\rho_{\nu,m} = (1 - 3w_\nu)\rho_\nu$ .

Considering that we know the scalings in  $a$  of each of the components in the total energy density  $\rho = \rho_m + \rho_r + \rho_\Lambda$ , we can express Eq. (1.15) in the more convenient form

$$H^2(z) = H_0^2 E^2(z) = H_0^2 \left[ \Omega_m (1+z)^3 + \Omega_r (1+z)^4 + \Omega_k (1+z)^2 + \Omega_\Lambda \right]. \quad (1.18)$$

We have defined for each fluid component  $i$  the dimensionless density parameters

$$\Omega_i \equiv \frac{\rho_{i,0}}{\rho_c}, \quad (1.19)$$

where  $\rho_c$  is the so called *critical density* today  $\rho_c \equiv 3H_0^2/8\pi G$ . It is sometimes more convenient to express the physical energy densities as  $\omega_i \equiv \Omega_i h^2$ , where  $h$  denotes the Hubble constant in units of 100 km/s/Mpc. The curvature density parameter has a different definition,  $\Omega_k \equiv -k/(a_0 H_0)^2$ , and it describes a flat ( $\Omega_k = 0$ ), spherical ( $\Omega_k < 0$ ) or hyperbolic ( $\Omega_k > 0$ ) geometry depending on whether the total energy density today  $\rho(a_0)$  is respectively equal, larger or smaller than the critical density  $\rho_c$ . In Fig. 1.5 we show the time-dependent fractional densities  $\Omega_i(z) = 8\pi G\rho_i(z)/3H^2(z)$  for various species in the cosmic inventory. According to the best-fit  $\Lambda$ CDM cosmology from Planck18

$$\Omega_r \simeq 9.1 \times 10^{-5}, \quad \Omega_b \simeq 0.05, \quad \Omega_{\text{cdm}} \simeq 0.26, \quad \Omega_\Lambda \simeq 0.69, \quad |\Omega_k| < 0.003. \quad (1.20)$$

In Sect. 1.6.5 we will describe in detail how these parameters are determined from the CMB temperature anisotropy spectra. Given these values of  $\Omega_i$ , one could now integrate directly Eq. (1.18) to obtain the evolution of the scale factor  $a(t)$ . However, the very different scalings of matter ( $a^{-3}$ ), radiation ( $a^{-4}$ ) and dark energy ( $a^0$ ) mean that for most of its history, the universe has been dominated by a single component (first radiation, then matter, then dark energy). We can thus consider only one single component  $i$  in Eq. (1.18) and integrate to get  $a(t)$  in each era. Restricting to a spatially flat universe, we can write down the solutions for the scale factor and the Hubble parameter in each era, expressed in terms of both cosmic and conformal time.

- *Radiation era:*

$$a \propto t^{1/2} \propto \tau, \quad H = \frac{1}{2t}, \quad \mathcal{H} = \frac{1}{\tau}. \quad (1.21)$$

- *Matter era:*

$$a \propto t^{2/3} \propto \tau^2, \quad H = \frac{2}{3t}, \quad \mathcal{H} = \frac{2}{\tau}. \quad (1.22)$$

- $\Lambda$  era:

$$a \propto e^{Ht} \propto (C - \tau)^{-1}, \quad H = \text{const.}, \quad \mathcal{H} \propto \frac{1}{C - \tau}, \quad (1.23)$$

where  $C$  is an integration constant determined by the initial conditions of the  $\Lambda$  era. These solutions assume that in each era we are far from the transition times, which are given by

$$\text{RM equality :} \quad \rho_r(a_{\text{eq}}) = \rho_m(a_{\text{eq}}) \implies a_{\text{eq}} = \frac{\Omega_r}{\Omega_m} \implies z_{\text{eq}} \simeq 3400, \quad (1.24)$$

$$\text{MA equality :} \quad \rho_m(a_\Lambda) = \rho_\Lambda(a_\Lambda) \implies a_\Lambda = \left(\frac{\Omega_m}{\Omega_\Lambda}\right)^{1/3} \implies z_\Lambda \simeq 0.3. \quad (1.25)$$

where we used the values from Eq. (1.20)<sup>9</sup>. Close to the transition redshifts given in Eq. (1.24) and Eq. (1.25), one should take into account the effects of the two components. For a universe full of matter and radiation, one can get an analytical expression for  $a$  in terms of conformal time  $\tau$ , but not in terms of cosmic time  $t$ . Nevertheless, it is possible to get the inverse relation  $t(a)$ :

$$t(a) = \frac{4a_{\text{eq}}^2}{3H_0\sqrt{\Omega_r}} \left[ 1 - \left(1 - \frac{a}{2a_{\text{eq}}}\right) \left(1 + \frac{a}{a_{\text{eq}}}\right)^{1/2} \right]. \quad (1.26)$$

For  $a \ll a_{\text{eq}}$  ( $a \gg a_{\text{eq}}$ ), one recovers the solutions for the radiation (matter) eras given in Eq. (1.21) and Eq. (1.22). In the case of matter and  $\Lambda$ , one can derive an analytical expression for  $a(t)$ :

$$a(t) = \left(\frac{\Omega_m}{\Omega_\Lambda}\right)^{1/3} \sinh^{2/3} \left(\frac{3}{2}\sqrt{\Omega_\Lambda}H_0t\right). \quad (1.27)$$

For  $H_0t \ll 1$  ( $H_0t \gg 1$ ) we arrive at the solutions for matter ( $\Lambda$ ) eras shown in Eq. (1.22) and Eq. (1.23).

Let us end this section by giving the expression of a very relevant quantity in cosmology, the age of the universe  $t_0$ . This can be obtained thanks to the useful relation  $dt = da/\dot{a} = da/(aH(a)) = -dz/((1+z)H(z))$ . Therefore, we get

$$t_0 = \int_0^\infty \frac{dz}{(1+z)H(z)} \simeq \frac{2}{3H_0\sqrt{\Omega_\Lambda}} \ln \left( \frac{1 + \sqrt{\Omega_\Lambda}}{\sqrt{\Omega_m}} \right), \quad (1.28)$$

where in the last step we assumed a universe full of dust and  $\Lambda$  (the contribution from radiation is negligible since this was dominating during only a tiny fraction of the total age). Using  $\Omega_\Lambda \simeq 0.69$ ,  $\Omega_m \simeq 0.31$ ,  $H_0 \simeq 67.6$  km/s/Mpc, and bearing in mind the conversion  $1\text{km/s/Mpc} = 1.02 \times 10^{-3}$  Gyr<sup>-1</sup>, we get  $t_0 \simeq 13.8$  Gyr, which is the value we quoted at the end of Sect. 1.1.

### 1.3.3 Distances in cosmology

As a consequence of the cosmological expansion, the notion of distance is not uniquely defined for very distant objects, and different operational procedures will yield in general different results. In this section we will introduce the concepts of

<sup>9</sup>The acceleration of the universe actually started a bit before dark energy domination. Indeed, from Eq. (1.16) we see that  $\ddot{a} = 0$  implies  $z_{\text{acc}} = (2\Omega_\Lambda/\Omega_m)^{1/3} - 1 \simeq 0.6$ .



particle horizon, Hubble radius, luminosity distance and angular diameter distance.

### Horizons

Let us start by rewriting the FLRW metric of Eq. (1.3) in terms of conformal time and a new radial coordinate  $d\chi = dr/\sqrt{1-kr^2}$ , such that

$$ds^2 = a(\tau)^2 \left( -d\tau^2 + d\chi^2 + r_m^2(\chi) \left( d\theta^2 + \sin^2(\theta)d\varphi^2 \right) \right), \quad (1.29)$$

with the function  $r_m(\chi)$  given by

$$r_m(\chi) = \begin{cases} \sinh(\chi) & k = -1, \\ \chi & k = 0, \\ \sin(\chi) & k = +1. \end{cases} \quad (1.30)$$

Now, photons travel along null geodesics ( $ds^2 = 0$ ) and, because of the isotropy of the FLRW metric, one can always assume that they follow a radial path ( $d\theta^2 = d\varphi^2 = 0$ ). Then, according to Eq. (1.29), the comoving distance  $\chi$  travelled by a photon emitted at a given time  $t_{\text{em}}$  and observed at a time  $t_{\text{obs}}$  is given by

$$\chi = \tau_{\text{obs}} - \tau_{\text{em}} = \int_{t_{\text{em}}}^{t_{\text{obs}}} \frac{dt}{a(t)} = \frac{1}{a_0} \int_{z_{\text{obs}}}^{z_{\text{em}}} \frac{dz'}{H(z')}. \quad (1.31)$$

For a photon emitted at a very early time  $t_i$  (i.e.  $z_{\text{em}} \rightarrow \infty$ ) and observed at a later time  $t$  (i.e.  $z_{\text{obs}} = z$ ), the previous expression describes what is known as *particle horizon*  $\chi_p(z)$ . This corresponds to the maximum comoving distance from which an observer can receive information at a certain time  $t$ , and it is equal to the elapsed conformal time between  $t_i$  and  $t$  (in units of  $c = 1$ ). In other words, two observers separated by a distance  $\lambda > \chi_p(t)$  could have never been in causal contact. If a light signal is received today on Earth ( $z_{\text{obs}} = 0$ ), then the distance given by  $a_0\chi_p(a_0)$  can be interpreted as the radius of the observable universe (although we will see that in practice the oldest light we have been able to observe comes from the *surface of last scattering*, located at  $z_{\text{em}} \simeq 1100$ ). For the parameter values given in Eq. (1.20), the radius of the observable universe is approximately equal to  $a_0\chi_p(a_0) \simeq 1.41 \times 10^4$  Mpc  $\simeq 45$  Glyr, which is about three times larger than the naive  $\sim 13.8$  Glyr that one would estimate by neglecting the cosmic expansion.

A related quantity is the so called *Hubble radius*,

$$R_H \equiv \frac{1}{aH} = \frac{d\chi_p}{d\ln a}, \quad (1.32)$$

which corresponds to the comoving distance that light can travel in the course of a Hubble time,  $t_H = H^{-1}$ . That is, two observers separated by a distance  $\lambda > R_H(t)$  can't be in causal contact at a given time  $t$ . For a dominant fluid component satisfying  $1 + 3w > 0$  (such as radiation or dust), the particle horizon and the Hubble radius are of the same order, and grow with time,  $\chi_p(t) \sim R_H(t) \sim a(t)^{\frac{1}{2}(1+3w)}$ . This is the reason why one typically refers to both the particle horizon and the Hubble radius simply as the horizon. However, for a dominant component satisfying  $1 + 3w < 0$ ,  $\chi_p(t) \gg R_H(t)$ , and the Hubble radius actually decreases with time, a case which is very relevant for inflation (see Sect. 1.4) as well as dark energy.

### Luminosity distance

Even if the concepts of Hubble radius and particle horizon are extremely important in cosmology (as we shall see later), these distances are not directly observable. One way to make a link with observations is to consider a pointlike source, of which we know the absolute luminosity  $L$  (units of emitted energy per second), *i.e.* a *standard candle*. Then, the observed flux  $\mathcal{F}$  (units of emitted energy per second per receiving area) can be used to infer the *luminosity distance* of the source. In a static Euclidean space, the flux is given by

$$\mathcal{F} = \frac{L}{4\pi r^2}, \quad (1.33)$$

where  $r$  represents the distance between the source and the observer. In an expanding universe, the previous formula needs to be modified in three different ways:

1. Emitted photons are spread over a sphere of area  $4\pi(a_0 r_m(\chi))^2$ , where  $r_m(\chi)$  is given by Eq. (1.30) and  $\chi$  denotes now the comoving distance between the source (that emitted light at  $z_{\text{em}} = z$ ) and us ( $z_{\text{obs}} = 0$ ).
2. The rate of arrival of photons is lower than the one at the moment of emission by a factor  $(1/\Delta t_{\text{obs}})/(1/\Delta t_{\text{em}}) = a/a_0 = (1+z)^{-1}$ .
3. The energy of photons has decreased by the same factor  $\Delta E(t_{\text{em}})/\Delta E(t_{\text{obs}}) = (1+z)^{-1}$  since the time of emission.

Taking these aspects into account, the observed flux can be written as

$$\mathcal{F} = \frac{1}{(1+z)^2} \frac{L}{4\pi a_0^2 r_m^2(\chi)} \equiv \frac{L}{4\pi d_L^2}. \quad (1.34)$$

In the previous expression, the luminosity distance  $d_L$  has been introduced in order to keep the same relation between  $\mathcal{F}$  and  $L$  as the one given by Eq. (1.33). Hence, we can write  $d_L$  as

$$d_L(z) = (1+z)a_0 r_m(\chi) = \frac{(1+z)}{H_0 \sqrt{\Omega_k}} \sinh \left( \sqrt{\Omega_k} \int_0^z \frac{dz'}{E(z')} \right), \quad (1.35)$$

where in the last equality we have used the definition of  $\Omega_k$  in order to eliminate  $a_0$ <sup>10</sup>. A well-known example of standard candles are Supernovae Ia. As opposed to Supernovae II or Ib (which arise from the core-collapse of very massive stars), Supernovae Ia are thought to be nuclear explosions in binary systems, which occur when a white dwarf accretes mass from its companion star above the Chandrasekhar limit of  $\sim 1.4M_\odot$ . An interesting characteristic of SNIa is that they all exhibit qualitatively similar light curves, *i.e.* they first brighten to a peak and then fade away after a period of few weeks. One is typically interested in the apparent magnitude at this peak. The *apparent magnitude*  $m_x$  in some spectral band  $x$  is simply a logarithmic measurement of the flux,  $m_x \equiv -2.5 \log_{10}(\mathcal{F}_x/\mathcal{F}_{x,0})$ , where  $\mathcal{F}_{x,0}$  is the flux of some reference object. In a similar way, one can define the *absolute magnitude*  $M_x$  as the apparent magnitude an observer would perceive at a distance of 10 pc to the object. By subtracting these quantities we can get rid of  $\mathcal{F}_{x,0}$ ,

$$\mu = m_x - M_x = -2.5 \log_{10} \left( \frac{\mathcal{F}(d_L)}{\mathcal{F}(10 \text{ pc})} \right). \quad (1.36)$$

<sup>10</sup>Notice that Eq. (1.35) includes in a compact way also the flat and spherical geometries, as can be seen by using the mathematical identities  $\lim_{x \rightarrow 0} \sin(ax)/x = a$  and  $\sinh(ix) = i \sin(x)$ , respectively.

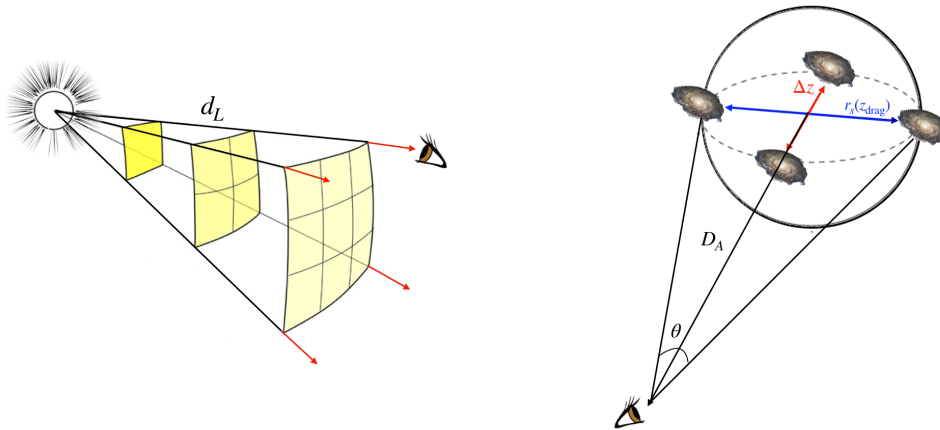


**Figure 1.6** – Geometries corresponding to the notions of luminosity distance to SNIa (**left**) and angular diameter distance to the BAO feature in the galaxy distribution (**right**).

The quantity  $\mu$  is commonly referred as *distance modulus*, since it can be directly linked to the  $d_L$  of SNIa if their peak luminosity is a constant in space and time <sup>11</sup>

$$\mu = -2.5 \log_{10} \left( \frac{(10 \text{ pc})^2}{d_L^2} \right) = 5 \log_{10} \tilde{d}_L + 25, \quad (1.37)$$

where  $\tilde{d}_L$  is the luminosity distance measured in units of Mpc. By comparing observations of  $m_{x,i}$  vs.  $z_i$  in a SNIa sample against the predicted values of  $d_L(z_i)$ , we can infer the underlying cosmology. Regarding the absolute magnitude, two strategies exist: 1) fit  $M_x$  to the data together with the rest of cosmological parameters (in which case it becomes totally degenerate with  $H_0$ ), or 2) get a direct measurement of  $M_x$  using a cosmic distance ladder method (see Sect. 2.2). As discussed at the end of Sect. 1.1, it is thanks to the observations of SNIa light curves up to  $z \sim 1$  that dark energy was discovered in 1998.

### Angular diameter distance

Another way of measuring distances is to consider an extended object of known physical transverse size  $L$ , *i.e.* a *standard ruler*. If this object emitted light at  $z_{\text{em}} = z$  and is at a comoving distance  $\chi$  from us, then according to Eq. (1.29) its transverse size is given by

$$L = a(t_{\text{em}}) r_m(\chi) \theta, \quad (1.38)$$

where  $\theta$  is the angular scale subtended by this object on the sky. The angular diameter distance  $d_A$  is defined in analogy with the formula in static Euclidean space,  $L/d_A \equiv 2 \tan(\theta/2) \simeq \theta$ , where in the last equality we assumed  $\theta \ll 1$  (which is true for all cosmological objects). Combining this with Eq. (1.38), we get

$$d_A = a(t_{\text{em}}) r_m(\chi) = \frac{a_0}{1+z} r_m(\chi). \quad (1.39)$$

<sup>11</sup>In practice, SNIa are not truly standard candles, since their peak luminosity vary from one SNIa to another. However, the peak luminosity is tightly correlated with other parameters, such as the width  $x_1$  or color  $c$  of the light curve, meaning they are *standardisable*. Hence, it is possible to correct the absolute magnitude  $M' = M + \alpha x_1 + \beta c$  (where  $\alpha, \beta$  are some empirical parameters to be fitted to data) such that  $M'$  is common to all SNIa (MANDEL *et al.* 2017).

The angular diameter distance measures the distance between us and the object at the moment of the emission (see Fig. 1.6). A widely used standard ruler is the so called comoving sound horizon at recombination,  $r_s(\tilde{z})$ , where  $\tilde{z}$  is of the order of  $10^3$ . As we will discuss in Sect. 1.6.4, the sound horizon corresponds to the maximum distance acoustic waves could propagate in the primordial plasma up to a certain redshift  $\tilde{z}$ . Depending on the observable, this redshift can correspond to the moment of photon decoupling,  $z_{\text{dec}} \simeq 1090$ , or the time at which baryons were released from photons (typically called the baryon drag epoch), which takes place slightly after photon decoupling,  $z_{\text{drag}} \simeq 1060 < z_{\text{dec}}$ . The sound horizon is mainly determined by the relative abundances of photons, baryons and dark matter, and it is of the order of 100 Mpc. This scale is imprinted in the map of CMB anisotropies as well as in the large scale distribution of galaxies, and can be seen as a characteristic angle that we can express in general as

$$\theta_X = \frac{r_X}{D_A}, \quad (1.40)$$

where  $D_A = a^{-1}d_A$  denotes the comoving angular diameter distance to the redshift at which observations are made,  $z_{\text{obs}}$ . In the case of the CMB measurements, one observes the photons ( $r_s = r_s(z_{\text{dec}})$ ) at the surface of last scattering,  $z_{\text{obs}} = z_{\text{dec}}$ , and the angle in Eq. (1.40) defines the position of the peaks in the angular correlation function of photon temperature fluctuations. In the case of LSS data, one observes the baryonic matter ( $r_d = r_s(z_{\text{drag}})$ ) at the redshifts accessible by galaxy surveys,  $0 \lesssim z_{\text{obs}} \lesssim 3$ , and the angle in Eq. (1.40) results from a feature in the galaxy correlation function perpendicular to the line of sight. The LSS determinations of this angular scale are commonly referred as Baryon Acoustic Oscillations (BAO), and when complemented with a knowledge on  $r_s(z_{\text{drag}})$ , they probe the distance-redshift relation at small  $z$ <sup>12</sup>. Hence, BAO data provide an alternative to SNIa to constrain the late-time expansion history, and allow to break parameter degeneracies when combined with other probes. In particular, the combination of CMB anisotropy with BAO or SNIa data indicate that our universe is flat to a high degree of accuracy. For these reasons and for simplicity, we will assume  $\Omega_k = 0$  in the rest of the text.

Let us end this part by noting that the angular diameter and luminosity distances are not independent. Indeed, by comparing Eq. (1.39) with Eq. (1.35), we observe that

$$d_L = (1+z)^2 d_A, \quad (1.41)$$

which is also known as the Etherington distance duality relation. At very small redshifts,  $z \lesssim 0.1$ , all distances essentially reduce to the Hubble law

$$d_L \simeq d_A \simeq a_0 \chi \simeq \frac{z}{H_0} \simeq \frac{v}{H_0}, \quad (1.42)$$

where we used the fact that the recessional velocity is approximately given by  $v \simeq z$  for nearby objects. Notice that the Hubble law also breaks down at even shorter distances, for which the peculiar velocities  $v_{\text{pec}} \equiv a\dot{\chi}$  become comparable to the Hubble flow. Thus, in full generality one writes  $v = \dot{d} = d(a\dot{\chi})/dt = Hd + v_{\text{pec}}$ .

<sup>12</sup>BAO observations also measure a feature in the galaxy correlation *parallel to the line of sight*, in which case they constrain the combination  $\Delta z = r_s(z_{\text{drag}})H(z_{\text{obs}})$ , see Fig. 1.6.

## 1.4 A few words on inflation

Cosmic inflation is a paradigm which was proposed in the '80s while investigating the problem of why no magnetic monopoles are seen today. It was quickly realized that inflation would resolve many other long-standing problems in Standard FLRW Cosmology (GUTH 1981):

- *The horizon problem.* Spacetime regions that could not have been in causal contact appear to have the same properties. This is reflected in the fact that spots in the CMB with non-overlapping past light-cones have an almost identical temperature. We can estimate the size of these spots by computing the angle subtended by the particle horizon at the moment of photon decoupling,

$$\theta_H = \frac{a_{\text{dec}}\chi_p(a_{\text{dec}})}{d_A(a_{\text{dec}})} = \frac{\int_{z_{\text{dec}}}^{\infty} dz/H(z)}{\int_0^{z_{\text{dec}}} dz/H(z)} = \frac{(1+z_{\text{dec}})^{-1/2}}{1-(1+z_{\text{dec}})^{-1/2}} \simeq 0.03 \simeq 1.7^\circ, \quad (1.43)$$

where we assumed matter domination at all times in order to simplify the calculations. This corresponds to  $4\pi/0.03^2 \sim 10^4$  patches in the CMB sky which are causally disconnected. How can we explain the homogeneity of regions that have not had sufficient time to communicate?

- *The curvature problem.* Using the Friedmann equation Eq. (1.18), it is easy to see that the evolution of the time-dependent curvature density parameter is approximately given by  $|\Omega_k(a)| \equiv |k|(aH(a))^{-2} \sim |k|a^{1+3w}$ , where  $w$  is the EoS of the dominating energy component in the universe. During the radiation and matter eras,  $1+3w > 0$ , implying that the curvature parameter increases with time. Hence, in order to explain why we observe the present curvature parameter  $|\Omega_k(a_0)|$  to be very close to zero, we would need an “incredibly” small value of curvature in the early universe, which appears very unnatural.
- *Initial conditions.* Standard cosmology is able to tell how perturbations have evolved during the history of the universe, until they grew enough to collapse and form the rich structure that we see. However, it does not provide a physical origin for these perturbations.

Inflation solves these problems by considering that, at very early times, the comoving Hubble radius was actually *decreasing* with time, rather than increasing. In this way, two points that *appear* not to be causally connected at the moment of decoupling (meaning they were separated by a comoving distance  $\lambda > (a_{\text{dec}}H(a_{\text{dec}}))^{-1}$ ), were actually in causal contact early on, *i.e.*  $\lambda < (a_{\text{ini}}H(a_{\text{ini}}))^{-1}$ . Put differently, the decreasing Hubble sphere can lead to a physical size particle horizon at the moment of decoupling,  $a_{\text{dec}}\chi_p(a_{\text{dec}})$  which can now encompass all the scales observed in the CMB. The condition of a decreasing Hubble radius,  $\dot{R}_H < 0$ , is equivalent to consider a period of early rapid accelerated expansion,  $\ddot{a} > 0$ , which in turn is equivalent to consider a dominant energy source satisfying  $1+3w < 0$ . To be more precise, inflation solves the horizon problem by requiring a growth of spacetime between the beginning and the end of inflation of at least  $a_{\text{end}}/a_{\text{ini}} \sim e^{60}$ . The curvature problem is also solved, since the curvature parameter  $|\Omega_k(a)|$  now rapidly decreases with time, and becomes very tiny by the end of inflation. In this way, the curvature parameter needs not to be fine-tuned to an incredibly small value at initial times.

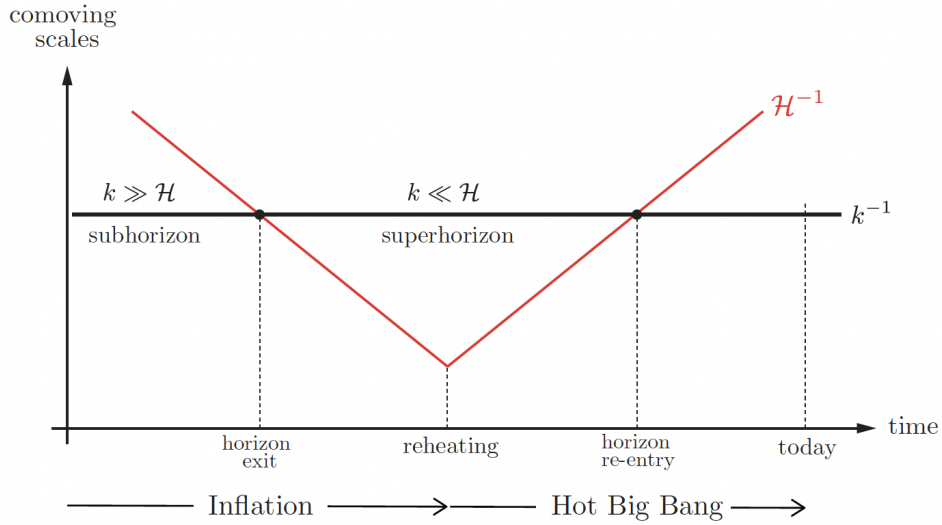


**Figure 1.7** – Evolution of the comoving Hubble radius during and after inflation. Taken from BAUMANN 2021.

Many inflation models consider a scalar field, the inflaton  $\phi(t, x^i)$ , as the mechanism responsible for driving the accelerated expansion. The stress-energy of a scalar field is given by

$$T^\mu{}_\nu = \partial^\mu \phi \partial_\nu \phi - \delta^\mu_\nu \left( \frac{g^{\alpha\beta}}{2} \partial_\alpha \phi \partial_\beta \phi + V(\phi) \right), \quad (1.44)$$

where  $V(\phi)$  is the scalar field potential. Assuming a FLRW background, the homogeneous part of the scalar field satisfies  $\partial_i \phi = 0$ , and the stress energy tensor in the previous equation has the same form as the one of a perfect fluid (see Eq. (1.12)). Hence, we can identify the energy density and pressure as

$$\rho_\phi = \frac{1}{2} \dot{\phi}^2 + V(\phi), \quad P_\phi = \frac{1}{2} \dot{\phi}^2 - V(\phi). \quad (1.45)$$

Applying the continuity equation of Eq. (1.14) to  $\rho_\phi$  and  $P_\phi$ , we find the Klein-Gordon equation that dictates the dynamical evolution of the scalar field,

$$\ddot{\phi} + 3H\dot{\phi} + \frac{dV}{d\phi} = 0, \quad \text{where } H^2 = \frac{8\pi G}{3} \rho_\phi. \quad (1.46)$$

By looking at Eq. (1.45), we see that the condition for cosmic acceleration,  $1 + 3w_\phi < 0$ , can be satisfied as long as the potential dominates over the kinetic energy. In addition, this period of cosmic acceleration should last enough time to solve the horizon problem. This amounts to saying that the scalar field should be initially at a high part of the potential and then roll slowly towards its minimum. In order to quantify these effects, it is useful to introduce the so called *slow-roll* parameters,

$$\varepsilon \equiv -\frac{\dot{H}}{H^2}, \quad \eta \equiv \frac{\dot{\varepsilon}}{H\varepsilon}. \quad (1.47)$$

Successful inflation happens when  $\varepsilon \ll 1$  and  $|\eta| \ll 1$ , *i.e.* a quasi-de Sitter expansion ( $H \simeq \text{const.}$ ) is maintained during a sufficiently long time. Assuming  $\frac{1}{2} \dot{\phi}^2 \ll V$  and



$\ddot{\phi} \ll H\dot{\phi}$ , we can write the *slow-roll* parameters in terms of the scalar field potential as

$$\varepsilon \simeq \frac{M_{\text{pl}}^2}{2} \left( \frac{V_{,\phi}}{V} \right)^2, \quad \eta \simeq 2M_{\text{pl}}^2 \left( \left( \frac{V_{,\phi}}{V} \right)^2 - \frac{V_{,\phi\phi}}{V} \right), \quad (1.48)$$

where  $M_{\text{pl}} = 1/\sqrt{8\pi G} \simeq 2.4 \times 10^{18}$  GeV is the reduced Planck mass. Inflation ends when  $\varepsilon = 1$ . Then, if  $V(\phi)$  is of the form  $V(\phi) \propto \phi^n$  (with  $n \gtrsim 2$ ) close to its minimum, the inflaton starts to oscillate rapidly, and releases all its energy to the Standard Model particles through decay processes. This is the reheating era that preceded the standard hot Big-Bang epoch, which we will describe in the following section.

The global picture that emerges is the following: at the beginning of inflation, all comoving scales  $\lambda$  that we observe today on the CMB were sub-horizon, *i.e.* they were inside the Hubble radius. In terms of the corresponding Fourier mode,  $k = 2\pi/\lambda$ , this condition can be expressed as  $k \gg \mathcal{H}$ . As  $\mathcal{H}^{-1}$  decreased during inflation, these scales exited the Hubble radius and became super-horizon ( $k \ll \mathcal{H}$ ). In this process, the microscopic quantum fluctuations of the inflaton got stretched to cosmic sizes and became classical. After inflation ended and  $\mathcal{H}^{-1}$  started to grow, the scales  $k^{-1}$  gradually re-entered the Hubble radius. This is depicted in Fig. 1.7. The small fluctuations of the inflaton provide the initial conditions for the evolution of perturbations of the different components in the universe.

## 1.5 In and out of equilibrium

Until now, we have taken a macroscopic view of the energy content of the universe. That is, we have always expressed the stress-energy tensor in terms of thermodynamic quantities, as the density and the pressure (related by the EoS parameter). However, in many cases of interest, it is possible to switch to a microscopic point of view, where all thermodynamic quantities can be derived from a distribution function of the particles in phase space,  $f(x^\mu, P^\mu)$ . This function gives the number of particles at a given time  $t$  and at a certain point in the phase-space  $(x^i, P^0, P^i)$  (in practice  $P^0$  is not an independent variable because of the mass-shell condition,  $g_{\mu\nu}P^\mu P^\nu = -m^2$ ). In terms of the phase-space distribution (PSD), one can define the particle current density and the stress energy tensor as

$$n^\mu(x^i, t) = g \int \frac{d^3\vec{P}}{(2\pi)^3} (-\det(g))^{-1/2} \frac{P^\mu}{P^0} f(x^i, P^i, t), \quad (1.49)$$

$$T^\mu{}_\nu(x^i, t) = g \int \frac{d^3\vec{P}}{(2\pi)^3} (-\det(g))^{-1/2} \frac{P^\mu P_\nu}{P^0} f(x^i, P^i, t), \quad (1.50)$$

where  $g$  represents the internal degrees of freedom of the particle, and the integration is over covariant 3-momenta  $P_i$ . Since we are assuming a FLRW background, we can make some simplifications. First, we notice that  $\det(g) = -a^6$  and  $P_i = \sum_j g_{ij}P^j = \sum_j a^2\delta_{ij}P^j$ , so that  $d^3\vec{P}(-\det(g))^{-1/2} = d^3p$ , which means that the integration is now over physical 3-momenta  $p^i \equiv aP^i$ . By construction, this vector has a norm  $\sqrt{\sum_i (p^i)^2} = \sqrt{\sum_{ij} a^2\delta_{ij}P^iP^j} = \sqrt{\sum_{ij} g_{ij}P^iP^j} = p$ , so the integral measure in spherical coordinates reads  $d^3\vec{p} = d\Omega p^2 dp$ . Second, homogeneity and isotropy imply that  $f(x^i, P^i, t) = f(p, t)$ . Hence, by virtue of the integrals  $\int d\Omega P^i = 0$  and  $\int d\Omega P^i P_j = 0$  (for  $i \neq j$ ), we see that the components  $n^i$ ,  $T^0_i$  and  $T^i_j$  (for  $i \neq j$ ) necessarily vanish. The remaining non-zero components correspond to the particle number density,

the energy density and the pressure

$$n(t) = n^0 = \frac{g}{2\pi^2} \int dp p^2 f(p, t), \quad (1.51)$$

$$\rho(t) = -T^0_0 = \frac{g}{2\pi^2} \int dp p^2 E f(p, t), \quad (1.52)$$

$$P(t) \equiv \frac{1}{3} \sum_i T^i_i = \frac{g}{2\pi^2} \int dp p^2 \frac{p^2}{3E} f(p, t). \quad (1.53)$$

We can alternatively express them in terms of the comoving momentum modulus  $q = ap$  and comoving energy  $\mathcal{E} = aE$ :

$$n(t) = \frac{4\pi}{a^3} \int dq q^2 f(q, t), \quad (1.54)$$

$$\rho(t) = \frac{4\pi}{a^4} \int dq q^2 \mathcal{E} f(q, t), \quad (1.55)$$

$$P(t) = \frac{4\pi}{a^4} \int dq q^2 \frac{q^2}{3\mathcal{E}} f(q, t), \quad (1.56)$$

where we have absorbed a factor  $g/(2\pi)^3$  inside  $f(q, t)$ . From the previous equations we see that, regardless of the shape of the PSD function, relativistic particles ( $E = p$ ) satisfy  $P/\rho = 1/3$ , while for non-relativistic particles ( $E \simeq m$ ) we have  $\rho \simeq mn$  and  $P/\rho \sim \langle p^2 \rangle / m^2 \ll 1$ .

### 1.5.1 The Boltzmann formalism

What about the shape of the PSD function? The almost perfect blackbody spectrum of the CMB gives a firm proof that the early universe was well characterized by *local thermodynamic equilibrium*. Indeed, the enormous temperatures after reheating favored the collisions between particles, making them exchange energy and momentum very efficiently. In this case, particles were distributed in the phase space according to the Bose-Einstein or Fermi-Dirac distributions. As the universe cooled, interactions became less frequent and particles progressively exited from equilibrium. The key to quantify this effect is to compare the interaction rate,  $\Gamma$ , to the expansion rate of the universe,  $H$ . For two-to-two interactions of the form  $1 + 2 \leftrightarrow 3 + 4$ , the interaction rate for the species 1 is given by

$$\Gamma_1 = n_2 \langle \sigma v \rangle, \quad (1.57)$$

where  $\langle \sigma v \rangle$  denotes the *thermally averaged cross-section* (a formal definition will be given below). Equilibrium is maintained if  $\Gamma_1 \gg H$ . When  $\Gamma_1 \ll H$ , particles decouple from the thermal bath and start free-streaming through the universe. In order to accurately describe the departures from equilibrium, we need to use the Boltzmann formalism. For a species 1 interacting with  $i = 2, \dots, N$  species, the Boltzmann equation reads

$$\mathcal{L}[f_1] \equiv \frac{df_1(x^\mu(\sigma), P^\mu(\sigma))}{d\sigma} = \mathcal{C}[f_1; f_2, \dots, f_N], \quad (1.58)$$

where  $\mathcal{L}[f]$  is the so-called Liouville operator, and  $\mathcal{C}[f_1; f_i]$  is the collision integral, whose expression depends on the particular type of interactions considered. Let us focus first on the l.h.s. of Eq. (1.58). In the absence of interactions, the collisionless Boltzmann equation,  $\mathcal{L}[f_1] = 0$ , can be expressed in the following way

$$\mathcal{L}[f_1] = \frac{\partial f_1}{\partial x^\mu} \frac{dx^\mu}{d\sigma} + \frac{\partial f_1}{\partial P^\mu} \frac{dP^\mu}{d\sigma} = \frac{\partial f_1}{\partial x^\mu} P^\mu - \frac{\partial f_1}{\partial P^\mu} \Gamma^\mu_{\alpha\beta} P^\alpha P^\beta = 0, \quad (1.59)$$



simply reflecting the fact that  $f_1$  is conserved as we follow a geodesic in phase space. In the FLRW background, we have  $f_1 = f_1(t, p)$ , and we can use the expression for the Christoffels in Eq. (1.7), to arrive at

$$\mathcal{L}[f_1] = E \left( \frac{\partial f_1}{\partial t} - Hp \frac{df_1}{dp} \right) = 0. \quad (1.60)$$

We will sometimes find convenient to switch to the modulus of the comoving momentum,  $q \equiv ap$ , which doesn't evolve with time. In terms of this new variable,

$$\frac{\partial f_1(t, q)}{\partial t} = \frac{\partial f_1}{\partial t} + \frac{\partial f_1}{\partial q} \frac{dq}{dp} \dot{p} = \frac{\partial f_1}{\partial t} - Hp \frac{\partial f_1}{\partial p} = 0, \quad (1.61)$$

which means that any PSD which depends exclusively on comoving momentum,  $f = f(q)$ , is automatically a solution of the collisionless Boltzmann equation. We can easily express Eq. (1.60) in terms of the number density  $n_1$  by integrating over  $(g/2\pi^2) \int dp_1 p_1^2$ . Doing integration by parts on the second term and assuming that  $f_1 \rightarrow 0$  for  $p \rightarrow \infty$ , then we get

$$\dot{n}_1 + 3Hn_1 = 0, \quad (1.62)$$

meaning that, in the absence of interactions, the number of particles is conserved on a comoving volume,  $n_1 \propto a^{-3}$ .

Let us now move to the r.h.s. of Eq. (1.58). For two-to-two interactions, the collision integral is written as

$$\begin{aligned} \mathcal{C}[f_1; f_2, f_3, f_4] &= \int \frac{d^3 \vec{p}_2}{(2\pi)^3 2E_2} \frac{d^3 \vec{p}_3}{(2\pi)^3 2E_3} \frac{d^3 \vec{p}_4}{(2\pi)^3 2E_4} \delta^4(P_1 + P_2 - P_3 - P_4) (2\pi)^4 \\ &\times \left[ |\mathcal{M}_{34,12}|^2 f_3 f_4 (1 \pm f_1) (1 \pm f_2) - |\mathcal{M}_{12,34}|^2 f_1 f_2 (1 \pm f_3) (1 \pm f_4) \right]. \end{aligned} \quad (1.63)$$

We have introduced the Lorentz-invariant amplitudes  $\mathcal{M}_{34,12}$  and  $\mathcal{M}_{12,34}$  for the processes  $3 + 4 \rightarrow 1 + 2$  and  $1 + 2 \rightarrow 3 + 4$  (which include the sum over all internal degrees of freedom). These amplitudes are equal in modulus for interactions with a time reversal symmetry, which is often the case. The Dirac delta is inserted just to guarantee the energy-momentum conservation. From Eq. (1.63), we see that the collision integral is simply giving the difference between the rate of production of species 1 (proportional to  $f_3 f_4$ ) and the rate of destruction of species 1 (proportional to  $f_1 f_2$ ). Finally, the factors  $(1 \pm f_i)$  account for the stimulated emission for bosons (+) and Pauli blocking effects for fermions (-). Similar equations as Eq. (1.63) can be written for species 2, 3 and 4. In the most general case, one should therefore solve a complicated system of coupled integro-differential equations.

In a static universe, equilibrium distributions can be obtained by demanding that the collision term vanishes, which is sometimes called the *detailed balance condition*. We remark that this doesn't imply at all that collisions aren't happening. Rather, it is reflecting the idea that forward and backward collision rates should be equal in equilibrium. Using the unitarity of  $\mathcal{M}_{ij,kl}$  and taking  $\mathcal{C} = 0$  in Eq. (1.63) yields

$$\prod_{a=1,2} \frac{1 \pm f_a}{f_a} = \prod_{b=3,4} \frac{1 \pm f_b}{f_b}. \quad (1.64)$$

By taking the logarithm of Eq. (1.64), we see that the quantity  $\mathcal{S} \equiv \sum_a \ln[(1 \pm f_a)/f_a]$  remains unchanged during collisions. This can be achieved if  $\mathcal{S}$  is a linear combination of conserved quantities in the collisions, such as 4-momentum  $P_a^\mu$  or any other conserved charge  $Q_a$  (like baryon number or electric charge). Thus, we can write

$$\ln\left(\frac{1 \pm f_a}{f_a}\right) = \beta E_a + \xi Q_a, \quad (1.65)$$

where we took  $P_a^i = 0$  since we assume a fluid whose center of mass is not moving. The coefficients  $\beta$  and  $\xi$  characterize the different equilibrium states, so in order to make a connection with thermodynamic quantities we can set  $\beta = 1/T$  and  $\xi Q_a = \mu_a/T$ , where  $T$  is the temperature and  $\mu_a$  the chemical potential associated with the conserved charge  $Q_a$ . Solving for  $f_a$  yields the Fermi-Dirac and Bose-Einstein equilibrium distributions,

$$f_a = \frac{1}{e^{(E_a - \mu_a)/T} \mp 1}, \quad (1.66)$$

where the sign  $-$  stands for bosons and the sign  $+$  for fermions. Notice that the distribution of Eq. (1.66) satisfies  $\mathcal{C} = 0$  for all kind of two-to-two interactions as long as all particles share the same temperature  $T$  (*kinetic equilibrium* condition) and the chemical potentials fulfill the *chemical equilibrium* condition,

$$\mu_1 + \mu_2 = \mu_3 + \mu_4. \quad (1.67)$$

Since particles and antiparticles carry opposite charges, their chemical potentials must be opposite in sign,  $\mu_a = -\mu_{\bar{a}}$ . Furthermore, photons carry no additive charges (*i.e.* they are equal to their antiparticles), so they can't have a chemical potential,  $\mu_\gamma = 0$ . For a non-degenerate fluid satisfying  $E_a - \mu_a \gg T$  (which is relevant for many applications in cosmology), the distribution in Eq. (1.66) reduces to the classical Maxwell-Boltzmann distribution

$$f_a \simeq e^{-(E_a - \mu_a)/T}. \quad (1.68)$$

Now, to see if the PSD in Eq. (1.66) is also an equilibrium solution in an expanding universe, we should check if they are also in the kernel of the Liouville operator,  $\mathcal{L}[f_a] = 0$ . Inserting Eq. (1.66) in Eq. (1.60) and allowing the independent variables  $T$  and  $\mu_a$  to vary with time, yields the conditions

$$\frac{\dot{\mu}_a}{\mu_a} = \frac{\dot{T}}{T} = -\frac{p^2}{E_a^2} H. \quad (1.69)$$

Specializing to the case of massless particles,  $E_a = p$ , we find that the temperature and chemical potential evolve as  $\mu_a \propto T \propto a^{-1}$ . For the case of massive particles, there is no general solution to Eq. (1.69). The reason for this is that, strictly speaking, there are no equilibrium solutions for massive particles in a FLRW geometry. However, one can show that the PSD function of massive particles remains always very close to the equilibrium form of Eq. (1.66) as long as interactions are very efficient,  $\Gamma_1/H \gg 1$  (BERNSTEIN 1988).

An important conclusion that can be extracted from the previous considerations is that any species that decouples while being relativistic (*i.e.* a hot relic), will approximately retain an equilibrium distribution with a decreasing temperature also at

later times. To see this, let's consider that a hot species decouples instantaneously at some temperature  $T_D$  (that is, we neglect the fact that the decoupling process actually takes some time). Before decoupling, the collision term is zero since forward and backward rates exactly compensate, meaning that the PSD of the species will be either a Bose-Einstein or Fermi-Dirac until  $T_D$ :

$$f(q) = \frac{1}{e^{(q-a_D\mu_D)/a_D T_D} \mp 1}. \quad (1.70)$$

After decoupling, the collision term is still zero because the species don't interact anymore with the rest of particles, and it will keep its equilibrium form with a decreasing temperature and chemical potential. Indeed, the distribution on Eq. (1.70) depends only on comoving momentum  $q$  provided that  $aT = a_D T_D = \text{const.}$  and  $a\mu = a_D \mu_D = \text{const.}$ , so it is automatically a solution of the collisionless Boltzmann equation by virtue of Eq. (1.61). This is the reason why CMB photons exhibit an almost perfect black body spectrum, even if they decoupled at  $z_D \sim 10^3$ . Another example of hot relics are neutrinos, which decoupled from the plasma much earlier, at  $z_D \sim 10^9$ . Even if neutrinos have nonzero masses of the order  $m_\nu \lesssim \mathcal{O}(0.1)$  eV, they decoupled at a temperature of the order  $T_D \sim 1$  MeV  $\gg m_\nu$ , so they were clearly relativistic at that epoch. However, we will see that the fact the decoupling process wasn't exactly instantaneous induces some small distortions in their Fermi-Dirac distribution.

### 1.5.2 Relativistic degrees of freedom and entropy conservation

Let us now compute the different thermodynamic quantities for particles in equilibrium. Inserting the Fermi-Dirac or Bose-Einstein distribution in Eq. (1.51), Eq. (1.52) and Eq. (1.53), we get

$$n_{\text{eq}} = \frac{g}{2\pi^2} \int \frac{dp p^2}{\exp[(\sqrt{p^2 + m^2} - \mu)/T] \mp 1}, \quad (1.71)$$

$$\rho_{\text{eq}} = \frac{g}{2\pi^2} \int \frac{dp p^2 \sqrt{p^2 + m^2}}{\exp[(\sqrt{p^2 + m^2} - \mu)/T] \mp 1}, \quad (1.72)$$

$$P_{\text{eq}} = \frac{g}{2\pi^2} \int \frac{dp p^4}{3\sqrt{p^2 + m^2}(\exp[(\sqrt{p^2 + m^2} - \mu)/T] \mp 1)}. \quad (1.73)$$

In general, the previous integrals have to be computed numerically. However, it is possible to get analytical expressions in some limiting cases. Let us start considering the relativistic limit,  $T \gg m$ . In this regime, the chemical potentials of all particles are typically so small that we can safely neglect them<sup>13</sup>. Hence, we get

$$n_{\text{eq}} = \frac{\zeta(3)}{\pi^2} g T^3 \begin{cases} 1 & \text{bosons} \\ \frac{3}{4} & \text{fermions} \end{cases} \quad (1.75)$$

<sup>13</sup>The chemical potential of electrons and protons can't be exactly zero, since a non-zero value of  $\mu$  is required to account for the particle-antiparticle asymmetry that we observe. As an example, consider temperatures  $m_p \gg T \gg m_e$ , such that the universe is full of non-relativistic protons  $p^+$  as well as relativistic electrons  $e^-$  and positrons  $e^+$ . One can then compute the ratio  $r \equiv (n_{e^-} - n_{e^+})/n_\gamma$  using the relativistic limit of Eq. (1.71) for fermions and  $\mu_{e^-} = -\mu_{e^+} \neq 0$ . This yields

$$r = \frac{g_e}{g_\gamma} \frac{\pi^2}{6\zeta(3)} \left( \frac{\mu_{e^-}}{T} + \frac{1}{\pi^2} \frac{\mu_{e^-}^3}{T^3} \right). \quad (1.74)$$

This ratio stays constant after the  $e^\pm$  annihilation stage, and can be related to the baryon-to-photon ratio  $\eta \equiv n_b/n_\gamma \simeq n_p/n_\gamma = r$ , where the last equality follows from the neutrality of the universe. Observations

$$\rho_{\text{eq}} = 3P_{\text{eq}} = \frac{\pi^3}{30} g T^4 \begin{cases} 1 & \text{bosons} \\ 7/8 & \text{fermions} \end{cases} \quad (1.76)$$

In the non-relativistic limit  $T \ll m$ , and for chemical potentials  $\mu_a \ll m$ , we can use the Maxwell Boltzmann distribution of Eq. (1.68), to obtain

$$n_{\text{eq}} = g \left( \frac{mT}{2\pi} \right)^{3/2} e^{(-m+\mu)/T}, \quad (1.77)$$

$$\rho_{\text{eq}} \simeq m n_{\text{eq}}, \quad P_{\text{eq}} = n_{\text{eq}} T \ll \rho_{\text{eq}}. \quad (1.78)$$

From Eq. (1.77) we see that, for null chemical potentials, the number density of non-relativistic components is exponentially suppressed as the temperature decreases. This is a result of particle-antiparticle annihilations, which aren't prevented from any conservation law (since  $\mu = 0$ ) and can't be balanced by particle-antiparticle pair production (which are inefficient for  $T \lesssim m$ )<sup>14</sup>.

Thanks to Eq. (1.76), we can easily compute the total energy density associated to radiation

$$\rho_r = \sum_i \rho_i = \frac{\pi^2}{30} g_*(T) T^4, \quad (1.79)$$

where  $g_*(T)$  is the *effective number of relativistic degrees of freedom* at a temperature  $T$ . Since we are summing over relativistic species with a negligible chemical potential, we can write  $g_*(T)$  as

$$g_*(T) = \sum_{i,\text{boson}} g_i \left( \frac{T_i}{T} \right)^4 + \frac{7}{8} \sum_{i,\text{fermion}} g_i \left( \frac{T_i}{T} \right)^4, \quad (1.80)$$

where we have allowed the possibility that particles might have different temperatures from photons,  $T_i \neq T$ . When the temperature drops below the mass  $m_i$  of a certain species, its contribution is removed from Eq. (1.80), consequently decreasing  $g_*(T)$ .

Let us consider now a very important quantity to describe the early universe, the entropy density,  $s = S/V$ , where  $V \propto a^3$ . Here  $S$  is the total entropy, which stays constant in equilibrium. From the thermodynamic identity  $s = \frac{\partial P}{\partial T}|_{\mu}$ , and using Eq. (1.66), one can show that the entropy density is given by

$$s = \frac{\rho + P - \mu n}{T}. \quad (1.81)$$

For relativistic particles, since  $\rho \propto P \propto \mu n \propto T^4$ , the entropy density  $s$  scales as  $a^{-3}$ , so that  $S$  is conserved. In a similar way as we did for the energy density, we

---

of CMB and BBN indicate that  $\eta \simeq 5.5 \times 10^{-10}$  ( $\omega_b/0.02$ ). Comparing this with the previous formula for  $r$ , we obtain  $\mu_{e^-}/T \sim 10^{-9}$ , which confirms that the contribution of  $\mu_{e^-}$  to the number and energy density is actually very small.

<sup>14</sup>The fact that annihilations can't be balanced by pair production doesn't contradict the idea that forward and backward rates are equal in chemical equilibrium. Indeed, when the number density is exponentially suppressed, the pair production cross-section is reduced accordingly, such that annihilation and pair production rates remain equal.

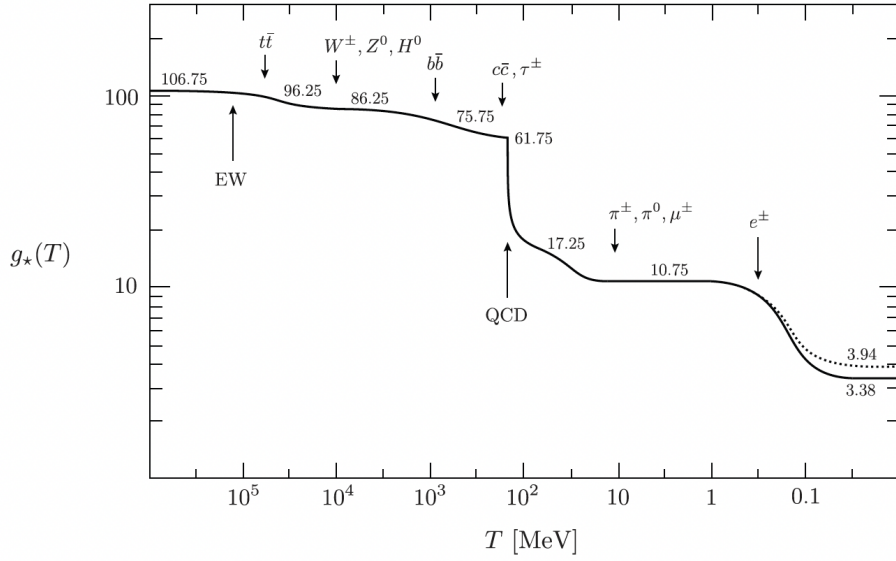


**Figure 1.8** – Temperature evolution of the effective number of relativistic degrees of freedom  $g_*(T)$ , assuming the particle content of the Standard Model. The dotted line indicates the effective number of degrees of freedom in entropy,  $g_{*,S}(T)$ . Taken from [BAUMANN 2021](#).

can compute the total entropy associated to radiation. For relativistic particles with vanishing chemical potentials,

$$s_r = \sum_i \frac{4}{3} \frac{\rho_i}{T_i} = \frac{2\pi^2}{45} g_{*,S}(T) T^3, \quad (1.82)$$

where  $g_{*,S}(T)$  is the *effective number of degrees of freedom in entropy*,

$$g_{*,S}(T) = \sum_{i,\text{boson}} g_i \left( \frac{T_i}{T} \right)^3 + \frac{7}{8} \sum_{i,\text{fermion}} g_i \left( \frac{T_i}{T} \right)^3. \quad (1.83)$$

We note that  $g_{*,S}(T) = g_*(T)$  as long as all relativistic particles share the same temperature of the photon bath,  $T_i = T$ . As we will see, this is the case until the  $e^\pm$  annihilation stage. In [Fig. 1.8](#) we show the evolution of  $g_*(T)$  as well of  $g_{*,S}(T)$ , assuming the particle content of the Standard Model. Applying entropy conservation  $S_r = \text{const.}$  to [Eq. \(1.82\)](#), we can readily obtain the evolution of the photon temperature in equilibrium,

$$a^3 g_{*,S}(T) T^3 = \text{const.}, \quad \implies \quad T \propto g_{*,S}^{-1/3} a^{-1}. \quad (1.84)$$

We see that, away from mass thresholds, the temperature evolves as  $T \propto a^{-1}$ . When a particle becomes non-relativistic, the factor  $g_{*,S}^{-1/3}$  makes  $T$  to decrease more slowly, which is simply reflecting the fact that annihilations are transferring entropy to the other species in the thermal bath.

### 1.5.3 Neutrino decoupling and evolution

An interesting application of entropy conservation is the calculation of neutrino temperature. At temperatures  $T > 1$  MeV, neutrinos were in equilibrium with the rest of the plasma through processes like  $\nu_e + \bar{\nu}_e \leftrightarrow e^- + e^+$  and  $e^- + \nu_e \leftrightarrow e^- + \nu_e$ .

The cross-section for these processes are of the order  $\langle\sigma v\rangle \sim G_F^2 T^2$  (where  $G_F \simeq 1.17 \times 10^{-5} \text{ GeV}^{-2}$  is Fermi's constant) meaning that  $\Gamma_\nu \sim G_F^2 T^5$ . The decoupling temperature can thus be estimated by comparing this interaction rate with the expansion rate, which by virtue of Eq. (1.79) is given by

$$H = \left( \frac{\rho_r}{3M_{\text{pl}}^2} \right)^{1/2} \simeq \frac{\pi}{3} \left( \frac{g_\star}{10} \right)^{1/2} \frac{T^2}{M_{\text{pl}}}. \quad (1.85)$$

Setting  $\Gamma_\nu = H$  and using the useful conversion  $1 \text{ eV} = 11605 \text{ K}$  yields a decoupling temperature of around  $T_D \sim 1 \text{ MeV}$ . As we already discussed, after decoupling the neutrinos inherit a Fermi-Dirac distribution with a temperature  $T_\nu \propto a^{-1}$ . This means that their entropy is also separately conserved, so we can just consider the entropy of the only relativistic species that were present in the plasma for  $T < 1 \text{ MeV}$ : electrons, positrons and photons. When electrons and positrons annihilate at  $T = m_e \sim 0.5 \text{ MeV}$ , they inject entropy that reheats the photons. The relation between the temperature of photons before and after  $e^\pm$  annihilation can be derived using entropy conservation of the  $e^\pm\gamma$  fluid:

$$\frac{T_{\text{before}}}{T_{\text{after}}} = \left( \frac{g_{\star,\text{after}}}{g_{\star,\text{before}}} \right)^{1/3}. \quad (1.86)$$

The number of relativistic degrees of freedom before and after  $e^\pm$  annihilation is  $g_{\star,\text{before}} = 2 + \frac{7}{8}(2 + 2) = 11/2$  and  $g_{\star,\text{after}} = 2$ , respectively. Thus, the photon temperature increases by a factor  $T_{\text{before}}/T_{\text{after}} = (4/11)^{1/3}$ . Neutrinos don't feel this raise of temperature, since they already decoupled from the plasma by the time electrons and positrons were annihilating, meaning that  $T_\nu = T_{\text{before}}$ . We conclude that the relation between neutrino and photon temperature at  $T_\gamma = T_{\text{after}} < m_e$  is the following

$$\frac{T_\nu}{T_\gamma} = \left( \frac{4}{11} \right)^{1/3} \simeq 0.71. \quad (1.87)$$

After  $e^\pm$  annihilation, photons and neutrinos constituted the sole relativistic species in the universe. In this context, we can use Eq. (1.87) to write the total density in radiation as

$$\rho_r = \rho_\gamma \left( 1 + N_{\text{eff}} \frac{7}{8} \left( \frac{4}{11} \right)^{4/3} \right), \quad (1.88)$$

where  $N_{\text{eff}}$  is the *effective number of neutrino species*. This parameter would be equal to the number of neutrino flavors,  $N_{\text{eff}} = 3$ , only if the assumptions we have made until now were valid; namely, if neutrinos decoupled instantaneously and they were described by Fermi-Dirac distributions with null chemical potentials. In practice, a  $N_{\text{eff}} \neq 3$  is used to capture deviations from these hypothesis. For instance, neutrinos with different momenta decoupled at slightly different times, and some of the energy released in  $e^\pm$  annihilations did leak to the more energetic neutrinos. The full calculation of neutrino decoupling yields a value of  $N_{\text{eff}} \simeq 3.044$  (J. J. BENNETT et al. 2020). It is customary to also use  $N_{\text{eff}}$  to parameterize the presence of any possible massless invisible species (*dark radiation*) in the early universe, which would be constrained by BBN and CMB data. To be more precise, the energy density of this dark radiation,  $\rho_{\text{dr}}$ , is re-absorbed as change in the effective number of neutrinos, given by  $\Delta N_{\text{eff}} \equiv N_{\text{eff}} - 3.044 = \rho_{\text{dr}}/\rho_{1\nu}$ , where  $\rho_{1\nu}$  is the density of a single relativistic neutrino.



At late times, the mass of neutrinos becomes important compared to their energy, so Eq. (1.88) is not valid anymore. Neutrinos become non-relativistic when the average momentum per neutrino species  $i$ ,

$$\langle p \rangle = \frac{\int dp p^3 (\exp(p/T_\nu) + 1)^{-1}}{\int dp p^2 (\exp(p/T_\nu) + 1)^{-1}} = \frac{7\pi^4}{180\zeta(3)} T_\nu \simeq 3.15 T_\nu, \quad (1.89)$$

drops below its mass  $m_{\nu,i}$  (SHOJI et al. 2010). Solving  $3.15 T_{\nu,0}(1 + z_{\text{nr}}) = m_{\nu,i}$  leads to

$$1 + z_{\text{nr},i} \simeq 1890 \left( \frac{m_{\nu,i}}{1 \text{ eV}} \right). \quad (1.90)$$

As we will discuss in Sect. 4.2, oscillation experiments tell us that at least two neutrinos need to have mass, whose minimum values correspond to  $m_{2,\text{min}} \simeq 0.01 \text{ eV}$  and  $m_{3,\text{min}} \simeq 0.05 \text{ eV}$  in the case of normal mass ordering, and to  $m_{2,\text{min}} \sim m_{1,\text{min}} \simeq 0.05 \text{ eV}$  in the case of an inverted mass ordering. Combining this information with Eq. (1.90), we see that at least two neutrinos are necessarily non-relativistic today. In addition, current CMB data places a stringent upper limit on the sum of neutrino masses of  $\sum_i m_i \lesssim 0.12 \text{ eV}$  (AGHANIM et al. 2020b), which by virtue of Eq. (1.90) implies that neutrinos became non-relativistic after decoupling,  $z_{\text{nr},i} < z_{\text{dec}}$ . The present contribution of neutrinos to the total energy density can easily be computed by summing over all neutrinos that are non-relativistic today

$$\Omega_\nu = \frac{\sum_i m_i n_{i,0}}{\rho_c} \simeq \frac{\frac{3}{11} n_\gamma \sum_i m_i}{\rho_c} \simeq \frac{\sum_i m_i}{94.1 h^2 \text{ eV}}. \quad (1.91)$$

This means that neutrinos can only constitute at present a very small fraction of the total energy budget of the universe.

#### 1.5.4 WIMP freeze-out

We have now two alternative ways to compute the evolution of thermodynamic quantities in equilibrium. On the one hand, we can use the integrated collisionless Boltzmann equation, which yields  $n \propto a^{-3}$ , as we saw in Eq. (1.62). On the other hand, we know that the temperature of the bath evolves as  $T \propto a^{-1}$  (away from mass thresholds), so plugging this in the relativistic equilibrium functions shown in Eq. (1.75), we recover  $n \propto a^{-3}$ . However, if we plug  $T \propto a^{-1}$  in the non-relativistic equilibrium function of Eq. (1.77) with  $\mu = 0$ , then we don't recover  $n \propto a^{-3}$ . This means that something must have happened to non-relativistic particles that prevented the exponential suppression  $\exp(-m/T)$  to develop further. There are two possibilities:

- Massive particles in chemical equilibrium have a non-zero chemical potential  $\mu$  associated with a charge conserved by all interactions in the thermal bath. This is the case of baryons (protons and neutrons) as well as electrons. The chemical potential adjusts itself as a function of temperature,  $\mu(T)$ , to ensure that the abundance of baryon matches the value that we observe,  $n_b = \eta n_\gamma \sim 5.5 \times 10^{-10} n_\gamma$ . Stated otherwise, if there's an initial excess of baryons over antibaryons, and all interactions conserve a non-zero baryonic charge,  $B = \frac{n_B - n_{\bar{B}}}{s} \neq 0$ , then particles acquire a positive chemical potential (such that  $\mu/T$  grows as  $T$  decreases) that cancels the effect of the exponential factor. Conversely, antiparticles are rapidly depleted because their chemical potential is negative,  $-\mu/T$ .

- Massive species with no particle-antiparticle asymmetry ( $\mu = 0$ ) might exit from chemical equilibrium after they become non-relativistic, when their interaction rate becomes smaller than the Hubble rate. In other words, when the expansion timescale starts to dominate over the interaction timescale, particles and antiparticles cannot find each other to annihilate, so their comoving number density  $a^3 n$  freezes out at a certain value. This is the case of weakly interacting massive particle (WIMP) scenario for CDM, that we proceed to discuss now.

In order to describe the departure from equilibrium for the WIMP dark matter, we are going to derive a simplified version of the Boltzmann equation in Eq. (1.58) for two-to-two interactions of the form  $1 + 2 \leftrightarrow 3 + 4$ . The assumptions we will make are sufficiently general so that the resulting equations can be applied to many situations of interest. First, we will assume that the particles are in kinetic equilibrium with other particles in the plasma thanks to fast scattering processes. Second, we will consider that particles are either non-relativistic, or relativistic with negligible or vanishing chemical potential (as in the case of photons), which means that all the effects due to quantum statistics can be neglected. The distribution functions can then be written in general as  $f_i = e^{(-E_i + \mu_i)/T} \ll 1$ . Taking  $\mathcal{M}_{12,34} = \mathcal{M}_{34,12} = \mathcal{M}$ , the integrand of the collision operator in Eq. (1.63) simplifies to

$$f_3 f_4 (1 \pm f_1)(1 \pm f_2) - f_1 f_2 (1 \pm f_3)(1 \pm f_4) \rightarrow e^{-(E_1 + E_2)/T} \left( e^{(\mu_3 + \mu_4)/T} - e^{(\mu_1 + \mu_2)/T} \right), \quad (1.92)$$

where we used energy conservation  $E_1 + E_2 = E_3 + E_4$ . In this context, the Boltzmann equation describes how the chemical potentials evolve from a chemical equilibrium configuration where  $\mu_1 + \mu_2 = \mu_3 + \mu_4$  to more general values that will fix the number densities of particles after they have decoupled from each other. Nevertheless, we can choose to evolve the number densities instead of the chemical potentials, since they keep a simple relation,

$$n_i = e^{\mu_i/T} n_i^{(0)}, \quad \text{where} \quad n_i^{(0)} \equiv \frac{g_i}{2\pi^2} \int dp p^2 e^{-E_i/T}. \quad (1.93)$$

We introduced the variable  $n_i^{(0)}$  to simplify notation, but we remark that it is not necessarily equal to the equilibrium distribution, since it is lacking the factor with  $\mu_i$ . Integrating the Boltzmann equation Eq. (1.58) over  $(g/2\pi^2) \int dp_1 p_1^2$ , we arrive at the following differential equation for the number density of species 1,

$$a^{-3} \frac{d(n_1 a^3)}{dt} = n_1^{(0)} n_2^{(0)} \langle \sigma v \rangle \left( \frac{n_3 n_4}{n_3^{(0)} n_4^{(0)}} - \frac{n_1 n_2}{n_1^{(0)} n_2^{(0)}} \right), \quad (1.94)$$

where  $\langle \sigma v \rangle$  is the thermally averaged cross section

$$\langle \sigma v \rangle \equiv \frac{1}{n_1^{(0)} n_2^{(0)}} \int d\Pi_1 d\Pi_2 d\Pi_3 d\Pi_4 \delta^4(P_1 + P_2 - P_3 - P_4) (2\pi)^4 e^{-(E_1 + E_2)/T} |\mathcal{M}|^2, \quad (1.95)$$

with  $d\Pi_i \equiv \frac{d^3 \vec{p}_i}{(2\pi)^3 2E_i}$ . Eq. (1.94) can be interpreted straightforwardly. The l.h.s. of the equation is of the order  $n_1 H$ , while the r.h.s. is of the order  $n_1 n_2 \langle \sigma v \rangle$ . Therefore, if the interaction rate  $\Gamma_1 = n_2 \langle \sigma v \rangle$  is much bigger than the Hubble rate  $H$ , the term in parenthesis in Eq. (1.94) needs to vanish,

$$\left. \frac{n_1 n_2}{n_3 n_4} \right|_{\text{eq}} = \frac{n_1^{(0)} n_2^{(0)}}{n_3^{(0)} n_4^{(0)}}. \quad (1.96)$$



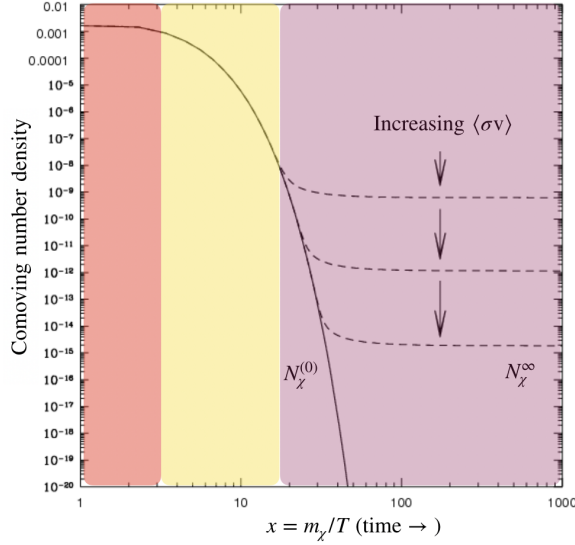


**Figure 1.9** – Schematic view of dark matter freeze-out. A comoving density is plotted against  $m_\chi/T$ . The red region corresponds to a time when annihilations and pair productions compensate. The yellow region, a time when pair productions become inefficient. The purple region, a time when annihilations stop due to the cosmic expansion. Adapted from [D. HOOPER \(2008\)](#)

This is an alternative way of expressing chemical equilibrium, and it is often referred to as the *Saha equation*. When  $\Gamma_1$  drops below  $H$ , the r.h.s. of Eq. (1.94) goes to zero, and the comoving number density  $n_1 a^3$  approaches a constant value.

Let us now apply Eq. (1.94) to the case of WIMP dark matter. The standard scenario considers that the dark matter particle  $\chi$  and its antiparticle  $\bar{\chi}$  are initially in chemical equilibrium with light SM fermions  $f$  and antifermions  $\bar{f}$  through annihilation processes



We assume there's no particle-antiparticle asymmetry for the dark matter particles (*i.e.*  $\mu_\chi = 0$  initially), so that  $n_\chi = n_{\bar{\chi}}$  and  $n_\chi^{(0)} = n_{\bar{\chi}}^{(0)}$ . In addition, we assume that the fermions are in chemical and kinetic equilibrium with the rest of the plasma (*i.e.*  $\mu_f = -\mu_{\bar{f}}$  is always satisfied), meaning that  $n_f n_{\bar{f}} = n_f^{(0)} n_{\bar{f}}^{(0)}$ . Then, the Boltzmann equation for  $n_\chi$  reads

$$a^{-3} \frac{d(n_\chi a^3)}{dt} = -\langle\sigma v\rangle \left( n_\chi^2 - (n_\chi^{(0)})^2 \right) \quad (1.98)$$

It is convenient to express the previous equation in terms of a comoving density  $N_\chi \equiv n_\chi/T^3$  and the time variable  $x \equiv m_\chi/T$ ,

$$\frac{dN_\chi}{dx} = -\frac{\lambda}{x^2} \left( N_\chi^2 - (N_\chi^{(0)})^2 \right), \quad \text{where } \lambda \equiv \frac{m_\chi^3 \langle\sigma v\rangle}{H(m_\chi)}. \quad (1.99)$$

We will take  $\lambda$  as a constant, since many theories predict the so-called *s*-wave annihilation channels, where  $\langle\sigma v\rangle$  is independent of temperature. In general, Eq. (1.99) needs to be solved numerically. In Fig. 1.9 we show the qualitative aspect of the solution. We see that the Boltzmann equation correctly predicts the transition from

the exponentially suppressed  $N_\chi^{(0)}$  to the *relic constant value* of  $N_\chi^\infty \equiv N_\chi(x_f \rightarrow \infty)$ <sup>15</sup>. This happens soon after the freeze-out temperature  $x_f$  defined by  $n_\chi(x_f)\langle\sigma v\rangle = H(x_f)$ , which one can show is of the order  $x_f \sim 10$ . Assuming that  $N_\chi(x > x_f) \gg N_\chi^{(0)}$  and that  $N_\chi^\infty \ll N_\chi(x_f)$ , we can analytically solve Eq. (1.99) to estimate the value of the  $N_\chi^\infty$ ,

$$N_\chi^\infty \simeq \frac{x_f}{\lambda}. \quad (1.100)$$

The relic density is inversely proportional to the cross section  $\langle\sigma v\rangle$ , which makes sense intuitively, since the larger the interaction rate is, the longer the particles stay in the exponentially suppressed regime. Using this result, it is possible to compute the present CDM abundance, and one notices that in order to reproduce the observed value  $\Omega_{\text{cdm}}h^2 \sim 0.1$ , a cross-section of roughly  $\langle\sigma v\rangle \simeq 2.6 \times 10^{-9} \text{ GeV}^{-2} \simeq 3 \times 10^{-26} \text{ cm}^3\text{s}^{-1}$  is required (see DODELSON (2003) for details). This is precisely the value we expect from a new particle in the 100 GeV mass range that interacts via the weak force. The fact that such a simple production mechanism leads to the right DM abundance, and the required energy scale corresponds to the one that can be currently probed at colliders, is what is known as *the WIMP miracle*.

As we already said, the Boltzmann equation in the form of Eq. (1.94) has many interesting applications beyond WIMP freeze-out, such as BBN or hydrogen recombination, that we are going to introduce in the following subsections.

### 1.5.5 Big-Bang Nucleosynthesis

We briefly discuss here the formation of the light elements during the first few minutes in the history of the universe. This is one of the pillars of the standard Big-Bang model, and the earliest cosmological probe to which we have access. In general, BBN has to be described through a complicated system of coupled Boltzmann equations, in order to track all nuclear abundances (WAGONER et al. 1967; M. S. SMITH et al. 1993). However, with very simple tools it is possible to get an analytical estimate of the  ${}^4\text{He}$  fraction, which is the most abundant nucleus that is formed during this epoch. That's the goal of this subsection.

The starting point to describe BBN is to consider temperatures slightly above  $T \sim 1 \text{ MeV}$ , when the primordial soup was full of relativistic electrons, positrons and neutrinos, as well as small traces of non-relativistic baryons (including free protons and neutrons). Firstly, we determine the relative abundances of protons and neutrons. At those temperatures, protons and neutrons were coupled by weak interactions of the type



We can compute the neutron to proton ratio  $n_n/n_p$  using the non-relativistic profile in Eq. (1.77). Notice that protons and neutrons share the same baryon number ( $\mathcal{B} = +1$ ) so the associated chemical potential is also equal,  $\mu_n = \mu_p = \mu_{\mathcal{B}}$ . Therefore,

$$\left. \frac{n_n}{n_p} \right|_{\text{eq}} = \frac{n_n^{(0)}}{n_p^{(0)}} = \left( \frac{m_n}{m_p} \right)^{3/2} e^{-\Delta m/T} \simeq e^{-\Delta m/T}, \quad (1.103)$$

<sup>15</sup>In terms of chemical potentials, the PSD of the dark matter has evolved from  $f_\chi = e^{-E_\chi/T}$  initially to  $f_\chi = e^{\mu_\chi^\infty/T} e^{-E_\chi/T}$  after chemical decoupling, where  $\mu_\chi^\infty(T)$  satisfies  $e^{\mu_\chi^\infty/T} = n_\chi^\infty/n_\chi^{(0)}$ .

where  $\Delta m \equiv m_n - m_p \simeq 1.3$  MeV. It is useful to express the previous result in terms of the free neutron fraction,  $X_n \equiv n_n/n_b$ , where the baryon abundance at that time was roughly  $n_b \simeq n_n + n_p$ . Then,

$$X_n^{\text{eq}} = \frac{e^{-\Delta m/T}}{1 + e^{-\Delta m/T}}. \quad (1.104)$$

Initially  $T \gg \Delta m$ , so there are as many neutrons as protons ( $X_n = 1/2$ ). Later, when  $T \ll \Delta m$ , the neutron abundance becomes exponentially smaller. However, we saw already in Sect. 1.5.3 that weak interactions switch off at around  $T_D \sim 1$  MeV, although a more accurate computation gives a value of  $T_D \simeq 0.8$  MeV. We can take the equilibrium neutron fraction at this temperature  $T_D$  as a proxy for the neutron fraction at freeze-out,  $X_n^\infty \sim X_n^{\text{eq}}(T_D)$  (the precise calculation of  $X_n^\infty$  would require solving the Boltzmann equation). In reality, the neutron fraction keeps evolving even after freeze-out, because neutrons decay to protons through the weak decay  $n \rightarrow p^+ + e^- + \bar{\nu}_e$ . The neutron lifetime ( $\tau_n \simeq 890$  s) is comparable with the age of the universe at that time, so this should be taken into account. Putting all together, the neutron fraction for  $T < T_D$  reads

$$X_n(t) \simeq X_n^{\text{eq}}(T_D)e^{-t/\tau_n}. \quad (1.105)$$

At this point,  ${}^4\text{He}$  still cannot form since reactions involving three or more incoming particles are very rare. The first nucleus that can form is deuterium through



Once deuterium is produced, two-particle reactions allow  ${}^4\text{He}$  and other heavier nuclei to be sequentially built from lighter ones,



Let us focus on deuterium production. We can apply the Saha condition in Eq. (1.96) to the process in Eq. (1.106), and use that photons satisfy  $n_\gamma = n_\gamma^{(0)}$ , to get the following ratio at chemical equilibrium

$$\left. \frac{n_D}{n_p n_n} \right|_{\text{eq}} = \frac{n_D^{(0)}}{n_p^{(0)} n_n^{(0)}} = \frac{3}{4} \left( \frac{4\pi}{m_p T} \right) e^{B_D/T}, \quad (1.109)$$

where  $B_D \equiv m_n + m_p - m_D = 2.22$  MeV is the deuterium binding energy, and we used  $m_D \simeq 2m_n$  in the prefactor, as well as  $g_D = 3$ ,  $g_p = g_n = 2$ . To get an order of magnitude, we can approximate the neutron abundance as  $n_n^{(0)} \sim n_b = \eta n_\gamma$  (since  $X_n$  was not much smaller than 1 at the time) and apply Eq. (1.75) to compute  $n_\gamma$ . This yields

$$\frac{n_D^{(0)}}{n_p^{(0)}} \simeq \eta \left( \frac{T}{m_p} \right)^{3/2} e^{B_D/T}. \quad (1.110)$$

Because of the smallness of  $\eta$ , temperature needs to decrease well below  $B_D$  in order for deuterium to form in significant amounts. Thus, heavier elements cannot be formed until deuterium is produced, even if they have larger binding energies. This is the so called *deuterium bottleneck*. The temperature of formation of these elements can

hence be estimated as the temperature  $T_{\text{BBN}}$  at which the ratio in Eq. (1.110) is equal to 1. Setting  $n_D^{(0)}/n_p^{(0)} = 1$  in Eq. (1.110) gives <sup>16</sup>

$$T_{\text{BBN}} \simeq 0.06 \text{ MeV} \longrightarrow t_{\text{BBN}} \simeq 340 \text{ s}. \quad (1.111)$$

After  $t_{\text{BBN}}$ ,  ${}^4\text{He}$  is produced almost immediately, given that its binding energy ( $B_{\text{He}} = 7.1$  MeV per nucleon) is much larger than the one of deuterium. We can thus assume that effectively all remaining neutrons at  $t \sim t_{\text{BBN}}$  are incorporated into  ${}^4\text{He}$ . Since each  ${}^4\text{He}$  nucleus contains 2 neutrons,  $n_{\text{He}}^{\text{tot}} = \frac{1}{2}n_n(t_{\text{BBN}})$  <sup>17</sup>, or equivalently,

$$f_{\text{He}} \equiv \frac{n_{\text{He}}^{\text{tot}}}{n_{\text{H}}^{\text{tot}}} \simeq \frac{\frac{1}{2}n_n(t_{\text{BBN}})}{n_p} = \frac{\frac{1}{2}X_n(t_{\text{BBN}})}{1 - X_n(t_{\text{BBN}})} \sim \frac{1}{16}, \quad (1.112)$$

where we used Eq. (1.105) to compute  $X_n(t_{\text{BBN}})$ . Traditionally, this result is expressed as the mass fraction of  ${}^4\text{He}$ , which is formally defined as

$$Y_p \equiv \frac{\rho_{\text{He}}^{\text{tot}}}{\rho_b}. \quad (1.113)$$

We can take  $\rho_b \simeq \rho_{\text{He}}^{\text{tot}} + \rho_{\text{H}}^{\text{tot}}$  (notice that the abundances of the rest of nuclei produced during BBN, like  $D$ ,  ${}^3\text{He}$  or  ${}^7\text{Li}$ , are too small to have any cosmological impact). In addition,  $\rho_{\text{H}}^{\text{tot}} \simeq m_{\text{H}}n_{\text{H}}^{\text{tot}}$  and  $\rho_{\text{He}}^{\text{tot}} \simeq m_{\text{He}}n_{\text{He}}^{\text{tot}}$ , where  $m_{\text{He}} \simeq 4m_{\text{H}}$ . Hence,

$$Y_p \simeq \frac{4f_{\text{He}}}{1 + 4f_{\text{He}}} \sim 0.2. \quad (1.114)$$

The result of the full Boltzmann calculation yields  $Y_p \simeq 0.24$ , which is not too far from the very rough estimate of Eq. (1.114). This prediction is in excellent agreement with current observations, as can be seen in Fig. 1.10. This constitutes one of the major triumphs of the standard cosmological model. Notice that Fig. 1.10 shows the predicted element abundances in terms of the baryon-to-photon ratio  $\eta$  (or equivalently,  $\Omega_b$ ), which in the standard case constitutes the only free parameter of BBN. More generally, BBN physics are also very sensible to the extra number neutrino species  $\Delta N_{\text{eff}}$  and many other deviations from the standard cosmological model, such as exotic electromagnetic energy injection or variations of fundamental constants. It is thus a very powerful probe to constrain new physics (POSPELOV et al. 2010).

As we will discuss in the following subsection, the value of  $Y_p$  has a non-negligible impact on recombination and thus on the shape of the CMB spectra. Additionally, the value of  $\Omega_b$  that is inferred from CMB analysis affects the prediction of  $Y_p$ . Therefore, in order to determine the value of  $Y_p$  self-consistently, the **CLASS** code reads a table produced with the BBN code **ParthENoPE** (PISANTI et al. 2008), that gives  $Y_p$  as a function of  $\Omega_b$  and  $N_{\text{eff}}$ .

<sup>16</sup>To convert BBN temperature to BBN time, it suffices to integrate Eq. (1.85),

$$\frac{T}{1 \text{ MeV}} \simeq 1.5g_*^{-1/4} \left( \frac{1 \text{ s}}{t} \right)^{1/2},$$

and apply  $g_* = 3.38$  (see Fig. 1.8).

<sup>17</sup>We use the superscript “tot” to indicate the total  $H$  and  ${}^4\text{He}$  in the universe, which initially are only in ionized forms ( $n_{\text{H}}^{\text{tot}} = n_p$  and  $n_{\text{He}}^{\text{tot}} = n_{\text{He}}^{++}$ ), but will be gradually converted into neutral atoms during the recombination era, that we discuss in the following section.

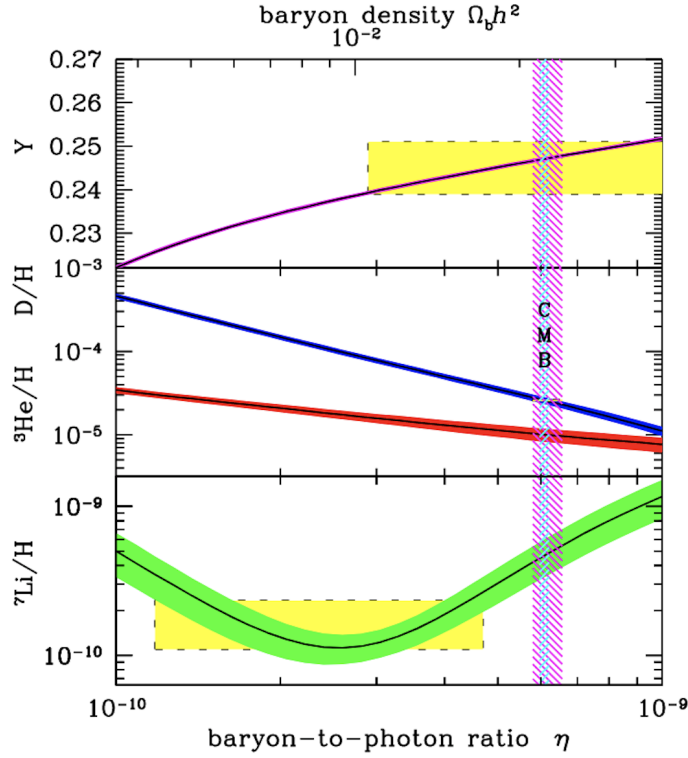


**Figure 1.10** – Predicted primordial abundances of  ${}^4\text{He}$ ,  $D$ ,  ${}^3\text{He}$  and  ${}^7\text{Li}$  as a function of  $\eta$  or  $\Omega_b$ . The colored bands indicate theoretical 95 % CL uncertainty. Yellow boxes indicate observed element abundances. The narrow vertical band indicates the CMB measurement on  $\Omega_b$  from [ADE et al. 2016a](#) – hereafter referred to as [Planck15](#). Taken from [TANABASHI et al. \(2018\)](#)

### 1.5.6 Hydrogen recombination

We focus here on the recombination<sup>18</sup> between electrons and protons to form neutral hydrogen. As we will see later, a precise knowledge of the recombination history is essential to understand the shape of the CMB anisotropy spectra.

#### Saha equilibrium

At temperatures above 1 eV, the universe consisted in a plasma of free electrons, free protons and light nuclei such as helium. Photons were strongly coupled to electrons through Compton scattering  $e^- + \gamma \leftrightarrow e^- + \gamma$ , whereas electrons and protons were coupled via Coulomb scattering  $e^- + p^+ \leftrightarrow e^- + p^+$ . There was very little hydrogen at that epoch: temperature needs to drop well below the binding energy of hydrogen  $H$  until recombination can happen. To see why, let's consider the following process in chemical equilibrium



We labelled the ground state  $1s$  for hydrogen, since we will discuss excited states later.

It is possible to get an estimate of the time of recombination thanks to the Saha condition [Eq. \(1.96\)](#). We take into account that protons, electrons and hydrogen have

<sup>18</sup>The term *recombination* is misleading: this is the first time electrons and nuclei combined.

a non-relativistic profile, given that  $m_H, m_p, m_e \gg T_b$  (here  $T_b$  is the temperature of the baryon fluid, which is equal to the photon temperature if photons and baryons are in kinetic equilibrium,  $T_b = T$ ). We can write

$$\left. \frac{n_{H,1s}}{n_e n_p} \right|_{\text{eq}} = \frac{n_{H,1s}^{(0)}}{n_e^{(0)} n_p^{(0)}} = \frac{g_{H,1s}}{g_e g_p} \left( \frac{m_H}{m_e m_p} \frac{2\pi}{T} \right)^{3/2} e^{(m_p + m_e - m_H)/T}. \quad (1.116)$$

In the prefactor of Eq. (1.116) we can approximate  $m_H \simeq m_p$ , but in the exponential the difference between  $m_p + m_e$  and  $m_H$  is crucial: it is the binding energy of hydrogen,  $\varepsilon_0 = m_p + m_e - m_H = 13.6$  eV. The number of internal degrees of freedom are  $g_{H,1s} = 4$  and  $g_p = g_e = 2$ . At this stage, it is useful to introduce the *free electron fraction*,

$$X_e \equiv \frac{n_e}{n_H^{\text{tot}}} = \frac{n_e}{n_p + n_{H,1s}}, \quad (1.117)$$

*i.e.*, it is the ratio of free electrons to total hydrogen, both in ionized and neutral form. As a consequence of the neutrality of the universe, we have  $n_e \simeq n_p$  (we are neglecting some small amount of ionized helium in the r.h.s. of this equation). Using the definition of the  ${}^4\text{He}$  mass fraction (*c.f.* Eq. (1.113)), we can write the total hydrogen density in terms of baryon density as  $n_H^{\text{tot}} = n_b - 4n_{\text{He}}^{\text{tot}} = n_b(1 - 4m_H n_{\text{He}}^{\text{tot}}/(m_H n_b)) \simeq n_b(1 - Y_p)$ . Bearing all of this in mind, we can recast Eq. (1.116) in terms of  $X_e$ ,

$$\left. \frac{X_e^2}{1 - X_e} \right|_{\text{eq}} = \frac{1}{\eta(1 - Y_p)} \left( \frac{m_e}{T} \right)^{3/2} \frac{\sqrt{\pi}}{2^{5/2} \zeta(3)} e^{-\varepsilon_0/T}, \quad (1.118)$$

where we used  $n_b = \eta n_\gamma$ , and applied Eq. (1.75) to compute  $n_\gamma$ . We see that, when  $T \sim \varepsilon_0$ , the r.h.s. of Eq. (1.118) is of order  $10^9 (m_e/T)^{3/2} \sim 10^{15}$ . Thus, the denominator at the l.h.s. needs to be very close to zero, *i.e.* almost all hydrogen is still ionized,  $X_e \simeq 1$ . This is because the number of photons compared to baryons is so high, that even for  $T < \varepsilon_0$  the high-energy tail of the photon distribution still contains many ionizing photons with  $E > \varepsilon_0$ . In fact, we can use Eq. (1.118) to estimate the temperature  $T_{\text{rec}}$  at which  $X_e = 0.1$  (this could serve as a definition of recombination temperature), to get

$$T_{\text{rec}} \simeq 0.3 \text{ eV} \simeq 3600 \text{ K}. \quad (1.119)$$

Using  $T_{\text{rec}} = T_0(1 + z_{\text{rec}})$ , this leads to a recombination redshift of around  $z_{\text{rec}} \sim 10^3$ .

One could now compute the time at which photons decoupled from the plasma, or in other words, the time of last scattering. For this, it would suffice to compare the photon scattering rate  $\Gamma_\gamma \sim \sigma_T n_b X_e$  (where  $\sigma_T \simeq 2 \times 10^{-3} \text{ MeV}^{-2}$  is the Thomson cross-section) with the Hubble rate,  $H = H_0 \sqrt{\Omega_m} (T/T_0)^{3/2}$ . This procedure yields a value of the order  $z_{\text{dec}} \sim 10^3$ , indicating that photon decoupling took place around recombination. In Sect. 1.6.5, we will give a more precise definition of  $z_{\text{dec}}$  as the maximum of the visibility function.

Even if the Saha equation gives a correct estimate of the time of recombination, it fails at predicting the residual amount of free electrons at later times. To track accurately the evolution of  $X_e$ , we need to apply the Boltzmann equation. Using Eq. (1.94) for the electron density  $n_1 = n_e$  gives

$$a^{-3} \frac{d(n_e a^3)}{dt} = - \langle \sigma v \rangle \left( n_e^2 - \frac{n_e^{(0)} n_p^{(0)}}{n_{H,1s}^{(0)}} n_{H,1s} \right), \quad (1.120)$$



It is more convenient to rewrite Eq. (1.120) in terms of the free electron fraction  $X_e$ . Using Eq. (1.116) and Eq. (1.117), we obtain

$$\frac{dX_e}{dt} = (1 - X_e)\beta - \alpha n_H^{\text{tot}} X_e^2, \quad (1.121)$$

where  $\beta$  and  $\alpha$  denote the photoionization and recombination rates,

$$\beta \equiv \alpha \left( \frac{m_e T_b}{2\pi} \right)^{3/2} e^{-\varepsilon_0/T_b}, \quad \alpha \equiv \langle \sigma v \rangle \quad (1.122)$$

However, Eq. (1.121) is still an incomplete description of the recombination process, as we shall see. The first compelling model of recombination was developed by ZELDOVICH et al. (1968) and PEEBLES (1968), that we briefly discuss in the following.

### The effective three-level model

This recombination model assumes that hydrogen can be in three different states

1. Hydrogen in the ground state  $1s$ , ( $n_{H,1s}$ ).
2. Hydrogen in the excited states, mostly  $2p$  or  $2s$  ( $n_{H,2l}$ ).
3. Ionized hydrogen ( $n_p \simeq n_e$ ).

This is schematically depicted in the left panel of Fig. 1.11. If the different atomic levels of hydrogen are in kinetic equilibrium between each other, they obey a simple relation

$$\frac{n_{H,n'l'}}{n_{H,n}} \Big|_{\text{eq}} = \frac{(2l'+1)}{n^2} e^{-(E_{n'}-E_n)/T}, \quad (1.123)$$

where  $n_{H,n} = \sum_{l=0}^{n-1} n_{H,nl}$  and  $E_n = -\varepsilon_0/n^2$  are the corresponding energies of each atomic level.

The first important thing to note is that recombination to the ground state ( $n = 1$ ) is very inefficient, since the emitted photon has enough energy to reionize another neutral hydrogen atom, leaving  $X_e$  unaffected. Indeed, the cross section for absorption of photons just above 13.6 eV is  $\sigma_{\text{pi}} \simeq 6 \times 10^{-18} \text{ cm}^2$  (C. HIRATA 2006), while the total density of hydrogen is around  $n_H^{\text{tot}} = (1 - Y_p)\eta n_\gamma \sim 200[(1+z)/1000]^3 \text{ cm}^{-3}$  (we temporarily restore I.S. units). The typical time before a photon is reabsorbed is thus of order

$$t_{\text{reabs}} \sim \frac{1}{n_H^{\text{tot}} x_{1s} \sigma_{\text{pi}} c} \sim \frac{10^4}{x_{1s}} \left( \frac{1000}{1+z} \right)^3 \text{ s}, \quad (1.124)$$

where  $x_{1s} \equiv n_{H,1s}/n_H^{\text{tot}}$ . We see that around recombination, and as long as  $x_{1s} > 10^{-9}$ , this reabsorption time is much smaller than the typical expansion time,  $t_H = 1/H = \Omega_m^{-1/2} H_0^{-1} (1+z)^{-3/2} \sim 10^{13} \text{ s}$ . Hence, efficient recombination only happens when electrons initially get captured into an excited state  $n \geq 2$ . In this case, the population of the  $n = 2$  states are suppressed with respect to  $n = 1$  states by a factor  $e^{-3\varepsilon_0/4T} \sim 10^{-17}$  (according to Eq. (1.123)), so there is no reabsorption problem. Therefore, the  $\alpha$  factor in Eq. (1.121) has to be replaced by the so called *case B recombination rate*,

$$\alpha_B = \sum_{n=2}^{\infty} \sum_{l=0}^{n-1} \langle \sigma_{[p+e \rightarrow H(nl)+\gamma]} v \rangle. \quad (1.125)$$

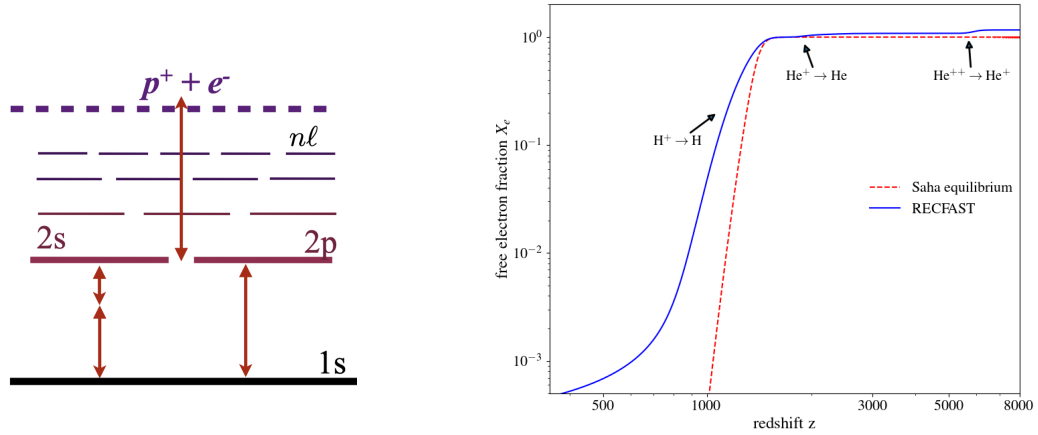


**Figure 1.11 – Left panel:** Schematic view of the three-level model of recombination. Taken from [https://cosmo.nyu.edu/yacine/teaching/cmb\\_fudan/lecture\\_2\\_yah.pdf](https://cosmo.nyu.edu/yacine/teaching/cmb_fudan/lecture_2_yah.pdf). **Right panel:** Evolution of the free electron fraction, computed using either the Saha equation in Eq. (1.118) or the **RECFAST** code. We note that **RECFAST** also takes into account the two Helium recombinations. We have assumed  $Y_p = 0.24$  and  $\Omega_b = 0.049$ .

This process is then followed by a fast radiative cascade to  $n = 2$ . The resulting excited hydrogen atom could subsequently reach the ground state in a much slower decay, through one of the following processes:

$$H(2s) \longleftrightarrow H(1s) + \gamma + \gamma, \quad (1.126)$$

$$H(2p) \longleftrightarrow H(1s) + \gamma_{Ly\alpha}. \quad (1.127)$$

The two-photon decay process has a rate  $\Lambda_{2\gamma} \simeq 8.2 \text{ s}^{-1}$ , and neither of the emitted photons has enough energy to excite another hydrogen atom. On the contrary, the emitted Lyman- $\alpha$  photons are usually re-absorbed by other hydrogen atoms, since the optical depth for these photons during recombination is very large. This effectively delays recombination. However, expansion eventually redshifts the Lyman- $\alpha$  photons off the resonance, so that they can no longer be re-absorbed by other atoms. This is characterized by the quantity  $\Lambda_\alpha \equiv \frac{H\omega_{Ly\alpha}^3}{\pi^2 n_H^{\text{tot}}(1-X_e)}$  (where  $\hbar\omega_{Ly\alpha} = 3\varepsilon_0/4$  is the Lyman- $\alpha$  energy), which gives the net  $2p \rightarrow 1s$  transition rate accounting for re-absorptions. To properly include all those effects, the r.h.s. of Eq. (1.121) gets an additional factor (see C. HIRATA (2006) for a proof),

$$C = \frac{\Lambda_\alpha + \Lambda_{2\gamma}}{\Lambda_\alpha + \Lambda_{2\gamma} + 4\beta_B}, \quad (1.128)$$

where  $\beta_B = \alpha_B \left(\frac{m_e T_b}{2\pi}\right)^{3/2} e^{-\varepsilon_0/4T_b}$  is the photoionization rate from  $n = 2$ . We see that  $C$  gives the probability for an electron in the excited  $n = 2$  state to reach the ground state before being ionized. The equation describing the evolution of  $X_e$  then reads

$$\frac{dX_e}{dz} = -\frac{C}{(1+z)H} \left[ (1-X_e)\alpha_B \left(\frac{m_e T_b}{2\pi}\right)^{3/2} e^{-\varepsilon_0/T_b} - \alpha_B n_H^{\text{tot}} X_e^2 \right]. \quad (1.129)$$

Given that the recombination rate per free electron  $C\alpha_B n_H^{\text{tot}} X_e$  is always much smaller than  $H$ , this model predicts that recombination happens much slower than in Saha



equilibrium. In addition, it gives a non-zero freeze-out electron fraction of  $X_e^\infty \sim 10^{-4}$ .

### Evolution of the baryon temperature

So as to complete the description of recombination, we need to track not only the free electron ratio  $X_e$ , but also the baryon temperature  $T_b$ , which enters in several places in Eq. (1.129). The assumption  $T_b = T$  is valid in the early universe, but it ceases to be true at later times. The evolution of matter temperature receives two main contributions (C. HIRATA 2006)

$$\frac{dT_b}{dz} = \underbrace{\frac{2T_b}{1+z}}_{\text{adiabatic}} + \underbrace{\frac{1}{(1+z)H} \frac{8\sigma_T a_r T^4}{3m_e c} \frac{X_e}{1+f_{\text{He}}+X_e} (T_b - T)}_{\text{Compton scattering}} = \frac{1}{1+z} [2T_b + \gamma(T_b - T)]. \quad (1.130)$$

Here we introduced the dimensionless parameter

$$\gamma \equiv \frac{X_e}{1+f_{\text{He}}+X_e} \frac{8\sigma_T a_r T^4}{3Hm_e}, \quad (1.131)$$

where  $a_r = 4\sigma_B/c = \pi^2 k_B^4 / (15\hbar^3 c^3)$  is the radiation constant. The first term in Eq. (1.130) simply describes the effect of the cosmic expansion, while the second one describes the Compton scattering between CMB photons and the gas. Initially  $\gamma \gg 1$ , so the second term dominates and Compton interactions couple baryons to radiation, so that  $T_b = T \propto a^{-1}$ . Later on, the  $\gamma$  factor decreases until becoming very suppressed (at a redshift of around  $z \sim 150$ ), time after which baryons start to cool down adiabatically,  $T_b \propto a^{-2}$ . The gas temperature will eventually increase again in the reionization era, due to the ionizing radiation emitted by the first stars and galaxies.

### Modern recombination codes

It was realized by the end of the 90s that the upcoming high-precision CMB data from the *Planck* satellite was going to require to compute the recombination history with a  $\sim 0.1\%$  precision. Thus, many improvements have been added to the three-level model in the last years, such as:

- Following not only  $n = 2$ , but a virtually infinite number of excited levels.
- Computing accurately the radiative transfer in the Lyman- $\alpha$  line.
- Including Helium recombination.

These corrections have been implemented approximately in the code **RECFAST** (SEAGER et al. 1999), which adds some fudge factors to Eq. (1.129) to match a complicated multilevel calculation, and exactly in the more sophisticated codes **HYREC** (ALI-HAIMOUD et al. 2011) and **COSMOREC** (CHLUBA et al. 2011). The three recombination codes are currently implemented in **CLASS**. In the right panel of Fig. 1.11, we show the evolution of the free electron fraction using both the Saha equilibrium condition in Eq. (1.118) and the more advanced calculation with **RECFAST**.

As a side note, **RECFAST** also includes the first and second Helium recombinations,  $\text{He}^{++} \rightarrow \text{He}^+$  and  $\text{He}^+ \rightarrow \text{He}$ , whose binding energies are respectively given by  $\varepsilon_{\text{He}^{++}} =$

$4\varepsilon_0 = 54.4$  eV and  $\varepsilon_{\text{He}^+} = 24.6$  eV. Since these energies are higher than the H binding energy  $\varepsilon_0$ , He recombines first. The first He recombination (happening between  $5000 \leq z \leq 8000$ ) can be safely described by Saha equilibrium, while the second He recombination requires a more careful treatment. Therefore, **RECFAST** actually solves for three variables (coupled between each other): the proton fraction  $X_p \equiv n_p/n_H^{\text{tot}}$ , the singly-ionized He fraction  $X_{\text{He}^+} \equiv n_{\text{He}^+}/n_{\text{He}}^{\text{tot}}$  (where  $n_{\text{He}}^{\text{tot}} = n_{\text{He}} + n_{\text{He}^+} + n_{\text{He}^{++}}$ ), and the baryon temperature  $T_b$ . From the neutrality condition  $n_e = n_p + n_{\text{He}^+} + 2n_{\text{He}^{++}}$ , we see that the free electron fraction is given by

$$X_e = X_p + f_{\text{He}}(X_{\text{He}^+} + 2X_{\text{He}^{++}}), \quad (1.132)$$

where  $f_{\text{He}} \simeq Y_p/(4(1 - Y_p))$  (c.f. Eq. (1.114)). Eq. (1.132) tells us that, even when hydrogen still hasn't recombined ( $X_p = 1$ ), we can still have  $X_e > 1$  due to He recombinations not being completed yet ( $X_{\text{He}^+} \neq 0$  and  $X_{\text{He}^{++}} \neq 0$ ). This explains the small bumps that can be seen in  $X_e$  at high  $z$  in the right panel of Fig. 1.11.

### Reionization

A few hundred million years after recombination, the first stars and galaxies were born. Around these objects, bubbles of ionized plasma formed due to the emitted ultraviolet radiation. Over time, these bubbles grew and eventually overlapped, leaving the IGM fully ionized again (except for some small traces of neutral hydrogen).

As opposed to what happens with recombination, the details of this epoch of reionization are very poorly understood, both at the theoretical and observational level. The best probe that we have nowadays comes from the optical spectra of very distant quasars, such as the one we show in Fig. 1.12. The Lyman- $\alpha$  absorption lines in these spectra are a very good indicator of the presence of neutral hydrogen. If a quasar from the epoch of reionization shines photons with  $\lambda < \lambda_{\text{Ly}\alpha} = 121.57$  nm, then these photons get stretched due to the cosmic expansion, until reaching  $\lambda = \lambda_{\text{Ly}\alpha}$  and being absorbed by the neutral hydrogen in the surrounding medium. This leads to the so-called Gunn-Peterson (GP) trough, which was predicted in 1965 (GUNN et al. 1965). The GP trough has been observed only in the spectra of quasars located at  $z \gtrsim 6$  (BECKER et al. 2015), indicating that the universe had to be completely reionized below this redshift. Notice that photons reaching  $\lambda = \lambda_{\text{Ly}\alpha}$  after the end of reionization can still be absorbed, due to encounters with individual clouds of neutral hydrogen along their path. This produces a jagged region in the quasar spectra that is known as *the Lyman- $\alpha$  forest*.

Observations of the CMB can also probe the EoR. The increase in  $X_e(z)$  at low redshifts enhances the scattering rate between photons and electrons, which leads to peculiar patterns in the temperature and polarization spectra (as we will discuss in Sect. 1.6.5). The CMB spectra are primarily sensitive to the column density of electrons along the line of sight, and therefore to the *optical depth at reionisation*, defined by

$$\tau_{\text{reio}} \equiv \int_0^{z_{\text{reio,start}}} X_e(z) n_H^{\text{tot}}(z) \sigma_T \frac{dt}{dz} dz, \quad (1.133)$$

where  $z_{\text{reio,start}}$  is the redshift at the beginning of reionization. For reionization histories centered around  $z \sim 6 - 7$  (as expected from GP measurements), the predicted  $\tau_{\text{reio}}$  is rather small, in agreement with the values recently reported by Planck18. Because of the large theoretical uncertainties associated with the EoR and the fact that the CMB

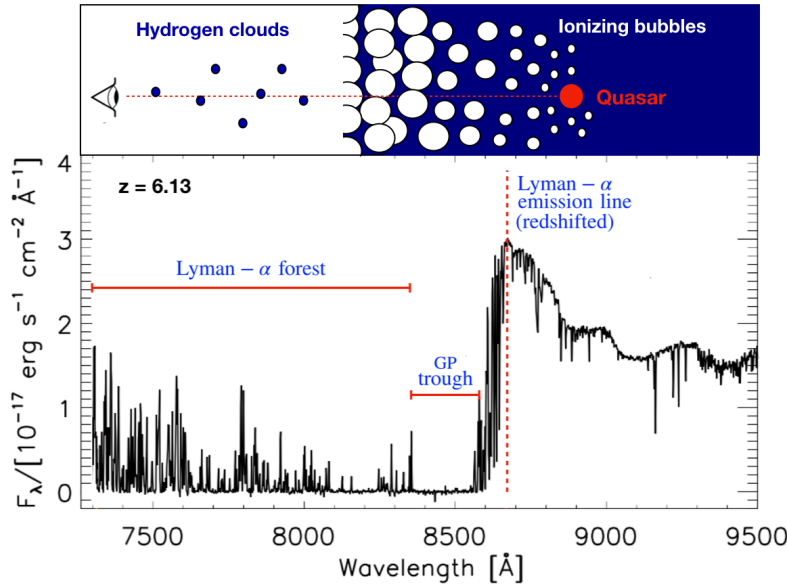


**Figure 1.12** – Optical spectra of quasar ULAS J1319+0959 at  $z = 6.13$ , accompanied by a pictorial description of the reionization process. The image has been adapted from Figure 1 in BECKER et al. (2015).

is not very sensitive to the details of reionization, Boltzmann codes usually adopt parametrizations, that interpolate a low  $X_e$  at high- $z$  to a  $X_e \sim 1$  at low- $z$ . The most common parametrization and the one used in **CLASS** by default is

$$X_e(z) = \frac{1 + f_{\text{He}}}{2} \left[ 1 + \tanh \left( \frac{y(z_{\text{reio}}) - y(z)}{\Delta y} \right) \right], \quad (1.134)$$

where  $y = (1+z)^{3/2}$  and  $\Delta y = \frac{3}{2}(1+z_{\text{reio}})^{1/2}\Delta z$ , with  $\Delta z = 0.5$ . With this parametrisation, there is a one-to-one relation between the mid-point redshift of reionisation  $z_{\text{reio}}$  and  $\tau_{\text{reio}}$ . For other parametrisations or approaches to model reionization sources, we refer to POULIN (2017). There is a current effort in planning and building instruments to observe the 21-cm hyperfine line of neutral hydrogen, such as HERA (ABDURASHIDOVA et al. 2022) or SKA (BARRY et al. 2021) radio interferometers. These observations promise to open a new window onto the dark ages and the beginning of reionization.

## 1.6 The linearly perturbed universe

Until now, we have been considering the universe as perfectly isotropic and homogeneous. However, to understand the pattern of temperature and polarization fluctuations of the CMB, or how the primordial fluctuations eventually formed all the large-scale structures, we need to introduce anisotropies and inhomogeneities. We can treat them in *linear perturbation theory* as long as these perturbations remain small. This provides an excellent description of the CMB physics, which are mostly determined by processes in the early universe, when over-densities were of the order  $\mathcal{O}(10^{-5})$ . For small scales at small redshift, non-linear effects become important, and perturbation theory needs to be replaced by more complicated descriptions, such as N-body simulations.

The basic idea of cosmological perturbation theory is to decompose all relevant quantities into spatial averages (from now on, denoted by an overline) plus a linear perturbation,

$$g_{\mu\nu}(\tau, \vec{x}) = \bar{g}_{\mu\nu}(\tau) + \delta g_{\mu\nu}(\tau, \vec{x}), \quad T^\mu{}_\nu(\tau, \vec{x}) = \bar{T}^\mu{}_\nu(\tau) + \delta T^\mu{}_\nu(\tau, \vec{x}). \quad (1.135)$$

Here  $\bar{g}_{\mu\nu}(\tau)$  is the FLRW metric, which for a flat spacetime in cartesian coordinates reads

$$ds^2 = \bar{g}_{\mu\nu} dx^\mu dx^\nu = a(\tau)^2 \left( -d\tau^2 + \delta_{ij} dx^i dx^j \right), \quad (1.136)$$

while  $\bar{T}^\mu{}_\nu(\tau)$  is the stress energy tensor of a perfect fluid that we introduced in Eq. (1.12). We will often switch from real to Fourier space when expressing equations for the perturbations. This is very advantageous, because it will allow to reduce a partial differential equation to several (decoupled) ordinary differential equations, one per mode  $\vec{k}$ . Put another way, in linear theory each mode evolves independently. We will adopt the common practice (not suitable to mathematicians) of calling the variables in real space in the same way as in Fourier space. For instance, the Fourier transform of the density contrast  $\delta(\tau, \vec{x}) \equiv \rho(\tau, \vec{x})/\bar{\rho}(\tau) - 1$  will read

$$\delta(\tau, \vec{x}) = \int \frac{d^3\vec{k}}{(2\pi)^3} \delta(\tau, \vec{k}) e^{i\vec{k}\cdot\vec{x}} \quad \longrightarrow \quad \delta(\tau, \vec{k}) = \int d^3\vec{x} \delta(\tau, \vec{x}) e^{-i\vec{k}\cdot\vec{x}}. \quad (1.137)$$

It is customary to express the perturbed metric components in the following way

$$\delta g_{00} = -2a^2(\tau)A, \quad \delta g_{0i} = a^2(\tau)B_i, \quad \delta g_{ij} = a^2(\tau)H_{ij}, \quad (1.138)$$

where  $A$ ,  $B_i$  and  $H_{ij}$  are generic functions of space and time. On the other hand, perturbing the stress-energy tensor in Eq. (1.12) gives

$$\delta T^\mu{}_\nu = (\delta\rho + \delta P)\bar{U}^\mu\bar{U}_\nu + (\bar{\rho} + \bar{P})(\delta U^\mu\bar{U}_\nu + \bar{U}^\mu\delta U_\nu) + \delta P\delta^\mu{}_\nu + S^\mu{}_\nu. \quad (1.139)$$

The perturbed stress-energy tensor can now receive a contribution from the anisotropic stress tensor  $S^\mu{}_\nu$  (whose non-zero elements are the off-diagonal components of  $\delta T^i{}_j$ ). This can be relevant for some fluids such as neutrinos, as we shall see later. In addition, perturbations can induce non-vanishing energy flux  $T^0{}_j$ , as well as momentum density  $T^i{}_0$ . So as to give an expression for each of the  $\delta T^\mu{}_\nu$  components in Eq. (1.139), we first need to know the expression for the four velocity  $U^\mu = \bar{U}^\mu + \delta U^\mu$ . As we show in App. A.1, it can be written as

$$U^\mu = \frac{1}{a}[1 - A, v^i], \quad (1.140)$$

where  $v^j$  is the coordinate velocity. With this, the covariant four-velocity is easily obtained from  $U_\mu = g_{\mu\nu}U^\nu$ ,

$$U_\mu = a[-(1 + A), v_i + B_i]. \quad (1.141)$$

Inserting Eq. (1.140) and Eq. (1.141) in Eq. (1.139), we arrive at

$$\delta T^0{}_0 = -\delta\rho, \quad \delta T^i{}_0 = -(\bar{\rho} + \bar{P})v^i, \quad \delta T^0{}_j = (\bar{\rho} + \bar{P})(v_j + B_j), \quad \delta T^i{}_j = \delta P\delta^i{}_j + S^i{}_j. \quad (1.142)$$

### Scalar-vector-tensor decomposition

Both tensors  $g_{\mu\nu}$  and  $T_{\mu\nu}$  are symmetric, so in the most general case each one contains 10 degrees of freedom (d.o.f). It was shown in [BARDEEN \(1980\)](#) that these d.o.f. can be decomposed in scalar, vector and tensors (SVT). Here the notion of scalar, vector or tensor is referred to their transformation properties under the group of spatial rotations  $SO(3)$ , which is a symmetry of the FLRW metric. This SVT decomposition is extremely useful, because *Einstein equations for scalars, vectors and tensors don't mix at linear order*. This powerful result is known as *the decomposition theorem*, and a proof can be found in [KNOBEL \(2012\)](#). For  $B_i$  the decomposition is simply

$$B_i = \partial_i B + \hat{B}_i, \quad (1.143)$$

with  $\partial^i \hat{B}_i = 0$  (divergenceless quantities are denoted with hats). For the tensor  $H_{ij}$  the decomposition reads ([STEWART 1990](#)):

$$\begin{aligned} H_{ij} = & 2C\delta_{ij} + 2\left(\partial_i\partial_j - \frac{\delta_{ij}}{3}\nabla^2\right)E \\ & + \left(\partial_i\hat{E}_j + \partial_j\hat{E}_i\right) \quad \text{with } \partial^i\hat{E}_i = 0 \\ & + 2\hat{E}_{ij} \quad \text{with } \partial^i\hat{E}_{ij} = 0 \text{ and } \hat{E}^i_i = 0. \end{aligned} \quad (1.144)$$

Thus we have split the 10 d.o.f. of the metric into:

- 4 scalar d.o.f. corresponding to  $A, B, C, E$ .
- 4 vector d.o.f. corresponding to the independent components of  $\hat{B}_i$  and  $\hat{E}_i$
- 2 tensor d.o.f. corresponding to the independent components of  $\hat{E}_{ij}$

In the presence of matter sources, scalars represent the response of the metric to irrotational velocity fields (that is, with vanishing vorticity). Vectors represent the response of the metric to vorticity, and they are usually irrelevant in cosmology, since they decay with the cosmic expansion. Tensor perturbations are the only ones that can propagate in vacuum, and their d.o.f. describe the two polarizations of gravitational waves. In this work we will exclusively concentrate on scalars (the only modes with a newtonian analog among the three) and their associated matter perturbations, although we'll say a few words about tensors in [Sect. 1.6.5](#).

It is also possible to perform a SVT decomposition for the stress-energy tensor. For the coordinate velocity  $v^i$  we may write,

$$v_i = \partial_i v + \hat{v}_i, \quad (1.145)$$

while for the anisotropic tensor  $S_{ij}$ ,

$$S_{ij} = \left(\partial_i\partial_j - \frac{\delta_{ij}}{3}\nabla^2\right)S + \frac{1}{2}\left(\partial_i\hat{S}_j + \partial_j\hat{S}_i\right) + \hat{S}_{ij}. \quad (1.146)$$

In practice, we will be only interested in  $v$  and  $S$ , since we just focus on the scalar sector. It is traditional to trade the scalar components of the stress-energy tensor

$(\delta\rho, v, \delta P, S)$  for the more common variables  $(\delta, \theta, \Pi, \sigma)$ , which are defined by:

$$\bar{\rho}\delta \equiv -\delta T^0_0, \quad (1.147)$$

$$(\bar{\rho} + \bar{P})\theta \equiv \sum_i \partial_i \delta T^0_i, \quad (1.148)$$

$$\bar{\rho}\Pi \equiv \frac{1}{3} \sum_i T^i_i, \quad (1.149)$$

$$(\bar{\rho} + \bar{P})\nabla^2\sigma \equiv -\sum_{i,j} \left( \partial_i \partial_j - \frac{\delta_{ij}}{3} \nabla^2 \right) \delta T^i_j. \quad (1.150)$$

Comparing previous equations with Eq. (1.142), Eq. (1.145) and Eq. (1.146), we find the relations <sup>19</sup>

$$\delta = \delta\rho/\bar{\rho}, \quad \Pi = \delta P/\bar{\rho}, \quad \theta = \sum_i \partial_i v_i = \nabla^2 v, \quad (\bar{\rho} + \bar{P})\nabla^2\sigma = -\frac{2}{3}\nabla^2\nabla^2 S. \quad (1.151)$$

The total stress-energy tensor is simply obtained by summing over the stress-energy tensor of each species. To give an example, the total perturbed density is  $\delta\rho_{\text{tot}} = \sum_I \bar{\rho}_I \delta_I$ , from which we infer that  $\delta_{\text{tot}} = \sum_I \bar{\rho}_I \delta_I / \bar{\rho}_{\text{tot}}$ .

### 1.6.1 The gauge problem

In the FLRW universe, there is only one possible slicing of constant-time hypersurfaces compatible with the assumption of homogeneity. On the contrary, in the perturbed FLRW universe, there are infinite possibilities of time slicings compatible with perturbation theory (*i.e.* such that on each constant-time hypersurface, all quantities remain close to the average value). For example, the density perturbation is defined by  $\delta\rho(\tau, \vec{x}) \equiv \rho(\tau, \vec{x}) - \bar{\rho}(t)$ . While  $\rho(\tau, \vec{x})$  is an unambiguously defined quantity,  $\bar{\rho}(t)$  depends on the particular time slicing passing through  $(\tau, \vec{x})$  over which we have decided to perform the average. Hence,  $\delta\rho(\tau, \vec{x})$  also depends on this choice, as illustrated in Fig. 1.13.

A gauge is simply a choice of time slicing, with a specific choice of spatial coordinates on these constant-time slices. Gauge transformations are thus induced by coordinate transformations,

$$x^\mu \longrightarrow \tilde{x}^\mu = x^\mu + \xi^\mu(\tau, \vec{x}), \quad (1.152)$$

where  $\xi^0 \equiv T$  and  $\xi^i \equiv L^i = \partial^i L + \hat{L}^i$ . These coordinate transformations map the points of one slicing to those of another slicing. We remark that not all coordinate transformations give rise to valid gauge transformations. The parameters  $T$  and  $L^i$  need to be small so that perturbed quantities remain at linear order after the transformation.

To see how metric elements transform under this gauge transformation, it suffices to use the transformation law for tensors,

$$g_{\mu\nu}(x) = \frac{\partial \tilde{x}^\alpha}{\partial x^\mu} \frac{\partial \tilde{x}^\beta}{\partial x^\nu} \tilde{g}_{\alpha\beta}(\tilde{x}). \quad (1.153)$$

<sup>19</sup>We take  $B = 0$  since we can always use the gauge freedom to do so, as we will see promptly.



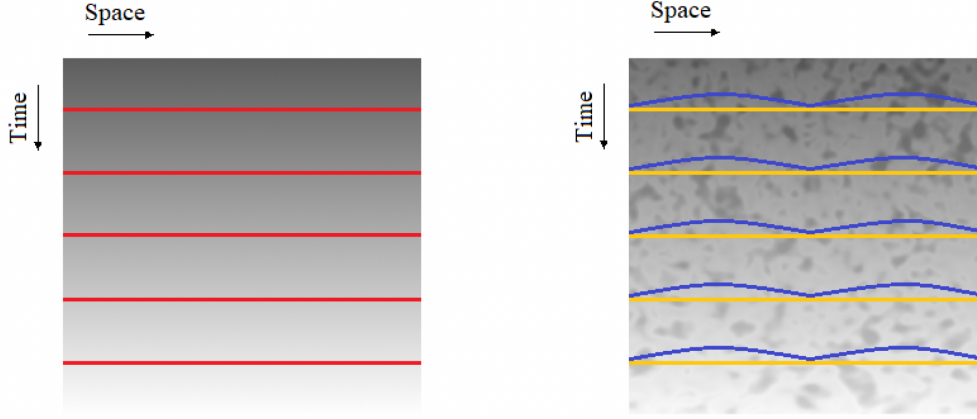


**Figure 1.13** – The gauge ambiguity. Darker (brighter) regions have larger (smaller) density, diluting with the cosmic expansion. **Left panel:** A homogeneous universe, with the only valid time slicing shown in red. **Right panel:** A universe with perturbations. In this case there are many possible time slicings, two of them are shown in blue and yellow. In both slicings, density remains homogeneous on average

Substituting Eq. (1.152) and Eq. (1.138) in Eq. (1.153), we arrive at the following transformation rules

$$A \longrightarrow \tilde{A} = A - T' - \mathcal{H}T, \quad (1.154)$$

$$B_i \longrightarrow \tilde{B}_i = B_i + \partial_i T - L'_i, \quad (1.155)$$

$$H_{ij} \longrightarrow \tilde{H}_{ij} = H_{ij} - (\partial_i L_j + \partial_j L_i) - 2\mathcal{H}T\delta_{ij}. \quad (1.156)$$

We give a proof of Eq. (1.155) in App. A.2 as an example. It will be convenient to express Eq. (1.154), Eq. (1.155) and Eq. (1.156) in terms of the SVT decomposition:

$$A \longrightarrow A - T' - \mathcal{H}T, \quad (1.157)$$

$$B \longrightarrow B + T - L', \quad \hat{B}_i \longrightarrow \hat{B}_i - \hat{L}'_i, \quad (1.158)$$

$$C \longrightarrow C - \mathcal{H}T - \frac{1}{3}\nabla^2 L, \quad (1.159)$$

$$E \longrightarrow E - L, \quad \hat{E}_i \longrightarrow \hat{E}_i - \hat{L}_i, \quad \hat{E}_{ij} \longrightarrow \hat{E}_{ij}. \quad (1.160)$$

In a similar vein, one can obtain the gauge transformation rules for the stress-energy tensor using,

$$T^\mu{}_\nu(x) = \frac{\partial x^\mu}{\partial \tilde{x}^\alpha} \frac{\partial \tilde{x}^\beta}{\partial x^\nu} \tilde{T}^\alpha{}_\beta(\tilde{x}). \quad (1.161)$$

Plugging Eq. (1.152) and Eq. (1.142) in Eq. (1.161) yields

$$\delta\rho \longrightarrow \delta\tilde{\rho} = \delta\rho - T\tilde{\rho}', \quad (1.162)$$

$$\delta P \longrightarrow \delta\tilde{P} = \delta P - T\tilde{P}', \quad (1.163)$$

$$v_i \longrightarrow \tilde{v}_i = v_i + L'_i, \quad (1.164)$$

$$S_{ij} \longrightarrow \tilde{S}_{ij} = S_{ij}. \quad (1.165)$$

We have proved Eq. (1.162) in App. A.2 to show the spirit of the calculation. We have seen that cosmological perturbations are subject to gauge freedom, and also

how the metric and the stress-energy tensor components change under these gauge transformations. However, this freedom can be problematic, since it can easily produce fake perturbations with no physical meaning. There are two strategies to deal with this issue: either work with gauge invariant quantities, or fix a gauge. We describe these two strategies in the following.

### Gauge invariant variables

By looking at the way the metric perturbations change under gauge transformations, one can define linear combinations of them that are left invariant. These are the so-called *Bardeen variables*:

$$\psi \equiv A + \mathcal{H}(B - E') + (B - E')', \quad (1.166)$$

$$\phi \equiv -C - \mathcal{H}(B - E') + \frac{1}{3}\nabla^2 E, \quad (1.167)$$

$$\hat{\phi}_i \equiv \hat{E}'_i - \hat{B}_i, \quad \hat{E}_{ij}. \quad (1.168)$$

We note that there are 6 d.o.f. in the Bardeen variables: this is exactly what we expect from the original 10 d.o.f. with 4 gauge choices. Using Eq. (1.157)-Eq. (1.160), one can easily check that the Bardeen variables are indeed gauge invariant.

In a similar way, having a look at Eq. (1.162)-Eq. (1.164) as well as Eq. (1.157)-Eq. (1.160), it is possible to construct linear combinations of the stress-energy tensor components which are gauge-invariant:

$$\delta\rho^{\text{GI}} \equiv \delta\rho - \bar{\rho}'(E' - B), \quad (1.169)$$

$$\delta P^{\text{GI}} \equiv \delta P - \bar{P}'(E' - B), \quad (1.170)$$

$$v_i^{\text{GI}} \equiv v_i + \partial_i(E' - B). \quad (1.171)$$

One could study the dynamical equations of perturbations in terms of these gauge invariant variables. In practice, this is not what it is usually done, since these equations can be quite tricky.

### Gauge fixing

This just consists in introducing a condition such that the time slicing is unique. In the scalar sector, this is typically achieved by using the freedom of the transformation variables  $T$  and  $L$  in order to set two of the four scalar metric perturbations to zero. There is no problem with this method, since observable quantities do not depend on the gauges, only the computations do. Different gauges have their advantages. We are going to discuss the two gauge choices that are more commonly used in the literature.

- **The Newtonian gauge.** This is defined by the choice  $\tilde{B} = \tilde{E} = 0$ , which can be achieved by setting  $L = E$  and  $T = E' - B$ . This prescription fixes a unique time slicing. A big advantage of this gauge is that the metric is diagonal and that the perturbed quantities can be trivially linked to the Bardeen variables. Namely,  $A = \psi$  and  $C = -\phi$ . Thus, the metric reads

$$ds^2 = a^2(\tau) \left[ -(1 + 2\psi)d\tau^2 + (1 - 2\phi)\delta_{ij}dx^i dx^j \right]. \quad (1.172)$$

The name of the gauge stems from the fact that Eq. (1.172) looks very similar to the weak-field limit of GR about the Minkowski metric. In fact,  $\psi$  plays the role of



the Newtonian gravitational potential on sub-horizon scales. Furthermore, the term  $a^2(\tau)(1 - 2\phi)$  represents a scale factor with a local distortion.

- **The synchronous gauge.** This gauge, originally introduced by LIFSHITZ (1946), is obtained by the choice  $\tilde{A} = \tilde{B} = 0$ , which can be achieved by picking  $L$  and  $T$  such that  $T' + \mathcal{H}T = A$  and  $L' = T + B$ . Thus, scalar perturbations only enter in the spatial part of the metric:

$$ds^2 = a^2(\tau) \left[ -d\tau^2 + (\delta_{ij} + H_{ij})dx^i dx^j \right], \quad (1.173)$$

where  $H_{ij} = 2C\delta_{ij} + 2(\partial_i\partial_j - \frac{\delta_{ij}}{3}\nabla^2)E$ . It is traditional to trade  $C$  and  $E$  for the scalar variables  $h$  and  $\eta$ . The first is defined as the trace of  $H_{ij}$ ,  $h \equiv \sum_i H^i_i = 6C$ , while the second is defined through the relation  $2\nabla^2 E = 6\eta + h$ . Hence, we can write in Fourier space:

$$-2k^2 E = 6\eta + h, \quad (1.174)$$

$$H_{ij} = \frac{\delta_{ij}}{3}h - 2\left(k_i k_j - \frac{\delta_{ij}}{3}k^2\right)E = \hat{k}_i \hat{k}_j h + \left(\hat{k}_i \hat{k}_j - \frac{\delta_{ij}}{3}\right)6\eta, \quad (1.175)$$

where  $\hat{k}_i \equiv k_i/k$ . Unfortunately, this still doesn't fix the gauge. Indeed,  $\tilde{A} = 0$  is obtained for any  $T$  satisfying  $T' + \mathcal{H}T = A$ , i.e.  $aT = \int d\tau aA + c_1$ , so the time slicings haven't yet been fixed due to this integration constant  $c_1$ . It is always possible to use the synchronous gauge as long as one uses some extra condition that eliminates the residual gauge freedom. One common approach is to set the initial velocity divergence of the CDM to zero,  $\theta_{\text{cdm}}^{\text{ini}} = 0$  (synchronous gauge *comoving* with the CDM).

It is practical to have equations that relate both gauges. For the metric perturbations, this can be straightforwardly achieved using the Bardeen variables in Eq. (1.166) and Eq. (1.167). Setting  $B = E = 0$  for the Newtonian gauge and  $A = B = 0$  for the synchronous gauge, we get (in Fourier space):

$$\psi = \mathcal{H}\alpha + \alpha', \quad (1.176)$$

$$\phi = \eta - \mathcal{H}\alpha, \quad (1.177)$$

where  $\alpha \equiv -E' = (6\eta + h)'/2k^2$ . In a very similar manner, we can relate elements of the perturbed stress-energy tensor using the gauge invariant variables that we defined in Eq. (1.169)-Eq. (1.171). We obtain:

$$\delta\rho^{\text{new}} = \delta\rho^{\text{syn}} + \bar{\rho}'\alpha, \quad (1.178)$$

$$\delta P^{\text{new}} = \delta P^{\text{syn}} + \bar{P}'\alpha, \quad (1.179)$$

$$v_i^{\text{new}} = v_i^{\text{syn}} - \partial_i\alpha. \quad (1.180)$$

The last equation can equivalently be expressed as  $\theta^{\text{new}} = \theta^{\text{syn}} + k^2\alpha$  (after taking the divergence and going to Fourier space). We observe that all the terms with  $\alpha$  at the r.h.s. of Eq. (1.178)-Eq. (1.180) are of the order  $\sim \mathcal{H}^2/k^2$  or  $\sim \mathcal{H}/k$ , meaning that they are very suppressed on sub-Hubble scales ( $k \gg \mathcal{H}$ ). Indeed, well inside the Hubble radius we expect to recover a Newtonian perturbation theory, where the gauge ambiguity (which is a purely relativistic effect) is absent.

The synchronous gauge is the one that is commonly adopted in Boltzmann codes, owing to its numerical stability. For this reason, it is also the one we have adopted in the Chapter 2, Chapter 3 and Chapter 4. However, physics is more intuitive using the Newtonian gauge, so we will restrict to this gauge for the rest of this Chapter.

### 1.6.2 Perturbation equations

Now that we have defined the perturbation d.o.f and fixed a gauge, it is time to concentrate on the dynamical evolution of these perturbed variables. More precisely, we need to know:

1. How the evolution of matter fluctuations is influenced by gravitational potentials and by the interactions among the different species.
2. How gravitational potentials respond to changes in the matter fluctuations.

The latter is dictated by the perturbed version of Einstein equations (see Eq. (1.10)). For the former, there are a priori several strategies. We have seen that there are four scalar variables in the perturbed stress-energy tensor, that can be taken to be the density contrast  $\delta$ , the perturbed pressure  $\delta P$ , the velocity divergence  $\theta$  and the anisotropic stress  $\sigma$ . The stress-energy conservation  $\nabla_\mu T^{\mu\nu} = 0$  (see Eq. (1.13)) leads to two dynamical equations in the scalar sector, the continuity and the Euler equation. Therefore, two more relations are needed to close the system. For ideal fluids, adiabaticity allows to relate the sound speed  $c_s^2 \equiv \delta P / \bar{\rho} \delta$  with the EoS  $w$ , whereas isotropy imposes  $\sigma = 0$ . In the most general case, for fluids which are non-ideal and/or have non-negligible interactions with other species, the stress-energy conservation provides an incomplete description. The most general description is obtained thanks to the perturbed version of the Boltzmann equation Eq. (1.58), that we proceed to discuss.

#### Perturbed Boltzmann equations

Let us consider a particle with mass  $m$  and energy  $E = \sqrt{m^2 + p^2}$ , where we remind that the amplitude of the physical three-momentum is defined as  $p \equiv \sqrt{\sum_{ij} g_{ij} P^i P^j}$ . As we show in App. A.3, the elements of the 4-momentum vector  $P^\mu = \frac{dx^\mu}{d\sigma} = (P^0, P^i)$  are given by

$$P^0 = \frac{E}{a}(1 - \psi), \quad P^i = \frac{p \hat{n}^i}{a}(1 + \phi). \quad (1.181)$$

In terms of these variables, the 0 component of the geodesic equation leads to (see App. A.3 for the derivation)

$$\frac{dq}{d\tau} = q\phi' - \mathcal{E} \hat{n} \cdot \vec{\nabla} \psi, \quad (1.182)$$

where  $q = ap$  is the comoving momentum and  $\mathcal{E} = aE$  is the comoving energy. This equation describes the change in comoving momentum for a particle following geodesic motion in a perturbed FLRW universe. The first term at the r.h.s of Eq. (1.182) accounts for a *local* energy loss due to dilation, *i.e.* the fact that (locally) the expansion is a bit ahead or behind the average. The second term describes the energy increase for photons falling in gravitational wells, or the energy decrease of those leaving the gravitational wells. In absence of inhomogeneities,  $\phi = \psi = 0$ , we recover the familiar momentum redshift,  $q = \text{const.}$ , *i.e.*  $p \propto a^{-1}$ . A crucial observation is that for massless particles, we can use  $\mathcal{E} = q$  and rewrite Eq. (1.182) as

$$\frac{1}{q} \frac{dq}{d\tau} = \phi' - \hat{n} \cdot \vec{\nabla} \psi. \quad (1.183)$$

That is, for massless particles, the *relative* change in momentum doesn't depend on momentum itself. This means that any massless particle that was in equilibrium in the early universe, will retain the Fermi-Dirac or Bose-Einstein form, even at the level of perturbations. The only way for this massless particle to acquire non-thermal distortions is through non-gravitational interactions. On the contrary, gravitational interactions can induce nonthermal distortions for massive particles, since the momentum dependence can't be eliminated from the r.h.s. of Eq. (1.182). This will be important when discussing the evolution of perturbations for massive neutrinos.

We are ready to derive the Boltzmann equation for the PSD  $f$  in a inhomogeneous universe. According to Eq. (1.58) we have

$$\frac{df}{d\sigma} = P^0 \frac{df}{d\tau} = \mathcal{C}[f]. \quad (1.184)$$

Using the chain rule, we can expand the derivative  $df/d\tau$ , taking account that the PSD has in this case a general dependence  $f = f(\tau, x^i, q, \hat{n}^i)$ . Hence,

$$\frac{df}{d\tau} = \frac{\partial f}{\partial \tau} + \frac{\partial f}{\partial x^i} \frac{dx^i}{d\tau} + \frac{\partial f}{\partial q} \frac{dq}{d\tau} + \frac{\partial f}{\partial \hat{n}^i} \frac{d\hat{n}^i}{d\tau}. \quad (1.185)$$

Both factors  $\partial f/\partial \hat{n}^i$  and  $d\hat{n}^i/d\tau$  are first order in perturbations, since particles follow straight lines in a homogeneous universe. Thus, we can discard the last term in Eq. (1.185). For the factor  $dx^i/d\tau$ , we notice that  $dx^i/d\tau = (dx^i/d\sigma)(d\sigma/d\tau) = P^i/P^0$ . Finally, for  $dq/d\tau$ , we insert the result of the geodesic equation Eq. (1.182). We get

$$\frac{\partial f}{\partial \tau} + \frac{q\hat{n}^i}{\mathcal{E}} \frac{\partial f}{\partial x^i} + q \frac{\partial f}{\partial q} \left[ \phi' - \frac{\mathcal{E}}{q} \hat{n}^i \frac{\partial \psi}{\partial x^i} \right] = \frac{\mathcal{C}[f]}{P^0}. \quad (1.186)$$

At this stage, it is useful to switch to Fourier space, which means that the PSD is now a function of the type  $f = f(\tau, q, k, \mu)$ , where  $\mu \equiv \hat{k} \cdot \hat{n}$ . Notice that the unit vector  $\hat{n}$  enters only through  $\mu$ , *i.e.* through the cosine of the angle between the direction of propagation and the wavenumber. This indicates a rotational symmetry around  $\hat{n}$ , which arises just due to the isotropy of the FLRW background. It is customary to split the PSD between a background and a linearly perturbed contribution

$$f(\tau, q, k, \mu) = \bar{f}(\tau, q)(1 + \Psi(\tau, q, k, \mu)). \quad (1.187)$$

Plugging the decomposition of Eq. (1.187) into Eq. (1.186), we get two equations, one at zeroth-order,

$$\frac{\partial \bar{f}}{\partial \tau} = \frac{a^2}{\mathcal{E}} \mathcal{C}^{(0)} \stackrel{!}{=} 0, \quad (1.188)$$

and another at first-order

$$\frac{\partial \Psi}{\partial \tau} + i\mu \frac{kq}{\mathcal{E}} \Psi + \frac{d\ln \bar{f}}{d\ln q} \left[ \phi' - i\mu \frac{k\mathcal{E}}{q} \psi \right] = \frac{a^2}{\bar{f}\mathcal{E}} \mathcal{C}^{(1)}, \quad (1.189)$$

where we have split the collision term in a zeroth-order and first-order contribution,  $\mathcal{C} = \mathcal{C}^{(0)} + \mathcal{C}^{(1)}$ . In Eq. (1.188), we set  $\mathcal{C}^{(0)} = 0$  since we assume that the relevant interactions are such that they maintain an equilibrium distribution for  $\bar{f}$ . This is the case for the Compton scattering between baryons and photons, that we shall discuss later. Eq. (1.189) is the master equation governing the evolution of perturbations of all relevant species in cosmology: photons, neutrinos, dark matter and baryons.

In the following, we will particularize [Eq. \(1.189\)](#) for each species, by specifying the energy-momentum relation and the collision term.

Before doing this task, let us detail how to obtain the elements of the perturbed stress-energy tensor from  $\Psi$ . For this, it is convenient to eliminate the dependence of  $\Psi$  on  $\mu$  by doing an expansion over Legendre multipoles

$$\Psi(\tau, q, k, \mu) = \sum_{\ell} (-i)^{\ell} (2\ell + 1) \Psi_{\ell}(\tau, q, k) P_{\ell}(\mu) \quad (1.190)$$

We already showed in [Eq. \(1.50\)](#) how the stress-tensor components are obtained from moments of the PSD. The linearly perturbed version of this equation is

$$\delta T^{\mu}_{\nu}(\tau, k) = g \int \frac{d^3 \vec{P}}{(2\pi)^3} (-\det(g))^{-1/2} \frac{P^{\mu} P_{\nu}}{P^0} \bar{f}(\tau, q) \Psi(\tau, q, k, \mu). \quad (1.191)$$

As we show in [App. A.4](#), the elements of  $\delta T^{\mu}_{\nu}$  can be obtained from the multipoles  $\Psi_{\ell}$  in the following manner:

$$\bar{\rho} \delta = \frac{4\pi}{a^4} \int_0^{\infty} dq q^2 \mathcal{E} \bar{f} \Psi_0, \quad (1.192)$$

$$(\bar{\rho} + \bar{P}) \theta = \frac{4\pi k}{a^4} \int_0^{\infty} dq q^2 q \bar{f} \Psi_1, \quad (1.193)$$

$$\bar{\rho} \Pi = \frac{4\pi}{3a^4} \int_0^{\infty} dq q^2 \frac{q^2}{\mathcal{E}} \bar{f} \Psi_0, \quad (1.194)$$

$$(\bar{\rho} + \bar{P}) \sigma = \frac{8\pi}{3a^4} \int_0^{\infty} dq q^2 \frac{q^2}{\mathcal{E}} \bar{f} \Psi_2. \quad (1.195)$$

From [Eq. \(1.194\)](#) and [Eq. \(1.195\)](#), we see that the perturbed pressure and anisotropic stress of non-relativistic particles is suppressed by a factor  $q/am \ll 1$ . Let us now describe the dynamics of each cosmological species.

### Photons

Before decoupling, photons were in kinetic equilibrium with electrons thanks to the frequent Compton interactions. We have seen that after decoupling the photon distribution maintains the Bose-Einstein form both at the background (*c.f.* [Eq. \(1.70\)](#)) and the linearly perturbed level (*c.f.* [Eq. \(1.183\)](#)). Hence, the only way the photon PSD can acquire anisotropies and inhomogeneities is through the temperature. Thus, we can write the photon PSD as

$$f_{\gamma}(\tau, q, k, \mu) = \left[ \exp \left( \frac{q}{a\bar{T}(1 + \Theta(\tau, k, \mu))} \right) - 1 \right]^{-1}, \quad (1.196)$$

where  $\Theta \equiv \delta T/\bar{T}$  stands for the relative temperature shift. Expanding at first order,

$$f_{\gamma} = \bar{f}_{\gamma} + \frac{\partial \bar{f}_{\gamma}}{\partial \bar{T}} \bar{T} \Theta = \bar{f}_{\gamma} - q \frac{\partial \bar{f}_{\gamma}}{\partial q} \Theta. \quad (1.197)$$

We have used the fact that the background PSD  $\bar{f}_{\gamma} = \left[ \exp(q/a\bar{T}) - 1 \right]^{-1}$  satisfies  $\frac{\partial \bar{f}_{\gamma}}{\partial \bar{T}} = -\frac{q}{\bar{T}} \frac{\partial \bar{f}_{\gamma}}{\partial q}$ . This implies a very interesting relation

$$\Psi_{\gamma}(\tau, q, k, \mu) = -\frac{d \ln \bar{f}}{d \ln q} \Theta(\tau, k, \mu) \quad (1.198)$$

That is, the perturbed PSD  $\Psi$  is a separable function on  $q$  and  $k$ . Inserting Eq. (1.198) in Eq. (1.189), and using  $\mathcal{E} = q$ , we get

$$\frac{\partial\Theta}{\partial\tau} + ik\mu\Theta - \phi' + ik\mu\psi = -\frac{a^2}{q^2\frac{\partial\bar{f}}{\partial q}}\mathcal{C}_\gamma^{(1)} = -\frac{a}{p^2\frac{\partial\bar{f}}{\partial p}}\mathcal{C}_\gamma^{(1)} \quad (1.199)$$

We have carried out the full derivation of the collision integral for photons,  $\mathcal{C}_\gamma^{(1)}$ , in App. A.5. The final result reads

$$\frac{\partial\Theta}{\partial\tau} + ik\mu\Theta - \phi' + ik\mu\psi = a\bar{n}_e\sigma_T \left[ \Theta_0 - \Theta + \mu v_b - \frac{P_2(\mu)}{2}\Theta_2 \right] \quad (1.200)$$

where  $v_b \equiv |\vec{v}_b| = \theta_b/ik$  is the common bulk velocity of baryons and electrons. The terms  $\Theta_0 \equiv \frac{1}{4\pi} \int d\Omega\Theta$  and  $\Theta_2 \equiv \frac{1}{4\pi} \int d\Omega P_2(\mu)\Theta$  denote the monopole and quadrupole perturbation, respectively. In Eq. (1.200) we have neglected for simplicity some extra terms associated with photon polarization, which don't affect the qualitative behavior of  $\Theta$ . We will say a few words about polarization in Sect. 1.6.5. The interaction term at the r.h.s. of Eq. (1.200) can be understood intuitively, by considering the so called *tightly coupled limit* ( $\Gamma_\gamma = a\bar{n}_e\sigma_T \gg \mathcal{H}$ ). In this limit, Compton scattering enforces  $\Theta_2 \rightarrow 0$  (as we will see more clearly later), and the temperature perturbation becomes equal to  $\Theta = \Theta_0 + \mu v_b$ , *i.e.* it is isotropic up to a dipole term accounting for the relative motion between the photon-baryon fluid and the observer. This just reflects the idea that, when interactions are strong, photons and electrons behave as a single fluid. In this context, one typically introduces the *optical depth*, giving the opacity of the universe at a given time  $\tau$  seen from today

$$\kappa_\gamma(\tau) \equiv \int_\tau^{\tau_0} d\tau' a\bar{n}_e\sigma_T, \quad \longrightarrow \quad \kappa'_\gamma = -a\bar{n}_e\sigma_T. \quad (1.201)$$

The optical depth tends to infinity at very early times, drops below one at recombination, and then decreases like  $a\bar{n}_e \sim a^{-2}$  (except during reionization, when it slightly increases). Notice that the optical depth at reionization shown in Eq. (1.133) is computed in the same way as in Eq. (1.201), but in a restricted time interval.

It is useful to perform a Legendre decomposition for  $\Theta$ , similar to the one we did for  $\Psi$ :

$$\Theta(\tau, k, \mu) = \sum_\ell (-i)^\ell (2\ell + 1) \Theta_\ell(\tau, k) P_\ell(\mu) \quad (1.202)$$

We can relate the temperature multipoles  $\Theta_\ell$  with elements of the perturbed stress-tensor by inserting  $\Psi_{\gamma,\ell} = -\frac{d\ln\bar{f}}{d\ln q}\Theta_\ell$  in Eq. (1.192)-Eq. (1.195). After doing integration by parts,  $q^4\frac{d\bar{f}}{dq} = \frac{d}{dq}(\bar{f}q^4) - 4\bar{f}q^3$ , and discarding the total derivative term (since we assume  $\bar{f}$  decreases sufficiently rapid for  $q \rightarrow \infty$ ), we end up with

$$\delta_\gamma = 4\Theta_0, \quad \theta_\gamma = 3k\Theta_1, \quad \sigma_\gamma = 2\Theta_2. \quad (1.203)$$

The factor 4 in the  $\delta_\gamma - \Theta_0$  relation could have been anticipated by noting that the photon density scales with temperature as  $\rho_\gamma \propto T^4$ . We can use the multipole expansion in Eq. (1.202) in order to eliminate the  $\mu$  dependence from the Boltzmann equation. The inverse relation of Eq. (1.202) is

$$\Theta_\ell = (-i)^{-\ell} \int_{-1}^{+1} \frac{d\mu}{2} P_\ell(\mu) \Theta(\mu), \quad (1.204)$$

so the idea is to perform the integral  $(-i)^{-\ell} \int_{-1}^{+1} \frac{d\mu}{2} P_\ell(\mu)$  on each side of Eq. (1.200)<sup>20</sup>. This leads to the following hierarchy of equations for the photon multipoles:

$$\delta'_\gamma = -\frac{4}{3}\theta_\gamma + 4\phi', \quad (1.206)$$

$$\theta'_\gamma = k^2 \left[ \frac{\delta_\gamma}{4} - \sigma_\gamma + \psi \right] + \kappa'_\gamma (\theta_\gamma - \theta_b), \quad (1.207)$$

$$\sigma'_\gamma = \frac{4}{15}\theta_\gamma - \frac{6}{5}k\Theta_3 + \frac{9}{10}\kappa'_\gamma\sigma_\gamma, \quad (1.208)$$

$$\Theta'_\ell = \frac{k}{2\ell+1} [\ell\Theta_{\ell-1} - (\ell+1)\Theta_{\ell+1}] + \kappa'_\gamma\Theta_\ell, \quad \forall \ell > 2. \quad (1.209)$$

From the previous equations, we can understand why the anisotropic stress  $\sigma_\gamma$  and higher moments are very suppressed in the tightly coupled limit,  $\kappa_\gamma \gg 1$ . The l.h.s. of Eq. (1.208) is of order  $\sigma_\gamma/\tau$ , which is much smaller than the third term at the r.h.s., of the order  $\kappa_\gamma\sigma_\gamma/\tau$ . Neglecting also the term with  $\Theta_3$ , we see that  $\sigma_\gamma \sim \tau\theta_\gamma/\kappa_\gamma$ , so  $\sigma_\gamma$  is very suppressed with respect to  $\theta_\gamma$ . In general, one shows that in the tightly coupled regime,  $\Theta_\ell \sim k\tau\Theta_{\ell-1}/\kappa_\gamma$  (which is the reason why we neglected the  $\Theta_3$  term before).

Obviously, the infinite hierarchy of Eq. (1.206) -Eq. (1.207) needs to be truncated at some multipole  $\ell_{\max}$ . The truncation scheme that has been recently adopted by all Boltzmann codes is the one proposed by MA et al. (1995)

$$\Theta'_{\ell_{\max}} \simeq k\Theta_{\ell_{\max}-1} - \frac{\ell_{\max}+1}{\tau}\Theta_{\ell_{\max}} + \kappa'_\gamma\Theta_{\ell_{\max}}. \quad (1.210)$$

The first two terms at the r.h.s. are inspired by the recurrence relation for spherical Bessel functions. Indeed, in the absence of time-varying gravitational potentials or interaction terms, one can show that the exact solution of the Boltzmann hierarchy gives  $\Theta_\ell(\tau, k) \propto j_\ell(k\tau)$  for  $\ell > 0$ . As a side note, the Boltzmann hierarchy for massless neutrinos is identical to the one showed in Eq. (1.206) -Eq. (1.208), except that all collision terms proportional to  $\kappa'_\gamma$  are set to zero.

### Massive neutrinos

Neutrinos decoupled from the thermal plasma in the very early universe, as we already saw in Sect. 1.5.3, so their collision term in Eq. (1.189) can be safely set to zero,  $C_\nu^{(1)} = 0$ . Even if their background PSD is well described by a Fermi-Dirac because they decoupled when they were relativistic, gravitational interactions induce non-thermal distortions at the linearly perturbed level, due to the late-time effects of their non-zero mass (*c.f.* Eq. (1.182)). Hence, the momentum d.o.f. cannot be integrated out from the Boltzmann equation as was done for photons, and we have to follow the full evolution in phase space.

Following the same logic that we applied to photons, we can eliminate the  $\mu$  dependence from the Boltzmann equation using the expansion in Legendre multipoles. The inverse relation of Eq. (1.190) is  $\Psi_\ell = (-i)^{-\ell} \int_{-1}^{+1} \frac{d\mu}{2} P_\ell(\mu)\Psi(\mu)$ , so performing the

<sup>20</sup>Doing this procedure, one encounters the integral  $\int_{-1}^{+1} d\mu\mu P_\ell(\mu)\Theta(\mu)$ . In order to handle this term, we use the recurrence relation

$$\mu P_\ell(\mu) = \frac{1}{2\ell+1} [(\ell+1)P_{\ell+1}(\mu) + \ell P_{\ell-1}(\mu)]. \quad (1.205)$$



integral  $(-i)^{-\ell} \int_{-1}^{+1} \frac{d\mu}{2} P_\ell(\mu)$  in Eq. (1.189), we arrive at the following hierarchy of equations for the neutrino multipoles <sup>21</sup>

$$\Psi'_{\nu,0} = -\frac{kq}{\mathcal{E}} \Psi_{\nu,1} - \frac{d\ln\bar{f}}{d\ln q} \phi', \quad (1.211)$$

$$\Psi'_{\nu,1} = \frac{kq}{3\mathcal{E}} [\Psi_{\nu,0} - 2\Psi_{\nu,2}] - \frac{\mathcal{E}k}{3q} \frac{d\ln\bar{f}}{d\ln q} \psi, \quad (1.212)$$

$$\Psi'_{\nu,\ell} = \frac{kq}{(2\ell+1)\mathcal{E}} [\ell\Psi_{\nu,\ell-1} - (\ell+1)\Psi_{\nu,\ell+1}], \quad \forall \ell > 1. \quad (1.213)$$

A similar truncation scheme as the one formerly discussed has been proposed for massive neutrinos (MA et al. 1995)

$$\Psi'_{\ell_{\max}} \simeq \frac{qk}{\mathcal{E}} \Psi_{\ell_{\max}-1} - \frac{\ell_{\max}+1}{\tau} \Psi_{\ell_{\max}}. \quad (1.214)$$

It is possible to derive conservation equations for the neutrinos by integrating the Boltzmann hierarchy over the phase space. Indeed, if we integrate Eq. (1.211) over  $4\pi a^{-4} \int dq q^2 \mathcal{E} \bar{f}$  and Eq. (1.212) over  $4\pi k a^{-4} \int dq q^3 \bar{f}$ , we arrive at the continuity and Euler equations (see App. A.6 for a proof):

$$\delta'_\nu = -3\mathcal{H}(c_s^2 - w_\nu) \delta_\nu - (1 + w_\nu) (\theta_\nu - 3\phi'), \quad (1.215)$$

$$\theta'_\nu = -\mathcal{H}(1 - 3c_g^2) \theta_\nu + k^2 \left( \frac{c_s^2}{1 + w_\nu} \delta_\nu + \psi - \sigma_\nu \right), \quad (1.216)$$

where  $c_s^2 \equiv \delta P_\nu / \delta \rho_\nu$  is the sound speed of the fluid and  $c_g^2 \equiv \bar{P}'_\nu / \bar{\rho}'_\nu$  is the adiabatic sound speed. In general,  $c_s^2$  is a spatially- and gauge-dependent quantity, as opposed to  $c_g^2$ . Eq. (1.215) and Eq. (1.216) could have been alternatively obtained using the covariant conservation of the stress-energy tensor,  $\nabla_\mu T^{\mu\nu} = 0$  (c.f. Eq. (1.13)). However, these conservation equations don't provide a closed evolution of the system, unless one specifies some recipe to compute  $c_s^2$  and  $\sigma_\nu$ . The full description of the system has to be obtained by solving for the multipoles  $\Psi_\ell(\tau, q, k)$  in the Boltzmann hierarchy Eq. (1.211)-Eq. (1.213), and then using the momentum integrals in Eq. (1.192)-Eq. (1.195) to get the elements of  $\delta T^\mu_\nu$ . As this is very time-consuming, several approximate descriptions for the neutrino dynamics have been proposed. These approaches typically describe neutrinos as a imperfect fluid, where the sound speed is set to  $c_s^2 \simeq c_g^2$ , and the anisotropic stress  $\sigma_\nu$  is expressed in terms of other thermodynamic quantities (see for example SHOJI et al. (2010) or LESGOURGUES et al. (2011)). We will make use of such approximation to describe the warm decay products of dark matter in Chapter 3.

## Cold Dark Matter

Dark matter is also assumed to have decoupled very early from the primordial bath, through some process such as the freeze-out mechanism that we sketched in Sect. 1.5.4. Thus, its collision term in Eq. (1.189) can be set to zero,  $\mathcal{C}_{\text{cdm}}^{(1)} = 0$ . CMB and LSS observations indicate that all or most of the dark matter needs to be *cold*, i.e. non-relativistic. Therefore, the description of CDM is easily achieved by

<sup>21</sup>This set of equations can also be applied to describe any kind of collisionless warm dark matter component.

taking the non-relativistic limit of Eq. (1.215) and Eq. (1.216):  $c_s^2 \simeq c_g^2 \simeq 0$ ,  $w \simeq 0$  and  $\sigma \simeq 0$ . This yields

$$\delta'_{\text{cdm}} = -\theta_{\text{cdm}} + 3\phi', \quad (1.217)$$

$$\theta'_{\text{cdm}} = -\mathcal{H}\theta_{\text{cdm}} + k^2\psi. \quad (1.218)$$

Let us express previous equations also in the synchronous gauge, since this will be relevant for our discussion about decaying dark matter in Chapter 3. This can be done straightforwardly with the help of the relations between the two gauges that we wrote in Eq. (1.176)-Eq. (1.177) and Eq. (1.178)-Eq. (1.180). Applying these transformations to the continuity equation, we get  $(\delta_{\text{cdm}}^{\text{new}})' = (\delta_{\text{cdm}}^{\text{syn}} - 3\mathcal{H}\alpha)' = -\theta_{\text{cdm}}^{\text{new}} + 3\phi' = -\theta_{\text{cdm}}^{\text{syn}} - k^2\alpha + 3\eta' - 3(\mathcal{H}\alpha)'$ . We see that the terms  $-3(\mathcal{H}\alpha)'$  cancel out and that  $-k^2\alpha + 3\eta' = -\frac{h'}{2}$ . We do the same game with the Euler equation:  $(\theta_{\text{cdm}}^{\text{new}})' = (\theta_{\text{cdm}}^{\text{syn}} + k^2\alpha)' = -\mathcal{H}\theta_{\text{cdm}}^{\text{new}} + k^2\psi = -\mathcal{H}\theta_{\text{cdm}}^{\text{syn}} - \mathcal{H}k^2\alpha + \mathcal{H}k^2\alpha + k^2\alpha'$ . In this case, both terms  $\mathcal{H}k^2\alpha$  and  $k^2\alpha'$  cancel out. In summary, the CDM equations in the synchronous gauge read

$$\delta'_{\text{cdm}} = -\frac{h'}{2}, \quad (1.219)$$

$$\theta'_{\text{cdm}} = -\mathcal{H}\theta_{\text{cdm}}. \quad (1.220)$$

As we already mentioned at the end of Sect. 1.6.1, to fully fix the synchronous gauge, one typically imposes the initial condition  $\theta_{\text{cdm}}^{\text{ini}} = 0$ . Since  $\theta'_{\text{cdm}}$  is just proportional to  $\theta_{\text{cdm}}$  according to Eq. (1.220), we see that in this case the velocity divergence of the CDM remains zero at all times,  $\theta_{\text{cdm}} = 0$ . This is the reason why in the synchronous gauge comoving with the CDM, the only dynamical variable to describe CDM at the perturbed level is  $\delta_{\text{cdm}}$ .

## Baryons

In the context of CMB physics, the only fully non-relativistic particles of the “visible” sector with a non-negligible cosmic abundance are hydrogen and helium (both in neutral and ionized forms) as well as electrons. At all epochs of interest, electrons and protons remain tightly coupled thanks to frequent Coulomb scatterings. In addition, neutral atoms keep a high scattering rate with protons, even after recombination (when the free proton ratio as small as  $X_p \sim 10^{-4}$ ) (HANNESTAD 2001). Hence, baryons and electrons can be generally described by a single fluid with  $\delta_e = \delta_b$  and  $\theta_e = \theta_b$ . Since the energy density is dominated by baryons ( $m_p \gg m_e$ ), cosmologists often refer to the baryon-electron fluid simply as baryons. Electrons and photons remain coupled until recombination due to Compton interactions, as we already mentioned. The Compton scattering between protons and photons can be neglected, because the Thomson cross-section scales as  $\sigma_T \propto 1/m^2$ , and thus  $\sigma_T^p/\sigma_T^e \sim 10^{-6}$ .

The dynamical equations of such baryon fluid can be derived by considering a separate Boltzmann equation like Eq. (1.189) for each species (electrons, protons and neutral atoms), adding them together, and integrating over the phase space. Given that baryons and electrons are non-relativistic, the non-collisional part of such equations looks like the continuity and Euler equations for CDM (c.f. Eq. (1.217)-Eq. (1.218)), except for the inclusion of a pressure term,  $k^2 c_s^2 \delta_b$  (that we will motivate later). Regarding the collision term, the contributions from electron-baryon interactions cancel out (as a consequence of particle number and momentum conservation), and we are only left with the Compton electron-photon interaction



term. This can only enter through the Euler equation, given that Compton scattering conserves the number of particles.

The collision term in the  $\theta'_b$  equation can easily be calculated using the covariant conservation of energy flux in the photon-baryon fluid,  $\nabla_\mu (\delta T^\mu_i|_b + \delta T^\mu_i|\gamma) = 0$ . This means that the collision terms in the equations for  $[(\bar{\rho}_\gamma + \rho_\gamma)\theta_\gamma]'$  and  $[(\bar{\rho}_b + \rho_b)\theta_b]'$  have to cancel out,  $\tilde{C}_\gamma = -\tilde{C}_b$ <sup>22</sup>. However, we are writing equations for  $\theta'_i$  (with  $i = \gamma, b$ ), so the associated collision term in each case is actually  $C_i \equiv \frac{\tilde{C}_i}{(\bar{\rho}_i + P_i)}$ . In Eq. (1.207) we already showed the collision term appearing in the  $\theta'_\gamma$  equation:  $C_\gamma = \kappa'_\gamma(\theta_\gamma - \theta_b)$ . Therefore, for baryons we have  $C_b = \frac{\tilde{C}_b}{(\bar{\rho}_b + P_b)} = -\frac{\tilde{C}_\gamma}{(\bar{\rho}_b + P_b)} = -\frac{(\bar{\rho}_\gamma + \bar{P}_\gamma)}{(\bar{\rho}_b + P_b)} C_\gamma$ . In summary, the equations for the baryon fluid read

$$\delta'_b = -\theta_b + 3\phi', \quad (1.221)$$

$$\theta'_b = -\mathcal{H}\theta_b + k^2 c_s^2 \delta_b + k^2 \psi + R^{-1} \kappa'_\gamma (\theta_b - \theta_\gamma), \quad (1.222)$$

where we defined  $R \equiv 3\bar{\rho}_b/4\bar{\rho}_\gamma$ . We see that for  $\bar{\rho}_b \rightarrow \infty$ , the collision term vanishes, reflecting the fact that photons cannot change the electron velocity if the average mass of the baryon-electron fluid is infinite. It is possible to define the *drag depth* for baryons, similar to the optical depth of photons, but taking into account the extra factor  $R^{-1}$

$$\kappa_{\text{dr}}(\tau) = \int_\tau^{\tau_0} d\tau' R^{-1} a \bar{n}_e \sigma_T. \quad (1.223)$$

This also goes from infinity in the early tightly-coupled regime to zero after decoupling. The time of *baryon drag* is defined by the condition  $\kappa_{\text{dr}}(\tau_{\text{dr}}) = 1$ , giving the moment at which baryons stop dragging the photons towards gravitational wells. Because recombination happened already during the matter era,  $R = 3\bar{\rho}_b/4\bar{\rho}_\gamma < 1$ , so baryon drag took place slightly after photon decoupling,  $z_{\text{drag}} < z_{\text{dec}}$ .

What about the pressure term  $k^2 c_s^2 \delta_b$ ? The motivation for including this term is that it can become important for scales smaller than the so called *Jeans length*. To see this more clearly, let's suppose we have some non-relativistic decoupled species  $I$  which dominates the energy content of the universe. It can thus be described by equations like Eq. (1.221)-Eq. (1.222), but without the collision term. As we will see in the next subsection, it is often a good approximation to neglect the time variation of gravitational potentials,  $\phi' \simeq 0$ . Furthermore, on sub-Hubble scales we can use the Poisson equation (c.f. Eq. (1.229)) to infer that  $k^2 \psi \simeq 4\pi G a^2 \bar{\rho}_{\text{tot}} \delta_I = \frac{3}{2} \mathcal{H}^2 \delta_I$ . Then, combining the time derivative of the continuity equation with the Euler equation, we arrive at a closed equation for the evolution of  $\delta_i$ :

$$\delta''_I + \mathcal{H}\delta'_I + (k^2 - k_J^2) c_s^2 \delta_I = 0, \quad (1.224)$$

<sup>22</sup>The fact that  $\tilde{C}_\gamma = -\tilde{C}_b$  is by itself a consequence of momentum conservation. Indeed, since these collision terms appear in the equation for  $(\bar{\rho} + P)\theta$  (c.f. Eq. (1.193)), they are given by

$$\begin{aligned} \tilde{C}_\gamma &= \int d\Pi_2 p_2 \mathcal{C}_\gamma = \int d\Pi_1 d\Pi_2 d\Pi_3 d\Pi_4 |\mathcal{M}|^2 \delta^4(P_1 + P_2 - P_3 - P_4) (2\pi)^4 [f_e(p_3) f_\gamma(p_4) - f_e(p_1) f_\gamma(p_2)] p_1, \\ \tilde{C}_b &= \int d\Pi_1 p_1 \mathcal{C}_b = \int d\Pi_1 d\Pi_2 d\Pi_3 d\Pi_4 |\mathcal{M}|^2 \delta^4(P_1 + P_2 - P_3 - P_4) (2\pi)^4 [f_e(p_3) f_\gamma(p_4) - f_e(p_1) f_\gamma(p_2)] p_2, \end{aligned}$$

where  $d\Pi_i \equiv \frac{d^3 \vec{p}_i}{(2\pi)^3 2E_i}$ . The total collision term in the photon-baryon fluid is thus  $\tilde{C}_{\gamma b} = \tilde{C}_\gamma + \tilde{C}_b$ . Applying momentum conservation in the integrand of  $\tilde{C}_{\gamma b}$ ,  $p_1 + p_2 = p_3 + p_4$ , and relabelling  $p_1 \leftrightarrow p_3$  and  $p_2 \leftrightarrow p_4$ , one quickly notices that  $\tilde{C}_{\gamma b} = -\tilde{C}_{\gamma b} \rightarrow \tilde{C}_{\gamma b} = 0$ .

where  $k_J \equiv \sqrt{\frac{3}{2}} \frac{\mathcal{H}}{c_s}$  is the Jeans scale. When  $k > k_J$ , the effective mass term  $(k^2 - k_J^2)c_s^2$  becomes positive, and  $\delta_I$  develops oscillations. Hence, we see that the Jeans length is the scale below which pressure prevents gravitational collapse of the fluid. The same scale can be defined for neutrinos, although in that context it is typically referred as *free-streaming* scale  $k_{\text{fs}}$ , and  $c_s$  is referred as the velocity dispersion.

The baryon sound speed is typically identified with the adiabatic sound speed,  $c_s^2 = c_g^2$ . Since the baryon pressure follows the ideal gas law (c.f. Eq. (1.78)),  $\bar{P}_b = \bar{n}_b \bar{T}_b$ , the baryon EoS reads  $w_b = \frac{\bar{T}_b}{\mu}$ , where  $\mu$  is the *mean molecular weight*

$$\mu \equiv \frac{\bar{\rho}_b}{\bar{n}_b} \simeq \frac{\bar{\rho}_H^{\text{tot}} + \bar{\rho}_{\text{He}}^{\text{tot}}}{\bar{n}_H^{\text{tot}} + \bar{n}_{\text{He}}^{\text{tot}} + \bar{n}_e} \simeq m_H \frac{1 + 4f_{\text{He}}}{1 + f_{\text{He}} + X_e}. \quad (1.225)$$

Neglecting the time variation of  $\mu$ , and assuming  $\bar{\rho}'_b \simeq -3\mathcal{H}\bar{\rho}_b$ , the baryon sound speed can then be computed as:

$$c_s^2 = \frac{\bar{P}'_b}{\bar{\rho}'_b} = w_b \left( 1 + \frac{w'_b \bar{\rho}_b}{w_b \bar{\rho}'_b} \right) = \frac{\bar{T}_b}{\mu} \left( 1 - \frac{1}{3} \frac{d \ln \bar{T}_b}{d \ln a} \right), \quad (1.226)$$

where the evolution of  $\bar{T}_b$  is given by Eq. (1.130).

### Perturbed Einstein equations

To close the system of Boltzmann equations presented before, we still need to determine the gravitational potentials  $\psi$  and  $\phi$ . This can be achieved thanks to Einstein equations, which relate  $\psi$  and  $\phi$  with the total perturbed stress-energy tensor. In the scalar sector, there are four independent Einstein equations, two of which are redundant. This is just a consequence of Bianchi identities: Einstein equations can be combined to arrive at the continuity and Euler equation for the total stress-energy tensor. We have given a derivation of the four linearly perturbed Einstein equation in App. A.7. The traceless longitudinal part of the  $(ij)$  components gives

$$k^2(\phi - \psi) = 12\pi G a^2 \sum_I (\bar{\rho}_I + \bar{P}_I) \sigma_I, \quad (1.227)$$

where  $I$  runs over all cosmic species. This equation tells us that in a universe full of perfect fluids (with  $\sigma_I = 0$ ), the two metric perturbations are the same. In practice, neutrinos and photons can have non-negligible anisotropic stress. For photons, we already saw that  $\sigma_\gamma$  remains very suppressed until recombination, due to the tight coupling with baryons. After recombination,  $\sigma_\gamma$  can be sizeable, but  $\bar{\rho}_\gamma$  is already very small because photons decoupled during the matter era. This makes the overall contribution of photons to the r.h.s of Eq. (1.227) still very minor. On the contrary, neutrinos are free-streaming from the first instants of the universe (*i.e.* for  $T \lesssim 1$  MeV), and behave relativistically until late times (after recombination). Hence, they are the only components capable of producing a significant departure of  $\phi - \psi$  from zero. This happens mainly during the radiation era, when the contribution from both  $\bar{\rho}_\nu$  and  $\sigma_\nu$  is important. Afterwards, neutrinos transition to the non-relativistic regime, and the metric perturbations become equal,  $\phi = \psi$ .

We still need one more Einstein equation to close the system. We can use the (00) component, which gives

$$k^2 \phi + 3\mathcal{H}(\phi' + \mathcal{H}\psi) = -4\pi G a^2 \sum_I \delta \rho_I, \quad (1.228)$$

Deep inside the Hubble radius,  $k \gg \mathcal{H}$ , the previous equation simply reduces to the Poisson equation

$$-\frac{k^2}{a^2}\phi = 4\pi G \sum_I \delta\rho_I, \quad (1.229)$$

where  $-\frac{k^2}{a^2}$  is the Fourier transform of the Laplacian in physical coordinates. We note that it is only the total perturbed density  $\delta\rho_{\text{tot}}$  and not  $\bar{\rho}_{\text{tot}}$  what sources the gravitational potential. Indeed, in a FLRW universe without over-densities or under-densities, there is no possibility for gravitational forces to appear.

Under some simplifying assumptions, it is possible to derive a closed equation for the evolution of the gravitational potential  $\phi$ , from which we can extract some qualitative aspects of its evolution. This is important in order to understand some of the key features in the CMB spectra that we will discuss in Sect. 1.6.4. First, let us neglect the effects of the anisotropic stress from neutrinos, such that  $\phi = \psi$ . In this case, the trace of the  $(ij)$  Einstein equation (written in Eq. (A.89)), simplifies to

$$\phi'' + 3\mathcal{H}\phi' + (2\mathcal{H}' + \mathcal{H}^2)\phi = 4\pi G a^2 \sum_I \delta P_I. \quad (1.230)$$

As we will explain in Sect. 1.6.3, if the universe is dominated by a single component with a constant EoS  $w$ , and in addition we assume its fluctuations evolve adiabatically, then we have  $\delta P_{\text{tot}} \simeq w\delta\rho_{\text{tot}}$ . This allows to relate Eq. (1.230) with Eq. (1.228). The resulting equation can be simplified by noting that  $2\mathcal{H}' + \mathcal{H}^2(1 + 3w) = 0$ , as a consequence of Friedmann equations. We end up with the following closed equation for the evolution of  $\phi$

$$\phi'' + 3\mathcal{H}\phi'(1 + w) + wk^2\phi = 0. \quad (1.231)$$

One could now move to solve Eq. (1.231) for matter, radiation and  $\Lambda$  eras, by looking at the corresponding  $\mathcal{H}$  and  $w$  in each case. On super-Hubble scales, the growing mode solution is always  $\phi = \text{const.}$  The fact that  $\phi$  is frozen reflects the natural expectation that no causal physics should influence perturbations outside the horizon (although this result is in reality only valid in the Newtonian gauge). However,  $\phi$  can still change of value on super-Hubble scales during the transition between eras. For instance, it is a famous result of linear theory that the super-Hubble values of  $\phi$  during matter dominated and radiation dominated eras are related by: <sup>23</sup>

$$\phi_{\text{MD}} = \frac{9}{10}\phi_{\text{RD}}. \quad (1.233)$$

It is interesting to find how density perturbations behave on super-Hubble scales. To do that, let us express the generalized Poisson equation Eq. (1.228) in the following manner

$$\delta_{\text{tot}} = \frac{\delta\rho_{\text{tot}}}{\bar{\rho}_{\text{tot}}} = -\frac{2}{3}\frac{k^2}{\mathcal{H}^2}\phi - \frac{2}{\mathcal{H}}\phi' - 2\phi. \quad (1.234)$$

<sup>23</sup>This can be shown by using the expression for the comoving curvature perturbation  $\mathcal{R}$  in Eq. (1.254). As we discuss later, this quantity is conserved on super-Hubble scales. In this case, we can use that  $\phi' \simeq 0$  and  $\mathcal{H}^2 = \frac{8\pi G}{3}a^2\bar{\rho}_{\text{tot}}$ , in order to rewrite  $\mathcal{R}$  as

$$\mathcal{R} = \frac{5 + 3w}{3 + 3w}\phi. \quad (1.232)$$

Evaluating  $\mathcal{R}$  in the matter ( $w = 0$ ) and radiation eras ( $w = 1/3$ ), we find  $\mathcal{R} = \frac{5}{3}\phi_{\text{MD}} = \frac{3}{2}\phi_{\text{RD}}$  and hence  $\phi_{\text{MD}} = \frac{9}{10}\phi_{\text{RD}}$ .

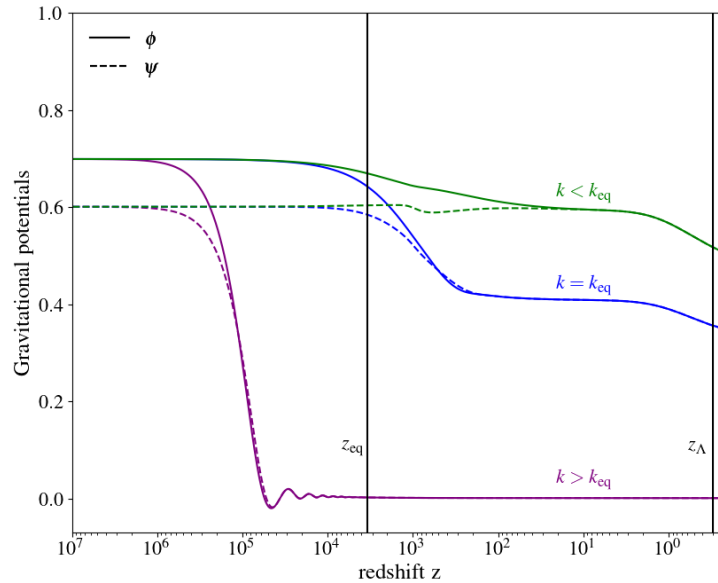


**Figure 1.14** – Evolution of the two scalar metric perturbations in the Newtonian gauge,  $\phi$  and  $\psi$ . This is shown for three different wavenumbers,  $k = 1 \text{ Mpc}^{-1}$  (purple),  $k = 10^{-2} \text{ Mpc}^{-1}$  (blue) and  $k = 10^{-3} \text{ Mpc}^{-1}$  (green), which crossed the horizon before, during and after matter-radiation equality, respectively.

On super-Hubble scales,  $\phi' \simeq 0$  and  $k/\mathcal{H} \ll 1$ , so we find that the total overdensity is also frozen and its value is given by

$$\delta_{\text{tot}} = -2\phi. \quad (1.235)$$

Regarding the sub-Hubble limit of Eq. (1.231), the behavior is different depending on which epoch we consider. During radiation domination, the metric potential oscillates with an amplitude that decreases as  $a^{-2}$ , while it stays constant during matter domination. In summary, the gravitational potential only evolves when the EoS of the universe changes (on all scales), and during the radiation era on sub-Hubble scales. All those aspects are illustrated in Fig. 1.14, where we show the numerical resolution of  $\phi$  and  $\psi$  for different wavenumbers

### 1.6.3 Initial conditions

Before moving with our discussion about linear perturbations, it is essential to introduce two important concepts related with the study of initial conditions: adiabatic/isocurvature modes and the primordial power spectrum.

#### Adiabatic and isocurvature modes

Any mode of interest (those that can be observed on the CMB and linear matter spectra) was outside the Hubble radius  $R_H$  if we look far enough into the past (*i.e.* for  $z \gtrsim 10^5$ ). Inflation establishes the initial conditions for these super-Hubble modes. Let us suppose that the universe was initially filled with  $N$  decoupled perfect fluids. This means that at the linearly perturbed level, each fluid is completely specified by  $\delta_I$  and  $\theta_I$ , so there are  $2N$  first-order equations, requiring  $2N$  independent initial

conditions <sup>24</sup>. One can show that half of them seed decaying solutions and are thus irrelevant for most applications. Therefore, the task is to find which combinations of the remaining  $N$  initial conditions get excited. There is one combination that is particularly simple and well-motivated.

In scenarios of single-field inflation, perturbations are generated due to a common, local shift in time  $\delta\tau(\vec{x})$  of the background quantities:

$$\rho_I(\tau, \vec{x}) = \bar{\rho}_I(\tau + \delta\tau(\vec{x})) \simeq \bar{\rho}_I(\tau) + \bar{\rho}'_I \delta\tau(\vec{x}), \quad (1.236)$$

$$P_I(\tau, \vec{x}) = \bar{P}_I(\tau + \delta\tau(\vec{x})) \simeq \bar{P}_I(\tau) + \bar{P}'_I \delta\tau(\vec{x}), \quad (1.237)$$

meaning that  $\delta\rho = \bar{\rho}'_I \delta\tau$  and  $\delta P = \bar{P}'_I \delta\tau$ . Using the fact that  $\delta\tau(\vec{x})$  is the same for all species and Eq. (1.14), we can write

$$\delta\tau = \frac{\delta\rho_I}{\bar{\rho}'_I} = \frac{\delta\rho_J}{\bar{\rho}'_J} \quad \longrightarrow \quad \frac{\delta_I}{1+w_I} = \frac{\delta_J}{1+w_J}, \quad (1.238)$$

for all species  $I$  and  $J$ . This is a great simplification, implying that in the early universe there is a single inhomogeneous degree of freedom, from which the rest of initial conditions can be derived. For example, if the universe is initially filled with photons ( $w_\gamma = 1/3$ ), baryons and cold dark matter ( $w_b \simeq w_{\text{cdm}} \simeq 0$ ), we have

$$\delta_{\text{cdm}} = \delta_b = \frac{3}{4} \delta_\gamma. \quad (1.239)$$

Eq. (1.236)-Eq. (1.237) have other interesting consequences:

- The pressure  $P_I$  of each species can be generally expressed as a function of the density  $\rho_I$  and the entropy  $S_I$ . Performing a Taylor expansion around the background quantities, we get

$$P_I(\rho_I, S_I) \simeq P_I(\bar{\rho}_I, \bar{S}_I) + c_{s,I}^2 \delta\rho_I + \Upsilon_I \delta S_I, \quad (1.240)$$

where  $c_{s,I}^2 \equiv \partial P_I / \partial \rho_I|_{S_I}$  is the sound speed and  $\Upsilon_I \equiv \partial P_I / \partial S_I|_{\rho_I}$ . From Eq. (1.236) and Eq. (1.237) we have  $\delta P_I = (\bar{P}'_I / \bar{\rho}'_I) \delta\rho_I$ , meaning that

$$c_{s,I}^2 = \frac{\bar{P}'_I}{\bar{\rho}'_I} = c_{g,I}^2, \quad \delta S_I = 0, \quad (1.241)$$

*i.e.* the sound speed of each component is adiabatic and the entropy perturbations vanish. For this reason, such kind of initial condition is often referred as *adiabatic or isentropic mode*. If in addition the EoS is constant for every species,  $w_I = \text{const.}$ , then  $c_{s,I}^2 = c_{g,I}^2 = w_I$ .

- The total pressure perturbation is also described by a sound speed  $c_s^2$  which is a weighted sum of the sound speeds for each species

$$\frac{\delta P_{\text{tot}}}{\delta\rho_{\text{tot}}} = \frac{\sum_I c_{g,I}^2 \delta\rho_I / \delta\tau}{\sum_I \delta\rho_I / \delta\tau} = \frac{\sum_I c_{g,I}^2 (\bar{\rho}_I + \bar{P}_I)}{\sum_I (\bar{\rho}_I + \bar{P}_I)} \equiv c_s^2. \quad (1.242)$$

From the previous equation we see that, even if  $c_{g,I}^2 = w_I$  for every component, in general we will have  $c_s^2 \neq w_{\text{tot}}$  in the presence of several components.

<sup>24</sup>This is still true for imperfect fluids that were initially tightly coupled to other species, such as photons. Indeed, we already saw that in the tightly coupled limit, all photon multipoles above  $\ell = 0$  and  $\ell = 1$  are negligible. The initial conditions for neutrinos are a bit more subtle and we don't discuss them here, we refer to LESGOURGUES et al. (2018) for details about this topic.

Remark that adiabatic modes don't necessarily have to remain adiabatic at later times. In fact, without assuming Eq. (1.236)-Eq. (1.237), the relations Eq. (1.239), Eq. (1.241) and Eq. (1.242) are not even true at initial times. In general, the total pressure perturbation can be arranged as a sum over  $N$  independent functions

$$\delta P_{\text{tot}} = c_s^2 \delta \rho_{\text{tot}} + \sum_{I \neq J} \Upsilon_{IJ} \left[ \frac{\delta \rho_I}{\bar{\rho}_I + \bar{P}_I} - \frac{\delta \rho_J}{\bar{\rho}_J + \bar{P}_J} \right]. \quad (1.243)$$

The term in brackets corresponds to the entropy perturbation  $\delta S_{IJ}$  of the fluid  $I$  with respect to a reference fluid  $J$  (typically the photons), while  $\Upsilon_{IJ} = \partial P_{\text{tot}} / \partial S_{IJ}|_{\rho_{\text{tot}}}$ . The initial entropy perturbations  $\delta S_{IJ}$  are also commonly referred as *isocurvature modes*. To understand the origin for the name, let us rewrite the defining condition for adiabatic modes in terms of the number densities of each species,  $n_I$ . From  $n_I(\tau, \vec{x}) = \bar{n}_I(\tau + \delta\tau(\vec{x})) = \bar{n}_I(\tau) + \bar{n}'_I \delta\tau(\vec{x})$ , we observe

$$\delta\tau = \frac{\delta n_I}{\bar{n}'_I} = \frac{\delta n_J}{\bar{n}'_J} \quad \longrightarrow \quad \frac{\delta n_I}{\bar{n}_I} = \frac{\delta n_J}{\bar{n}_J} \quad \longrightarrow \quad \delta \left( \frac{n_I}{n_J} \right) = 0. \quad (1.244)$$

That is, for the adiabatic mode, the relative ratios in number densities are unperturbed. It is associated with a global perturbation in the matter content, which is translated into a fluctuation of the spatial curvature via Einstein's equations (see Eq. (1.252)). The isocurvature modes  $\delta S_{IJ} = \frac{\delta n_I}{\bar{n}_I} - \frac{\delta n_J}{\bar{n}_J}$  are thus the complement of adiabatic modes, since they are characterized by variations in the particle number ratios, but with a vanishing curvature perturbation (LANGLOIS 2003). In summary, the most general initial condition can be expanded in a basis formed by 1 adiabatic mode,  $N - 1$  isocurvature modes, and  $N$  decaying modes which are unobservable. From the previous discussion, it is clear that non-adiabatic modes are generated when there are more than one inhomogeneous degrees of freedom in the early universe (for example, this could naturally arise in scenarios of multi-field inflation). The presence of isocurvature modes is tightly constrained by Planck18 data (N. LEE et al. 2021), so in the following we will restrict to adiabatic initial conditions.

### Primordial power spectrum

The theory of cosmological perturbations is stochastic by nature. Its main goal is to determine how the probability distribution of perturbed quantities evolves in time. The simplest hypothesis that is in agreement with observations is that primordial perturbations follow gaussian statistics. As long as perturbations are linear, it is guaranteed that the gaussian shape of the distributions is preserved, so that all observable properties can be encoded in two-point correlation functions. For some arbitrary perturbed quantity  $A(\tau, \vec{x})$ , the two-point correlation function in real space is given by

$$\langle A(\tau, \vec{x}), A(\tau, \vec{x}') \rangle = \xi_A(\tau, \vec{x}, \vec{x}') = \xi_A(\tau, r), \quad (1.245)$$

with  $r = |\vec{x}' - \vec{x}|$ . The symbol  $\langle \dots \rangle$  indicates an average over many different realizations. The last equality in Eq. (1.245) follows as a consequence of statistical isotropy and homogeneity of the perturbed FLRW universe. The two-point correlation function is often written in Fourier space. Following our Fourier convention in Eq. (1.137) and using that  $A^*(\tau, \vec{k}) = A(\tau, -\vec{k})$  for a real quantity,

$$\langle A(\tau, \vec{k}), A^*(\tau, \vec{k}') \rangle = \int d^3\vec{x} d^3\vec{x}' \xi_A(\tau, |\vec{x}' - \vec{x}|) e^{-i\vec{k}\cdot\vec{x} + i\vec{k}'\cdot\vec{x}'}. \quad (1.246)$$



Now, changing variables from  $\vec{x}'$  to  $\vec{r} = \vec{x}' - \vec{x}$ , and using the identity  $\int d^3\vec{x} e^{i(\vec{k}' - \vec{k}) \cdot \vec{x}} = (2\pi)^3 \delta^3(\vec{k}' - \vec{k})$ , we get

$$\langle A(\tau, \vec{k}), A^*(\tau, \vec{k}') \rangle = \delta^3(\vec{k}' - \vec{k}) \int d^3\vec{r} \xi_A(\tau, r) e^{i\vec{k}' \cdot \vec{r}} = \delta^3(\vec{k}' - \vec{k}) 4\pi \int_0^\infty dr r^2 \xi_A(\tau, r) \frac{\sin(kr)}{kr},$$

where we have absorbed the factor  $(2\pi)^3$  inside  $\xi_A$ . If we define the *power spectrum* of the quantity  $A$  as

$$P_A(\tau, k) \equiv 4\pi \int_0^\infty dr r^2 \xi_A(\tau, r) \frac{\sin(kr)}{kr}, \quad (1.247)$$

we thus arrive at the very important relation

$$\langle A(\tau, \vec{k}), A^*(\tau, \vec{k}') \rangle = P_A(\tau, k) \delta^3(\vec{k}' - \vec{k}). \quad (1.248)$$

The Dirac delta indicates that different wavenumbers are uncorrelated, and arises as a consequence of statistical homogeneity. On the other hand, the fact that  $P_A$  only depends on  $k = |\vec{k}|$  is a consequence of statistical isotropy. It is common to introduce the *dimensionless power spectrum*, defined as

$$\mathcal{P}_A(k, \tau) \equiv \frac{k^3}{2\pi^2} P_A(\tau, k). \quad (1.249)$$

The motivation for the definition of  $\mathcal{P}_A$  is that it frequently appears convoluted with some window function  $W(k)$  when computing the average of a certain quantity in real space

$$\int \frac{d^3\vec{k}}{(2\pi)^3} P_A(k) W(k) = 4\pi \int \frac{dk k^2}{(2\pi)^3} P_A(k) W(k) = \int d\ln k \mathcal{P}_A(k) W(k). \quad (1.250)$$

The notion of “scale-invariant power spectrum” refers to  $\mathcal{P}_A$  being independent of  $k$ , *i.e.*  $P_A \propto k^{-3}$ .

It is useful to present the primordial power spectrum in terms of some variable that is conserved on super-Hubble scales. Let us consider the spatial part of the metric in some arbitrary gauge,  $g_{ij} = a^2 \left[ (1 + 2C) \delta_{ij} + 2 \left( \partial_i \partial_j - \frac{\delta_{ij}}{3} \nabla^2 \right) E \right]$ . One can show that the three-dimensional Ricci scalar associated with  $g_{ij}$  is given by  $a^2 R^{(3)} = 4\nabla^2 \left( -C + \frac{1}{3} \nabla^2 E \right)$  (BAUMANN 2021). The term in parenthesis is the so called *comoving curvature perturbation*, and it is defined in the comoving gauge (where  $B = 0$  and  $v_{\text{tot}} = 0$ ):

$$\mathcal{R} = \left[ -C + \frac{1}{3} \nabla^2 E \right]_{B=v_{\text{tot}}=0}. \quad (1.251)$$

It is more convenient to have a gauge-invariant expression for  $\mathcal{R}$ . Since  $B$  and  $v_{\text{tot}}$  vanish by definition in the comoving gauge, it is always possible to add linear combination of these to  $\mathcal{R}$  so as to make  $\mathcal{R}$  gauge invariant. By looking at the gauge transformations Eq. (1.157)-Eq. (1.160) and Eq. (1.164), one quickly realizes that the following combination is gauge-invariant <sup>25</sup>

$$\mathcal{R} \equiv -C + \frac{1}{3} \nabla^2 E - \mathcal{H}(B + v_{\text{tot}}). \quad (1.253)$$

<sup>25</sup>There is an alternative way to make  $-C + \frac{1}{3} \nabla^2 E$  gauge-invariant, which results in a similar quantity

$$\zeta \equiv -C + \frac{1}{3} \nabla^2 E + \mathcal{H} \frac{\delta \rho_{\text{tot}}}{\bar{\rho}'_{\text{tot}}}. \quad (1.252)$$

This is called the *constant density curvature perturbation*, and it corresponds to the comoving curvature defined in the uniform density gauge (where  $B = 0$  and  $\delta \rho_{\text{tot}} = 0$ ). Both  $\mathcal{R}$  and  $\zeta$  are widely used, and it can be shown that on super-Hubble scales,  $\mathcal{R} \simeq \zeta$  (FERGUSON 2015).



We can now evaluate  $\mathcal{R}$  in any gauge, such as the Newtonian one. In this gauge,  $B = E = 0$  and  $C = -\phi$ . In addition, we can express  $v_{\text{tot}} = -\theta_{\text{tot}}/k^2$  in terms of the metric potentials using the  $0i$  Einstein equation (see Eq. (A.86)). This yields,

$$\mathcal{R} = \phi + \frac{\mathcal{H}(\phi' + \mathcal{H}\psi)}{4\pi G a^2(\bar{\rho}_{\text{tot}} + \bar{P}_{\text{tot}})}. \quad (1.254)$$

In App. A.8 we show that  $\mathcal{R}$  is conserved on super-Hubble scales and for adiabatic initial conditions. This is a big advantage, since it allows to relate predictions made at horizon exit (given by some inflationary theory) to observables at horizon re-entry. The power spectrum in Eq. (1.248) can be decomposed into the primordial spectrum  $P_{\mathcal{R}}(k)$  and the square of the so called *transfer function*  $A(\tau, k)$ :

$$\langle A(\tau, \vec{k}), A^*(\tau, \vec{k}') \rangle = \delta^3(\vec{k}' - \vec{k}) A(\tau, k)^2 P_{\mathcal{R}}(k). \quad (1.255)$$

The transfer function accounts for the linear evolution of  $A(\tau, \vec{k})$ , irrespective of its initial conditions. It is given by  $A(\tau, k) = A(\tau, \vec{k})/\mathcal{R}(\vec{k})$ , where it is common to normalize initially  $\mathcal{R}(\vec{k}) = 1$ . Note that we have written the transfer function with the same name as the original variable. The only difference is that the transfer function doesn't depend on  $\vec{k}$ , only on the modulus  $k = |\vec{k}|$ . This just reflects the idea that isotropy is respected by the linear evolution of perturbations in a FLRW background.

The dimensionless primordial spectrum  $\mathcal{P}_{\mathcal{R}}$  is usually parameterized as a power-law near some reference scale (often taken to be  $k_* = 0.05 \text{ Mpc}^{-1}$ ):

$$\mathcal{P}_{\mathcal{R}} = A_s \left( \frac{k}{k_*} \right)^{n_s - 1}. \quad (1.256)$$

Here  $A_s$  is the *scalar amplitude* and  $n_s$  is the *scalar spectral index*. Inflation predicts small deviations from a scale invariant primordial spectrum ( $n_s = 1$ ) as a consequence of a nearly constant energy density during the inflationary period. In fact, one can relate the spectral index with the slow-roll parameters that we introduced in Sect. 1.4 as (BAUMANN 2021):

$$n_s - 1 = -2\varepsilon - \eta. \quad (1.257)$$

The last measurements from Planck18 indicate strong evidence for a nearly scale-invariant spectrum with  $n_s = 0.9665 \pm 0.0038$ . This constitutes one of the great triumphs of the inflationary paradigm. In Chapter 2, we will comment on the consequences of the Hubble tension for this measurement.

#### 1.6.4 Acoustic oscillations

The goal of Boltzmann codes such as CLASS is to solve numerically the set of perturbed Einstein and Boltzmann equations that we presented in Sect. 1.6.2. However, one can adopt several approximations in order to gain a semi-analytic understanding of the evolution of photon and baryon perturbations. This is essential in order to understand the features in the CMB anisotropy spectra that we will describe in Sect. 1.6.5.

As we discussed earlier, photons and baryons form a tightly coupled fluid until recombination. Photons exert a strong pressure on this fluid that counteracts gravitational forces. As a consequence, inhomogeneities in the photon-baryon fluid don't

experience a continuous growth, but rather propagate in the form of acoustic waves. The sound speed at which waves propagate can be computed as

$$c_s^2 = \frac{\delta P_\gamma + \delta P_b}{\delta \rho_\gamma + \delta \rho_b} \simeq \frac{3\delta \rho_\gamma}{\delta \rho_\gamma + \delta \rho_b} \simeq \frac{1}{3(1+R)}, \quad (1.258)$$

where we have used that the baryon pressure is negligible compared to that of the photons,  $\delta P_b \ll \delta P_\gamma = 3\delta \rho_\gamma$ , and that tight-coupling imposes  $\delta_b = 3\delta_\gamma/4$ . Since  $R = 3\bar{\rho}_b/(4\bar{\rho}_\gamma) \propto a$ , we see that the sound speed is close to the speed of light during the radiation era,  $c_s \simeq 1/\sqrt{3}$ , and then slowly drops down to zero during the matter era.

With this, we can define a quantity which is extremely relevant in the context of CMB physics (and for the Hubble tension as we shall see): the sound horizon. At a fixed time  $t$ , this corresponds to the comoving distance travelled by a wavefront since some initial time  $t_i$ , and it is given by

$$r_s(\tau) = \int_{\tau_{\text{ini}}}^{\tau} c_s(\tau') d\tau' = \int_{t_{\text{ini}}}^t \frac{c_s(t) dt}{a(t)} = \int_z^{z_{\text{ini}}} \frac{c_s(z') dz'}{H(z')}. \quad (1.259)$$

This quantity is independent on the choice of  $\tau_{\text{ini}}$  as long as  $\tau_{\text{ini}} \ll \tau$ . During the radiation era, the sound speed is constant and thus the sound horizon is of the order of the particle horizon,  $r_s \simeq c_s \tau \simeq \chi_p/\sqrt{3}$ .

We can get more insight about the details of these acoustic oscillations by building an equation that dictates the evolution of  $\Theta_0 = \delta_\gamma/4$  at leading order in the tight-coupling limit. When the optical depth  $\kappa_\gamma$  is very large, we have already seen that the photon hierarchy Eq. (1.206)-Eq. (1.208) implies  $\sigma_\gamma \rightarrow 0$  and  $\theta_\gamma \rightarrow \theta_b$ . Combining Eq. (1.207) for  $\theta'_\gamma$  with Eq. (1.222) for  $\theta'_b$ , we can get rid of the interaction term (notice the baryon pressure term is totally negligible in this context). Then, we can combine with Eq. (1.206) for  $\delta'_\gamma$  in order to eliminate  $\theta_\gamma$ . Using  $R\mathcal{H} = R'$  and  $3(1+R) = c_s^{-2}$  in the remaining equation, we end up with

$$\Theta_0'' + \frac{R'}{1+R} \Theta_0' + k^2 c_s^2 \Theta_0 = -\frac{k^2}{3} \psi + \frac{R'}{1+R} \phi' + \phi''. \quad (1.260)$$

This corresponds to the equation of an harmonic oscillator with a time-dependent frequency  $k^2 c_s^2$ , a baryon-induced friction term  $\frac{R'}{1+R} \Theta_0'$  and a gravitational forcing function on the r.h.s. If we were to consider a constant  $R$  and ignore the gravitational terms, Eq. (1.260) becomes the equation of a perfect harmonic oscillator, whose solution is

$$\Theta_0(\tau, k) = \Theta_{\text{ini}} \cos(kc_s\tau + \varphi), \quad (1.261)$$

where  $\Theta_{\text{ini}}$  and  $\varphi$  stand for the two integration constants. On the super-Hubble limit,  $k\tau \ll 1$ , the value of  $\Theta_0$  should be frozen (for instance, Eq. (1.235) tells us that during radiation era,  $\delta_{\text{tot}} \simeq \delta_\gamma = -2\phi = \text{const.}$ ). This fixes the phase to  $\varphi = 0$ . On the sub-Hubble limit, we expect oscillations to appear. However, from Eq. (1.261) we see that the threshold between constant and oscillatory behavior is set by  $kc_s\tau$  and not by  $k\tau$ . In particular, the oscillatory condition  $kc_s\tau \gg 1$  is equivalent to say that a comoving wavelength  $\lambda = 2\pi/k$  has entered the sound horizon,  $r_s \simeq c_s\tau \gg \lambda$ . Modes with smaller  $\lambda$  crossed the sound horizon earlier and therefore experienced more oscillations. Since the phase  $kc_s\tau$  of the cosine roughly stands for  $2\pi r_s/\lambda$ , the number of oscillations is given by the ratio  $r_s/\lambda$ .

There is another important effect that cannot be described with Eq. (1.260). This equation assumes that the scattering rate is infinite, *i.e.* that the distance between scatters is virtually zero. Close to recombination, this approximation breaks down, and inhomogeneities are washed out by random scatterings on small scales, below the *diffusion length* (SILK 1968). One can get an estimate of this length by treating photon diffusion as a random walk. The mean-free path of photons is given by  $r_{\text{mfp}}^2 = 1/\Gamma_\gamma$ , where  $\Gamma_\gamma = a\bar{n}_e\sigma_T$  is the comoving photon scattering rate. Then, at a given time  $\tau$ , the comoving distance travelled by a photon since some initial time  $\tau_i$  is

$$r_d^2(\tau) \simeq \int_{\tau_{\text{ini}}}^{\tau} d\tau' \Gamma_\gamma r_{\text{mfp}}^2 = \int_{\tau_{\text{ini}}}^{\tau} \frac{d\tau'}{an_e\sigma_T}. \quad (1.262)$$

This equation is essentially telling us that the diffusion length is of the order  $r_d \sim r_{\text{mfp}}\sqrt{N}$ , where  $N \sim \tau\Gamma_\gamma$  is the total number of scatters. This distance is close to zero in the tight-coupling limit, and abruptly increases when approaching the time of photon decoupling. A more accurate estimate for  $r_d$  can be obtained by considering a non-zero quadrupole  $\Theta_2$  in the Boltzmann hierarchy Eq. (1.206)-Eq. (1.208). The idea is to combine this set of equations with Eq. (1.222) for  $\theta'_b$ , restrict to small scales (where the metric potentials can be neglected), and try solutions of the form  $e^{i\int w d\tau}$ . The imaginary part of  $w$  in the resulting dispersion relation then accounts for damping. The result is (see DODELSON (2003) for details):

$$r_d^2 = (2\pi)^2 \int_{\tau_{\text{ini}}}^{\tau} \frac{d\tau'}{an_e\sigma_T} \left[ \frac{R^2 + \frac{8}{9}(1+R)}{6(1+R)^2} \right]. \quad (1.263)$$

Had we included polarization terms in the photon hierarchy, the numerical factor 8/9 would be replaced by 16/15 (HU et al. 1997).

We proceed now to discuss the behavior of  $\Theta_0$  in the different parts of the  $(k, \tau)$  space. In Fig. 1.15, we have labelled four different regions, in order to highlight for which times and scales the different effects of baryon damping, gravitational driving and diffusion damping can play a role. Fig. 1.15 also depicts three different lines corresponding to Hubble crossing ( $k = \mathcal{H}$ ), sound horizon crossing ( $k = 1/r_s$ ) and diffusion damping crossing ( $k = 1/r_d$ ). Let us discuss each of the regions separately:

- On super-Hubble scales, we've already seen that the perturbation  $\Theta_0$  is frozen. However, its constant value is different in the matter and radiation domination epochs. Using Eq. (1.235) and considering adiabatic initial conditions, one quickly realizes that

$$\Theta_0 = -\frac{\psi}{2} = -\frac{\phi}{2} \quad (\text{Radiation era}), \quad (1.264)$$

$$\Theta_0 = -\frac{2\psi}{3} = -\frac{2\phi}{3} \quad (\text{Matter era}). \quad (1.265)$$

- The region 1 corresponds to modes that are crossing the sound horizon before photon decoupling. In this region, gravitational source terms are important. A key consequence is that the zero point of oscillations is shifted. An approximation to the new zero-point of oscillations is achieved by setting to zero all time derivatives in Eq. (1.260)

$$\Theta_0^{\text{eq}} = -\frac{1}{3c_s^2}\psi = -(1+R)\psi. \quad (1.266)$$

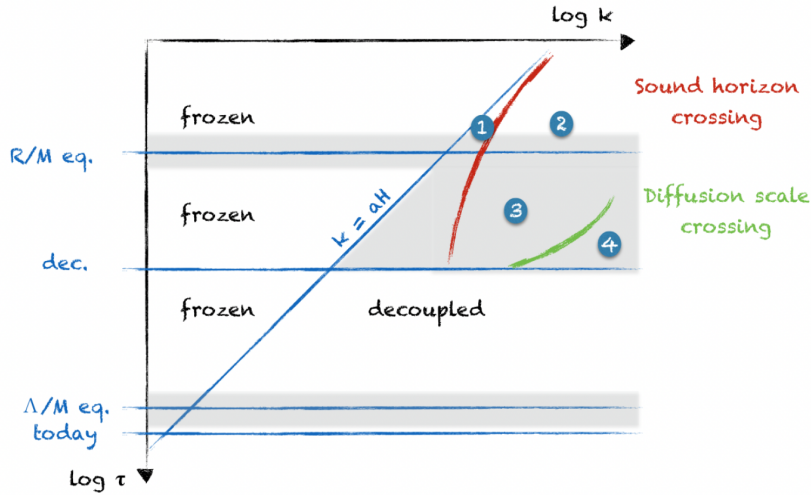


**Figure 1.15** – Different portions of the  $(k, \tau)$  space, leading to specific behaviors of  $\Theta_0$ . The shaded areas indicate regions in which the gravitational potentials decay. Taken from [POULIN \(2017\)](#).

This only lasts a small time, since  $\psi$  rapidly decays on sub-sound horizon scales during the radiation era. Remark that the shifting effect crucially depends on  $R$  and thus on the baryon fraction.

- The region 2 refers to scales that are inside the sound horizon during the radiation era. In this region, the metric potentials have decayed, the friction terms are negligible since  $R \ll 1$ , and  $c_s \simeq 1/\sqrt{3}$ . Thus, this is the case of the perfect harmonic oscillator solution for  $\Theta_0$  that we showed in [Eq. \(1.261\)](#).
- The region 3 is located between matter-radiation equality and decoupling, on scales well below  $r_s$ . Here the metric potentials have decayed, but the effects of baryons are important ( $R$  cannot be neglected). Hence the oscillator equation has a friction term (increasing with time) and a time-dependent pressure term (decreasing with time). This results in damped oscillations. The damping effect is controlled by the duration of the stage between equality and decoupling.
- The region 4 corresponds to scales inside the diffusion length  $r_d$ , that we wrote in [Eq. \(1.262\)](#). This scale increases rapidly close to decoupling, encompassing a big portion of the sub-sound horizon scales. Fluctuations become strongly damped, as diffusion tends to erase any small-scale photon perturbation.

In addition, [Fig. 1.15](#) shows in which parts of the  $(k, \tau)$  space the gravitational potentials decay. This will be important when discussing the integrated Sachs-Wolfe effect in [Sect. 1.6.5](#).

To get a confirmation of the qualitative description we just gave, we show in [Fig. 1.16](#) a numerical resolution of the photon transfer function  $\Theta_0(\tau, k)$ , evaluated at the times of radiation-matter equality and photon decoupling. We also show the zero-point of oscillations,  $\Theta_0^{\text{eq}} = -(1+R)\psi$ , at the decoupling time. We observe that  $\Theta_0$  is frozen on super-Hubble scales, and starts oscillating when  $kr_s(\tau) > 1$ . The negative values of  $\Theta_0$  and  $-\psi$  in the long-wavelength limit come from the fact that transfer functions are all normalized with respect to the curvature perturbation,  $\mathcal{R} = 1$ . Notice

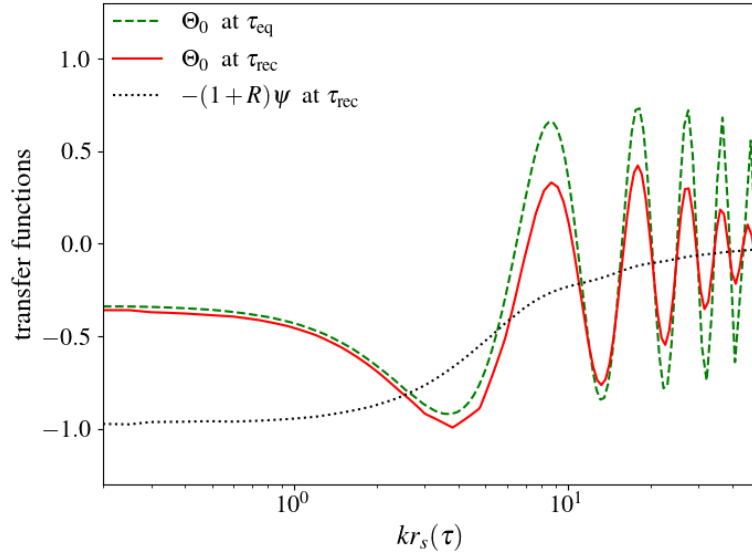


**Figure 1.16** – A snapshot of the photon transfer function  $\Theta_0$  and the zero-point of oscillations,  $\Theta_0^{\text{eq}} = -(1+R)\psi$ , at the time of photon decoupling. The former is also shown at the time of matter-radiation equality, in order to highlight the differences in the shape of the oscillations. In the x axis, we have rescaled the wavenumbers by the corresponding value of the sound horizon, to indicate that the phase of the oscillations is given by  $kr_s(\tau)$ .

also that the super-Hubble values of  $\Theta_0$  are not exactly the same at  $\tau_{\text{eq}}$  and  $\tau_{\text{rec}}$ . In fact, combining Eq. (1.233) with Eq. (1.264)-Eq. (1.265), one finds that the values of  $\Theta_0$  during radiation and matter domination are related by  $\Theta_0^{\text{MD}} = \frac{6}{5}\Theta_0^{\text{RD}}$ .

Moving to the sub-sound-horizon limit in Fig. 1.16, we clearly see differences between the shape of the oscillations at  $\tau_{\text{eq}}$  and  $\tau_{\text{rec}}$ . At equality,  $\Theta_0$  exhibits oscillations with constant amplitude, roughly symmetric around  $\Theta_0^{\text{eq}} = -\psi \simeq 0$ . At decoupling,  $\Theta_0$  is affected by the three important effects we discussed previously: a suppression in the global amplitude due to baryon friction, a shift in the zero point of oscillations by an amount  $-R\psi$ , and the exponential damping at  $k$  larger than the diffusion wavenumber  $k_d = 2\pi/r_d$ . Importantly, the shift of the zero-point leads to an enhancement of the absolute value of the odd extrema in  $\Theta_0$  with respect to the even extrema.

### 1.6.5 The CMB power spectra

We would like to understand the pattern of anisotropies appearing the famous temperature map of the CMB (shown in Fig. 1.4). Note that although temperature fluctuations depend on space and time,  $\Theta(\tau, \vec{x}, \hat{n})$ , we only measure them on Earth (that for simplicity we can take at the origin  $\vec{x} = \vec{0}$ ) and at present time ( $\tau = \tau_0$ ). All the information that we can extract comes from the variations in temperature for each direction of the incoming photons,  $\hat{n}$ . Then, one can expand the temperature map in spherical harmonics

$$\frac{\delta T(\hat{n})}{\bar{T}} = \Theta(\tau_0, \vec{0}, -\hat{n}) = \sum_{\ell=0}^{\infty} \sum_{m=-\ell}^{m=\ell} a_{\ell m} Y_{\ell m}(\hat{n}), \quad (1.267)$$

(since when observing at  $\hat{n}$ , we see photons traveling in the opposite direction). In an all sky experiment, an observer can collect the coefficients  $a_{\ell m}$ 's, given by the inverse of the previous relation

$$a_{\ell m} = (-1)^\ell \int d\Omega_{\hat{n}} Y_{\ell m}^*(\hat{n}) \Theta(\tau_0, \vec{0}, \hat{n}), \quad (1.268)$$

where we did a change of variables  $\hat{n} \rightarrow -\hat{n}$  and used the properties  $\int d\Omega_{-\hat{n}} = \int d\Omega_{\hat{n}}$  as well as  $Y_{\ell m}(-\hat{n}) = (-1)^\ell Y_{\ell m}(\hat{n})$ . We can relate the coefficients  $a_{\ell m}$ 's with theoretical quantities such as the photon multipoles  $\Theta_\ell(\tau, \vec{k})$ . To do so, we can expand  $\Theta(\tau_0, \vec{0}, \hat{n})$  in Fourier space and in Legendre multipoles, and then make use of the following identity

$$P'_\ell(\hat{k} \cdot \hat{n}) = \frac{4\pi}{2^{\ell'} + 1} \sum_{m'=-\ell'}^{m'+\ell'} Y_{\ell' m'}^*(\hat{k}) Y_{\ell' m'}(\hat{n}). \quad (1.269)$$

Proceeding in this way,

$$\begin{aligned} a_{\ell m} &= \frac{(-1)^\ell}{(2\pi)^3} \int d\Omega_{\hat{n}} Y_{\ell m}^*(\hat{n}) \int d^3\vec{k} \sum_{\ell'=0}^{\infty} (-i)^{\ell'} (2\ell' + 1) P_{\ell'}(\hat{k} \cdot \hat{n}) \Theta_{\ell'}(\tau_0, \vec{k}) \\ &= \frac{(-1)^\ell}{2\pi^2} \int d^3\vec{k} \sum_{\ell' m'} (-i)^{\ell'} \underbrace{\int d\Omega_{\hat{n}} Y_{\ell m}^*(\hat{n}) Y_{\ell' m'}(\hat{n}) Y_{\ell' m'}^*(\hat{k})}_{\delta_{mm'} \delta_{\ell\ell'}} \Theta_{\ell'}(\tau_0, \vec{k}) \\ &= \frac{i^\ell}{2\pi^2} \int d^3\vec{k} Y_{\ell m}^*(\hat{k}) \Theta_\ell(\tau_0, \vec{k}), \end{aligned} \quad (1.270)$$

where to reach the last equality we used the orthogonality of the spherical harmonics. We see that the  $a_{\ell m}$ 's and  $\Theta_\ell(\tau, \vec{k})$  linearly related. Hence, for gaussian linear perturbations, the statistics of the  $a_{\ell m}$ 's is fully encoded in the two-point correlation function  $\langle a_{\ell m}^* a_{\ell' m'} \rangle$ . Using again the orthogonality of the spherical harmonics and

$$\langle \Theta_\ell(\vec{k}) \Theta_{\ell'}(\vec{k}') \rangle = \Theta_\ell(k) \Theta_{\ell'}(k) \frac{2\pi^2}{k^3} \mathcal{P}_{\mathcal{R}}(k) \delta^3(\vec{k} - \vec{k}'), \quad (1.271)$$

it is straightforward to get the two-point correlation function for the  $a_{\ell m}$ 's

$$\langle a_{\ell m}^* a_{\ell' m'} \rangle = \delta_{mm'} \delta_{\ell\ell'} \int \frac{d\ln k}{2\pi^2} \Theta_\ell^2(\tau_0, k) \mathcal{P}_{\mathcal{R}}(k) \equiv \delta_{mm'} \delta_{\ell\ell'} C_\ell^{\text{TT}}. \quad (1.272)$$

The quantity  $C_\ell^{\text{TT}}$  is referred as *the power spectrum of temperature anisotropies* (in harmonic space). The fact that  $\langle a_{\ell m}^* a_{\ell' m'} \rangle$  is proportional to  $\delta_{mm'} \delta_{\ell\ell'}$  indicates that different multipoles are uncorrelated, while the fact that  $C_\ell^{\text{TT}}$  is independent of  $m$  is a consequence of statistical isotropy.

An important caveat is that we can never really observe the true harmonic spectrum. This is because  $C_\ell^{\text{TT}}$  is obtained by carrying out an average of the  $a_{\ell m}$ 's over many realizations of the theory, *i.e.* over many universes obeying the same cosmological model. However, we only observe the CMB sky of our universe. This implies there will necessarily be some scattering around  $C_\ell^{\text{TT}}$ . We can reduce this scattering by taking advantage of the fact that, for a given  $\ell$ -mode, the distribution of the observed  $a_{\ell m}^* a_{\ell m}$  is independent of  $m$ . Thus, for an ideal full sky observation, the best estimator of the true  $C_\ell^{\text{TT}}$  ( $= C_\ell$ , to shorten notation) is the average of the coefficients  $a_{\ell m}^* a_{\ell m}$  over all  $m$ -modes

$$\hat{C}_\ell \equiv \frac{1}{2\ell + 1} \sum_{m=-\ell}^{m=\ell} a_{\ell m}^* a_{\ell m}. \quad (1.273)$$



We notice that the mean of  $\hat{C}_\ell$  is given by

$$\langle \hat{C}_\ell \rangle = \frac{1}{2\ell + 1} \sum_{m=-\ell}^{m=\ell} \underbrace{\langle a_{\ell m}^* a_{\ell m} \rangle}_{C_\ell} = C_\ell, \quad (1.274)$$

which means that it is an unbiased estimator of the true  $C_\ell$ . However, there is a non-zero variance associated to  $\hat{C}_\ell$ :

$$\sigma_{C_\ell}^2 = \frac{\langle (\hat{C}_\ell - C_\ell)(\hat{C}_\ell - C_\ell) \rangle}{C_\ell^2} = \frac{\langle \hat{C}_\ell \hat{C}_\ell \rangle - 2C_\ell \langle \hat{C}_\ell \rangle + C_\ell^2}{C_\ell^2} = \frac{\langle \hat{C}_\ell \hat{C}_\ell \rangle}{C_\ell^2} - 1, \quad (1.275)$$

where  $\langle \hat{C}_\ell \hat{C}_\ell \rangle = (2\ell + 1)^{-2} \sum_{m,m'} \langle a_{\ell m}^* a_{\ell m} a_{\ell m'}^* a_{\ell m'} \rangle$ . To compute this quantity, we can make use of the Wick's probability theorem, which says that for gaussian distributions, any even  $N$ -point correlation function is a sum over all possible pairings of the products of 2-point functions. Hence  $\langle a_{\ell m}^* a_{\ell m} a_{\ell m'}^* a_{\ell m'} \rangle = \langle a_{\ell m}^* a_{\ell m} \rangle \langle a_{\ell m'}^* a_{\ell m'} \rangle + \langle a_{\ell m}^* a_{\ell m'}^* \rangle \langle a_{\ell m} a_{\ell m'} \rangle + \langle a_{\ell m}^* a_{\ell m'} \rangle \langle a_{\ell m} a_{\ell m'}^* \rangle$ . Now, from the requirement that  $\Theta(\hat{n})$  has to be real, one infers the property  $a_{\ell m}^* = (-1)^m a_{\ell -m}$ , and thus  $\langle a_{\ell m} a_{\ell m'} \rangle = \langle a_{\ell m}^* a_{\ell m'}^* \rangle = \delta_{m-m'} (-1)^m C_\ell$ . In short, we can write the variance  $\sigma_{C_\ell}^2$  as

$$\sigma_{C_\ell}^2 = \frac{1}{(2\ell + 1)^2 C_\ell^2} \sum_{m,m'} (C_\ell^2 + \delta_{m-m'}^2 C_\ell^2 + \delta_{mm'}^2 C_\ell^2) - 1 = \frac{2}{2\ell + 1}. \quad (1.276)$$

We see that  $\sigma_{C_\ell}^2$  decreases for larger  $\ell$ , which is to be expected, because at high- $\ell$  there are more  $m$ -modes available to sample the distribution. This fundamental uncertainty, which can be seen as theoretical error, is known as *cosmic variance*.

Let us discuss how we compute in practice the temperature power spectrum that we wrote before,

$$C_\ell^{\text{TT}} = \int \frac{d \ln k}{2\pi^2} \Theta_\ell^2(\tau_0, k) \mathcal{P}_{\mathcal{R}}(k). \quad (1.277)$$

In the previous expression, we didn't specify the integration limits of the  $k$ -integral. For  $k_{\min}$ , a reasonable choice is the inverse of the present Hubble radius,  $k_{\min} \sim \mathcal{H}_0 \sim \tau_0^{-1}$ , since  $R_H = \mathcal{H}_0^{-1}$  gives roughly the largest scale we can observe. What about  $k_{\max}$ ? To find the best choice, we have to remember that the approximate solution for  $\Theta_\ell(\tau, k)$  (*i.e.* when neglecting the gravitational source terms) is given in terms of the spherical Bessel function as  $\Theta_\ell(\tau, k) \propto j_\ell(k\tau)$ . The functions  $j_\ell(x)$  peak near  $x = \ell + \frac{1}{2}$ , and present damped oscillations for  $x > \ell$ . Therefore, at present time  $\tau_0$  and as a function of  $\ell$ ,  $\Theta_\ell(\tau_0, k)$  peaks around  $\ell \sim k\tau_0$ , while multipoles with  $\ell \gg k\tau_0$  are very suppressed. This can be understood from a geometrical point of view. The multipoles index is given by  $\ell = \pi/\theta$ , where  $\theta$  is the angle subtending a comoving scale  $\lambda/2 = \theta D_A(\tau_{\text{rec}})$  on the last scattering surface, with  $D_A(\tau_{\text{rec}})$  the comoving angular distance at decoupling<sup>26</sup> (see Fig. 1.17). This implies the following relation between  $\ell$  and  $k$ :

$$\frac{\lambda}{2} = \frac{\pi}{k} = \theta D_A(\tau_{\text{rec}}) \quad \longrightarrow \quad k = \frac{\ell}{D_A(\tau_{\text{dec}})}. \quad (1.278)$$

In a flat universe, the comoving angular distance at decoupling is simply given by  $D_A(\tau_{\text{rec}}) = (\tau_0 - \tau_{\text{dec}})$ , meaning

$$k = \frac{\ell}{(\tau_0 - \tau_{\text{rec}})}, \quad (1.279)$$

<sup>26</sup>The reason for dividing  $\lambda$  by 2 is that, in harmonic space,  $\theta$  is the angle between a maximum and a minimum, while in Fourier space the distance between a maximum and a minimum is  $\lambda/2$ .



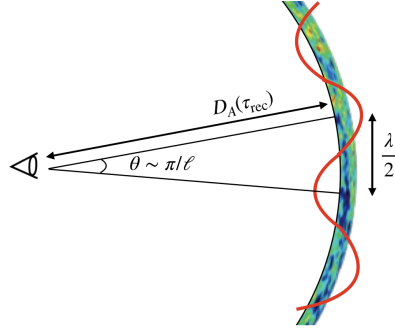


**Figure 1.17** – Diagram to illustrate the geometric relation between the multipole  $\ell$  and the Fourier scale  $\lambda$  observed on the last scattering surface. Adapted from [LESGOURGUES \(2013\)](#).

where  $(\tau_0 - \tau_{\text{rec}}) \simeq \tau_0$ . Hence, if the CMB experiment is observing multipoles up to  $\ell_{\text{max}}$ , the maximum wavenumber should be chosen of the order  $k_{\text{max}} \sim \ell_{\text{max}}/\tau_0$ . This guarantees that the multipoles of the photon transfer function,  $\Theta_\ell(\eta_0, k)$ , are very suppressed for  $\ell > \ell_{\text{max}}$ , so it is safe to compute them just until  $\ell_{\text{max}}$ . Remark that the one-to-one relation between  $\ell$  and  $k$  in [Eq. \(1.279\)](#) is only valid for small angles, or equivalently, for large values of  $\ell$ .

A brute-force approach for computing  $C_\ell^{\text{TT}}$  would consist in truncating the photon Boltzmann hierarchy [Eq. \(1.206\)](#)-[Eq. \(1.208\)](#) at  $\ell_{\text{max}}$ , *i.e.* to solve as many equations as observed multipoles. The problem is that this task is extremely time-consuming, since for a *Planck*-like experiment the maximum multipole is of the order  $\ell_{\text{max}} \sim \mathcal{O}(10^3)$ . In the next subsection, we introduce the alternative line-of-sight formalism, which allows to get  $\Theta_\ell(\eta_0, k)$  up to  $\ell_{\text{max}}$  without having to solve thousands of differential equations. In addition, it makes the underlying physics much more transparent.

### The line-of-sight formalism

The main idea of the line-of-sight formalism, originally introduced by [ZALDARRIAGA et al. \(1995\)](#), is to integrate the Boltzmann equation over the photon trajectory and relate the temperature anisotropies observed today to that at the last scattering surface. In doing this, it is assumed that photons travel along a straight line. Strictly speaking, this is not true, since matter fluctuations produce deviations in the travel direction of photons. However, this effect can be neglected when restricting to first-order perturbations. The starting point is to re-express the photon Boltzmann equation [Eq. \(1.200\)](#) in the following manner (we will neglect the quadrupole  $\Theta_2$  for simplicity):

$$e^{-ik\mu\tau + \kappa_\gamma} \frac{d}{d\tau} \left[ \Theta e^{ik\mu\tau - \kappa_\gamma} \right] = \phi' - ik\mu\psi - \kappa'_\gamma [\Theta_0 + \mu v_b] \equiv \tilde{S}_T(k, \mu, \tau). \quad (1.280)$$

We integrate this equation between some initial time  $\tau_{\text{ini}}$  and today  $\tau_0$ , and use that  $\kappa_\gamma(\tau_0) = 0$ , to get

$$\Theta(\tau_0, k, \mu) = \int_{\tau_{\text{ini}}}^{\tau_0} d\tau \tilde{S}_T(k, \mu, \tau) e^{ik\mu(\tau - \tau_0) - \kappa_\gamma(\tau)}. \quad (1.281)$$

We have also used the fact that  $\tau_{\text{ini}}$  is early enough so that  $e^{-\kappa_\gamma(\tau_{\text{ini}})} \ll 1$ . Now, we would like to remove the dependence of  $\tilde{S}_T$  on  $\mu$ , so that the only factor that depends on  $\mu$

in the integrand is the exponential. This can be achieved by noting that  $\mu e^{ik\mu(\tau-\tau_0)} = \frac{1}{ik} \frac{d}{d\tau} [e^{ik\mu(\tau-\tau_0)}]$ . After performing integration by parts for the two terms with  $\mu$  in  $S_T$  and using  $v_b = \theta_b/ik$ , we get

$$\Theta(\tau_0, k, \mu) = \int_{\tau_{\text{ini}}}^{\tau_0} d\tau e^{ik\mu(\tau-\tau_0)} \left\{ e^{-\kappa_\gamma} (\phi' - \kappa'_\gamma \Theta_0) + \frac{d}{d\tau} \left[ e^{-\kappa_\gamma} \left( \psi - \frac{\theta_b \kappa'_\gamma}{k^2} \right) \right] \right\}. \quad (1.282)$$

We have dropped all surface terms, including one that yields  $\psi(\tau_0, k)$ . In real space, this corresponds to an isotropic term  $\psi(\tau_0, \vec{0})$  that cannot be distinguished from a shift in the average photon temperature. This justifies that we discarded  $\psi(\tau_0, k)$  in the previous expression. At this point, it is useful to introduce the so-called *visibility function*

$$g(\tau) = -\kappa'_\gamma e^{-\kappa_\gamma}. \quad (1.283)$$

This gives the probability that the photons that we see today last scattered at the time  $\tau$  (notice it is correctly normalized,  $\int_0^{\tau_0} g(\tau) d\tau = 1$ ). The visibility function is sharply peaked around the time of photon decoupling. Indeed, at early times (when  $\kappa_\gamma \gg 1$ ), the exponential  $e^{-\kappa_\gamma}$  is very small, while later (after  $\tau_{\text{dec}}$ ), the term  $\kappa'_\gamma = -a\bar{n}_e\sigma_T$  is also very tiny. Thus, the time of photon decoupling can be defined as the peak of  $g(\tau)$ . The terms of Eq. (1.282) inside brackets can now be expressed in terms of this function. Then we can multiply each side by  $i^\ell P_\ell(\mu)/2$  and integrate over  $\mu$ . Using the identity,

$$i^\ell \int_{-1}^{+1} \frac{d\mu}{2} P_\ell(\mu) e^{ik\mu(\tau-\tau_0)} = j_\ell(k(\tau_0 - \tau)), \quad (1.284)$$

we arrive at

$$\Theta_\ell(\tau_0, k) = \int_{\tau_{\text{ini}}}^{\tau_0} d\tau \left\{ g(\Theta_0 + \psi) + (gk^{-2}\theta_b)' + e^{-\kappa_\gamma} (\phi' + \psi') \right\} j_\ell(k(\tau_0 - \tau)). \quad (1.285)$$

This is what we were looking for. This equation allows to obtain any  $\Theta_\ell(\tau_0, k)$  in terms of only a few transfer functions:  $\Theta_0, \theta_b, \psi, \dots$ . The truncation scheme should be designed to compute with accuracy only these quantities. To give an example, truncating the Boltzmann hierarchy in Eq. (1.206)-Eq. (1.208) at  $\ell_{\text{max}, \gamma} \sim \mathcal{O}(10)$  is enough for computing  $\Theta_\ell(\tau_0, k)$  (and hence  $C_\ell^{\text{TT}}$ ) up to  $\ell_{\text{max}} \sim \mathcal{O}(10^3)$ . Notice that, even if we have significantly reduced the number of differential equations to solve, it is  $\ell_{\text{max}}$  and not  $\ell_{\text{max}, \gamma}$  that should be used to compute the maximum wavenumber,  $k_{\text{max}} \sim \ell_{\text{max}}/\tau_0$ .

In order to gain further insight from Eq. (1.285), we will make the *instantaneous decoupling approximation*. That is, we consider that the transition from an opaque to a transparent universe was very abrupt. This means that we can approximate the visibility function as a Dirac delta,  $g(\tau) \simeq \delta(\tau - \tau_{\text{dec}})$ , and the exponential as a step function,  $e^{-\kappa_\gamma} \simeq \Theta_H(\tau - \tau_{\text{dec}})$ . By integrating the  $\theta_b$  term by parts, we get

$$\begin{aligned} \Theta_\ell(\tau_0, k) &\simeq [\Theta_0(\tau_{\text{dec}}, k) + \psi(\tau_{\text{dec}}, k)] j_\ell(k(\tau_0 - \tau_{\text{dec}})) && \longleftarrow \text{SW} \\ &+ k^{-2} \theta_b(\tau_{\text{dec}}, k) j'_\ell(k(\tau_0 - \tau_{\text{dec}})) && \longleftarrow \text{Doppler} \\ &+ \int_{\tau_{\text{dec}}}^{\tau_0} d\tau (\phi' + \psi') j_\ell(k(\tau_0 - \tau)) && \longleftarrow \text{ISW} \end{aligned} \quad (1.286)$$

Here the prime ' in the Bessel function indicates derivative with respect to its argument. As we see, there are three different contributions to  $\Theta_\ell(\tau_0, k)$ . Let us describe each of them separately

- The first contribution is called the Sachs-Wolfe (SW) term, in honor of the first scientists that studied the large-scale anisotropies (SACHS et al. 1967). It corresponds to the quantity  $\Theta_0 + \psi$  evaluated at the last-scattering surface, conveying the general idea that the CMB map is “the picture of the universe when it was only 380 000 years old”. The presence of  $\psi$  simply indicates that photons have to climb out of their potential wells to reach us today. Its interpretation becomes more clear when moving to real space. To do this, we can first go back to angle space using Eq. (1.204) and Eq. (1.284), and then integrate over  $\int \frac{d^3\vec{k}}{(2\pi)^3}$ , to get:

$$\Theta^{\text{SW}}(\tau_0, \vec{0}, \hat{n}) \simeq \Theta_0(\tau_{\text{dec}}, \vec{x}_{\text{dec}}, \hat{n}) + \psi(\tau_{\text{dec}}, \vec{x}_{\text{dec}}), \quad (1.287)$$

where  $\vec{x}_{\text{dec}} = (\tau_{\text{dec}} - \tau_0)\hat{n}$  is the comoving coordinate of the photon arriving from a direction  $-\hat{n}$ . For large (super-Hubble) scales and during the matter era, we know from Eq. (1.265) that there is a relation  $\Theta_0 = -2\psi/3$ . Hence, the SW contribution to the CMB anisotropies smoothed over small scales is written as

$$\Theta^{\text{SW,smoothed}}(\tau_0, \vec{0}, \hat{n}) \simeq \frac{1}{3}\psi(\tau_{\text{dec}}, \vec{x}_{\text{dec}}) \simeq -\frac{1}{2}\Theta_0(\tau_{\text{dec}}, \vec{x}_{\text{dec}}, \hat{n}). \quad (1.288)$$

Surprisingly, hot regions in the observed CMB map corresponds to cold regions on the last scattering surface, and vice-versa. This just arises because the gravitational redshift effect of photons climbing out of the potential well wins against their intrinsic temperature monopole.

- The second contribution is the standard Doppler term. Photons are emitted from a tightly coupled baryon-electron fluid with a different peculiar velocity at different points on the last scattering surface. The projection along the line of sight induces a Doppler shift in the photon wavelength.
- The third contribution is called the Integrated Sachs-Wolfe (ISW) term, and appears in the presence of time variations of the metric fluctuations. Physically, the integral over  $\psi'$  describes a cumulative temperature shift acquired by photons in the presence of a non-conservative gravitational potential. That is, for non-static potentials, it is not true that the integral along the line-of-sight of the gradient,  $\int_{\tau_{\text{dec}}}^{\tau_0} d\tau \hat{n} \cdot \vec{\nabla} \psi$ , is simply equal to  $\psi(\tau_0) - \psi(\tau_{\text{dec}})$ . In a similar manner, the integral over  $\phi'$  accounts for the cumulative effect of local time dilation.

In this formalism, the temperature spectrum  $C_\ell^{\text{TT}}$  is obtained by computing  $\Theta_\ell$  with the line-of-sight integral of Eq. (1.285) and then taking its square and convoluting with the primordial spectrum as demanded by Eq. (1.277). Therefore,  $C_\ell^{\text{TT}}$  receives contributions from the three terms we just discussed: the SW, Doppler and ISW contributions. These are shown in Fig. 1.18.

We can understand the qualitative shape of the different contributions to  $C_\ell^{\text{TT}}$  by making two simplifying assumptions. First, we assume again that decoupling happened instantaneously. Second, we restrict to high- $\ell$  (*i.e.* small scales), for which the functions  $j_\ell(x)$  and  $j'_\ell(x)$  are very peaked in  $x \simeq \ell$ . This means that the  $k$ -integrals mainly receive contributions from  $\ell \simeq k(\tau_0 - \tau_{\text{dec}})$ , which has a simple geometrical interpretation as we discussed around Eq. (1.279). Hence, in these two limits, the SW, Doppler and ISW contributions are roughly given by <sup>27</sup>

<sup>27</sup>The SW contribution to  $C_\ell^{\text{TT}}$  can actually be computed analytically assuming large (super-Hubble) scales instead of small ones, and considering also a scale invariant primordial spectrum,  $n_s = 1$ . From

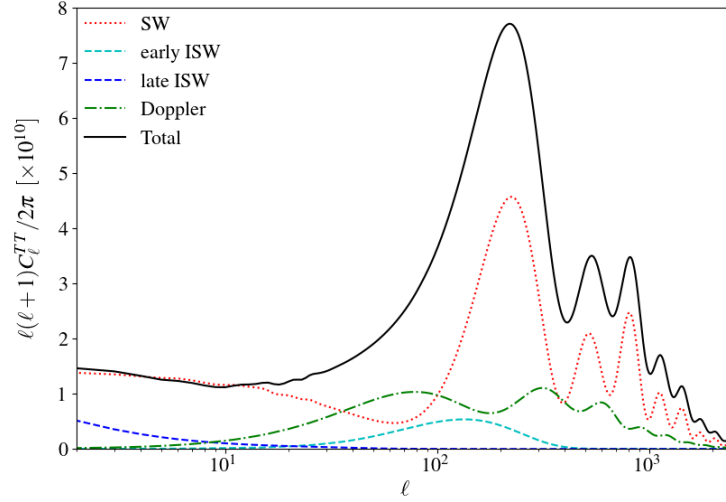


**Figure 1.18** – Different contributions to the temperature anisotropy spectrum  $C_\ell^{\text{TT}}$ .

$$C_\ell^{\text{SW}} \sim \langle |\Theta_0 + \psi|^2 \rangle_{(\tau, k) \simeq (\tau_{\text{dec}}, \ell / (\tau_0 - \tau_{\text{dec}}))}, \quad (1.290)$$

$$C_\ell^{\text{Doppler}} \sim \langle |\theta_b|^2 \rangle_{(\tau, k) \simeq (\tau_{\text{dec}}, \ell / (\tau_0 - \tau_{\text{dec}}))}, \quad (1.291)$$

$$C_\ell^{\text{ISW}} \sim \int_{\tau_{\text{dec}}}^{\tau_0} d\tau (\tau_0 - \tau) \langle |\phi' + \psi'|^2 \rangle_{(\tau, k) \simeq (\tau, \ell / (\tau_0 - \tau))}. \quad (1.292)$$

Note that  $C_\ell^{\text{TT}}$  is not exactly given by the sum of these three contributions because of the different correlations among terms. Let us start discussing the SW part. From Eq. (1.290), it is clear that the shape of the SW contribution should be qualitatively similar to the square of the transfer function  $\Theta_0 + \psi$  at the time of decoupling, as can be confirmed by comparing with Fig. 1.16. At low- $\ell$ , corresponding to super-Hubble scales at decoupling, we see a plateau since perturbations are frozen. On larger  $\ell$ , we see a series of acoustic peaks modulated by the effects we discussed in Sect. 1.6.4. Notoriously, we observe an enhancement of the odd peaks with respect to the even peaks (due to the shift in the zero point of oscillations), as well as an exponential diffusion damping for multipoles above  $\ell_d \sim k_d(\tau_0 - \tau_{\text{dec}})$ . Moving to the Doppler term, we see that its contribution is negligible at low- $\ell$ , whereas at high- $\ell$  it exhibits oscillations with a phase shifted by  $\pi/2$  with respect to those of the SW term. The former can be again explained by the fact that super-horizon perturbations are frozen. The latter can be understood by noting that in the tight-coupling limit, and neglecting variations of the metric potential, the baryon velocity is of the order  $\theta_b \sim \theta_\gamma \sim \Theta'_0 \sim \sin(kc_s\tau)$  (see Eq. (1.206)). Finally, the ISW contribution is only important

Eq. (1.232) and Eq. (1.288), we see that the SW transfer function on large scales is simply  $\Theta_0 + \psi = \frac{\psi}{3} = \frac{1}{5}$  (remember that we set  $\mathcal{R}(\vec{k}) = 1$ ). Hence,

$$C_\ell^{\text{SW,smoothed}} = \frac{A_s}{2\pi^2} \int_0^\infty \frac{dk}{k} (\Theta_0 + \psi)^2 j_\ell^2(k(\tau_0 - \tau_{\text{dec}})) = \frac{A_s}{2\pi^2} \frac{1}{25} \int_0^\infty dx j_\ell^2(x) = \frac{A_s}{100\pi^2} \frac{1}{\ell(\ell+1)}. \quad (1.289)$$

This is the reason why it is common to plot  $\mathcal{D}_\ell = \ell(\ell+1)C_\ell$ , in order to roughly get a plateau at small  $\ell$ .

when  $\phi' \neq 0$  and  $\psi' \neq 0$ . In Fig. 1.15, we had indicated in which regions of the  $k - \tau$  plane the gravitational potentials decay:

- Since the moment of decoupling happened shortly after the beginning matter domination, the metric fluctuations (which have decayed inside the Hubble radius during the radiation era) didn't completely stabilize. This produces a residual variation in  $\psi$  and  $\phi$ , which is known as the *Early Integrated Sachs Wolfe* (EISW) effect.
- At late times, when dark energy begins to dominate the energy budget of the universe, the metric fluctuations start decaying again. This produces the so called *Late Integrated Sachs Wolfe* (LISW) effect.

It can be shown that both the EISW and LISW decrease as a function of  $\ell$ . Since the EISW effect is only relevant inside the sound horizon after decoupling, its contribution is peaked around  $\ell \sim 200$  (as can be seen in Fig. 1.18), enhancing the first acoustic peak. The LISW effect happens at all scales, so it peaks at the smallest  $\ell$ , slightly tilting the Sachs-Wolfe plateau.

### Parameter dependence of $C_\ell$

We have now everything we need to understand the specific effects of the different cosmological parameters on the shape of  $C_\ell^{\text{TT}}$ . For simplicity, we consider a spatially flat universe. We also ignore the effects of free-streaming neutrinos, which are discussed in great details in LESGOURGUES et al. (2018). Nevertheless, we will sketch the dominant effects of a non-zero neutrino mass when discussing decaying neutrinos in Chapter 4.

There are many parameter basis that can be chosen. For convenience, we will take the six free parameters to be

$$\{A_s, n_s, \omega_b, \omega_{\text{cdm}}, \Omega_\Lambda, \tau_{\text{reio}}\}, \quad (1.293)$$

where we remind that  $\omega_i \equiv \Omega_i h^2$ . Remark that the dimensionless Hubble parameter  $h$  is not included since it can be obtained from the condition  $\omega_m h^{-2} = 1 - \Omega_\Lambda$ . The radiation density parameter is not included either, as it can be obtained from the very precise measurement of the present CMB temperature ( $T_0 = 2.7255 \pm 0.0006$  K), and the theoretical prediction of the effective number of neutrino species,  $N_{\text{eff}} \simeq 3.044$ . It is important to remember that the scale factors at matter-radiation and matter- $\Lambda$  equality are controlled by the ratios  $\omega_r/\omega_m$  and  $((1 - \Omega_\Lambda)/\Omega_\Lambda)^{1/3}$ , respectively (c.f. Eq. (1.24)-Eq. (1.25)). Since we assume  $\omega_r$  to be fixed, in practice the scale factor at equality only depends on  $\omega_m$ . The degrees of freedom that sculpt the shape of the temperature spectrum are:

1. The position of the peaks. All the peaks of the CMB spectrum in multipole space,  $C_\ell^{\text{TT}}$ , correspond to the harmonics of one single correlation length of the CMB spectrum in real space,  $C^{\text{TT}}(\theta)$ . This characteristic length is precisely the sound horizon,  $r_s(\tau_{\text{dec}})$ , giving the comoving distance travelled by a wavefront by the time of the decoupling. In multipole space, the peak location is given by  $\pi/\ell_{\text{peak}} = \theta_s = r_s(z_{\text{dec}})/D_A(z_{\text{dec}})$ . The sound horizon depends on the pre-decoupling expansion history and on the sound speed, and thus is affected by  $\omega_m$  and  $\omega_b$ . The comoving angular distance  $D_A(z_{\text{dec}})$  depends on the post-decoupling expansion history and thus it is affected by  $\Omega_\Lambda$  and  $\omega_m$ .

2. The ratio of odd/even peaks. As we have already discussed, the asymmetry between odd and even peaks arises from squaring acoustic oscillations that are shifted with respect to 0 by an amount  $-(1+R)\psi$ . This effects depends on  $R$  and therefore on  $\omega_b$ .
3. The overall amplitude of the peaks. Between the time of radiation-matter equality and decoupling, the amplitude of acoustic oscillations decreases due to baryon friction (see region 3 in Fig. 1.15). If radiation-matter equality happened later, there would be fewer time for oscillations to decrease, and thus all peaks in the spectrum would move upwards. The first peak would be additionally increased by a larger EISW, since metric fluctuations would be less stabilized at decoupling. Those effects are controlled by  $\omega_m$ .
4. The damping envelope. The diffusion processes induce an exponential cutoff shaped like  $\exp(-(\ell/\ell_d)^2)$ , being  $\ell_d = \pi/\theta_d$  with  $\theta_d = r_d(z_{\text{dec}})/D_A(z_{\text{dec}})$ . The diffusion length at decoupling,  $r_d(z_{\text{dec}})$  depends on  $\omega_m$  (governing the conformal time at equality) and  $\omega_b$  (governing the evolution of the free electron fraction). In addition,  $D_A(z_{\text{dec}})$  depends on  $\Omega_\Lambda$  and  $\omega_m$ , as we said earlier.
5. The overall amplitude of the spectrum. The global amplitude of the spectrum depends on  $A_s$ , since this just enters as a multiplicative factor in the expression Eq. (1.277) for  $C_\ell^{\text{TT}}$ .
6. The overall tilt of the spectrum. The global slope of the spectrum depends on the one of the primordial spectrum,  $\mathcal{P}_{\mathcal{R}}(k)$ , controlled by  $n_s$ .
7. Tilting of the plateau. The plateau at small  $\ell$  is tilted further as a result of the LISW. This comes from the fact that  $\psi$  and  $\phi$  start decaying again after matter- $\Lambda$  equality. Consequently, this effect is enhanced by a larger value of  $\Omega_\Lambda$ .
8. Effect of reionization. A small fraction of the CMB photons that we see today last-scattered not at the time of recombination, but at the time of reionization. These rescattered photons come in random directions that average to zero, so they tend to erase the CMB anisotropies. This produces a steplike suppression in the overall amplitude of the peaks starting at  $\ell \sim 40$  (which corresponds to modes crossing the Hubble radius around  $z \sim 10$ ). This effect depends on the optical depth at reionization,  $\tau_{\text{reio}}$ .

We have assumed for simplicity that the redshift of recombination is fixed, but in reality it has a small dependence on the baryon density  $\omega_b$  and the helium mass fraction  $Y_p$ . Notice also that  $\tau_{\text{reio}}$  and  $\Omega_\Lambda$  are poorly constrained by the temperature spectrum, since they are inferred from measurements of the lowest multipoles, dominated by cosmic variance. Fortunately, the combination with polarization anisotropy data and low-redshift probes breaks parameter degeneracies that allow to constrain  $\tau_{\text{reio}}$  and  $\Omega_\Lambda$  (respectively) with better precision.

### A few words on CMB Polarization

At each point in space, photons are described by their temperature, but also by a set of Stokes parameters specifying their polarization state. The invariant amplitude for Thomson scattering depends on photon polarization, more precisely on the product  $|\hat{\epsilon} \cdot \hat{\epsilon}'|^2$ , where  $\hat{\epsilon}$  and  $\hat{\epsilon}'$  denote the polarizations of the incoming and



outgoing photons. However, during the tight-coupling regime, isotropy implies that photons cannot acquire a net polarization in the scatterings with electrons, so they remain unpolarized on average. The situation changes close to the epoch of photon decoupling. Photons experienced their last interactions in regions with increasing anisotropies. The quadrupole  $\Theta_2(\tau, \vec{x})$  associated to these anisotropies produces a net linear polarization of scattered photons. As a consequence, polarization patterns appear on the last scattering surface, which are strongly correlated with the temperature patterns.

The polarization map is described by a vector field on a sphere, as opposed to the temperature map, which is a scalar field. Therefore, it can be decomposed into two scalar maps, a gradient and a curl field, or an  $E$ -polarization and  $B$ -polarization component, by analogy with electromagnetism. It is possible to define harmonic power spectra for these polarization modes. It can be shown that scalar perturbations can produce both temperature and  $E$ -polarization anisotropies. If the primordial universe features only gaussian scalar fluctuations, all the information of the CMB maps is encapsulated in the temperature power spectrum,  $C_\ell^{\text{TT}}$ , the  $E$ -type polarization power spectrum  $C_\ell^{\text{EE}}$ , and also the cross-correlation between both,  $C_\ell^{\text{TE}}$ . The latter really adds new information, since polarization anisotropies are only partially correlated with temperature anisotropies.

At this stage, it is convenient to say a few words about tensor modes. As we mentioned at the beginning of [Sect. 1.6](#), tensor modes are associated to the traceless divergenceless spatial components of the metric and the stress-energy tensor, and their d.o.f. represent the polarization states of gravitational waves (GW). Tensor perturbations can interact with any species having non-negligible tensor components in their perturbed stress tensor  $\delta T_{\mu\nu}$  (such as photons after recombination), and generate temperature and polarization anisotropies, including  $B$ -type polarization. But how are these tensor modes produced? Decoupled neutrinos and photons possess non-zero anisotropic stress that can seed tensor perturbations, but these are far too small to generate any detectable effect. The most famous generation mechanism is inflation. [STAROBINSKY \(1979\)](#) showed that, during inflation, quantum fluctuations of the metric can generate a significant amount of primordial GWs, which are described by a nearly scale-invariant power spectrum,  $P_h = A_t \left(\frac{k}{k_*}\right)^{n_t}$ . The amplitude of this spectrum is directly related to the square of the Hubble parameter when observable wavelengths crossed the Hubble radius during inflation. Hence, these primordial GWs directly probe the energy scale of inflation. In this scale is large enough, they can contribute to  $C_\ell^{\text{TT}}$ , but only at  $\ell \lesssim 100$ , because GWs quickly decay inside the Hubble radius. They also generate  $E$ -type and  $B$ -type polarization (at all scales). However, temperature and  $E$ -polarization anisotropies are predominantly dominated by scalars. A better way to detect primordial GWs by measuring the  $B$ -type polarization spectrum,  $C_\ell^{\text{BB}}$ , since in this case there is no scalar contamination. In practice, weak gravitational lensing of the CMB produce a leak from  $E$ -type to  $B$ -type polarization, so disentangling the tensor contribution to  $C_\ell^{\text{BB}}$  is challenging. Tensors have not been observed yet, so current experiments set an upper limit on the tensor amplitude normalized to the scalar one, *i.e.* on the so called *tensor-to-scalar* ratio  $r \equiv A_t/A_s$ . The last measurements from [Planck18](#) indicate  $r < 0.10$  (at 95 % CL). Notice that, even in the presence of tensors, the cross-correlation spectra  $C_\ell^{\text{TB}}$  and  $C_\ell^{\text{EB}}$  should vanish. Indeed,  $T$  and  $E$  modes remain unchanged under parity transformations, while



$B$  changes sign, so in the absence of parity violating physics we expect  $C_\ell^{\text{TB}} = C_\ell^{\text{EB}} = 0$ .

The calculation of  $C_\ell^{\text{EE}}$  and  $C_\ell^{\text{TE}}$  in a universe featuring just scalar perturbations can be performed along the same line as for  $C_\ell^{\text{TT}}$ . The photon polarization is described by a new degree of freedom,  $\Theta_P(\tau, k, \mu)$ , whose evolution is described by a new Boltzmann equation coupled to the Boltzmann equation for the photon temperature perturbation  $\Theta(\tau, k, \mu)$ . We neglected this effect when writing Eq. (1.200), but it turns out that the impact of polarization on photon temperature anisotropies is quite small, so our previous qualitative discussion on  $C_\ell^{\text{TT}}$  remains valid. One can express the photon polarization as the line-of-sight integral of an appropriate source function, and then expand in Legendre multipoles (just as for temperature). For brevity, we just quote the final result without providing any explicit calculation (we refer to DURRER (2020) for more details on this rich subject). Under the assumption of instantaneous decoupling, and restricting to small scales ( $k\tau_0 \gg 1$ ), one can show that the photon polarization multipoles today are roughly given by

$$\begin{aligned} E_\ell(\tau_0, k) = \Theta_{P,\ell}(\tau_0, k) &\simeq \frac{15}{8} \Theta_2(k, \tau_{\text{dec}}) \frac{\ell^2 j_\ell(k\tau_0)}{(k\tau_0)^2} \\ &\simeq \frac{5k}{6\kappa'_\gamma(\tau_{\text{dec}})} \Theta_1(k, \tau_{\text{dec}}) \frac{\ell^2 j_\ell(k\tau_0)}{(k\tau_0)^2}, \end{aligned} \quad (1.294)$$

where the last equality follows from the tight-coupling condition,  $\Theta_2 \simeq -4k\Theta_1/(9\kappa'_\gamma)$ . There are three important aspects to discuss. First, the polarization spectrum is seen to be smaller than the temperature spectrum by a factor of order  $k/\kappa'_\gamma$  at recombination. This arises as a combination of the facts that polarization can only be generated by a quadrupole, and the quadrupole is suppressed in the early universe due to the frequent Compton interactions. Second, we see that,  $E_\ell \propto \Theta_1$ , so we expect the polarization spectrum to exhibit oscillations which are out of phase with the temperature spectrum. Finally, there is no analogue to the ISW effect, since polarization is not induced by photons moving through time-varying metric potentials.

Measuring the  $EE$  and the  $TE$  power spectrum is interesting, since it contains additional information that allows to break some degeneracies among parameters. For instance, reionization imprints a very characteristic effect on  $C_\ell^{\text{EE}}$ , as we illustrate in Fig. 1.19. A small fraction of photons rescattered during reionization acquire additional polarization that manifests as a bump at  $\ell \lesssim 10$  in  $C_\ell^{\text{EE}}$ . This effect is so large that, despite cosmic variance,  $\tau_{\text{reio}}$  can be well determined using polarization data. In Chapter 4, we will see the implications of this measurement for a model of decaying neutrinos.

### A few words on CMB lensing

The anisotropies measured in the CMB can be classified as *primary* or *secondary*, depending on whether they are affected by processes around the time of recombination or at much later times, respectively. We have already discussed two examples of secondary anisotropies: the LISW effect and reionization. There is still a very important secondary anisotropy that we haven't described: CMB lensing. In general, gravitational lensing occurs when matter deflects the path of light as it travels from a source to the observer. There are three types of gravitational lensing. Strong lensing occurs when the deflection is large and multiple images are formed. Microlensing

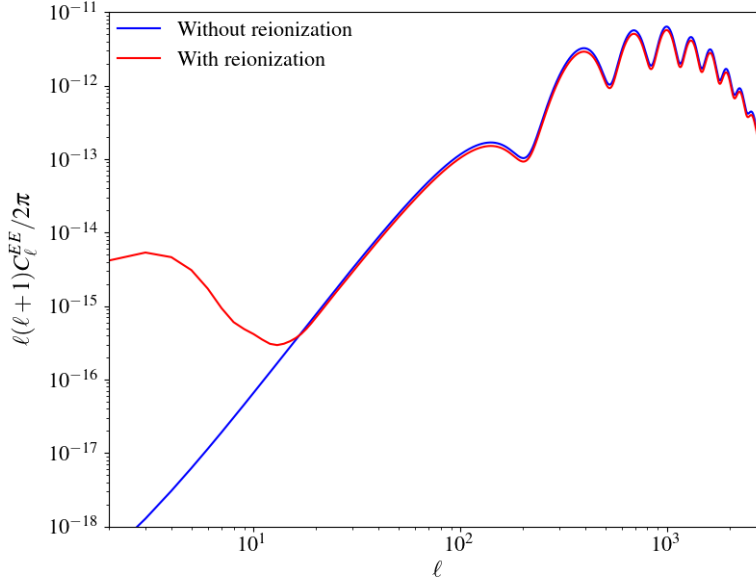


**Figure 1.19** – Type- $E$  polarization spectrum, with and without including the effects of the cosmic reionization at low redshift.

occurs when the angular separation of images is too small to be resolved, and instead the source is temporarily brightened. Finally, weak lensing occurs when the deflection is small, and no multiple images are formed. The latter is the one which is most relevant in cosmology. The main idea of weak CMB lensing is that the trajectories of photons coming from the last scattering surface are deflected by matter fluctuations localized at redshifts  $z \lesssim 3$ . At leading order in perturbations, it's possible to describe CMB lensing in terms of a two-dimensional deflection field  $\hat{d}(\hat{n})$ , giving the difference between the direction  $\hat{n}$  at which photons are emitted, and the observed direction  $\hat{n} + \hat{d}(\hat{n})$ . Using the spatial component  $\mu = i$  of the perturbed geodesic equation, one can show that the deflection field is given by the gradient of a lensing potential  $\varphi$ , related to the Newtonian metric potentials  $\phi$  and  $\psi$  through a convolution along the line of sight (see [DODELSON \(2003\)](#) for details)

$$\varphi(\hat{n}) = - \int_{\tau_{\text{rec}}}^{\tau_0} d\tau \frac{\chi(\tau_{\text{rec}}) - \chi(\tau)}{\chi(\tau_{\text{rec}})\chi(\tau)} (\phi + \psi)_{(\tau, \vec{x}=r(\tau)\hat{n})}, \quad (1.295)$$

where  $\chi(\tau)$  represents the comoving distance introduced in [Eq. \(1.31\)](#). During the matter era and inside the Hubble radius, we can relate  $\psi = \phi$  to the total matter density fluctuations  $\delta_m$  using the Poisson equation [Eq. \(1.229\)](#). Hence, the harmonic power spectrum  $C_\ell^{\varphi\varphi}$  of a given map  $\varphi(\hat{n})$  can be obtained from the matter power  $P_m(z, k)$  (which we define in [Eq. \(1.296\)](#)) convolved with an appropriate kernel. Using  $C_\ell^{\varphi\varphi}$ , one can compute the two-point statistics associated to the lensed temperature map  $\tilde{\Theta}(\hat{n}) = \Theta(\hat{n} + \hat{d}(\hat{n}))$  from that of the unlensed map  $\Theta(\hat{n})$  ([LEWIS et al. 2006](#)). Lensing smoothes out the peaks in the temperature power spectrum, and adds power on very small scales, as we illustrate in [Fig. 1.20](#). The lensing effects are so small that they are only evident in the fractional differences. However, these effects are already larger than the error bars in current CMB experiments, so lensing needs to be taken into account.

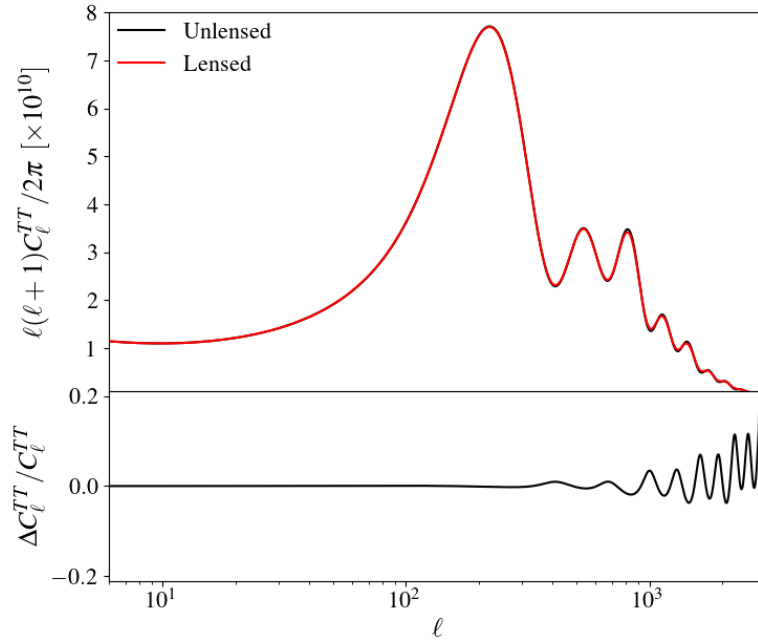


**Figure 1.20 – Top panel:** Temperature power spectrum before and after lensing corrections are applied. **Bottom panel:** Fractional difference between these two spectra.

Inferring the lensing spectrum  $C_\ell^{\varphi\varphi}$  from observations is not a trivial task, since we only observe CMB anisotropies after lensing effects have taken place. Luckily, lensing produces non-zero correlations between off-diagonal modes of the temperature maps, *i.e.*  $\langle \tilde{\Theta}(\vec{\ell})\tilde{\Theta}(\vec{\ell}') \rangle = f^{TT}(\vec{\ell}, \vec{\ell}')\varphi(\vec{\ell} - \vec{\ell}') \neq 0$  for  $\vec{\ell} \neq \vec{\ell}'$  (here  $\tilde{\Theta}(\vec{\ell})$  denotes the flat-sky 2D Fourier transform of  $\tilde{\Theta}(\hat{n})$ ). Thanks to this effect, one can build estimators that allow to reconstruct the deflection potential  $\varphi(\hat{n})$  directly from the anisotropy maps  $\tilde{\Theta}(\hat{n})$  (OKAMOTO et al. 2003).

As we will see in Chapter 3 and Chapter 4, secondary CMB anisotropies (and specially, CMB lensing) are essential for constraining unstable relics, such as decaying dark matter or decaying neutrinos, since these scenarios typically produce deviations from  $\Lambda$ CDM only after recombination.

### 1.6.6 The matter power spectrum

Many Large Scale Structure (LSS) observables can be inferred from the matter power spectrum at different scales and redshifts,  $P_m(z, k)$ , which is defined as

$$\langle \delta_m(z, \vec{k})\delta_m^*(z, \vec{k}') \rangle = P_m(z, k)\delta^{(3)}(\vec{k} - \vec{k}'). \quad (1.296)$$

Here  $\delta_m$  is the total density contrast of non-relativistic matter components. In the  $\Lambda$ CDM model, it receives contributions from CDM, baryons and non-relativistic neutrinos

$$\delta_m = \frac{\delta\rho_m}{\bar{\rho}_m} = \frac{\bar{\rho}_{\text{cdm}}\delta_{\text{cdm}} + \bar{\rho}_b\delta_b + \bar{\rho}_\nu\delta_\nu}{\bar{\rho}_{\text{cdm}} + \bar{\rho}_b + \bar{\rho}_\nu}. \quad (1.297)$$

In the following, we will discuss the shape of the matter power spectrum in the linear regime (although we will briefly comment the importance of non-linearities later

on). The assumptions of linearity and gaussian initial conditions imply that, at any time, the matter power spectrum can be expressed as the product of the primordial spectrum and the square of the transfer function  $\delta_m(z, k)$ :

$$P_m(z, k) = \frac{2\pi^2}{k^3} A_s \left( \frac{k}{k_*} \right)^{n_s-1} \delta_m^2(z, k). \quad (1.298)$$

Hence, one can get some insight about the shape of  $P_m(z, k)$  by studying the qualitative evolution of  $\delta_m(z, k)$ , as we proceed to do now.

### Theoretical understanding

For simplicity, let us first consider a neutrinoless universe with a negligible amount of baryons  $\Omega_b \ll \Omega_{\text{cdm}}$ . This means that  $\delta_m \simeq \delta_{\text{cdm}}$ , so all we need to know is the evolution of CDM perturbations. By combining the first derivative of the continuity equation Eq. (1.217) with the Euler equation Eq. (1.218), we easily arrive at a master equation for the evolution of  $\delta_{\text{cdm}}$

$$\delta_{\text{cdm}}'' + \mathcal{H}\delta_{\text{cdm}}' = -k^2\psi + 3\phi'' + 3\mathcal{H}\phi'. \quad (1.299)$$

This equation tells us that the evolution of  $\delta_{\text{cdm}}$  is governed by a competition between friction due to the cosmic expansion ( $\mathcal{H}\delta_{\text{cdm}}'$ ), gravitational forces ( $-k^2\psi$ ) and dilation effects ( $3\phi'' + 3\mathcal{H}\phi'$ ).

As we have already discussed,  $\delta_{\text{cdm}}$  is frozen on super-Hubble scales, and only varies when the EoS of the universe changes (assuming the Newtonian gauge). Let us focus on the evolution at sub-Hubble scales. In this regime, we saw earlier that the dilation terms can be safely ignored. What about the gravitational force term  $k^2\psi$ ? The Poisson equation tells us that  $k^2\psi \simeq -4\pi G a^2 \delta\rho_{\text{tot}} \simeq -4\pi G a^2 (\bar{\rho}_{\text{cdm}}\delta_{\text{cdm}} + \bar{\rho}_\gamma\delta_\gamma)$ . During matter and  $\Lambda$  domination, the contribution from photons is negligible, so we can simply replace  $k^2\psi$  by  $-4\pi G a^2 \bar{\rho}_{\text{cdm}}\delta_{\text{cdm}}$ . During radiation domination, the situation is more subtle, since both  $\delta_{\text{cdm}}$  and  $\delta_\gamma$  can be important. As pointed out by WEINBERG (2002), in this case the full solution of the system can be decomposed into fast modes (oscillating with a pulsation of the order  $k$  or  $k c_s$ ) and slow modes (evolving over a Hubble time scale). It turns out the gravitational back reaction between the two modes (through the Poisson equation) can be neglected. Since we are only looking at CDM, we just need to consider slow modes and thus make the same replacement as for the matter era,  $k^2\psi = -4\pi G a^2 \bar{\rho}_{\text{cdm}}\delta_{\text{cdm}}$ . In short, inside the Hubble radius we can rewrite Eq. (1.299) as

$$\delta_{\text{cdm}}'' + \mathcal{H}\delta_{\text{cdm}}' - \frac{3}{2}\mathcal{H}^2\Omega_{\text{cdm}}(\tau)\delta_{\text{cdm}} = 0, \quad (1.300)$$

where  $\Omega_{\text{cdm}}(\tau) = \bar{\rho}_{\text{cdm}}(\tau)/\bar{\rho}_c(\tau) = 8\pi G \bar{\rho}_{\text{cdm}}(\tau)/3H^2(\tau)$  is the time dependent abundance of CDM. This equation is sometimes referred as *the Mészáros equation* (MESZAROS 1974). It is possible to get analytical solutions at all times, which are scale independent since the Mészáros equation doesn't involve  $k$ . However, the integration constants can generally depend on  $k$ , and their expression is obtained by matching to the solutions at horizon crossing. For simplicity, we don't detail this procedure here. In fact, for understanding the shape of the matter spectrum, it will be enough to just look at the asymptotic solutions:

- During the radiation era ( $\Omega_{\text{cdm}}(a) \ll 1$ ) the growing solution has a sub-Hubble limit  $\delta_{\text{cdm}} \propto \log(ka) \propto \log(k\tau)$ . The full solution (valid at all scales) involves the cosine integral, and its expression can be found in Eq. (22) of GREEN et al. (2005).
- During the matter era ( $\Omega_{\text{cdm}}(\tau) \simeq 1$ ), the growing sub-Hubble solution evolves linearly with the scale factor  $\delta_{\text{cdm}} \propto a \propto \tau^2$ . This is a famous result from linear theory; it means that it is necessary to wait until the universe becomes matter dominates in order for CDM perturbations to grow appreciably.
- During the  $\Lambda$  era, the growth of structures is slowed down, since  $\Lambda$  enhances the expansion rate and consequently the friction term. It is common to parametrize the sub-Hubble solution as  $\delta_{\text{cdm}} \propto ag(a, \Omega_m)$ , where  $g(a, \Omega_m)$  is a function capturing the deviations from the linear evolution with  $a$ : it is equal to 1 deep in the matter era, and monotonically decreases afterwards.  $g(a, \Omega_m)$  can be written in terms of a hypergeometric function, but simple fitting formulas in terms of  $\Omega_m = 1 - \Omega_\Lambda$  can be found in the literature (e.g. see Eq. (A4) in EISENSTEIN et al. (1998)).

We have everything we need to understand the global shape of the matter spectrum as a function of time. We will have to consider three different wavenumbers, corresponding to modes crossing the Hubble radius at the time of matter-radiation equality, matter- $\Lambda$  equality and today:  $k_{\text{eq}} = a_{\text{eq}}H_{\text{eq}}$ ,  $k_\Lambda = a_\Lambda H_\Lambda$ , and  $k_0 = a_0 H_0$ . Let us now describe the evolution of  $P_m(k)$  with respect to time.

1. At initial times, all modes of interest were super-horizon, so  $P_m$  just follows the shape of the primordial spectrum  $\mathcal{P}_{\mathcal{R}}(k)$ . Assuming a scale invariant spectrum for simplicity ( $n_s = 1$ ), then  $P_m(k) \propto k^{-3}$ .
2. During the radiation era, sub-Hubble modes evolve like  $\log(k\tau)$ . Thus, at matter-radiation equality, super-Hubble modes ( $k \ll k_{\text{eq}}$ ) are shaped like initially ( $P_m(k) \propto k^{-3}$ ), whereas the sub-Hubble modes ( $k \gg k_{\text{eq}}$ ) have been amplified by a  $k$ -dependent factor  $[\delta_{\text{cdm}}(\tau_{\text{eq}}, k)/\delta_{\text{cdm}}(\tau_{\text{ini}}, k)]^2 \simeq [\log(k\tau_{\text{eq}})]^2$  (meaning that  $P_m(k) \propto k^{-3} [\log(k)]^2$ ).
3. At the time of matter- $\Lambda$  equality, super-Hubble modes ( $k \ll k_\Lambda$ ) keep being shaped like initially. Modes with  $k \gg k_{\text{eq}}$  have been enhanced during the matter era by a  $k$ -independent factor  $[\delta_{\text{cdm}}(\tau_\Lambda, k)/\delta_{\text{cdm}}(\tau_{\text{eq}}, k)]^2 \simeq (\tau_\Lambda/\tau_{\text{eq}})^4$ . Finally, intermediate modes crossing the Hubble radius during matter domination ( $k_\Lambda \ll k \ll k_{\text{eq}}$ ) have been amplified by a  $k$ -dependent factor  $(\tau_\Lambda/\tau_*)^4$ , where  $\tau_*$  is their time of Hubble crossing,  $\tau_* \simeq 1/k$ . In summary, the spectrum has three branches, which scale like
  - $P_m(k) \propto k^{-3}$ , for  $k < k_\Lambda$ ,
  - $P_m(k) \propto k^{-3}k^4 = k$ , for  $k_\Lambda < k < k_{\text{eq}}$ ,
  - $P_m(k) \propto k^{-3}(\log k)^2$ , for  $k > k_{\text{eq}}$ .
4. During the  $\Lambda$  era,  $\delta_{\text{cdm}}$  grows more slowly than  $\tau^2$ , but this suppression of growth is the same for all scales. Hence, the shape of the matter spectrum is unaffected by this stage, and the three branches are the same as during the matter era. The only difference is that the primordial spectrum  $P_m \propto k^{-3}$  is now recovered for scales  $k < k_0$ , which in practice are never directly observed.

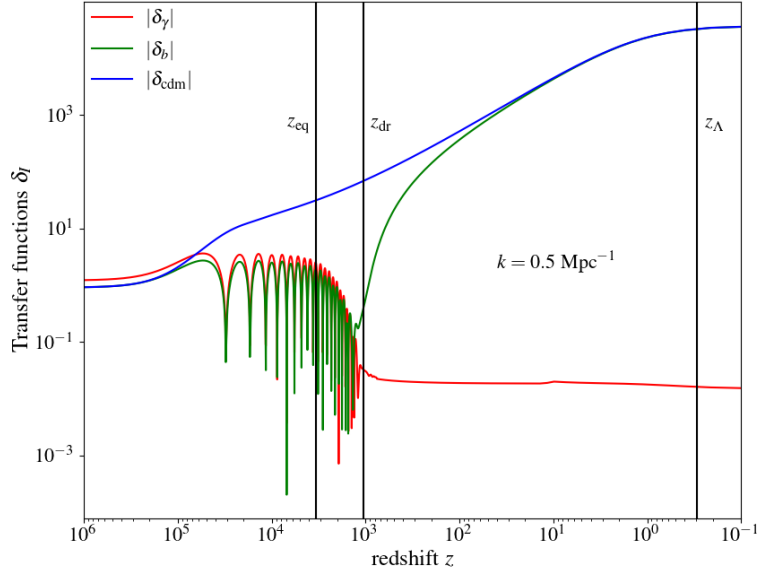


**Figure 1.21** – Linear evolution of the density perturbations for photons, baryons and CDM, corresponding to a mode ( $k = 0.5 \text{ Mpc}^{-1}$ ) that crossed the Hubble radius during radiation domination.

It still remains to see the effects associated to baryons, since in reality  $\Omega_b$  is not negligible. As we already discussed in Sect. 1.6.2, baryons remain coupled to photons until the time of baryon drag, which took place slightly after photon decoupling,  $\tau_{\text{dr}} > \tau_{\text{dec}}$ . After that time, the collision term vanishes, and the evolution of baryons is dictated by an identical equation as that for CDM, *i.e.* Eq. (1.299) (notice that will always consider scales bigger than the Jean’s length, which means that we can discard the baryon pressure term). Let us discuss separately the evolution of modes that crossed the Hubble radius before and after baryon drag.

For modes that crossed the Hubble radius after baryon drag, the evolution of baryons is trivial, since it matches that of CDM,  $\delta_b = \delta_{\text{cdm}}$ . Indeed, baryon and CDM density perturbations are equal on super-Hubble scales due to the adiabatic initial conditions. After Hubble crossing, they are subject to the same evolution equation of the form Eq. (1.299), so they remain equal at all times.

The situation is a bit more complex for modes that crossed the Hubble radius before baryon drag. In this case, baryons develop the same oscillatory behavior as photons, since the tight-coupling between these species enforces  $\delta_b = \frac{3}{4}\delta_\gamma$ . This means that baryons experience all the effects discussed in Sect. 1.6.4, such as decreasing oscillations during the matter era, diffusion damping on the small scales, etc. As long as baryons remain coupled to photons, they don’t cluster, but still contribute to enhance the expansion rate. This is translated into a reduced growth of CDM. For instance, one can consider sub-Hubble scales during the matter era, and solve a Mészáros equation identical to Eq. (1.300) but including the contribution from baryons in  $\mathcal{H}$ . This gives a solution  $\delta_{\text{cdm}} \propto a^{1-\frac{3}{5}f_b}$ , with  $f_b \equiv \frac{\bar{\rho}_b}{\bar{\rho}_b + \bar{\rho}_{\text{cdm}}}$ . This reduction of



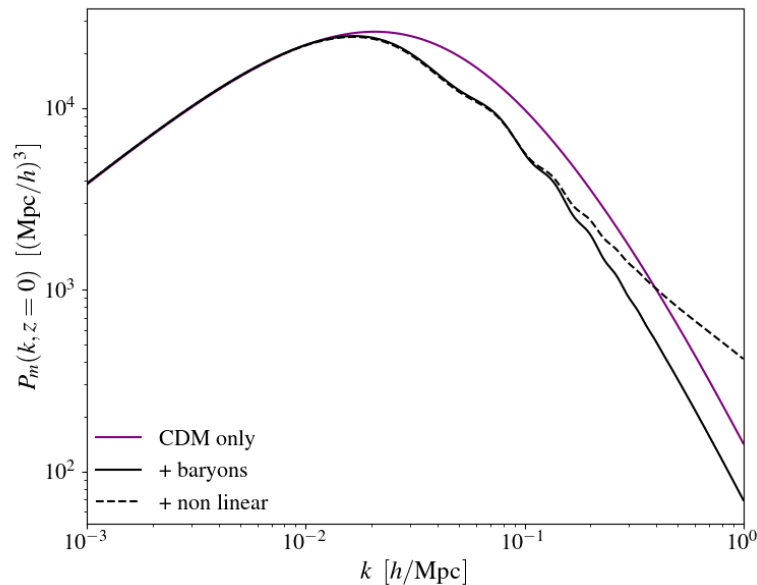


**Figure 1.22** – The matter power spectrum at  $z = 0$  computed with only CDM, adding baryons ( $\omega_b = 0.022$ ), and including non-linear corrections with **HALOFIT** (R. E. SMITH et al. 2003; R. TAKAHASHI et al. 2012). In all cases, the present matter abundance is set to  $\omega_m = 0.142$ .

linear growth of the CDM perturbations produces a suppression in the matter power spectrum for wavenumbers  $k > k_{\text{eq}}$ .

After baryon drag, baryons and CDM are collisionless species feeling the same gravitational forces, so their perturbations are described the following set of coupled equations at sub-Hubble scales

$$\delta''_{\text{cdm}} + \mathcal{H}\delta'_{\text{cdm}} = 4\pi G a^2 (\bar{\rho}_{\text{cdm}}\delta_{\text{cdm}} + \bar{\rho}_b\delta_b), \quad (1.301)$$

$$\delta''_b + \mathcal{H}\delta'_b = 4\pi G a^2 (\bar{\rho}_{\text{cdm}}\delta_{\text{cdm}} + \bar{\rho}_b\delta_b). \quad (1.302)$$

By solving this system of equations, one notices that  $\delta_b$  (which at baryon drag was much more suppressed than  $\delta_{\text{cdm}}$ ) rapidly approaches  $\delta_{\text{cdm}}$ . In other words, baryons fall into the potential gravitational wells created by the CDM. The time needed to reach  $\delta_b = \delta_{\text{cdm}}$  is greater for smaller scales, because in the large- $k$  limit the ratio  $|\delta_b/\delta_{\text{cdm}}|$  is smaller at  $\tau_{\text{dr}}$  due to Silk damping. This phenomenon, essential to understand the formation of large-scale structures, is illustrated in Fig. 1.21, where we show the numerical resolution of  $\delta_\gamma$ ,  $\delta_b$  and  $\delta_{\text{cdm}}$  for a mode that entered the Hubble radius deep in the radiation era ( $k = 0.5 \text{ Mpc}^{-1}$ ). Hence, in order to get an approximate description of the matter power spectrum, it is enough to perform a matching of the solution  $\delta_c = \delta_b$  for  $\tau > \tau_{\text{dr}}$  with the individual solutions  $\delta_c$  and  $\delta_b$  during  $\tau < \tau_{\text{dr}}$  (as described in detail in EISENSTEIN et al. (1998)). The important outcome is that baryons imprint small oscillations as a function of  $k$  in the matter power spectrum, which are known as *Baryon Acoustic Oscillations* (BAO).

In Fig. 1.22 we show a numerical calculation of the matter power spectrum at  $z = 0$ , with and without taking baryons into account<sup>28</sup>. The shape of  $P_m(k)$  agrees very well

<sup>28</sup>Let us briefly motivate the choice of displaying  $k$  in units of  $h/\text{Mpc}$ . The evolution of sub-Hubble perturbations depends primarily on how deep inside the Hubble radius a given mode is, *i.e.* on the ratio



with our qualitative discussion. It shows a peak at  $k = k_{\text{eq}}$ , with the two branches at  $k < k_{\text{eq}}$  and  $k > k_{\text{eq}}$  going roughly as  $P_m \propto k$  and  $P_m \propto k^{-3}[\log(k)]^2$ , respectively. In addition, baryons lead to an overall suppression for  $k > k_{\text{eq}}$  and imprint the BAO feature, which has already been detected in galaxy surveys (EISENSTEIN et al. 2005).

### Parameter dependence of $P_m(k)$

We can now discuss the effects of the different cosmological parameters on the shape of the matter power spectrum, similarly as we did in Sect. 1.6.5 with the CMB temperature spectrum. In this case,  $P_m(k)$  is impacted by only 5 parameters, since the optical depth at reionization only affects the scattering rate of photons. Taking as a parameter basis,

$$\{A_s, n_s, \omega_b, \omega_{\text{cdm}}, \Omega_\Lambda\}, \quad (1.303)$$

we can enumerate each of the different effects.

1. The time of equality fixes the location of the peak,  $k_{\text{eq}}$ . In units of  $h/\text{Mpc}$ , this scale is entirely determined by  $z_{\text{eq}}$  and  $\Omega_m$ , or equivalently, by  $\omega_m$  and  $\Omega_\Lambda = 1 - \Omega_m$ .
2. The abundance of baryons relative to CDM controls the branch at  $k > k_{\text{eq}}$ . A higher fraction  $\omega_b/\omega_{\text{cdm}}$  implies more suppression at these scales and BAOs more pronounced.
3. The phase of the BAOs is dictated by the comoving sound horizon at baryon drag,  $r_d = r_s(\tau_{\text{dr}})$ . Similarly to the scale of the acoustic oscillations in the CMB spectra,  $r_d$  depends on  $\omega_b$  and  $\omega_m$ . However,  $r_d$  depends much more strongly on  $\omega_b$ , because the time of baryon drag is affected by  $R = 3\bar{\rho}_b/4\bar{\rho}_\gamma$ .
4. The global amplitude depends on the amplitude of the primordial spectrum,  $A_s$ , but also on  $\Omega_\Lambda$ , since we have seen that the  $\Lambda$  produces a scale-independent suppression of growth during the  $\Lambda$  era.
5. The global tilt depends directly on the tilt of the primordial spectrum, *i.e.* on  $n_s$ .

For simplicity we have not included a description of the effects of neutrinos, which are nicely explained in LESGOURGUES et al. (2018). Let us just mention that massive neutrinos have a very strong impact on the matter spectrum. In particular, they induce a smooth steplike suppression on wavenumbers larger than the free-streaming wavenumber at the non-relativistic transition,  $k_{\text{nr}} = k_{\text{fs}}(z_{\text{nr}})$  (where the function  $k_{\text{fs}}(z)$  exhibits a minimum). Indeed, on scales  $k > k_{\text{nr}}$ , neutrinos do not contribute to clustering but still enhance the Hubble friction term, producing a reduced growth of CDM perturbations (akin to the suppression due to baryons). We will encounter a very similar behavior when discussing the dynamics of warm particles arising from DM decays in Chapter 3.

### Probes of structure formation

The theory of linear cosmological perturbations cannot provide a description of matter fluctuations at small scales and small redshifts, where the approximation

---

$k/aH$ . Thus, it is convenient to plot the matter power spectrum as a function of  $k/(a_0H_0)$ , such that any other choice of  $H_0$  would leave the overall shape of the spectrum invariant. However,  $H_0 = h/3000 \text{ Mpc}^{-1}$  and it is typically assumed  $a_0 = 1$ , so in practice it is equivalent to simply write  $k$  in units of  $h/\text{Mpc}$ .

$\delta(\vec{x}, z) \ll 1$  breaks down. LSS observations are sensitive to such range of  $z$  and  $k$ , so it is important to be able to compute the power spectra on mildly or even strongly non-linear scales, in order to extract as much information as possible from these observables <sup>29</sup>. This is typically done with the help of  $N$ -body simulations. In this approach, CDM (and eventually other species like baryons or neutrinos) is represented as a set of  $N$ -body particles, with masses of the order of million solar masses (not to be confused with real particles!). Initially, these particles are distributed inside a box such that the power spectrum of the smoothed distribution is given by the linear spectrum  $P_m(z_{\text{ini}}, k)$  for a given cosmology. Afterwards, particles are evolved using equations from Newtonian gravity, but including the effects of the expansion through a Hubble friction term. These simulations are performed in boxes in comoving space with periodic boundary conditions. Their associated spatial resolution simply scales like the volume of the box divided by the number of particles  $N$ . State-of-the-art codes such as GADGET-2 (SPRINGEL et al. 2001; SPRINGEL 2005) are based on the Tree Particle-Mesh (Tree-PM) approach, which is an intelligent algorithm that avoids having to compute  $N(N - 1)$  forces between pairs of particles, as would be required in a brute-force calculation. The Boltzmann solver **CLASS** makes use of an accurate fitting formula based on the results of the GADGET-2 code, called **HALOFIT** (R. E. SMITH et al. 2003; R. TAKAHASHI et al. 2012), improved to account for the effects of massive neutrinos (BIRD et al. 2012). We show in Fig. 1.22 the impact of the non-linear matter power spectrum, which starts to deviate from the linear one at  $k \sim 0.1h/\text{Mpc}$ . In Chapter 2, we will use the **HALOFIT** code to compute the non-linear matter spectrum associated to a model of Early Dark Energy, in order to test this model against LSS data.

Many LSS observables probe the  $\sigma_8$  parameter, measuring the present strength of clustering on a certain range of scales. Given the importance that this parameter has for the so-called “ $S_8$  tension” and for this work, it is worth pausing for a moment to define this parameter properly. Often, one would like to smooth the matter density field  $\delta_m(\vec{x}, z)$  over some “window” in space. In fact, the actual density field is grainy due to the presence of structures (stars, galaxies, etc) and the theory can only predict the statistics of a smoothed density field. There are several choices for the smoothing function, a popular one is the top-hat window function in real space:

$$W_R(r) = \frac{1}{(4\pi/3)R^3} \Theta_H(R - r), \quad (1.304)$$

where  $r = |\vec{x}' - \vec{x}|$  and  $\Theta_H$  is the Heaviside step function. The smoothed density field is obtained by a convolution with the window function

$$\delta_{m,R}(\vec{x}, z) = \int d^3\vec{x}' W_R(|\vec{x}' - \vec{x}|) \delta_m(\vec{x}', z). \quad (1.305)$$

In Fourier space, this corresponds to a simple multiplication  $\delta_{m,R}(\vec{k}, z) = W_R(k) \delta_m(\vec{k}, z)$ , where  $W_R(k)$  is the Fourier transform of the top-hat window function

$$W_R(k) = 3 \frac{\sin(kR) - kR \cos(kR)}{(kR)^3}. \quad (1.306)$$

---

<sup>29</sup>Note however, that the amount of information that can be extracted tends to saturate at large  $k_{\text{max}}$ , because, deeply in the non-linear regime, the non-linear matter spectrum gradually loses memory of initial conditions, *i.e.* of early linear perturbations.

Hence, the smoothed matter power spectrum reads  $P_{m,R}(k, z) = |W_R(k)|^2 P_m(k, z)$ . Now, from Eq. (1.247) we know how to obtain the matter power spectrum  $P_m(k, z)$  from the 2-point correlation function in real space,  $\xi_m(r, z)$ . One can perform the inverse Fourier-transform and evaluate the *zero-lag* correlation function  $\xi_m(r = 0, z)$ ,

$$\xi_m(r = 0, z) = \frac{1}{2\pi^2} \int_0^\infty dk k^2 P_m(k, z) \lim_{r \rightarrow 0} \frac{\sin(kr)}{kr} = \int_0^\infty d \ln k \mathcal{P}_m(k, z), \quad (1.307)$$

with  $\mathcal{P}_m(k, z) = k^3 P_m(k, z) / 2\pi^2$ . We can now consider the autocorrelation function associated to the smoothed matter power spectrum (often referred as  $\sigma^2(R, z) = \xi_{m,R}(r = 0, z)$  in the literature),

$$\sigma^2(R, z) = \int_0^\infty d \ln k |W_R(k)|^2 \mathcal{P}_m(k, z). \quad (1.308)$$

This gives the r.m.s. amplitude of mass fluctuations smoothed over a scale  $R$ . Historically, cosmologists have first studied clustering on scales about the size of a galaxy cluster ( $5 - 10 h^{-1} \text{Mpc}$ ), so an important quantity to choose was

$$\sigma_8 \equiv \sigma(R = 8 h^{-1} \text{Mpc}, z = 0). \quad (1.309)$$

The  $\sigma_8$  parameter also provides an alternative way to normalize the matter power spectrum, since it is proportionally related to the primordial amplitude  $A_s$  (but note this relation is model-dependent). In the  $\Lambda$ CDM framework,  $\sigma(R, z)$  increases smoothly with decreasing  $R$ , corresponding to a “bottom-up” scenario where the smallest, least massive objects form first (such as stars and galaxies), and the larger, more massive objects (like galaxy clusters) form later. Notice that the matter power spectrum entering in the definition of  $\sigma_8$  is the *linear one*. In fact, one can estimate the redshift at which a given scale  $R$  enters in the non-linear regime from the condition  $\sigma(R, z_{\text{nl}}) \sim 1$ .

Let us briefly comment on one technique used to probe the large-scale structures, called galaxy weak lensing, which is very relevant in the context of the  $S_8$  tension. The images of distant galaxies are slightly distorted due to the gravitational lensing of the intervening large scale structures. The two main areas of galaxy weak lensing are cosmic shear, the study of correlations between the shapes of pairs of galaxies, and galaxy-galaxy lensing, the study of correlations between the position of foreground galaxies and background galaxy shapes. Cosmic shear allows to probe the LSS more directly than galaxy-galaxy lensing, where one needs to make assumptions about the relation between galaxies and the underlying matter distribution.

The basic observable in weak lensing studies is the ellipticity of a galaxy. The measured ellipticity receives contributions from the intrinsic galaxy ellipticity and the shear effect due to gravitational lensing (*i.e.* the squeezing of the image in one direction, and its stretching on the orthogonal direction). In the weak lensing regime, the intrinsic ellipticity largely dominates over the small shear, so it is necessary to perform an average over many galaxies. The main idea behind this approach is that galaxies are intrinsically randomly oriented on the sky, so the intrinsic ellipticities average to zero, leaving just the shear. Like for CMB lensing, galaxy lensing is described by a deflection potential, which is related to the Newtonian metric potentials  $\phi$  and  $\psi$  through

$$\varphi(\hat{n}) = - \int_0^{\tau_0} d\tau_s g(\tau_s) \int_{\tau_s}^{\tau_0} d\tau \frac{\chi(\tau_s) - \chi(\tau)}{\chi(\tau_s)\chi(\tau)} (\phi + \psi)_{(\tau, \vec{x}=r(\tau)\hat{n})}, \quad (1.310)$$

This expression is very similar to the one we wrote in Eq. (1.295) when presenting the CMB lensing, although there are two important differences. First, the source is now located at an arbitrary comoving distance  $\chi(\tau_s)$ , rather than on the last-scattering surface. Second, since we are measuring the distortions for an ensemble of galaxies, we need to consider a distribution of galaxy redshifts,  $g(\tau_s)$ , normalized such that  $\int_0^{\tau_0} d\tau_s g(\tau_s) = 1$ . As for the CMB lensing spectrum, the associated harmonic spectrum  $C_\ell^{\varphi\varphi}$  is obtained by a convolution of the matter power spectrum  $P_m(k, z)$  with an appropriate kernel. However, as opposed to the CMB lensing, it is strictly necessary to consider the *non linear* matter power spectrum, since galaxy lensing covers much smaller scales. Often, it is possible to split the catalog of galaxies in several redshift bins  $i$ , described by selection functions  $g_i(\tau)$  such that  $g(\tau) = \sum_i g_i(\tau)$ , and to measure the lensing spectrum  $C_\ell^{\varphi_i\varphi_j}$  at each redshift bin. This tomographic approach is particularly useful for measuring neutrino masses as well as dark energy properties. Observational constraints are often reduced to the parameter combination to which weak lensing surveys are mostly sensitive. In particular, constraints are typically quoted in terms of  $S_8 \equiv \sigma_8 \sqrt{\Omega_m/0.3}$ , which modulates the amplitude of weak lensing measurements. We remark that the  $S_8$  parameter is not directly measured by the collaborations, but inferred from Eq. (1.308) by adjusting the  $\Lambda$ CDM model to their weak-lensing data (HEYMANS et al. 2021).

Let us just mention that other LSS probes can be similarly obtained from the matter power spectrum. For instance, galaxy clustering probes measure the galaxy power spectrum, which in the simplest formulation is assumed to be  $P_g(z, k, \mu) = (b_g(z) + f\mu^2)^2 P_m(z, k)$ , where the first term includes the light-to-mass bias function  $b_g(z)$ , and the second term proportional to the growth rate  $f \equiv d\ln(D(a))/d\ln a$  (with  $D(a) = ag(a)/g(a_0)$ ) is accounting for Redshift Space Distortions (KAISER 1987). On the other hand, probes of the Lyman- $\alpha$  forest measure the flux power spectrum  $P_F(k)$ , linearly related to the one-dimensional matter spectrum  $P_{m,1D}(k) = \frac{1}{2\pi} \int_k^\infty dk' k' P_m(k')$  through another scale-dependent bias function,  $P_F(k) = b^2(k) P_{m,1D}$  (MURGIA et al. 2017).

## 1.7 Successes and challenges of the $\Lambda$ CDM paradigm

The  $\Lambda$ CDM model provides outstanding explanation for a wide variety of early universe data, such as Cosmic Microwave Background (CMB) and Big Bang Nucleosynthesis (BBN), as well as late universe observations of Large Scale Structure (LSS) including the Baryon Acoustic Oscillation (BAO), and uncalibrated luminosity distance to SuperNovae of type Ia (SNIa). In Fig. 1.23 we show a schematic representation of the approximate redshift  $z$  and wavenumber  $k$  corresponding to different cosmological observables. The fact that the  $\Lambda$ CDM model agrees well with such a disparate compilation of observations (spanning many orders of magnitude in time and scale) is an impressive proof of its success. Nevertheless, the  $\Lambda$ CDM model does not teach us about the intrinsic nature of its dark sector, made up of both cold dark matter and dark energy. In addition, as the accuracy of cosmological observations has improved, the concordance cosmological model starts showing several experimental discrepancies. In the following, we proceed to discuss each of these problems.

### 1.7.1 The nature of the dark sector

During the last couple of decades, a myriad of models have been proposed to describe the dark components of the universe. Unfortunately, their nature remains a

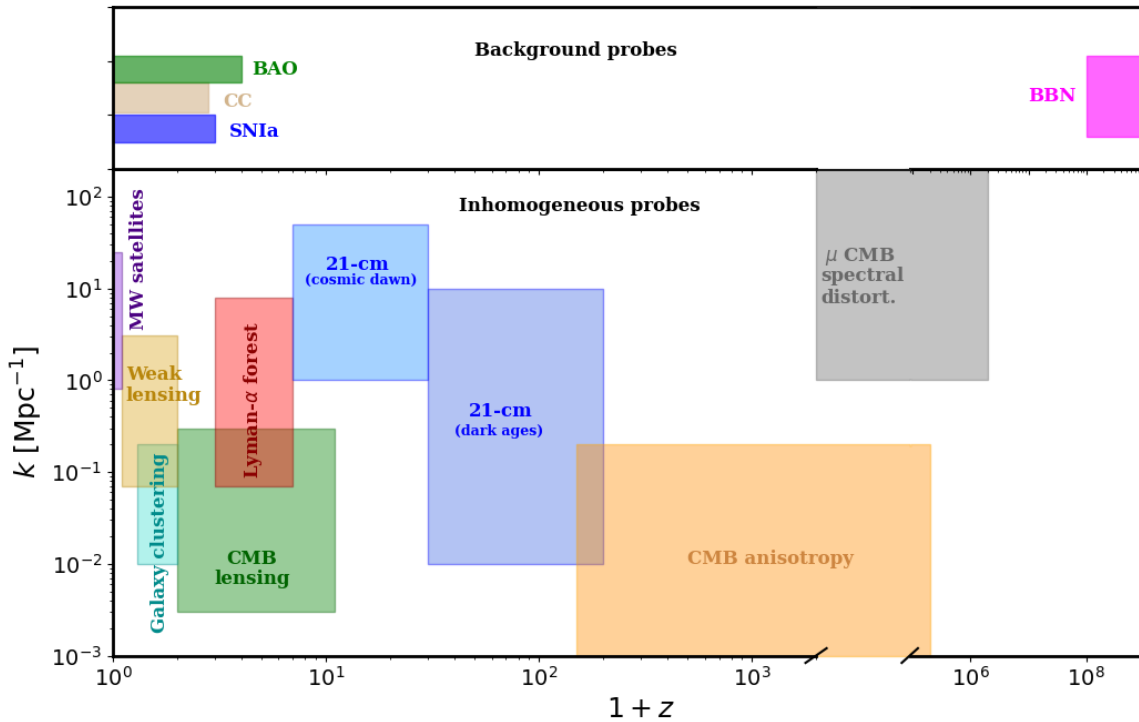


**Figure 1.23** – Schematic view of the coverage of current and future cosmological probes across various epochs and scales. The ranges of each individual probes are approximate. Similar figures can be found in [BODDY et al. \(2022\)](#) and [SABTI et al. \(2022\)](#).

mystery, due to the absence of a clear signal independent from the gravitational ones. Below we sketch some of the main candidates for dark matter and dark energy.

### Dark matter candidates

- **WIMPs.** These remain amongst the most popular models, due to their simple production mechanism in the primordial universe (discussed in [Sect. 1.5.4](#)), and the fact that they are excellent CDM candidates ([B. W. LEE et al. 1977](#)). Indeed, they are neutral, stable, have masses in the GeV-TeV range, and interact weakly with the SM. Specific WIMP models arise for example in Supersymmetry (SUSY). This is an extension of the gauge theories that was introduced in the 70s in order to fill some of the gaps of the SM, such as the electro-weak hierarchy problem. It predicts that each particle should have a super-partner with a spin that differs by a half-integer, *i.e.* all fermions have bosonic super-partners and vice-versa. The lightest of the *neutralinos* (which are the mass eigenstates of four neutral super-partners, namely, two Higgsinos, the bino and the wino) has all the required properties to be a WIMP candidate. Another good candidate for WIMP DM is the *gravitino*, the super-partner of the graviton (see [JUNGMAN et al. \(1996\)](#) for a review on SUSY DM). Outside the SUSY framework, WIMPs also arise in models of *extra-dimensions*. These models are based on the seminal work by [KALUZA \(1921\)](#) and [KLEIN \(1926\)](#), who pursued to unify electromagnetism and gravity by postulating the existence of a compact fifth dimension. Modern examples of extra-dimension theories include the Randall-Sundrum model ([RANDALL et](#)



al. 1999) and the Universal Extra Dimensions (UED) model (APPELQUIST et al. 2001). In this context, particles that are allowed to propagate through all dimensions exhibit excited, more massive states, denominated *Kaluza-Klein (KK) states*. In UED, all SM particles can propagate in all dimensions, and the lightest KK particle (LKP), if stable and neutral, becomes a perfect WIMP candidate. During the recent years, WIMPs have lost their quasi-monopoly due to the null searches in colliders and direct/indirect detection experiments, and the community is starting to focus on other candidates.

- **Axions.** This corresponds to a very different class of DM candidates, which were originally introduced to solve the CP (charge-parity) problem of the SM. This is a fine-tuning problem that deals with the question of why there is no experimental sign of CP-violating physics in strong interactions, even if the QCD Lagrangian requires in full generality a CP-violating term. In a nutshell, the idea is to introduce a new global chiral symmetry  $U(1)_{\text{PQ}}$  that is spontaneously broken at scales much higher than the QCD confinement scale ( $f_a \gg \Lambda_{\text{QCD}} \sim 150 \text{ MeV}$ ). This generates the “axion” field as a pseudo-scalar Goldstone boson, whose dynamics are such that it can naturally cancel the CP-violating term in QCD (PECCEI et al. 1977; WEINBERG 1978; WILCZEK 1978). The axion field, which is initially massless, acquires a non-zero mass when temperature of the bath drops below  $T \sim \Lambda_{\text{QCD}}$ . At this point, the field starts rolling down to the minimum of its potential, oscillating and diluting in the same way as a CDM fluid,  $\bar{\rho}_a \propto a^{-3}$ . One can show that the axion mass scales as  $m_a \propto 1/f_a$ , and in order to produce the right DM abundance, it should fall in the range  $10 \mu\text{eV} < m_a < 0.1 \text{ eV}$ . Many axion models predict a coupling to photons,  $g_{a\gamma}$ , which is the source of Primakoff effect: the conversion of axions into detectable photons in a strong magnetic field. With the years, QCD axions have paved the way to the study of more generic light bosons, such as *axion-like particles* (generalizing the QCD axion but not necessarily connected to the strong CP-problem) or ultralight axions (with masses as low as  $m_a \sim 10^{-22} \text{ eV}$ ), making what is known as *fuzzy DM* (see MARSH (2016) for a review on axion cosmology).
- **Sterile neutrinos.** These particles arise in the context of the neutrino mass puzzle. Even if active neutrinos are assumed to be massless in the SM, oscillation experiments have provided convincing evidence that at least two of them must possess tiny non-zero masses (see Sect. 4.2). One simple construction to explain the smallness of neutrino masses is given by the *type-I seesaw* mechanism (DREWES et al. 2017). The main idea is to add to the SM content a right-handed, sterile neutrino, *i.e.* a fermion which is a singlet for all interactions. Then, one can construct the most general mass matrix that is allowed by gauge invariance, and from its eigenvalues one finds that the mass of the active neutrino is inversely proportional to the mass of the heavy sterile neutrino. Notice that, a priori, the mass of sterile neutrinos can cover a wide range of values. Those with masses of the order  $M_{N_R} \sim \mathcal{O}(\text{keV})$  have all the necessary properties to constitute cold DM or warm DM, *i.e.* they are neutral, stable on cosmological scales, and possess very weak interactions with other particles (if the mixing angles are small). Interestingly, sterile neutrinos can decay into an active neutrino and a photon, providing a clean astrophysical signature than can be searched with X-ray observations (see BOYARSKY et al. (2019) for a recent review).

- **Primordial black holes.** DM models don't necessarily have to introduce new particles. Primordial black holes (PBHs) are a class of non-baryonic MACHOs (standing for Massive Astrophysical Compact Halo Object) that are naturally good DM candidates. PBHs are believed to have formed in the very early universe, from rare and extremely large density fluctuations that collapsed into BHs right after entering the Hubble radius (ZEL'DOVICH et al. 1967; HAWKING 1971; CARR et al. 1974). The abundance of PBHs is controlled by the amplitude of the primordial spectrum, and should be vanishingly small if the latter were at the level constrained by CMB and LSS observations. Nonetheless, this amplitude remains very unconstrained at small scales, so it could still be possible that PBHs represent a sizable fraction of the DM. There has been recently a renewed interest in PBHs thanks to the latest observations of black hole binary mergers with the LIGO/Virgo gravitational wave detectors (B. P. ABBOTT et al. 2016; BIRD et al. 2016). However, they are subject to many observational constraints, such as those coming from  $\gamma$ -rays, microlensing, the CMB or the Ly- $\alpha$  forest, to name a few examples (see GREEN et al. (2021) for a recent compilation of constraints).

### Dark energy candidates

- **Cosmological constant.** The simplest possible explanation for the cosmic acceleration which is in agreement with current observations is that dark energy is in the form of a cosmological constant  $\Lambda$ , whose energy is independent of space and time. However, this triggers a number of questions. First, the stress-energy tensor associated to  $\Lambda$  has the same form of that associated to the ground state energy of the vacuum,  $T_{\mu\nu}^{\Lambda} = -\rho_{\Lambda}g_{\mu\nu}$ , with  $\rho_{\Lambda} = \Lambda/8\pi G$ . Unfortunately, the predicted size of the vacuum energy  $\rho_{\text{vac}}$  from the zero-point energy suggested by quantum field theory is completely off,  $\rho_{\text{vac}}/\rho_{\Lambda} \sim 10^{120}$ . This is known as *the cosmological constant (CC) problem*. Another issue is related to the fact that the present abundance of dark energy  $\Omega_{\Lambda}$  is extremely similar to that of matter  $\Omega_m$ , despite the very different scalings of each one ( $\rho_{\Lambda} \propto a^0$  and  $\rho_m \propto a^{-3}$ ). This is the so-called *coincidence problem*. Faced with these questions, theorists have developed extensions of GR, which are pursued to understand gravity at a more fundamental level. But how should one modify gravity? In fact, GR turns out to be a very unique theory. According to Lovelock's theorem (LOVELOCK 1971), in a four-dimensional space-time, the only second order equations derived from an action that depends only on the metric,  $S = \int d^4x \mathcal{L}(g_{\mu\nu})$ , are precisely Einstein field equations (c.f. Eq. (1.10)). Hence, new theories of gravity can be built by breaking some of the assumptions of this theorem, e.g. by considering new fields, extra dimensions, higher-order equations etc. It should be stressed that, even if most of these models address the coincidence problem, there is still no widely accepted solution for the CC problem.
- **Quintessence.** This is one of the simplest extensions, which consists in adding a scalar field  $\phi$  (playing the role of dark energy) minimally coupled to gravity and described by some generic potential  $V(\phi)$  (COPELAND et al. 2006). A well-known example is the Ratra-Peebles potential  $V(\phi) = k/\phi^{\alpha}$  (RATRA et al. 1988). In quintessence models, the EoS is simply given by  $w_{\phi} = \frac{\dot{\phi}^2/2 - V(\phi)}{\dot{\phi}^2/2 + V(\phi)}$ , so the scalar field can produce cosmic acceleration ( $w_{\phi} < -1/3$ ) as long as the field is in slow-roll ( $V(\phi) \gg \dot{\phi}^2/2$ ), similarly to inflationary models. However, the EoS can never



become strictly smaller than  $w_\phi = -1$ . The regime  $w < -1$  actually defines a different class of models, dubbed *phantom dark energy*. These scenarios produce such a rapid acceleration that a *big rip* can take place, *i.e.*,  $a \rightarrow \infty$  is reached in a finite amount of time, meaning that all the matter in the universe is eventually torn apart (R. R. CALDWELL 2002; R. R. CALDWELL et al. 2003).

- **Scalar-tensor theories.** These theories postulate the existence of one extra scalar field, with a possible non-minimal coupling to gravity. This leads to a vast array possibilities, from the simplest forms of Brans-Dicke theories (BRANS et al. 1961) to the most recent higher-derivative theories, where the scalar and the metric dynamics are strongly intertwined. Scalar-tensor theories are constrained by local tests of GR and the equivalence principle, and by cosmological probes (since they typically modify the growth of large-scale structures). Moreover, the recent precise measurement of the gravitational wave speed from the detection of GW170817 has already put under pressure many scalar-tensor theories designed to account for the cosmic acceleration (CREMINELLI et al. 2017). It was recently discovered that scalar-tensor theories can generally be grouped in the Horndeski action, which was first written down in HORNDESKI (1974). This action gives the most general scalar-tensor theory described by second order equations of motions and universally coupled to matter. The Horndeski action covers quintessence, Brans-Dicke,  $f(R)$ , covariant Galileons as well as many other exotic modifications (see CLIFTON et al. (2012) for a review).
- **Other theories of modified gravity.** There are many other proposals of modified gravity outside the scalar-tensor framework. For instance, theories of massive gravity propose that the elementary spin-2 excitations of the gravitational field (*the gravitons*) can have a non-zero mass. In order to satisfy current constraints, this mass must be tiny (less than  $10^{-23}$  eV), but can already have effects on the very large scales (RHAM 2014). Another important class of models are higher-dimension theories. They are based on the idea that our universe contains extra hidden dimensions only visible by gravity, while the rest of SM particles are confined in a four-dimensional *brane*. A well-known example is the Dvali–Gabadadze–Porrati (DGP) model (DVALI et al. 2000). These models share many features with massive gravity and scalar-tensor theories, but the behavior at large distances is different.

## 1.7.2 Cosmic discordance

### The $H_0$ tension

The so-called “Hubble tension” refers to the inconsistency between local measurements of the current expansion rate of the Universe, *i.e.* the Hubble constant  $H_0$ , and the value inferred from early-Universe data using the flat  $\Lambda$ CDM model. This tension is predominantly driven by the Planck collaboration’s observation of the cosmic microwave background (CMB), which predicts a value in  $\Lambda$ CDM of  $H_0 = (67.27 \pm 0.60)\text{km/s/Mpc}$  (AGHANIM et al. 2020b), and the value measured by the SHOES collaboration using the Cepheid-calibrated cosmic distance ladder, whose latest measurement yields  $H_0 = (73.04 \pm 1.04)\text{km/s/Mpc}$  (RIESS et al. 2021a). Taken at face value, these observations alone result in a  $5\sigma$  tension.

The problem, however, is more severe than the naïve comparison between Planck and SHOES may suggest. Today, there exist a variety of different techniques for calibrating  $\Lambda$ CDM, and subsequently inferring the value of  $H_0$ , which do not involve Planck data – for example, one can use alternative CMB data sets such as WMAP (C. L. BENNETT et al. 2013), ACT (S. K. CHOI et al. 2020), or SPT (DUTCHER et al. 2021), or one can remove observations of the CMB altogether and combine measurements of Big Bang nucleosynthesis (BBN) with data from baryonic acoustic oscillations (BAO) (AUBOURG et al. 2015; BLOMQVIST et al. 2019; CUCEU et al. 2019; SCHÖNEBERG et al. 2019) or with supernovae constraints (VERDE et al. 2017; BERNAL et al. 2021)<sup>30</sup>. These probes, which invoke at least one measurement from high redshifts, are often dubbed “early-Universe calibrations”, and all result in  $H_0$  values below 70 km/s/Mpc (typically in strong agreement with the value inferred by Planck using  $\Lambda$ CDM). Similarly, several alternative methods for directly measuring the local expansion rate have been proposed in the literature. A large number of these techniques offer alternative methods for calibrating the cosmic distance ladder, removing any bias introduced from Cepheid observations. One example is the recent determination of  $H_0$  obtained by the Chicago-Carnegie Hubble program (CCHP), which calibrates SNIa using the tip of the red giant branch (TRGB); this observation yielded a value of  $H_0 = (69.8 \pm 0.6 \text{ (stat)} \pm 1.6 \text{ (sys)})$  km/s/Mpc (FREEDMAN et al. 2019; FREEDMAN 2021), in between the Planck CMB prediction and the SHOES calibration measurement. However, alternative analyses using similar techniques have yielded values significantly closer to the value obtained by SHOES, in particular the latest calibration of the TRGB using the parallax measurement of  $\omega$ -Centauri from GAIA DR3 leads to  $H_0 = (72.1 \pm 2.0)$  km/s/Mpc (YUAN et al. 2019; SOLTIS et al. 2021). Additional methods intended to calibrate SNIa at large distances include: surface brightness fluctuations of galaxies (KHETAN et al. 2021), MIRAS (HUANG et al. 2019), or the Baryonic Tully Fisher relation (SCHOMBERT et al. 2020). There also exists a variety of observations which do not rely on observations of SNIa – these include e.g. time-delay of strongly lensed quasars (BIRRER et al. 2020; K. C. WONG et al. 2020), maser distances (PESCE et al. 2020), or gravitational waves as “standard sirens” (B. P. ABBOTT et al. 2021). In Fig. 1.24 we show an updated compilation of some of the direct and indirect determinations of  $H_0$  we just discussed. While not all measurements are in tension with Planck, these direct probes tend to yield values of  $H_0$  systematically larger than the value inferred by Planck<sup>31</sup>. Depending on how one chooses to combine the various measurements, the tension may be elevated to as much as  $6\sigma$  (DI VALENTINO et al. 2021b).

Intense experimental efforts are underway to establish whether this discrepancy can be caused by yet unknown systematic effects (appearing in either the early or late Universe measurements, or both). This includes (but is not limited to) issues in SNIa dust extinction modeling and intrinsic variations (MORTSELL et al. 2021a,b), the importance of Cepheid metallicity correction (EFSTATHIOU 2020), differences in TRGB calibration in the LMC (FREEDMAN et al. 2019; YUAN et al. 2019; FREEDMAN et al. 2020) and in the Milky Way (CERNY et al. 2020; SOLTIS et al. 2021), different population of SNIa at low- $z$  and high- $z$  (RIGAULT et al. 2015; JONES et al. 2018; RIGAULT et al. 2020; BROUT et al. 2021), and the existence of a local void biasing  $H_0$  estimates (KENWORTHY

<sup>30</sup>The robustness of such probes have been investigated for example in BERNAL et al. (2020) and CARTER et al. (2020).

<sup>31</sup>However, there is some debate about the robustness and independence of these additional measurements, see e.g. FREEDMAN (2021).

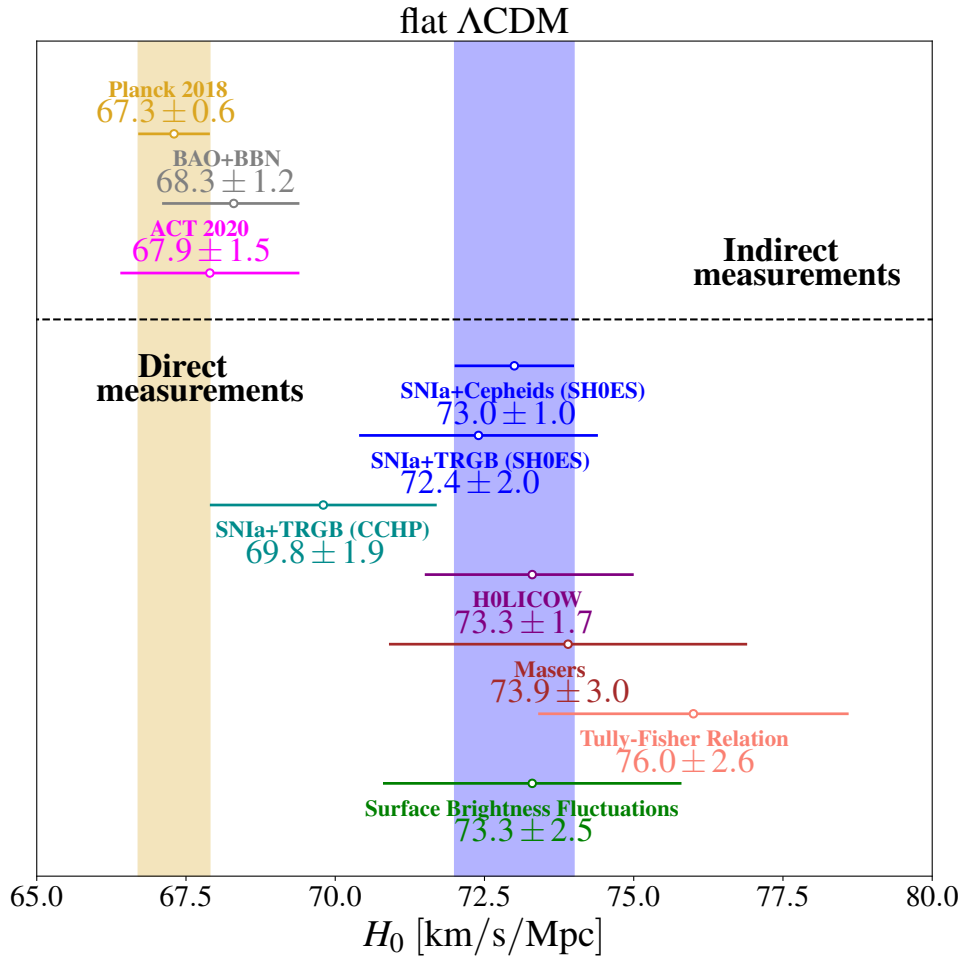


**Figure 1.24** – Whisker plot showing 68% CL determinations of the Hubble constant  $H_0$  through a series of direct and indirect measurements. The yellow vertical band denotes the  $H_0$  value from *Planck18* (AGHANIM et al. 2020b), whereas the blue vertical band denotes the  $H_0$  value reported by SH0ES (RIESS et al. 2021a). For clarity, we restricted to a subset of constraints with error bars smaller than  $\sigma_{H_0} \lesssim 3 \text{ km/s/Mpc}$ , a full compilation of measurements can be found in DI VALENTINO et al. (2021b).

et al. 2019; LOMBRISER 2020) (for a more complete review, see DI VALENTINO et al. (2021b)). Yet, the appearance of this discrepancy across a wide array of probes seems to suggest that a single systematic effect may not be sufficient to resolve this discrepancy. The alternative possibility is that the Hubble tension reflects a breakdown of the  $\Lambda$ CDM model; properly accounting for new physics operating either in the early- or late-Universe could change the inference of  $H_0$  from the early-Universe probes to be in agreement with the direct measurements. In Chapter 2 we will explain that any viable  $\Lambda$ CDM extension likely requires reducing the sound horizon at recombination.

### The $S_8$ tension

The “ $S_8$  tension” is a longstanding discrepancy between the strength of matter clustering measured by large-scale structure probes, and the value inferred from early-Universe data. In particular, the value of the clustering strength estimated by the primary anisotropies of the CMB (as measured by *Planck*) is typically  $2 - 3\sigma$  higher than that obtained from lower redshift probes, such as weak gravitational lensing and

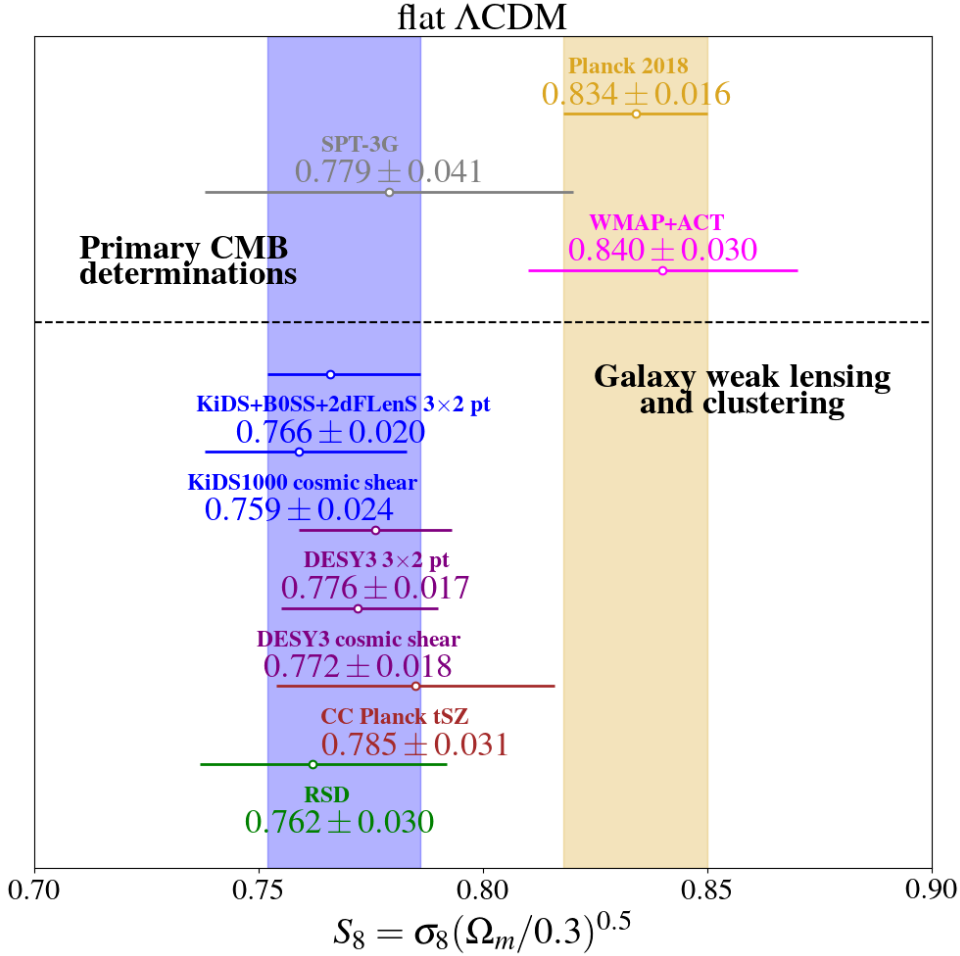


**Figure 1.25** – Whisker plot showing 68% CL determinations of the  $S_8$  parameter by various CMB experiments and other low-redshift cosmological probes. The yellow vertical band denotes the  $S_8$  value from [Planck18](#) ([AGHANIM et al. 2020b](#)), whereas the blue vertical band denotes the  $S_8$  value reported by the joint analysis of KIDS1000+B0SS+2dfLenS ([HEYMANS et al. 2021](#)). For clarity, we restricted to a subset of constraints with error bars smaller than  $\sigma_{S_8} \lesssim 0.03$ , a full compilation of measurements can be found in [ABDALLA et al. \(2022\)](#).

galaxy clustering. As mentioned in [Sect. 1.6.6](#), this is often quantified through the  $S_8 \equiv \sigma_8 \sqrt{\Omega_m / 0.3}$  parameter, where  $\sigma_8$  is the root mean square of matter fluctuations on a  $8h^{-1}$  Mpc scale, and  $\Omega_m$  is the total matter abundance. This parameter combination is chosen to encapsulate the main degeneracy direction of weak lensing measurements. The  $S_8$  parameter is intimately related to  $f\sigma_8(z=0)$  measured by redshift space distortions (RSD) ([GIL-MARIN et al. 2017](#)), where  $f = [\Omega_m(z)]^{0.55}$  approximates the growth rate in GR. Notice that measuring  $S_8$  is model dependent, and all current experimental determinations assume the flat  $\Lambda$ CDM model.

The CMB anisotropy data from [Planck18](#) TT,TE,EE+lowE yields a constraint  $S_8 = 0.834 \pm 0.016$ , which can be tightened when adding the CMB lensing reconstruction,  $S_8 = 0.832 \pm 0.013$ . As we mention later, this high  $S_8$  estimate could be related to an excess of lensing inferred from the smoothing of the acoustic peaks within *Planck* data. However, the combination of high- $\ell$  data from ACT ([S. K. CHOI et al. 2020](#)) with the low- $\ell$  measurements from WMAP ([C. L. BENNETT et al. 2013](#)) also yields a high value,  $S_8 = 0.834 \pm 0.016$ , despite not exhibiting any lensing anomaly.

On the side of the low- $z$  probes, there is a host of galaxy weak lensing surveys that have provided accurate measurements of  $S_8$ . The Canada France Hawaii Lensing Survey (CFHTLenS) (HEYMANS et al. 2013) was the first to report a  $\sim 2\sigma$  tension in  $S_8$  with the initial *Planck* data release (ADE et al. 2014), which has persisted with subsequent analysis of CFHTLenS data (JOUDEKI et al. 2017a). This motivated the weak lensing community to carry out blinding procedures in their analysis. The first blinded analysis of this type was performed by the Kilo Degree Survey on their first 450 square degrees of data (KiDS-450, HILDEBRANDT et al. 2017), which found a  $2.3\sigma$  lower value of  $S_8$  compared to *Planck* 2015 (ADE et al. 2016a). All subsequent published results from weak-lensing measurements have obtained  $S_8$  values which are systematically lower than the high- $z$  estimates. The first year of data from the Dark Energy Survey (DES-Y1, TROXEL et al. 2018) and Hyper Suprime Cam (HSC, HIKAGE et al. 2019) found slightly higher but consistent values with the results of KiDS-450. The improved analysis of KiDS-450 with photometric data from VIKING (KV450) consistently found low  $S_8$  results (HILDEBRANDT et al. 2020). A combination of KV450 and DES-Y1 was performed in ASGARI et al. (2020), finding stronger constraints in good agreement with former results. The latest analysis of KiDS (KiDS-1000, ASGARI et al. 2021) and DES (DES-Y3, SECCO et al. 2022) show a similar trend with a better precision. The  $S_8$  parameter can also be measured from redshift-space galaxy clustering; in particular, with the BOSS full-shape galaxy power spectrum and bispectrum:  $S_8 = 0.751 \pm 0.039$  (PHILCOX et al. 2022). The precision of these measurements can be improved in a joint analysis with weak lensing data. The combination of cosmic shear, galaxy-galaxy lensing and galaxy clustering at the level of 2-point statistic is known as “ $3 \times 2$ pt” analysis. For instance, the recent  $3 \times 2$ pt analysis by KIDS1000+BOSS+2dfLenS has yielded a constraint  $S_8 = 0.766^{+0.020}_{-0.014}$ , which has the overall same precision as *Planck* but it is  $\sim 3\sigma$  smaller. This kind of combined analysis between galaxy clustering with weak lensing allows to break the degeneracy between  $\sigma_8$  and  $\Omega_m$ , revealing that the tension is driven by  $\sigma_8$ , rather than  $\Omega_m$ . Another possibility to measure  $S_8$  is to use the number density of DM halos, which is very sensitive to the growth of structure through the cosmological halo mass function. The *Planck* mission has provided measurements of the number counts of galaxy clusters detected through the Sunyaev-Zel’dovich (SZ) effect, reporting a deficit with respect to the value expected from the fiducial *Planck* TT,TE,EE+lowE  $\Lambda$ CDM model (ADE et al. 2016b). This can be translated into a  $2 - 3\sigma$  tension in  $S_8$ , which has been confirmed by other cluster count experiments (PRATT et al. 2019). In Fig. 1.25 we show an updated compilation of some of the high- $z$  and low- $z$  determinations of  $S_8$  we just discussed.

There is a large number of known systematic effects that can affect the low-redshift measurements of large-scale structures. Weak-lensing systematics include: noise bias affecting the galaxy shape measurements (MELCHIOR et al. 2012), errors in photometrically determined redshift distributions (HUTERER et al. 2006), intrinsic alignment of galaxies (BRIDLE et al. 2007), uncertainties in the modeling of baryon feedback (MEAD et al. 2020) and small-angle approximations (KITCHING et al. 2017). Regarding the galaxy clustering systematics, there can be issues with stellar contamination, atmospheric extinction and blurring (ROSS et al. 2012), fiber collisions (HAHN et al. 2017) and selection bias (C. M. HIRATA 2009). Finally, the dominant source of systematic uncertainty in cluster count observations is the hydrostatic bias parameter relating the mass observed through the hot gas and the true mass of the host halo,  $1 - b = M_{\text{obs}}/M_{\text{true}}$  (BLANCHARD et al. 2021). Still, the appearance of this mismatch



across such a variety of probes suggest that a single systematic might not be enough to explain the discrepancy, similarly to what happens with the  $H_0$  parameter. Hence, the  $S_8$  tension could also be a signal of a failure of the  $\Lambda$ CDM model. In particular, it seems to point towards a suppression of power in the matter spectrum  $P_m(k)$  at the scales selected by the window function  $k^2|W_8(k)|^2$ , *i.e.* for  $k \sim (0.1 - 1)h/\text{Mpc}$ . In [Chapter 3](#), we will study a model that can achieve precisely this type of suppression.

### The $A_{\text{lens}}$ anomaly and other discrepancies

Another well studied ‘curiosity’ in the recent literature consists in the anomalous amount of lensing estimated from the smoothing of the acoustic peaks at high- $\ell$ ’s within *Planck* data, as quantified by the ‘ $A_{\text{lens}}$ ’ parameter ([CALABRESE et al. 2008](#); [AGHANIM et al. 2017](#); [EFSTATHIOU et al. 2019](#); [AGHANIM et al. 2020b](#)). However, this anomalous ‘lensing’ is not supported by the lensing power spectrum reconstruction, such that it is now commonly admitted that this tension (oscillating between the  $2 - 3\sigma$  statistical level) cannot originate from a true lensing effect. On the other hand, it has been understood that this anomaly can be easily resolved if the universe is closed ([DI VALENTINO et al. 2019](#); [EFSTATHIOU et al. 2020](#); [HANDLEY 2021](#)), in certain modified gravity theories ([MOSHAFI et al. 2021](#)), or in early-universe scenarios inducing a pattern of primordial oscillatory features ([X. CHEN 2010](#); [CHLUBA et al. 2015](#); [SLOSAR et al. 2019](#); [DOMÈNECH et al. 2020](#)). In fact, it has already been noted that this anomaly could be related to the  $S_8$  tension: indeed, once including  $A_{\text{lens}}$  as an extra free-parameter in the analysis, it has been shown that the reconstructed cosmology has a smaller  $A_s$  and  $\omega_{\text{cdm}}$  (as well as a higher  $H_0$ ), showing no  $S_8$  tension, but a remnant  $\sim 3.5\sigma$  Hubble tension ([DI VALENTINO et al. 2018a](#); [MOTLOCH et al. 2018, 2020](#)). Interestingly, the cosmology deduced once marginalizing over the lensing information is in better agreement with the recent results from the SPTPol and SPT-3G ([HENNING et al. 2018](#); [CHUDAYKIN et al. 2020a](#); [DUTCHER et al. 2021](#)), which shows no tension with the LSS measurement of  $S_8$ , a weaker  $H_0$  tension, and no lensing anomaly. Pin-pointing the source of such lensing anomaly (perhaps a simple statistical fluke, although quantifying its likelihood and how to treat it is complicated) is therefore of utmost importance to understand whether the  $S_8$  tension derives from it. In [Chapter 2](#) and [Chapter 3](#) we will study the implications of the  $A_{\text{lens}}$  anomaly for models of Early Dark Energy and Decaying Dark Matter, respectively.

There are many other intriguing anomalies that we haven’t addressed in this thesis, such as those related to the small-scale crisis of  $\Lambda$ CDM ([BULLOCK et al. 2017](#)), the Lithium problem ([MATHEWS et al. 2020](#)), the cosmic dipole tension ([SECRET et al. 2021](#); [DALANG et al. 2022](#)) or the Ly- $\alpha$  tension in  $n_s$  ([PALANQUE-DELABROUILLE et al. 2020](#); [D. C. HOOPER et al. 2022](#)) (a thorough review of cosmological tensions can be found in [ABDALLA et al. \(2022\)](#)).

## 1.8 Outline

After this general introduction, the rest of the document is divided into three other chapters. In [Chapter 2](#), we reassess the viability of a pre-recombination Early Dark Energy component as a solution to the Hubble tension, by confronting the model against a host of high- and low-redshift measurements, including LSS observations from recent weak lensing surveys, as well as CMB, BAO and SNIa data. We also

---

perform a systematic comparison of seventeen different models which have been proposed to resolve the  $H_0$  tension, and quantify the relative success of each using different metric and a variety of datasets. In [Chapter 3](#) we perform the first thorough cosmological analysis of a scenario in which dark matter can decay into massless and massive invisible particles, showing that the model can successfully explain the low- $S_8$  measurements reported by weak-lensing surveys. Finally, in [Chapter 4](#) we update the bounds on the mass and lifetime of neutrinos decaying into dark radiation after becoming non-relativistic, thanks to the latest *Planck* data release and an improved Boltzmann formalism.

Complementary information can be found in the numerous appendices. In [App. A](#) we detail some important calculations concerning linear perturbation theory. In [App. B](#) we say a few words about statistical analysis and parameter inference. In [App. C](#), [App. D](#) and [App. E](#) we provide tables, plots and calculations that are intended to complement the content of [Chapter 2](#) , [Chapter 3](#) and [Chapter 4](#), respectively.





# II

---

## Early dark energy and the $H_0$ tension

---

*“Sometimes science is more art than science, Morty.  
Lot of people don’t get that.”*

*Rick character in Rick and Morty*

### Contents

---

2.1	Best-fit EDE cosmology solving the $H_0$ discrepancy . . . . .	<b>100</b>
2.2	Guidelines to solve the $H_0$ tension . . . . .	<b>102</b>
2.3	Formalism of Early dark energy . . . . .	<b>107</b>
2.3.1	Basic equations . . . . .	107
2.4	Cosmological constraints . . . . .	<b>109</b>
2.4.1	Baseline analysis: anatomy of the 3-parameter EDE model . . . . .	110
2.4.2	Towards a 1-parameter resolution to the $H_0$ tension . . . . .	114
2.4.3	Confronting EDE to weak-lensing data . . . . .	115
2.4.4	EDE and the $S_8$ tension in light of the $A_{\text{lens}}$ anomaly . . . . .	123
2.5	EDE in the context of other proposed solutions . . . . .	<b>127</b>
2.5.1	Brief overview of competitors . . . . .	127
2.5.2	Statistical tests to quantify model success . . . . .	129
2.5.3	Results of the contest . . . . .	131
2.6	Summary and outline . . . . .	<b>135</b>

---

This Chapter is based on:

R. Murgia, [G. F. Abellán](#), V. Poulin

*“Early dark energy resolution to the  $H_0$  tension in light of weak lensing surveys and lensing anomalies”*

**PRD 103 063502 (2021)**; [arXiv:2009.10733](#)

N. Schöneberg, [G. F. Abellán](#), A. P. Sánchez, S. Witte, V. Poulin, J. Lesgourgues

*“The  $H_0$  Olympics: A fair ranking of proposed models”*

**Phys. Rept. 984 1-55 (2022)**; [arXiv:2107.10291](#)

## 2.1 Best-fit EDE cosmology solving the $H_0$ discrepancy

Early dark energy (EDE) refers to a model in which a scalar field  $\phi$  is frozen-in at times prior to recombination, thus behaving during this epoch like a dark energy component. EDE representing  $\sim 10\%$  of the total energy density of the universe around matter-radiation equality and diluting faster than radiation afterwards has been shown to provide a very good resolution to the  $H_0$  tension. To be more precise, the reconstructed parameters from the [Planck15+BAO+SNIa+SHOES](#) analysis of [T. L. SMITH et al. \(2020\)](#) indicate <sup>1</sup>

$$f_{\text{EDE}} = 0.10 \pm 0.03, \quad \text{Log}_{10}(z_c) = 3.57^{+0.05}_{-0.14}, \quad H_0 = 71.4 \pm 1.2 \text{ km/s/Mpc}. \quad (2.1)$$

However, taken at face value, this model triggers a number of questions. On the theoretical side, it suffers from a strong coincidence problem as the fluid needs to become dynamical around a key era of the universe, matter-radiation equality  $z_c \simeq 3500$ . However, this coincidence might be the sign of a very specific dynamics to be uncovered; in fact there exist models in which the field becomes dynamical precisely around matter-radiation equality, either because of a phase-transition triggered by some other process ([SAKSTEIN et al. 2020](#)) or because of a non-minimal coupling to the Ricci curvature ([BRAGLIA et al. 2020a](#)). Other models set on a stronger theoretical ground have been proposed in the literature, see for example [ALEXANDER et al. \(2019\)](#), [KALOPER \(2019\)](#), [BERGHAUS et al. \(2020\)](#), [BRAGLIA et al. \(2020b\)](#), [GONZALEZ et al. \(2020\)](#), [NIEDERMANN et al. \(2020\)](#), [ALLALI et al. \(2021\)](#), [FREESE et al. \(2021\)](#), [GOGOI et al. \(2021\)](#), [MCDONOUGH et al. \(2021\)](#), [NIEDERMANN et al. \(2021a\)](#), [KARWAL et al. \(2022\)](#), and [SABLA et al. \(2022\)](#).

Furthermore, in order to preserve a good fit to CMB data while solving the  $H_0$  tension, EDE predicts values of some of the cosmological parameters which are somewhat different from those of baseline  $\Lambda$ CDM:

- A higher spectral index  $n_s$ . For instance, a [Planck18+BAO+SNIa+SHOES](#) analysis of the EDE model indicates  $n_s = 0.988 \pm 0.007$  (see [Tab. \(2.1\)](#)), *i.e.* it is compatible with a scale-invariant primordial spectrum at less than  $2\sigma$ . If this trend turns out to be confirmed with future data, it might require going beyond the simplest slow-roll scenarios for inflation (see [F. TAKAHASHI et al. \(2021\)](#) for a recent discussion on inflationary models that can achieve  $n_s = 1$ ).
- A smaller age of the universe  $t_0$ . To give an example, the age of the universe derived from a [Planck18+BAO+SNIa+SHOES](#) analysis of the EDE gives  $t_0 = 13.24 \pm 0.17$  Gyrs. This feature is actually generic to any early-time solution, since these models increase  $H_0$  while leaving  $\Omega_m$  and  $\Omega_\Lambda$  unaffected. As a consequence, the age of the universe, which scales as  $t_0 \propto 1/H_0$  (*c.f.* [Eq. \(1.28\)](#)), decreases roughly by the same amount as  $H_0$  increases. This can therefore be tested against measurements of the age of old objects such as globular clusters of stars, which was recently determined as  $t_0 = 13.5 \pm 0.027$  Gyrs ([VALCIN et al. 2020, 2021](#)). This issue was discussed in great details in the context of the EDE cosmology, but current data are not accurate enough to play a decisive role in arbitrating

<sup>1</sup>As we'll explain later, these phenomenological parameters can be mapped into the theory parameters entering into the scalar field potential. They correspond roughly to an ultra-light axion with a mass  $m \sim 10^{-27}$  eV and a decay constant  $f \sim M_{\text{pl}}$ . The latter value is in stark contrast with the expectation from the Weak Gravity Conjecture ([HILL et al. 2020](#)), but we remark that the EDE potential considered here is just a way to capture the phenomenology that is required to explain the  $H_0$  tension.

the tension (BERNAL et al. 2021; BOYLAN-KOLCHIN et al. 2021; VAGNOZZI et al. 2021b).

- Higher values of  $\omega_{\text{cdm}}$  and  $S_8$ . Namely, the Planck18+BAO+SNIa+SHOES analysis indicates  $\omega_{\text{cdm}} = 0.130 \pm 0.004$  and  $S_8 = 0.838 \pm 0.013$ . This is related to some “unexpected” effects within CMB power spectra, introduced by the increase in  $H(z)$  at early-times. More precisely, the increase in  $\omega_{\text{cdm}}$  needed for EDE is required to match the observed height of the first CMB peak (POULIN et al. 2019; VAGNOZZI 2021). Additionally, it was noted that a similar increase in  $\omega_{\text{cdm}}$  is required to simultaneously preserve the BAO angular scale, because of the different  $r_s - H_0$  degeneracy lines for BAO and CMB data (JEDAMZIK et al. 2021). As a consequence of the larger  $\omega_{\text{cdm}}$ , the peak of the matter power spectrum is shifted, and the growth rate of perturbation at late times increases. This leads to a larger value of  $\sigma_8$  and hence a larger value of  $S_8$ .

The last point is the focus of this work. As explained in Sect. 1.7.2, a number of cosmic shear surveys (CFHTLenS (HEYMANS et al. 2013), KiDS/Viking (HILDEBRANDT et al. 2020), DES (T. M. C. ABBOTT et al. 2018), HSC (HIKAGE et al. 2019)) have provided accurate measurements of the cosmological parameter  $S_8$  which are systematically lower than the  $\Lambda$ CDM prediction. Since EDE predicts a higher value of  $S_8$  than  $\Lambda$ CDM, taken at face values these experiments pose a challenge to EDE cosmologies, and could exclude these models as a resolution to the Hubble tension (HILL et al. 2020). A similar conclusion was reached in IVANOV et al. (2020) and D’AMICO et al. (2021b) with the inclusion of BOSS data in the effective field theory (EFT) of LSS framework.

In the first part of this chapter, we analyze the EDE cosmology resolving the Hubble tension in light of the latest Planck18 data (and the more precise polarization measurement) and confront it to the KiDS-VIKING measurement of the cosmic shear power spectrum (ASGARI et al. 2020) and the joint measurement of  $S_8$  from KiDS-VIKING+DES<sup>2</sup>. The KiDS-VIKING+DES measurements however rely on modeling the non-linear matter power spectrum on relatively small scales. This is done within numerical Einstein-Boltzmann solvers such as CAMB (LEWIS et al. 2000) or CLASS (LESGOURGUES 2011), through the HALOFIT (R. E. SMITH et al. 2003; R. TAKAHASHI et al. 2012) or HMCODE (MEAD et al. 2015) algorithms, which have not been calibrated for EDE cosmologies. We thus check the predictions of these algorithms against the results of a set of dedicated cosmological  $N$ -body simulations, confirming that the qualitative departures from  $\Lambda$ CDM arising in the EDE cosmology are small enough to make use of these standard algorithms. We perform a series of Monte Carlo Markov Chain (MCMC) analyses with various combination of the latest Planck, BAO, growth factor and SNIa Luminosity distance measurements, the SHOES measurement of  $H_0$ , and KiDS/Viking/DES data, in order to assess whether current observations exclude the EDE resolution to the Hubble tension.

We find that, even if the  $S_8$  prediction from the best fit EDE cosmology is indeed  $\sim 2.5\sigma$  higher than the weak-lensing determinations, KiDS data currently provide very little constraining power on the EDE parameters. Yet, it has been found in ASGARI et al. (2020) and JOUDAKI et al. (2020) that a combination of KiDS and DES-Y1 (after re-calibration of the DES photo-metric redshifts) yields  $S_8 = 0.755^{+0.019}_{-0.021}$ , a result that

<sup>2</sup>The re-analysis of BOSS data in the EFT of LSS has been performed in T. L. SMITH et al. (2021).

is in  $3.2\sigma$  tension with Planck  $\Lambda$ CDM prediction<sup>3</sup>. At such a level of discrepancy, one should be cautious when interpreting results obtained from combining Planck and WL data, even within  $\Lambda$ CDM. Indeed, we show that despite the inclusion of a Gaussian  $S_8$  likelihood, the resulting cosmological model yields a very bad fit to the  $S_8$  data, while providing very strong constraints on any parameter correlated with  $S_8$  (e.g.  $\omega_{\text{cdm}}$ ,  $A_s$ ,  $f_{\text{EDE}}$ ). It is easily conceivable that the resolution to the  $S_8$  tension lies elsewhere (whether new physics related – or not – to the EDE, or systematic effects), such that any constraints derived from these combined data are artificial.

As already mentioned in Sect. 1.7.2, It is also possible that the  $S_8$  tension is related to the ‘ $A_{\text{lens}}$ ’ anomaly, *i.e.* the anomalous amount of lensing estimated from the smoothing of the acoustic peaks at high- $\ell$ ’s within *Planck* data. Motivated by this fact, we perform an analysis of the  $\Lambda$ CDM and EDE cosmology against *Planck* and a prior on  $S_8$  from the joint DES-Y1 and KiDS results, while marginalizing over the lensing information. We find that both the unlensed  $\Lambda$ CDM and EDE cosmology spectrum agrees better with LSS data, and that the presence of EDE does not affect the amount of anomalous lensing. This means that the anomalous lensing is not due to the EDE, and also that the success of EDE is not due to opening up a new degeneracy direction with some exotic lensing parameters.

In the last part, we make a systematic comparison of seventeen different models which have been proposed to resolve the  $H_0$  tension (spanning both early- and late-Universe solutions), and quantify the relative success of each model using a series of metrics and a vast array of data combinations. Among these models, we include the EDE proposal as well as the decaying DM scenario discussed in Chapter 3. We note that the ranking that we’ve established is based on a full reanalysis of all models, and not just on a bibliographic compilation. This analysis establishes a foundation of tests which will allow the success of novel proposals to be meaningfully “benchmarked”. In particular, it shows that the EDE scenario currently stands as one of the most promising mechanisms that could be responsible for the observed discrepancy.

The rest of this chapter is structured as follows. In Sect. 2.2 we discuss the general characteristics that any model attempting to solve the Hubble tension might require. In Sect. 2.3 we present the basic equations of the EDE scenario. In Sect. 2.4 we present the results of our different data analyses for the EDE model. In Sect. 2.5 we discuss the different aspects of the “ $H_0$  olympics”: the proposed models, the tests to quantify model success and the results of the contest. Finally, in Sect. 2.6 we draw our conclusions.

## 2.2 Guidelines to solve the $H_0$ tension

The inference of  $H_0$  from “early-Universe” probes (like the CMB) heavily depends on the assumed cosmological model, as opposed to local determinations (such as the cosmic distance ladder). For this reason, it is commonly stated that the  $H_0$  tension necessarily signals a breakdown of the  $\Lambda$ CDM model, if not originated by unaccounted systematics. Let us explore this statement in more details, focusing on

<sup>3</sup>The joint analysis of KIDS1000+BOSS+2dfLenS has determined  $S_8 = 0.766^{+0.020}_{-0.014}$  (HEYMANS et al. 2021) in  $3\sigma$  tension with Planck. Making use of these data would not affect our conclusions.

the CMB and cosmic-distance ladder determinations of  $H_0$ .

Most local determinations aim to obtain  $H_0$  from the slope of the Hubble diagram, which gives the luminosity distance  $d_L(z)$  to some standard candle (typically, SNIa) in terms of redshift. The redshift range should be chosen to reduce as much as possible the dependence on peculiar velocities at low- $z$  and the dependence on cosmology at high- $z$ . As already mentioned in [Chapter 1](#), a SNIa can be standardized using light curve color  $c$  and shape  $x$  corrections, such that the peak absolute magnitude in the  $B$ -band,  $M_b$ , is common to all SNIa. Hence, the peak apparent magnitude  $m_b$  at redshift  $z$  can be written as:

$$\begin{aligned} m_b(z) &= M_b + 25 + \log_{10} d_L(z) \\ &= -5a_b + 5\log_{10} \hat{d}_L(z), \end{aligned} \quad (2.2)$$

where  $5a_b \equiv -(M_b + 25 - 5\log_{10} H_0)$  is the intercept and  $\hat{d}_L(z) \equiv H_0 d_L(z)$  is the uncalibrated luminosity distance. For a spatially flat universe, the low- $z$  expansion of  $\hat{d}_L(z)$  gives

$$\hat{d}_L(z) = z \left[ 1 + (1 - q_0) \frac{z}{2} - \frac{1}{6} (1 - q_0 - 3q_0^2 + j_0) z^2 \right], \quad (2.3)$$

where  $q_0 \equiv -\frac{\ddot{a}a}{\dot{a}^2} \Big|_0$  and  $j_0 \equiv \frac{\dddot{a}a^2}{\dot{a}^3} \Big|_0$  are the deceleration and jerk parameters, respectively. Therefore, in order to get  $H_0$  from the value of  $a_b$ , a knowledge of  $M_b$  is required, *i.e.*, the luminosity distances of SNIa need to be calibrated. The goal of the cosmic distance ladder is precisely to calibrate the distances to SNIa by using a succession of overlapping methods, where each rung of the “ladder” is needed to determine greater distances at the next rung. Getting direct measurements of distance is only possible for nearby galaxies (anchors), located at a few  $\sim$  kpc from us. The anchor galaxies considered by SHOES include the megamaser host NGC 4258, the Milky Way where distances are obtained using parallaxes, and the Large Magellanic Cloud (LMC) where distances are measured by detached eclipsing binaries. Those galaxies host a class of pulsating stars known as *Cepheids*. These were the first standard candles to be identified, when Henrietta Leavitt discovered that they exhibit a strong correlation between their period and their intrinsic luminosity ([LEAVITT et al. 1912](#)). The Wesenheit apparent magnitude <sup>4</sup> of a  $j$ th Cepheid in the  $i$ th galaxy can generally be written as

$$m_{H,i,j}^W = \mu_i + M_H^W + b_W [P]_{i,j} + Z_W [O/H]_{i,j}. \quad (2.5)$$

Here  $\mu_i$  is the distance modulus to the galaxy,  $M_H^W$  is the zeropoint Cepheid absolute magnitude corresponding to a period  $P = 10$  days, and  $b_W, Z_W$  denote the slope parameters that capture the dependence on period,  $[P] \equiv \log_{10} P - 1$  (with  $P$  in units of days), as well as metallicity,  $[O/H] \equiv \log_{10}(O/H) - \log_{10}(O/H)_\odot$  (with  $O$  and  $H$  the number of oxygen and hydrogen atoms per unit of volume, respectively). Thus, the first step of the ladder consists in measuring distances to the aforementioned anchors (hosting 980 Cepheids according to the latest SHOES data release), in such a way to

<sup>4</sup>The dereddened apparent magnitude  $m_H^W$  is connected to the Wesenheit dust extinction parameter  $R_W$  as ([PERIVOLAROPOULOS et al. 2022](#))

$$m_H^W \equiv m_H - R_W(V - I), \quad (2.4)$$

where  $m_H$  is the apparent magnitude in the near-infrared  $H$  (F160W) band,  $V$  (F555W) and  $I$  (F814W) are optical apparent magnitudes in the corresponding bands.



determine  $M_H^W, b_W$  and  $Z_W$ . Once the calibration of the period-luminosity-metallicity relation is achieved, one can measure distances to much farther Cepheids. In the second step of the ladder, a few thousands of Cepheids are observed in galaxies hosting SNIa (at distances between  $\sim$  kpc to  $\sim$  Mpc), hence permitting a calibration of SNIa. In particular, the latest SHOES analysis considers 37 galaxies with redshifts  $0.0015 \lesssim z \lesssim 0.011$  hosting 2150 Cepheids and 42 SNIa. This procedure yields (see [RIESS et al. 2021b](#) for details)

$$M_b = 19.2435 \pm 0.0373 \quad (2.6)$$

In the third and last step of the ladder, the Hubble constant is determined from the observations of SNIa in the Hubble flow (at distances of the order of  $\sim$  Gpc). More precisely, the SHOES team converts the intrinsic magnitude  $M_b$  into a value of  $H_0$  via the magnitude-redshift relation (see [Eq. \(2.2\)](#)) of 277 SNIa from the Pantheon catalog ([SCOLNIC et al. 2018](#)) in the redshift range  $0.023 < z < 0.15$ . In this procedure, the deceleration and jerks parameters are set to  $q_0 = -0.55$  and  $j_0 = 1$  (corresponding to the standard cosmological model). From this, we see that the SHOES determination of  $H_0$  is not fully cosmology-independent. However, this procedure is expected to be very robust under changes in the cosmological model, since  $H_0$  is extrapolated from measurements at very low  $z$ , as opposed to the early universe probes, which extrapolate  $H_0$  from observations at  $z \sim \mathcal{O}(10^3)$ .

Let us move to describe the “early-Universe” determination of the Hubble constant. The key scales at play in the  $\Lambda$ CDM prediction are the observed angular scale of sound horizon at recombination  $\theta_s$ , measured at  $\mathcal{O}(0.1\%)$  precision in CMB data, and the related angular scale of sound horizon at baryon drag  $\theta_d$ , measured at  $\mathcal{O}(1\%)$  precision within the latest BOSS data. As discussed in [Chapter 1](#), these angular scales are defined as  $\theta_X \equiv r_X/D_A(z_{\text{obs}})$ , where the numerator is either the sound horizon at recombination  $r_s$  or sound horizon at baryon drag  $r_d$ , while the denominator is the comoving angular diameter distance  $D_A(z_{\text{obs}})$  to recombination,  $z_{\text{obs}} \simeq z_{\text{rec}}$ , or to the redshift of the survey,  $z_{\text{obs}} \simeq 0.1 - 3$ . Given that the relationship between  $r_s$  and  $r_d$  is fixed within the  $\Lambda$ CDM cosmology, it is common to say that one can calibrate BAO using the CMB sound horizon measurement. The sound horizon is calculated as

$$r_s = \int_{z_{\text{rec}}}^{\infty} \frac{c_s dz}{H(z)}, \quad (2.7)$$

while the comoving angular diameter distance in flat space is given by :

$$D_A(z_{\text{obs}}) = \int_0^{z_{\text{obs}}} \frac{dz}{H(z)}. \quad (2.8)$$

There are different ways to approach the question of how the angles  $\theta_X$  depend on the Hubble parameter. Let us take the view in which the physical densities  $\bar{\rho}_I$  contribute to the Hubble parameter  $H(z)$  via the Friedmann law (in other words, we parametrize densities with  $\omega_i$ , rather than  $\Omega_i$ ). One recognizes that a change of the Hubble parameter today ( $H_0 \equiv H(z=0)$ ) can only be produced by a change in the total physical density *at present*. Therefore, this change in  $H_0$  yields an impact on the angular diameter distance  $D_A$  (affected by densities at  $z \in [0, z_{\text{obs}}]$ ), but not on the sound horizon  $r_s$  (affected by densities at  $z \in [z_{\text{rec}}, \infty]$ ). This means that there are two ways to increase the inferred value of  $H_0$  while keeping the angles  $\theta_X$  fixed



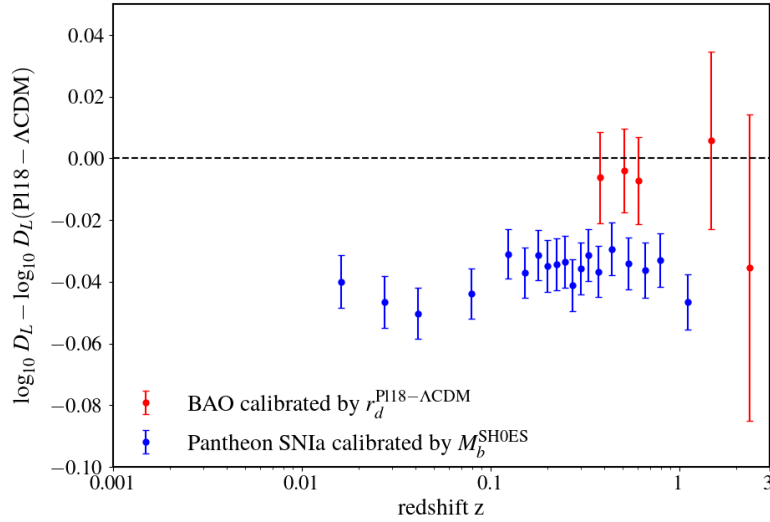


**Figure 2.1** – Differences in the luminosity distances, with respect to the prediction from the best-fit  $\Lambda$ CDM model from [Planck18](#). These distances are obtained from two sets of data: measurements of SNIa apparent magnitudes calibrated using  $M_b^{\text{SHOES}} = 19.2435 \pm 0.0373$  ([RIESS et al. 2021b](#)), and BAO measurements calibrated with  $r_d^{\text{P118-}\Lambda\text{CDM}} = 147.18 \pm 0.29$  Mpc ([AGHANIM et al. 2020b](#)) and converted into luminosity distance with  $d_L(z) = (1+z)D_A(z)$ . The blue dots correspond to SNIa data from the Pantheon catalog ([SCOLNIC et al. 2018](#)), while the red dots correspond to BAO data from BOSS DR12 at  $z = 0.38, 0.51$  and  $0.61$  ([ALAM et al. 2017](#)), eBOSS DR16 quasars at  $z = 1.48$  ([HOU et al. 2020](#)), and the joint constraints from the eBOSS DR14 Ly- $\alpha$  cross-correlation at  $z = 2.35$  ([BLOMGVIST et al. 2019](#)).

- **Early time solutions.** This class of solutions aim to decrease the sound horizon  $r_s$ , by changing the physics before or around recombination,  $z \gtrsim z_{\text{rec}}$ . In this way, the shift in  $\theta_X$  is compensated by an increase of  $H_0$ , which rescales the angular diameter distance.
- **Late time solutions.** Those solutions change physics well after recombination ( $z \ll z_{\text{rec}}$ ) in such a way to attain a higher energy density today and thus a higher  $H_0$ . However, given that  $r_s$  is unchanged, one has to be careful to keep the angular diameter distance fixed in order not to change the measured  $\theta_X$ . This can be accomplished by requiring the energy density to be smaller in the past (but still at  $z < z_{\text{rec}}$ ), in such a way so as to compensate for the higher energy density today. This is known as the “geometrical degeneracy” within CMB data

The problem for late time solutions, however, arises from the multitude of low redshift measurements (such as supernovae, BAO, cosmic chronometers), which tightly constrain  $H(z)/H_0$  in a redshift range of around  $z \lesssim 2$ . This becomes particularly clear when combining BAO and supernovae data. Notice that, because of the distance duality relation in [Eq. \(1.41\)](#), those two sets of observations are actually providing a measurement of the same type of distance. This is illustrated in [Fig. 2.1](#), where we show the difference in luminosity distances with respect to the prediction from the best-fit [Planck18](#)  $\Lambda$ CDM model (P118- $\Lambda$ CDM, to shorten notation), for two different datasets: 1) the Pantheon SNIa calibrated using the SHOES value of  $M_b$ , and 2) the BAO data calibrated using the P118- $\Lambda$ CDM value of  $r_d$  and converted from angular

diameter distance with<sup>5</sup>  $d_L(z) = (1+z)D_A(z)$ . We see a clear discrepancy between the BAO and SNIa data. This makes it hard for late-time modifications to resolve the tension, as it is not possible to fit simultaneously BAO and SNIa data without changing  $r_d$ . This problem can be reformulated in several equivalent ways:

- The “inverse distance ladder” determination of  $M_b$ , obtained from the combination of  $d_L(z) = (1+z)D_A(z)$  as extracted from the P18- $\Lambda$ CDM-calibrated BAO data and the apparent magnitudes from the Pantheon survey, cannot be made compatible with the direct determination from SHOES. This has been shown for example in CAMARENA et al. (2021) and EFSTATHIOU (2021).
- The value of the sound horizon  $r_s$  obtained from a combination of  $D_A(z) = d_L(z)/(1+z)$  as extracted from the SHOES-calibrated SNIa data and the BAO data, is in disagreement with that inferred from Planck18 under  $\Lambda$ CDM. This was highlighted in BERNAL et al. (2016), KNOX et al. (2020) and AYLOR et al. (2019).
- The reconstructed expansion histories  $H(z)$  inferred from P18- $\Lambda$ CDM-calibrated BAO data and SHOES-calibrated SNIa data are inconsistent with each other. This was the approach of LEMOS et al. (2019) and POULIN et al. (2018b).

We conclude that in order to quantify the ability of a certain model to solve the tension with SHOES, it is very important to use a prior on the intrinsic SNIa magnitude,  $M_b$ , rather than a prior on  $H_0$ , for two main reasons:

1. *It is a fully cosmology-independent approach.* Indeed, we saw earlier that what the SHOES team directly measures is  $M_b$ , and not  $H_0$ . Focusing on  $M_b$  allows to derive  $H_0$  from the supernovae self-consistently within the given exotic expansion history. This point is effectively irrelevant for early-Universe solutions<sup>6</sup>, but might be important for late-Universe solutions. Nevertheless, DHAWAN et al. (2020) explored several parametric forms of the expansion history at late times, and concluded that the distance ladder values of  $H_0$  inferred from these expansion histories agreed to within about 0.5 km/s/Mpc. Hence, a SHOES-like determination of  $H_0$  is expected to be quite robust under late-time changes in the model. Still, using a  $M_b$  prior is very important for the reason given below.
2. *It highlights the inconsistency between the SHOES-calibrated Pantheon data and the  $\Lambda$ CDM-calibrated BAO data.* In fact, one could further split the late-Universe solutions into two different categories. The first type considers smooth modifications of the expansion history at late times. This is the case of the decaying dark matter scenario that we will discuss in Chapter 3. For this kind of solutions, the inconsistency between SNIa and BAO data shown in Fig. 2.1 already prevents them from predicting a high value of  $H_0$ , even when a SHOES prior is imposed. The second type of late-time solutions generically consider sharp transitions in the dark energy equation of state at very low  $z$  (BENEVENTO et al. 2020). Such kind of solutions can in principle predict a high value of  $H_0$ , even when both BAO and SNIa data are considered, giving the impression that they have resolved the tension after imposing a SHOES  $H_0$  prior. However, they are not resolving the true origin of the tension, namely, the inconsistency between the distance ladder and

<sup>5</sup>This is sometimes referred as the the “inverse distance ladder”.

<sup>6</sup>In fact, all our EDE analysis presented in Sect. 2.4 consider a SHOES prior on  $H_0$ .

inverse distance ladder calibration of SNIa. In order to correctly penalize this kind of models, the use of a prior on  $M_b$  is essential.

From the above discussion, it becomes clear that a minimum ingredient that any model attempting to solve the tension should have (although likely not the only one) is the ability to decrease the sound horizon at recombination. In the next section we proceed to describe one of such models.

## 2.3 Formalism of Early dark energy

The idea that an anomalous era of expansion arising from EDE at early times might resolve the Hubble tension was first suggested in KARWAL et al. (2016), where computation only at the level of the background was shown to partially alleviate the tension. However, it is the work of POULIN et al. (2019) that showed through a fluid approximation the key role played by perturbations in the scalar field to allow for a resolution of the Hubble tension. In particular, it has been shown that *Planck* data not only provide a detection of the background dynamics of the EDE component, but also severely restricts the dynamics of perturbations, favoring either a non-canonical kinetic term, whereby the equation of state  $w$  is approximately equal to the effective sound speed  $c_s^2$  (M.-X. LIN et al. 2019), or a potential that flattens close to the initial field value (T. L. SMITH et al. 2020).

### 2.3.1 Basic equations

In this work, we study the modified axion potential introduced in KAMIONKOWSKI et al. (2014), KARWAL et al. (2016), POULIN et al. (2018a, 2019), and T. L. SMITH et al. (2020),

$$V_n(\Theta) = m^2 f^2 [1 - \cos(\Theta)]^n, \quad (2.9)$$

where  $m$  represents the axion mass,  $f$  the axion decay constant, and  $\Theta \equiv \phi/f$  is a re-scaled dimensionless field variable defined such that  $-\pi \leq \Theta \leq \pi$ . This potential is a phenomenological generalization of the well motivated axion-like potential (which can be recovered by setting  $n = 1$ ) that arise generically in string theory (SVRCEK et al. 2006; DOUGLAS et al. 2007; ARVANITAKI et al. 2010; MARSH 2016). Such a potential may be generated by higher-order instanton corrections (KAPPL et al. 2016), but taken at face values would suffer from strong fine-tuning issues necessary to the cancelling of the lowest orders instantons (if  $n > 1$ ). Therefore, it should not be interpreted beyond a phenomenological description.

The dynamics of EDE are dictated by the Klein-Gordon equations at the background level

$$\phi'' + 2\mathcal{H}\phi' + a^2 V_{n,\phi} = 0, \quad (2.10)$$

and at the linearly perturbed level

$$\delta\phi'' + 2\mathcal{H}\delta\phi' + \left(k^2 + a^2 V_{n,\phi\phi}\right) \delta\phi = -\frac{h'}{2}\phi', \quad (2.11)$$

where  $h$  denotes the scalar metric potential in the synchronous gauge. The elements of the scalar field stress-energy tensor are given by<sup>7</sup>

$$\bar{\rho}_\phi = a^{-2} \frac{\phi'^2}{2} + V_n, \quad \bar{P}_\phi = a^{-2} \frac{\phi'^2}{2} - V_n, \quad (2.13)$$

$$\delta\rho_\phi = a^{-2} \phi' \delta\phi' + V_{n,\phi} \delta\phi, \quad \delta P_\phi = a^{-2} \phi' \delta\phi' - V_{n,\phi} \delta\phi, \quad (2.14)$$

$$(\bar{\rho}_\phi + \bar{P}_\phi) \theta_\phi = k^2 a^{-2} \phi' \delta\phi, \quad \sigma_\phi = 0. \quad (2.15)$$

We assume that the field always starts in slow-roll,  $\Theta'_i = 0$  (as enforced by the very high value of the Hubble rate at early times), and without loss of generality we restrict  $0 \leq \Theta_i \leq \pi$ . The model at this point has four free parameters:  $\{m, f, n, \Theta_i\}$ . Given that the dynamics are relatively insensitive to changes of  $2 \lesssim n \lesssim 4.5$  (AGRAWAL et al. 2019; T. L. SMITH et al. 2020), we further restrict the parameter space by taking  $n = 3$ . In order to make this model more physically accessible, instead of parameterizing the dynamics using the mass  $m$  and decay constant  $f$ , we use the critical redshift when the field becomes dynamical,  $z_c$ , and the fractional energy density at this redshift,  $f_{\text{EDE}}(z_c) \equiv \bar{\rho}_\phi(z_c)/\bar{\rho}_{\text{tot}}(z_c)$ , which is roughly the maximum energy contribution induced by EDE. The final degree of freedom is encoded in the dynamics of the linear perturbations, which is fully characterized via the effective sound speed  $c_s^2$ , and physically related to the curvature of the potential close to the initial field value – note that after fixing all other phenomenological parameters, this is fully described by  $\Theta_i$  (POULIN et al. 2018a; T. L. SMITH et al. 2020).

The background dynamics of EDE is easy to understand: at early times the scalar field is frozen-in due to Hubble friction and contributes as dark energy to the expansion; once the Hubble rate drops below its mass, Hubble friction is removed and the field begins to perform damped oscillations about the minimum of the potential; the rate of energy dilution is related to the period-averaged equation of state, roughly given by  $w(n) = (n-1)/(n+1)$ . In Fig. 2.2 we show the redshift evolution for the fractional energy density and the equation of state in the EDE. We see that EDE provides exactly the required behavior to explain a high value of  $H_0$ : thanks to the very peaked shape of its energy injection, it can boost the expansion rate just prior to recombination, thereby reducing the value of the sound horizon.

To perform our analyses, we use the modified version of **CLASS** presented in T. L. SMITH et al. (2020). The code is publicly available at <https://github.com/PoulinV/AxiCLASS>. The main goal of this code is to solve the Klein-Gordon equations Eq. (2.10) and Eq. (2.11), and to perform a shooting method in order to map a choice of  $\{z_c, f_{\text{EDE}}\}$  into the theory parameters  $\{m, f\}$ .

<sup>7</sup>The expressions for the overdensity, perturbed pressure, energy flux and shear can easily be obtained by considering linear perturbations in the general expression for the stress energy tensor of a scalar field in Eq. (1.44),

$$\begin{aligned} \delta T^\mu{}_\nu &= \partial^\mu \phi \partial_\nu \delta\phi + \partial^\mu \delta\phi \partial_\nu \phi - \delta^\mu_\nu \left( \frac{\bar{g}^{\alpha\beta}}{2} (\partial_\alpha \phi \partial_\beta \delta\phi + \partial_\alpha \delta\phi \partial_\beta \phi) + V_{n,\phi} \delta\phi \right) \\ &= -\delta^\mu_0 a^{-2} \phi' \partial_\nu \delta\phi + \delta^\mu_\nu \phi' \bar{g}^{\alpha\mu} \partial_\alpha \delta\phi + \delta^\mu_\nu (a^{-2} \phi' \delta\phi' - V_{n,\phi} \delta\phi), \end{aligned} \quad (2.12)$$

and then using the definitions of  $\delta\rho$ ,  $\delta P$ ,  $\theta$  and  $\sigma$  in Eq. (A.30).

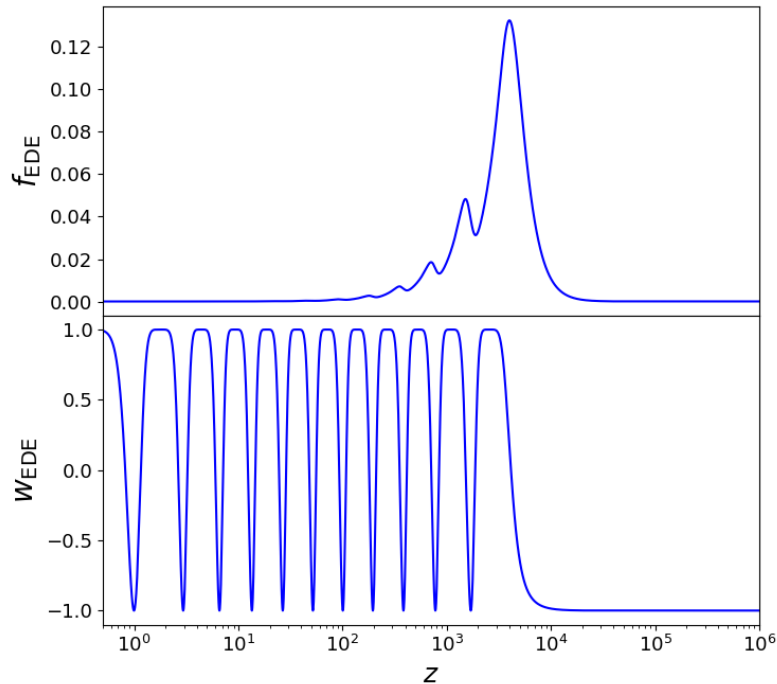


**Figure 2.2** – Fractional energy density (**upper**) and equation of state (**lower**) in the EDE as a function of redshift. Cosmological parameters are set to the best-fit values from the [Planck18+BAO+SNIa+SHOES](#) analysis (see third column of [Tab. \(2.1\)](#)).

In the following section, we detail the results of our different data analyses for the EDE model. We start by performing an ‘anatomy’ of the EDE resolution to the Hubble tension, to understand how each data set reacts to the presence of EDE. We additionally introduce the new baseline 1-parameter EDE model that is favored by [Planck18](#) 2018 data. Then, we present our  $N$ -Body simulations validating for the first time the HMcode prediction and confront the 1-parameter EDE model against WL data. We end by discussing the  $H_0$  and  $S_8$  tension in light of the lensing-marginalized CMB spectrum.

## 2.4 Cosmological constraints

In this section, we test the EDE scenario with various combinations of data-sets, in order to extract the cosmology that would resolve the Hubble tension, and compare with results from past literature making use of [Planck 2015](#) data.

- $\text{PLANCK}^{\text{TTTEEE}+\phi\phi}$ : the high- $\ell$  TT,TE,EE, low- $\ell$  TT and EE data from [Planck 2018](#) through the baseline PLIK, COMMANDER and SIMALL likelihoods ([AGHANIM et al. 2020a,c](#)), alone and combined with the lensing amplitude reconstruction (SIMCA likelihood); we make use of a Cholesky decomposition to handle the large number of nuisance parameters ([LEWIS 2013](#)). Following the procedure of [Planck 2018](#), we don’t consider the low- $\ell$  TE part of the spectra, given its lower signal-to-noise ratio ([AGHANIM et al. 2020a](#)).

- BAO: the measurements from 6dFGS at  $z = 0.106$  (BEUTLER et al. 2011), SDSS MGS at  $z = 0.15$  (ROSS et al. 2015), and BOSS DR12 data at  $z = 0.38, 0.51$  and  $0.61$  (ALAM et al. 2017).
- FS: the measurements of the growth function  $f\sigma_8(z)$  (FS) from the CMASS and LOWZ galaxy samples of BOSS DR12 at  $z = 0.38, 0.51,$  and  $0.61$  (ALAM et al. 2017). In practice, we make use of the “consensus” BAO and FS result that combines both in a single likelihood
- PANTHEON: the Pantheon SNIa catalogue, spanning redshifts  $0.01 < z < 2.3$ ; we marginalize over the nuisance parameter  $\mathcal{M}$  describing the SNIa calibration (SCOLNIC et al. 2018).
- SHOES: the SHOES result, modeled with a Gaussian likelihood centered on  $H_0 = 74.03 \pm 1.42$  km/s/Mpc (RIESS et al. 2019). We could have alternatively considered a prior on  $M_b$  as advocated in Sect. 2.2, but this is not expected to affect the results, given that EDE only changes physics at very early times.

### 2.4.1 Baseline analysis: anatomy of the 3-parameter EDE model

Our baseline cosmology consists in the following combination of the six  $\Lambda$ CDM parameters  $\{\omega_b, \omega_{\text{cdm}}, H_0, n_s, A_s, \tau_{\text{reio}}\}$ , plus three parameters describing the EDE sector, namely  $\{f_{\text{EDE}}(a_c), \text{Log}_{10}(a_c), \Theta_i\}$ <sup>8</sup>. We use wide flat priors on all these parameters. We follow the Planck convention and assume two massless neutrinos and one massive with  $m_\nu = 0.06$  eV. We perform our MCMC analyses using `MontePython-v3`<sup>9</sup> (AUDREN et al. 2013; BRINCKMANN et al. 2019a), and consider chains to be converged with the Gelman-Rubin criterion<sup>10</sup>  $R - 1 < 0.1$  (GELMAN et al. 1992). To extract best-fit parameters, we make use of the MINUIT algorithm (JAMES et al. 1975) through the `iMinuit` python package<sup>11</sup>. Starting from Planck only, we now discuss the impact of adding data-sets on the reconstructed EDE parameters. We compare the evolution of the  $\chi^2$  in the EDE cosmology as we add data-sets, to that of the  $\Lambda$ CDM model in the same combined fit, with and without SHOES data. The results are presented in Tab. (2.1) and we show the 1D and 2D posterior distributions of  $\{H_0, f_{\text{EDE}}(z_c), \Theta_i, \text{Log}_{10}(z_c), \omega_{\text{cdm}}, n_s, S_8\}$  in Fig. 2.3. All relevant  $\chi^2$  information is given in App. C.1.

**Planck TT,TE,EE only:** with  $\text{PLANCK}^{\text{TTTEEE}}$  data only and three free parameters, the EDE model under study is not detected. In agreement with HILL et al. (2020) and NIEDERMANN et al. (2020), we find that the fraction of EDE at  $z_c$  is limited to<sup>12</sup>  $f_{\text{EDE}}(z_c) < 0.088$ , while  $\text{Log}_{10}(z_c)$  and  $\Theta_i$  are unconstrained. Interestingly, we also find that the best fit within `Planck18` data only has  $\{f_{\text{EDE}}(z_c) \sim 8.5\%, \text{Log}_{10}(z_c) \sim 3.56, \Theta_i \sim 2.8, H_0 \sim 70.5$  km/s/Mpc $\}$  and a  $\Delta\chi_{\text{min}}^2 \equiv \chi_{\text{min}}^2(\Lambda\text{CDM}) - \chi^2(\text{EDE}) \simeq -5$  in favor of

<sup>8</sup>One could have alternatively considered a logarithmic prior on  $f_{\text{EDE}}$ , but this would have given more weight to very small values of  $f_{\text{EDE}}$ , which are uninteresting in the context of finding a solution to the Hubble tension.

<sup>9</sup>[https://github.com/brinckmann/montepython\\_public](https://github.com/brinckmann/montepython_public)

<sup>10</sup>Most chains are in fact converged at the  $R - 1 \sim 0.01$  level, this somewhat ‘loose’ but reasonable criterion was only used once including KIDS-VIKING data, which are much longer to converge.

<sup>11</sup><https://iminuit.readthedocs.io/>

<sup>12</sup>Hereinafter, we quote 1-sided constraints at 95%C.L., and two-sided ones at 68%C.L.



3-parameter EDE cosmology				
Parameter	PLANCK <sup>TTTEEE</sup>	+SHOES	+PLANCK <sup>φφ</sup> +BAO+PANTHEON	+FS
$H_0$ [km/s/Mpc]	68.29(70.49) <sup>+0.75</sup> <sub>-1.3</sub>	71.49(73.05) ± 1.2	71.34(72.41) <sup>+1</sup> <sub>-1.1</sub>	71.01(71.96) <sup>+1.1</sup> <sub>-1.1</sub>
100 $\omega_b$	2.252(2.270) <sup>+0.019</sup> <sub>-0.023</sub>	2.284(2.281) <sup>+0.022</sup> <sub>-0.024</sub>	2.282(2.292) <sup>+0.021</sup> <sub>-0.022</sub>	2.28(2.285) <sup>+0.021</sup> <sub>-0.022</sub>
$\omega_{\text{cdm}}$	0.1232(0.1278) <sup>+0.0019</sup> <sub>-0.004</sub>	0.13(0.135) <sup>+0.0042</sup> <sub>-0.004</sub>	0.1297(0.1327) <sup>+0.0036</sup> <sub>-0.0039</sub>	0.1289(0.1323) ± 0.0039
10 <sup>9</sup> $A_s$	2.116(2.124) <sup>+0.035</sup> <sub>-0.041</sub>	2.153(2.160) <sup>+0.036</sup> <sub>-0.042</sub>	2.152(2.183) <sup>+0.031</sup> <sub>-0.035</sub>	2.144(2.135) <sup>+0.032</sup> <sub>-0.033</sub>
$n_s$	0.9706(0.9829) <sup>+0.0058</sup> <sub>-0.0087</sub>	0.9889(0.9966) <sup>+0.0076</sup> <sub>-0.0075</sub>	0.9878(0.9963) <sup>+0.0066</sup> <sub>-0.007</sub>	0.9859(0.9895) <sup>+0.007</sup> <sub>-0.0071</sub>
$\tau_{\text{reio}}$	0.0552(0.0524) <sup>+0.0076</sup> <sub>-0.0086</sub>	0.0586(0.0558) <sup>+0.0077</sup> <sub>-0.0091</sub>	0.0585(0.0633) <sup>+0.007</sup> <sub>-0.008</sub>	0.0574(0.0528) <sup>+0.007</sup> <sub>-0.0079</sub>
$f_{\text{EDE}}(z_c)$	< 0.088(0.085)	0.108(0.152) <sup>+0.035</sup> <sub>-0.028</sub>	0.106(0.133) <sup>+0.031</sup> <sub>-0.028</sub>	0.097(0.126) <sup>+0.035</sup> <sub>-0.029</sub>
$\text{Log}_{10}(z_c)$	3.705(3.569) <sup>+0.37</sup> <sub>-0.22</sub>	3.612(3.569) <sup>+0.13</sup> <sub>-0.49</sub>	3.615(3.602) <sup>+0.11</sup> <sub>-0.029</sub>	3.61(3.572) <sup>+0.13</sup> <sub>-0.054</sub>
$\Theta_i$	unconstrained (2.775)	2.604(2.756) <sup>+0.33</sup> <sub>-0.0087</sub>	2.722(2.759) <sup>+0.17</sup> <sub>-0.092</sub>	2.557(2.705) <sup>+0.37</sup> <sub>-0.025</sub>
100 $\theta_s$	1.04165(1.04371) <sup>+0.00039</sup> <sub>-0.00034</sub>	1.04131(1.04070) <sup>+0.00039</sup> <sub>-0.0004</sub>	1.04143(1.04122) <sup>+0.00036</sup> <sub>-0.00039</sub>	1.04145(1.04098) <sup>+0.00038</sup> <sub>-0.00039</sub>
$r_s(z_{\text{rec}})$	142.8(140.1) <sup>+1.9</sup> <sub>-0.72</sub>	138.8(136.4) <sup>+1.7</sup> <sub>-1.9</sub>	139(137.5) <sup>+1.7</sup> <sub>-1.7</sub>	139.4(137.8) <sup>+1.7</sup> <sub>-1.9</sub>
$S_8$	0.839(0.834) <sup>+0.018</sup> <sub>-0.019</sub>	0.838(0.842) <sup>+0.018</sup> <sub>-0.019</sub>	0.838(0.846) ± 0.013	0.837(0.838) ± 0.013
$\Omega_m$	0.314(0.304) <sup>+0.0088</sup> <sub>-0.0091</sub>	0.3004(0.2969) <sup>+0.0079</sup> <sub>-0.0084</sub>	0.301(0.2980) <sup>+0.0051</sup> <sub>-0.0055</sub>	0.3022(0.3009) <sup>+0.0053</sup> <sub>-0.0054</sub>
$\Delta\chi_{\text{min}}^2$ ( $\Lambda$ CDM w/ SHOES)	–	-20.8	-19.1	-18.7
$\Delta\chi_{\text{min}}^2$ ( $\Lambda$ CDM w/o SHOES)	-4.9	-1.5	-0.02	-0.6

**Table 2.1** – The mean (best-fit)  $\pm 1\sigma$  error of the cosmological parameters reconstructed from the combined analysis of various data sets (from left to right, each column adds a set of data to the previous one). We also report the  $\Delta\chi_{\text{min}}^2$  with respect to a  $\Lambda$ CDM fit to the same data-sets, with and without a prior on  $H_0$  from SHOES.

the EDE model<sup>13</sup>. One can already note a curiosity: the best fit value of  $f_{\text{EDE}}(z_c)$  is very close to the  $2\sigma$  bound that we obtain. This, as we will discuss later, is due to the choice of flat, uninformative prior on  $\text{Log}_{10}(z_c)$  and  $\Theta_i$ .

**Planck TT,TE,EE+SHOES:** Once a prior on  $H_0$  given by SHOES is included in the analysis, the sampler explores more easily a part of parameter space with higher  $H_0$  values, and the EDE is now well detected:  $\{f_{\text{EDE}}(z_c) \simeq 0.11_{-0.031}^{+0.036}, \text{Log}_{10}(z_c) = 3.6_{-0.039}^{+0.14}, \Theta_i = 2.569_{-0.032}^{+0.36}\}$ , with  $H_0 = 71.4 \pm 1$  km/s/Mpc. This is in excellent agreement with results from past literature (M.-X. LIN et al. 2019; POULIN et al. 2019; NIEDERMANN et al. 2020; T. L. SMITH et al. 2020). Remarkably, the best fit values of both  $\Theta_i$  and  $\text{Log}_{10}(z_c)$  are in perfect agreement with that obtained Planck18 only. This is highly non-trivial, and seem to indicate that Planck18 does favor the region of the  $\{\text{Log}_{10}(z_c), \Theta_i\}$ -space that resolves the Hubble tension. However, the best fit fraction reaches 15%, a value that one would naively consider to be strongly excluded by the Planck18 only analysis. In fact, that is not the case, as the the fit to Planck18 data is barely affected by the additional  $H_0$  prior, while one can get an excellent fit of SHOES data. Concretely, the  $\chi_{\text{min}}^2$ (EDE) when fitting Planck18+SHOES increases by  $\sim 3$ , such that even in this combined fit, the  $\chi^2$  of Planck18 data is smaller than that of  $\Lambda$ CDM fitted on Planck18 data only. This indicates that the limit on  $f_{\text{EDE}}(z_c)$  derived in a Planck18 only analysis is not robust, as it is entirely driven by our choice of flat priors. This was also discussed in NIEDERMANN et al. (2020) and T. L. SMITH et al. (2020), and the reason for that is clear<sup>14</sup>: there exists a strong  $\chi^2$  degeneracy in Planck18 data between  $\Lambda$ CDM and the EDE cosmology, that, given our choice of uninformative priors on  $\Theta_i$  and  $\text{Log}_{10}(z_c)$ , leads to an artificially strong bound on  $f_{\text{EDE}}(z_c)$ . Indeed, once  $f_{\text{EDE}}(z_c)$  drops below  $\lesssim 4\%$  (as seen from the 2D posterior), its impacts on the power spectrum is not detectable given current measurement accuracy. As a result, the quantity  $\text{Log}_{10}(z_c)$  and  $\Theta_i$  have no impact on observables, such that any choice of  $\text{Log}_{10}(z_c)$  and  $\Theta_i$  leads to a

<sup>13</sup>To guide the reader, we mention that a  $1\sigma$  shift in the quality of the fit to Planck18 data roughly corresponds to a  $\Delta\chi^2$  of  $\sim 6$  (see the distribution of Planck18's  $\chi^2$  in the tables available at this link).

<sup>14</sup>Here, let us mention that IVANOV et al. (2020) make the comment that such degeneracy does not exist. This is of course only true because they include the  $3\sigma$  discrepant  $S_8$  data to their analysis. The degeneracy is very clear within Planck18 data.



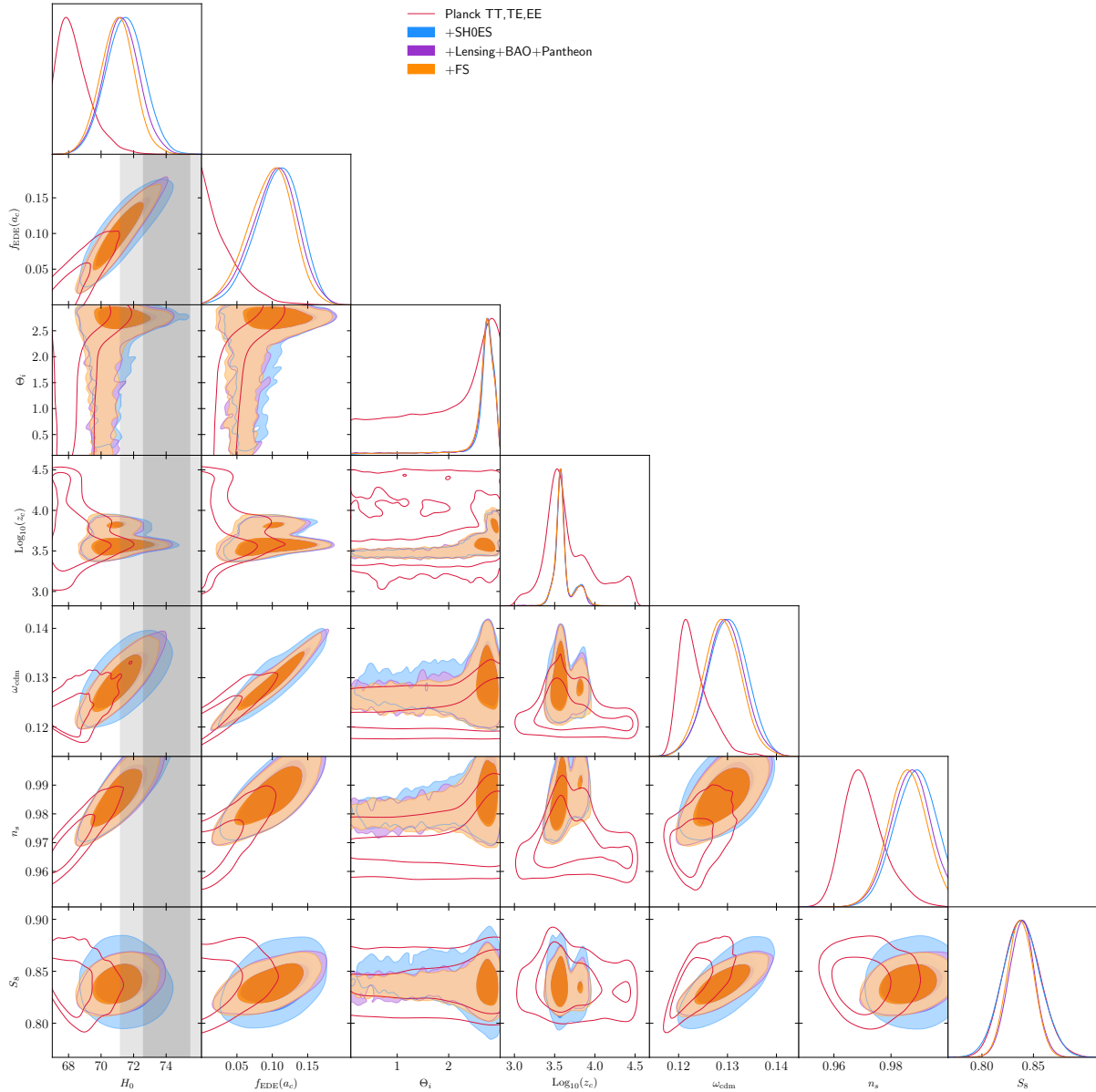


**Figure 2.3** – Reconstructed 2D posterior distributions of a subset of parameters for various data set combinations (see legend) in the 3-parameters EDE cosmology.

cosmology indistinguishable from  $\Lambda$ CDM. Therefore, the sampler spends much more time exploring this degeneracy direction, rather than efficiently sampling the narrow degeneracy between  $f_{\text{EDE}}(z_c)$  and  $H_0$ , which requires a specific choice of  $\text{Log}_{10}(z_c)$  and  $\Theta_i$  to appear<sup>15</sup>. Following NIEDERMANN et al. (2020), we will discuss a natural way to alleviate this issue in Sect. 2.4.2.

**Planck TT,TE,EE+PP+BAO+SNIa+SHOES:** We now add to our analysis the lensing reconstruction  $\text{PLANCK}^{\phi\phi}$ , the PANTHEON SNIa data-set, and the BAO data from BOSS. Strikingly, the addition of these three data-sets has

<sup>15</sup>Let us mention that HEROLD et al. (2022) recently derived new constraints on EDE with the profile likelihood method, which does not suffer from volume effects. Using *Planck* CMB and BOSS full-shape data, they obtain  $f_{\text{EDE}} = 0.072 \pm 0.036$ , which is extremely similar to the results of the 1-parameter EDE analysis of T. L. SMITH et al. (2021) using the same data-sets.

1-parameter EDE cosmology			
Parameter	PLANCK <sup>TTEEE</sup>	+PLANCK <sup>φφ</sup> +BAO+PANTHEON+FS	+SHOES
$H_0$ [km/s/Mpc]	70.10(70.83) $^{+1.4}_{-1.6}$	70.00(69.84) $^{+0.98}_{-1.4}$	71.71(72.21) $^{+1.0}_{-0.95}$
100 $\omega_b$	2.258(2.265) $^{+0.018}_{-0.018}$	2.259(2.263) $^{+0.015}_{-0.016}$	2.273(2.282) $\pm$ 0.013
$\omega_{\text{cdm}}$	0.1282(0.1306) $^{+0.0039}_{-0.0046}$	0.1270(0.1265) $^{+0.0033}_{-0.0043}$	0.1317(0.1310) $^{+0.0036}_{-0.0037}$
$10^9 A_s$	2.137(2.164) $^{+0.037}_{-0.042}$	2.131(2.118) $^{+0.03}_{-0.036}$	2.15(2.140) $^{+0.032}_{-0.031}$
$n_s$	0.9803(0.9851) $^{+0.0079}_{-0.0085}$	0.9795(0.9788) $^{+0.0063}_{-0.0074}$	0.9884(0.9917) $^{+0.0062}_{-0.0057}$
$\tau_{\text{reio}}$	0.0558(0.0602) $^{+0.0079}_{-0.0085}$	0.0553(0.0522) $^{+0.0069}_{-0.0075}$	0.0561(0.0536) $^{+0.0071}_{-0.0076}$
$f_{\text{EDE}}(z_c)$	0.082(0.104) $^{+0.037}_{-0.038}$	0.074(0.070) $^{+0.03}_{-0.036}$	0.118(0.122) $^{+0.029}_{-0.026}$
100 $\theta_s$	1.04147(1.0413) $^{+0.00036}_{-0.00035}$	1.04153(1.04159) $^{+0.00035}_{-0.00032}$	1.04157(1.04127) $\pm$ 0.00034
$r_s(z_{\text{rec}})$	140.1(138.9) $^{+2.2}_{-2.0}$	140.6(140.8) $^{+2.1}_{-1.6}$	138.2(138.2) $^{+1.6}_{-1.8}$
$S_8$	0.844(0.851) $^{+0.017}_{-0.018}$	0.838(0.835) $\pm$ 0.012	0.843(0.839) $^{+0.012}_{-0.013}$
$\Omega_m$	0.3084(0.3067) $^{+0.009}_{-0.0093}$	0.3067(0.3071) $^{+0.0055}_{-0.0058}$	0.3017(0.2962) $^{+0.0051}_{-0.0054}$
$\Delta\chi^2_{\text{min}} (\Lambda\text{CDM})$	-5	-6	-18.5 (-0.5)

**Table 2.2** – The mean (best-fit)  $\pm 1\sigma$  error of the cosmological parameters reconstructed from the combined analysis of various data-sets (from left to right, each column adds a sets of data to the previous one). We also report the  $\Delta\chi^2_{\text{min}}$  with respect to a  $\Lambda\text{CDM}$  fit to the same data-sets. In the last row, we also report the  $\Delta\chi^2$  with respect to  $\Lambda\text{CDM}$  fit to the combined data without SHOES in parenthesis.

almost no impact on the reconstructed posteriors, nor on the best fit. This is far from a trivial test to pass, as many of the suggested resolutions to the Hubble tension are strongly constrained by the addition of these data-sets (BERNAL et al. 2016; DI VALENTINO et al. 2017a,b; ZHAO et al. 2017; ADDISON et al. 2018; POULIN et al. 2018b; AYLOR et al. 2019; RAVERI 2020). However, as noted in POULIN et al. (2019), NIEDERMANN et al. (2020), and T. L. SMITH et al. (2020), we find that the reconstructed  $\omega_{\text{cdm}}$  and  $n_s$  in the EDE cosmology are somewhat higher than in  $\Lambda\text{CDM}$ , such that the  $S_8$  tension is slightly increased. As suggested in past literature (HILL et al. 2020; IVANOV et al. 2020; D’AMICO et al. 2021b), this opens up the possibility of constraining the EDE resolution using LSS data, and in particular the  $S_8$  measurement from weak gravitational lensing surveys. However, combining KiDS+VIKING/HSC data with Planck18 to constrain extension to  $\Lambda\text{CDM}$  can be problematic as: i) they require the ability to predict the non-linear power spectrum at relatively small scales in models beyond  $\Lambda\text{CDM}$ ; ii) the  $\Lambda\text{CDM}$  best fit model from Planck18 is not a good fit to these data.

**All Data:** As a starter, we add the ‘consensus’  $f\sigma_8$  BOSS likelihood to the analysis, which is consistent with the  $\Lambda\text{CDM}$  model from Planck18; we find a mild  $\sim 0.4\sigma$  decrease in the reconstructed mean, now being  $H_0 \simeq 71 \pm 1$  km/s/Mpc and  $f_{\text{EDE}} \simeq 0.1 \pm 0.03$ . This is consistent with the fact that the  $f\sigma_8$  measurements are sensibly lower than the  $\Lambda\text{CDM}$  prediction, while the EDE cosmology leads to slightly larger values. Still, the  $\chi^2$  of the FS data is barely affected; in fact, as before,  $\Lambda\text{CDM}$  provides a slightly worse fit to the joint data-set, even when the SHOES prior is not included in the analysis. Before including weak lensing measurements to the analysis, we therefore conclude that the 3-parameter EDE model under study performs very well in resolving the Hubble tension, but future measurement of  $f\sigma_8$  will certainly put the model under crucial tests.

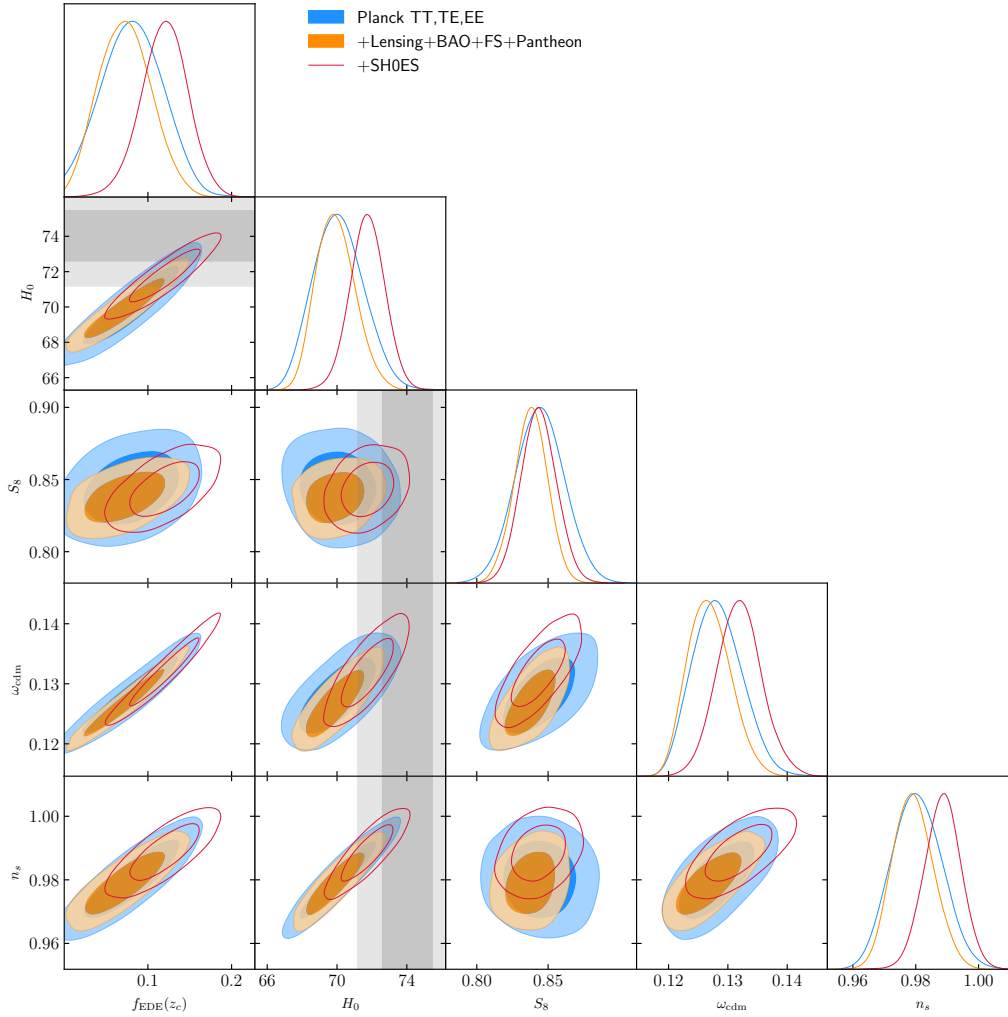


**Figure 2.4** – Reconstructed 2D posterior distributions of a subset of parameters for various data set combinations (see legend) in the 1-parameter EDE cosmology.

### 2.4.2 Towards a 1-parameter resolution to the $H_0$ tension

Before turning to the inclusion of WL data, we show that the apparently tight bounds obtained when the SHOES prior on  $H_0$  is not included is due to our choice of uninformative priors for  $\Theta_i$  &  $\text{Log}_{10}(z_c)$ . In fact, one can strongly weaken the bound on  $f_{\text{EDE}}$  by *reducing* the EDE parameter space to a suitable choice of  $\text{Log}_{10}(z_c)$  and  $\Theta_i$ . This might sound counter-intuitive: in principle, one expects to relax constraints on a given parameter by enlarging the parameter space such as to introduce a new degeneracy. Here however, it is the poor prior choice which leads to a strong bound on  $f_{\text{EDE}}(z_c)$  independently of the data combination. Fixing  $\text{Log}_{10}(z_c)$  and  $\Theta_i$  to some fiducial values surely rises the question of what values should one choose. In a realistic scenario, one might know these values a priori; one example is the scenario discussed in SAKSTEIN et al. (2020) in which a scalar field experiences a phase-transition around the redshift at which neutrinos become non-relativistic <sup>16</sup>, such that the critical redshift is specified by the value of the neutrino mass, while

<sup>16</sup>Current constraints on the sum of neutrino masses set  $\sum m_\nu < 0.12$  eV (Planck18+lensing+BAO), meaning that neutrinos become non-relativistic after recombination. Taken at face value, this would exclude the proposal of SAKSTEIN et al. (2020), but to confirm this one should perform a full analysis

$\Theta_i$  is set by the dynamics of the phase-transition (see also BERGHAUS et al. (2020), BRAGLIA et al. (2020a), GONZALEZ et al. (2020), and NIEDERMANN et al. (2020) for different EDE models with fewer free parameters). Here however, we have been considering a phenomenological model whose primary characteristic is to have enough freedom to extract information from the data to resolve the tension – we will therefore make use of that information and fix  $\Theta_i$  &  $\text{Log}_{10}(z_c)$  to their best fit value from *Planck18* data only – which, we recall, are close-to-identical to that obtained in the combined fit.

We report in Tab. (2.2) the reconstructed cosmological parameters from *Planck18* only and from the combined fit of all data, with and without including SHOES. We show the reconstructed 2D posteriors of  $\{f_{\text{EDE}}(z_c), H_0, S_8\}$  in Fig. 2.4. Notice how the degeneracy direction  $f_{\text{EDE}}(z_c) - H_0$  clearly opens up. Furthermore, the mild  $\Delta\chi^2$  preference in favor of the EDE cosmology now leads to reconstructing  $f_{\text{EDE}}(z_c) = 0.082 \pm 0.037$ , i.e., a  $\sim 2\sigma$  preference for non-zero EDE from *Planck18* data only. The inferred  $H_0 = 70.1 \pm 1.4 \text{ km/s/Mpc}$  is now in agreement with the SHOES determination at better than <sup>17</sup>  $2\sigma$ . The addition of BAO, FS and PANTHEON measurements has little impact; the reconstructed EDE fraction shifts downward by  $\sim 0.3\sigma$ , slightly degrading the success of the resolution to the Hubble tension, while the  $2\sigma$  preference for non-zero EDE is still present. These results are in excellent agreement with those presented in NIEDERMANN et al. (2020) for a different EDE model.

Finally, the inclusion of a prior from SHOES pulls up the fraction of EDE to  $f_{\text{EDE}}(z_c) = 0.118 \pm 0.029$  and the value of  $H_0 = 71.7 \pm 1 \text{ km/s/Mpc}$ , at the cost of a small degradation in  $\chi^2_{\text{min}}$  ( $\Delta\chi^2 \sim +6$ ). Yet, as before, the  $\chi^2_{\text{min}}$  of the *combined fit Planck18+BAO+FS+PANTHEON+SHOES* in the 1-parameter EDE cosmology is slightly lower than a  $\Lambda\text{CDM}$  fit to *Planck18+BAO+FS+PANTHEON* (no SHOES). This attests that, despite this small degradation in  $\chi^2_{\text{min}}$ , the goodness of fit is still excellent. However, as discussed previously, the values of  $S_8$  are in significant tension with weak lensing measurements, and one might expect that it is possible to strongly constrain the EDE model by including LSS data. We study this possibility in detail in Sect. 2.4.3, following HILL et al. (2020), IVANOV et al. (2020), and D’AMICO et al. (2021b).

### 2.4.3 Confronting EDE to weak-lensing data

In order to make use of weak gravitational lensing data to perform LSS analyses, one needs to accurately model the matter power spectrum in the late-time non-linear regime. To this purpose, one can adopt the **HALOFIT** semi-analytical prescription R. E. SMITH et al. (2003), as revised by R. TAKAHASHI et al. (2012), which has been shown to be accurate at 5% level in reproducing the non-linear power spectra of  $\Lambda\text{CDM}$  models up to wavenumbers  $k \leq 10 h/\text{Mpc}$ . However, the version developed by authors of R. TAKAHASHI et al. (2012) does not consider the impact of baryon feedback. A further improvement, dubbed as **HMCODE**, has been developed in MEAD et al. (2015), its main advantage being its flexibility to account for the effects of

---

accounting for the coupling between EDE and the neutrino sector, since adding non-standard neutrino interaction typically shifts neutrino mass constraints (see Chapter 4).

<sup>17</sup>For all the EDE analysis carried out in this section, we quote ‘tension’ and ‘agreement’ assuming Gaussian posteriors for simplicity. While this is surely a crude approximation, we believe this is justified because the posterior of interest ( $H_0, S_8$ ) are close to Gaussian. In Sect. 2.5 we use a different estimator of tension, following RAVERI et al. (2019), that allows to better capture the non-gaussian shape of the posteriors.

Model	Particles ( $N$ )	Box size ( $L$ )	Mass resolution	Label
$\Lambda$ CDM/EDE	$1024^3$	$250 h^{-1}$ Mpc	$1.2 \cdot 10^9 h^{-1} M_\odot$	HR
$\Lambda$ CDM/EDE	$1024^3$	$1000 h^{-1}$ Mpc	$7.5 \cdot 10^{10} h^{-1} M_\odot$	LB
$\Lambda$ CDM/EDE	$256^3$	$250 h^{-1}$ Mpc	$7.5 \cdot 10^{10} h^{-1} M_\odot$	LR

**Table 2.3** – Summary of the properties of the cosmological simulations used in this work. Notice that the Figures shown in this Section have been obtained by splicing together (for each redshift and model) the non-linear matter power spectra extracted from the first two simulations listed here, by using the third one to correct for finite-volume and resolution effects (see App. C.2 for details). The labels listed in the last column stand for High Resolution, Large Box, and Low Resolution, respectively.

baryon physics on the small-scale clustering of matter, particularly important at very low redshifts. Both **HALOFIT** and **HMCODE** have been shown to be suitable to describe the  $\Lambda$ CDM scenario, as well as some common extensions beyond it, such as models with varying DE EoS or massive neutrinos (JOUAKI et al. 2017b).

First, we confront the non-linear matter power spectra produced by using **HALOFIT** /**HMCODE** in the EDE framework, against the outputs of dedicated cosmological  $N$ -Body simulations, to explicitly demonstrate the accuracy of our LSS data analyses. Afterwards, we discuss the results of our MCMC analysis against weak lensing data.

### Non-linear matter power spectrum: a comparison with $N$ -Body simulations

The goal of this Section is to show that the impact on the non-linear matter power spectrum due to the presence of EDE is mainly due to changes in the standard  $\Lambda$ CDM free parameters with respect to their reference values, and therefore such impact can be safely studied without further modifying or re-calibrating **HALOFIT** /**HMCODE**.

To this end, we perform two sets of  $N$ -Body DM-only simulations (one set for the EDE and one for the  $\Lambda$ CDM scenarios), as reported in Tab. (2.3), by using the  $N$ -body code GADGET-3, a modified version of the publicly available numerical code GADGET-2 (SPRINGEL et al. 2001; SPRINGEL 2005). The initial conditions have been produced by displacing the DM particles from a cubic Cartesian grid according to second-order Lagrangian Perturbation Theory, with the 2LPTIC public code (CROCCE et al. 2006), at redshift  $z = 99$ . The corresponding input linear matter power spectra, for both the EDE and  $\Lambda$ CDM cases, were computed with AXICLASS, the aforementioned modified version (T. L. SMITH et al. 2020) of the publicly available code **CLASS** (BLAS et al. 2011). For all of the simulations, we kept the cosmological parameters fixed to their EDE best fit values from T. L. SMITH et al. (2020) (very close to ours), namely  $H_0 = 72.81$ ,  $\Omega_m = 0.2915$ ,  $A_s = 2.191 \cdot 10^{-9}$ ,  $n_s = 0.986$  for both cosmological scenarios; plus the additional parameters  $\log_{10}(z_c) = 3.53$ ,  $f_{\text{EDE}}(z_c) = 0.132$ ,  $\Theta_i = 2.72$ ,  $n = 2.6$  for the EDE model. To bind together the matter power spectra extracted from simulations with different resolutions we adopt a splicing technique described in detail in App. C.2. Our results are summarized in Fig. 2.5, and we refer to App. C.2 for a deeper technical discussion.

In the top panel of Fig. 2.5 we compare the matter power spectra extracted from our simulations, with the ones computed with **HALOFIT** /**HMCODE**, at redshift  $z = 0$ . The blue curves refer to the  $\Lambda$ CDM scenario – dubbed hereafter as  $\Lambda$ CDM “equivalent”

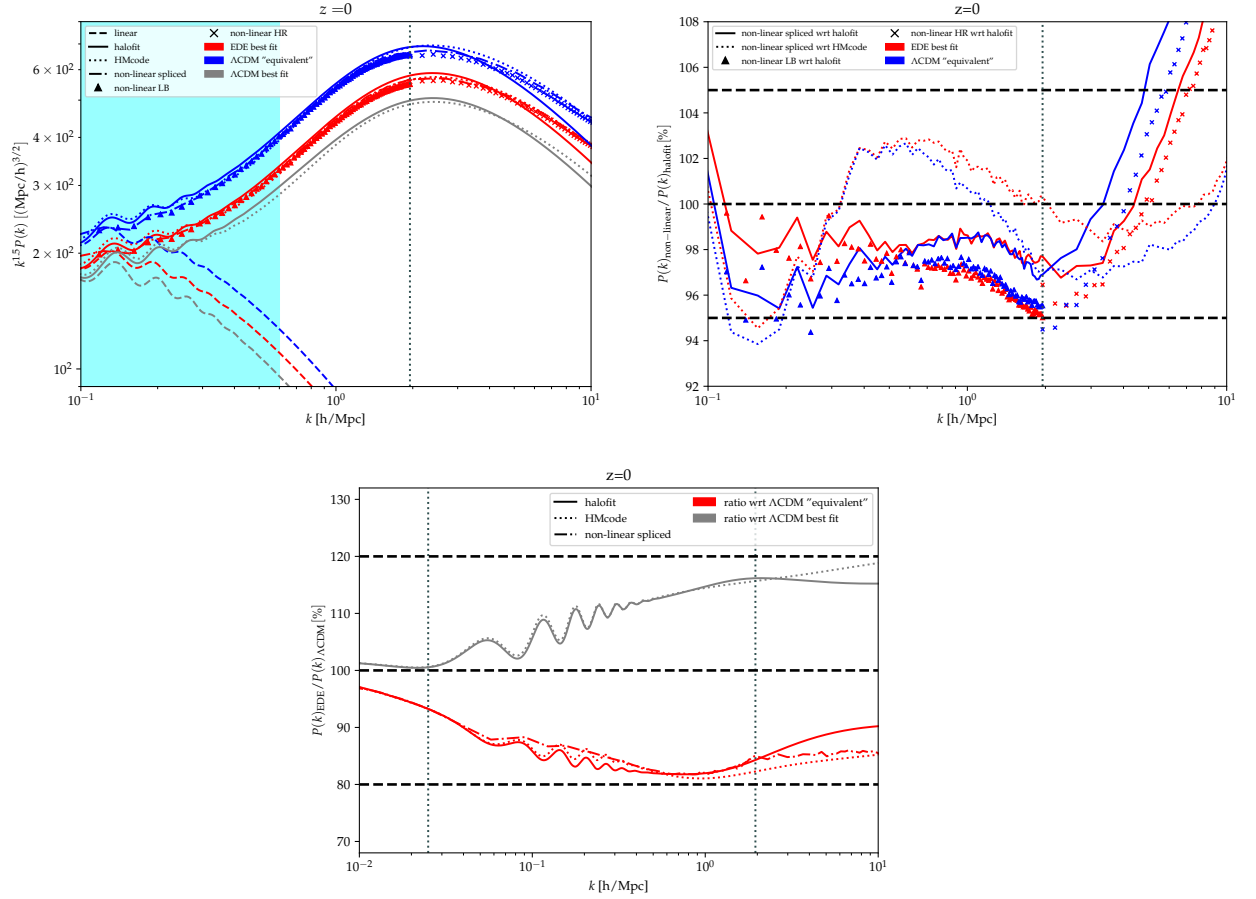


**Figure 2.5** – In the top left panel we show the matter power spectra extracted from our simulations, and the ones computed with **HALOFIT** /**HMCODE** . The blue curves refer to the  $\Lambda$ CDM scenario, while the red ones refer to the EDE best fit model. We also report the best fit  $\Lambda$ CDM case from Planck 2018. The spliced power spectra are reported as thick dot-dashed lines. Symbols stand for the outputs of the LB and HR simulations. The solid/dotted lines are the non-linear power spectra from **HALOFIT** /**HMCODE** , whereas the dashed lines are the corresponding linear power spectra used to produce the initial conditions for the simulations. The cyan shaded band roughly corresponds to the scales probed by DES-Y1. In the top right panel, we show the ratio between the non-linear matter power spectra from our simulations and the ones computed with **HALOFIT** /**HMCODE** , for both the  $\Lambda$ CDM “equivalent” and the EDE best fit models, adopting the same linestyle-code and color-code. In the bottom right panel we compare departures from the  $\Lambda$ CDM model in terms of ratios of non-linear matter power spectra, adopting the same linestyle-code and color-code.

– while the red ones refer to the EDE best fit model. As a reference, we also report the best fit  $\Lambda$ CDM case from Planck 2018. The spliced power spectra are denoted by thick dot-dashed lines. Symbols stand for the output power spectra of the “non-spliced” LB and HR simulations. The solid/dotted lines are the non-linear power spectra from **HALOFIT** /**HMCODE** , while the dashed lines are the corresponding linear power spectra used to set the initial conditions for the simulations. In the right panel, we adopt the same linestyle-code and color-code to show the ratio between the non-linear power spectra produced by **HALOFIT** /**HMCODE** with respect to the ones extracted from our simulations. The thick horizontal lines highlight  $\pm 5\%$  deviations.



In [App. C.2](#) we extend the analysis to three additional redshift bins –  $z = 0.5, 1.5, 2$  – obtaining analogous results. We can thus conclude that the differences between **HALOFIT** /**HMCODE** predictions with respect to the outputs of our  $N$ -Body simulations are below 5% level, for scales  $10^{-2} \lesssim k \lesssim 10 \text{ h/Mpc}$ , at redshifts  $0 \leq z \leq 2$ , for both  $\Lambda$ CDM and EDE models. Whereas this is a very well established result for the  $\Lambda$ CDM paradigm, this is not often the case for alternative cosmological scenarios, such as the one considered in this work. Let us note that the exponential increase in the difference between the outputs by simulations and **HALOFIT** at  $k \sim 10 \text{ h/Mpc}$  is absent when one compares the outputs from simulations with the predictions by **HMCODE**. As expected, the latter method is more accurate than **HALOFIT** in modeling the very small-scale and very low- $z$  regime. In this work, we therefore make use of **HMCODE** to model the non-linear evolution of perturbations, following the approach adopted by the KiDS collaboration.

We also present our results in terms of ratios between the matter power spectra in the EDE and the  $\Lambda$ CDM models in [Fig. 2.5](#) bottom panel. The comparison between the EDE best fit and the  $\Lambda$ CDM equivalent confirms that it is not the intrinsic presence of EDE that enhances the matter power spectrum on small scales, exacerbating the  $S_8$  tension. Rather, the EDE reduces the growth of perturbations at fixed  $\omega_{\text{cdm}}$ . As already pointed out, such power enhancement is instead due to variations in the standard  $\Lambda$ CDM parameters – mostly an increase in  $\omega_{\text{cdm}}$  – induced to balance the EDE impact on the CMB. This suggests that the limitations of the EDE are not intrinsic to its presence, but rather to an accidental degeneracy that could be alleviated in an extended model (*i.e.* by adding non-standard interactions to the dark matter sector, see [Chapter 3](#)).

In view of these considerations, it is straightforward to conclude that LSS surveys constitute an ideal counterpart to CMB data, given the complementarity between the regimes that they probe. However, in [section Sect. 2.4.3](#) we will show that currently available weak lensing data are not sensitive enough to unequivocally capture the signature of EDE. This will clearly not be the case when more precise data (e.g. from Euclid ([AMENDOLA et al. 2018](#))) will become available. As also our results suggest, it will soon be necessary to go beyond the **HALOFIT** /**HMCODE** prescription for modeling the non-linear power spectrum (see e.g. ([CHUDAYKIN et al. 2020b](#); [IVANOV et al. 2020](#); [D’AMICO et al. 2021b](#); [KLYPIN et al. 2021](#))). Furthermore, it might be already possible to test  $\mathcal{O}(20\%)$  deviations in the small-scale power, as the ones shown in the bottom panel of [Fig. 2.5](#), with current Lyman- $\alpha$  forest flux power spectrum data ([MURGIA et al. 2017, 2018](#); [ARCHIDIACONO et al. 2019](#); [MILLER et al. 2019](#); [BALDES et al. 2020](#)) and the EFT of LSS data analysis of BOSS data (see e.g. [IVANOV et al. \(2020\)](#) and [D’AMICO et al. \(2021b\)](#) for a recent analysis in the 3-parameter model). We leave these tasks for future work.

### MCMC analysis against weak lensing data

In the following, we will focus on the 1-parameter EDE cosmology, fixing  $\Theta_i$  and  $\text{Log}_{10}(z_c)$  to their best fit values from [Planck18](#) only. Firstly, we test the model against the KiDS-VIKING cosmic shear measurements. We follow the prescription described in [HILDEBRANDT et al. \(2020\)](#) and make use of the **HMCODE** algorithm ([MEAD et al. 2015](#)) (with 9 nuisance parameters) to model the non-linear matter power spectrum. Secondly, we perform an analysis trading KiDS-VIKING data for a split-normal

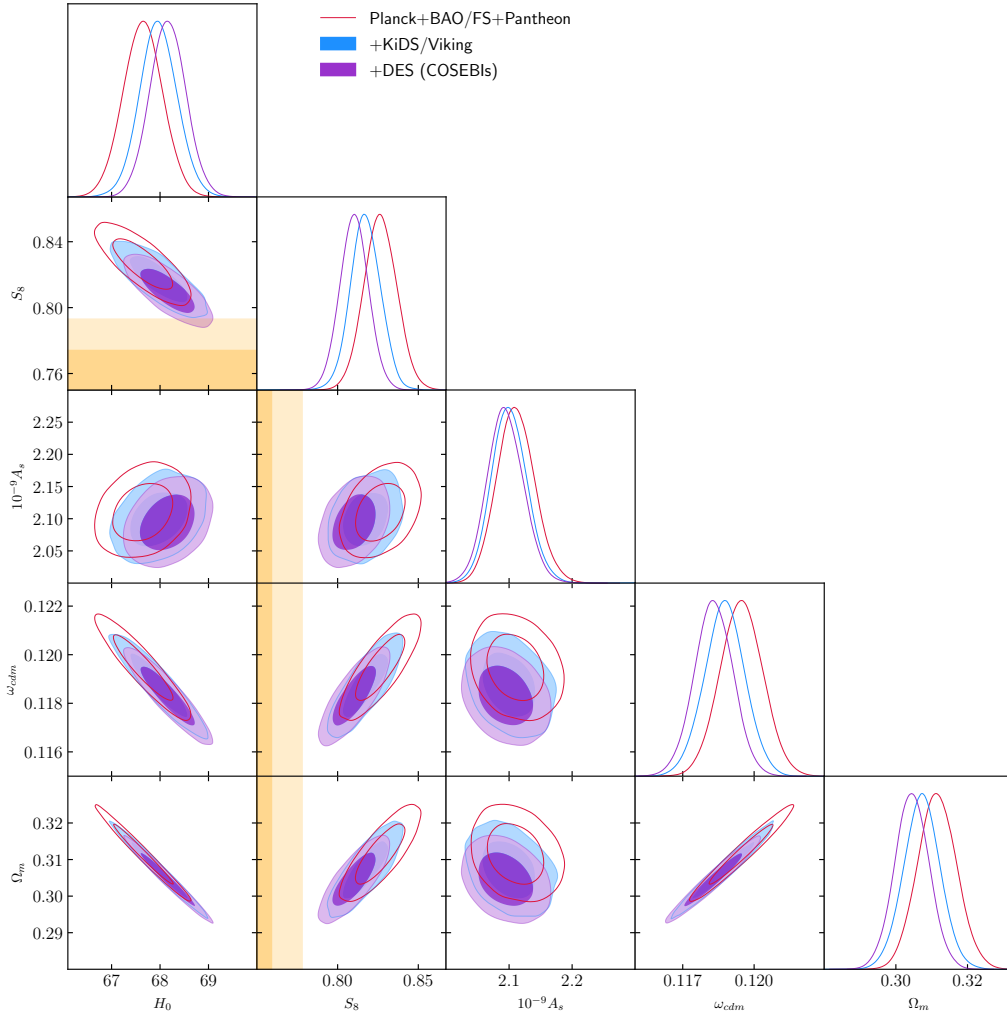


**Figure 2.6** – Reconstructed 2D posterior distributions of a subset of parameters for various data set combinations (see legend) in the  $\Lambda$ CDM cosmology.

likelihood on  $S_8$  as inferred from the joint KiDS-VIKING+DES data using Complete Orthogonal Sets of E/B-Integrals (COSEBIs), namely<sup>18</sup>  $S_8 = 0.755^{+0.019}_{-0.021}$  (ASGARI et al. 2020). We report results of MCMC analysis of  $\Lambda$ CDM and EDE against the KiDS-VIKING data and the joint KiDS-VIKING+DES data in table Tab. (2.4) and Tab. (2.5).

**Results for  $\Lambda$ CDM :** Starting with the  $\Lambda$ CDM cosmology, we find that combining Planck18 with KiDS-VIKING data leads to a mild degradation of the  $\chi^2_{\min}$  of the combined fit: While one might naively expect that the  $\chi^2_{\min}$  of the global fit should be roughly the sum of the  $\chi^2_{\min}$  of individual fits, we find that the global  $\chi^2_{\min}$  is degraded by  $\sim +6.5$ . Similarly, the inclusion of a tight Gaussian likelihood on  $S_8$  as measured by KiDS-VIKING+DES leads to a degradation in the combined  $\chi^2 \sim +15.5$ , while one expects  $\sim +1$  for a good fit. In Fig. 2.6, we show the reconstructed 2D posteriors of  $\{H_0, S_8, 10^{-9}A_s, \omega_{\text{cdm}}, \Omega_m\}$  in the  $\Lambda$ CDM model. One can see that the degradation in  $\chi^2_{\min}$  is accompanied by shifts in the mean of any parameter correlated with  $S_8$ , in

<sup>18</sup>We stress that  $S_8$  is a model-dependent quantity, and it is particularly sensitive to the treatment of the neutrino mass. We therefore make use of the value that was derived following our convention, i.e. at fixed  $\sum m_\nu = 0.06$  eV.

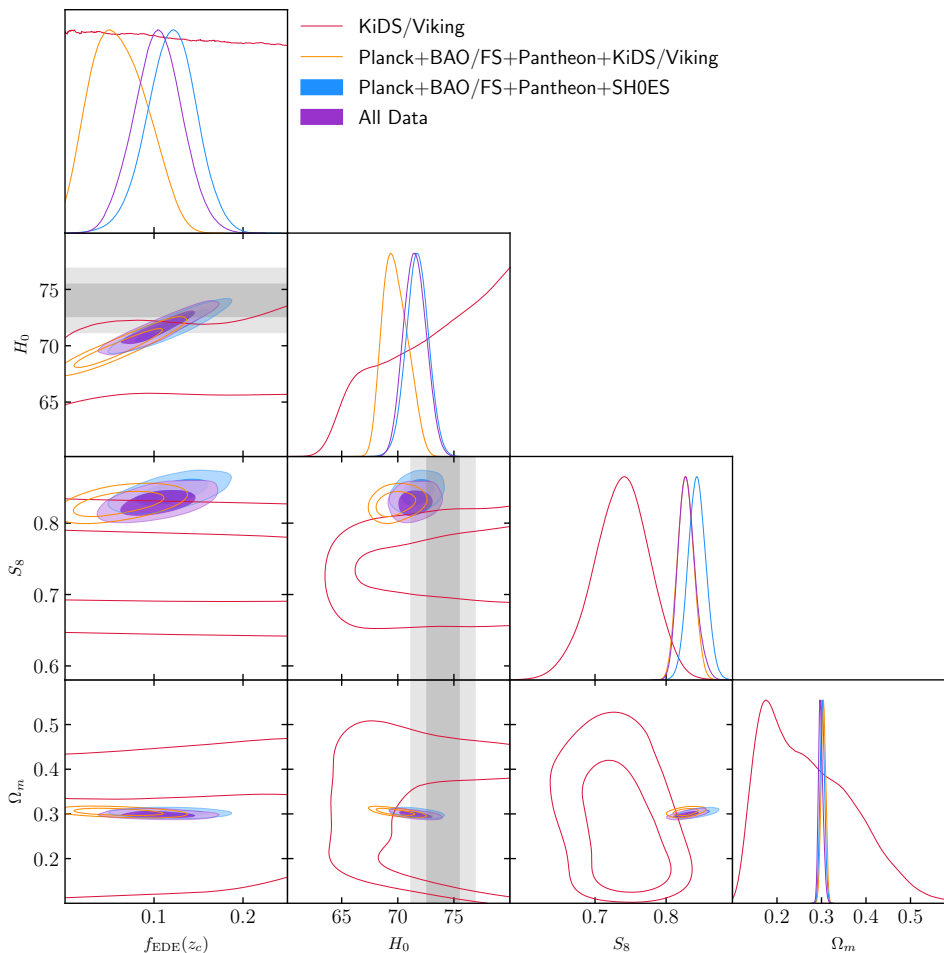


**Figure 2.7** – Reconstructed 2D posterior distributions of a subset of parameters for various data set combinations (see legend) in the 1-parameter EDE cosmology. “All data” stands for the combination Planck+BAO/FS+Pantheon+SH0ES+KiDS/Viking.

particular  $A_s$ ,  $\omega_{\text{cdm}}$  and  $H_0$ , without succeeding in getting a good fit to the WL data. We therefore stress that any of the combined results should be taken with a grain of salt, even in the  $\Lambda$ CDM framework. This joint analysis serves mostly to demonstrate that the EDE cosmology does not sensibly degrade the fit to the  $S_8$  measurement as compared to  $\Lambda$ CDM, and that currently available WL measurements do not strongly constrain the EDE resolution to the Hubble tension.

**Results for EDE against Planck+KiDS-VIKING:** In Fig. 2.7 we show the reconstructed 2D posteriors of  $\{f_{\text{EDE}}(z_c), H_0, S_8, \Omega_m\}$  in the 1-parameter EDE realization for various data combinations. We start by performing an analysis of EDE against KiDS-VIKING data only; as expected we find that the KiDS-VIKING data have no constraining power on the fraction of EDE. However, the reconstructed  $S_8 = 0.738^{+0.041}_{-0.038}$  is  $\sim 2.4\sigma$  discrepant with that obtained from previous analyses, suggesting a potential discordance between the cosmologies. For comparison, the prediction for  $S_8$  in the  $\Lambda$ CDM model obtained from Planck18 data is  $2.3\sigma$  discrepant with that from KiDS-VIKING data (HILDEBRANDT et al. 2020). Therefore, although the mean value has increased, the level of the  $S_8$  tension in the EDE cosmology is similar to that in  $\Lambda$ CDM because of larger error bars. Combining

Model Parameter	$\Lambda$ CDM		EDE	
	Base+KiDS/VIKING	+SHOES	Base+KiDS/VIKING	+SHOES
$H_0$ [km/s/Mpc]	$67.97 \pm 0.38$	$68.4 \pm 0.38$	$69.75(68.95)^{+0.99}_{-1.1}$	$71.58(72.22)^{+1}_{-0.97}$
$100 \omega_b$	$2.248(2.248) \pm 0.013$	$2.257(2.256) \pm 0.013$	$2.261(2.253)^{+0.014}_{-0.015}$	$2.277(2.282)^{+0.013}_{-0.015}$
$\omega_{\text{cdm}}$	$0.1187(0.1188) \pm 0.0009$	$0.1179(0.1180) \pm 0.0009$	$0.1245(0.1235)^{+0.0028}_{-0.0039}$	$0.1291(0.1310) \pm 0.0034$
$10^9 A_s$	$2.10(2.08) \pm 0.028$	$2.11(2.12)^{+0.03}_{-0.032}$	$2.117(2.116)^{+0.03}_{-0.033}$	$2.136(2.130)^{+0.03}_{-0.033}$
$n_s$	$0.9685(0.9667)^{+0.0038}_{-0.0036}$	$0.9708(0.9691)^{+0.0039}_{-0.0035}$	$0.9778(0.9740)^{+0.0061}_{-0.0068}$	$0.9872(0.9907)^{+0.0064}_{-0.0055}$
$\tau_{\text{reio}}$	$0.0556(0.0520)^{+0.0069}_{-0.0066}$	$0.0585(0.0589)^{+0.0074}_{-0.0075}$	$0.0547(0.0559)^{+0.0067}_{-0.0074}$	$0.0552(0.0536)^{+0.0068}_{-0.0073}$
$f_{\text{EDE}}(z_c)$	–	–	$0.058(0.042)^{+0.028}_{-0.034}$	$0.104(0.122)^{+0.029}_{-0.025}$
$100 \theta_s$	$1.04198(1.04165) \pm 0.00028$	$1.04207(1.04210) \pm 0.00028$	$1.04165(1.04181)^{+0.00035}_{-0.00032}$	$1.04146(1.04130)^{+0.00031}_{-0.00034}$
$S_8$	$0.8172(0.8137)^{+0.009}_{-0.0096}$	$0.8092(0.8094)^{+0.0091}_{-0.0098}$	$0.826(0.831) \pm 0.011$	$0.829(0.828)^{+0.012}_{-0.011}$
$\Omega_m$	$0.307(0.309) \pm 0.005$	$0.302(0.302) \pm 0.005$	$0.3037(0.3085)^{+0.0054}_{-0.0055}$	$0.2976(0.2962)^{+0.005}_{-0.0051}$
$\chi^2_{\text{min}}$	3996.82	4011.16	3992.11	3997.67

**Table 2.4** – The mean (best-fit)  $\pm 1\sigma$  error of the cosmological parameters reconstructed from the combined analysis of KiDS/Viking with other data. The ‘Base’ dataset refers to Planck18+BAO/FS+PANTHEON. We also report the  $\chi^2_{\text{min}}$  for each model and data set combination.

Model Parameter	$\Lambda$ CDM		EDE	
	Base+KiDS/VIKING/DES	+SHOES	Base+KiDS/VIKING/DES	+SHOES
$H_0$ [km/s/Mpc]	$68.16(68.15) \pm 0.38$	$68.56(68.69)^{+0.38}_{-0.39}$	$69.56(69.55)^{+0.72}_{-1.2}$	$71.29(71.81)^{+0.94}_{-0.94}$
$100 \omega_b$	$2.251(2.253) \pm 0.013$	$2.26(2.263)^{+0.013}_{-0.014}$	$2.262(2.270)^{+0.014}_{-0.015}$	$2.278(2.288) \pm 0.014$
$\omega_{\text{cdm}}$	$0.1183(0.1183)^{+0.00084}_{-0.00082}$	$0.1175(0.1172)^{+0.00085}_{-0.00083}$	$0.1223(0.1199)^{+0.002}_{-0.0036}$	$0.1264(0.1270)^{+0.003}_{-0.0032}$
$10^9 A_s$	$2.094(2.091)^{+0.029}_{-0.03}$	$2.104(2.115)^{+0.029}_{-0.032}$	$3.046(2.107)^{+0.014}_{-0.015}$	$2.121(2.117) \pm 0.031$
$n_s$	$0.9691(0.9705) \pm 0.0037$	$0.9712(0.9731) \pm 0.0037$	$0.9765(0.9782)^{+0.0051}_{-0.0065}$	$0.9854(0.9892)^{+0.0055}_{-0.0057}$
$\tau_{\text{reio}}$	$0.0546(0.0538)^{+0.0069}_{-0.0073}$	$0.0576(0.0602)^{+0.0069}_{-0.0077}$	$0.05339(0.0559)^{+0.0071}_{-0.0072}$	$0.05441(0.05254)^{+0.007}_{-0.0072}$
$f_{\text{EDE}}(z_c)$	–	–	$< 0.094(0.029)$	$0.087(0.097)^{+0.029}_{-0.024}$
$100 \theta_s$	$1.04198(1.04195)^{+0.00028}_{-0.00029}$	$1.04207(1.04209)^{+0.00028}_{-0.00029}$	$1.04178(1.04190)^{+0.00032}_{-0.00031}$	$1.04157(1.04149)^{+0.00033}_{-0.00032}$
$S_8$	$0.8043(0.8102)^{+0.0055}_{-0.0057}$	$0.8039(0.8023)^{+0.0056}_{-0.0058}$	$0.8145(0.8036)^{+0.0098}_{-0.01}$	$0.817(0.812)^{+0.01}_{-0.011}$
$\Omega_m$	$0.3045(0.3046)^{+0.0048}_{-0.005}$	$0.2994(0.2978) \pm 0.0049$	$0.3008(0.2961)^{+0.0054}_{-0.0053}$	$0.2949(0.2919)^{+0.0047}_{-0.005}$
$\chi^2_{\text{min}}$	3821.93	3837.98	3820.46	3826.35

**Table 2.5** – The mean (best-fit)  $\pm 1\sigma$  error of the cosmological parameters reconstructed from the combined analysis of the KiDS/Viking/DES data with other data discussed in the text, with and without a prior on  $H_0$  from SHOES. The ‘Base’ dataset refers to Planck18+BAO/FS+PANTHEON. We also report the  $\chi^2_{\text{min}}$  for each model and data set combination.

KiDS-VIKING to Planck18+BAO+PANTHEON+FS, a non-zero EDE contribution is still favored at  $\sim 1.5\sigma$ , but the reconstructed mean fraction has moved downwards by  $\sim 0.7\sigma$ . This was expected, given the positive correlation between  $f_{\text{EDE}}(z_c)$  and  $S_8$ . In this cosmology, Planck18 data are still slightly better fitted ( $\Delta\chi^2_{\text{min}} \sim -6$ ) than in  $\Lambda$ CDM, while the fit to KiDS-VIKING data is degraded by  $\sim +2$ . Once a prior on  $H_0$  from SHOES is added, we find again  $f_{\text{EDE}}(z_c) \sim 10 \pm 3\%$ , at the cost of increasing the total  $\chi^2_{\text{min}} \sim +5.5$ . The increase in  $\chi^2$  is partly due to the inclusion of SHOES ( $\chi^2 \sim 1.62$ , a reasonably good fit), and also to a mild degradation in the fit to Planck18 ( $\sim +3$ ) and BAO ( $\sim +1.6$ ). The reason is that the inclusion of KiDS-VIKING data reduces the degeneracy between  $f_{\text{EDE}}(z_c)$  and the  $\Lambda$ CDM parameters, in particular the one with  $\omega_{\text{cdm}}$ . Note that the goodness of Planck18 fit is not sensibly degraded as compared to  $\Lambda$ CDM, since the  $\chi^2$  stays better than that from  $\Lambda$ CDM fitted on Planck18 only. In fact, when compared to  $\Lambda$ CDM, the combined  $\chi^2$  is improved by  $\sim -13$  (for one extra parameter), indicating a significant preference for EDE despite the presence of KiDS-VIKING data. Looking at the individual  $\chi^2_{\text{min}}$ , we find indeed that the quality of the fit to KiDS-VIKING data in the EDE cosmology that resolves the Hubble tension is barely changed ( $\Delta\chi^2 \sim +1.6$  for 195 data points (HILDEBRANDT et al. 2020)) compared to the  $\Lambda$ CDM fit to the same data set.

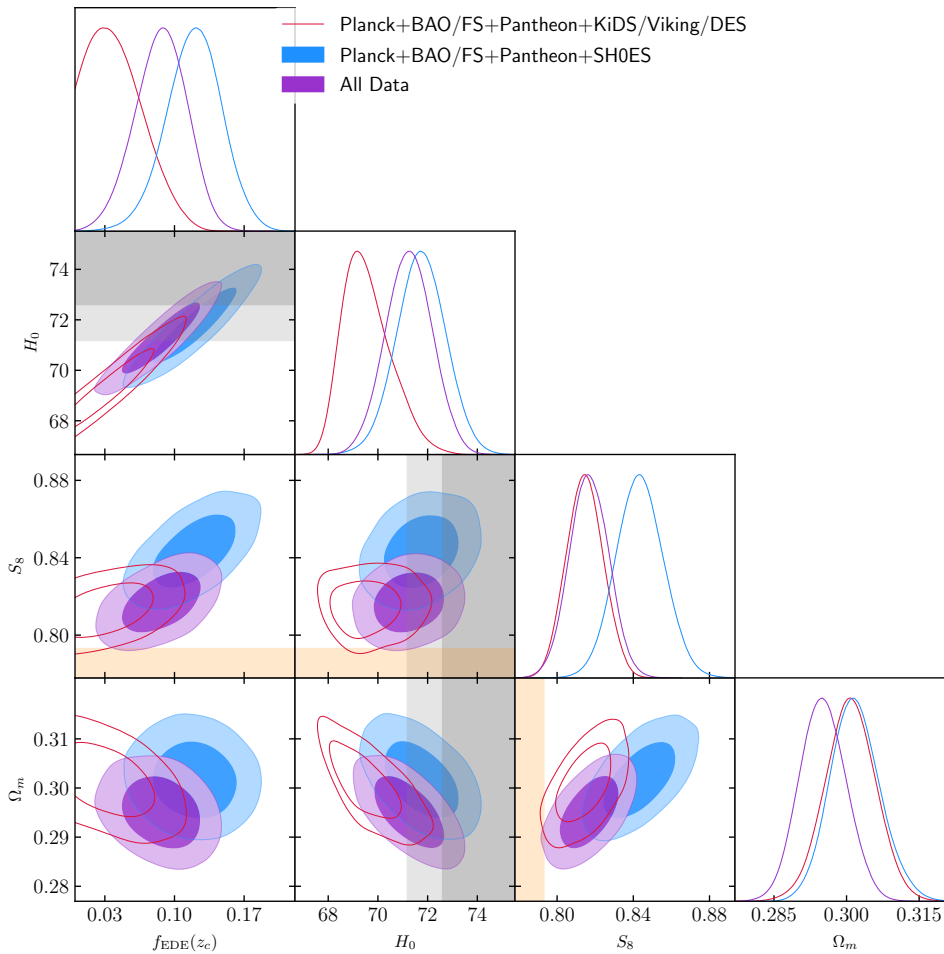


**Figure 2.8** – Reconstructed 2D posterior distributions of a subset of parameters for various data set combinations (see legend) in the 1-parameter EDE cosmology. “All data” stands for the combination Planck+BAO/FS+Pantheon+SH0ES+KiDS/Viking/DES.

**Results for EDE against Planck+KIDS+DES:** We now trade KIDS-VIKING data for a split-normal likelihood on  $S_8$  as inferred from the joint KIDS-VIKING+DES data. We note that the tension between the value of this joint  $S_8$  measurement and that predicted by our fiducial EDE model (obtained from the global fit of Planck18+BAO+FS+PANTHEON+SH0ES) is at the  $\sim 3.8\sigma$  level (slightly increased from  $3.2\sigma$  tension in  $\Lambda$ CDM). It would be interesting to quantify the level of tension between these data sets in the  $\Lambda$ CDM framework using more robust statistical tools than the ‘difference in the mean’ used here, as done for instance in HANDLEY et al. (2019) and RAVERI et al. (2019). However, we note that authors from RAVERI et al. (2019) found that the less precise KIDS-VIKING data available at that time were already in significant statistical disagreement with the prediction from  $\Lambda$ CDM. We anticipate that this more robust approach would strengthen the case for a statistically significant discrepancy, even in  $\Lambda$ CDM, and therefore the need to apply caution when drawing conclusions from the combined analyses. We show the reconstructed 2D posteriors of  $\{f_{\text{EDE}}(z_c), H_0, S_8, \Omega_m\}$  in the 1-parameter EDE model in Fig. 2.8.

Without the SH0ES prior,  $f_{\text{EDE}}(z_c)$  is compatible with 0 at  $1\sigma$ , and we find an upper limit on  $f_{\text{EDE}}(z_c) < 0.094$  at 95% C.L. This constraint is significantly weaker than that derived in HILL et al. (2020), despite the fact that we have *reduced* the parameter



Model Parameter	$\Lambda$ CDM		EDE	
	PLANCK <sup>TTTEEE</sup> +PLANCK <sup><math>\phi\phi</math></sup>	All Data	PLANCK <sup>TTTEEE</sup> +PLANCK <sup><math>\phi\phi</math></sup>	All Data
$H_0$ [km/s/Mpc]	68.44(68.66) <sup>+0.74</sup> <sub>-0.72</sub>	69.16(69.37) $\pm$ 0.41	71.17(72.18) <sup>+1.4</sup> <sub>-1.6</sub>	71.64(72.07) <sup>+0.94</sup> <sub>-1</sub>
100 $\omega_b$	2.262(2.269) $\pm$ 0.018	2.277(2.284) $\pm$ 0.014	2.284(2.292) $\pm$ 0.02	2.292(2.294) $\pm$ 0.015
$\omega_{\text{cdm}}$	0.1179(0.1174) $\pm$ 0.0016	0.1164(0.1159) $\pm$ 0.00087	0.1253(0.1286) <sup>+0.0037</sup> <sub>-0.0045</sub>	0.1248(0.1255) <sup>+0.003</sup> <sub>-0.0033</sub>
10 <sup>9</sup> $A_s$	2.069(2.071) <sup>+0.038</sup> <sub>-0.035</sub>	2.048(2.053) <sup>+0.039</sup> <sub>-0.032</sub>	2.101(2.122) $\pm$ 0.041	2.064(2.066) <sup>+0.047</sup> <sub>-0.033</sub>
$n_s$	0.9718(0.9730) $\pm$ 0.005	0.9755(0.9786) $\pm$ 0.0037	0.9862(0.9925) <sup>+0.008</sup> <sub>-0.0088</sub>	0.9884(0.9925) <sup>+0.0059</sup> <sub>-0.0056</sub>
$\tau_{\text{reio}}$	0.0494(0.0506) <sup>+0.0089</sup> <sub>-0.0079</sub>	0.0464(0.0480) <sup>+0.0093</sup> <sub>-0.0074</sub>	0.0507(0.0529) <sup>+0.0087</sup> <sub>-0.008</sub>	0.0429(0.0431) <sup>+0.012</sup> <sub>-0.0071</sub>
$A_1^{\phi\phi}$	1.071(1.075) <sup>+0.04</sup> <sub>-0.043</sub>	1.104(1.110) <sup>+0.034</sup> <sub>-0.038</sub>	1.064(1.056) <sup>+0.04</sup> <sub>-0.043</sub>	1.093(1.099) <sup>+0.035</sup> <sub>-0.039</sub>
$A_{\text{lens}}^{\text{TTTEEE}}$	1.195(1.208) <sup>+0.066</sup> <sub>-0.07</sub>	1.247(1.266) <sup>+0.06</sup> <sub>-0.066</sub>	1.187(1.188) <sup>+0.065</sup> <sub>-0.07</sub>	1.222(1.238) <sup>+0.061</sup> <sub>-0.067</sub>
$f_{\text{EDE}}(z_c)$	–	–	0.078(0.108) <sup>+0.035</sup> <sub>-0.038</sub>	0.082(0.092) $\pm$ 0.027
100 $\theta_s$	1.04205(1.04207) $\pm$ 0.00031	1.04215(1.04214) $\pm$ 0.00029	1.04165(1.04343) <sup>+0.00036</sup> <sub>-0.00035</sub>	1.04165(1.04164) $\pm$ 0.00034
$S_8$	0.800(0.795) <sup>+0.019</sup> <sub>-0.02</sub>	0.780(0.776) $\pm$ 0.011	0.801(0.812) $\pm$ 0.02	0.794(0.793) $\pm$ 0.013
$\Omega_m$	0.302(0.297) <sup>+0.009</sup> <sub>-0.01</sub>	0.2924(0.2883) <sup>+0.0049</sup> <sub>-0.0051</sub>	0.2938(0.2870) <sup>+0.0095</sup> <sub>-0.01</sub>	0.2891(0.2870) $\pm$ 0.0052
$\chi_{\text{min}}^2$ ( $\Lambda$ CDM)	2765.98	3816.23	2761.98	3808.40

**Table 2.6** – The mean (best-fit)  $\pm 1\sigma$  error of the cosmological parameters reconstructed from the lensing-marginalized [Planck18](#) data only and in combination with BAO/FS+PANTHEON+KIDS-VIKING-DES. We also report the  $\chi_{\text{min}}^2$  for each model and data set combination.

space. We have simply adopted a different ‘prior’ choice on  $\Theta_i$  and  $\text{Log}_{10}(z_c)$  (i.e. here we fix them), demonstrating that the current constraints from WL – besides being derived from statistically inconsistent data set <sup>19</sup> – are not robust. Looking at  $\chi_{\text{min}}^2$ , we find that the resulting best fit cosmology degrades the fit to Planck by  $\sim +6$  while providing a poor fit to the  $S_8$  likelihood ( $\chi^2 = 8.3$  for a single data point). Still, the best-fit is marginally better than that of  $\Lambda$ CDM adjusted on the same sets of data ( $\Delta\chi_{\text{min}}^2 \sim -1.5$ ). Once we include the SHOES prior, we find again  $f_{\text{EDE}}(z_c)$  to be non-zero at more than  $3\sigma$ ,  $f_{\text{EDE}}(z_c) \simeq 9 \pm 3\%$ , with a global  $\Delta\chi_{\text{min}}^2 \simeq -11.6$ . Looking at individual  $\chi_{\text{min}}^2$ , we find that the fit to PLANCK<sup>TTTEEE</sup>, PLANCK <sup>$\phi\phi$</sup> , BAO and FS data is somewhat degraded compared to the best fit EDE cosmology obtained without  $S_8$  prior, as a consequence of the breaking of the  $f_{\text{EDE}}(z_c) - \omega_{\text{cdm}}$  degeneracy. However, as expected, we note that the  $S_8$  likelihood has a  $\chi^2 \simeq 9$ , which is not particularly worst than the one obtained in the  $\Lambda$ CDM case without SHOES ( $\chi^2 \simeq 8.3$ ). This indicates that any constraint on the EDE derived from this combined analysis should be regarded with caution, as the cosmology reconstructed from the analysis does not provide a good fit to the  $S_8$  data. This naturally impacts the reconstructed  $H_0$ , which is  $\sim 0.6\sigma$  lower than without the  $S_8$  likelihood, although the fit to SHOES is still reasonably good ( $\chi^2 \simeq 2.4$ ). We therefore conclude that current  $S_8$  measurements do not exclude the EDE resolution to the Hubble tension; however, they do call for new physics beyond EDE – or unknown systematics – to explain the intriguingly low measured  $S_8$  values.

#### 2.4.4 EDE and the $S_8$ tension in light of the $A_{\text{lens}}$ anomaly

It has been noted that there exists a number of ‘curiosities’ in [Planck18](#) that can potentially shed light on cosmological tensions. In particular, there is a residual oscillatory feature in the [Planck18](#) TT data at  $1100 \lesssim \ell \lesssim 2000$  compared to the best fit  $\Lambda$ CDM prediction ([AGHANIM et al. 2017, 2020b](#)). This feature can be captured by an extra source of smoothing of the acoustic peaks, as modelled by the ‘ $A_{\text{lens}}^{\phi\phi}$ ’

<sup>19</sup>Since P18 –  $\Lambda$ CDM provides an even worse fit to SHOES data, one could argue that Planck and SHOES are also statistically inconsistent. However, we remind that the notion of “statistically inconsistent datasets” is generally model-dependent (specially when including CMB or other early-universe data), and in fact P18 – EDE gives a very good fit to SHOES. This latter point is only evident when looking at the long tails of the EDE posteriors, so to properly quantify the agreement with SHOES one should consider metrics that generalize the standard Gaussian Tension estimators, as we do in [Sect. 2.5.2](#).



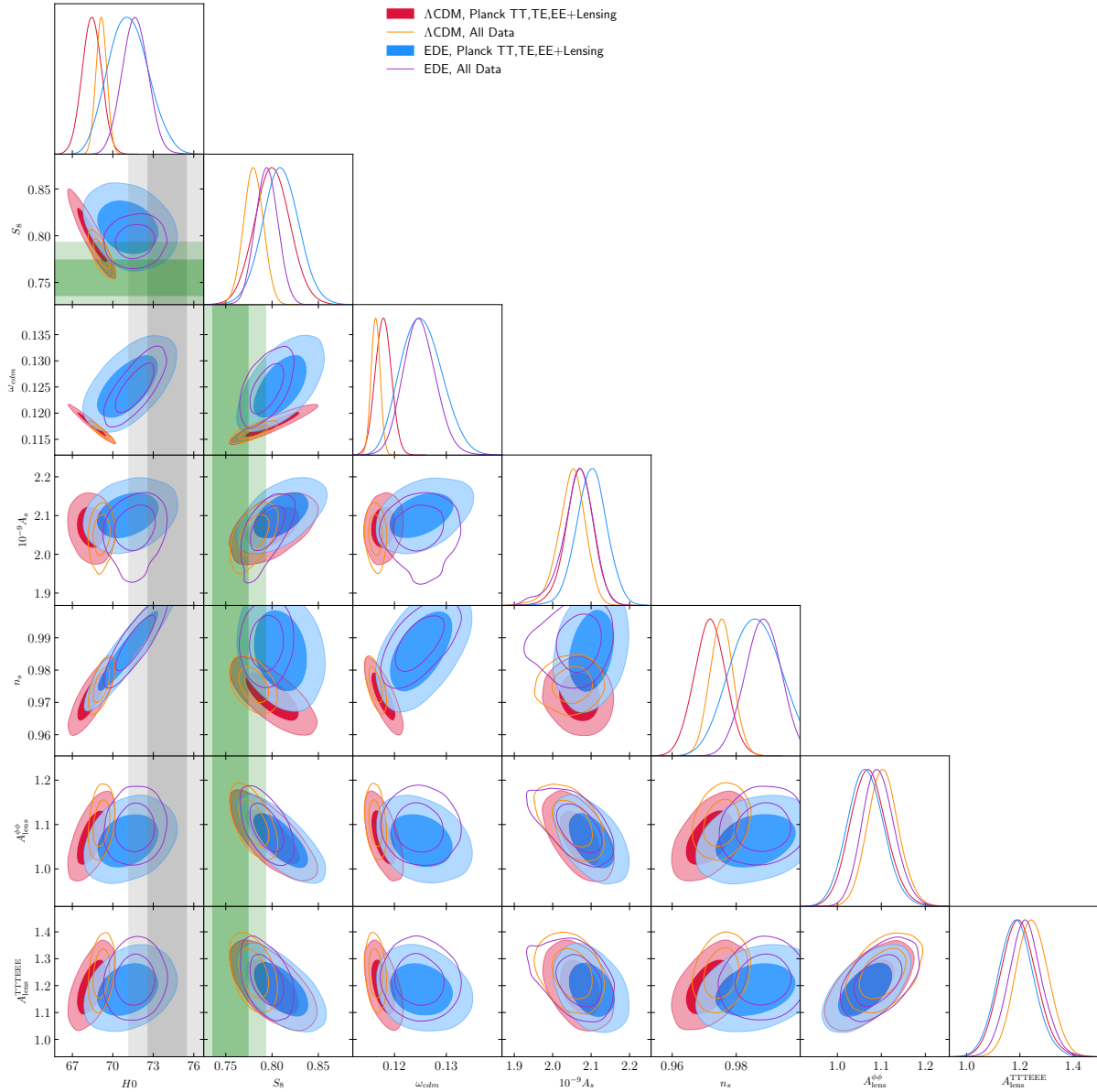


**Figure 2.9** – Reconstructed 1- and 2D-posteriors of a subset of parameters in the  $\Lambda$ CDM and 1-parameter EDE cosmology for various data sets (see legend), once marginalizing over  $A_{\text{lens}}$  and  $A_{\text{lens}}^{\phi\phi}$

parameter which is used to re-scale the amplitude of the lensing potential power spectrum  $C_{\ell}^{\phi\phi} \rightarrow A_{\text{lens}}^{\phi\phi} C_{\ell}^{\phi\phi}$ , at every point in parameter space. However, the amplitude of the lensing potential power spectrum can also be estimated directly from the lensing-reconstruction and is compatible with the  $\Lambda$ CDM expectation, such that while this extra smoothing looks like lensing, it cannot be attributed to actual gravitational lensing. A thorough investigation of the lensing-like tensions in the Planck legacy release was performed in AGHANIM et al. (2017) and MOTLOCH et al. (2018, 2020). It has been noted in particular that, once marginalizing over the lensing information, the ‘unlensed’ CMB temperature and polarization power spectra favor a cosmology with a lower  $A_s$  and  $\Omega_{\text{cdm}} h^2$ . Indeed, these parameters are strongly correlated with the amplitude of the lensing power spectrum, such that the lensing-like anomaly pulls these parameters up. Additionally, since the acoustic feature of the CMB tightly

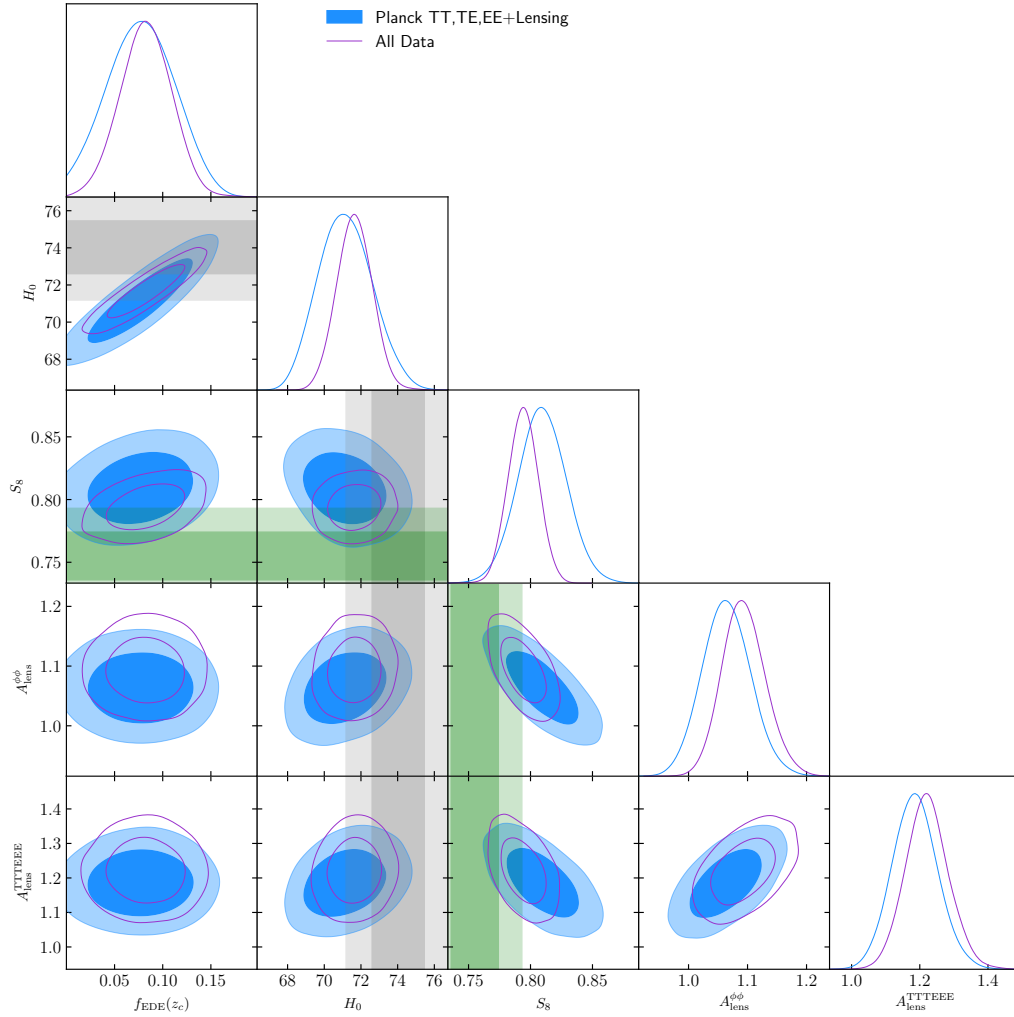


**Figure 2.10** – Reconstructed 1- and 2D-posterior of a subset of parameters in the 1-parameter EDE cosmology for various data sets (see legend), once marginalizing over  $A_{\text{lens}}$  and  $A_{\text{lens}}^{\phi\phi}$ .

constraints the parameter combination  $\Omega_m h^3$ , a lower  $\Omega_{\text{cdm}} h^2$  is compensated by a higher  $H_0$ . As a consequence, the unlensed  $\Lambda$ CDM cosmology shows no  $S_8$  tension, and a milder (although still  $> 3.5\sigma$  significant)  $H_0$  tension. It was also pointed out that this ‘unlensed’ cosmology is in good agreement with the  $\Lambda$ CDM cosmology reconstructed from the SPTPol data (HENNING et al. 2018; CHUDAYKIN et al. 2020a).

It is therefore reasonable to ask what is the impact of such anomalies on extensions to  $\Lambda$ CDM like the EDE under study. To that end, we introduce two additional parameters  $A_{\text{lens}}$  and  $A_{\text{lens}}^{\phi\phi}$  whose goal is to marginalize over the lensing information in Planck<sup>20</sup>. The latter parameter re-scales the amplitude of the theory lensing potential power spectrum, while the former only re-scales the amplitude of the acoustic peak smoothing. In practice, the amplitude of the acoustic peak smoothing is then determined by the product  $A_{\text{lens}}^{\text{TTTTEEE}} \equiv A_{\text{lens}} \times A_{\text{lens}}^{\phi\phi}$ . We first perform MCMC analysis of the  $\Lambda$ CDM and EDE cosmologies against Planck18 data. In a

<sup>20</sup>An alternative, more thorough, way is to use CMB lensing principal components as introduced in MOTLOCH et al. (2018, 2020). As we will show shortly, our reconstructed ‘unlensed’ cosmologies are in good agreement. Our approach follows that introduced in SIMARD et al. (2018) and WU et al. (2019).

second step, we perform a global analysis combining all the data considered in this work. As before, the joint KiDS-VIKING+DES results is modeled via a split-normal likelihood distribution on  $S_8$ . The results of these analysis are reported in Tab. (2.6) and shown in Fig. 2.9 and Fig. 2.10 .

**Results for  $\Lambda$ CDM:** We start by analyzing the  $\Lambda$ CDM cosmology in light of the ‘unlensed’ Planck spectra. We confirm the results of AGHANIM et al. (2020b) and MOTLOCH et al. (2020): we find that the amount of lensing determined from the peak smoothing  $A_{\text{lens}}^{\text{TTTTTEE}}$  is  $\sim 2.8\sigma$  higher than the expectation from the  $\Lambda$ CDM model deduced from the ‘unlensed’ CMB power spectrum. Moreover, the difference between the reconstructed  $A_{\text{lens}}^{\phi\phi} \simeq 1.07 \pm 0.04$  and  $A_{\text{lens}}^{\text{TTTTTEE}} \simeq 1.2 \pm 0.07$  illustrates the fact that this extra smoothing component cannot be due to actual gravitational lensing. Still, this  $\Lambda$ CDM ‘unlensed’ cosmology is now in much better agreement with the  $S_8$  measurements from KiDS and DES, as can be seen in Fig. 2.9. This is due to the fact that the reconstructed  $A_s$  and  $\omega_{\text{cdm}}$  are lower than in the analysis including lensing information. We then perform a global analysis, including all data sets considered in this work. We find that the ‘unlensed’  $\Lambda$ CDM cosmology can indeed accommodate a low  $S_8$ , however this is at the cost of worsening somewhat the fit to BAO+FS data ( $\Delta\chi^2 \simeq +3.5$ ), when compared to the ‘concordance’  $\Lambda$ CDM model obtained from a fit to the full Planck data, BAO and FS (without  $S_8$  priors). Additionally, we note that accommodating such a low  $S_8$  requires a somewhat smaller  $\omega_{\text{cdm}}$  and  $A_s$  (by a little less than  $1\sigma$ ), which are compensated for by pulling up the  $A_{\text{lens}}^{\phi\phi}$  and  $A_{\text{lens}}^{\text{TTTTTEE}}$  by a similar amount. The fit to SHOES on the other hand is still very poor,  $\chi_{\text{min}}^2 \simeq 10$ , suggesting that the global unlensed cosmology is still in strong tension with SHOES.

**Results for EDE:** Turning now to the 1-parameter EDE model, we wish to check whether the EDE cosmology deduced from ‘unlensed’ Planck18 spectra only is in better agreement with both  $S_8$  and  $H_0$  direct measurements <sup>21</sup>. As one can see from Fig. 2.10, the lensing-marginalized CMB data does favor non-zero  $f_{\text{EDE}}(z_c)$  at  $\sim 2\sigma$  ( $\Delta\chi_{\text{min}}^2 \simeq -4$  with respect to  $\Lambda$ CDM) and predicts  $H_0 \simeq 71.2 \pm 1.5$  and  $S_8 \simeq 0.81 \pm 0.02$ . Compared to the EDE cosmology reconstructed from the full Planck data, the ‘tension’ with  $H_0$  and  $S_8$  has therefore decreased by  $\sim 1\sigma$  due to a shift in the mean of the reconstructed posterior in the unlensed cosmology. It is now in  $1.4\sigma$  agreement with SHOES but stays in mild ( $\sim 2.7\sigma$ ) tension with the combined  $S_8$  measurement. The  $S_8$  prediction is however in very good agreement with the KiDS-VIKING and DES measurements when considered individually (an important note since the combined low  $S_8$  value relies on a re-calibration of DES’photo-metric redshift by the KiDS-VIKING team). Additionally, the  $A_{\text{lens}}^{\phi\phi}$  and  $A_{\text{lens}}^{\text{TTTTTEE}}$  parameters are unchanged with respect to that reconstructed in the  $\Lambda$ CDM cosmology. Therefore, while the anomalous amount of lensing in Planck18 data is not an effect due to the presence of the EDE, these parameters do not correlate with a non-zero  $f_{\text{EDE}}(z_c)$ , i.e., they do not take values different from the  $\Lambda$ CDM ones to ‘hide’ the effect of the EDE.

Once all data sets are included in the analysis, a non-zero fraction of EDE is favored at  $\sim 3.5\sigma$ . Interestingly, most of the reconstructed parameters do not shift by more than  $\sim 0.5\sigma$ ; rather, the uncertainty on the reconstructed parameters tighten significantly, as one would expect from making use of additional data. However,

<sup>21</sup>A similar study was performed in MOTLOCH et al. (2020) for  $N_{\text{eff}}$ . There, it was found that polarization and BAO data exclude  $N_{\text{eff}}$  as a resolution to the Hubble tension, even after marginalizing over the lensing anomaly in Planck18.

similarly to what happens in the  $\Lambda$ CDM cosmology, the inclusion of the tight-and-low  $S_8$  value does force a slightly ( $\sim 1\sigma$ ) smaller  $A_s$ , that is compensated by slightly higher  $A_{\text{lens}}^{\phi\phi}$  and  $A_{\text{lens}}^{\text{TTTTTEE}}$  parameters. The fit to SHOES is good ( $\chi^2 \sim 1.9$ ) and stable when compared to that obtained including Planck lensing information. On the other hand, as expected, the fit to the joint KiDS-VIKING+DES  $S_8$  is better than in the ‘lensed’ cosmology ( $\Delta\chi^2 \sim -4.3$ ), but its value is still somewhat poor ( $\chi^2 \sim 4$ ). We emphasize again that the fit to individual  $S_8$  measurements, on the other hand, is excellent. If future  $S_8$  measurements stay low while becoming more precise, they will be in tension even with the ‘unlensed’ cosmology (whether  $\Lambda$ CDM or EDE), confirming the need for new physics beyond EDE (or an unknown systematic effect).

## 2.5 EDE in the context of other proposed solutions

We have seen that EDE provides an excellent fit to Planck and SHOES data, even when LSS data is considered in the analysis. However, there are hundreds of solutions beyond the  $\Lambda$ CDM framework that have been proposed in the recent years, so it is fair to ask whether these models perform worse, better or equally good than EDE in explaining the  $H_0$  discrepancy. Hence, in the second part of this Chapter, we seek to ascertain the relative success of various cosmological models proposed to solve the  $H_0$  tension. We do this by systematically confronting each of the considered models to data from the early and late Universe, assessing at each point the extent to which the tension between the Planck and local measurements remains. This allows a direct comparing between EDE and other proposed solutions, but the broader intent is really to better understand the successes and drawbacks of each approach, and to generate a meaningful set of benchmarks for future proposals.

### 2.5.1 Brief overview of competitors

We have considered seventeen different models which are intended to be representative of the wide variety of models presented in the literature, such as those listed in [DI VALENTINO et al. \(2021b\)](#). For clarity, we split the models in three different categories: early Universe models that invoke extra relativistic dark relics (in addition to other ingredients), alternative early Universe models that do not involve dark radiation, and finally, models modifying the cosmological expansion at late times (*i.e.* well after recombination). Below we list all the models that we have considered.

#### Dark Radiation solutions

- Free-streaming Dark Radiation [ $\Delta N_{\text{ur}}$ ].
- Self-Interacting Dark Radiation [SIDR].
- Free-streaming plus self-interacting Dark Radiation [mixed DR], ([BRUST et al. 2017](#); [BLINOV et al. 2020b](#)).
- Self-interacting Dark Radiation scattering on Dark Matter [DR-DM], ([LESGOURGUES et al. 2016](#); [BUEN-ABAD et al. 2018](#); [ARCHIDIACONO et al. 2019](#)).
- Self-interacting neutrinos plus free-streaming Dark Radiation [SI $\nu$ +DR], ([PARK et al. 2019](#); [KREISCH et al. 2020](#)).

- Interacting neutrinos with a Majoron [Majoron],  
([ESCUDERO et al. 2020a, 2021](#)).

Let us emphasize that it has been shown in many different studies (*e.g.* [BERNAL et al. \(2016\)](#), [POULIN et al. \(2019\)](#), and [DI VALENTINO et al. \(2020a\)](#)) that  $\Delta N_{\text{eff}}$  fails at resolving the Hubble tension. Thus, rather than a real competitor, we will treat it as a useful benchmark model, in order to assess the extent to which the additional complexity introduced by other models really helps for relieving the Hubble tension. Remark also that the SIDR model is very similar to the  $\Delta N_{\text{ur}}$  model, except that the anisotropic stress vanishes,  $\sigma_{\text{dr}} = 0$ , in order to reflect the fact that the dark radiation behaves as a perfect fluid due to the strong self-interactions.

### Other early Universe solutions

- primordial magnetic field [primordial B],  
([JEDAMZIK et al. 2011, 2020](#)).
- varying effective electron mass [varying  $m_e$ ],  
([HART et al. 2018, 2020](#)).
- varying effective electron mass in a curved universe [varying  $m_e + \Omega_k$ ],  
([SEKIGUCHI et al. 2021](#); [SOLOMON et al. 2022](#)).
- Early Dark Energy [EDE].  
This is the model introduced in [Sect. 2.3](#) of this Chapter.
- New Early Dark Energy [NEDE],  
([NIEDERMANN et al. 2020, 2021a](#)).
- Early Modified Gravity [EMG],  
([BRAGLIA et al. 2021](#)).

We note that, in order to decrease the sound horizon at recombination  $r_s(z_{\text{rec}})$ , the first three models in this category increase the recombination redshift  $z_{\text{rec}}$ , while the last three models change the expansion rate  $H(z)/H_0$  near recombination. The combination varying  $m_e + \Omega_k$  might appear surprising (since curvature has an entirely disjoint cosmological effect to that of a varying electron mass), but it is mainly included because it produces a strong shift in  $H_0$ . The reason for this degeneracy is further explained in [SEKIGUCHI et al. \(2021\)](#). We have verified explicitly that this is a peculiar degeneracy that uniquely appears in this model – allowing curvature to float in other models seems to have no significant impact.

### Late Universe solutions

- Late Dark Energy with Chevallier-Linder-Polarski parametrization [CPL],  
([CHEVALLIER et al. 2001](#); [LINDER 2003](#)).
- Phenomenological Emergent Dark Energy [PEDE],  
([LI et al. 2019](#); [PAN et al. 2020](#); [YANG et al. 2021a](#)).

- Generalized Phenomenological Emergent Dark Energy [GPEDE], (YANG et al. 2021b).
- fraction of CDM decaying into DR [DM  $\rightarrow$  DR], (AUDREN et al. 2014; POULIN et al. 2016; NYGAARD et al. 2021).
- CDM decaying into DR and WDM [DM  $\rightarrow$  DR+WDM].  
This model will be discussed in detail in Chapter 3.

Similarly, to the case of  $\Delta N_{\text{eff}}$ , it is already well known that the CPL model does not resolve the Hubble tension (POULIN et al. 2019; DI VALENTINO et al. 2020a). Therefore, rather than a real competitor, we will consider the CPL parameterization of the Dark Energy equation of state as a historical benchmark model, useful to gauge the extent to which more complex late-universe models truly performs. In addition, notice that the PEDE model considers a parametrization of the DE energy density with no new free parameters (*i.e.* it has not  $\Lambda$ CDM limit), while GPEDE has an additional parameter such that  $\Lambda$ CDM can be recovered for a particular value of this parameter.

### 2.5.2 Statistical tests to quantify model success

For each model  $\mathcal{M}$  and compilation of data sets  $\mathcal{D}$ , we discuss three ways to quantify the tension between the cosmological inferred value and the SHOES experiment <sup>22</sup>, each one related to a different question:

- **Criterion 1:** *When considering a dataset  $\mathcal{D}$  not including SHOES, what is the residual level of tension between the posterior on  $M_b$  inferred using  $\mathcal{D}$  and the SHOES measurement?*

The tension on  $x = M_b$  can be quantified through the Gaussian Tension (GT), defined as

$$\frac{\bar{x}_{\mathcal{D}} - \bar{x}_{\text{SHOES}}}{(\sigma_{\mathcal{D}}^2 + \sigma_{\text{SHOES}}^2)^{1/2}}, \quad (2.16)$$

where  $\bar{x}_i$  and  $\sigma_i$  are the mean and standard deviation of observation  $i$ . A problem of this metric is that it is only strictly valid if the parameter's posteriors are Gaussian, and it could disfavor models with long tails in the posterior. This can happen for instance if the data set  $\mathcal{D}$  cannot disentangle between  $\Lambda$ CDM and a more complex model which has parameters that become irrelevant when others are close to their  $\Lambda$ CDM limit. As a result, the posterior is necessarily dominated by the Gaussian  $\Lambda$ CDM limit, and the easing power of the model can only show up in the aforementioned tails of the probability distribution (this is precisely what happens with EDE cosmologies, as we saw in Sect. 2.4.2). In addition, this criterion does not quantify how good (or bad) the  $\chi^2$  of the new model is. As a result, a model which does not contain the  $\Lambda$ CDM best fit (like the PEDE model) can appear arbitrarily good. In order to avoid such problems, we instead use the two additional tests listed below.

- **Criterion 2:** *How does the addition of the SHOES measurement to the data set  $\mathcal{D}$  impact the fit within a particular model  $\mathcal{M}$ ?*

<sup>22</sup>We treat SHOES not as a model-dependent measurement of  $H_0$ , but as a direct measurement of the intrinsic magnitude of supernovae Ia (SNIa),  $M_b = -19.2435 \pm 0.0373$  (RIESS et al. 2021b). As discussed in Sect. 2.2, this allows to take into account the correlation between the information contained in SHOES and Pantheon catalog of remote SNIa.



We compute the change in the effective best-fit chi-square  $\chi^2 = -2 \ln \mathcal{L}$  between the combined data set and the dataset  $\mathcal{D}$  as

$$\Delta\chi^2 = \chi_{\min, \mathcal{D}+\text{SHOES}}^2 - \chi_{\min, \mathcal{D}}^2. \quad (2.17)$$

In the  $\Lambda$ CDM framework, the  $\chi^2$  of the combined fit to  $\mathcal{D}+\text{SHOES}$  is notably worse than the sum of the separate best-fitting  $\chi^2$  to  $\mathcal{D}$  and to SHOES, reflecting the fact that the data sets are in tension. Since we are comparing the  $\chi^2$  values within a given model, there is no change in the number of model parameters, and the tension can simply be expressed as  $\sqrt{\Delta\chi^2}$  in units of  $\sigma$ , which is identical to the  $Q_{\text{DMAP}}$  metric discussed in [RAVERI et al. \(2019\)](#). This criterion naturally generalizes the commonly used criterion discussed in point 1 to the case of non-Gaussian posteriors. Indeed, for any Gaussian posterior, it is equivalent to that criterion. However, it is sensitive to the effect of over-fitting (i.e. a model with arbitrarily large number of parameters could fit any features better than  $\Lambda$ CDM), which usually requires Bayesian methods to compute Occam’s razor factors. For this reason, we also consider a third criterion, which attempts to penalize overly complex models, and to quantify the intrinsic success of a model.

- **Criterion 3:** *When the dataset  $\mathcal{D}$  includes the SHOES likelihood, does the fit within a particular model  $\mathcal{M}$  significantly improve upon that of  $\Lambda$ CDM?*

We compute the Akaike Information Criterion (AIC) of the extended model  $\mathcal{M}$  relative to that of  $\Lambda$ CDM, defined as

$$\Delta\text{AIC} = \chi_{\min, \mathcal{M}}^2 - \chi_{\min, \Lambda\text{CDM}}^2 + 2(N_{\mathcal{M}} - N_{\Lambda\text{CDM}}), \quad (2.18)$$

where  $N_{\mathcal{M}}$  stands for the number of free parameters of the model. This metric attempts to penalize models which introduce new parameters that do not subsequently improve the fit. Thus, the ability of a model  $\mathcal{M}$  to resolve the tension at a significant level despite having more parameters can be assessed through  $\Delta\text{AIC}$ , with more negative values indicating larger model success. While this metric does indicate whether a model is favored compared to  $\Lambda$ CDM for the combined data set, it does not quantify whether this improvement stems from improving the Hubble tension or from simply fitting better other data sets such as Planck data. This criterion is thus especially useful if applied together with criterion 1 or 2 above. The  $\Delta\text{AIC}$  criterion offers the advantage of being numerically cheap and prior independent, as opposed to several Bayesian estimators ([VERDE et al. 2013](#); [RAVERI et al. 2021](#)), including the Bayes factor ratio ([KASS et al. 1995](#)), or the related “suspiciousness” ([HANDLEY et al. 2019](#)).

In the case of Tests 1 and 2, we require models to reduce the tension below the  $3\sigma$  level. This may not seem like a very stringent threshold for success since, at the end of the day,  $3\sigma$  may still be considered as a significant tension. However, we will show that only a limited number of models are capable of reducing the tension to this rather meager level. In addition, it is important to bear in mind that some of the current data likelihoods might underestimate systematic errors. In the future, as long as systematic errors are revised slightly but not drastically, there is a good chance that the models that do not pass our  $3\sigma$  criteria will remain excluded, while the models not passing some possible  $2\sigma$  criterion could be rescued. For Test 3, we demand that the preference for the extended cosmology  $\mathcal{M}$  over  $\Lambda$ CDM is larger than a “weak preference” on Jeffrey’s scale ([JEFFREYS 1961](#); [NESSERIS et al. 2013](#)), that is,  $p = 10^{1.5}$ . Using  $\exp(\Delta\text{AIC}/2) = p$  in the AIC formalism, this leads to the criterion

$\Delta\text{AIC} \leq -6.91$ .

Since the questions addressed by criteria 1 and 2 are very similar <sup>23</sup>, and since criterion 2 does not assume Gaussian posteriors, we consider that criterion 2 supersedes criterion 1. On the other hand, criteria 2 and 3 address significantly different questions. Each of them has its pros and cons and they complement each other. Thus, as long as the  $\Delta\chi^2$  computed for the AIC test is negative (*i.e.* as long as a model is not giving a worse combined fit than  $\Lambda\text{CDM}$ ), we will conservatively consider that it is successful when one of criterion 2 or 3 is fulfilled. To summarize the success of each suggested solution we attribute “medals” to models passing our tests: A model passing either criterion 2 (obtaining a good combined fit) or 3 (strongly improving the fit over  $\Lambda\text{CDM}$ ) receives a bronze medal. A model passing both criteria receives a silver medal. We reserve the gold medal for models that additionally pass criterion 1, that is, whose posterior distributions allow for high values of  $H_0$  (or  $M_B$ ) independently of the inclusion of a local distance ladder prior.

### 2.5.3 Results of the contest

For our baseline dataset,  $\mathcal{D}_{\text{baseline}}$ , where

$$\begin{aligned} \mathcal{D}_{\text{baseline}} = & \text{Planck18 (including TTTEEE and lensing)} \\ & + \text{BAO (including BOSS DR12 (ALAM et al. 2017) + MGS (ROSS et al. 2015)} \\ & + \text{6dFGS (BEUTLER et al. 2011)) + Pantheon (SCOLNIC et al. 2018)}, \end{aligned}$$

the result of our main tests ( $Q_{\text{DMAP}}$  for  $M_b$  and Akaike Information Criterion) are summarized in Tab. (2.7) and represented graphically in Fig. 2.11. For the sake of completeness, we also present the results obtained using criterion 1 (Gaussian Tension on  $M_b$ ), both in Tab. (2.7) and in the discussion. First and foremost, no model is perfect – in fact, none of the models studied here are capable of reducing the tension below the  $\sim 1.6\sigma$  level. A number of models, however, are capable of passing the criteria identified above (with varying levels of success). We enumerate the results for each of the test criteria below:

- Adopting the GT estimator, only four models can reduce the tension to the  $3\sigma$  level, with the best model (varying  $m_e + \Omega_k$ ) showing a residual  $2.0\sigma$  tension. From best to worse, they are: varying  $m_e + \Omega_k$ , PEDE, varying  $m_e$  in a flat universe, and the Majoron.
- Making use instead of the more robust  $Q_{\text{DMAP}}$  criterion, which compares  $\chi^2$  of models with and without the inclusion of the SHOES determination of  $M_b$ , we find that models with non-Gaussian tails perform significantly better. This most strongly impacts the two models of EDE and the EMG model, reducing their level of tension from roughly  $3.1 - 3.7\sigma$  to  $1.6 - 2.3\sigma$ . From best to worse, models that pass criterion 2 are: EDE, varying  $m_e + \Omega_k$ , NEDE, EMG, PEDE, varying  $m_e$ , and the Majoron.
- Adopting the  $\Delta\text{AIC}$  criterion, which attempts at quantifying the role of enlarged model complexity in the improvement of the fit to  $\mathcal{D}_{\text{baseline}} + \text{SHOES}$ , we find that

<sup>23</sup>The most notable difference is that one is based on average properties of the posterior distribution, as opposed to the  $\chi^2$  of a single point, and the ability to capture the effect of long tails in non-Gaussian posterior distributions.

Model	$\Delta N_{\text{param}}$	$M_B$	Gaussian Tension	$Q_{\text{DMAP}}$ Tension		$\Delta\chi^2$	$\Delta\text{AIC}$		Finalist
$\Lambda\text{CDM}$	0	$-19.416 \pm 0.012$	$4.4\sigma$	$4.5\sigma$	X	0.00	0.00	X	X
$\Delta N_{\text{nr}}$	1	$-19.395 \pm 0.019$	$3.6\sigma$	$3.8\sigma$	X	-6.10	-4.10	X	X
SIDR	1	$-19.385 \pm 0.024$	$3.2\sigma$	$3.3\sigma$	X	-9.57	-7.57	✓	✓ 🟡
mixed DR	2	$-19.413 \pm 0.036$	$3.3\sigma$	$3.4\sigma$	X	-8.83	-4.83	X	X
DR-DM	2	$-19.388 \pm 0.026$	$3.2\sigma$	$3.1\sigma$	X	-8.92	-4.92	X	X
SI $\nu$ +DR	3	$-19.440^{+0.037}_{-0.039}$	$3.8\sigma$	$3.9\sigma$	X	-4.98	1.02	X	X
Majoron	3	$-19.380^{+0.027}_{-0.021}$	$3.0\sigma$	$2.9\sigma$	✓	-15.49	-9.49	✓	✓ 🟡
primordial B	1	$-19.390^{+0.018}_{-0.024}$	$3.5\sigma$	$3.5\sigma$	X	-11.42	-9.42	✓	✓ 🟡
varying $m_e$	1	$-19.391 \pm 0.034$	$2.9\sigma$	$2.9\sigma$	✓	-12.27	-10.27	✓	✓ 🟡
varying $m_e + \Omega_k$	2	$-19.368 \pm 0.048$	$2.0\sigma$	$1.9\sigma$	✓	-17.26	-13.26	✓	✓ 🟡
EDE	3	$-19.390^{+0.016}_{-0.035}$	$3.6\sigma$	$1.6\sigma$	✓	-21.98	-15.98	✓	✓ 🟡
NEDE	3	$-19.380^{+0.023}_{-0.040}$	$3.1\sigma$	$1.9\sigma$	✓	-18.93	-12.93	✓	✓ 🟡
EMG	3	$-19.397^{+0.017}_{-0.023}$	$3.7\sigma$	$2.3\sigma$	✓	-18.56	-12.56	✓	✓ 🟡
CPL	2	$-19.400 \pm 0.020$	$3.7\sigma$	$4.1\sigma$	X	-4.94	-0.94	X	X
PEDE	0	$-19.349 \pm 0.013$	$2.7\sigma$	$2.8\sigma$	✓	2.24	2.24	X	X
GPEDE	1	$-19.400 \pm 0.022$	$3.6\sigma$	$4.6\sigma$	X	-0.45	1.55	X	X
DM $\rightarrow$ DR+WDM	2	$-19.420 \pm 0.012$	$4.5\sigma$	$4.5\sigma$	X	-0.19	3.81	X	X
DM $\rightarrow$ DR	2	$-19.410 \pm 0.011$	$4.3\sigma$	$4.5\sigma$	X	-0.53	3.47	X	X

**Table 2.7** – Test of the models based on dataset  $\mathcal{D}_{\text{baseline}}$ , using the direct measurement of  $M_b$  by SHOES as the GT for the quantification of the tension (4th column), the  $Q_{\text{DMAP}}$  criterion (5th column), or the computation of the  $\Delta\text{AIC}$  (7th column).

eight models are capable of significantly improving over  $\Lambda\text{CDM}$  <sup>24</sup>. They are, in decreasing level of success: EDE, varying  $m_e + \Omega_k$ , NEDE, EMG, varying  $m_e$ , the Majoron model, a primordial magnetic field, and SIDR.

Before declaring the official *finalists*, let us briefly comment on models that do not make it to the final, starting with late-universe models. The CPL parameterization, our “late-universe defending champion”, only reduces the tension to  $3.7\sigma$ , inducing a minor improvement to the global fit. The PEDE model noticeably degrades the  $\chi^2$  of BAO and Pantheon data, leading to an overall worse fit than  $\Lambda\text{CDM}$ . Thus, according to our general rules, we must exclude PEDE from the final. The GPEDE model, which generalises PEDE to include  $\Lambda\text{CDM}$  as a limiting case, does not pass any of the tests. This shows the danger of using only criterion 1 or 2 for models that do not include  $\Lambda\text{CDM}$  as a limit. Ideally, one should always perform a test equivalent to the  $\Delta\text{AIC}$  or consider models in which  $\Lambda\text{CDM}$  is nested. As emphasized in Sect. 2.2, for late-time modifications of  $\Lambda\text{CDM}$ , it is also important to treat the SHOES observation as a model-independent measurement of  $M_b$ , rather than a model-dependent measurement of  $H_0$ . We checked explicitly that using a SHOES likelihood on  $H_0$  rather than  $M_b$  incorrectly yields more favorable results for these late-time models, a result consistent with the claims of (BENEVENTO et al. 2020; CAMARENA et al. 2021; EFSTATHIOU 2021). Finally, the models of decaying dark matter studied here are only capable of reducing the tension from  $4.4\sigma$  to  $4.2\sigma$ , despite only introducing two new parameters. Consequently, the  $\Delta\text{AIC}$  criteria disfavors both DDM models. We thus conclude that the late-time DE and dark matter decay models

<sup>24</sup>None of our models show a significant preference in AIC over  $\Lambda\text{CDM}$  when only considering the baseline  $\mathcal{D}_{\text{baseline}}$

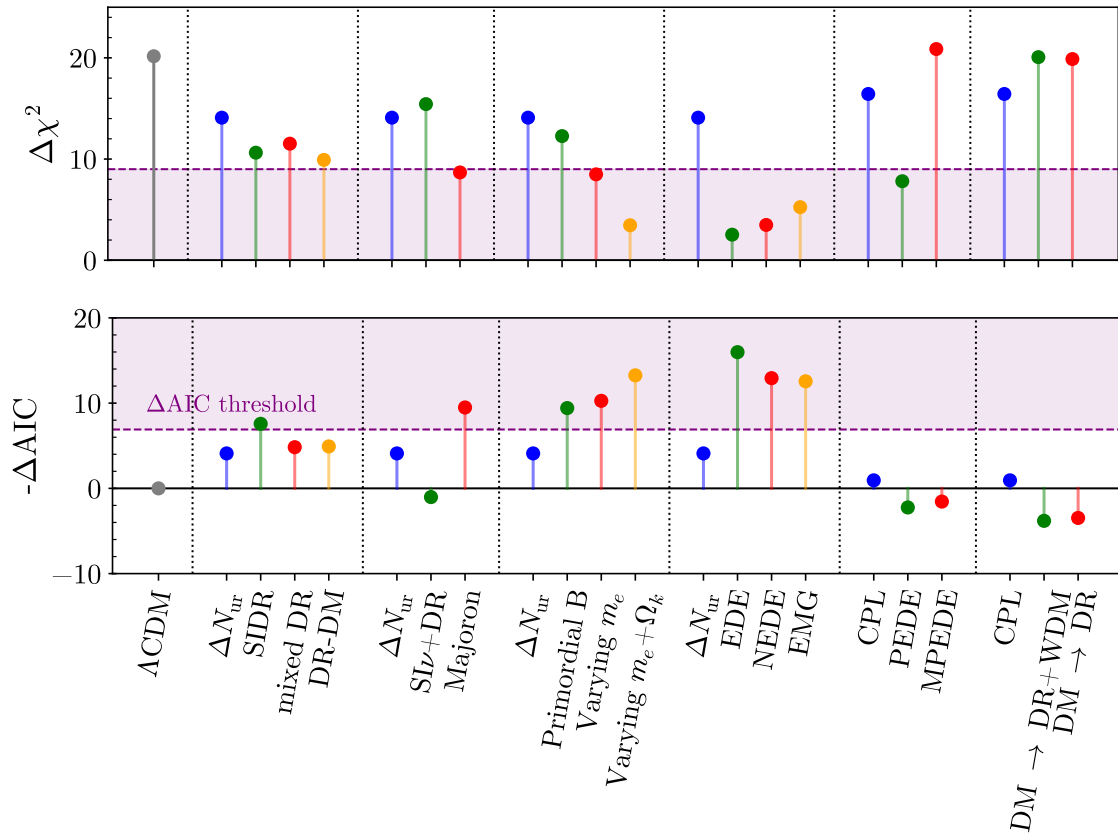


**Figure 2.11** –  $\Delta\chi^2$  (Test 2) and  $\Delta AIC$  (Test 3) of the various models considered in this work. We additionally display the thresholds that have to be reached as purple dashed lines, and the regions of successful models as a purple region.

considered in this work cannot resolve the Hubble tension.

Secondly, the class of models invoking extra relativistic degrees of freedom perform significantly better than late-universe models, but a majority are not successful enough to pass our pre-determined thresholds. Self-Interacting Dark Radiation [SIDR], Self-interacting Dark Radiation scattering on Dark Matter [DR-DM], and Free-streaming plus self-interacting Dark Radiation [mixed DR], all improve upon the “early-universe defending champion”, that is, free-streaming DR (for all three criteria). However, none of them reduces the tension below the  $\sim 3.2\sigma$  level. Perhaps the most surprising case is that of Self-interacting neutrinos plus free-streaming Dark Radiation [SI $\nu$ +DR], which has long been claimed as a promising solution to the Hubble tension, but performs worse on  $\Delta AIC$  and  $Q_{\text{DMAP}}$  than the benchmark of free-streaming DR. It may also sound surprising that the DR-DM model does not perform significantly better than the SIDR model (the latter model passing the  $\Delta AIC$  criterion). We emphasize that in several previous papers, the success of this model was boosted by a lower prior on the amount of DR that excluded  $\Lambda$ CDM as a limit, a situation comparable to that of PEDE. The only model which successfully passes both criteria is that of the Majoron, which reduces the tension to the level of  $\sim 2.9\sigma$  and shows a significant improvement to the fit. It is perhaps interesting to point out that this is the only model in this categoriza-

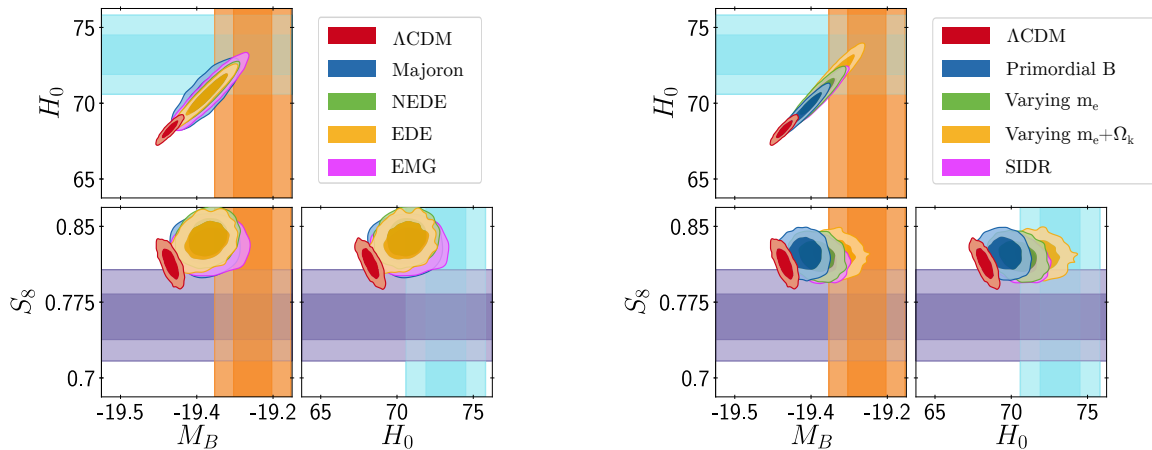


**Figure 2.12** – Contours of  $\{H_0, M_b, S_8\}$  obtained when considering the  $\mathcal{D}_{\text{extended}}$  dataset for the finalists models compared to  $\Lambda\text{CDM}$ . The purple band represents the  $S_8$  measurement from KiDS-1000 (ASGARI et al. 2021).

tion which invokes a non-trivial evolution of  $H(z)$ . It is thus in some ways more similar to Early Dark Energy than to the other Dark Radiation models presented here.

In summary, the models that pass at least one of criterion 2 or 3 without leading to a worse global fit, ranked from the best to worst  $\Delta\text{AIC}$ , are the following:

1. EDE,
2. varying  $m_e + \Omega_k$ ,
3. NEDE,
4. EMG,
5. primordial B,
6. varying  $m_e$ ,
7. Majoron,
8. SIDR.

These models constitute our “finalist” sample. In Fig. 2.12 we highlight the predicted distributions of  $S_8$  for each of the finalist models<sup>25</sup>. As we can see, none of these models are able to relieve the  $S_8$  tension, however neither do any of the models dramatically increase the tension. As discussed extensively in Sect. 2.4 and in other works (HILL et al. 2020; IVANOV et al. 2020; D’AMICO et al. 2021b; NIEDERMANN et al. 2021b; T. L. SMITH et al. 2021), the inclusion of LSS data doesn’t spoil the resolution to the  $H_0$  tension provided by the EDE and NEDE models, even if they slightly increase the mean value of  $S_8$ . Nevertheless, this figure clearly illustrates that resolving the both  $H_0$  and  $S_8$  tensions will likely require multiple extensions.

There has been attempts in the literature at resolving both tensions simultaneously. In particular, models of DM-DR interactions seemed particularly promising given that they predict both a higher  $H_0$  and a smaller  $S_8$  (BUEN-ABAD et al. 2015; CHACKO et al. 2016; BUEN-ABAD et al. 2018). However, none passed the tests we considered in this work. Similarly, the primordial magnetic field model was advertised as promising to resolve both tensions (JEDAMZIK et al. 2020). While it does pass our  $\Delta\text{AIC}$

<sup>25</sup>We remark that this analysis corresponds to an extended dataset  $\mathcal{D}_{\text{extended}} = \mathcal{D}_{\text{baseline}} + \text{Redshift-Space-Distortions (from BOSS DR12 (ALAM et al. 2017), 6dFGS (BEUTLER et al. 2011), MGS (ROSS et al. 2015) and eBOSS DR 14 quasars (ZARROUK et al. 2018))} + \text{Cosmic Chronometers (VAGNOZZI et al. 2021a)} + \text{Lyman-}\alpha \text{ based high-}z \text{ BAO (BLOMQUIST et al. 2019; SAINTE AGATHE et al. 2019)}$ .



criterion, it only reduces the  $H_0$  tension at the  $3.5\sigma$  level, and the  $S_8$  tension is barely affected ( $S_8$  is even slightly larger than in  $\Lambda$ CDM). Nevertheless, it is possible that the resolutions of the  $S_8$  and  $H_0$  tension lie in different sectors, or require more involved modifications than the ones discussed here. In fact, as we discussed in Sect. 1.7.2, it is becoming clear that the  $S_8$  tension lies in the amplitude of fluctuation  $\sigma_8$  rather than  $\Omega_m$ , in particular due to constraints on  $\Omega_m$  from uncalibrated SNIa data (SCOLNIC et al. 2018), and from the cross-correlation of weak lensing and galaxy surveys that breaks the  $\Omega_m - \sigma_8$  degeneracy (HEYMANS et al. 2021). Therefore, one might expect that the  $\sigma_8$  tension hints at new perturbation properties, while  $H_0$ , which is a measure of the total energy density, hints at a new background contribution. Many models discussed so far are mainly motivated by their impact at the background level, and it is perhaps not surprising that they fail at simultaneously reducing  $\sigma_8$  due to the small freedom they have at the level of perturbations. For instance, it was recently noted that extending the (N)EDE sector with an additional ultra-light axion of mass  $m \sim 10^{-26}$  eV representing  $\sim 5\%$  of the DM would resolve both tensions (ALLALI et al. 2021). Alternatively, while less pleasing from the Occam’s razor point of view, new properties of DM, such as decays (see Chapter 3), cannibalism (HEIMERSHEIM et al. 2020), interactions with DR (BUEN-ABAD et al. 2015; CHACKO et al. 2016), with neutrinos (DI VALENTINO et al. 2018b; MOSBECH et al. 2021) or with DE (DI VALENTINO et al. 2020b; LUCCA 2021), as well as new neutrino properties (KREISCH et al. 2020; DAS et al. 2022) could independently resolve the  $\sigma_8$  tension, and leave unaffected the (relative) success of the models studied here at resolving the  $H_0$  tension. In this context, it was recently shown that a naïve combination of the EDE model with the DM  $\rightarrow$  DR+WDM decay scenario can indeed address both tensions successfully (CLARK et al. 2021b).

## 2.6 Summary and outline

In the first part of this work, we have reassessed the viability of the EDE against a host of high- and low-redshift measurements, by combining LSS observations from recent weak lensing surveys KIDS-VIKING and DES with Planck18 2018 CMB data, BOSS-DR12 BAO and growth function measurements, and the PANTHEON compilation of luminosity distance to SNIa. Our results can be summarized as follows:

1. Within a phenomenological 3-parameters EDE model (3pEDE), we confirm that Planck18+ BAO+FS+PANTHEON+SHOES favor  $f_{\text{EDE}}(z_c) \simeq 0.1 \pm 0.03$ ,  $z_c \simeq 4000_{-500}^{+1400}$  and  $\Theta_i = 2.6_{-0.03}^{+0.4}$ , with a  $\Delta\chi^2 = -18.7$  compared to  $\Lambda$ CDM fitted on the same data set. The inclusion of the latest Planck18 data (and in particular the more precise polarization measurements) does not spoil the success of the EDE resolution to the Hubble tension. When compared to the ‘concordance’  $\Lambda$ CDM model (i.e. obtained from analysis without SHOES data), the EDE cosmology fits Planck18+BAO+FS+ PANTHEON equally well, but can additionally accommodate the high local  $H_0$  values.
2. Following the approach of NIEDERMANN et al. (2020), we have then shown that *reducing* the parameter space to a 1-parameter EDE (1pEDE) model by fixing  $\text{Log}_{10}(z_c)$  and  $\Theta_i$  to their best fit values as obtained from a Planck18 data only analysis – which strikingly coincide with those from the combined analysis with SHOES – leads to  $\sim 2\sigma$  preference for non-zero EDE, namely  $f_{\text{EDE}}(z_c) \simeq 0.08 \pm 0.04$  from Planck18 CMB data alone. In this cosmology, the inferred  $H_0 \simeq 70 \pm 1.5$  km/s/Mpc is in agreement at better than  $2\sigma$  with its local measurement from



SHOES. The addition of BAO, FS and PANTHEON data has no significant impact on the result. Including a prior on  $H_0$  from SHOES pulls up the reconstructed fraction to the  $\sim 10\%$  level, with  $H_0 \simeq 71.7 \pm 1$ , while the fit to [Planck18](#) is slightly better than in the concordance  $\Lambda$ CDM cosmology ( $\Delta\chi^2 \sim -5$ ).

3. To justify the inclusion of LSS data in our analyses, we have confronted the EDE non-linear matter power spectrum as predicted by standard semi-analytical algorithms against a dedicated set of  $N$ -body simulations. We have then tested the 1pEDE cosmology against WL data, finding that it does not significantly worsen the fit to the  $S_8$  measurements as compared to  $\Lambda$ CDM, and that current WL observations do not exclude the EDE resolution to the Hubble tension.
4. We also caution against the interpretation of constraints obtained from combining [Planck18](#) with KiDS-VIKING+DES. As we showed, the ‘compromise’ cosmology that is obtained is a poor fit to KiDS-VIKING+DES and degrades the fit to [Planck18](#) data, even in  $\Lambda$ CDM. This illustrates that these data sets are statistically inconsistent in a  $\Lambda$ CDM framework, and it is easily conceivable that the resolution of this tension lies elsewhere (whether systematic effect or new physics).
5. In light of the CMB lensing anomaly, we have shown that the lensing-marginalized CMB data favor non-zero EDE at  $\sim 2\sigma$ , predicts  $H_0$  in  $1.4\sigma$  agreement with SHOES and  $S_8$  in  $1.5\sigma$  and  $0.8\sigma$  agreement with KiDS-VIKING and DES, respectively. There still exists however a  $\sim 2.5\sigma$  tension with the joint results from KiDS-VIKING and DES. Moreover, the presence of EDE does not affect the amount of anomalous lensing. This suggests that the anomalous lensing is not due to the presence of EDE, but also that the success of EDE is not due to opening up a new degeneracy direction with some exotic lensing parameters.

Interestingly, recent analysis of the 3pEDE model using data from the Atacama Cosmology Telescope’s fourth data release (ACT DR4) ([S. K. CHOI et al. 2020](#)) alone have shown a slight ( $\sim 2.2\sigma$ ) preference for the presence of an EDE component with a fraction  $f_{\text{EDE}}(z_c) \sim 0.15$  and  $H_0 \sim 74$  km/s/Mpc ([HILL et al. 2021](#); [POULIN et al. 2021](#)). These studies showed that the inclusion of large-scale CMB temperature measurements by the Wilkinson Microwave Anisotropy Probe (WMAP) ([C. L. BENNETT et al. 2013](#)) or [Planck18](#) restricted to the WMAP multipole range increases the preference to  $\sim 3\sigma$ . A similar analysis using the third generation South Pole Telescope 2018 (SPT-3G) data ([DUTCHER et al. 2021](#)) was presented in [LA POSTA et al. \(2022\)](#). There is no evidence for 3pEDE over  $\Lambda$ CDM using SPT-3G alone or when combined with the *Planck* temperature power spectrum restricted to the WMAP multipole range. Combining ACT and/or SPT-3G with the full *Planck* CMB power spectra returns an upper limit on  $f_{\text{EDE}}(z_c)$ , albeit less restrictive than for *Planck* alone. In [HILL et al. \(2021\)](#) and [POULIN et al. \(2021\)](#) it was argued that the ACT preference for 3pEDE is mainly driven by a feature in the ACT EE power spectrum around  $\ell \sim 500$  when ACT is considered alone, with an additional broadly-distributed contribution from the TE spectrum when in combination with restricted *Planck* TT data ( $\ell < 650$  or  $\ell < 1060$ ). Building on these previous studies, in [T. L. SMITH et al. \(2022\)](#) we derived constraints on 3pEDE using ACT DR4, SPT-3G 2018, *Planck* polarization, and restricted *Planck* temperature data, finding a  $3.3\sigma$  preference for EDE over  $\Lambda$ CDM. This is the first time that a moderate preference for EDE has been

reported for these combined CMB data sets including Planck polarization. However, with the inclusion of *Planck* TT data at  $\ell > 1300$ , the constraint on  $f_{\text{EDE}}(z_c)$  becomes compatible with  $\Lambda\text{CDM}$  at  $1\sigma$ . In addition, we explored whether systematic errors in the *Planck* polarization data could affect our conclusions and found that changing the TE polarization efficiencies<sup>26</sup> significantly reduces the *Planck* preference for EDE. More work will be necessary to establish whether these hints for EDE within CMB data alone are the sole results of systematic errors or an opening to new physics.

In the second part of this work, we have used a common analysis pipeline to compare and contrast the relative success of seventeen models (including EDE) proposed to ease the Hubble tension; this approach is thus intended as a fair comparison between proposed solutions, and provides a useful benchmark for those wishing to put forth novel ideals. We have broken down the various models into three generic categories: those that modify the sound horizon by including a component of Dark Radiation (DR) impacting the early expansion history, solutions which modify the sound horizon through some other mechanism (such as a delay of recombination or some pre-recombination contribution to the expansion), and solutions that attempt to modify the late-time expansion history.

For each model and data-set, we quantify the residual tension using a series of metrics, each of which has both advantages and shortcomings, and attempting to answer slightly different questions, namely: given a model, (i) to what extent does confrontation with data (other than SHOES) generate posteriors compatible with high values of  $H_0$ , (ii) to what extent can one obtain a good combined fit to all data, and (iii) to what extent is that model favored over  $\Lambda\text{CDM}$ ? The summary of our findings is that no model does perfectly well in all of our tests – all models are left with a residual tension, with the most promising reducing the tension to the  $\sim 1.6\sigma$  level, and with very few models actually reducing the tension below  $3\sigma$ . Similarly, only a small subset of the models are capable of improving the fit sufficiently to pass the AIC test. Six models, EDE, NEDE, EMG, varying  $m_e$  (with and without curvature), and the Majoron, are able to simultaneously satisfy the  $Q_{\text{DMAP}}$  and  $\Delta\text{AIC}$  criteria. Furthermore, only the varying  $m_e$  (with and without curvature) passes the Gaussian criterion and allows for high  $H_0$  (or  $M_B$ ) without a SHOES prior, receiving the only “gold medal” of our tournament.

Additionally we note that, besides EDE, none of the models of interest alleviate (nor exacerbate) the  $S_8$  tension. Some models which had previously shown some success in reducing the  $S_8$  tension, namely DM-DR and the strongly interacting neutrinos, are now disfavored by the data. Finding a common resolution to both tensions would certainly reinforce the degree of belief into the new concordance cosmology; however, we reiterate that the resolution of these tensions could arise from independent sectors – either from new physics or systematics. We conclude that some of the models presented in this work can provide a good combined fit to all data considered (including SHOES), demonstrating that there at least exist potential solutions to the  $H_0$

---

<sup>26</sup>Polarization efficiencies are calibration factors multiplying polarization spectra. In principle, the polarization efficiencies found by fitting the TE spectra should be consistent with those obtained from EE. However, in *Planck*, small differences (at the level of  $2\sigma$ ) are found between the two estimates at 143 GHz. There are two possible choices: the ‘map-based’ approach, which adopts the estimates from EE (which are about a factor of 2 more precise than TE) for both the TE and EE spectra; or the ‘spectrum-based’ approach, which applies independent estimates from TE and EE.

tension, but there are still many difficulties to be overcome in the model building and in explaining the growing  $S_8$ -tension. Further work must be done to establish whether these remaining theoretical and observational issues can be overcome in a new concordant cosmology, one that may either build upon the models studied here, or perhaps lie in a yet unexplored direction.

# III

---

## Decaying dark matter and the $S_8$ tension

---

*“Caminante, son tus huellas  
el camino y nada más;  
Caminante, no hay camino,  
se hace camino al andar.  
Al andar se hace el camino,  
y al volver la vista atrás  
se ve la senda que nunca  
se ha de volver a pisar.  
Caminante no hay camino  
sino estelas en la mar. .”*

*Antonio Machado, Proverbios y cantares*

### Contents

---

3.1	Unstable dark matter and cosmic tensions . . . . .	<b>140</b>
3.2	Formalism of the two-body Dark Matter decay . . . . .	<b>141</b>
3.2.1	Background equations . . . . .	144
3.2.2	Linear perturbation equations . . . . .	146
3.2.3	Fluid approximation for the warm component . . . . .	148
3.2.4	Dynamics of perturbations . . . . .	149
3.3	Observable effects of the Dark Matter decay . . . . .	<b>151</b>
3.3.1	Impact on the matter power spectrum . . . . .	151
3.3.2	Impact on the CMB anisotropy spectra . . . . .	153
3.4	Cosmological constraints . . . . .	<b>155</b>
3.4.1	General constraints: background vs. linear perturbations . . . . .	156
3.4.2	Implications for the $S_8$ tension . . . . .	158
3.4.3	Implications for other cosmic tensions and the XenonIT anomaly . . . . .	163
3.4.4	Detecting DDM in the CMB: impact of current and future data . . . . .	165
3.5	Summary and outline . . . . .	<b>171</b>

---

This Chapter is based on:

G. F. Abellán, R. Murgia, V. Poulin, J. Lavallo

*“Implications of the  $S_8$  tension for decaying dark matter with warm decay products”*

**PRD 105 063525 (2022)**; arXiv:2008.09615

G. F. Abellán, R. Murgia, V. Poulin

*“Linear cosmological constraints on two-body decaying dark matter scenarios and the  $S_8$  tension”*

**PRD 104 123533 (2021)**; arXiv:2102.12498

### 3.1 Unstable dark matter and cosmic tensions

From the point of view of particle physics model building, the stability over cosmological timescales is one of the most peculiar property of the dark matter particle, reviewed e.g. in HAMBYE (2011). Often, an additional symmetry (typically a discrete  $Z_2$  symmetry) has to be assumed to make the DM candidate stable. Nevertheless, DM decays at late-times are known signatures of many models in the literature such as (for instance) models with R-parity violation (BEREZINSKY et al. 1991; KIM et al. 2002), super Weakly Interacting Massive particles (super WIMPs) (COVI et al. 1999; FENG et al. 2003; ALLAHVERDI et al. 2015), sterile neutrinos (ABAZAJIAN et al. 2012) or models with an additional  $U(1)$  gauge symmetry (C.-R. CHEN et al. 2009; G. CHOI et al. 2020a,c)<sup>1</sup>.

Decays to electromagnetically charged particles are tightly constrained by *Planck* data (POULIN et al. 2017; SLATYER et al. 2017),  $\gamma$ -ray (CIRELLI et al. 2012; ESSIG et al. 2013) and cosmic-ray searches (JIN et al. 2013; GIESEN et al. 2015), typically requiring  $\Gamma^{-1} > \mathcal{O}(10^{26}\text{s})$ , with some level of dependence on the decay channel. Still, a purely gravitational constraint, although weaker, is very interesting in the spirit of being ‘model-independent’, while applying to models with decay to a dark sector, or to (non-interacting) neutrinos. The canonical example is perhaps that of the keV majoron (BEREZINSKY et al. 1993; LATTANZI 2008) decaying into relativistic neutrinos. Models of CDM decays with massive daughters have also been invoked as a potential solution to the observational discrepancies with CDM on small (sub-galactic) scales after structure formation (W. B. LIN et al. 2001; CEMBRANOS et al. 2005; KAPLINGHAT 2005; PETER et al. 2010a,b). Even more recently, decaying dark matter models were proposed (G. CHOI et al. 2020b; XU et al. 2021) as a way to explain the excess of events in the electronic recoils reported by the Xenon1T collaboration (APRILE et al. 2020).

In the literature, most studies restricted themselves to massless daughter particles (AUDREN et al. 2014; POULIN et al. 2016; NYGAARD et al. 2021), with the benefit of greatly simplifying the cosmological analysis, but limiting the true ‘model-independence’ of the bound, and therefore its robustness. Nevertheless, some studies have attempted at including the effect of massive daughters in a cosmological context but either neglected cosmological perturbations of the daughter particles (VATTIS et al. 2019; HARIDASU et al. 2020; CLARK et al. 2021a) or were limited by computational power to perform a complete analysis against a host of cosmological data (AOYAMA et al. 2011, 2014).

It has originally been suggested that DM decaying into massless daughters could help with cosmological tensions (BEREZHIANI et al. 2015; ENQVIST et al. 2015), but careful analysis of this scenario in light of *Planck* 2015 data has excluded this possibility (CHUDAYKIN et al. 2016; POULIN et al. 2016) (although see BRINGMANN et al. (2018) for a different conclusion if the decay rate is not constant). Attempting to go beyond these studies, the authors of VATTIS et al. (2019) suggested that considering a non-zero mass for (at least one of) the decay product would affect the phenomenology and allow for a resolution of the Hubble tension. However, a recent

<sup>1</sup>Recently, the authors of G. CHOI et al. (2022) engineered a model in the context of supergravity that explicitly reproduces the kind of late 2-body decays considered here, and also provides a natural explanation for the small mass splitting that seems to be favoured by cosmic data.

study based on a combination of both BAO and uncalibrated SNIa data-sets has been carried out in HARIDASU et al. (2020). As opposed to VATTIS et al. (2019), they conclude that a  $\Lambda$ DDM scenario does not predict higher  $H_0$  values. This is in good agreement with model-independent analyses existing in the literature in which it has been established that a combination of BAO and uncalibrated SNIa data strongly constrain any late-time modification as a resolution to the Hubble tension (see our discussion in Sect. 2.2). A similar conclusion is also reached when CMB data are considered (CLARK et al. 2021a). Yet, these recent analyses were limited to the study of the effects of  $\Lambda$ DDM on the background evolution of the universe.

In this work, we reassess the phenomenology of this 2-body Decaying Cold Dark Matter (DCDM) scenario, where the decay products are one massive Warm DM (WDM) particle and one (massless) DR component, interacting only through gravitation with the standard model particles. We will refer to the full model as  $\Lambda$ DDM. We perform the first thorough analysis of the  $\Lambda$ DDM model including a realistic treatment of linear cosmological perturbations. To that end, we introduce a new approximation scheme that allows to accurately and quickly compute the dynamics of the WDM linear perturbations by treating the WDM species as a viscous fluid. Thanks to this new fluid approximation, we show that the  $\Lambda$ DDM model, while unable to ease the Hubble tension, can fully explain the low- $S_8$  measurement from recent weak lensing surveys. We then investigate the implications for the ‘ $S_8$  tension’ against a number of changes in the analysis: different  $S_8$  priors, marginalization over the lensing information in *Planck* data, trading *Planck* high- $\ell$  polarization data for those from the SPTpol and ACTPol surveys, and the inclusion of the recent results from the Xenon1T collaboration. We conclude that the preference for decaying DM, apparent only when the  $S_8$  value determined from weak lensing data is added to the analysis, does not sensibly degrade the fit to any of the cosmological data-sets considered, and that the model could potentially explain the anomalous electron recoil excess reported by the Xenon1T collaboration. Furthermore, we explicitly show that while current CMB data alone are not sensitive enough to distinguish between standard CDM and decaying DM, next-generation CMB observations (CMB-S4) can unambiguously detect its signature.

The rest of this chapter is structured as follows. In Sect. 3.2 we introduce the formalism of  $\Lambda$ DDM (both at the background and linearly perturbed level) and the novel approximation scheme for the WDM species. In Sect. 3.3 we discuss in detail the impact of the  $\Lambda$ DDM model on the CMB and linear matter power spectra. In Sect. 3.4 we discuss the results of our numerous data analyses. Finally, in Sect. 3.5 we draw our conclusions.

## 3.2 Formalism of the two-body Dark Matter decay

Hereafter, we adopt the Boltzmann formalism by AOYAMA et al. (2014), where the time-evolution of the PSD for both the mother and the daughter particles was derived. However, in Sect. 3.2.1 we explicitly show that, at the background level, such formalism is equivalent to the one by BLACKADDER et al. (2014).

While the (cold) mother particle can be safely described as a perfect fluid, computing the density perturbation evolution for the daughter particles requires a



more sophisticated treatment. The central role in the game is played by  $\ell_{\max}$ , i.e. the highest multipole to consider when drawing up the hierarchy of equations describing the PSD of the daughter particles. In the massless case, the degrees of freedom associated to momentum can be removed after the PSD multipole decomposition and integration over  $q$  (AUDREN et al. 2014). Due to its non-trivial energy-momentum relation, this approach is not possible for the warm daughter particle. One has to study the full evolution in phase space, which would be computationally prohibitive when performing MCMC analyses. For this reason, in Sect. 3.2.3 we provide a detailed description of a novel approximation scheme, based on describing the WDM component as a viscous fluid on sub-Hubble scales. This allows us to integrate out the momentum degrees of freedom and the hierarchy of equations to be truncated at  $\ell_{\max} = 1$ . We will show that the new, computationally faster scheme is accurate enough to be used for cosmological analyses, allowing to establish accurate and robust CMB limits on this class of models.

Our framework is characterized by two additional free parameters with respect to  $\Lambda$ CDM: the DCDM lifetime,  $\Gamma^{-1}$ , and the fraction of DCDM rest mass energy converted into DR, given by (BLACKADDER et al. 2014):

$$\varepsilon = \frac{1}{2} \left( 1 - \frac{m_{\text{wdm}}^2}{m_{\text{dcdm}}^2} \right), \quad (3.1)$$

where  $0 \leq \varepsilon \leq 1/2$ . The lower limit corresponds to the standard CDM case, so that  $\Omega_{\text{cdm}} = \Omega_{\text{dcdm}} + \Omega_{\text{wdm}}$ , whereas  $\varepsilon = 1/2$  corresponds to DM decaying solely into DR. In general, small  $\varepsilon$  values (*i.e.* heavy massive daughters) and small  $\Gamma$  values (*i.e.* lifetimes much longer than the age of the universe) induce little departures from  $\Lambda$ CDM.

We choose to work in the synchronous gauge co-moving with the mother particle (that we introduced in Sect. 1.6.1), where the scalar metric potentials are referred as  $h$  and  $\eta$ . This gauge choice, in conjunction with the assumption that the mother particles are fully cold, imply the PSD of mother particles should be proportional to the Dirac delta function of  $\vec{q}$  (AOYAMA et al. 2014):

$$f_{\text{dcdm}}(k, q, \tau) = N_{\text{dcdm}}(k, \tau) \delta^{(3)}(\vec{q}) = N_{\text{dcdm}}(k, \tau) \frac{\delta(q)}{4\pi q^2}, \quad (3.2)$$

where

$$N_{\text{dcdm}}(k, \tau) \equiv \frac{a^3 \rho_{\text{dcdm}}(k, \tau)}{m_{\text{dcdm}}} = \frac{a^3 \bar{\rho}_{\text{dcdm}}(\tau)}{m_{\text{dcdm}}} (1 + \delta_{\text{dcdm}}(\tau, k)) \quad (3.3)$$

denotes the comoving number density of the DCDM. Then, the Boltzmann equations describing the evolution of the  $I$ -th dark component ( $I = \{\text{dcdm}, \text{dr}, \text{wdm}\}$ ) reads <sup>2</sup>

$$\frac{\partial f_I}{\partial \tau} + i\mu \frac{kq}{\mathcal{E}_I} f_I + \frac{\partial f_I}{\partial q} \frac{dq}{d\tau} = \left( \frac{\partial f_I}{\partial \tau} \right)_{\text{C}}, \quad (3.4)$$

where the evolution of the comoving momentum is related to the metric potentials as

$$\frac{1}{q} \frac{dq}{d\tau} = \eta' - \frac{h' + 6\eta'}{2} \mu^2, \quad (3.5)$$

<sup>2</sup>The second term at the l.h.s. of Eq. (3.4) is assumed to be a first order perturbation, see App. D.1.

and the collision terms of each species are

$$\left(\frac{\partial f_{\text{dcdm}}}{\partial \tau}\right)_C = -a\Gamma f_{\text{dcdm}}, \quad (3.6)$$

$$\left(\frac{\partial f_{\text{dr}}}{\partial \tau}\right)_C = \left(\frac{\partial f_{\text{wdm}}}{\partial \tau}\right)_C = \frac{a\Gamma N_{\text{dcdm}}}{4\pi q^2} \delta(q - ap_{\text{max}}). \quad (3.7)$$

In the previous expression  $p_{\text{max}} = p_{\text{wdm}} = p_{\text{dr}} = m_{\text{wdm}}\varepsilon/\sqrt{1-2\varepsilon}$ <sup>3</sup> denotes the modulus of the initial physical momentum of the daughter particles. We provide a derivation of Eq. (3.4)-Eq. (3.7) in App. D.1.

Let us decompose the PSD function of the  $I$ -th dark component into a background contribution  $\bar{f}_I$  plus a linear perturbation  $\Delta f_I$  as

$$f_I(k, q, \mu, \tau) = \bar{f}_I(q, \tau) + \Delta f_I(k, q, \mu, \tau). \quad (3.8)$$

Notice that this time we are considering an *absolute* perturbation to the background PSD, instead of the *relative* perturbation we considered in Eq. (1.187). As a matter of fact, the zeroth order collision term for decaying dark matter is not zero (as opposed to the standard species we discussed in Sect. 1.6.2), so the Boltzmann equations for the daughter particles are simpler when expressed in terms of an absolute perturbation. As usual, the linear perturbation term  $\Delta f_I$  is expanded over Legendre polynomials:

$$\Delta f_I(k, q, \mu, \tau) = \sum_{\ell=0}^{\infty} (-i)^\ell (2\ell + 1) \Delta f_{I,\ell}(k, q, \tau) P_\ell(\mu). \quad (3.9)$$

We remind that the mean energy density and pressure are obtained by

$$\bar{\rho}_I = \frac{4\pi}{a^4} \int_0^\infty dq q^2 \mathcal{E}_I \bar{f}_I, \quad (3.10)$$

$$\bar{P}_I = \frac{4\pi}{3a^4} \int_0^\infty dq q^2 \frac{q^2}{\mathcal{E}_I} \bar{f}_I, \quad (3.11)$$

while perturbed energy density, pressure, energy flux and shear stress are given by

$$\delta\rho_I = \bar{\rho}_I \delta_I = \frac{4\pi}{a^4} \int_0^\infty dq q^2 \mathcal{E}_I \Delta f_{I,0}, \quad (3.12)$$

$$\delta P_I = \bar{\rho}_I \Pi_I = \frac{4\pi}{3a^4} \int_0^\infty dq q^2 \frac{q^2}{\mathcal{E}_I} \Delta f_{I,0}, \quad (3.13)$$

$$(\bar{\rho}_I + \bar{P}_I) \theta_I = \frac{4\pi k}{a^4} \int_0^\infty dq q^2 q \Delta f_{I,1}, \quad (3.14)$$

$$(\bar{\rho}_I + \bar{P}_I) \sigma_I = \frac{8\pi}{3a^4} \int_0^\infty dq q^2 \frac{q^2}{\mathcal{E}_I} \Delta f_{I,2}. \quad (3.15)$$

Throughout the rest of this Chapter and unless stated otherwise, we compare  $\Lambda$ DDM models at fixed  $\omega_{\text{dcdm}}^{\text{ini}} \equiv \Omega_{\text{dcdm}}^{\text{ini}} h^2$  with  $\Lambda$ CDM models having the same  $\omega_{\text{cdm}}$ . All other cosmological parameters are fixed to  $\{H_0 = 67.7 \text{ km/s/Mpc}, \omega_{\text{cdm}} = \omega_{\text{dcdm}}^{\text{ini}} = 0.1194, \omega_{\text{b}} = 0.0224, n_s = 0.9673, \ln(10^{10} A_s) = 3.052, \tau_{\text{reio}} = 0.0582\}$ , which constitutes our baseline  $\Lambda$ CDM model. These values correspond to the best-fit from the combined

<sup>3</sup>This expression is easily derived using energy-momentum conservation. In the rest frame of the DCDM, we have  $E_{\text{dcdm}} = m_{\text{dcdm}} = E_{\text{wdm}} + E_{\text{dr}}$ , with  $E_{\text{wdm}} = \sqrt{p_{\text{wdm}}^2 + m_{\text{dcdm}}^2}$  and  $E_{\text{dr}} = p_{\text{dr}} = p_{\text{wdm}}$ . Solving for  $p_{\text{wdm}}$  yields  $p_{\text{wdm}} = (m_{\text{dcdm}}/2)(1 - m_{\text{wdm}}^2/m_{\text{dcdm}}^2) = m_{\text{dcdm}}\varepsilon = m_{\text{wdm}}\varepsilon/\sqrt{1-2\varepsilon}$ .

analysis (including  $S_8$  data from weak lensing) that we present in Sect. 3.4.2 (see fourth column of Tab. (3.1)), which are however very similar to the  $\Lambda$ CDM best-fit parameters from Planck18. We implement the equations describing the  $\Lambda$ DDM model in a modified version of CLASS (BLAS et al. 2011; LESGOURGUES et al. 2011). Our code is available at [https://github.com/PoulinV/class\\_majoron](https://github.com/PoulinV/class_majoron).

### 3.2.1 Background equations

Gathering the zeroth order terms of the Boltzmann equations Eq. (3.4), we arrive at the background evolution of the mother and daughter particles

$$\bar{f}'_{\text{dcdm}} = -a\Gamma\bar{f}_{\text{dcdm}}, \quad (3.16)$$

$$\bar{f}'_{\text{dr}} = \bar{f}'_{\text{wdm}} = \frac{a\Gamma\bar{N}_{\text{dcdm}}}{4\pi q^2}\delta(q - ap_{\text{max}}). \quad (3.17)$$

Here  $\bar{N}_{\text{dcdm}} = a^3\bar{\rho}_{\text{dcdm}}/m_{\text{dcdm}}$  denotes the mean value of the DCDM comoving number density. From Eq. (3.16), one sees that it evolves as  $\bar{N}_{\text{dcdm}} = (\Omega_{\text{dcdm}}^{\text{ini}}\rho_c/m_{\text{dcdm}})e^{-\Gamma t}$ <sup>4</sup>. By combining Eq. (3.10) and Eq. (3.11) with Eq. (3.16) and Eq. (3.17) we obtain:

$$\bar{\rho}'_{\text{dcdm}} = -3\mathcal{H}\bar{\rho}_{\text{dcdm}} - a\Gamma\bar{\rho}_{\text{dcdm}}, \quad (3.18)$$

$$\bar{\rho}'_{\text{dr}} = -4\mathcal{H}\bar{\rho}_{\text{dr}} + \varepsilon a\Gamma\bar{\rho}_{\text{dcdm}}, \quad (3.19)$$

$$\bar{\rho}'_{\text{wdm}} = -3(1+w)\mathcal{H}\bar{\rho}_{\text{wdm}} + (1-\varepsilon)a\Gamma\bar{\rho}_{\text{dcdm}}. \quad (3.20)$$

Here  $w(\tau) \equiv \bar{P}_{\text{wdm}}/\bar{\rho}_{\text{wdm}}$  refers to the WDM Equation of State<sup>5</sup>. We give a proof of Eq. (3.20) in App. D.2.

Eq. (3.20) will be useful to analytically derive the fluid equations that we present in Section Sect. 3.2.3, but for a numerical resolution it is much simpler to use an integral formula for  $\bar{\rho}_{\text{wdm}}$ , as it was done in BLACKADDER et al. (2014). This formula can be obtained by integrating Eq. (3.17) firstly with respect to  $\tau$ , and then with respect to  $q$ . The first integration requires using the relation  $\delta(q - ap_{\text{max}}) = \delta(\tau - \tau_q)/q\mathcal{H}$ , where  $\tau_q$  represents the conformal time when daughter particles with co-moving momentum  $q$  are born,  $q = a(\tau_q)p_{\text{max}}$  (AOYAMA et al. 2014). This yields

$$\bar{f}_{\text{wdm}}(\tau, q) = \frac{a_q\Gamma\bar{N}_{\text{dcdm}}(\tau_q)}{4\pi q^3\mathcal{H}_q}\Theta(\tau - \tau_q). \quad (3.21)$$

where  $a_q = a(\tau_q)$  and  $\mathcal{H}_q \equiv \mathcal{H}(a_q)$ . Now, we can obtain an expression for  $\bar{\rho}_{\text{wdm}}$  by taking the integral  $4\pi a^{-4}\int_0^\infty dq q^2\mathcal{E}_{\text{wdm}}$  at each side of the equation. Then, changing the integration variable from  $q$  to  $a_q$ , and applying the Heaviside function  $\Theta(a - a_q)$  leads to

$$\bar{\rho}_{\text{wdm}}(a) = \frac{\rho_c\Omega_{\text{dcdm}}^{\text{ini}}\Gamma}{a^4}\int_0^a da_q \frac{e^{-\Gamma t_q}}{\mathcal{H}_q}\sqrt{\varepsilon^2 a_q^2 + (1-2\varepsilon)a^2}, \quad (3.22)$$

where  $t_q \equiv t(a_q)$ . We note the equivalence between Eq. (3.22) and the analogous expression derived in BLACKADDER et al. (2014) with a different formalism. Concerning

<sup>4</sup>The initial abundance of DCDM,  $\Omega_{\text{dcdm}}^{\text{ini}}$ , is related to the present DCDM abundance by  $\Omega_{\text{dcdm}}^0 \equiv \Omega_{\text{dcdm}}^{\text{ini}}e^{-\Gamma t_0}$ , with  $t_0$  the age of the universe.

<sup>5</sup>This expression does not coincide with the EoS used in BLACKADDER et al. (2014), which regarded it as an average squared velocity.

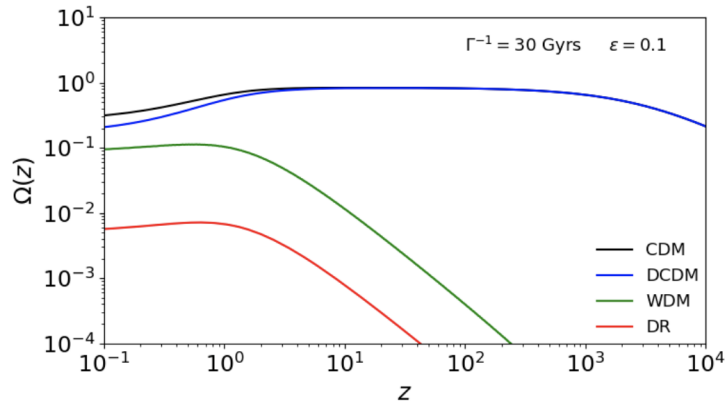


**Figure 3.1** – Redshift evolution of the abundances of the DCDM, WDM and DR species, assuming  $\Gamma^{-1} = 30$  Gyrs and  $\varepsilon = 0.1$ . We also show the abundance for a standard CDM species with  $\Omega_{\text{cdm}}^0 = \Omega_{\text{dcdm}}^{\text{ini}}$ .

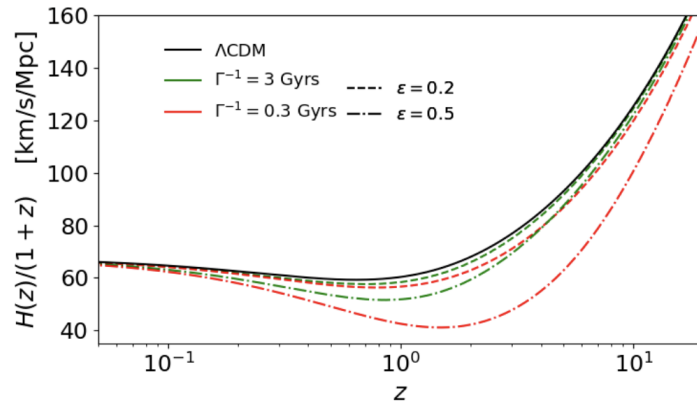


**Figure 3.2** – Redshift evolution of the Hubble parameter for the  $\Lambda$ CDM and four different  $\Lambda$ DDM models. The Hubble parameter today is fixed to  $H_0 = 67.7$  km/s/Mpc.

the mean energy density of the massless DR species,  $\bar{\rho}_{\text{dr}}$ , we simply take the limit  $\varepsilon \rightarrow 1/2$  of Eq. (3.22).

In both cases, the background evolution Eq. (3.22) needs to be solved iteratively, as the Hubble parameter  $\mathcal{H}$  depends on  $\bar{\rho}_{\text{wdm}}$  and  $\bar{\rho}_{\text{dr}}$  through the Friedmann equation. For a flat universe, this equation reads

$$\mathcal{H}^2(a) = \frac{8\pi G a^2}{3} \sum_i \bar{\rho}_i(a), \quad (3.23)$$

where

$$\sum_i \bar{\rho}_i(a) = \bar{\rho}_{\text{dcdm}}(a) + \bar{\rho}_{\text{dr}}(a) + \bar{\rho}_{\text{wdm}}(a) + \bar{\rho}_\gamma(a) + \bar{\rho}_\nu(a) + \bar{\rho}_b(a) + \bar{\rho}_\Lambda. \quad (3.24)$$

Here  $\bar{\rho}_\gamma$ ,  $\bar{\rho}_\nu$ ,  $\bar{\rho}_b$  and  $\bar{\rho}_\Lambda$  denote the mean densities of photons, neutrinos, baryons and dark energy, respectively.

In Fig. 3.2, we show the evolution of the Hubble parameter for  $\Lambda$ CDM and several  $\Lambda$ DDM models. In Fig. 3.1, we also show the evolution of the fractional densities  $\Omega_{\text{dcdm}}(z)$ ,  $\Omega_{\text{wdm}}(z)$  and  $\Omega_{\text{dr}}(z)$  for a particular  $\Lambda$ DDM model ( $\Gamma^{-1} = 30$  Gyrs and  $\varepsilon = 0.1$ )

as well as  $\Omega_{\text{cdm}}(z)$  with the same initial amount of dark matter, namely  $\Omega_{\text{cdm}}^0 = \Omega_{\text{dcdm}}^{\text{ini}}$ . The two new parameters affect  $\mathcal{H}(a)$  as follows: at fixed  $\varepsilon$ , a shorter lifetime  $\Gamma^{-1}$  implies a lower Hubble parameter. This is clearly visible at  $z \gtrsim 1$ . The behavior below  $z \sim 1$  is due to our assumption of a flat universe and the requirement of fixing  $H_0$ : to fulfill the budget equation, a lower DM abundance requires a larger  $\Omega_\Lambda$ , meaning that the period of accelerated expansion begins earlier with respect to  $\Lambda$ CDM. At fixed lifetime  $\Gamma^{-1}$ , a larger  $\varepsilon$  also induces a lower  $\mathcal{H}(a)$ , because more energy is converted into radiation, which dilutes faster. We thus anticipate a negative correlation between  $\Gamma^{-1}$  and  $\varepsilon$  at the background level. The degeneracy can be captured by the matter contribution from the WDM species,  $\Omega_{\text{wdm}}^{\text{m}} \equiv \Omega_{\text{wdm}}^0(1 - 3w)$ , which is well constrained by data. This quantity is roughly approximated by <sup>6</sup>

$$\Omega_{\text{wdm}}^{\text{m}} \simeq \Omega_{\text{dcdm}}^{\text{ini}}(1 - e^{-\Gamma t_0})\sqrt{1 - 2\varepsilon}, \quad (3.25)$$

For small  $\Gamma$  and small  $\varepsilon$ ,  $\Omega_{\text{wdm}}^{\text{m}} \propto \Gamma(1 - \varepsilon)$  and we expect data to constrain a parameter combination of the form  $\varepsilon \propto \Gamma^{-1}$ .

### 3.2.2 Linear perturbation equations

The continuity and the Euler equations for the DCDM can be obtained by integrating over momenta the first two multipoles ( $\Delta f_{\text{dcdm},0}$  and  $\Delta f_{\text{dcdm},1}$ ) of the Boltzmann equation in Eq. (3.4). The calculation is analogous to one we have done in App. A.6 to arrive at the conservation equations for massive neutrinos. The main differences is that we have to take into account the fact that DCDM is pressureless and has a non-zero collision term associated to the decay. When rewriting the equations for  $\delta\rho_{\text{dcdm}}$  and  $\bar{\rho}_{\text{dcdm}}\theta_{\text{dcdm}}$  as equations for  $\delta_{\text{dcdm}}$  and  $\theta_{\text{dcdm}}$  (respectively), the decay terms coming from the background and perturbed equations cancel out and we are left with the same equations as for CDM (*c.f.* Eq. (1.219)-Eq. (1.220)):

$$\delta'_{\text{dcdm}} = -\frac{h'}{2}, \quad (3.26)$$

$$\theta'_{\text{dcdm}} = -\mathcal{H}\theta_{\text{dcdm}}. \quad (3.27)$$

Given our gauge choice,  $\theta_{\text{dcdm}}^{\text{ini}} = 0$ , so we can set  $\theta_{\text{dcdm}} = 0$  at all times. Let us recall that, strictly speaking, the synchronous gauge in **CLASS** (BLAS et al. 2011) is coded with respect to the CDM. Nevertheless, for adiabatic initial conditions, one can choose  $\theta_{\text{ini,dcdm}} = \theta_{\text{ini,cdm}} = 0$ , such that the gauge co-moving with CDM is also co-moving with DCDM at all times (AUDREN et al. 2014). Hence, hereinafter we neglect this irrelevant complication.

To obtain the dynamical equations for the daughter particles, we plug the Legendre decomposition of Eq. (3.9) in the Boltzmann equation of Eq. (3.4), so that we have the following hierarchy of equations

<sup>6</sup>One can arrive at this expression simply by taking the limit  $\varepsilon \ll 1$  in Eq. (3.22) and then performing the integral analytically noticing that  $da_q/\mathcal{H}_q = dt_q$ .

$$\frac{\partial(\Delta f_{I,0})}{\partial\tau} = -\frac{qk}{\mathcal{E}_I}\Delta f_{I,1} + q\frac{\partial\bar{f}_I}{\partial q}\frac{h'}{6} + \frac{a\Gamma\bar{N}_{\text{dcdm}}}{4\pi q^2}\delta(q - ap_{\text{max}})\delta_{\text{dcdm}}, \quad (3.28)$$

$$\frac{\partial(\Delta f_{I,1})}{\partial\tau} = \frac{qk}{3\mathcal{E}_I}[\Delta f_{I,0} - 2\Delta f_{I,2}], \quad (3.29)$$

$$\frac{\partial(\Delta f_{I,2})}{\partial\tau} = \frac{qk}{5\mathcal{E}_I}[2\Delta f_{I,1} - 3\Delta f_{I,3}] - q\frac{\partial\bar{f}_I}{\partial q}\frac{(h' + 6\eta')}{15}, \quad (3.30)$$

$$\frac{\partial(\Delta f_{I,\ell})}{\partial\tau} = \frac{qk}{(2\ell + 1)\mathcal{E}_I}[\ell\Delta f_{I,\ell-1} - (\ell + 1)\Delta f_{I,\ell+1}] \quad (\ell \geq 3), \quad (3.31)$$

where  $I = \{\text{dr}, \text{wdm}\}$ . The system of Eq. (3.28)-Eq. (3.31) is in the same form as the one for massive neutrinos (MA et al. 1995), except for the last term in Eq. (3.28) and the fact that the partial derivative  $\partial\bar{f}_I/\partial q$  in Eq. (3.28) and Eq. (3.30) is now time-dependent.

Given that the DR species satisfies the condition  $q/\mathcal{E}_{\text{dr}} = 1$ , the hierarchy of equations can be simplified by taking the moments <sup>7</sup>

$$F_{\text{dr},\ell} \equiv \frac{1}{\rho_c} \int_0^\infty dq 4\pi q^2 q \Delta f_{\text{dr},\ell} \quad (3.32)$$

of Eq. (3.28)-Eq. (3.31), and integrating over all the momentum degrees of freedom, so that

$$F'_{\text{dr},0} = -kF_{\text{dr},1} - \frac{2}{3}r_{\text{dr}}h' + r'_{\text{dr}}\delta_{\text{dcdm}}, \quad (3.33)$$

$$F'_{\text{dr},1} = \frac{k}{3}F_{\text{dr},0} - \frac{2k}{3}F_{\text{dr},2}, \quad (3.34)$$

$$F'_{\text{dr},2} = \frac{2k}{5}F_{\text{dr},1} - \frac{3k}{5}F_{\text{dr},3} + \frac{4}{15}r_{\text{dr}}(h' + 6\eta'), \quad (3.35)$$

$$F'_{\text{dr},\ell} = \frac{k}{(2\ell + 1)}[\ell F_{\text{dr},\ell-1} - (\ell + 1)F_{\text{dr},\ell+1}] \quad (\ell \geq 3). \quad (3.36)$$

We have adopted the convention  $r_{\text{dr}} \equiv a^4\bar{\rho}_{\text{dr}}/\rho_c$ , as in POULIN et al. (2016), which in the 2-body decay scenario under study leads to:

$$r'_{\text{dr}} = \varepsilon a\Gamma(\bar{\rho}_{\text{dcdm}}/\bar{\rho}_{\text{dr}})r_{\text{dr}}. \quad (3.37)$$

The first three multipoles are given by:

$$F_{\text{dr},0} = r_{\text{dr}}\delta_{\text{dr}}, \quad F_{\text{dr},1} = \frac{4r_{\text{dr}}}{3k}\theta_{\text{dr}}, \quad F_{\text{dr},2} = 2\sigma_{\text{dr}}r_{\text{dr}}. \quad (3.38)$$

We choose the maximum multipole  $\ell_{\text{max}}$  to truncate the hierarchies of equations according to the scheme proposed in MA et al. (1995) for both massless and massive neutrinos, *i.e.*

$$F'_{\text{dr},\ell_{\text{max}}} = kF_{\text{dr},\ell_{\text{max}}-1} - \frac{\ell_{\text{max}} + 1}{\tau}F_{\text{dr},\ell_{\text{max}}}, \quad (3.39)$$

$$\Delta f'_{\text{wdm},\ell_{\text{max}}} = \frac{qk\Delta f_{\text{wdm},\ell_{\text{max}}-1}}{\mathcal{E}_{\text{wdm}}} - \frac{\ell_{\text{max}} + 1}{\tau}\Delta f_{\text{wdm},\ell_{\text{max}}}. \quad (3.40)$$

<sup>7</sup>Even if the momentum degrees of freedom are integrated out, we can not write equations in terms of temperature multipoles as we did for photons in Sect. 1.6.2, since the DR species are never in thermal equilibrium.



### 3.2.3 Fluid approximation for the warm component

In order to compute the WDM dynamics one cannot integrate over the momentum degrees of freedom, as we did in the DR case. Indeed, when taking the moments of the hierarchy of Eq. (3.28)-Eq. (3.31), higher velocity-weight integrals appearing at  $\ell = 2$  cannot be computed from the system of equations itself. Therefore, one has to follow the evolution of the full time-dependent PSD to obtain the elements of the perturbed stress-energy tensor  $\delta_{\text{wdm}}$ ,  $\theta_{\text{wdm}}$  and  $\sigma_{\text{wdm}}$  through Eq. (3.12)-Eq. (3.15). A typical set-up for CMB analyses requires roughly  $\sim 500$  wavenumbers,  $\sim 20$  multipoles and  $\sim 10^4$  momentum bins, i.e.  $\mathcal{O}(10^8)$  linear differential equations to be computed. On a single processor, this leads to runs with a CPU time of 1 – 2 days per each parameter choice, making a systematic scan of the parameter space computationally prohibitive.

To overcome the problem, we make use of a new fluid approximation for the WDM species, where the momentum dependence is removed, and one only needs to track the evolution of the first two multipoles. The number of linear differential equations to be solved is now reduced to  $\mathcal{O}(10^3)$ , with a CPU time per single run  $\sim 30 - 40$  s. The novel approximation scheme is based on the treatment of massive neutrinos as a viscous fluid by LESGOURGUES et al. (2011), and it is only valid at scales deeply inside the Hubble radius, where high- and low- $\ell$  modes are effectively decoupled. In App. D.4 we explicitly demonstrate the accuracy of this approximation.

Similarly to the DR case, the fluid equations can be derived by multiplying both sides of Eq. (3.28) and Eq. (3.29) by  $4\pi q^2 \mathcal{E}_{\text{wdm}} a^{-4}$  and  $4\pi q^3 k a^{-4}$ , respectively, and integrating over  $q$ . Then, by using Eq. (3.12)-Eq. (3.15) and Eq. (3.20), one can write down the continuity equation,

$$\delta'_{\text{wdm}} = -3\mathcal{H}(c_s^2 - w)\delta_{\text{wdm}} - (1 + w) \left( \theta_{\text{wdm}} + \frac{h'}{2} \right) + (1 - \varepsilon) a \Gamma \frac{\bar{\rho}_{\text{dcdm}}}{\bar{\rho}_{\text{wdm}}} (\delta_{\text{dcdm}} - \delta_{\text{wdm}}), \quad (3.41)$$

and the Euler equation,

$$\theta'_{\text{wdm}} = -\mathcal{H}(1 - 3c_g^2)\theta_{\text{wdm}} + \frac{c_s^2}{1 + w} k^2 \delta_{\text{wdm}} - k^2 \sigma_{\text{wdm}} - (1 - \varepsilon) a \Gamma \frac{1 + c_g^2}{1 + w} \frac{\bar{\rho}_{\text{dcdm}}}{\bar{\rho}_{\text{wdm}}} \theta_{\text{wdm}}. \quad (3.42)$$

Notice that we have introduced the WDM sound speed in the synchronous gauge,  $c_s^2 \equiv \delta P_{\text{wdm}} / \delta \rho_{\text{wdm}}$ , and the WDM adiabatic sound speed,  $c_g^2 \equiv \bar{P}'_{\text{wdm}} / \bar{\rho}'_{\text{wdm}}$ . The latter can be written as

$$c_g^2 = w \frac{\bar{P}'_{\text{wdm}}}{\bar{P}_{\text{wdm}}} \left( \frac{\bar{\rho}'_{\text{wdm}}}{\bar{\rho}_{\text{wdm}}} \right)^{-1}, \quad (3.43)$$

and it can be computed as follows

$$c_g^2 = w \left( 5 - \frac{\mathfrak{p}_{\text{wdm}}}{\bar{P}_{\text{wdm}}} - \frac{\bar{\rho}_{\text{dcdm}}}{\bar{\rho}_{\text{wdm}}} \frac{a\Gamma}{3w\mathcal{H}} \frac{\varepsilon^2}{1 - \varepsilon} \right) \left( 3(1 + w) - \frac{\bar{\rho}_{\text{dcdm}}}{\bar{\rho}_{\text{wdm}}} \frac{a\Gamma}{\mathcal{H}} (1 - \varepsilon) \right)^{-1}. \quad (3.44)$$

Here  $\mathfrak{p}_{\text{wdm}}$  denotes the so-called pseudo-pressure, a higher momenta integral of  $\bar{f}_{\text{wdm}}$  which reduces to the standard pressure in the relativistic limit (LESGOURGUES et al. 2011). Taking the relativistic limit of Eq. (3.41) and Eq. (3.42) and multiplying the decay terms by 2 (to account for the decay into two massless particles), we recover the conservation equations for DR written in POULIN et al. (2016). We give a complete

proof of Eq. (3.41)-Eq. (3.44) in App. D.3.

Obtaining an analytical expression for  $c_s^2$  is less straightforward, since we do not have a dynamical equation for the pressure perturbation  $\delta P_{\text{wdm}}$ . In LESGOURGUES et al. (2011) it is assumed that  $c_s^2$  is scale-independent and approximately equal to  $c_g^2$ . For the WDM species, we have found that this assumption leads to accurate results for the CMB power spectrum, but not for the matter power spectrum. In fact, calculations using the full Boltzmann hierarchy of Eq. (3.28)-Eq. (3.31) reveal that  $c_s^2$  exhibits a particular  $k$ -dependence that cannot be captured by a background quantity such as  $c_g^2$ . In particular,  $c_s^2$  gets slightly enhanced on scales  $k > k_{\text{fs}}$ , where  $k_{\text{fs}}$  is the free-streaming scale of the WDM species, defined as (c.f. Eq. (1.224))

$$k_{\text{fs}}(\tau) \equiv \sqrt{\frac{3}{2}} \frac{\mathcal{H}(\tau)}{c_g(\tau)}. \quad (3.45)$$

It is possible to gain a semi-analytic understanding of this behavior by building a formal equation for the evolution of  $c_s^2$ , as detailed in App. D.3.5. To account for such an enhancement, we adopt the following prescription

$$c_s^2(k, \tau) = c_g^2(\tau) [1 + (1 - 2\varepsilon)T(k/k_{\text{fs}})], \quad (3.46)$$

where the function  $T(x) = 0.2\sqrt{x}$  has been fitted to the sound speed obtained using the full Boltzmann hierarchy, for the parameter values  $\varepsilon = 0.5, 0.1, 0.01, 0.001$  and  $\Gamma/H_0 = 0.1, 1, 10$ . The factor  $(1 - 2\varepsilon)$  is inserted to make the  $k$ -dependent correction vanishingly small close to the relativistic limit, where  $c_s^2 \simeq c_g^2 \simeq 1/3$ .

In order to trace the evolution of the shear  $\sigma_{\text{wdm}}$  one could follow a similar approach to that of LESGOURGUES et al. (2011), where the authors obtained a dynamical equation for the neutrino shear by means of an improved truncation scheme at  $\ell_{\text{max}} = 2$ . We tested the implementation of a generalization of that equation suitable to the decaying case (which can be found in App. D.3), but we found it to be only relevant close to the relativistic case  $\varepsilon \simeq 1/2$ , when it reduces to the DR shear equation from ENQVIST et al. (2015). In this regime, the dynamics of the daughter particles do not significantly impact the CMB and matter power spectra, we thus decided to not include any dynamical equation for the shear of the WDM species, when switching to the fluid approximation. In practice, we simply set  $\sigma_{\text{wdm}}$  to a constant value, obtained via integration of the second PSD multipole in the Boltzmann hierarchy (see Eq. (3.15)). We explicitly checked that this approach yields better results rather than simply setting  $\sigma_{\text{wdm}} = 0$  in the fluid equations, or than using the DR shear equation of ENQVIST et al. (2015) when  $\varepsilon = 1/2$ .

### 3.2.4 Dynamics of perturbations

Before discussing the signatures of varying the parameters  $\Gamma$  and  $\varepsilon$  on the relevant cosmological observables, it is worth having a look at the linear perturbations of the mother and daughter particles. In Fig. 3.3 we show the evolution of the linear density perturbations for the  $\Lambda$ CDM, WDM and DR species, corresponding to a mode that enters the horizon very early (i.e.  $k = 1 \text{ Mpc}^{-1}$ ). To clarify the impact of the two extra free parameters, the perturbations are shown for  $\Lambda$ CDM lifetimes similar and smaller than the age of the universe ( $\Gamma^{-1} = H_0^{-1} \sim 14.5 \text{ Gyrs}$  and  $\Gamma^{-1} = (10H_0)^{-1} \sim 1.5 \text{ Gyrs}$ ), and for massive daughters behaving either as warm or cold particles ( $\varepsilon = 10^{-2}$  and

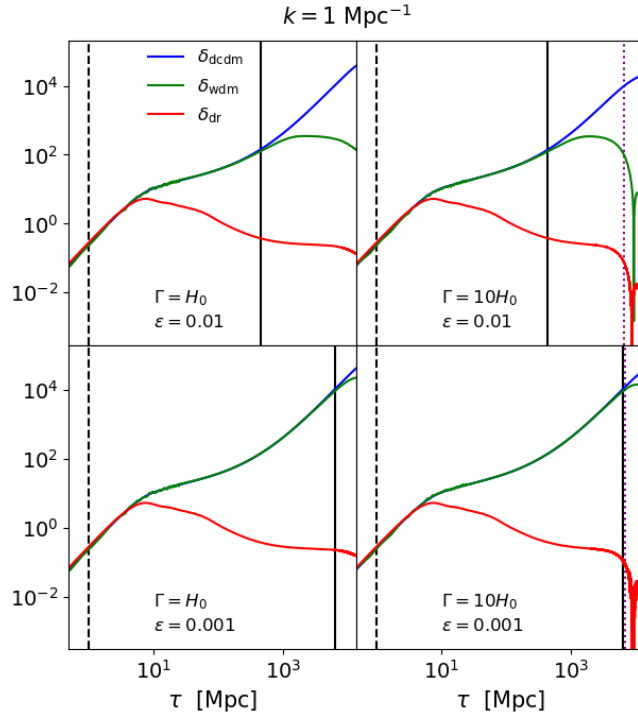


**Figure 3.3** – Time evolution of the linear density perturbations of the DCDM, WDM and DR species, corresponding to a wavenumber  $k = 1 \text{ Mpc}^{-1}$ . Each panel displays the perturbations for a different combination of the parameters  $\Gamma$  and  $\varepsilon$ . The black dashed and solid lines indicate the times of horizon crossing (at  $\mathcal{H}(\tau) = k$ ) and WDM free-streaming scale crossing (at  $k_{\text{fs}}(\tau) = k$ ), respectively. The purple dotted line indicates the characteristic decay time, given by  $t(\tau) = \Gamma^{-1}$ .

$\varepsilon = 10^{-3}$ ).

One can see that initially, the perturbations of the daughter species always track those of the mother, because the coupling term dominates the dynamics (*i.e.* the ratios  $\rho_{\text{dcdm}}/\rho_{\text{wdm}}$  and  $\rho_{\text{dcdm}}/\rho_{\text{dr}}$  are large). When a mode crosses the free-streaming scale, the pressure support of the daughter particles becomes important and the perturbations develop oscillatory features. For the DR species, the free-streaming scale simply corresponds to the horizon ( $k_{\text{fs}} \sim \mathcal{H}$ ), while for the WDM it corresponds to a larger value, given by  $k_{\text{fs}} \sim \mathcal{H}/c_g$  (see Eq. (3.45)). This time- and scale-dependent power suppression, together with the different background dynamics, lead to key signatures on the CMB and matter power spectra, as we discuss later.

By comparing upper and lower panels of Fig. 3.3, it is clear that the value of the WDM free-streaming scale is essentially determined by the value of  $\varepsilon$ , as expected. On the other hand, by comparing left and right panels, one notices that the intensity of the oscillations due to the pressure support can be compensated by the coupling to the DCDM if the lifetime is long enough, as the daughter particles keep being produced.

Interestingly, the decoupling time of the daughter perturbations from the mother perturbations is always set by the free-streaming crossing time, and not by the characteristic decay time. In order to illustrate that, in Fig. 3.4 we show perturbations corresponding to a smaller wave-number,  $k = 10^{-2} \text{ Mpc}^{-1}$ , that enters the horizon

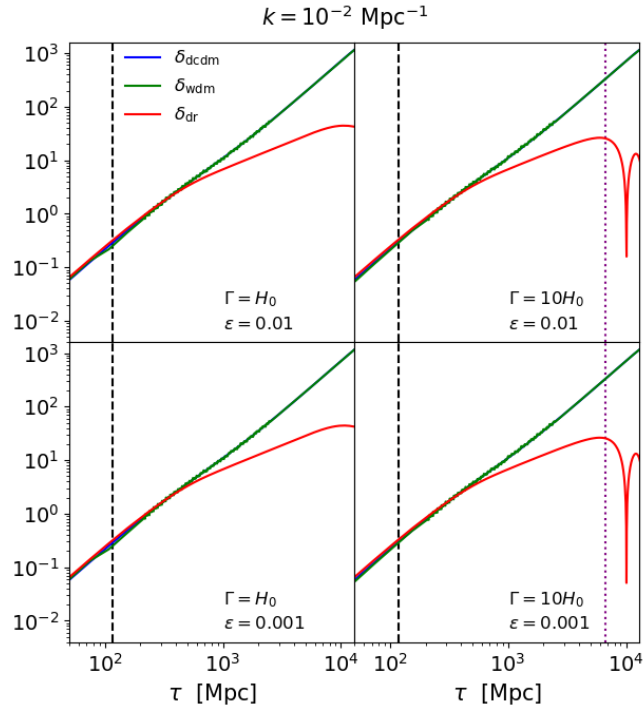


**Figure 3.4** – Same as in Fig. 3.3, but corresponding to a wavenumber  $k = 10^{-2} \text{ Mpc}^{-1}$ . In this case, the WDM perturbations never cross the free-streaming scale.

much later. For this mode, the WDM species does not have time to cross the free-streaming length (the crossing will occur in the future), so that  $\delta_{\text{dcdm}}$  and  $\delta_{\text{wdm}}$  remain equal, even if the lifetime is smaller than the age of the universe. This can be understood from the fluid description in Eq. (3.41)-Eq. (3.42): when the decay term that includes  $\Gamma$  is relevant,  $\delta_{\text{wdm}}$  is driven by  $\delta_{\text{dcdm}}$ . Therefore, the WDM density perturbation  $\delta_{\text{wdm}}$  will continue to track the behaviour of  $\delta_{\text{dcdm}}$ , as long as the free-streaming scale is not crossed, *i.e.*, as long as the pressure term, containing  $c_s^2 k^2 \delta_{\text{wdm}}$ , is small compared to  $\delta_{\text{wdm}}'' \sim \delta_{\text{wdm}} \mathcal{H}^2$ .

### 3.3 Observable effects of the Dark Matter decay

#### 3.3.1 Impact on the matter power spectrum

Firstly, we focus on describing the effects of the 2-body decay on the linear matter power spectrum, since this will allow to better understand some of the effects on the CMB spectra. In this section, we use the same  $\Lambda$ CDM parameters as in Sect. 3.2.1, except for fixing  $100\theta_s = 1.04217$  instead of  $H_0$ , to better connect with CMB observations, that accurately pin down  $\theta_s$ . In Fig. 3.5, we compare the residual differences in the linear power spectra (at redshifts  $z = 0$  and  $z = 2$ ) with respect to our baseline  $\Lambda$ CDM. The left panel shows several lifetimes and a fixed DR energy fraction  $\varepsilon = 0.1$ , while the right panel shows a fixed lifetime  $\Gamma^{-1} = 30 \text{ Gyrs}$  and several values of the DR energy fraction  $\varepsilon$ .

One important feature of the C+WDM scenarios, such as the one considered in this work, is that they are expected to produce a suppression in the linear matter power spectrum at scales smaller than a ‘cutoff scale’, with a non-trivial shape

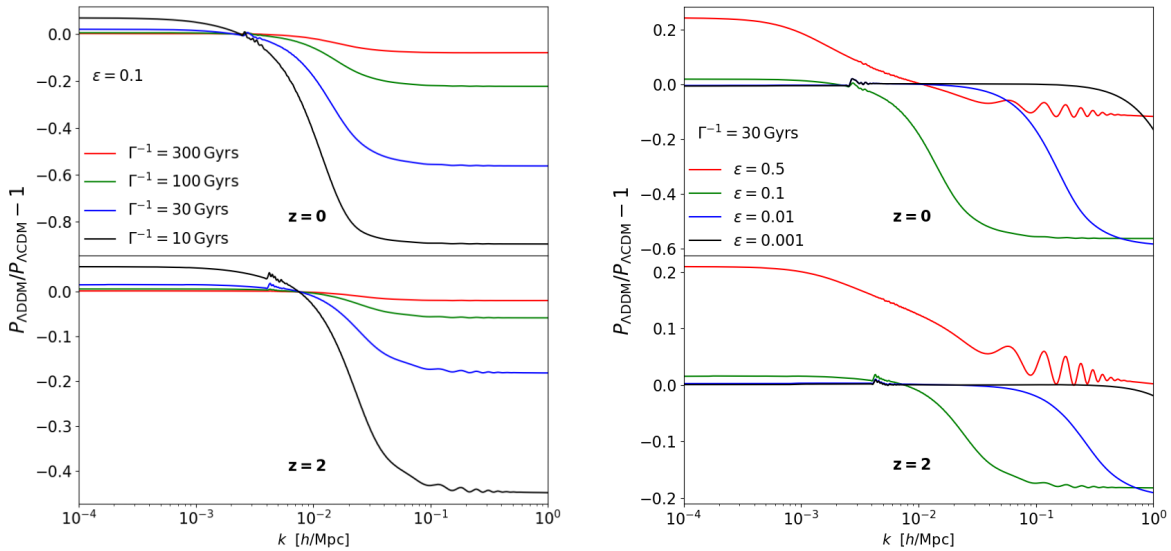


**Figure 3.5 – Left panel:** Residuals of the linear matter power spectrum at  $z = 0$  (upper) and  $z = 2$  (lower) for several values of the lifetime  $\Gamma^{-1} = 10, 30, 100, 300$  Gyrs and a fixed DR energy fraction  $\varepsilon = 0.1$ . Residuals are taken with respect our baseline  $\Lambda$ CDM model. **Right panel:** Same as in the left, but for several DR energy fractions  $\varepsilon = 0.5, 0.1, 0.01, 0.001$  and a fixed lifetime  $\Gamma^{-1} = 30$  Gyrs.

(MURGIA et al. 2017, 2018; MILLER et al. 2019; BOHR et al. 2020). The cut-off scale is determined by the free-streaming scale of the WDM species,  $k_{\text{fs}}$ , given by Eq. (3.45). On scales  $k > k_{\text{fs}}$ , pressure becomes important and WDM particles cannot stay confined in gravitational potential wells, which inhibits structure formation. Fig. 3.5 clearly illustrates that: while the parameter  $\varepsilon$  fixes the value of the cut-off  $k_{\text{fs}}$ <sup>8</sup>, the lifetime  $\Gamma^{-1}$  essentially determines the depth of the suppression at very small scales. This is to be expected, since the amount of power suppression grows with the WDM abundance, which increase for smaller lifetimes. In a similar way, the effects of decay become less important when considering the matter spectrum at a higher redshift  $z = 2$ , since the abundance of WDM was smaller in the past.

In general, for late-time decay scenarios (well after recombination) as the one studied in this work, it is possible to distinguish three different regimes depending on the value of  $\varepsilon$ , as it is shown in the right panel of Fig. 3.5:

- **Non-relativistic decay:** if  $\varepsilon \lesssim 0.001$  (black curve), the WDM leaves the expansion rate unaffected, since its contribution to the matter density,  $\bar{\rho}_{\text{wdm}}(1 - 3\omega) \simeq \bar{\rho}_{\text{wdm}}$ , compensates the reduction in the DCDM density,  $\bar{\rho}_{\text{cdm}}$ . In addition, the WDM free-streaming length is very small, inducing a power suppression at  $k \gtrsim 1 \text{ hMpc}^{-1}$ . Such scales are beyond the range of scales probed by the observables considered in this work, so in this regime the WDM is almost degenerate with standard CDM.

<sup>8</sup>By looking at Eq. (3.44) and Eq. (3.45), we see that for small values of  $\varepsilon$ , the cut-off approximately satisfies the scalings  $k_{\text{fs}} \propto c_g^{-1} \propto w^{-1/2} \propto \varepsilon^{-1}$ .

- **Relativistic decay:** if  $\varepsilon \simeq 0.5$  (red curve), the WDM component acts as DR, which can appreciably reduce the expansion rate<sup>9</sup>. Moreover, the free-streaming length  $k_{\text{fs}}$  gets as large as the horizon, so that the WDM does not cluster at all. The reduction in the Hubble friction is balanced by a reduction in the clustering density of the daughter particles,  $\delta\rho_{\text{wdm}} \simeq \delta\rho_{\text{dr}} \simeq 0$ , inducing a very little overall suppression of the growth of fluctuations. However, there is an impact coming from another background effect: the significant decrease in the co-moving matter density,  $a^3\rho_{\text{m}}$ , leading in turn to an increase of the angular diameter distance, thereby a reduction of  $\theta_s$ . This effect can be compensated by increasing  $H_0$ , which shifts the location of the peak,  $k_{\text{eq}}/(a_0H_0)$ , towards smaller  $k$  in the matter power spectrum – since we are keeping the matter-radiation equality era fixed. The net effect on the residuals is twofold, a large-scale enhancement and small-scale suppression of power.
- **Warm decay:** For intermediate values of  $\varepsilon$ , namely  $0.001 \lesssim \varepsilon \lesssim 0.5$  (green and blue curves), the WDM component partially contributes to the matter energy density, leaving to an expansion rate almost unchanged. However, the values of  $k_{\text{fs}}$  that determine the cut-off scale in the matter power spectrum are not as small as in the case of non-relativistic decay, leading to  $\delta\rho_{\text{wdm}} \simeq 0$  for  $k > k_{\text{fs}}$ . Hence, on scales  $k > k_{\text{fs}}$  the Hubble friction gets enhanced with respect to the clustering density  $\delta\rho_{\text{tot}}$ , slowing down the growth of  $\Lambda$ CDM perturbations. The net impact on the matter power spectrum is thus a suppression on intermediate scales, somewhat similar to that induced by massive active neutrinos (LESGOURGUES et al. 2006; GIUSARMA et al. 2016; PARIMBELLI et al. 2019).

### 3.3.2 Impact on the CMB anisotropy spectra

We now discuss the impact of the 2-body decay scenario on the CMB anisotropy temperature and polarization angular power spectra, as well as on the lensing potential power spectrum reconstructed from the CMB 4-point correlation function. In the left panel of Fig. 3.6 we report the residuals of the (lensed) TT, EE and lensing potential power spectra with respect to our baseline  $\Lambda$ CDM, for different lifetimes  $\Gamma^{-1}$  and a fixed DR energy fraction  $\varepsilon = 0.1$ . The effects, more and more pronounced as the lifetime decreases, can be understood as follows:

- At the background level, the decay decreases the value of  $\Omega_{\text{m}}$  with respect to  $\Lambda$ CDM. This is compensated by an increase in  $\Omega_{\Lambda}$  (earlier beginning of  $\Lambda$ -domination) and thus an enhancement in the Late Integrated Sachs-Wolfe (LISW) effect, leaving a signature in the low- $\ell$  TT power spectrum. Furthermore, a modified background history alters quantities integrated along  $z$ , such as  $\tau_{\text{reio}}$ , which impacts the multipoles  $\ell \sim 10$  in the EE power spectrum.
- At the perturbation level, the late-time reduction of  $a^3\bar{\rho}_{\text{dcdm}}$  implies a reduction of the quantity  $a^2\delta\rho_{\text{dcdm}}$ , which acts as a source of gravity through the Poisson equation. This induces a damping in the metric fluctuations, and hence yields a further enhancement of the LISW effect. Furthermore, the suppression in the matter power spectrum and in  $\Omega_{\text{m}}$  lowers the amplitude of the lensing potential

<sup>9</sup>Note that since now we are fixing  $100\theta_s$  instead of  $H_0$ , the Hubble rate  $H(z)$  can increase with respect to  $\Lambda$ CDM at  $z \lesssim 1$ , once dark energy starts to dominate. However, this effect is small for long lifetimes, and at early times the Hubble rate is still smaller than in  $\Lambda$ CDM.



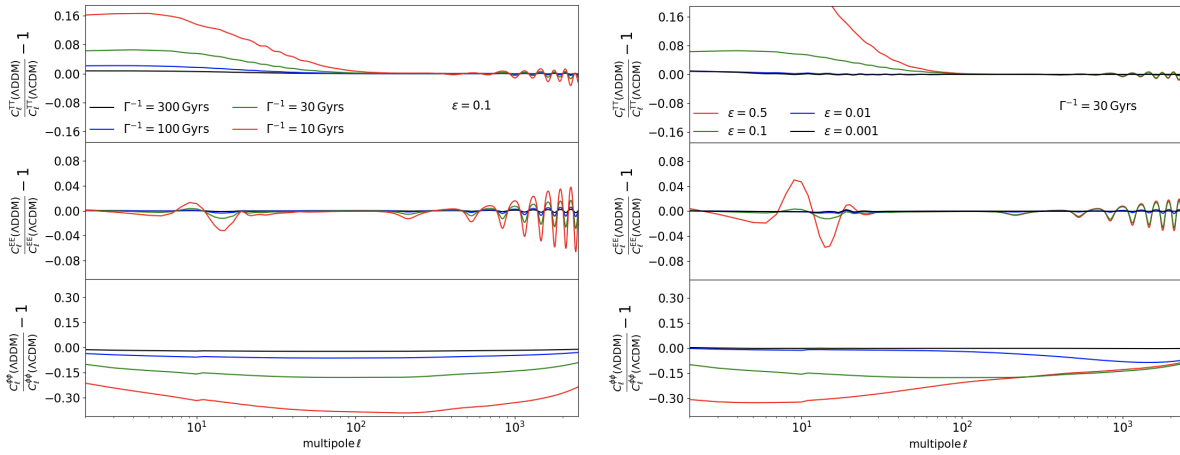


**Figure 3.6 – Left panel:** Residuals (with respect our baseline  $\Lambda$ CDM model) of the CMB lensed TT (upper), EE (middle) and lensing potential (lower) power spectra for several values of the lifetime  $\Gamma^{-1} = 10, 30, 100, 300$  Gyrs and a fixed DR energy fraction  $\varepsilon = 0.1$ . **Right panel:** Same as in the left, but for several values of the DR energy fraction  $\varepsilon = 0.5, 0.1, 0.01, 0.001$  and a fixed lifetime  $\Gamma^{-1} = 30$  Gyrs.

power spectrum, consequently reducing the smoothing of the peaks in the high- $\ell$  part of both the TT and EE spectra, as one can see from the ‘wiggles’ in the corresponding plots.

In the right panel of [Fig. 3.6](#) we show the CMB residuals for a fixed  $\Gamma^{-1}$  and various values of  $\varepsilon$ . The effects can be readily understood:

- At the background level, smaller values of  $\varepsilon$  weaken the effects previously discussed, because the decay product dilute in a way similar to dark matter. Namely, the decrease in  $\Omega_m$  is less prominent due to the significant WDM contribution (*i.e.* the increase in  $\Omega_\Lambda$  is shallower), and the impact on  $\tau_{\text{reio}}$  is smaller. Therefore, the signatures in the low- $\ell$  part of the TT and EE spectra become less visible.
- At the level of perturbations,  $\varepsilon$  leads to some interesting signatures on the LISW effect and on the lensing potential. Since the LISW effect is only relevant for small multipoles  $\ell$  (*i.e.* very large scales), one just needs to look at wavenumbers such that  $k < k_{\text{fs}}$ . On these scales, the growth suppression does not play any role, and the decrease in  $a^2\delta\rho_{\text{dcdm}}$  due to the decay gets partially compensated by the increase in  $a^2\delta\rho_{\text{wdm}}$ , which is more significant for smaller values of  $\varepsilon$ . Thus, the damping in the metric fluctuations is less relevant for smaller  $\varepsilon$ , reducing the LISW enhancement.
- Regarding the effects on the lensing potential, one can see that the suppression in the corresponding power spectrum monotonically decreases for smaller  $\varepsilon$ . Naively, one might expect the opposite, since we have argued that the matter power suppression increases for small  $\varepsilon$ . This can be understood by looking at the CMB lensing kernel  $W(z)$ , given by the following expression ([MANZOTTI 2018](#))

$$W(z) = \frac{3\Omega_m}{2} \frac{H_0^2}{H(z)} (1+z)\chi(z) \frac{\chi_* - \chi(z)}{\chi_*}, \quad (3.47)$$

where  $\chi_*$  is the co-moving distance to the last-scattering surface. Firstly, the CMB lensing kernel peaks at  $z \sim 2$ , where the suppression is less important (see bottom panels of Fig. 3.5). Secondly, it gets highly suppressed for higher values of  $\varepsilon$ , and this effect can dominate over the effect on the matter power spectrum. This suppression happens mainly due to the smaller  $\Omega_m$ , as we have verified by computing  $W(z)$  for several  $\Lambda$ DDM models, with and without including the factor  $\Omega_m$ . Note that coincidentally, the effects on the lensing power spectrum at high  $\ell$  are very similar for  $\varepsilon = 0.5$  and  $\varepsilon = 0.1$ : this is because in the former case  $\Omega_m$  is highly reduced and the small scales power spectrum is almost unaffected, while the opposite occurs in the latter case.

Let us finally remark that, even if the effects of varying either  $\varepsilon$  or  $\Gamma$  on the observables are different, one can easily exploit the degeneracy mentioned at the background level to get different couples of values (large  $\Gamma$  and small  $\varepsilon$  or vice-versa) with a similar cosmological signature, especially on the CMB. We do indeed expect the Monte Carlo analysis to show a negative correlation in the reconstructed 2D posteriors for  $\varepsilon$  and  $\Gamma$ .

### 3.4 Cosmological constraints

We now confront the  $\Lambda$ DDM cosmology to a host of recent cosmological observations. Our goal is to set constraints on the lifetime of DM and the mass-ratio of the mother and daughter particles. We also wish to check to what extent the  $\Lambda$ DDM model can play a role in resolving cosmological tensions. To that end, we perform comprehensive MCMC analyses with the `MontePython-v3` (AUDREN et al. 2013; BRINCKMANN et al. 2019a) code interfaced with our modified version of `CLASS`, considering various combinations of the following data-sets:

- The BAO measurements from 6dFGS at  $z = 0.106$  (BEUTLER et al. 2011), SDSS DR7 at  $z = 0.15$  (ROSS et al. 2015), BOSS DR12 at  $z = 0.38, 0.51$  and  $0.61$  (ALAM et al. 2017), and the joint constraints from eBOSS DR14 Ly- $\alpha$  auto-correlation at  $z = 2.34$  (SAINTE AGATHE et al. 2019) and cross-correlation at  $z = 2.35$  (BLOMQUIST et al. 2019).
- The measurements of the growth function  $f\sigma_8(z)$  (FS) from the CMASS and LOWZ galaxy samples of BOSS DR12 at  $z = 0.38, 0.51$ , and  $0.61$  (ALAM et al. 2017).
- The Pantheon SNIa catalogue, spanning redshifts  $0.01 < z < 2.3$  (SCOLNIC et al. 2018).
- The low- $\ell$  CMB TT, EE, and the high- $\ell$  TT, TE, EE data <sup>10</sup> + the gravitational lensing potential reconstruction from Planck18.
- The KIDS-1000+BOSS+2dFLens (HEYMANS et al. 2021), DES-Y1 (T. M. C. ABBOTT et al. 2018) and KIDS-1000+Viking+DES-Y1 (JOUAKI et al. 2020) weak lensing data, compressed as a split-normal likelihood, *i.e.*,  $S_8 = 0.766^{+0.02}_{-0.014}$ ,  $S_8 = 0.773^{+0.026}_{-0.02}$ ,  $S_8 = 0.755^{+0.019}_{-0.021}$ , respectively.
- The local measurement of the Hubble constant from SHOES <sup>11</sup>, modelled with a Gaussian likelihood centered on  $H_0 = 74.03 \pm 1.42$  km/s/Mpc (RIESS et al. 2019).

<sup>10</sup>In our main analysis, we use the ‘lite’ version of the CLIK likelihood. We have verified that this leads to negligible differences with respect to the full likelihood.

<sup>11</sup>A new version of the SHOES measurement (RIESS et al. 2021a) was published during completion of this work. We do not expect it to have any impact on our conclusions.

We start by performing two distinct sets of studies in order to illustrate the importance of taking CMB data into account when studying the  $\Lambda$ DDM scenarios, even in the long-lived regime (*i.e.* when the DCDM decays after photon decoupling):

- (1) A background-only analysis against BAO <sup>12</sup> and Pantheon SNIa data.
- (2) A full analyses including linear perturbations, where we combine the data-set used in (i) with CMB TT, TE, EE + lensing data, with and without including the aforementioned informative priors on  $S_8$  and  $H_0$ .

In the case of (1), the parameter space is fully characterized by the following free parameters:

$$\left\{ \Omega_{\text{dcdm}}^{\text{ini}}, H_0, \Gamma, \varepsilon \right\},$$

whereas in (2) the whole parameter space is described by:

$$\left\{ \Omega_b h^2, \ln(10^{10} A_s), n_s, \tau_{\text{reio}}, \Omega_{\text{dcdm}}^{\text{ini}}, H_0, \Gamma, \varepsilon \right\}.$$

For both (1) and (2) we adopt logarithmic priors on  $\varepsilon$  and  $\Gamma$  <sup>13</sup>, namely,

$$\begin{aligned} -4 &\leq \text{Log}_{10} \varepsilon \leq \text{Log}_{10}(0.5), \\ -4 &\leq \text{Log}_{10} (\Gamma/\text{Gyrs}^{-1}) \leq 1, \end{aligned}$$

and a flat prior on the initial DCDM abundance:

$$0 \leq \Omega_{\text{dcdm}}^{\text{ini}} \leq 1.$$

Secondly, we explore the possibility of resolving the infamous Hubble and  $S_8$  tensions, and the ‘ $A_{\text{lens}}$ ’ anomaly that exists within *Planck* data. We also briefly discuss the viability of the 2-body decay scenario as solution for the Xenon1T anomaly (APRILE et al. 2020). We then test the robustness of our results to various changes in the pipeline, and in particular to trading the high- $\ell$  *Planck* CMB data for those from the SPT collaboration (HENNING et al. 2018), which are known to be less in tension with local  $S_8$  measurements, as well as ACTPol data (AIOLA et al. 2020), which shows a level of tension with  $S_8$  measurements similar to *Planck*. We end by showing that next-generation CMB observations (CMB-S4) can detect the  $\Lambda$ DDM model.

We adopt flat priors on the rest of parameters, and we set two massless and one massive neutrino species with  $m_\nu = 0.06$  eV, following *Planck18* conventions. We assume our chains to be converged when the Gelman-Rubin criterion  $R - 1 < 0.02$  (GELMAN et al. 1992). To extract the best-fit parameters, we make use of the MINUIT algorithm (JAMES et al. 1975) through the `iMinuit` python package. In App. D.5 we report all individual  $\chi^2$ ’s per each of the analyses performed.

### 3.4.1 General constraints: background vs. linear perturbations

In Fig. 3.7 we show the  $2\sigma$  posterior distributions of the parameters characterizing the  $\Lambda$ DDM model,  $\text{Log}_{10}(\varepsilon)$  and  $\text{Log}_{10}(\Gamma/\text{Gyrs}^{-1})$ . Red contours refer to the

<sup>12</sup>As discussed in Sect. 3.1, we calibrate BAO data by imposing a Gaussian prior on the sound horizon at recombination  $r_s(z_{\text{rec}}) = 144.7 \pm 0.5$  Mpc, to not to spoil CMB data.

<sup>13</sup>For comparisons with previous works, an useful conversion is the following  $\text{Log}_{10}(\Gamma/\text{Gyrs}^{-1}) \simeq \text{Log}_{10}(\Gamma/\text{km s}^{-1}\text{Mpc}^{-1}) - 2.991$ . We also note that the lower limits for the  $\Gamma$  and  $\varepsilon$  priors are simply chosen because we verified that the  $\Lambda$ CDM limit is fully recovered for  $\Gamma < 10^{-4}$  Gyrs $^{-1}$  and  $\varepsilon < 10^{-4}$  (at least for the observables considered in this work).

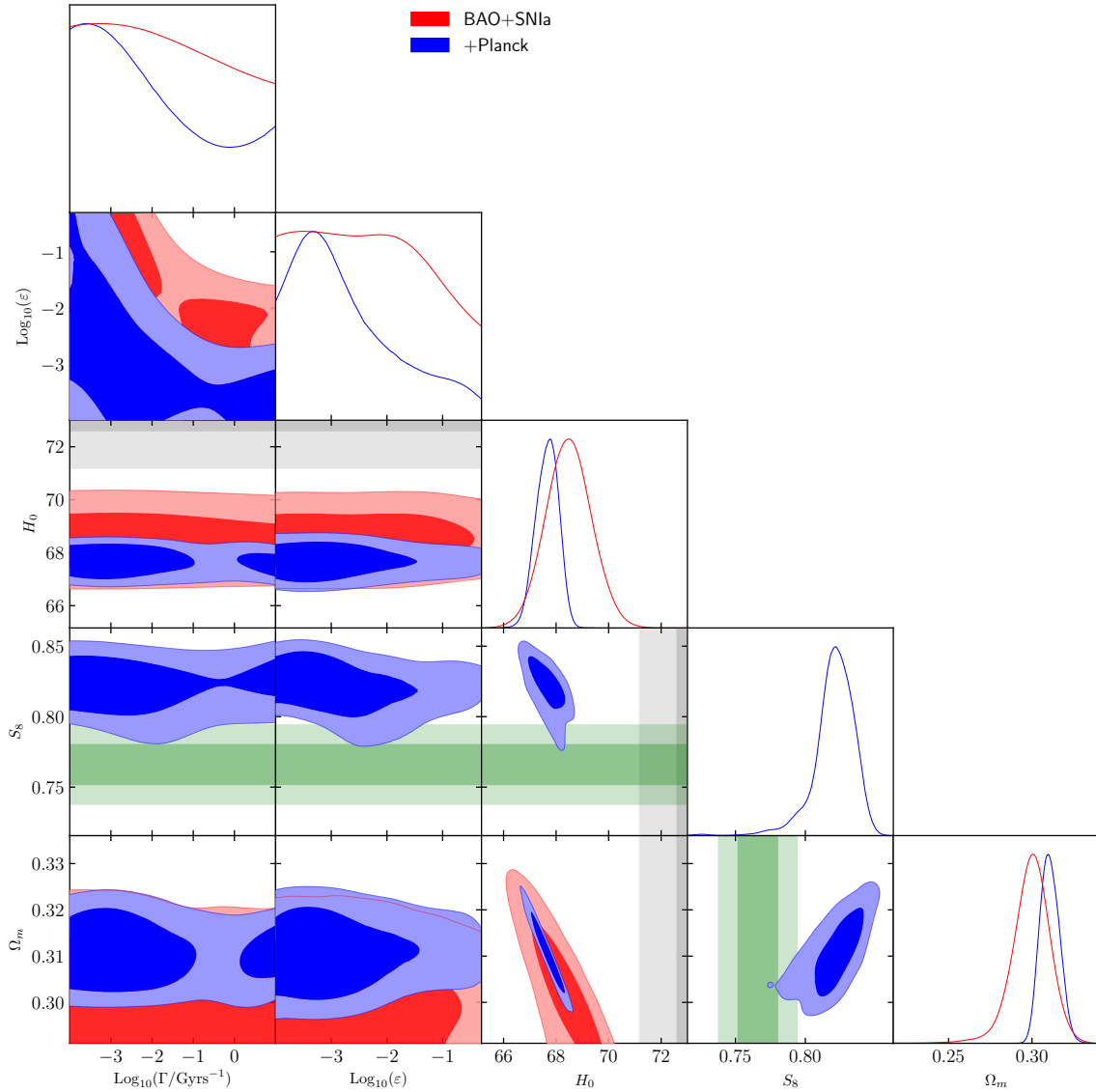


**Figure 3.7** – 1 and 2D marginalized posterior distributions for the cosmological parameters relevant for our analysis. Hereafter, unless otherwise stated, the green shaded bands refer to the joint  $S_8$  measurement from KiDS-1000+BOSS+2dFLens, while the gray bands stand for the  $H_0$  measurement by the SHOES collaboration. Note that the BAO+SNIa analysis is based on background evolution only, whereas the BAO+SNIa+CMB analysis also includes linear perturbations (see the main text for further details).

background-only analysis (1), while blue contours refer to the full analysis (2), at the perturbation level, when CMB data are also added <sup>14</sup>. From BAO+SNIa and *Planck* data, the DDM is not detected. We confirm our expectation from Sect. 3.2.1 and Sect. 3.3 that there is a negative correlation between  $\text{Log}_{10}(\epsilon)$  and  $\text{Log}_{10}(\Gamma/\text{Gyrs}^{-1})$ , apparent within all data sets: as  $\epsilon$  decreases, the 95% C.L. upper limit on  $\Gamma$  relaxes. In practice, we find that for decay rates  $\Gamma \sim 10^{-3} - 10^{-1} \text{Gyrs}^{-1}$ , our  $2\sigma$  exclusion curve is roughly described by  $\epsilon \simeq 1.6 \times 10^{-4} (\Gamma/\text{Gyrs}^{-1})^{-1.1}$ .

<sup>14</sup>The results of the full BAO+SNIa+*Planck* analysis are reported in the third column of Tab. (3.1)

For large  $\Gamma$  and small  $\varepsilon$ , the factor ‘ $1 - e^{-\Gamma t_0}$ ’ in Eq. (3.25) reaches 1 faster than  $\sqrt{1 - 2\varepsilon}$  (assuming  $t_0 \simeq 13.8$  Gyrs), explaining why our constraint on the DR energy fraction becomes flat even for very large decay rates. In particular, for small decay rates  $\text{Log}_{10}(\Gamma/\text{Gyrs}^{-1}) \lesssim -3$  and very massive daughters  $\text{Log}_{10}(\varepsilon) \lesssim -2.7$  the DCDM behaves like CDM, leading to departures indistinguishable from  $\Lambda$ CDM. Of utmost importance, we find that constraints on the  $\Lambda$ DDM free parameters become much stronger when CMB data are included, increasing by more than one order of magnitude over the whole parameter space, contrarily to the naive expectations that CMB data do not weigh-in on late-time decays.

Interestingly, we see that the background-only analysis predicts a value of  $H_0$  slightly higher than the one inferred assumed  $\Lambda$ CDM, though it can be noticed that the standard  $\Lambda$ CDM value for  $H_0$  is still perfectly compatible, due to larger uncertainties with respect to the full analysis, which anyhow pulls  $H_0$  back to its standard value. This suggests that this kind of models is not suitable for relieving the Hubble tension, contrarily to earlier claims (VATTIS et al. 2019), and in agreement with HARIDASU et al. (2020) and CLARK et al. (2021a). However, in contrast to CLARK et al. (2021a), we observe a significant decrease in the  $S_8$  contours for  $\varepsilon \sim 0.01$  and  $\Gamma^{-1} \sim 10^2$  Gyrs. We attribute this disagreement to the fact that CLARK et al. (2021a) does not include a treatment of WDM perturbations, which are responsible for the suppression in the matter power spectrum. Hence, the 2-body decay presented here could potentially reconcile the inferred value of  $S_8$  with its direct measurements from LSS observations. We present an explicit comparison of our constraints with those from CLARK et al. (2021a) in App. D.6.

Finally, in order to compare our constraints on  $\Gamma$  with previous literature, we have carried out a MCMC analysis including BAO + SNIa + *Planck* data, but fixing <sup>15</sup>  $\varepsilon = 0.5$  (*i.e.* in the limit in which the daughter particle behaves as dark radiation). We find a  $2\sigma$  upper limit on the DCDM decay rate of  $\log_{10}(\Gamma/[\text{Gyr}^{-1}]) \lesssim -2.67$ , corresponding to  $\Gamma^{-1} \gtrsim 468$  Gyrs. Our constraints on DM decays to DR are three times tighter than those found in works using older *Planck* data (AUDREN et al. 2014; POULIN et al. 2016) but also  $\sim 40\%$  tighter than NYGAARD et al. (2021) due to the use of a logarithmic prior on  $\Gamma$  as opposed to linear (as we argue in App. D.7, a logarithmic prior is more agnostic because it doesn’t carry any scale).

### 3.4.2 Implications for the $S_8$ tension

So as to quantify the ability of the model to solve the  $S_8$  tension, we have re-conducted the BAO + SNIa + *Planck* analysis for the  $\Lambda$ DDM scenario, but including the  $S_8$  prior as measured by KiDS-1000+BOSS+2dFLens. Note that we neglect the potential co-variance between  $S_8$  and BOSS BAO/FS data for simplicity, and we checked that removing the BAO/FS data from the analysis does not affect the result. To gauge the importance of the late-time decay in the success of the solution, we compare the  $\Lambda$ DDM model with another cosmological scenario that features a power suppression at small scales, namely massive neutrinos ( $\nu\Lambda$ CDM). We model these as three degenerate states and vary the total mass  $M_\nu$ , on top of the standard  $\Lambda$ CDM parameters.

<sup>15</sup>This is not equivalent to directly reading the constraints on  $\Gamma$  at  $\varepsilon = 0.5$  from the  $\Gamma$  vs.  $\varepsilon$  contours, since the 95% C.L. derived from a  $\chi^2$  distribution with different degrees of freedom correspond to different  $\Delta\chi^2$ .

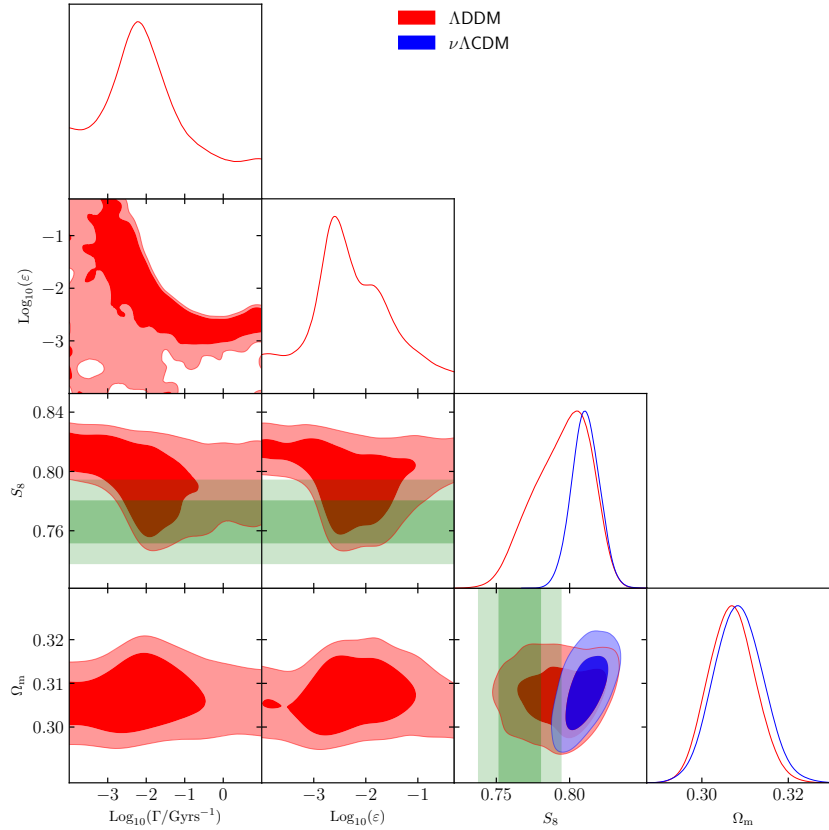


**Figure 3.8** – Reconstructed 2D posterior distributions of a subset of parameters in the  $\Lambda$ DDM and in the  $\nu\Lambda$ CDM models when confronted to BAO + SNIa + *Planck* data and a prior on  $S_8$  from KiDS-1000+BOSS+2dFLens.

We assess the remaining level of tension by computing the  $Q_{\text{DMAP}}$  (for “difference in the maximum a posteriori”) tension metric introduced in [RAVERI et al. \(2019\)](#), which essentially (for flat priors) makes use of the difference in  $\chi^2$  between the fit of a given model with and without including the  $S_8$  data point. The tension is then estimated as  $\sqrt{\Delta\chi^2}$  in unit of  $\sigma$ . Finally, we also compute the Bayesian evidence with the sampler [MULTINEST \(FEROZ et al. 2009\)](#), taking 1000 live points and a tolerance condition on the evidence for stopping the sampling equal to 0.1. We perform model comparison by calculating  $\Delta\log B = \log B(\Lambda\text{DDM}) - \log B(\nu\Lambda\text{CDM})$ .

Our results are reported in [Tab. \(3.1\)](#) and summarized in [Fig. 3.8](#): In the  $\Lambda$ DDM scenario (red contours) we find that the best-fit (when including the  $S_8$  prior) has  $\varepsilon \simeq 0.7\%$  and  $\Gamma^{-1} \simeq 55$  Gyrs, yielding  $S_8 \simeq 0.767$  and  $\Omega_m \simeq 0.31$ , in excellent agreement with the KiDS1000+BOSS+2dfLenS measurement. Moreover, the decrease in  $S_8$  is driven by a smaller  $\sigma_8$ , while  $\Omega_m$  is not affected, which is also what is favored by the data. We find a strong negative correlation between  $\varepsilon$  and  $\Gamma$ , which approximately scales like  $\Gamma^{-1} \simeq 55 (\varepsilon/0.007)^{1.4}$  Gyrs. On the other hand, the  $\nu\Lambda$ CDM model can only achieve  $S_8 \simeq 0.81$ , with  $M_\nu < 0.1614$  (95% C.L.). Remarkably, we find a  $\Delta\chi^2_{\text{min}} = \chi^2_{\text{min}}(\Lambda\text{DDM}) - \chi^2_{\text{min}}(\nu\Lambda\text{CDM}) \simeq -5.5$  in favor of the  $\Lambda$ DDM model. The negative  $\Delta\chi^2$  is driven entirely by the low  $S_8$  value (the  $\chi^2_{\text{min}}$  per experiment is reported in [App. D.5](#)). The fit to other data set is barely affected by the inclusion of a  $S_8$  prior in the  $\Lambda$ DDM model (but degrades in the  $\nu\Lambda$ CDM case), such that without the  $S_8$  prior, there is no preference for DDM and  $S_8$  seems unchanged. Looking at the reconstructed  $S_8 = 0.821^{+0.017}_{-0.011}$  in the  $\Lambda$ DDM model without the prior information, one



Model	$\nu\Lambda$ CDM		ADDMM	
	w/o $S_8$	w/ $S_8$	w/o $S_8$	w/ $S_8$
100 $\omega_b$	$2.245(2.242) \pm 0.013$	$2.251(2.253) \pm 0.013$	$2.243(2.244)_{-0.013}^{+0.014}$	$2.246(2.241) \pm 0.013$
$\omega_{\text{cdm}}$ or $\omega_{\text{dec dm}}^{\text{ini}}$	$0.1193(0.1194) \pm 0.0009$	$0.1182(0.1184)_{-0.0008}^{+0.0009}$	$0.1195(0.1195) \pm 0.00095$	$0.1191(0.1194)_{-0.001}^{+0.0009}$
$H_0$ /[km/s/Mpc]	$67.55(67.76)_{-0.44}^{+0.46}$	$67.85(68.08)_{-0.44}^{+0.47}$	$67.71(67.71) \pm 0.42$	$67.92(67.70)_{-0.42}^{+0.43}$
$\text{Ln}(10^{10} A_s)$	$3.052(3.045)_{-0.016}^{+0.014}$	$3.047(3.043)_{-0.015}^{+0.014}$	$3.051(3.052)_{-0.015}^{+0.014}$	$3.048(3.052)_{-0.016}^{+0.014}$
$n_s$	$0.9676(0.9663) \pm 0.0037$	$0.9697(0.9683)_{-0.0036}^{+0.0037}$	$0.9674(0.9672) \pm 0.0038$	$0.9682(0.9673) \pm 0.0037$
$\tau_{\text{reio}}$	$0.058(0.055)_{-0.008}^{+0.007}$	$0.0569(0.0549)_{-0.008}^{+0.007}$	$0.0576(0.0582)_{-0.0076}^{+0.0071}$	$0.0570(0.0582)_{-0.0077}^{+0.0071}$
$M_\nu$ /eV	$< 0.1395$	$< 0.1611$	–	–
$\text{Log}_{10}(\varepsilon)$	–	–	$-2.69(-2.97)_{-1.3}^{+0.32}$	$-2.28(-2.16)_{-1.5}^{+0.8}$
$\text{Log}_{10}(\Gamma/[\text{Gyr}^{-1}])$	–	–	unconstrained (-3.86)	$-1.89(-1.74)_{-1.5}^{+0.82}$
$\Omega_m$	$0.3127(0.3104)_{-0.0061}^{+0.0057}$	$0.3083(0.3061)_{-0.006}^{+0.0056}$	$0.3102(0.3109)_{-0.0058}^{+0.0056}$	$0.3071(0.3099)_{-0.0058}^{+0.0053}$
$S_8$	$0.824(0.824) \pm 0.011$	$0.81(0.816) \pm 0.01$	$0.821(0.828)_{-0.011}^{+0.017}$	$0.795(0.767)_{-0.016}^{+0.024}$
$\chi_{\text{min}}^2$	2053.4	2060.5	2053.4	2055.0
$\Delta \log B$	0	0	-1.4	-0.81
$Q_{\text{DMAP}}$ tension	$2.7\sigma$		$1.3\sigma$	

**Table 3.1** – The mean (best-fit)  $\pm 1\sigma$  errors of the cosmological parameters from the analysis of Planck, BAO/FS, SN1a data, with and without a split-normal likelihood on  $S_8$  from KiDS-1000+BOSS+2dFLens. For each model and data-set, we also report the best-fit  $\chi^2$ , the level of tension estimated through the  $Q_{\text{DMAP}}$  metric (RAVERI et al. 2019) and the Bayesian evidence.

might naively expect  $S_8 \simeq 0.767$  to be largely excluded. In fact, the combined  $\chi^2$  with the prior on  $S_8$  only increases by  $\sim +1.6$  (as opposed to  $\sim +7.1$  in the  $\nu\Lambda$ CDM). This is because  $S_8$  has a non-Gaussian posterior with a tail extending to low values due to the degeneracy between  $\Gamma$  and  $\varepsilon$ . This degeneracy becomes clear when incorporating the  $S_8$  prior. As a result, the  $Q_{\text{DMAP}}$  estimator indicates that the tension evolves from  $2.7\sigma$  within  $\Lambda$ CDM to  $1.3\sigma$  within ADDMM.

Nevertheless, the model comparison is slightly in favor of  $\nu\Lambda$ CDM,  $\Delta \log B = -0.81$ , although based on the modified Jeffrey’s scales (JEFFREYS 1961; TROTTA 2008; NESSERIS et al. 2013) the preference is ‘weak’ or ‘inconclusive’. We thus conclude that, while the tension between our baseline data set and  $S_8$  is resolved in the ADDMM, current data do not favor the model in a Bayesian sense<sup>16</sup>.

As we show later in Sect. 3.4.2, the  $\Lambda$ CDM model with two massless neutrinos and one massive with  $M_\nu = 0.06$  eV yields results very similar to the  $\nu\Lambda$ CDM model. Similarly, letting the neutrino masses free to vary in the ADDMM model does not affect the results (see App. D.8). We also note that making use of linear priors on  $\varepsilon$  and  $\Gamma$  does not affect the reconstructed  $S_8$  value, but the scale chosen for the prior (i.e. sampling over the original prior range or in a more restricted range where  $\varepsilon \sim \mathcal{O}(10^{-2})$ ) affects the reconstructed 2D posteriors of  $\varepsilon$  and  $\Gamma$ . We discuss these issues in more details in App. D.7.

### Best-fit cosmology solving the $S_8$ tension

To better understand the ADDMM success in resolving the  $S_8$  tension compared to the case of massive neutrinos, in Fig. 3.9 we shown the residual differences in

<sup>16</sup>Let us point out that, assuming the  $\Delta\chi^2$  is  $\chi^2$ -distributed with 2 degrees of freedom, the ADDMM model is favored at 93.3% ( $\sim 2\sigma$ ) over  $\Lambda$ CDM (in the combined analysis). This indicates that part of the ‘inconclusive’ evidence is driven by our choice of wide priors and that different choices can affect the Bayesian evidence.

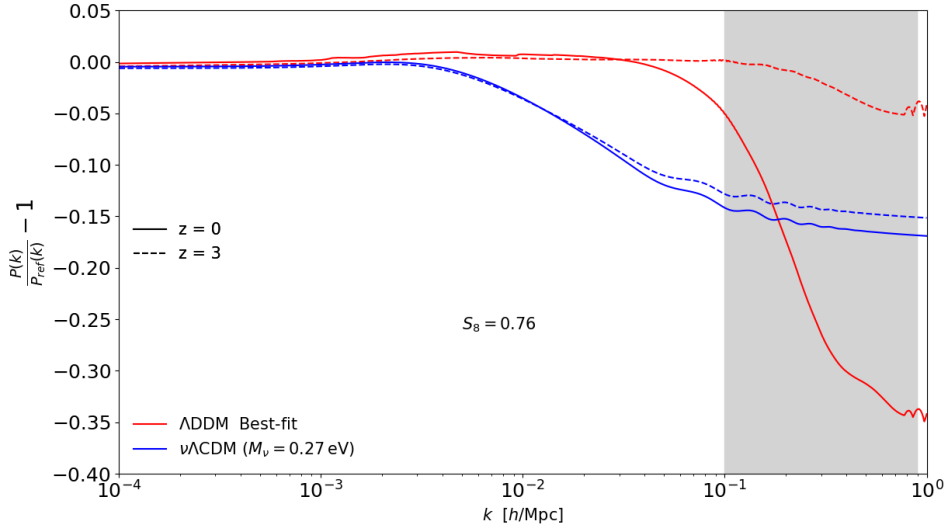


**Figure 3.9** – Residuals in the linear matter power spectrum  $P(k)$  at redshifts  $z = 0, 3$ , with respect to our baseline  $\nu\Lambda\text{CDM}$  model, for the best-fit  $\Lambda\text{DDM}$  model (red lines) and a  $\nu\Lambda\text{CDM}$  scenario yielding the same  $S_8$  (blue lines). The gray band indicates the approximate range of comoving wavenumbers contributing to  $\sigma_8$ .

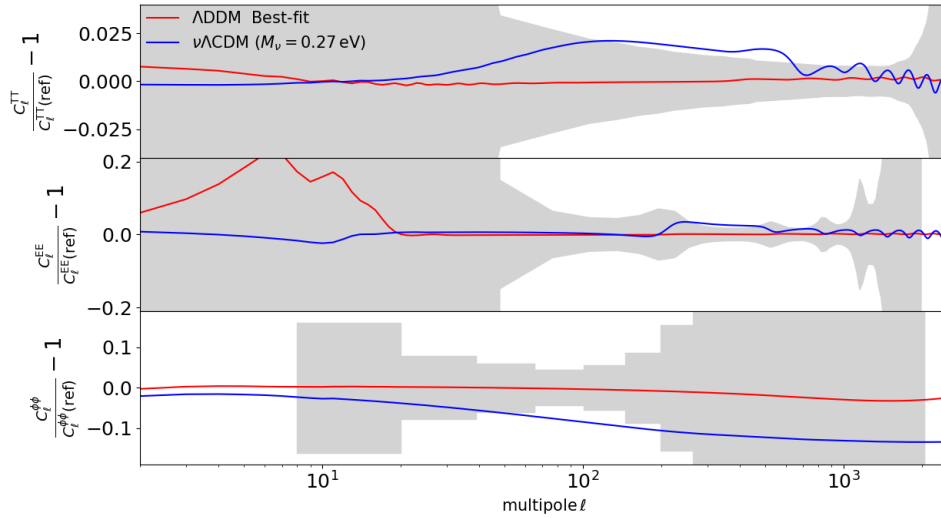


**Figure 3.10** – Same as in Fig. 3.9, for the (lensed) CMB TT, EE and lensing power spectrum. In this case, the gray bands show *Planck*  $1\sigma$  errors.

linear matter power spectrum  $P(k)$  with respect to our baseline  $\nu\Lambda\text{CDM}$  model (first column of Tab. (3.1)) for two models:

1. The best-fit  $\Lambda\text{DDM}$  scenario (fourth column of Tab. (3.1)).
2. A  $\nu\Lambda\text{CDM}$  model with three degenerate massive neutrinos of total mass  $M_\nu = 0.27$  eV<sup>17</sup>, which yields  $\sigma_8 \simeq 0.75$  and  $\Omega_m \simeq 0.31$ , in agreement with weak lensing data (HEYMANS et al. 2021).

<sup>17</sup>We adjust  $\omega_{\text{cdm}} = 0.1154$  whereas all other parameters are fixed to the baseline  $\nu\Lambda\text{CDM}$  model

These scenarios feature two key differences: i) a distinct redshift evolution for the power suppression. In the  $\Lambda$ DDM scenario, it is less significant at higher redshifts, since the abundance of the WDM daughter is smaller; ii) a time-evolving cut-off scale; in the  $\Lambda$ DDM model,  $k_{\text{fs}} = \sqrt{3/2}\mathcal{H}(a)/c_g(a)$ , while in the  $\nu\Lambda$ CDM it is obtained by evaluating  $k_{\text{fs}}$  at the redshift at which neutrinos become non-relativistic (LESGOURGUES et al. 2006). As a consequence, the CMB power spectra, well constrained by *Planck*, are vastly different. This is illustrated in Fig. 3.10, for both the best-fit  $\Lambda$ DDM scenario and the  $\nu\Lambda$ CDM model which yields the same  $S_8$  value. The  $\nu\Lambda$ CDM predicts different early-integrated Sachs-Wolfe effects, as well as different amount of lensing, because of a significant power suppression at  $z \sim 2 - 3$ , where the CMB lensing kernel peaks MANZOTTI 2018. On the other hand, the differences between  $\Lambda$ CDM and  $\Lambda$ DDM until  $z \sim 2$  are very small, explaining why *Planck* cannot disentangle between the two scenarios.

### The role of $S_8$ priors

Instead of using a split-normal likelihood on  $S_8$ , a more accurate approach would have been to include the full galaxy shear and clustering power spectra. Making use of the full likelihood would however require the ability to compute the matter power spectrum on non-linear scales in a  $\Lambda$ DDM universe, a task that is beyond the scope of this work. Let us note that it has been established in various cases that the reconstructed  $S_8$  value only mildly vary from one model to another. In particular, the KiDS collaboration has established that the reconstructed value of  $S_8$  is insensitive to the neutrino mass (HILDEBRANDT et al. 2020) – a model that has physical effects very similar to the  $\Lambda$ DDM model<sup>18</sup>. This provides confidence in making use of a prior on  $S_8$  derived in the  $\Lambda$ CDM context.

Nevertheless, to highlight the impact of a different  $S_8$  measurement, we conduct two extra BAO + SNIa + *Planck* +  $S_8$  runs for  $\Lambda$ DDM, but replacing the  $S_8$  prior from KiDS-1000+BOSS+2dFLens by the one determined in the combined analysis KiDS+Viking+DES-Y1<sup>19</sup> (JOUDAKI et al. 2020),  $S_8 = 0.755^{+0.019}_{-0.021}$  and with the DES-Y1 data only (T. M. C. ABBOTT et al. 2018),  $S_8 = 0.773^{+0.026}_{-0.02}$ . We also performed three analogous  $\Lambda$ CDM runs (one per each  $S_8$  prior), in order to compute  $\Delta\chi^2_{\text{min}} = \chi^2_{\text{min}}(\Lambda\text{DDM}) - \chi^2_{\text{min}}(\Lambda\text{CDM})$  in each case. From the reconstructed parameters and the  $\Delta\chi^2_{\text{min}}$ :

$$\begin{aligned} \text{Log}_{10}(\Gamma/[\text{Gyr}^{-1}]) &= -1.89^{+0.82}_{-1.5} && \text{KiDS1000 + BOSS + 2dFLens} \\ \text{Log}_{10}(\varepsilon) &= -2.28^{+0.8}_{-0.78} \\ S_8 &= 0.795^{+0.024}_{-0.016} \\ \Delta\chi^2_{\text{min}} &= -5.7, \end{aligned}$$

<sup>18</sup>The differences between the  $\Lambda$ DDM and  $\nu\Lambda$ CDM models that we have highlighted in Fig. 3.9 concern the shape of the power suppression with respect to a reference model *adjusted to Planck data*. This doesn't mean that similar differences will appear between these models when looking directly at the corresponding matter power spectra *adjusted to KiDS data*.

<sup>19</sup>Note that this combined analysis includes a photo-metric redshift correction applied to DES result, slightly lowering the  $S_8$  value compared to what is advocated by the DES collaboration (T. M. C. ABBOTT et al. 2018).

$$\begin{aligned}
\text{Log}_{10}(\Gamma/[\text{Gyr}^{-1}]) &= -1.62_{-1}^{+0.81} && \text{KiDS+ Viking + DES - Y1} \\
\text{Log}_{10}(\varepsilon) &= -2.23_{-0.59}^{+0.48} \\
S_8 &= 0.778_{-0.023}^{+0.025} \\
\Delta\chi_{\text{min}}^2 &= -8.6, \\
\\
\text{Log}_{10}(\Gamma/[\text{Gyr}^{-1}]) &= -2.15_{-1.8}^{+0.41} && \text{DES - only} \\
\text{Log}_{10}(\varepsilon) &= -2.52_{-1.5}^{+0.38} \\
S_8 &= 0.809_{-0.01}^{+0.021} \\
\Delta\chi_{\text{min}}^2 &= -2.3,
\end{aligned}$$

one can see that the level of preference is higher for the KiDS+Viking+DESY1 case while it is lower in the DES-only case. This explicitly demonstrates that the statistical significance of the DDM “detection” is strongly driven by the level of tension of the  $S_8$  value used in the analysis. If the  $S_8$  tension increases in the future, the preference for  $\Lambda$ DDM over  $\Lambda$ CDM would likely increase. On the other hand, if the  $S_8$  tension disappears, cosmological data would not favour the  $\Lambda$ DDM scenario compared to the standard  $\Lambda$ CDM scenario.

### 3.4.3 Implications for other cosmic tensions and the Xenon1T anomaly

#### The $H_0$ tension

In order to test the implications of the 2-body decay for the Hubble tension, we conduct a run that includes the local measurement of  $H_0$  from SHOES (RIESS et al. 2019), CMB, BAO and SNIa data. For the sake of brevity we do not report the results of the runs here. We find that the shape of the posterior probabilities is almost unchanged, except for a tiny shift in  $H_0$  to a higher value,  $H_0 = 68.21 \pm 0.4$  km/s/Mpc. We thus confirm the inability of this model to resolve the Hubble tension. In fact, any late-time solution that does not modify the sound horizon at recombination is expected to fail when combining BAO with SNIa data, as we discussed in Sect. 2.2. Although this is not of material importance in the context of the present work, let us note that a more correct way of combining Pantheon and SHOES is through a prior on the intrinsic magnitude of SNIa (see Sect. 2.2). Yet, this does not affect our conclusions, as it was explicitly shown in Sect. 2.5.

#### The $A_{\text{lens}}$ anomaly in *Planck* data

We focus now on the ‘ $A_{\text{lens}}$ ’ anomaly, *i.e.* the anomalous amount of lensing estimated from the smoothing of the acoustic peaks at high- $\ell$ ’s within *Planck* data, as quantified by the ‘ $A_{\text{lens}}$ ’ parameter. We wish to check whether this anomaly could impact constraints on the  $\Lambda$ DDM model, and conversely if the  $\Lambda$ DDM model could help explaining the existence of such anomalies, since it has already been noted that this anomaly could be related to the  $S_8$  tension (see our discussion in Sect. 1.7.2). To do so, we follow the approach of the SPTpol collaboration and implement two new parameters in **CLASS** that allows to (roughly) marginalize over the lensing information in *Planck*. The parameter  $A_{\text{lens}}^{\text{TTTEEE}}$  re-scales the amplitude of the lensing power spectrum entering in the high- $\ell$  part of the CMB TT,TE,EE spectra, while the parameter  $A_{\text{lens}}^{\phi\phi}$  re-scales the amplitude of the lensing power spectrum reconstruction. We present the result of a MCMC analysis including data from *Planck*

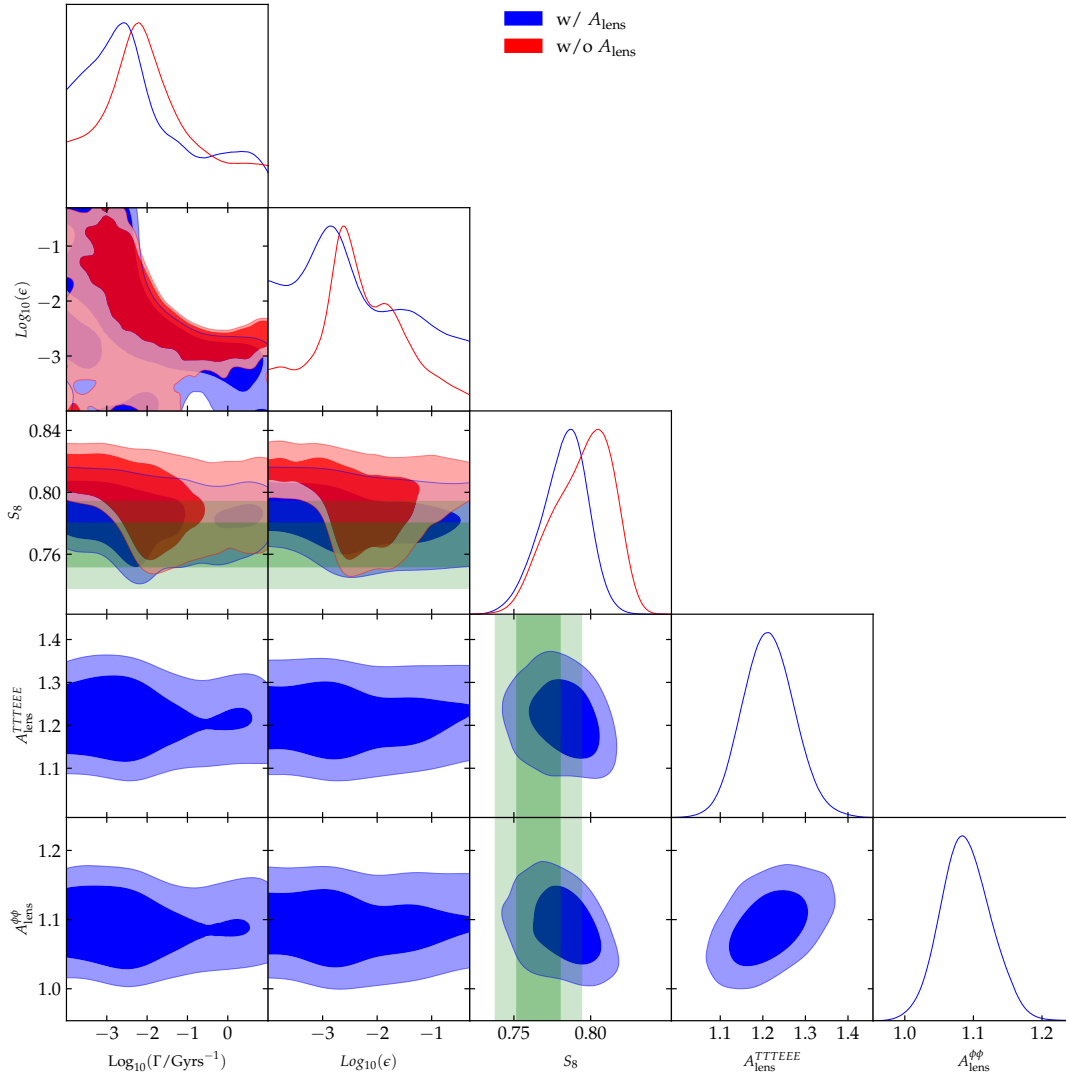


**Figure 3.11** – 2D posterior distribution of a subset of parameters from our BAO + SNIa + *Planck* +  $S_8$  (from KiDS+BOSS+2dFLens) analysis, with and without including the extra  $A_{\text{lens}}^{\text{TTTEEE}}$  and  $A_{\text{lens}}^{\phi\phi}$  to marginalize over CMB lensing information.

high- $\ell$  TT,TE,EE+lensing+BAO+SNIa+ $S_8$  (from KiDS-1000+BOSS+2dFLens) – with the two extra lensing parameters – in Tab. (3.2) and Fig. 3.11.

One can see that the  $S_8$  parameter reconstructed once marginalizing over the ‘ $A_{\text{lens}}$ ’ anomaly is lower by  $\sim 0.5\sigma$  than in the baseline analysis. However, the preference for  $\Lambda$ DDM decreases, with  $\text{Log}_{10}(\epsilon)$  now unconstrained. Note also that the  $A_{\text{lens}}^{\text{TTTEEE}}$  is still more than  $2\sigma$  away than the fiducial value  $A_{\text{lens}}^{\text{TTTEEE}} = 1$ . We can therefore conclude that the  $\Lambda$ DDM model cannot explain this anomaly and that the preference for  $\Lambda$ DDM would likely disappear if the  $S_8$  tension turns out to be explained by a systematic in *Planck* data leading to the anomalous value of the  $A_{\text{lens}}$  parameters.

### The Xenon1T excess

Let us explore the implications of the  $\Lambda$ DDM model for the excess of events in the electronic recoils recently reported by the Xenon1T Collaboration (APRILE et al.

Parameter	w/ $A_{\text{lens}}$
100 $\omega_b$	2.262(2.260) $^{+0.016}_{-0.015}$
$\Omega_{\text{dcdm}}^{\text{ini}}$	0.2506(0.2526) $^{+0.0049}_{-0.0059}$
$H_0$ /[km/s/Mpc]	68.56(68.38) $^{+0.5}_{-0.45}$
$\text{Ln}(10^{10} A_s)$	3.025(3.032) $^{+0.02}_{-0.018}$
$n_s$	0.9725(0.9718) $^{+0.0042}_{-0.0039}$
$\tau_{\text{reio}}$	0.0474(0.0506) $^{+0.0098}_{-0.008}$
$\text{Log}_{10}(\Gamma/[\text{Gyr}^{-1}])$	-2.10(-1.49) $^{+0.39}_{-1.9}$
$\text{Log}_{10}(\varepsilon)$	unconstrained (-2.47)
$\Omega_m$	0.2991(0.3009) $^{+0.0053}_{-0.0066}$
$S_8$	0.784(0.768) $^{+0.018}_{-0.014}$
$A_{\text{lens}}^{\text{TTTEEE}}$	1.208(1.192) $^{+0.066}_{-0.064}$
$A_{\text{lens}}^{\phi\phi}$	1.086(1.072) $^{+0.035}_{-0.041}$
$\chi_{\text{min}}^2$	2043.2

**Table 3.2** – The mean (best-fit)  $\pm 1\sigma$  errors of the cosmological parameters from our BAO + SNIa + *Planck* +  $S_8$  (from KiDS+BOSS+2dFLens) analysis performed by marginalizing over the amplitude of the lensing potential  $A_{\text{lens}}$ . We also report the best-fit  $\chi^2$ .

2020). It has been pointed out that this excess could potentially be explained by the elastic interactions of electrons with a fast DM component of mass  $m \gtrsim 0.1$  MeV and velocities  $0.05 \lesssim v/c \lesssim 0.13$  (KANNIKE et al. 2020). Interestingly, the WDM daughter species in the  $\Lambda$ DDM scenario could in principle play the role of such a fast component, since our results indicate that the  $1\text{-}\sigma$  range for the speed of the daughter particle extends up to  $v/c \simeq \varepsilon \simeq 0.05$ .

In order to test this hypothesis further, we perform another MCMC analysis including *Planck* high- $\ell$  TT,TE,EE+lensing+BAO+SNIa+ $S_8$  (from KiDS-1000+BOSS+2dFLens), with the DR energy fraction now fixed to  $\varepsilon = 0.05$ . This serves as a proxy for taking into account Xenon1T measurement (alternatively, one could enforce  $\varepsilon > 0.05$ ). The results are summarized in Fig. 3.12 and Tab. (3.3). We find best-fit values  $\text{Log}_{10}(\Gamma/\text{Gyrs}^{-1}) \simeq -2.4$  and  $S_8 \simeq 0.784$ , at the cost of a mild degradation in the fit to *Planck* data ( $\Delta\chi^2 \simeq +1.7$ ), indicating that the 2-body decaying scenario has indeed the potential to provide a common resolution to the  $S_8$  and Xenon1T anomalies. We leave the construction of a realistic model and study of the subsequent cosmological implications beyond the effect the decay to another study (see (G. CHOI et al. 2020b; XU et al. 2021) for examples).

### 3.4.4 Detecting DDM in the CMB: impact of current and future data

In this section, we confront the DDM model to additional CMB data from current ground based surveys and perform forecast for future surveys. In addition to *Planck*, we consider first, the high- $\ell$  CMB EE and TE ( $50 \leq \ell \leq 8000$ ) (HENNING et al. 2018) measurements and the reconstructed gravitational lensing potential ( $100 \leq \ell \leq 8000$ ) (BIANCHINI et al. 2020) from the 500deg SPTpol survey (CHUDAYKIN et al. 2020a). We then include the high- $\ell$  CMB TT, EE and TE ( $350 \leq \ell \leq 4125$ ) data from the DR4 of the ACTPol survey (AIOLA et al. 2020; S. K. CHOI et al. 2020). Finally, we demonstrate that an experiment like CMB-S4 can unambiguously detect the DDM model.



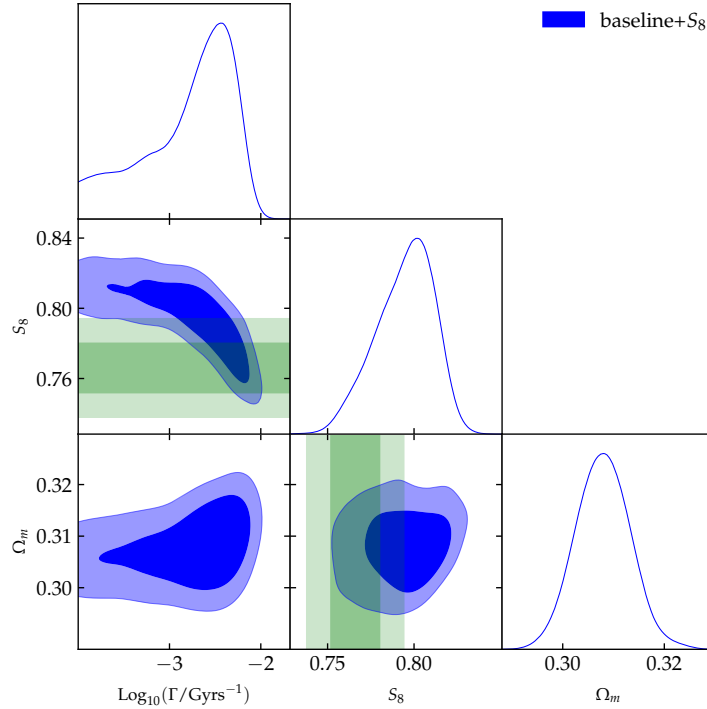


**Figure 3.12** – 2D posterior distribution of a subset of parameters in our BAO + SNIa + *Planck* +  $S_8$  (from KiDS+BOSS+2dFLens) analysis when fixing the DR energy fraction to a value motivated by the recent Xenon1T anomaly ( $\varepsilon = 0.05$ ).

Parameter	$\Lambda$ DDM ( $\varepsilon = 0.05$ )
$100 \omega_b$	$2.244(2.245)^{+0.014}_{-0.015}$
$\Omega_{\text{dcdm}}^{\text{ini}}$	$0.2597(0.2595)^{+0.0054}_{-0.0067}$
$H_0$ /[km/s/Mpc]	$67.76(67.78)^{+0.54}_{-0.45}$
$\ln(10^{10} A_s)$	$3.050(3.047)^{+0.015}_{-0.016}$
$n_s$	$0.9674(0.9674)^{+0.0042}_{-0.0039}$
$\tau_{\text{reio}}$	$0.0573(0.0559)^{+0.0073}_{-0.0079}$
$\log_{10}(\Gamma/[\text{Gyr}^{-1}])$	$-2.72(-2.44)^{+0.61}_{-0.21}$
$\Omega_m$	$0.3093(0.3090)^{+0.0057}_{-0.007}$
$S_8$	$0.794(0.786)^{+0.021}_{-0.015}$
$\chi^2_{\text{min}}$	2057.6

**Table 3.3** – The mean (best-fit)  $\pm 1\sigma$  errors of the cosmological parameters from our *Planck* high- $\ell$  TT,TE,EE+lensing+BAO+SNIa+ $S_8$  analysis, when fixing the DR energy fraction to  $\varepsilon = 0.05$ . We also report the best-fit  $\chi^2$ .

### Confronting $\Lambda$ DDM to SPTpol data

It is interesting to test the robustness of the DDM “detection” to a change of CMB data sets, especially given the impact of marginalizing over the ‘ $A_{\text{lens}}$ ’ anomaly as discussed in the previous section. We thus confront the  $\Lambda$ DDM scenario under study against a set of CMB data constituted by low- $\ell$  temperature and polarization as well as high- $\ell$  temperature data from *Planck*, in combination with high- $\ell$  polarization data from SPTpol (see Sect. 3.4 for further details and references). It has been shown indeed that such a joint analysis predicts an amount of CMB lensing consistent with the  $\Lambda$ CDM expectation (CHUDAYKIN et al. 2020a), *i.e.* no ‘ $A_{\text{lens}}$ ’ anomaly, and no  $S_8$  tension. This is manifest in Fig. 3.13, where we compare predictions from the

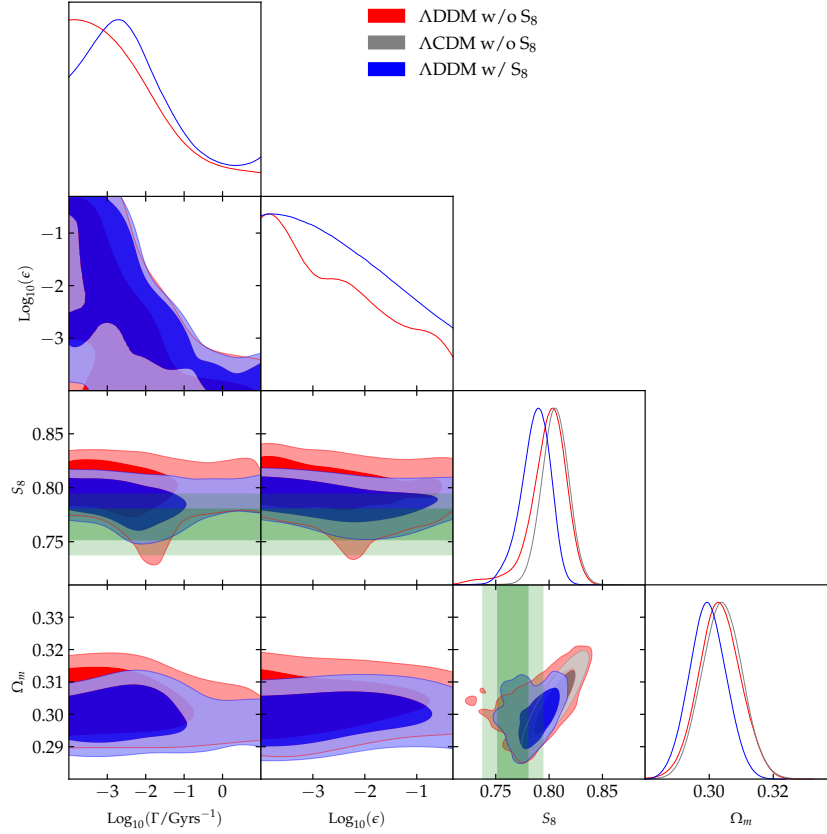


**Figure 3.13** – 2D posterior distribution of a subset of parameters in the joint BAO + SNIa + *Planck* + SPTpol analysis, with and without imposing a prior on  $S_8$  from KiDS+BOSS+2dFLens, compared to the  $\Lambda$ CDM scenario.

Data Parameter	BAO + SNIa + <i>Planck</i> TT + SPTpol	
	w/o $S_8$	w/ $S_8$
$100 \omega_b$	2.239(2.2378) $^{+0.019}_{-0.018}$	2.241(2.247) $^{+0.016}_{-0.019}$
$\Omega_{\text{dec dm}}^{\text{ini}}$	0.2544(0.2557) $^{+0.0057}_{-0.0061}$	0.2514(0.2532) $^{+0.0054}_{-0.0055}$
$H_0$ /[km/s/Mpc]	68.15(68.03) $^{+0.51}_{-0.48}$	68.39(68.25) $^{+0.47}_{-0.46}$
$\ln(10^{10} A_s)$	3.031(3.026) $^{+0.016}_{-0.017}$	3.026(3.018) $^{+0.017}_{-0.014}$
$n_s$	0.9701(0.9695) $^{+0.0041}_{-0.0042}$	0.9712(0.9707) $^{+0.0037}_{-0.004}$
$\tau_{\text{reio}}$	0.0509(0.0481) $^{+0.0074}_{-0.0081}$	0.0494(0.0457) $^{+0.0082}_{-0.0073}$
$\log_{10}(\Gamma/[\text{Gyr}^{-1}])$	-2.38(-1.73) $^{+0.38}_{-1.6}$	-2.25(-1.35) $^{+0.42}_{-1.7}$
$\log_{10}(\varepsilon)$	unconstrained(-2.73)	unconstrained(-2.57)
$\Omega_m$	0.3033(0.3046) $^{+0.0064}_{-0.0067}$	0.2999(0.3013) $^{+0.0059}_{-0.0062}$
$S_8$	0.799(0.798) $^{+0.022}_{-0.015}$	0.787(0.767) $^{+0.016}_{-0.013}$
$\chi_{\text{min}}^2$	1816.3	1816.8

**Table 3.4** – The mean (best-fit)  $\pm 1\sigma$  errors of the cosmological parameters from our BAO + SNIa + *Planck*TT + SPTpol analysis, with and without imposing a split-normal likelihood on  $S_8$  (from KiDS+BOSS+2dFLens). For each data-set, we also report the best-fit  $\chi^2$ .

$\Lambda$ CDM and the ADDM models, the latter both with and without including information on  $S_8$  from KIDS1000+BOSS+2dFLens. As one can easily see, both cosmological models predict a  $S_8$  value in excellent agreement with the KIDS1000+BOSS+2dFLens measurement, displayed as a green horizontal band. Our results regarding the

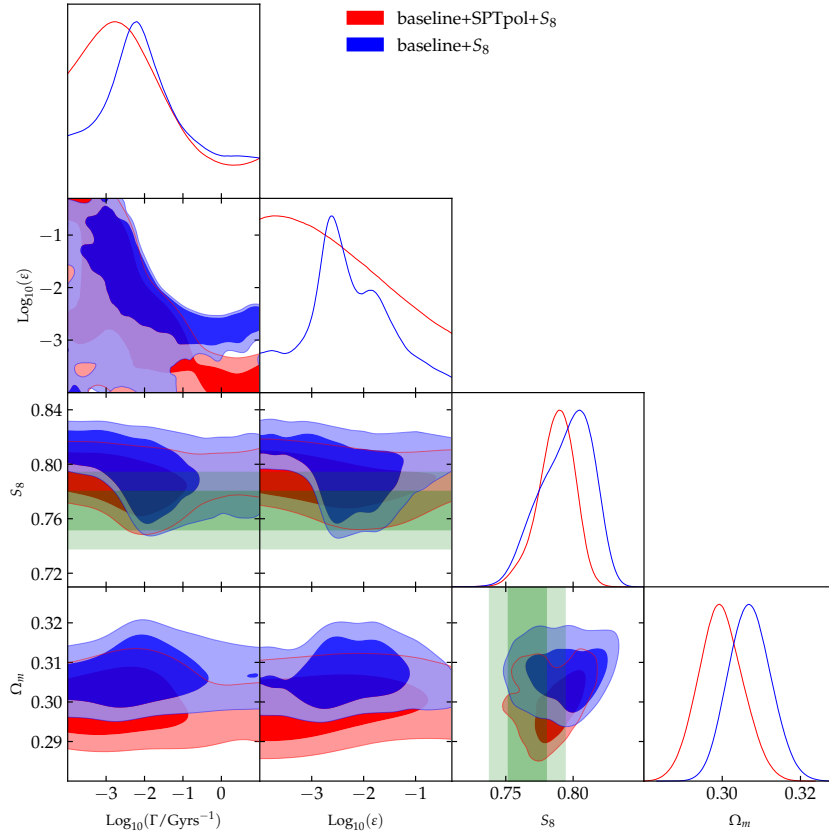


**Figure 3.14** – 2D posterior distribution of a subset of parameters in our from our BAO + SNIa + *Planck* +  $S_8$  (from KiDS+BOSS+2dFLens) analysis, compared to the joint BAO + SNIa + *Planck* + SPTpol +  $S_8$  analysis.

$\Lambda$ DDM model are also reported in Tab. (3.4).

In Fig. 3.14, instead, we report a comparison between our baseline  $\Lambda$ DDM analysis and the *Planck*+SPT one. First and foremost, SPTpol appears in very good agreement with the  $\Lambda$ DDM model resolution of the  $S_8$  tension required by *Planck*. However, the  $\Lambda$ DDM parameters are largely unconstrained in that case and no deviations from  $\Lambda$ CDM are visible, which further establishes that if the  $S_8$  tension turns out to be explained by a systematic in *Planck* high- $\ell$  polarization data, the preference for  $\Lambda$ DDM is likely to vanish.

### Confronting $\Lambda$ DDM to ACTpol data

Second, we confront the  $\Lambda$ DDM model to the combination of *Planck* and ACTPol data, to test whether more accurate measurements at high- $\ell$  can further constrain the model. Within  $\Lambda$ CDM, it has been found that ACTPol data (when combined with WMAP) also favor relatively high  $S_8$ , in  $2.1\sigma$  disagreement with KiDS1000+BOSS+2dFLens (AIOLA et al. 2020). To limit double counting of information, we follow the procedure of the ACT collaboration and truncate multipoles  $\ell < 1800$  in the ACT TT data. The results of this analysis are presented in Fig. 3.15 and Tab. (3.5). Interestingly, the  $\Lambda$ DDM parameter  $\epsilon$  is more precisely measured with the inclusion of the ACTPol data, while the mean value is barely affected. Compared with  $\Lambda$ CDM, the  $\Delta\chi^2$  in favor of  $\Lambda$ DDM is now  $-6.7$ , and the level of

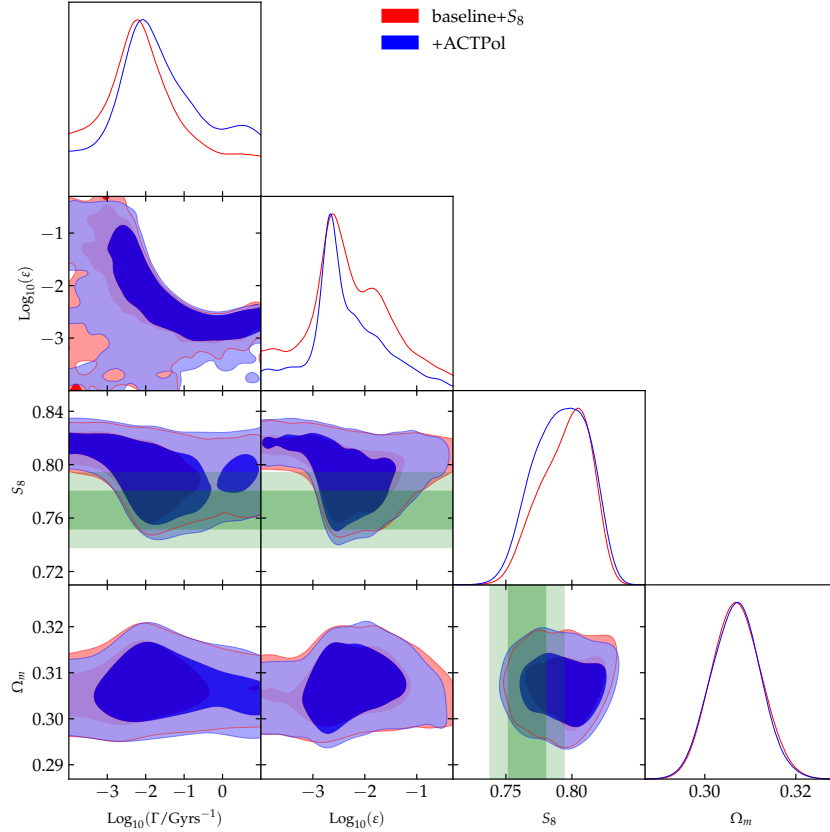


**Figure 3.15** – 2D posterior distribution of a subset of parameters in the case BAO + SNIa + *Planck* +  $S_8$  (from KiDS+BOSS+2dFLens), with and without the inclusion of ACT data.

Data Parameter	BAO + SNIa + <i>Planck</i> + ACTPol	
	w/o $S_8$	w/ $S_8$
$100 \omega_b$	$2.245(2.242) \pm 0.013$	$2.243(2.243) \pm 0.012$
$\Omega_{\text{dcdm}}^{\text{ini}}$	$0.26(0.261) \pm 0.005$	$0.2583(0.2591)_{-0.0051}^{+0.0048}$
$H_0/[\text{km/s/Mpc}]$	$67.77(67.73)_{-0.42}^{+0.33}$	$67.92(67.84) \pm 0.40$
$\ln(10^{10} A_s)$	$3.058(3.054) \pm 0.015$	$3.056(3.061) \pm 0.015$
$n_s$	$0.9703(0.9697)_{-0.004}^{+0.0034}$	$0.9708(0.9706) \pm 0.0036$
$\tau_{\text{reio}}$	$0.0571(0.0549)_{-0.0084}^{+0.0069}$	$0.0567(0.0592)_{-0.0075}^{+0.007}$
$\log_{10}(\Gamma/[\text{Gyr}^{-1}])$	$0.92(-2.92)_{-1.90}^{+0.55}$	$-1.56(-1.19)_{-1.50}^{+1.10}$
$\log_{10}(\epsilon)$	unconstrained (-3.88)	$-2.34(-2.54) \pm 0.65$
$\Omega_m$	$0.3094(0.3108)_{-0.0054}^{+0.0051}$	$0.3069(0.3068)_{-0.0056}^{+0.0050}$
$S_8$	$0.822(0.829)_{-0.011}^{+0.018}$	$0.792(0.772)_{-0.019}^{+0.025}$
$\chi_{\text{min}}^2$	2294.54	2296.20
$\Delta\chi^2(\Lambda\text{CDM})$	-0.12	-6.7

**Table 3.5** – The mean (best-fit)  $\pm 1\sigma$  errors of the cosmological parameters from our BAO + SNIa + *Planck* + ACTPol analysis, with and without imposing a split-normal likelihood on  $S_8$  (from KiDS+BOSS+2dFLens). For each data-set, we also report the best-fit  $\chi^2$  and the  $\Delta\chi^2(\Lambda\text{CDM}) \equiv \chi_{\text{min}}^2(\Lambda\text{DDM}) - \chi_{\text{min}}^2(\Lambda\text{CDM})$ .

tension between *Planck*+ACT+BAO+SNIa and  $S_8$  from KIDS1000+BOSS+2dFLens is  $1.3\sigma$ . We conclude that ACT data are in very good agreement with the  $\Lambda\text{DDM}$  model, slightly increasing its preference over  $\Lambda\text{CDM}$ .

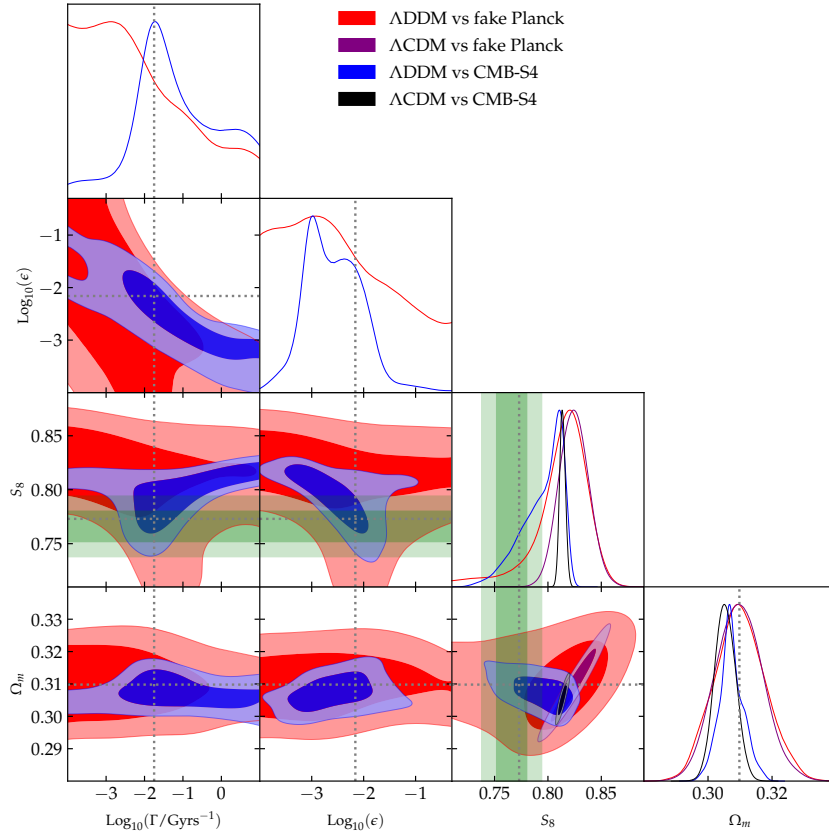


**Figure 3.16** – 2D posterior distribution of a subset of parameters reconstructed from a fit to simulated *Planck* and CMB-S4 data. The fiducial model has  $\text{Log}_{10}(\epsilon) = -2.16$  and  $\text{Log}_{10}(\Gamma/[\text{Gyr}^{-1}]) = -1.74$ , as denoted by the gray dotted lines.

### Towards detecting the $\Lambda$ DDM model with CMB-S4

As we have extensively discussed, current CMB data are not sensitive enough to detect DDM, so that the preference for non-standard values for  $\epsilon$  and  $\Gamma$  is fully driven by the inclusion of the  $S_8$  measurement from weak lensing data in the analysis. To further stress this aspect we have performed additional analyses fitting a set of mock CMB data generated starting from our reference best-fit  $\Lambda$ DDM model (*i.e.* that from the *Planck*+BAO+SNi+KiDS+BOSS+2dFLens run, reported in the fourth column of Tab. (3.1)). The resulting contour plots are shown in Fig. 3.16, where we compare the constraints that *Planck* would obtain if the “true” cosmological model actually contained DDM, with those that a future generation CMB survey (CMB-S4) would get. Concretely, this task was pursued by using the ‘Planck-fake-realistic’ and ‘CMB-S4’ likelihoods available in **MontePython-v3**. The former allowed us to generate synthetic *Planck* data, whereas the latter includes multipoles  $\ell$  from 30 to 3000, assuming a sky coverage of 40%, uncorrelated Gaussian error on each  $a_{\ell m}$ ’s, uncorrelated temperature and polarization noise, and perfect foreground cleaning up to  $\ell_{\text{max}}$ <sup>20</sup>. All details about the likelihood can be found in Tab. 1 of BRINCKMANN et al. (2019b).

<sup>20</sup>To overcome the lack of low- $\ell$  data in the CMB-S4 analysis, we have imposed a Gaussian prior on the optical depth to reionization, centered on its best-fit value from our reference *Planck*+BAO+SNi+KiDS+BOSS+2dFLens analysis, namely  $\tau_{\text{reio}} = 0.0582 \pm 0.008$ .

As expected, from Fig. 3.16 it is manifest that *Planck* alone could not detect DDM even if its signature was truly imprinted in CMB data. Note indeed that the red contours barely features an overlap at  $2\sigma$  in  $S_8$ , and only upper limits on  $\text{Log}_{10}\Gamma$ ,  $\text{Log}_{10}\varepsilon$ . This, as we explained earlier, is a consequence of the degeneracy that exists within  $\Lambda$ DDM and leads to a bias in the Bayesian analysis. Therefore, the information that matters in quantifying the success of the resolution is rather contained in the  $\chi^2$  values: just like in the analysis of real data, we find that, when testing the  $\Lambda$ CDM model against the mock data that contains the  $\Lambda$ DDM signal, the  $\chi^2$  in the  $\Lambda$ CDM model is identical to that of the  $\Lambda$ DDM model. This clearly shows that *Planck* cannot disentangle between  $\Lambda$ CDM and  $\Lambda$ DDM, while the  $S_8$  measurements favors  $\Lambda$ DDM (in terms of  $\chi^2$ ). This is not the case for CMB-S4, which contours are over-plotted in blue: if the real Universe contains DDM, CMB-S4 would unequivocally detect its signature, finding  $\varepsilon \neq 0$  at  $\gtrsim 2\sigma$  level. The  $\Delta\chi^2$  in favor of the  $\Lambda$ DDM model from (mock) CMB-S4 data alone is in fact  $\simeq +8$ .

### 3.5 Summary and outline

In this work, we have performed a comprehensive cosmological study of the CDM 2-body decay scenario dubbed ‘ $\Lambda$ DDM’, whereby decays are characterized both by the decay rate  $\Gamma$  and energy fraction converted to radiation  $\varepsilon$ , including for the first time a fully consistent treatment of the linear perturbations of the WDM daughter component. To that end, we have made use of a new approximation scheme, that allows to accurately and quickly compute the dynamics of the WDM linear perturbations by treating the WDM species as a viscous fluid. Close to the best-fit values, our approximation scheme is accurate at the  $\mathcal{O}(0.1\%)$  level in the CMB power spectra and  $\mathcal{O}(1\%)$  level in the linear matter power spectrum (see App. D.4). We have then discussed in detail the dynamics of linear density perturbations of the mother and daughter particles, as well as the physical effects of the  $\Lambda$ DDM model on the CMB and matter power spectra.

In a second part, we have performed a set of MCMC analyses of the  $\Lambda$ DDM model against a suite of up-to-date low- and high-redshift data-sets. We have compared the constraints obtained from BAO and SNIa data, thereby solely based on background effects, to those obtained from the full *Planck* data-set, that requires instead an accurate description of the WDM linear perturbations. We find that *Planck* CMB data constrain the  $\Lambda$ DDM model  $\sim 1$  order of magnitude better than current BAO+SNIa data. However, we also show that despite these constraints, the  $\Lambda$ DDM model provides a promising possibility to resolve the  $S_8$  tension.

We have then tested the robustness of the  $\Lambda$ DDM resolution to the  $S_8$  tension to a number of change in the analysis. We show that the mild preference for the  $\Lambda$ DDM model over  $\Lambda$ CDM is tied to the  $S_8$  value chosen in the analysis. Concretely, the  $S_8$  value from the KiDS+Viking+DES analysis, which has a higher level of tension with the *Planck*  $\Lambda$ CDM prediction than the baseline KiDS+BOSS+2dFLens value, leads to a stronger preference in favor of the  $\Lambda$ DDM model. However, the DES-only result, which is in reasonable agreement with *Planck*, leads to a weaker preference of the  $\Lambda$ DDM model. Similarly, once marginalizing over the lensing information in *Planck* through the  $A_{\text{lens}}$  parameter (we used two extra parameters in practice describing the normalization of the lensing power spectrum and the normalization of the lensing



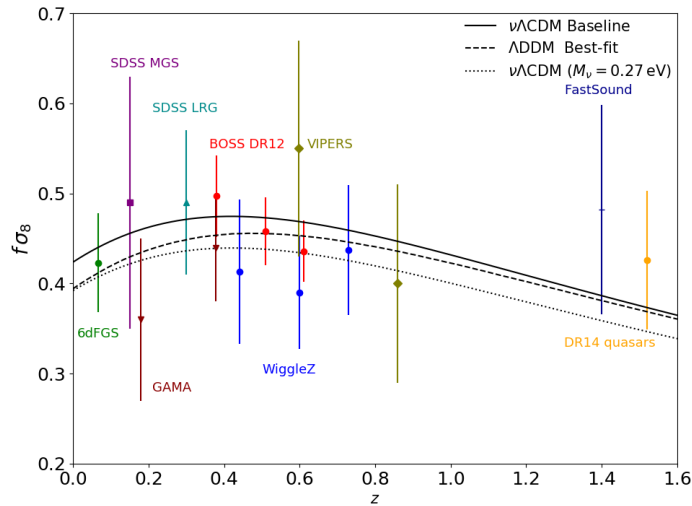


**Figure 3.17** – Growth rate of matter fluctuations for our baseline  $\nu\Lambda$ CDM model (solid line), compared to the best-fit  $\Lambda$ DDM model (dashed line) and to the  $\nu\Lambda$ CDM scenario yielding the same  $\sigma_8$  and  $\Omega_m$  (dotted line). The observational constraints are taken from AGHANIM et al. (2020b) and references therein.

smoothing effect in the high- $\ell$  TT,TE,EE power spectra), or when trading the *Planck* high- $\ell$  TE,EE power spectra for the SPTpol ones, the preference for the  $\Lambda$ DDM model decreases. This is because in these two cases the inferred  $\Lambda$ CDM model has a smaller  $S_8$  value, showing less of a tension with the weak lensing surveys. This indicates that if the  $S_8$  tension ends up coming from an unknown systematic within weak lensing surveys or within *Planck* data, the preference for the  $\Lambda$ DDM model would likely disappear. On the other hand, when combining *Planck* with ACTPol the mild preference for  $\Lambda$ DDM increases, and the remaining ‘tension’ with  $S_8$  is now only  $\sim 1.3\sigma$ .

We have also tested the intriguing possibility that the recent Xenon1T excess is due to the  $\Lambda$ DDM model. To that end, we have performed an additional MCMC analysis fixing  $\varepsilon = 0.05$  as required by Xenon1T. We find that it is easy to resolve the  $S_8$  tension in that case, pointing to a DCDM lifetime of  $\text{Log}_{10}(\Gamma/[\text{Gyr}^{-1}]) = -2.72^{+0.61}_{-0.21}$ . Interestingly, this comes at the cost of a very minor degradation in *Planck* fit ( $\Delta\chi^2 \simeq +1.7$ ), indicating that *Planck*, BAO and SNIa data are in good agreement with this model. Finally, by performing an analysis where we artificially introduce a DDM signal in a set of mock CMB data, we explicitly demonstrate that while current CMB data alone are not sensitive enough to distinguish between standard CDM and DDM, next-generation CMB experiments (CMB-S4) can unambiguously detect its signature.

It will be very interesting to go beyond the linear aspects discussed in this work and study the non-linear evolution of density perturbations, in order to be able to make use of the full power of the KiDS and DES likelihoods. This task would likely require using N-body simulations, as in WANG et al. (2012, 2014). This will be even more crucial with upcoming surveys such as Euclid (AMENDOLA et al. 2018), LSST (MANDELBAUM et al. 2018), and DESI (AGHAMOUSA et al. 2016). For instance, these surveys will be able to measure the differences between the growth rate  $f\sigma_8$  in the  $\Lambda$ DDM scenario and  $\Lambda$ CDM at  $0 \lesssim z \lesssim 1$ , which at present remain below the sensitivity of current experiments (see Fig. 3.17). It might also be possible to test the  $\Lambda$ DDM

model with current Lyman- $\alpha$  forest flux power spectrum data (WANG et al. 2013; MURGIA et al. 2017; ARCHIDIACONO et al. 2019; ENZI et al. 2021).

In SIMON et al. (2022), we have already extended the analysis to the mildly non-linear scales using the Effective Field Theory of LSS (EFTofLSS) (CHUDAYKIN et al. 2020b; D'AMICO et al. 2021a). This allowed us to test the  $\Lambda$ DDM model against the full shape galaxy power spectrum as measured by BOSS, significantly improving the constraints at 68 % C.L. on the CDM lifetime. We also showed that, in order to fit EFTofBOSS data while lowering  $S_8$  to match the values measured by weak-lensing surveys, the best-fit model has a longer lifetime  $\Gamma^{-1} \simeq 120$  Gyr and a larger kick velocity  $v_{\text{kick}}/c \simeq \varepsilon \simeq 1.2\%$  than without EFTofBOSS.

To finish, let us point out that the DES collaboration recently derived new constraints on the  $\Lambda$ DDM scenario using observations of Milky Way satellites (MAU et al. 2022). These constraints exclude  $\text{Log}_{10}(\Gamma/\text{Gyr}^{-1}) \gtrsim -1.5$  for  $\text{Log}_{10}(v_{\text{kick}}/c) \simeq \text{Log}_{10}(\varepsilon) \gtrsim -4$ . The best-fit model of our baseline BAO+SNIa+*Planck*+ $S_8$  analysis, and a large fraction of the 68 % C.L., lie well within the allowed region, but these observations certainly provide a crucial test of the  $\Lambda$ CDM cosmology, as a deficit of satellites compared to  $\Lambda$ CDM is expected in this model.



# IV

---

## New cosmological limits on the neutrino mass and lifetime

---

*“When I heard the learn’d astronomer,  
When the proofs, the figures, were ranged in columns before me,  
When I was shown the charts and diagrams, to add, divide, and  
measure them,  
When I sitting heard the astronomer where he lectured with much  
applause in the lecture-room,  
How soon unaccountable I became tired and sick,  
Till rising and gliding out I wander’d off by myself,  
In the mystical moist night-air, and from time to time,  
Look’d up in perfect silence at the stars.”*

*Walt Whitman, Leaves of Grass*

### Contents

---

4.1	Constraints on neutrino mass and lifetime from cosmological data . . .	176
4.2	The neutrino mass conundrum . . . . .	178
4.3	Parameter space of decaying neutrinos . . . . .	181
4.4	Formalism of invisible non-relativistic neutrino decay . . . . .	184
4.4.1	Derivation of Boltzmann equations . . . . .	184
4.4.2	Impact of the non-relativistic neutrino decay on the CMB spectral	88
4.4.3	Consistency of the implementation of the Boltzmann equations	189
4.5	Cosmological constraints . . . . .	192
4.5.1	Details of the analysis . . . . .	192
4.5.2	Updated limits on the neutrino mass and lifetime . . . . .	193
4.5.3	Comparison with former results and impact of <i>Planck</i> 2018 data	94
4.6	Summary and outline . . . . .	195

---

This Chapter is based on:

G. F. Abellán, Z. Chacko, A. Dev, P. Du, V. Poulin, Y. Tsai  
*“Improved cosmological constraints on the neutrino mass and lifetime”*

JHEP 08 076 (2022); arXiv:2112.13862

## 4.1 Constraints on neutrino mass and lifetime from cosmological data

Even though neutrinos were first detected more than six decades ago, they remain among the most mysterious particles in nature, with many of their fundamental properties still to be determined. In particular, although oscillation experiments have provided convincing evidence that neutrinos have non-vanishing masses, these measurements are only sensitive to the mass-squared splittings and consequently the spectrum of neutrino masses remains unknown. The lifetimes of the neutrinos are also poorly constrained, especially in comparison to the other particles in the Standard Model (SM). The determination of the masses and the lifetimes of these mysterious particles remain some of the most important open problems in fundamental physics.

The fact that cosmic neutrinos are among the most abundant particles in the universe, contributing significantly to the total energy density at early times, provides an opportunity to measure their properties. In particular, the evolution of the cosmological density fluctuations depends on  $\sum m_\nu$ , the sum of neutrino masses. This translates into characteristic effects on the CMB and LSS (BOND et al. 1980; HU et al. 1998) (for reviews see Y. Y. Y. WONG (2011), LATTANZI et al. (2018), and LESGOURGUES et al. (2018)), that are large enough to allow the sum of neutrino masses to be determined in the near future.

This determination is based on the observation that massive neutrinos contribute differently to cosmological observables than either massless neutrinos or CDM. At early times, while still relativistic, massive neutrinos contribute to the energy density in radiation, just as in the case of massless neutrinos. However, after neutrinos become non-relativistic, their energy density redshifts as matter and therefore contributes more to the expansion rate than massless neutrinos, which would continue to redshift as radiation. As a result, over a given redshift span, the higher expansion rate reduces the time available for the growth of matter density perturbations. However, since massive neutrinos retain pressure until late times, their contribution to the density perturbations on scales below their free streaming lengths is too small to compensate for the shorter structure formation time. Therefore, if neutrinos become non-relativistic after recombination, the net effect of non-vanishing neutrino masses is a suppression of the matter power spectrum and the CMB lensing potential. Based on this, current observations are able to place a bound on the sum of neutrino masses,  $\sum m_\nu \lesssim 0.12$  eV (AGHANIM et al. 2020b). It is important to note that this result assumes that neutrinos are stable on timescales of order the age of the universe. In scenarios in which the neutrinos decay (SERPICO 2007, 2009), or annihilate away into lighter species (BEACOM et al. 2004; FARZAN et al. 2016) on timescales shorter than the age of the universe, this bound is no longer valid and must be reconsidered.

Cosmological observations can also be used to place limits on the neutrino lifetime. In the case of neutrinos that decay to final states containing photons, the bounds on spectral distortions in the cosmic microwave background (CMB) can be translated into limits on the neutrino lifetime,  $\tau_\nu \gtrsim 10^{19}$  s for the larger mass splitting and  $\tau_\nu \gtrsim 4 \times 10^{21}$  s for the smaller one (AALBERTS et al. 2018). In the case of decays to invisible final states, the limits are much weaker. For neutrinos that decay

while still relativistic, the decay and inverse decay processes can prevent neutrinos from free streaming. Measurements of the CMB power spectra sets a lower bound on the neutrino lifetime,  $\tau_\nu \geq 4 \times 10^6 \text{ s } (m_\nu/0.05\text{eV})^5$ , in the case of decay into dark radiation (BARENBOIM et al. 2021)<sup>1</sup> (for earlier work, see HANNESTAD et al. (2005), BASBOLL et al. (2009), ARCHIDIACONO et al. (2014), and ESCUDERO et al. (2019)).

In the case of non-relativistic neutrino decays into dark radiation, the energy density of the decay products redshifts faster than that of stable massive neutrinos. Unstable neutrinos therefore have less of an effect on structure formation than stable neutrinos of the same mass. Consequently, cosmological observables depend both on the masses of the neutrinos and their lifetimes, and heavier values of  $\sum m_\nu$  may still be allowed by the data provided the neutrino lifetime is short enough. In CHACKO et al. 2020, Planck15 and LSS data were used to place constraints on the neutrino mass as a function of the lifetime, and found that values of  $\sum m_\nu$  as large as 0.9 eV were still allowed by the data. Future LSS measurements at higher redshifts may be able to break the degeneracy between the neutrino mass and lifetime and measure these parameters independently (CHACKO et al. 2021).

It is worth noting that there are also bounds on the neutrino lifetime from Supernova 1987A (FRIEMAN et al. 1988), solar neutrinos (BEACOM et al. 2002; JOSHIPURA et al. 2002; BANDYOPADHYAY et al. 2003; BERRYMAN et al. 2015), astrophysical neutrinos measured at IceCube (BAERWALD et al. 2012; PAGLIAROLI et al. 2015; BUSTAMANTE et al. 2017; DENTON et al. 2018; ABDULLAHI et al. 2020; BUSTAMANTE 2020), atmospheric neutrinos and long baseline experiments (GONZALEZ-GARCIA et al. 2008; GOMES et al. 2015; CHOUBEY et al. 2018; AHARMIM et al. 2019). However, these constraints are in general much weaker than the limits from cosmology.

We revisit the scenario in which neutrinos decay into dark radiation after becoming non-relativistic, and obtain updated limits based on the newer data from Planck18. In order to take advantage of the greater precision of the new data, the analysis we perform is also more accurate. We find that, under the assumption that neutrinos decay after becoming non-relativistic, the neutrino mass bound from Planck18 data (in combination with BOSS BAO data and Pantheon SN1a data) is relaxed to  $\sum m_\nu \lesssim 0.42 \text{ eV } (95\% \text{ C.L.})$ <sup>2</sup>. While this represents a remarkable relaxation of the constraints as compared to the case of stable neutrinos, we note that it is much stronger than the limit derived from Planck15 data for the same decaying neutrino scenario,  $\sum m_\nu \lesssim 0.9 \text{ eV } (95\% \text{ C.L.})$ . We show that the improvement of the bound arises primarily from the more precise low- $\ell$  polarization data from Planck18, which allows an improved determination of the optical depth to reionization  $\tau_{\text{reio}}$ , thereby breaking the correlation with  $\sum m_\nu$  that appears (for relatively high neutrino masses) through the impact of neutrinos on the overall height of the acoustic peaks

<sup>1</sup>More concretely, this work considered a scenario in which a heavier neutrino decays relativistically into a lighter neutrino and a massless scalar,  $\nu_H \rightarrow \nu_l + \phi$ , and derived bounds assuming  $m_{\nu_l} = 0$ . Recently, J. Z. CHEN et al. (2022) updated those bounds by accounting for the experimentally determined mass splittings between the parent and the daughter neutrino,  $\Delta m_\nu^2$ . They showed that, for a parent neutrino with  $m_{\nu_H} \lesssim 0.1 \text{ eV}$ , the constraints on its lifetime weaken by a factor 50 and  $10^5$ , if  $\Delta m_\nu^2$  corresponds to the atmospheric and solar mass gap, respectively.

<sup>2</sup>This is a factor of two weaker than the constraints advocated in LORENZ et al. (2021), which used a model-independent approach to constrain the neutrino mass as a function of redshift, but neglected the effect of the daughter particles.



(*i.e.* the “early integrated Sachs-Wolfe effect”) (LESGOURGUES et al. 2018).

Besides using up-to-date cosmological data, we also improve the analysis from CHACKO et al. 2020 – hereafter C19 – by incorporating higher order corrections due to neutrino decays into the Boltzmann equations that describe the evolution of Universe’s energy and metric fluctuations. Recently, BARENBOIM et al. 2021 – hereafter B20 – provided a complete set of Boltzmann equations for the neutrino decay, but did not conduct MCMC runs necessary to update the bounds on non-relativistic neutrino decays. In this work, we derive Boltzmann equations exactly valid in the absence of ‘inverse-decays’ and quantum statistics (*i.e.* Fermi blocking and Bose enhancement terms). For the numerical implementation, we follow a consistent  $T_{\text{dec}}/m_\nu$  expansion, where  $T_{\text{dec}}$  is the temperature at the time of the decay, so that the analysis is under control when neutrinos decay after become non-relativistic.

The rest of this chapter is organized as follows. In Sect. 4.2 we review the neutrino mass conundrum and its interplay with cosmology. In Sect. 4.3, we present a summary of constraints on the parameter space of decaying neutrinos. In Sect. 4.4, we derive the set of Boltzmann equations to describe neutrino decay that are valid in the non-relativistic regime and compare our improved analysis to past work. In Sect. 4.5, we present a MCMC analysis of the decaying neutrino scenario against up-to-date cosmological data. Finally, we conclude in Sect. 4.6.

## 4.2 The neutrino mass conundrum

Neutrinos are neutral fermions with spin  $1/2$  which were postulated by W. Pauli in 1930 in order to explain the continuous spectrum observed in the  $\beta$ -decay of nuclei. They come in three flavors which are paired to leptons within  $SU(2)_L$  doublets, and are charged only under the weak interaction. Because of this, neutrinos typically pass through matter unimpeded and therefore are very hard to detect. Electron neutrinos ( $\nu_e$ ) were discovered by Reines and Cowan in 1956, muon neutrinos ( $\nu_\mu$ ) in 1962 at Brookhaven and tau neutrinos ( $\nu_\tau$ ) in 2000 at Fermilab, by the DONUT experiment. Neutrinos were long thought to be massless, but this started to change with the observation of the solar neutrino flux. The sun is a potent source of  $\nu_e$  in the energy range  $E \sim \mathcal{O}(\text{MeV})$ , produced in thermonuclear fusion reactions inside the core. After the technology required to detect the solar neutrino flux was developed in the 70s, the observations showed that the number of detected solar  $\nu_e$  was only about one third of the number predicted by the standard solar model. This is the famous *solar neutrino problem*. The breakthrough came in 2001, thanks to the data from the SuperKamiokande experiment and the Sudbury Neutrino Observatory. Those combined observations allow to compare the total number of solar neutrinos of all types, to the number of just  $\nu_e$ : the first was in good agreement with theoretical expectations, while the second still showed the same deficit, pointing at *conversion of neutrino flavor* during their propagation. The most plausible explanation invoked *neutrino oscillations*, which were confirmed in subsequent experiments.

Neutrino oscillations had been theorized in the 50s by Bruno Pontecorvo (PONTECORVO 1957). They arise from a quantum mechanical phenomenon linked to the fact that neutrino possess non-zero masses. The principle of superposition allows the three flavor states to be (orthogonal) combinations of three neutrino states with

a definite mass. Introducing the Pontecorvo-Maki-Nakgawa-Sakata (PMNS) mixing matrix  $U$ , a  $3 \times 3$  unitary matrix, a certain “ket” state can generally be written as

$$|\nu_\alpha\rangle = \sum_{i=1}^3 U_{\alpha i}^* |\nu_i\rangle \quad \text{with } \alpha = e, \mu, \tau, \quad (4.1)$$

where greek (latin) indices label flavor (mass) states, and it is assumed the normalization  $\langle \nu_\alpha | \nu_\beta \rangle = \delta_{\alpha\beta}$  and  $\langle \nu_i | \nu_j \rangle = \delta_{ij}$ . Considering neutrinos propagating in vacuum at semi-relativistic speeds, one can compute the survival probability  $P_{\nu_\alpha \rightarrow \nu_\alpha}$  as a function of the distance of the detector from the neutrino source (GIUNTI et al. 2007)

$$P_{\nu_\alpha \rightarrow \nu_\alpha}(L) = 1 - 4 \sum_{i>j} |U_{\alpha i}|^2 |U_{\alpha j}|^2 \sin^2 \left( 2\pi \frac{L}{L_{ij}^{\text{osc}}} \right), \quad (4.2)$$

where  $L_{ij}^{\text{osc}}$  is the characteristic oscillation length

$$L_{ij}^{\text{osc}} \equiv \frac{4\pi E}{\Delta m_{ij}^2} \simeq 2.47 \frac{E/\text{MeV}}{\Delta m_{ij}^2/\text{eV}^2} \text{ m}, \quad (4.3)$$

and  $\Delta m_{ij}^2 \equiv m_i^2 - m_j^2$  denote the (squared) mass splittings. Therefore, flavor transitions can take place only if neutrinos are massive, their masses are non-degenerate, and the corresponding PMNS matrix elements are non-zero. From the argument of the sinusoidal function, we see that for a given distance  $L$  and source energy  $E$ , experiments are mainly sensitive to mass splittings  $\Delta m_{ij}^2$  such that  $L \gtrsim L_{ij}^{\text{osc}}$ . In fact, the sun is not the single source of neutrinos available. Nuclear reactors typically produce neutrinos with energy of the order  $E \sim \mathcal{O}(\text{MeV})$ , and are classified between short ( $L \sim 10$  m) (SBL), long ( $L \sim 1$  km) (LBL) and very long ( $L \sim 10^2$  km) (VLBL) baseline experiments, sensitive to  $\Delta m_{ij}^2 \gtrsim 0.1, 10^{-3}$  and  $10^{-5}$  eV<sup>2</sup>, respectively. An analogous classification can be made for neutrino beams produced at accelerators in the energy range  $E \sim \mathcal{O}(\text{GeV})$  due to the pion, kaon and muon decays. In this case, SBL are characterized by  $L \sim 1$  km and LBL by  $L \sim 10^3$  km, sensitive to  $\Delta m_{ij}^2 \gtrsim 0.1$  and  $10^{-3}$  eV<sup>2</sup>, respectively. Finally, *atmospheric neutrinos* are produced when cosmic rays, consisting mainly of protons, interact with atoms in our atmosphere. These interactions create a lot of pions which subsequently decay into muons and neutrinos. In this case, the energy and distance cover a very wide range, but neutrinos are typically detected with energies centered at  $E \sim \mathcal{O}(\text{GeV})$  and distances up to  $L \sim 10^4$  km (for neutrinos produced on the other side of the Earth), which corresponds to a sensitivity  $\Delta m_{ij}^2 \gtrsim 10^{-4}$  eV<sup>2</sup>.

The PMNS matrix is unitary, so it contains a priori nine real d.o.f. However, five of these real parameters can be absorbed as phases of the lepton fields, and thus the PMNS matrix is fully described by four parameters (assuming Dirac neutrinos), and can be parametrized in the following form

$$U = \begin{pmatrix} 1 & 0 & 0 \\ 0 & c_{23} & s_{23} \\ 0 & -s_{23} & c_{23} \end{pmatrix} \begin{pmatrix} c_{13} & 0 & s_{13}e^{-i\delta_{\text{CP}}} \\ 0 & 1 & 0 \\ -s_{13}e^{i\delta_{\text{CP}}} & 0 & c_{13} \end{pmatrix} \begin{pmatrix} c_{12} & s_{12} & 0 \\ -s_{12} & c_{12} & 0 \\ 0 & 0 & 1 \end{pmatrix}, \quad (4.4)$$

where  $c_{ij} = \cos(\theta_{ij})$  and  $s_{ij} = \sin(\theta_{ij})$ , with  $\theta_{ij}$  the mixing angle of mass states  $i$  and  $j$ , and  $\delta_{\text{CP}}$  is a Dirac CP violating phase. Hence, neutrino oscillations are described in general by six parameters, that can taken to be  $\{\theta_{13}, \theta_{23}, \theta_{12}, \delta_{\text{CP}}, \Delta m_{21}^2, \Delta m_{31}^2\}$ . However,

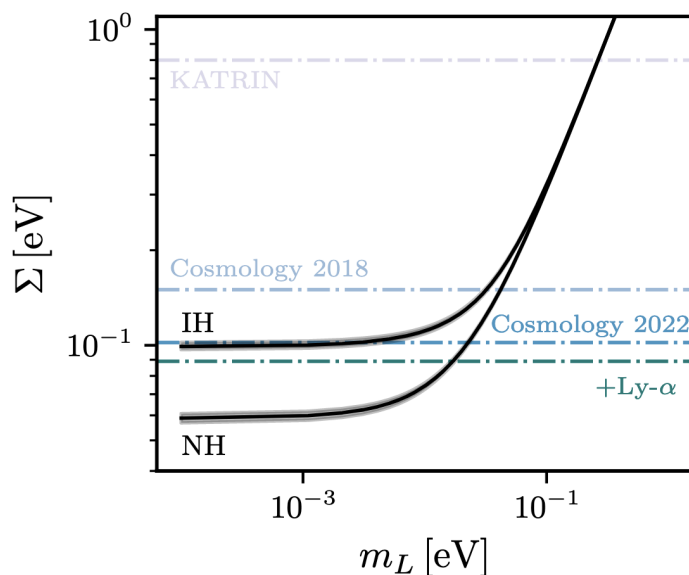


**Figure 4.1** – Sum of neutrino masses as a function of the lowest neutrino mass, together with the most recent upper limits (at 95 % C.L.) from cosmology and the estimated KATRIN sensitivity limit. The grey bands represent  $5\sigma$  uncertainty on the oscillation measurements. Taken from JIMENEZ et al. (2022).

in many cases, the observations can be understood in terms of oscillations driven by just one  $\Delta m_{ij}^2$ . Solar and VLBL reactor neutrino experiments (e.g. SNO, KamLAND) have measured the parameters  $\{\Delta m_{12}^2, \theta_{12}\}$ , while atmospheric and LBL accelerator experiments (e.g. SuperKamiokande, K2K, MINOS, OPERA) have measured the parameters  $\{|\Delta m_{31}^2 + \Delta m_{32}^2|/2, \theta_{23}\}$ . Finally, LBL reactor (e.g. Daya Bay, RENO, Double Chooz) have provided information on the mixing angle  $\theta_{13}$ . In a medium, the presence of a high energy density of electrons can enhance the effective mixing angle, an effect which is known as the Mikheyev-Smirnov-Wolfenstein (MSW) effect (WOLFENSTEIN 1978; MIKHEYEV et al. 1985). Because of the correction to the vacuum mixing picture, studies of solar neutrinos have been able to deduce the sign of  $\Delta m_{21}^2$ . The most recent determinations of the solar and atmospheric mass splittings indicate  $\Delta m_{21}^2 \simeq 7.6 \times 10^{-5} \text{ eV}^2$  and  $|\Delta m_{31}^2| \simeq 2.5 \times 10^{-3} \text{ eV}^2$ , respectively (SALAS et al. 2018). Since the sign of  $\Delta m_{31}^2$  is still unknown, this leaves two possibilities for the mass ordering of neutrinos: *normal hierarchy* (NH), if  $m_3 \gg m_2 > m_1$ , or *inverted hierarchy* (IH), if  $m_2 > m_1 \gg m_3$ . The absolute scale of neutrino mass is unknown as well. The sum of neutrino masses  $\sum m_\nu$  can be related to the mass splittings as follows

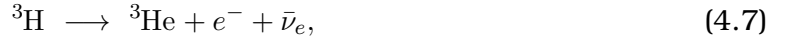
$$\sum m_\nu^{\text{NH}} = m_1 + \sqrt{m_1^2 + \Delta m_{21}^2} + \sqrt{m_1^2 + \Delta m_{31}^2}, \quad (4.5)$$

$$\sum m_\nu^{\text{IH}} = m_3 + \sqrt{m_3^2 + |\Delta m_{31}^2|} + \sqrt{m_3^2 + |\Delta m_{31}^2| + \Delta m_{21}^2}, \quad (4.6)$$

Hence, the minimum value for the total neutrino mass depends on the mass ordering. For the normal hierarchy, setting  $m_1 = 0$  gives  $\sum m_\nu^{\text{NH}} \gtrsim 0.06 \text{ eV}$ , while for the inverted hierarchy, setting  $m_3 = 0$  gives  $\sum m_\nu^{\text{IH}} \gtrsim 0.10 \text{ eV}$ . In Fig. 4.1 we show the sum of neutrino masses ( $= \Sigma$ , to shorten notation) as a function of the lowest neutrino mass ( $m_L$ ), together with some current and projected upper bounds on  $\Sigma$ . Currently, cosmology provides the strongest constraints on the sum of neutrino masses. As mentioned previously, the latest constraints from

Planck18 TT,EE,TE+lowE+lensing+BAO give  $\sum_{\text{cosmo}} < 0.12$  eV (AGHANIM et al. 2020b). This bound strengthens to  $\sum_{\text{cosmo}} < 0.102$  eV when combining with redshift-space distortions (RSD) from eBOSS (ALAM et al. 2021) and to  $\sum_{\text{cosmo}} < 0.089$  eV when combining with the Lyman- $\alpha$  forest 1D flux power spectrum (PALANQUE-DELABROUILLE et al. 2020).

It is also possible to measure the absolute neutrino mass scale with laboratory experiments on Earth. These experiments typically look at the energy spectrum of electrons emitted from the tritium beta decay



which have  $Q_\beta = m_{3\text{H}} - m_{3\text{He}} - m_e \simeq 18.58$  keV. The main idea is that the endpoint of the spectrum (or maximum electron energy) is shifted with respect to  $Q_\beta$  due to the presence of neutrino masses. Assuming mass splittings much smaller than the experimental energy resolution, one expects to measure a shift  $Q_\beta - m_{\nu_e}$ , where  $m_{\nu_e}$  is the effective electron mass

$$m_{\nu_e}^2 \equiv \sum_i |U_{ei}|^2 m_i^2. \quad (4.8)$$

The combination of the first and second campaign of the KARlsruhe TRITium Neutrino (KATRIN)  $\beta$ -experiment have yielded a constraint on the effective neutrino mass of  $m_{\nu_e} < 0.8$  eV (AKER et al. 2022), corresponding to  $\sum_{\text{KATRIN}} < 2.4$  eV<sup>3</sup> (at 90 % C.L.). The expected final sensitivity of KATRIN is  $\sum_{\text{KATRIN}} < 0.6 - 0.8$  eV. One important benefit of KATRIN is that the neutrino mass determination is fully model independent (even independent of the Dirac or Majorana nature of neutrinos), as opposed to the CMB/LSS determinations, which always rely on the cosmological model.

The origin of neutrino masses cannot be successfully explained in the framework of the SM of particle physics, so they currently provide the only certain evidence of physics beyond the SM (GIUNTI et al. 2007). Besides the absolute mass scale and hierarchy, other open questions in the neutrino sector include: their Majorana/Dirac nature, the existence of new sterile neutrinos (inducing a small non-unitarity in the mixing matrix) or the possibility of CP violation in the leptonic sector (possibly related to the matter-antimatter asymmetry). As we discussed in the previous section, massive neutrinos influence both the cosmic expansion as well as the growth of structure in the universe, so cosmological observations provide very valuable clues about their properties. Future LSS surveys such as Euclid (AMENDOLA et al. 2018) aim at a detection of the absolute neutrino mass scale. Notice also from the above discussion that a possible detection of  $\sum$  by KATRIN would immediately enter in conflict with CMB/LSS determinations. In the rest of this chapter, we study the cosmological implications of a model of decaying neutrinos that could potentially reconcile those measurements.

### 4.3 Parameter space of decaying neutrinos

Here we outline the constraints on the mass and lifetime of neutrinos decaying into dark radiation. As explained in Sect. 4.1, current cosmological observables

<sup>3</sup>For the range of masses probed by KATRIN, neutrino mass states are quasi-degenerate,  $m_i \simeq m$ , so the effective electron mass is roughly given by  $m_{\nu_e}^2 \simeq m^2 \sum_i |U_{ei}|^2 = m^2$ , where the last equality follows from unitarity. Hence the sum of neutrino masses is indeed given by  $\sum \sim 3m \sim 3m_{\nu_e}$ .

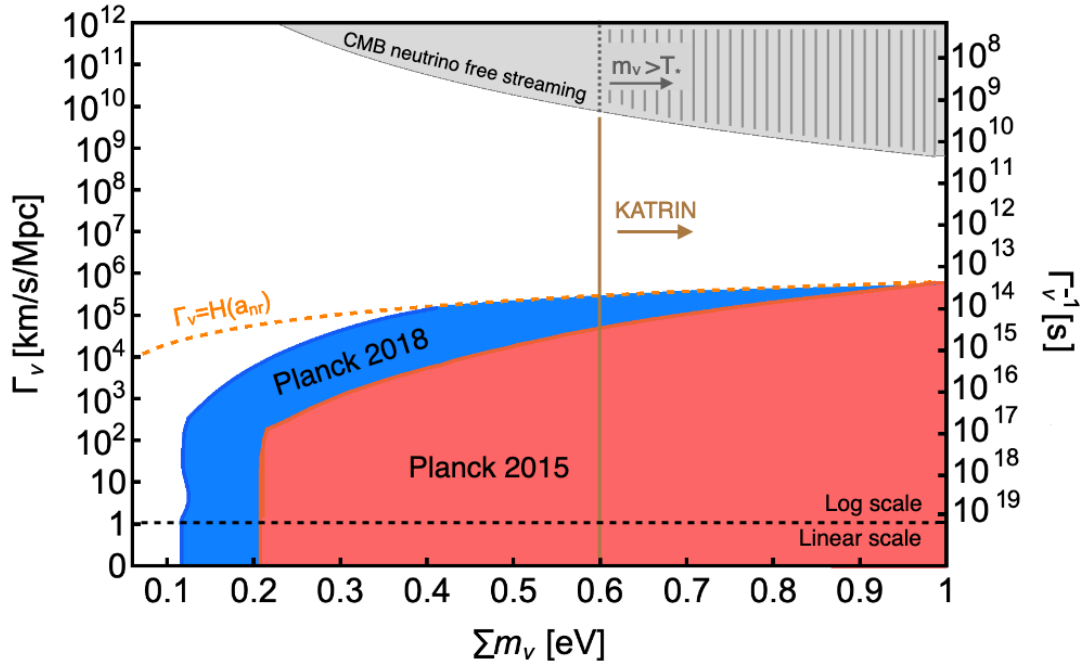


**Figure 4.2** – The plot shows the current constraints on decaying neutrinos in the  $\sum m_\nu - \Gamma_\nu$  parameter space. The colored regions are excluded by current data while the white region is allowed. The orange dashed line represents  $\Gamma_\nu = H(a_{nr})$ . Our study focuses on the region below this line, meaning decay happens after neutrinos have become non-relativistic. The light grey region shows current constraints on neutrino mass and lifetime coming from the requirement that neutrinos are free streaming close to recombination (B20). The shaded region indicates that this bound may not be applicable when neutrino mass is larger than the temperature of recombination:  $m_\nu > T_* \sim 0.2$  eV. Our analysis excludes the red (blue) region labelled “Planck 2015” (“Planck 2018”) based on the data (Planck+BAO+Pantheon). The vertical brown line shows the projected KATRIN sensitivity.

only place limits on a combination of the sum of neutrino masses and their lifetime. Therefore, in this study we will map out the constraints in the two-dimensional parameter space spanned by the sum of neutrino masses ( $\sum m_\nu$ ) and the neutrino decay width ( $\Gamma_\nu$ ), as shown in Fig. 4.2.

In our analysis we assume that all three neutrinos are degenerate in mass. This is a good approximation because the current bounds on  $\sum m_\nu$  are larger than the observed mass splittings (see Fig. 4.2). We further assume that all three neutrinos have the same decay width  $\Gamma_\nu$ . Since the mixing angles in the neutrino sector are large, this is a good approximation in many simple models of decaying neutrinos if the spectrum of neutrinos is quasi-degenerate. While this is a simple parameterization of neutrino decays, our bounds can easily be applied to specific models, as done in great details in ESCUDERO et al. (2020b).

The CMB can be used to constrain the masses and decay widths of neutrinos that decay prior to recombination. When neutrinos decay while still relativistic, decay and inverse decay can prevent neutrinos from free-streaming. If this happens before recombination, it can alter the well-known ‘neutrino drag’ effect that manifests as a phase-shift at high- $\ell$ ’s in the CMB power spectrum (BASHINSKY et al. 2004; AUDREN et al. 2015; FOLLIN et al. 2015; BAUMANN et al. 2016). Therefore, CMB data can



place a constraint on the decay width of neutrinos. The resulting bound depends on neutrino masses, and was recently updated in B20,  $\tau_\nu \geq 4 \times 10^6 \text{ s} (m_\nu/0.05 \text{ eV})^5$ . This bound excludes the grey region at the top of Fig. 4.2.

In addition, based on the analysis in this paper, part of the ‘late-decay’ parameter space can also be excluded based on the gravitational impacts of massive neutrinos on the CMB and LSS. Through the Monte Carlo study presented in Sect. 4.5, the blue (red) shaded region in Fig. 4.2 is excluded by the data combination Planck18 (Planck15) + BAO + Pantheon.<sup>4</sup> The orange dashed line in the figure ( $\Gamma_\nu = H(a_{\text{nr}})$ ) separates the region where neutrinos decay when non-relativistic from the region where they decay while still relativistic. Here  $a_{\text{nr}}$  corresponds to the approximate scale factor at the time that neutrinos transition to non-relativistic, and is defined as  $3T_\nu(a_{\text{nr}}) = m_\nu$ . This simple definition is based on the fact that for relativistic neutrinos at temperature  $T_\nu$ , the average energy per neutrino is approximately  $3T_\nu$ . The Hubble scale at  $a_{\text{nr}}$  is given by,

$$H(a_{\text{nr}}) = H_0 \sqrt{\Omega_m} \left( \frac{\sum m_\nu}{9T_{\nu,0}} \right)^{3/2} \quad (4.9)$$

$$\simeq 7.5 \times 10^5 \text{ km/s/Mpc} \left( \frac{H_0}{68 \text{ km/s/Mpc}} \right) \left( \frac{\Omega_m}{0.3} \right)^{1/2} \left( \frac{\sum m_\nu}{1 \text{ eV}} \right)^{3/2} \left( \frac{1.5 \times 10^{-4} \text{ eV}}{T_{\nu,0}} \right)^{3/2},$$

where  $T_{\nu,0}$  is the present neutrino temperature. Since our study focuses on the decay of neutrinos after they become non-relativistic, we only present constraints below the orange dashed line. Our analysis shows that  $\sum m_\nu$  as large as 0.42 eV is still allowed by the data.

Our results have important implications for current and future laboratory experiments designed to detect neutrino masses. As discussed in Sect. 4.2, next generation tritium decay experiments such as KATRIN (ANGRIK et al. 2005) are expected to be sensitive to values of  $m_{\nu_e}$  as low as 0.2 eV, corresponding to  $\sum m_\nu$  of order 0.6 eV. Naively, a signal in these experiments would conflict with the current cosmological bound for stable neutrinos,  $\sum m_\nu < 0.12 \text{ eV}$ . However, since the unstable neutrino paradigm greatly expands the range of neutrino masses allowed by current cosmological data, it is interesting to explore whether this scenario can accommodate a potential signal at KATRIN. In Fig. 4.2, we display a brown vertical line  $\sum m_\nu = 0.6 \text{ eV}$  that corresponds to the expected KATRIN sensitivity. We see that this value of  $\sum m_\nu$  is too large to be accommodated in the non-relativistic decay regime, where our analysis is valid. However, our result, in combination with those from the ‘relativistic decay’ scenario studied in B20, leaves open the interesting possibility that neutrinos decaying with a decay width between  $\text{Log}_{10} \left( \frac{\Gamma_\nu}{\text{km/s/Mpc}} \right) \sim 5.5 - 9$  could reconcile cosmological observations with a potential detection at KATRIN, thereby opening a large discovery potential for laboratory experiments. To confirm this conjecture, more work needs to be done to cover the ‘intermediate’ decay regime (i.e. where neutrinos are neither fully relativistic nor fully non-relativistic). We leave this for future work.

In recent years, a number of studies have attempted to constrain the neutrino mass ordering, showing that under the assumption of stable neutrinos, the inverted

<sup>4</sup>Note that in our analysis we scanned the region between  $0 \leq \text{Log}_{10} \left( \frac{\Gamma_\nu}{\text{km/s/Mpc}} \right) \leq 6$ . In Fig. 4.2, we have extrapolated the bound at  $\text{Log}_{10} \left( \frac{\Gamma_\nu}{\text{km/s/Mpc}} \right) = 0$  to  $\Gamma_\nu = 0$ , because the constraint on  $\sum m_\nu$  is independent of  $\Gamma_\nu$  when  $\Gamma_\nu \ll H_0$ .



ordering is now disfavored by a compilation of cosmological data (A. CALDWELL et al. 2017; GERBINO et al. 2017; SIMPSON et al. 2017; VAGNOZZI et al. 2017; DI VALENTINO et al. 2021a; JIMENEZ et al. 2022) (see also SCHWETZ et al. (2017), GARIAZZO et al. (2018), HERGT et al. (2021), and GARIAZZO et al. (2022) for a different take) as well as from Ly- $\alpha$  observations (PALANQUE-DELABROUILLE et al. 2020). However, these arguments are centered on the fact that these analyse leads to a constraint on  $\sum m_\nu$  at odds with the lower bound on the sum of neutrino masses in the case of inverted ordering,  $\sum m_\nu \gtrsim 0.1$  eV. Our result suggests that these constraints are strongly dependent on the assumption of neutrino stability over cosmological timescales, and therefore that the inverted ordering is not robustly excluded. It would be very interesting to extend our analysis to the inclusion of Ly- $\alpha$  data to confirm this conclusion.

## 4.4 Formalism of invisible non-relativistic neutrino decay

In this section, we revisit the set of Boltzmann equations describing the evolution of the phase space distribution (PSD) of massive particles decaying into daughter radiation. In our analysis, we assume the decay happens after the neutrinos have become non-relativistic so that the contribution from inverse decay processes and quantum statistics can be safely neglected.

### 4.4.1 Derivation of Boltzmann equations

We denote the phase space distribution of each species as  $f_I(k, q, \mu, \tau)$  (in Fourier space), where  $I = \{\nu, \text{dr1}, \text{dr2}\}$ , since we are assuming a two-body decay to massless daughters. As in previous chapters, we work in the synchronous gauge co-moving with the CDM (introduced in Sect. 1.6.1), where the scalar metric potentials are referred as  $h$  and  $\eta$ . In this gauge, and neglecting all terms that are at least second order in perturbations, the Boltzmann equations controlling the evolution of  $f_I$  is written as (c.f. Eq. (3.4)) :

$$\frac{\partial f_I}{\partial \tau} + i\mu \frac{kq}{\mathcal{E}_I} f_I + \frac{df_I}{d \ln q} \left( \eta' - \frac{h' + 6\eta'}{2} \mu^2 \right) = \left( \frac{\partial f_I}{\partial \tau} \right)_C. \quad (4.10)$$

The collision terms  $\left( \frac{\partial f_I}{\partial \tau} \right)_C$  describe the decay process

$$\nu(Q) \longrightarrow \text{DR}(Q_1) + \text{DR}(Q_2), \quad (4.11)$$

where we labelled the comoving four-momentum  $Q = (\mathcal{E}, \vec{q})$  of each species, and are given by (C19) :

$$\left( \frac{\partial f_\nu}{\partial \tau} \right)_C = - \frac{\alpha^2}{2\mathcal{E}_\nu} \int \frac{d^3 \vec{q}_1}{(2\pi)^3 2\mathcal{E}_1} \frac{d^3 \vec{q}_2}{(2\pi)^3 2\mathcal{E}_2} |\mathcal{M}|^2 (2\pi)^4 \delta^{(4)}(Q - Q_1 - Q_2) f_\nu(q), \quad (4.12)$$

$$\left( \frac{\partial f_{\text{dr1}}}{\partial \tau} \right)_C = + \frac{\alpha^2}{2\mathcal{E}_1} \int \frac{d^3 \vec{q}}{(2\pi)^3 2\mathcal{E}_\nu} \frac{d^3 \vec{q}_2}{(2\pi)^3 2\mathcal{E}_2} |\mathcal{M}|^2 (2\pi)^4 \delta^{(4)}(Q - Q_1 - Q_2) f_\nu(q), \quad (4.13)$$

$$\left( \frac{\partial f_{\text{dr2}}}{\partial \tau} \right)_C = + \frac{\alpha^2}{2\mathcal{E}_2} \int \frac{d^3 \vec{q}}{(2\pi)^3 2\mathcal{E}_\nu} \frac{d^3 \vec{q}_1}{(2\pi)^3 2\mathcal{E}_1} |\mathcal{M}|^2 (2\pi)^4 \delta^{(4)}(Q - Q_1 - Q_2) f_\nu(q). \quad (4.14)$$

To separate the Boltzmann equations into zeroth and first order contributions, we will eventually perform the same decomposition as in Eq. (3.8)

$$f_I(k, q, \mu, \tau) = \bar{f}_I(q, \tau) + \Delta f_I(k, q, \mu, \tau). \quad (4.15)$$

Let us start with the derivation of the zeroth order equations. As we show in [App. E.1](#), the collision term in [Eq. \(4.12\)](#) for the decaying neutrinos simplifies to

$$\left(\frac{\partial f_\nu}{\partial \tau}\right)_C = -\frac{a^2 \Gamma_\nu m_\nu}{\mathcal{E}_\nu} f_\nu = -\frac{a \Gamma_\nu}{\gamma} f_\nu, \quad (4.16)$$

where  $\gamma \equiv \mathcal{E}_\nu / (am_\nu)$  denotes the Lorentz boost factor. Hence, the background equation for the neutrino mother particles can be simply written as

$$\frac{\partial \bar{f}_\nu}{\partial \tau} = -\frac{a \Gamma_\nu}{\gamma} \bar{f}_\nu, \quad (4.17)$$

Multiplying each side of the former equation by  $4\pi a^{-4} q^2 \mathcal{E}_\nu$ , and integrating over  $q$ , we find the continuity equation for  $\bar{\rho}_\nu$ :

$$\bar{\rho}'_\nu + 3\mathcal{H}\bar{\rho}_\nu(1 + w_\nu) = -a\Gamma_\nu m_\nu \bar{n}_\nu, \quad (4.18)$$

where  $\bar{n}_\nu = 4\pi a^{-3} \int dq q^2 \bar{f}_\nu(q)$  is the neutrino number density. On the other hand, the continuity equation for the total background density of daughter radiation,  $\bar{\rho}_{\text{dr}} = 4\pi a^{-4} \sum_{i=1,2} \int dq_i q_i^3 \bar{f}_{\text{dri}}$ , is given by

$$\bar{\rho}'_{\text{dr}} + 4\mathcal{H}\bar{\rho}_{\text{dr}} = a\Gamma_\nu m_\nu \bar{n}_\nu, \quad (4.19)$$

where the term at the r.h.s. follows from [Eq. \(4.18\)](#) and conservation of energy. In practice, we never use [Eq. \(4.18\)](#) to solve for the evolution of the neutrino background density. Rather, we directly compute the PSD  $\bar{f}_\nu$  at each time step, and then integrate over momenta to find  $\bar{\rho}_\nu$  and  $\bar{n}_\nu$ . The formal solution  $\bar{f}_\nu(q, \tau)$  to the differential equation [Eq. \(4.17\)](#) is

$$\bar{f}_\nu(q, \tau) = \bar{f}_{\nu,i}(q) e^{-\Gamma_\nu \int_{\tau_i}^{\tau} \frac{ad\tau'}{\gamma(a)}}, \quad (4.20)$$

where  $\tau_i$  denotes the initial conformal time and  $\bar{f}_{\nu,i}$  represents the initial momentum distribution, which we take to be of the Fermi-Dirac form  $\bar{f}_{\nu,i} = 1/(e^{q/T_{\nu,0}} + 1)$ .

We now turn to the Boltzmann equations describing the perturbations of the PSD of decaying neutrinos and their decay products. From [Eq. \(4.10\)](#) and [Eq. \(4.16\)](#), the Boltzmann equation for  $\Delta f_\nu$  reads

$$\frac{\partial \Delta f_\nu}{\partial \tau} + i\mu \frac{kq}{\mathcal{E}_\nu} \Delta f_\nu + \frac{d\bar{f}_\nu}{d\ln q} \left( \eta' - \frac{h' + 6\eta'}{2} \mu^2 \right) = -\frac{a^2 \Gamma_\nu m_\nu}{\mathcal{E}_\nu} \Delta f_\nu. \quad (4.21)$$

As usual, we will expand  $\Delta f_I$  in Legendre multipoles

$$\Delta f_I(k, q, \mu, \tau) = \sum_{\ell=0}^{\infty} (-i)^\ell (2\ell + 1) \Delta f_{I,\ell}(k, q, \tau) P_\ell(\mu). \quad (4.22)$$

With this, we can turn [Eq. \(4.21\)](#) into the following hierarchy of equations

$$\Delta f'_{\nu,0} = -\frac{qk}{\mathcal{E}_\nu} \Delta f_{\nu,1} + q \frac{\partial \bar{f}_\nu}{\partial q} \frac{h'}{6} - \frac{a^2 \Gamma_\nu m_\nu}{\mathcal{E}_\nu} \Delta f_{\nu,0}, \quad (4.23)$$

$$\Delta f'_{\nu,1} = \frac{qk}{3\mathcal{E}_\nu} [\Delta f_{\nu,0} - 2\Delta f_{\nu,2}] - \frac{a^2 \Gamma_\nu m_\nu}{\mathcal{E}_\nu} \Delta f_{\nu,1}, \quad (4.24)$$

$$\Delta f'_{\nu,2} = \frac{qk}{5\mathcal{E}_\nu} [2\Delta f_{\nu,1} - 3\Delta f_{\nu,3}] - q \frac{\partial \bar{f}_\nu}{\partial q} \frac{(h' + 6\eta')}{15} - \frac{a^2 \Gamma_\nu m_\nu}{\mathcal{E}_\nu} \Delta f_{\nu,2}, \quad (4.25)$$

$$\Delta f'_{\nu,\ell>2} = \frac{qk}{(2\ell + 1)\mathcal{E}_\nu} [\ell \Delta f_{\nu,\ell-1} - (\ell + 1) \Delta f_{\nu,\ell+1}] - \frac{a^2 \Gamma_\nu m_\nu}{\mathcal{E}_\nu} \Delta f_{\nu,\ell}. \quad (4.26)$$

We have derived fluid equations for the decaying neutrinos in order to integrate out the dependency on momenta, similarly as we did for the warm daughter species in [Chapter 3](#). However, we found that it is not so trivial to relate the collision terms in the Boltzmann hierarchy for the DR daughter (see [Eq. \(4.34\)](#)-[Eq. \(4.37\)](#)) with the elements of the neutrino stress-energy tensor:  $\delta_\nu$ ,  $\theta_\nu$  and  $\sigma_\nu$ . In addition, the gain in speed provided by these fluid equations is not as high as for the decaying dark matter scenario of [Chapter 3](#). This is mainly because the **CLASS** code implements an optimal sampling in momentum space<sup>5</sup> that makes the resolution of the neutrino Boltzmann hierarchy very manageable. For these reasons, we don't use any fluid equations for our analysis, but we show them in [App. E.3](#) for the sake of completeness.

To study the perturbations of the daughter radiation, we can take moments of the perturbed PSD, following the same convention of [Chapter 3](#),

$$F_{\text{dr},\ell} \equiv \frac{4\pi}{\rho_c} \sum_{i=1,2} \int dq_i q_i^3 \Delta f_{\text{dr},i,\ell}, \quad (4.27)$$

In terms of  $F_{\text{dr},\ell}$ , the Boltzmann hierarchy for the radiation daughter reads

$$F'_{\text{dr},0} = -kF_{\text{dr},1} - \frac{2}{3}h' r_{\text{dr}} + C_0, \quad (4.28)$$

$$F'_{\text{dr},1} = \frac{k}{3}F_{\text{dr},0} - \frac{2k}{3}F_{\text{dr},2} + C_1, \quad (4.29)$$

$$F'_{\text{dr},2} = \frac{2k}{5}F_{\text{dr},1} - \frac{3k}{5}F_{\text{dr},3} + \frac{4(h' + 6\eta')}{15}r_{\text{dr}} + C_2, \quad (4.30)$$

$$F'_{\text{dr},\ell>2} = \frac{k}{(2\ell + 1)} [\ell F_{\text{dr},\ell-1} - (\ell + 1)F_{\text{dr},\ell+1}] + C_\ell, \quad (4.31)$$

where  $r_{\text{dr}} \equiv a^4 \bar{\rho}_{\text{dr}} / \rho_c$ . The terms  $C_\ell$  appearing in [Eq. \(4.28\)](#)-[Eq. \(4.31\)](#) arise from the integrated daughter collision terms in [Eq. \(4.13\)](#)-[Eq. \(4.14\)](#) projected in Legendre polynomials:

$$C_\ell = 2i^\ell \int \frac{d\Omega_k}{4\pi} P_\ell(\mu) \left( \frac{4\pi}{\rho_c} \int dq_1 q_1^3 \left( \frac{\partial f_{\text{dr}}}{\partial \tau} \right)_C [q_1, \mu] \right), \quad (4.32)$$

with  $\mu = \hat{k} \cdot q_1$ . The overall factor of two in the equation above arises because we are adding the collision integrals of the two massless daughters, which are of the same form,  $\left( \frac{\partial f_{\text{dr}1}}{\partial \tau} \right)_C = \left( \frac{\partial f_{\text{dr}2}}{\partial \tau} \right)_C = \left( \frac{\partial f_{\text{dr}}}{\partial \tau} \right)_C$ . In [App. E.2](#), we show that  $C_\ell$  can be written as

$$C_\ell = \left( \frac{8\pi m_\nu \Gamma_\nu a^2}{\rho_c} \right) \int \frac{dq}{\mathcal{E}_\nu} q \Delta f_{\nu,\ell} \int_{q_1^-}^{q_1^+} dq_1 q_1 P_\ell \left( \frac{2\mathcal{E}_\nu q_1 - a^2 m_\nu^2}{2qq_1} \right), \quad (4.33)$$

with  $q_1^\pm = \frac{1}{2}(\mathcal{E}_\nu \pm q)$ . [Eq. \(4.33\)](#) may also be obtained by taking the appropriate limit of the more general expression in [B20](#)<sup>6</sup>. Performing the integral over  $q_1$ , we can obtain

<sup>5</sup>The optimal momentum sampling of **CLASS** typically involves a Gauss-Laguerre quadrature, which is expected to give good results for PSD which are close to a Fermi-Dirac, like the one considered in [Eq. \(4.20\)](#). On the contrary, the PSD of the warm daughter particles considered in [Chapter 3](#) has a very different shape from a Fermi-Dirac, so that's why the optimal sampling was not used in that case.

<sup>6</sup>We note that the same Boltzmann hierarchy has been derived in the context of warm dark matter decaying into dark radiation ([BLINOV et al. 2020a](#)).

the following expressions for the first few  $C_\ell$ 's,

$$C_0 = \frac{4\pi a^2 \Gamma_\nu m_\nu}{\rho_c} \int dq q^2 \Delta f_{\nu,0}, \quad (4.34)$$

$$C_1 = \frac{4\pi a^2 \Gamma_\nu m_\nu}{\rho_c} \int dq q^2 \frac{q}{\mathcal{E}_\nu} \Delta f_{\nu,1}, \quad (4.35)$$

$$C_2 = \frac{4\pi a^2 \Gamma_\nu m_\nu}{\rho_c} \int dq q^2 g_2(q, \mathcal{E}_\nu) \Delta f_{\nu,2}, \quad (4.36)$$

$$C_3 = \frac{4\pi a^2 \Gamma_\nu m_\nu}{\rho_c} \int dq q^2 g_3(q, \mathcal{E}_\nu) \Delta f_{\nu,3}. \quad (4.37)$$

Here the functions  $g_2(q, \mathcal{E}_\nu)$  and  $g_3(q, \mathcal{E}_\nu)$  are given by,

$$g_2(q, \mathcal{E}_\nu) \equiv \frac{5}{2} - \frac{3}{2} \frac{\mathcal{E}_\nu^2}{q^2} + \frac{3}{4} \frac{(\mathcal{E}_\nu^2 - q^2)^2}{\mathcal{E}_\nu q^3} \ln \left( \frac{\mathcal{E}_\nu + q}{\mathcal{E}_\nu - q} \right), \quad (4.38)$$

$$g_3(q, \mathcal{E}_\nu) \equiv \frac{25}{2} \frac{\mathcal{E}_\nu}{q} - \frac{4q}{\mathcal{E}_\nu} - \frac{15}{2} \frac{\mathcal{E}_\nu^3}{q^3} + \frac{15}{4} \frac{(\mathcal{E}_\nu^2 - q^2)^2}{q^4} \ln \left( \frac{\mathcal{E}_\nu + q}{\mathcal{E}_\nu - q} \right). \quad (4.39)$$

Given the complicated integrals in Eq. (4.33), it is technically challenging to keep track of all the collision terms in the Boltzmann hierarchy. Instead, we choose to keep just the first few  $C_\ell$ 's for  $\ell \leq \ell_{\max}$ . The idea behind this approach is that  $C_\ell$  is of order  $O((T_{\text{dec}}/m_\nu)^\ell)$  around the time of decay. Therefore, for non-relativistic decay ( $T_{\text{dec}}/m_\nu \ll 1$ ), it is self-consistent to set  $C_{\ell > \ell_{\max}} = 0$  because those terms only have negligible effect on physical observables. To understand the scaling of  $C_\ell$ , we first note that the integral over  $q$  in Eq. (4.34)-Eq. (4.37) receives most of its support from the region around  $q \sim T_{\nu,0}$  because  $\Delta f_{\nu,\ell}$  inherits features of the Fermi-Dirac distribution from  $\bar{f}_{\nu,i} = 1/(e^{q/T_{\nu,0}} + 1)$ . Deep in the non-relativistic region,  $q \ll \mathcal{E}_\nu$  and  $T_{\nu,0} \ll am_\nu$ . In this regime, we can employ a Taylor expansion for the functions  $g_2$  and  $g_3$  in powers of  $q/\mathcal{E}_\nu$  to obtain,

$$g_2(q, \mathcal{E}_\nu) \approx \frac{4}{5} \frac{q^2}{\mathcal{E}_\nu^2}, \quad g_3(q, \mathcal{E}_\nu) \approx \frac{4}{7} \frac{q^3}{\mathcal{E}_\nu^3}, \quad \text{for } (q \ll \mathcal{E}_\nu). \quad (4.40)$$

Inserting Eq. (4.40) above into Eq. (4.34)-Eq. (4.37), it is straightforward to see that  $C_\ell \propto (T_{\nu,0}/am_\nu)^\ell$ . Moreover, if we assume decay happens deep in the non-relativistic region, we will get  $C_\ell \propto (T_{\text{dec}}/m_\nu)^\ell$  when decay happens, where  $T_{\text{dec}} = T_{\nu,0}/a_{\text{dec}}$ . Therefore,  $C_\ell$  is suppressed by powers of  $T_{\text{dec}}/m_\nu \ll 1$  for higher  $\ell$ . To further justify this argument, we show in Sect. 4.4.3 that setting  $\ell_{\max} = 2$  or  $\ell_{\max} = 3$  makes negligible difference to cosmological observables (see Fig. 4.5). Therefore, we only keep  $C_{\ell \leq 3}$  and set  $C_{\ell > 3} = 0$  in our numerical study for simplicity.

Physically, the expansion in the small parameter  $T_{\text{dec}}/m_\nu$  corresponds to perturbing about the ultra-nonrelativistic limit in which the momentum of the mother particle has completely redshifted away, so that it has come to rest in the cosmic frame. Energy and momentum conservation is respected order by order in this expansion. The earlier work C19 approximated the Boltzmann hierarchy for daughter radiation (Eq. (4.28)-Eq. (4.31)) by just keeping  $C_0$  and setting all the  $C_{\ell \geq 1} = 0$ . It is clear from the above discussion that this is a consistent approximation to zeroth order in an expansion in the small parameter  $T_{\text{dec}}/m_\nu$ . The authors in B20 argued that the Boltzmann hierarchy for daughter radiation in C19 does not reproduce the standard decaying CDM scenario and does not respect momentum conservation. Both criticisms can be addressed by considering the term  $C_1$ . Since  $C_1$  begins at  $O(T_{\text{dec}}/m_\nu)$ ,

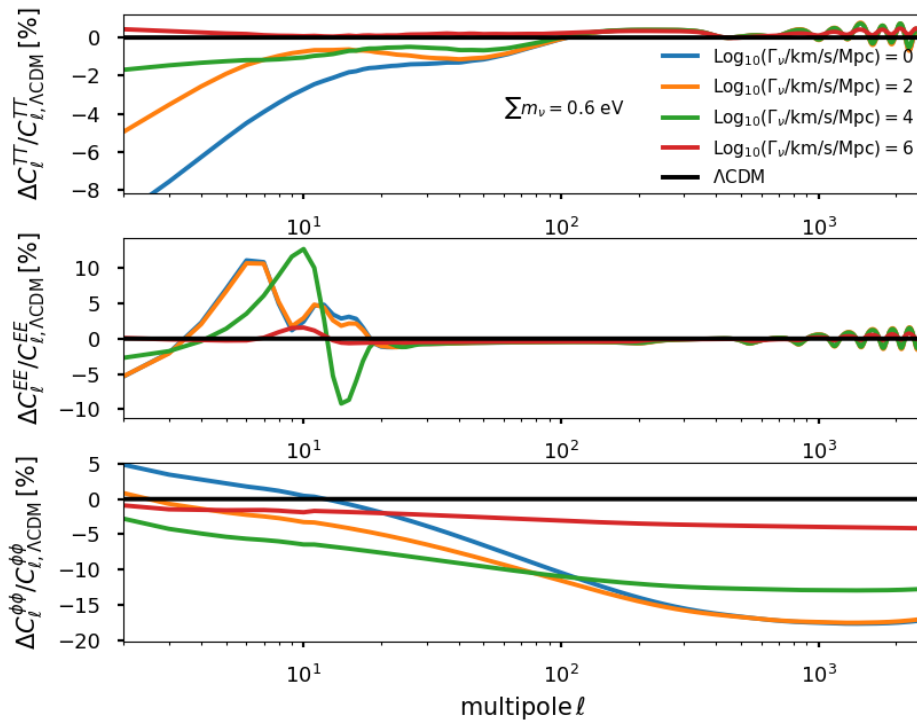


**Figure 4.3** – Residuals in the the CMB lensed TT (upper), EE (middle) and lensing (lower) spectrum for a fixed value of the neutrino mass and several decay widths. The residuals are taken with respect to the  $\Lambda$ CDM best-fit parameters from *Planck* 2018. The  $\Lambda$ CDM parameters are kept fixed in all cases.

we see that the Boltzmann hierarchy in C19 does in fact reproduce the decaying CDM scenario and respects momentum conservation up to  $O(T_{\text{dec}}/m_\nu)$  corrections, consistent with the approximation. In this limit, the momenta of the daughter particles arise entirely from the rest mass of the mother. In practice, since the contributions of neutrinos to the density perturbations are small, we will see that the higher order terms do not significantly affect the constraints derived in C19 with *Planck15* data.

#### 4.4.2 Impact of the non-relativistic neutrino decay on the CMB spectra

We briefly summarize the impact of the non-relativistic invisible neutrino decays on the CMB spectra, following the discussion in C19. In Fig. 4.3, we display the residuals in the CMB (lensed) TT, EE and lensing power spectra, for the sum of neutrino masses  $\sum m_\nu = 0.6$  eV and several decay widths  $\text{Log}_{10}(\Gamma_\nu/\text{km/s/Mpc}) = 0, 2, 4, 6$ . In all cases, the  $\Lambda$ CDM parameters are set to their best-fit values from *Planck18*, that is,  $\{100\theta_s = 1.04089, \omega_{\text{cdm}} = 0.1198, \omega_b = 0.02233, n_s = 0.9652, \ln(10^{10}A_s) = 3.043, \tau_{\text{reio}} = 0.0540\}$ . Our reference  $\Lambda$ CDM model makes use of the same parameters and assumes standard massless neutrinos.

For the value of the mass considered ( $\sum m_\nu = 0.6$  eV) and at fixed angular size of the sound horizon  $\theta_s$ , neutrino masses primarily impact the lensing spectrum. Indeed, as they reduce power below the free-streaming scale, they produce a significant matter power suppression at small scales, which leads to a  $\sim 20\%$

reduction in the  $C_\ell^{\phi\phi}$  at large  $\ell$  (blue curve in Fig. 4.3). Consequently, this power suppression decreases the smoothing in the high- $\ell$  part of the TT and EE spectra, which can be seen as ‘wiggles’ in the corresponding plots.

In addition, stable neutrinos dilute like non-relativistic matter at late times ( $\bar{\rho}_\nu \sim a^{-3}$ ), which increases the value of  $\Omega_m$ . As we impose the closure relation  $\Omega_m + \Omega_\Lambda = 1$  at late-times, this is compensated for by a decrease in  $\Omega_\Lambda$  (later beginning of  $\Lambda$ -domination), and thus a reduction in the Late Integrated Sachs-Wolfe effect (LISW), leaving a signature in the low- $\ell$  TT spectrum. Furthermore, the modified expansion history  $H(z)$  changes quantities integrated along  $z$ , such as  $\tau_{\text{reio}}$ , which affects the multipoles at  $\ell \sim 10$  in the EE spectrum.

When a non-negligible  $\Gamma_\nu$  is considered (orange, green and red curves in Fig. 4.3), one can see that the aforementioned effects typically become less prominent for earlier decays. This is particularly true for the high- $\ell$  part of the lensing spectrum (and consequently the smoothing at high- $\ell$  in TT and EE) since decay of neutrinos reduce their impact on structure formation. The reduction of the effect in the low- $\ell$  part of the TT and EE spectra is not entirely monotonic, as intermediate values of  $\Gamma_\nu$  can induce additional time variation in the gravitational potentials (thereby affecting the LISW effect), as well as time variations in  $H(z)$  (thereby affecting  $\tau_{\text{reio}}$ ). As a result, the  $\Lambda$ CDM limit is reached not only for small values of  $\sum m_\nu$ , but also for high values of  $\Gamma_\nu$ . This will be reflected in the MCMC analysis in Sect. 4.5, which shows a large positive correlation between both parameters. It is precisely this degeneracy which relaxes the neutrino mass bounds.

#### 4.4.3 Consistency of the implementation of the Boltzmann equations

We begin by comparing the approximation used in C19 for the background energy density of decaying massive neutrinos to the more accurate results obtained by evaluating the integral in Eq. (4.20) numerically. In C19, the phase space distribution of neutrinos in Eq. (4.20) is approximated through the following analytic formula,

$$\bar{f}_\nu(q, \tau) = \bar{f}_{\nu,i}(q) e^{-\Gamma_\nu t/\gamma}. \quad (4.41)$$

As argued in C19, this approximation is valid under the assumption that the decay happens deep in the non-relativistic regime. To see the difference between the approximation and the full result, we plot the ratio  $r \equiv (\bar{\rho}_\nu + \bar{\rho}_{\text{dr}})/\bar{\rho}_{\text{nr}}$  in Fig. 4.4, for several values of the decay width  $\Gamma_\nu$  and a fixed value of the total neutrino mass  $\sum m_\nu = 0.06$  eV. Here  $\bar{\rho}_{\text{nr}}$  denotes the energy density of stable massless neutrinos. If neutrinos decay while relativistic, this ratio always gives  $r \simeq 1$ . However, if the decay happens when the neutrinos are already non-relativistic ( $\bar{\rho}_\nu \sim a^{-3}$ ), then the ratio evolves from  $r \simeq 1$  to  $r \sim a$ , and will eventually reach a plateau once all the neutrinos have decayed. From Fig. 4.4, we can see that the approximate formula in Eq. (4.41) gradually improves as we go to smaller decay widths (that is, going deeper into the regime of non-relativistic decays), as expected. The error in the case of neutrinos decaying right around the time of the non-relativistic transition ( $\text{Log}_{10}(\Gamma_\nu/[\text{km/s/Mpc}]) \simeq 4$  for  $\sum 0.06$  eV) is around 25%. Nevertheless, as we argue below, the impact on observables is much smaller given that neutrinos only contribute a small fraction of the total energy density for masses considered in this work. Not surprisingly, the approximate formula fails in the relativistic regime, leading to  $r < 1$  at late-times. Therefore future work focusing on this regime should



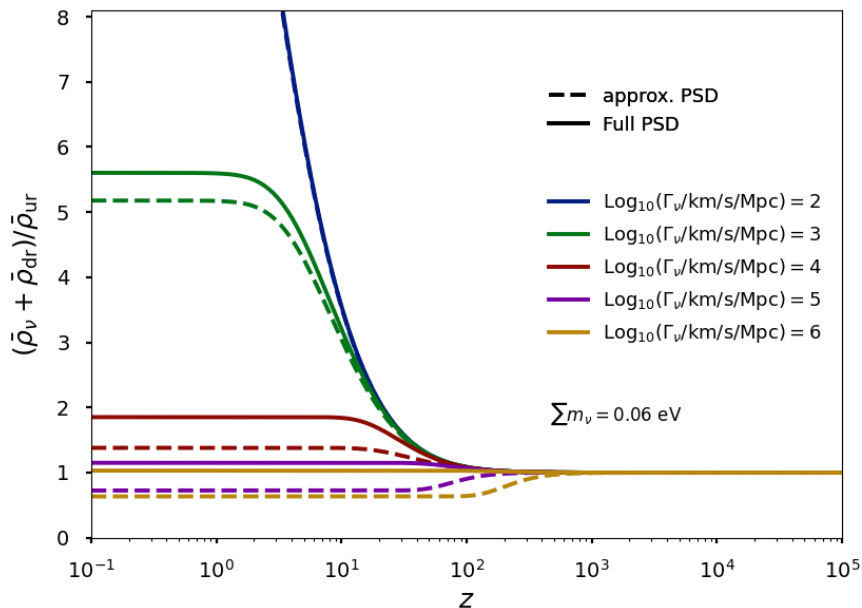


**Figure 4.4** – Redshift evolution of the quantity  $(\bar{\rho}_\nu + \bar{\rho}_{\text{dir}})/\bar{\rho}_{\text{ur}}$  (where  $\bar{\rho}_{\text{ur}}$  denotes the energy density of stable massless neutrinos), which should be equal to 1 in the limit of relativistic decays. We consider a very small value of the neutrino mass sum,  $\sum m_\nu = 0.06 \text{ eV}$ , and several values for the decay width,  $\text{Log}_{10}(\Gamma_\nu/\text{km/s/Mpc})$ . “approx. PSD” refers to the approximated phase space distribution in Eq. (4.41) while “Full PSD” refers to the exact solutions of Eq. (4.20).

make use of the exact formula.

In Fig. 4.5 and Fig. 4.6, we show the effects of various approximations in dealing with decaying neutrinos (at the background and perturbation level) on the CMB TT, EE and lensing spectra. We compare the impact of using either the approximated or the exact PSD of neutrinos discussed above, as well as the impact of only keeping  $C_{\ell \leq \ell_{\text{max}}}$  in the Boltzmann hierarchy of daughter particles in Eq. (4.28)-Eq. (4.31), where we vary  $\ell_{\text{max}}$  from zero to three. We show the residuals of these approximations with respect to the ‘optimal’ case (i.e. including all terms up to  $\ell_{\text{max}} = 3$  and the exact background PSD) for a fixed value of the neutrino mass ( $\sum m_\nu = 0.6 \text{ eV}$ ) and two different decay widths ( $\text{Log}_{10}(\Gamma_\nu/[\text{km/s/Mpc}]) = 5.5$  in Fig. 4.5 and  $\text{Log}_{10}(\Gamma_\nu/[\text{km/s/Mpc}]) = 4$  in Fig. 4.6). Fig. 4.5 corresponds to decays happening around the time of the non-relativistic transition,  $T_{\text{dec}}/m_\nu \simeq 0.3$ , where the effects of the approximations are expected to be largest. Fig. 4.6 on the other hand refers to decays happening deep in the non-relativistic regime,  $T_{\text{dec}}/m_\nu \simeq 0.03$ . We also show the [Planck18](#)  $1-\sigma$  error bars, as well as the (binned) cosmic variance.

For decays close to the non-relativistic transition  $T_{\text{dec}}/m_\nu \simeq 0.3$  shown in Fig. 4.5, we find that the biggest improvement in the CMB TT spectrum occurs when including  $C_{\ell \leq 1}$  (i.e., the contribution from the decaying neutrino bulk velocity) in the Boltzmann hierarchy of daughter radiation, which impacts the integrated Sachs-Wolfe (ISW) effect at multipoles  $\ell \lesssim 100$ . On the other hand, the approximate background distribution of neutrinos does not have a significant effect. For the CMB EE spectrum shown in the same figure, which is not sourced by the ISW effect, the impact of

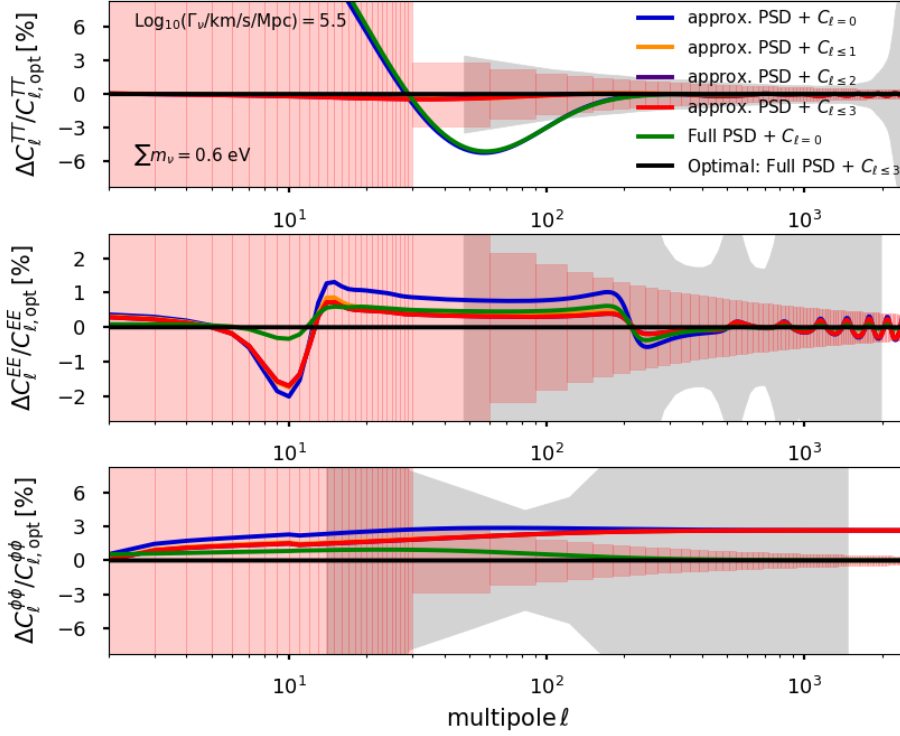


**Figure 4.5** – Fractional change in the CMB TT (upper), EE (middle) and lensing (lower) spectrum, when imposing different prescriptions for the background energy density distribution and Boltzmann hierarchies. “approx. PSD” refers to the approximate phase space distribution in Eq. (4.41) while “Full PSD” refers to the exact solution of Eq. (4.20). “ $C_\ell$ ” in the plot means we only keep those collision terms in Eq. (4.28)-Eq. (4.31). The chosen values of the neutrino mass ( $\sum m_\nu = 0.6$  eV) and decay width ( $\text{Log}_{10}(\Gamma_\nu/[\text{km/s/Mpc}]) = 5.5$ ) correspond to the case when neutrinos decay close to non-relativistic transition ( $T_{\text{dec}}/m_\nu \simeq 0.3$ ). The gray shaded region indicates Planck18  $1-\sigma$  uncertainties, while the pink boxes indicate the (binned) cosmic variance.

the approximate background distribution of neutrinos is comparable to the effect of the approximate perturbed hierarchy. Nevertheless, one can see that for  $\ell_{\text{max}} \geq 2$ , additional contributions to the daughter hierarchy have negligible impacts, which justifies our choice of cutting the collision term  $C_\ell$  contribution at  $\ell_{\text{max}} = 3$ . Finally for the CMB lensing spectrum, the effects due to the approximate treatment of the background PSD dominate over the ones due to including higher order terms in the Boltzmann hierarchy of the dark radiation. This is expected given that the matter power spectrum suppression scales approximately with  $\bar{\rho}_\nu/\bar{\rho}_m$  (HU et al. 1998; LESGOURGUES et al. 2018) where  $\bar{\rho}_m$  is the total matter density, while neutrino perturbations are very small well below the free-streaming scale, so that their detailed dynamics is not as important as on larger scales.

The impact of the various approximations in the case of decays deep in the non-relativistic regime  $T_{\text{dec}}/m_\nu \simeq 0.03$ , displayed in Fig. 4.6, is much less visible. In that case, one can therefore safely neglect  $C_{\ell>0}$  and consider the approximate PSD, as done in C19.

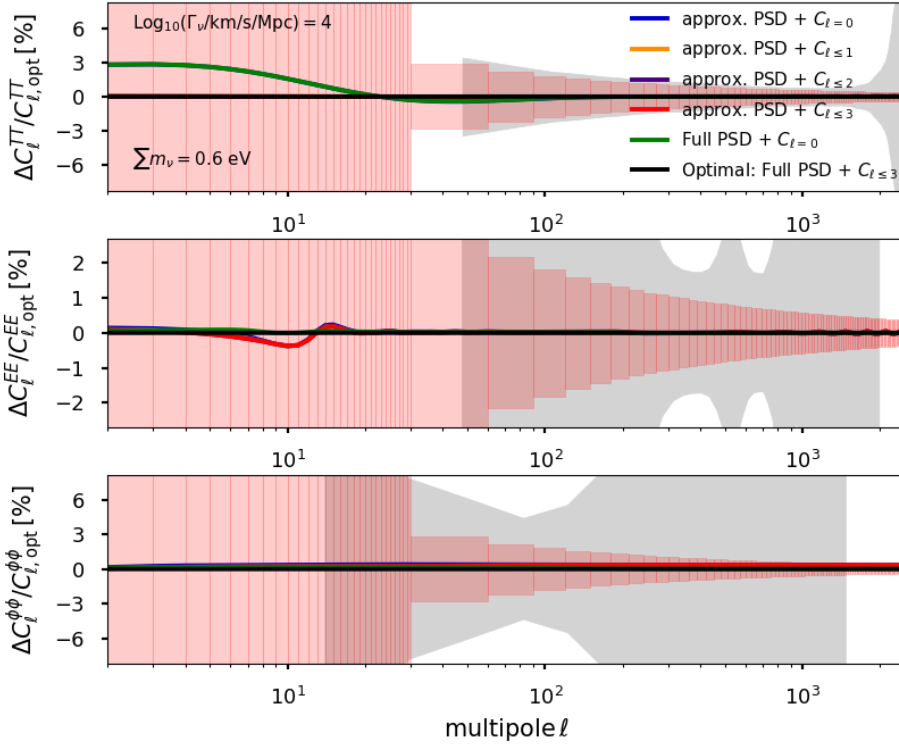


**Figure 4.6** – Same as in Fig. 4.5, but with a smaller decay width ( $\text{Log}_{10}(\Gamma_{\nu}/[\text{km/s/Mpc}]) = 4$ ), corresponding to a neutrino decay happening deep in the non-relativistic limit ( $T_{\text{dec}}/m_{\nu} \simeq 0.03$ ).

## 4.5 Cosmological constraints

### 4.5.1 Details of the analysis

In this section we perform a numerical scan over the parameter space to obtain updated limits on the neutrino mass and lifetime. We perform comprehensive MCMC analyses with the **MontePython-v3** (AUDREN et al. 2013; BRINCKMANN et al. 2019a) code interfaced with our modified version of **CLASS**. We fit the decaying neutrino model to a combination of the following data-sets:

- The **Planck18** high- $\ell$  TT, TE, EE + low- $\ell$  data TT, EE + lensing data. We will also compare these results with the use of **Planck15** data to disentangle the effects of our improved formalism and that of the new data.
- The BAO measurements from 6dFGS at  $z = 0.106$  (BEUTLER et al. 2011), SDSS DR7 at  $z = 0.15$  (ROSS et al. 2015), BOSS DR12 at  $z = 0.38, 0.51$  and  $0.61$  (ALAM et al. 2017), and the joint constraints from eBOSS DR14 Ly- $\alpha$  auto-correlation at  $z = 2.34$  (SAINTE AGATHE et al. 2019) and cross-correlation at  $z = 2.35$  (BLOMQVIST et al. 2019).
- The measurements of the growth function  $f\sigma_8(z)$  (FS) from the CMASS and LOWZ galaxy samples of BOSS DR12 at  $z = 0.38, 0.51, \text{ and } 0.61$  (ALAM et al. 2017).
- The Pantheon SNIa catalogue, spanning redshifts  $0.01 < z < 2.3$  (SCOLNIC et al. 2018).

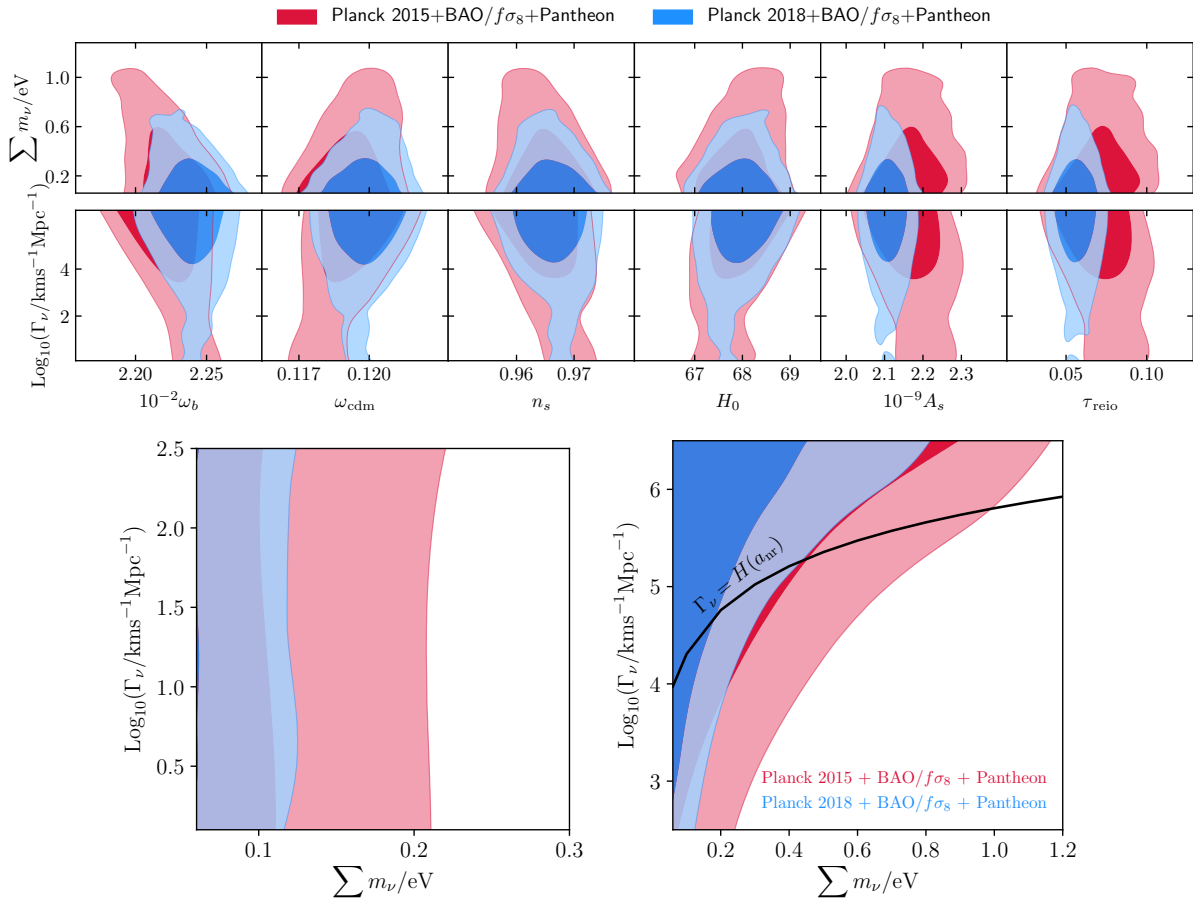


**Figure 4.7** – 2D posterior distribution of the decaying neutrino model reconstructed from the analysis of BAO + FS + Pantheon together with either [Planck15](#) or [Planck18](#) data. In the top panel, we show the correlation with other cosmological parameters.

We adopt flat priors on the following six  $\Lambda$ CDM parameters:  $\{\omega_b, \omega_{\text{cdm}}, H_0, n_s, A_s, \tau_{\text{reio}}\}$ . We assume three degenerate neutrinos decaying into massless radiation and consider flat priors on  $\sum m_\nu/\text{eV}$  and  $\text{Log}_{10}(\Gamma_\nu/[\text{km/s/Mpc}])$ . In order to accelerate convergence, we split the parameter space between  $\text{Log}_{10}(\Gamma_\nu/[\text{km/s/Mpc}]) \in [0.1, 2.5]$  and  $\text{Log}_{10}(\Gamma_\nu/[\text{km/s/Mpc}]) \in [2.5, 6.5]$ . In both cases we take wide priors on  $\sum m_\nu \in [0.06, 1.5]$  eV. We assume our MCMC chains to be converged when the Gelman-Rubin criterion  $R - 1 < 0.05$  (GELMAN et al. 1992). In our baseline analysis, we do not apply any specific cut to the parameter space, even if neutrinos decay in the (mildly-)relativistic regime (this occurs for low  $\sum m_\nu$  and high  $\Gamma_\nu$ ). In [App. E.4](#), we investigate the impact of excluding the parameter space corresponding to relativistic decay from our analysis and show that the limit at 95% on  $\sum m_\nu$  agrees within a few percent.

#### 4.5.2 Updated limits on the neutrino mass and lifetime

The results of our analyses are presented in [Fig. 4.7](#). For very late decays, corresponding to  $\text{Log}_{10}(\Gamma_\nu/[\text{km/s/Mpc}]) \lesssim 2.5$ , no relaxation of the constraints on  $\sum m_\nu/\text{eV}$  is visible, in agreement with what was found in [C19](#). The impact of the new *Planck* data is visible as a significantly improved bound on the sum of neutrino mass, namely we find  $\sum m_\nu < 0.127$  eV (95% C.L.), an improvement of about  $\sim 35\%$  over 2015 data, in good agreement with [AGHANIM et al. \(2020b\)](#). For  $\text{Log}_{10}(\Gamma_\nu/[\text{km/s/Mpc}]) \gtrsim 2.5$ , one can

see that the bound relaxes as expected, although not as much with [Planck18](#) data as for [Planck15](#) data. Taking the intersect of the non-relativistic decay line with our  $2\sigma$  limit, we find that [Planck18](#) excludes neutrino decaying non-relativistically with masses  $\sum m_\nu > 0.42$  eV (95% C.L.). This is significantly stronger than the limits from [Planck15](#) data, for which  $\sum m_\nu \sim 0.9$  eV was still allowed in the non-relativistic decay scenario.

Our result also has implications for laboratory searches. For  $\sum m_\nu = 0.6$  eV, the smallest mass scale that the KATRIN experiment is designed to probe, [Planck18](#) data requires decay rate  $\Gamma_\nu \gtrsim 10^{5.5}$  km/s/Mpc, a constraint roughly one order of magnitude stronger than from [Planck15](#) data. However, this value of the decay rate is now slightly beyond the regime of validity of our work <sup>7</sup>, indicating that, in the event of a neutrino mass discovery at KATRIN, a more involved analysis including inverse-decays would be necessary to confirm that the decay scenario can reconcile laboratory and cosmological measurements.

#### 4.5.3 Comparison with former results and impact of *Planck* 2018 data

Comparing with the constraints presented in [C19](#) for [Planck15](#), we find that, while the impact of our improved treatment is clearly visible in the CMB power spectra (and will be relevant for future experiments), it has only a marginal impact on the constraints, and our bounds are in very good agreement with those derived in [C19](#), which only included the leading order term in the daughter radiation hierarchy <sup>8</sup>. The bulk of the improvement is due to the newest [Planck18](#) data and can be understood as follows.

As shown in [Fig. 4.3](#), for the masses we consider, the main effect is an almost scale independent suppression of CMB lensing spectrum. This suppression can be compensated for by increasing the primordial amplitude  $A_s$  or by adjusting the matter density  $\omega_{\text{cdm}}$  (see [ARCHIDIACONO et al. \(2017\)](#) for a discussion of the correlation between  $\{\sum m_\nu, A_s, \tau_{\text{reio}}, \omega_{\text{cdm}}\}$ ). Due to the well-known degeneracy between  $A_s$  and  $e^{-2\tau_{\text{reio}}}$ , [Planck15](#) data, which was limited in polarization, were unable to place a tight constraint on  $A_s$ , and thus the constraining power on the sum of neutrino mass and lifetime was limited. The precise measurements of low- $\ell$  polarization from [Planck18](#) leads to constraints on  $\tau_{\text{reio}}$  that are tighter by a factor of two than those from [Planck15](#). As a result, parameters degenerate with  $\tau_{\text{reio}}$  such as  $A_s$  are now much better constrained. Consequently, the constraints on the sum of neutrino mass and lifetime have significantly improved with [Planck18](#) data.

To confirm this simple argument, we perform another run with [Planck15](#) data and a tight gaussian prior on  $\tau_{\text{reio}} = 0.0540 \pm 0.0074$ , chosen to match the optical depth to reionization reconstructed from [Planck18](#). Given that the constraints on  $\sum m_\nu$  are independent of  $\Gamma_\nu$  below  $\Gamma_\nu \lesssim 10^3$ , and the scaling above  $\Gamma_\nu \lesssim 10^{5.5}$  is monotonic, we focus on the parameter space  $\text{Log}_{10}(\Gamma_\nu/[\text{km/s/Mpc}]) \in [3, 5.5]$  to accelerate convergence. Our

<sup>7</sup>For  $\sum m_\nu = 0.6$  eV and assuming degenerate neutrino masses, the non-relativistic condition requires  $\Gamma_\nu < 10^{5.3}$  km/s/Mpc.

<sup>8</sup>Let us note that the implementation of the BAO/ $f\sigma_8$  DR12 likelihood used in [C19](#) within the MontePython code had an issue that led to constraints on  $\sum m_\nu$  that were somewhat milder than the true bounds. MontePython has since then been corrected, leading to an improvement on the constraints on the stable/long-lived ( $\Gamma_\nu < 10^3$  km/s/Mpc) case by about 20%. However, we have verified that this bug had no impact in the short-lived case ( $\Gamma_\nu > 10^{2.5}$  km/s/Mpc).

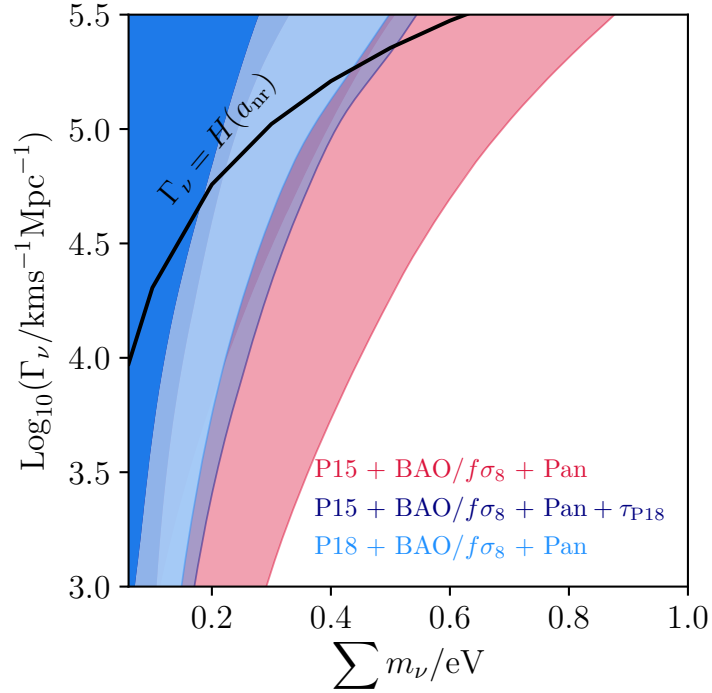


**Figure 4.8** – Posterior distribution of  $\sum m_\nu$  and  $\text{Log}_{10}(\Gamma_\nu/[\text{km/s/Mpc}])$  with [Planck18](#) and [Planck15](#) + a prior on  $\tau_{\text{reio}}$  from [Planck18](#).

results are presented in [Fig. 4.8](#), where one can see that this simple prescription leads to constraints that are very similar to those from the full [Planck18](#) data. We attribute the remaining differences to the additional constraining power of [Planck18](#) data on the parameters  $\omega_{\text{cdm}}$  and  $\omega_b$ , which are mildly correlated with  $\sum m_\nu$  (see [Fig. 4.7](#), top panel). Note that our constraints are a factor of two weaker than those advocated in [LORENZ et al. \(2021\)](#), which performed a ‘model-independent’ reconstruction of the neutrino mass as a function of redshift, but neglects the decay products. As we show here, including details about the daughter radiation is necessary to accurately compute the effect of neutrino decays even in the non-relativistic regime. Finally, as discussed in [ARCHIDIACONO et al. \(2017\)](#) and [CHACKO et al. \(2021\)](#), a combination of CMB data with future tomographic measurements of the power spectrum by DESI ([FONT-RIBERA et al. 2014](#)) or Euclid ([AMENDOLA et al. 2018](#)), and an improved determination of the optical depth to reionization by 21-cm observations with SKA ([MAARTENS et al. 2015](#); [LIU et al. 2016](#)), could greatly increase the sensitivity of cosmological probes to neutrino masses and lifetimes.

## 4.6 Summary and outline

Cosmological observations are known to set the strongest constraints on the sum of neutrino masses. Yet, the existing mass bound from CMB and LSS measurements, which assumes that neutrinos are stable, is significantly weakened if neutrinos decay. In this work, we provide up-to-date limits on the lifetime of massive neutrinos that decay into dark radiation after becoming non-relativistic, from a combination of CMB, BAO, growth factor measurements, and Pantheon SN1a data.



Compared to the earlier analysis in C19, we have incorporated higher-order corrections up to  $\mathcal{O}((T_{\text{dec}}/m_\nu)^3)$  when solving the dark radiation perturbations, and also performed the full calculation of the background energy density of the decaying neutrino using Eq. (4.20). The more precise treatment of the Boltzmann equations and the background energy evolution in our MCMC study improves the coverage of the case when the neutrinos decay early so that their average momenta are close to their masses. As shown in Fig. 4.6, if neutrinos decay when having  $T_\nu \ll m_\nu/3$ , the inclusion of higher moment perturbations  $C_{\ell \geq 2}$  gives a negligible change to the power spectra as compared to the experimental uncertainties. However, the complete calculation of the neutrino energy does improve the prediction for the power spectrum significantly from the approximate result using Eq. (4.41) when the decays happen semi-relativistically. Nevertheless, we have found that constraints from Planck15, given their limited precision, are unaffected by these considerations. However, we anticipate that these effects will be relevant for future experiments (as well as an essential contribution in the relativistic case, to be considered in the future).

In fact, we have shown that the bulk of the improvement in the constraining power compared to C19 comes from the use of Planck18 data. Indeed, we have demonstrated that the improved  $\tau_{\text{reio}}$  measurement from the low- $\ell$  polarization data helps breaking the degeneracy in the CMB power spectrum amplitude and strengthens the bound on the neutrino mass and lifetime. As a result, we have found that neutrinos with  $\sum m_\nu > 0.42$  eV ( $2\sigma$ ) cannot be made consistent with cosmological data if they decay while non-relativistic, a significant improvement from Planck15 data for which masses as high as  $\sum m_\nu \sim 0.9$  eV were consistent with the non-relativistic decay scenario (C19).

We have argued that one notable application of this result is that, if the KATRIN experiment sees an electron neutrino with  $m_\nu \approx 0.2$  eV (the advocated sensitivity), our result would constrain  $\Gamma_\nu \gtrsim 10^{5.5}$  km/s/Mpc, *i.e.* the neutrinos would need to decay between  $z \approx 2 \times 10^2 - 4 \times 10^3$ , while they are still relativistic, so that our bounds and the bounds studied in B20 would not apply. In case of a neutrino mass discovery at KATRIN, a more involved analysis including inverse-decays would be necessary to firmly confirm that the decay scenario can reconcile laboratory and cosmological measurements. Additionally, our results show that the tentative exclusion of the inverted mass ordering (SIMPSON et al. 2017; VAGNOZZI et al. 2017; PALANQUE-DELABROUILLE et al. 2020; DI VALENTINO et al. 2021a), based solely on the fact that the inverted ordering predicts  $\sum m_\nu > 0.1$  eV, is highly dependent on the hypothesis that neutrinos are stable on cosmological time-scales. Non-relativistic decays can still easily reconcile the inverted ordering with cosmological data.

Finally, let us mention that even though current exclusion bounds in Fig. 4.7 do not set independent constraints on the neutrino mass and lifetime, next generation measurements of the matter power spectrum at different redshifts can help break that degeneracy (CHACKO et al. 2021). It will be interesting to revisit the forecast on the sensitivity of future cosmological data to the sum of neutrino masses and their lifetime in light of our improved formalism.





# V

---

## Conclusions

---

The main goal of this work was to constrain or search for signs of exotic physics using current cosmological data. An important focus has been the theoretical interpretation of two longstanding experimental discrepancies in cosmology: the  $H_0$  and  $S_8$  tensions. While unknown systematic effects at the origin of these discrepancies are not excluded, the existence of several independent observations disfavoring the CMB predictions could point to a major failure of the  $\Lambda$ CDM scenario. I have put new and robust constraints on several extensions of  $\Lambda$ CDM that are targeted at explaining these tensions, such as Decaying Dark Matter and Early Dark Energy. Additionally, I have used cosmic data to better characterize the properties (mass and lifetime) of one of the most elusive particles in the universe, the neutrino. In all my projects, a special attention has been given to the CMB anisotropies, which provides a powerful tool to test deviations from the standard model of cosmology and the standard model of particle physics. My approach has always been very phenomenological, so that the derived constraints can apply to many different theoretical high-energy physics models.

In [Chapter 1](#), I started with a thorough review of the standard tools needed to compute the most relevant cosmological observables, including the CMB and matter power spectra. At the end of this Chapter, I briefly discussed the challenges that the  $\Lambda$ CDM paradigm has to face: the nature of the dark sector and the cosmological tensions.

In [Chapter 2](#), I have analyzed a model of Early Dark Energy, which has been shown to provide a simple resolution to the Hubble tension if the EDE component contributes a fraction  $f_{\text{EDE}} \simeq 10\%$  of the energy density of the universe at  $z_c \simeq 3500$ , and dilutes as or faster than radiation afterwards. However, some authors have pointed out that the best-fit EDE cosmology requires a larger value of  $S_8$ , so that including LSS data in the analysis highly restricts the resolution to the tension. I have reassessed this claim by confronting an EDE model whose only parameter is  $f_{\text{EDE}}(z_c)$  against a wide variety of datasets. This analysis shows that EDE is detected at  $\sim 2\sigma$  from *Planck* CMB data alone, and that the addition of BAO, SNIa and weak-lensing data does not significantly worsen the fit to the  $S_8$  measurements with respect to  $\Lambda$ CDM. The main conclusion is that current weak-lensing data is not constraining enough to rule out the resolution to the  $H_0$  tension provided by EDE.

In addition, I have participated in a review of different models that have proposed to resolve the Hubble tension, spanning early-time solutions (such as Early Dark Energy) and late-time solutions (such as Decaying Dark Matter). The main goal was to go beyond a simple bibliographic compilation, and quantify for the first time the relative success of several models in explaining the discrepancy. To achieve that, we confronted seventeen different models proposed in the literature against a variety of cosmological data, and quantified the relative success of each model using a series of metrics. This work provides a series of benchmarks for future model-builders wishing to assess the level of success of a given model/scenario.

In [Chapter 3](#), I have studied the cosmological impact of a scenario where CDM is allowed to decay into massless (dark radiation) and massive (warm DM) species. I have performed the first thorough analysis of this 2-body DM decay scenario including a realistic treatment of linear perturbations. In this way, I have obtained the strongest constraints up-to-date for these kind of models (using CMB, BAO and SNIa data), and showed that the  $S_8$  tension can be resolved if DM decays with a lifetime of  $\Gamma^{-1} \simeq 55$  Gyr and transfers around 0.7% of its rest-mass energy to the massless component. This analysis was possible thanks to a new and accurate fluid approximation scheme that I developed for the warm species, and which allowed to reduce the CPU time in the calculations from  $\sim 1$  day to only  $\sim 1$  minute. I also considered alternative CMB data-sets (like those from ACT-DR4 and SPTPol), discussed a potential connexion with the recent XENON1T excess, and showed that, while current data are not sensitive enough to distinguish between standard CDM and decaying DM, future CMB observations can unambiguously detect its signature.

In [Chapter 4](#), I have updated the constraints on the mass and lifetime of active SM neutrinos. Currently, the strongest limit of the sum of neutrino mass comes from cosmology,  $\sum m_\nu < 0.12$  eV, but these determinations assume that neutrinos are stable on cosmic timescales. The idea of neutrino decay is particularly interesting in the eventuality that laboratory experiments (like KATRIN) will measure a value of the neutrino mass bigger than the one inferred from cosmological observations. It has been shown that, for neutrinos decaying to dark radiation while being non-relativistic, the stringent CMB constraints on the sum of neutrino masses can be significantly relaxed (up to  $\sum m_\nu \sim 0.9$  eV). I have gone beyond previous work by improving the Boltzmann treatment of neutrino decays both at the background and linear perturbation level. This has allowed us to show that, given the new *Planck* 2018 CMB measurements, non-relativistic neutrino decays can relax the bound of neutrino masses only up to  $\sum m_\nu \sim 0.4$  eV.

The work presented here is based on the following publications

- [G. F. Abellán](#), [R. Murgia](#), [V. Poulin](#), [J. Laval](#)  
 “Implications of the  $S_8$  tension for decaying dark matter with warm decay products” **PRD 105 063525 (2022)**; [arXiv:2008.09615](#).
- [R. Murgia](#), [G. F. Abellán](#), [V. Poulin](#)  
 “Early dark energy resolution to the  $H_0$  tension in light of weak lensing surveys and lensing anomalies” **PRD 103 063502 (2021)**; [arXiv:2009.10733](#).
- [G. F. Abellán](#), [R. Murgia](#), [V. Poulin](#)  
 “Linear cosmological constraints on two-body decaying dark matter scenarios and the  $S_8$  tension” **PRD 104 123533 (2021)**; [arXiv:2102.12498](#).

- 
- N. Schöneberg, G. F. Abellán, A. P. Sánchez, S. Witte, V. Poulin, J. Lesgourgues “*The  $H_0$  Olympics: A fair ranking of proposed models*” **Phys. Rept.** **984 1-55 (2022)**; arXiv:2107.10291.
  - G. F. Abellán, Z. Chacko, A. Dev, P. Du, V. Poulin, Y. Tsai “*Improved cosmological constraints on the neutrino mass and lifetime*” **JHEP** **08 076 (2022)**; arXiv:2112.13862.

Besides the aforementioned articles, I have also been working on a few other projects, which are not included in this thesis, but have ended up in the following publications:

- T. Smith, M. Lucca, V. Poulin, G. F. Abellán, L. Balkenhol, K. Benabed, S. Galli, R. Murgia. “*Hints of Early Dark Energy in Planck, SPT, and ACT data: new physics or systematics?*” **PRD** **106 043526 (2022)**; arXiv:2202.09379.
- T. Simon, G. F. Abellán, P. Du, V. Poulin, Y. Tsai. “*Constraining decaying dark matter with BOSS data and the effective field theory of large-scale structures*” **PRD** **106 023516 (2022)**; arXiv:2203.07440.
- J. Iguaz, P. Serpico, G. F. Abellán. “*The QCD phase transition behind a PBH origin of LIGO/Virgo events?*” **JCAP** **07 008 (2022)**; arXiv:2204.07027.

In conclusion, current cosmological data carry a wealth of information that is still far from being fully exploited. It is an exciting time for cosmology, since the upcoming arrival of new and more precise data will allow to test models suggested to resolve cosmic tensions (such as the ones studied in this work), and to possibly establish a new concordance model. I hope that my research work has been useful in that direction.





# **Appendices**



# A

---

## Complements on linear perturbation theory

---

In this appendix we provide some important calculations regarding the theory of linear cosmological perturbations, that were a bit too long to be included in [Chapter 1](#). We always assume a spatially flat background metric.

### A.1 The four velocity in a generic gauge

The goal is to compute the four-velocity  $U^\mu = \bar{U}^\mu + \delta U^\mu$  at linear order in a generic gauge. We remind that metric perturbations are generically written as

$$\delta g_{00} = -2a^2(\tau)A, \quad \delta g_{0i} = a^2(\tau)B_i, \quad \delta g_{ij} = a^2(\tau)H_{ij}, \quad (\text{A.1})$$

For a comoving observer,  $\bar{U}^\mu = a^{-1}\delta_0^\mu$  (the  $a^{-1}$  factor appears because we are working in conformal time), which means  $\bar{U}_\mu = \bar{g}_{\mu\nu}\bar{U}^\nu = -a\delta_\mu^0$ . Let us now obtain  $\delta U^\mu$  and  $\delta U_\mu$ . Using that  $\bar{g}_{\mu\nu}\bar{U}^\mu\bar{U}^\nu = g_{\mu\nu}U^\mu U^\nu = -1$ , we get at linear order

$$\delta g_{\mu\nu}\bar{U}^\mu\bar{U}^\nu + 2\bar{U}_\nu\delta U^\nu = 0, \quad (\text{A.2})$$

from which we can infer that  $\delta U^0 = -a^{-1}A$ . Writing  $\delta U^i = a^{-1}v_i$ , where  $v_i$  is the *coordinate velocity*, we arrive at

$$U^\mu = \frac{1}{a}[1 - A, v^i]. \quad (\text{A.3})$$

### A.2 Gauge transformations

We want to prove the following gauge transformation for the  $0i$  metric perturbation

$$B_i \longrightarrow \tilde{B}_i = B_i + \partial_i T - L'_i \quad (\text{A.4})$$

We simply have to substitute the coordinate transformation [Eq. \(1.152\)](#) and the perturbed metric elements [Eq. \(A.1\)](#) in the transformation law for tensors [Eq. \(1.153\)](#).

Expanding the derivatives and always keeping linear order:

$$\begin{aligned}
g_{0i}(x) &= a^2(\tau)B_i = \frac{\partial \tilde{x}^\alpha}{\partial x^0} \frac{\partial \tilde{x}^\beta}{\partial x^i} \tilde{g}_{\alpha\beta}(\tilde{x}) \\
&= \frac{\partial \tilde{x}^0}{\partial x^0} \frac{\partial \tilde{x}^0}{\partial x^i} \tilde{g}_{00} + \frac{\partial \tilde{x}^0}{\partial x^0} \frac{\partial \tilde{x}^j}{\partial x^i} \tilde{g}_{0j} + \frac{\partial \tilde{x}^j}{\partial x^0} \frac{\partial \tilde{x}^0}{\partial x^i} \tilde{g}_{j0} + \frac{\partial \tilde{x}^l}{\partial x^0} \frac{\partial \tilde{x}^s}{\partial x^i} \tilde{g}_{ls} \\
&= a^2(\tau + T) \left( -\partial_i T (1 + T') (1 + 2\tilde{A}) + (1 + T') (\delta_{ij} + \partial_i L_j) \tilde{B}_j + L'_l (\delta_{ls} + \partial_l L_s) (\delta_{ls} + \tilde{H}_{ls}) \right) \\
&= a^2(\tau) (1 + 2\mathcal{H}T) \left( -\partial_i T + \tilde{B}_i + L'_i \right) = a^2(\tau) \left( -\partial_i T + \tilde{B}_i + L'_i \right). \tag{A.5}
\end{aligned}$$

Let us now prove the gauge transformation for the overdensity

$$\delta\rho \longrightarrow \delta\tilde{\rho} = \delta\rho - T\tilde{\rho}', \tag{A.6}$$

Expanding the derivatives in Eq. (1.161) and keeping linear order:

$$\begin{aligned}
T^0_0(x) &= -(\bar{\rho}(\tau) + \delta\rho) = \frac{\partial x^0}{\partial \tilde{x}^\alpha} \frac{\partial \tilde{x}^\beta}{\partial x^0} \tilde{T}^\alpha_\beta(\tilde{x}) \\
&= \frac{\partial x^0}{\partial \tilde{x}^0} \frac{\partial \tilde{x}^0}{\partial x^0} \tilde{T}^0_0 + \frac{\partial x^0}{\partial \tilde{x}^0} \frac{\partial \tilde{x}^i}{\partial x^0} \tilde{T}^0_i + \frac{\partial x^0}{\partial \tilde{x}^i} \frac{\partial \tilde{x}^0}{\partial x^0} \tilde{T}^i_0 + \frac{\partial x^0}{\partial \tilde{x}^i} \frac{\partial \tilde{x}^j}{\partial x^0} \tilde{T}^i_j \\
&= -(1 - T')(1 + T') (\bar{\rho}(\tau + T) + \delta\tilde{\rho}) = -(\bar{\rho}(\tau) + T\tilde{\rho}' + \delta\tilde{\rho}). \tag{A.7}
\end{aligned}$$

### A.3 The 0 component of the geodesic equation

The goal is to compute the 0 component of the geodesic equation. But for this, we first need to compute the Christoffel symbols in a perturbed FLRW universe, which will also be useful for other calculations. From now on, we work in conformal time and assume the Newtonian gauge. We will simply have to plug the elements of the metric

$$g_{00} = -a^2(1 + 2\psi), \quad g_{ij} = a^2(1 - 2\phi)\delta_{ij}, \tag{A.8}$$

and the inverse metric

$$g^{00} = -a^{-2}(1 - 2\psi), \quad g^{ij} = a^{-2}(1 + 2\phi)\delta^{ij}, \tag{A.9}$$

in the definition for the Christoffel symbols:

$$\Gamma^\mu_{\alpha\beta} = \frac{1}{2}g^{\mu\lambda} (\partial_\alpha g_{\beta\lambda} + \partial_\beta g_{\alpha\lambda} - \partial_\lambda g_{\alpha\beta}). \tag{A.10}$$

We start with  $\Gamma^0_{00}$ , systematically discarding all terms beyond linear order

$$\Gamma^0_{00} = \frac{g^{00}}{2} (2\partial_0 g_{00} - \partial_0 g_{00}) = \frac{g^{00}}{2} \partial_0 g_{00} = \frac{(1 - 2\psi)}{2a^2} \partial_0 [a^2(1 + 2\psi)] = \mathcal{H} + \psi'. \tag{A.11}$$

We compute in the same way the rest of Christoffels, having in mind that  $g^{0i} = g_{0i} = 0$ .

$\Gamma^0_{0i}$  :

$$\Gamma^0_{0i} = \frac{1}{2}g^{0\lambda} (\partial_0 g_{\lambda i} + \partial_i g_{0\lambda} - \partial_\lambda g_{0i}) = \frac{g^{00}}{2} \partial_i g_{00} = \frac{(1 - 2\psi)}{2a^2} 2a^2 \partial_i \psi = \partial_i \psi. \tag{A.12}$$

$\Gamma^i_{00}$  :

$$\begin{aligned}\Gamma^i{}_{00} &= \frac{1}{2}g^{i\lambda}(2\partial_0g_{0\lambda} - \partial_\lambda g_{00}) = \frac{1}{2}g^{ij}(2\partial_0g_{j0} - \partial_j g_{00}) = -\frac{1}{2}g^{ij}\partial_j g_{00} \\ &= \frac{\delta^{ij}}{2a^2}(1+2\phi)2a^2\partial_j\psi = \delta^{ij}\partial_j\psi.\end{aligned}\quad (\text{A.13})$$

$\Gamma^0{}_{ij}$  :

$$\begin{aligned}\Gamma^0{}_{ij} &= \frac{1}{2}g^{0\lambda}(\partial_j g_{j\lambda} + \partial_j g_{i\lambda} - \partial_\lambda g_{ij}) = -\frac{1}{2}g^{00}\partial_0 g_{ij} = \frac{\delta_{ij}}{2a^2}(1-2\psi)(a^2 - 2a^2\phi)' \\ &= (1-2\psi)\delta_{ij}(\mathcal{H} - \phi' - 2\phi\mathcal{H}) = \delta_{ij}(\mathcal{H} - \phi' - 2\mathcal{H}(\phi + \psi)).\end{aligned}\quad (\text{A.14})$$

$\Gamma^i{}_{j0}$  :

$$\begin{aligned}\Gamma^i{}_{j0} &= \frac{1}{2}g^{i\lambda}(\partial_j g_{0\lambda} + \partial_0 g_{j\lambda} - \partial_\lambda g_{j0}) = \frac{1}{2}g^{ik}\partial_0 g_{jk} = \frac{\delta^{ik}\delta_{jk}(1+2\phi)}{2a^2}(a^2 - 2\phi a^2)' \\ &= (1+2\phi)\delta^i{}_j(\mathcal{H} - \phi' - 2\phi\mathcal{H}) = \delta^i{}_j(\mathcal{H} - \phi').\end{aligned}\quad (\text{A.15})$$

$\Gamma^i{}_{jk}$  :

$$\begin{aligned}\Gamma^i{}_{jk} &= \frac{1}{2}g^{i\lambda}(\partial_j g_{k\lambda} + \partial_k g_{j\lambda} - \partial_\lambda g_{jk}) = \frac{1}{2}g^{il}(\partial_j g_{lk} + \partial_k g_{lj} - \partial_l g_{jk}) \\ &= \frac{a^2\delta^{il}(1+2\phi)}{2a^2}(-2\delta_{lk}\partial_j\phi - 2\delta_{lj}\partial_k\phi + 2\delta_{jk}\partial_l\phi) = -2\delta^i{}_j\partial_k\phi + \delta_{jk}\delta^{il}\partial_l\phi.\end{aligned}\quad (\text{A.16})$$

The remaining ingredients needed to compute the geodesic equation are the elements of the 4-momentum vector  $P^\mu = \frac{dx^\mu}{d\sigma} = (P^0, P^i)$ . For computing  $P^0$ , we can expand the closure relation

$$-m^2 = g_{\mu\nu}P^\mu P^\nu = -a^2(1+2\psi)(P^0)^2 + p^2. \quad (\text{A.17})$$

From this, we get that  $P^0 = \frac{E}{a\sqrt{1+2\psi}}$ . Now, to determine  $P^i$ , we write  $P^i = C\hat{n}^i$ , where  $\hat{n}^i$  is a unit vector and  $C$  is a constant to be determined. From the definition of  $p$ , we have

$$p^2 = C^2 \sum_{ij} g_{ij}\hat{p}^i\hat{p}^j = a^2(1-2\phi)C^2 \sum_{ij} \delta_{ij}\hat{n}^i\hat{n}^j = a^2(1-2\phi)C^2, \quad (\text{A.18})$$

which means  $C = \frac{p}{a\sqrt{1-2\phi}}$ . In short, using that  $(1+2\psi)^{-1/2} \simeq 1-\psi$  and  $(1-2\phi)^{-1/2} \simeq 1+\phi$ , we can write:

$$P^0 = \frac{E}{a}(1-\psi), \quad P^i = \frac{p\hat{n}^i}{a}(1+\phi). \quad (\text{A.19})$$

We are finally ready to compute the 0-component of the geodesic equation. Setting  $\mu = 0$  in Eq. (1.5):

$$\frac{dP^0}{d\sigma} = \frac{d\tau}{d\sigma} \frac{dP^0}{d\tau} = P^0 \frac{dP^0}{d\tau} = -\Gamma^0{}_{\alpha\beta} P^\alpha P^\beta. \quad (\text{A.20})$$

This can also be written as

$$\frac{d}{d\tau} \left[ \frac{E}{a}(1-\psi) \right] = -\Gamma^0{}_{\alpha\beta} \frac{P^\alpha P^\beta}{E} a(1+\psi), \quad (\text{A.21})$$



where we used  $(P^0)^{-1} \simeq \frac{a}{E}(1 + \psi)$ . By expanding the derivative and then multiplying by  $a(1 + \psi)$  we get (after dropping all quadratic terms):

$$\frac{dE}{d\tau} = E\mathcal{H} + E\frac{d\psi}{d\tau} - \Gamma^0_{\alpha\beta} \frac{P^\alpha P^\beta}{E} a^2(1 + 2\psi). \quad (\text{A.22})$$

Now, notice that we expand the derivative of  $\psi$  as  $\frac{d\psi}{d\tau} = \frac{\partial\psi}{\partial\tau} + \frac{dx^i}{d\tau} \frac{d\psi}{dx^i}$ , where  $\frac{dx^i}{d\tau} = \frac{P^i}{P^0} = \frac{p\hat{p}^i}{E} \frac{1+\phi}{1-\psi}$ . In addition, using that  $E = \sqrt{m^2 + p^2}$  we have  $\frac{dE}{d\tau} = \frac{p}{E} \frac{dp}{d\tau}$ . We can thus rewrite Eq. (A.22) as

$$\frac{dp}{d\tau} = \frac{E^2}{p}\mathcal{H} + \frac{E^2}{p} \left( \frac{\partial\psi}{\partial\tau} + \frac{p\hat{p}^i}{E} \frac{d\psi}{dx^i} \right) - \Gamma^0_{\alpha\beta} \frac{P^\alpha P^\beta}{p} a^2(1 + 2\psi). \quad (\text{A.23})$$

Using the expressions for the Christoffels that we derived in Eq. (A.11), Eq. (A.12) and Eq. (A.14), we can work out the factor  $\Gamma^0_{\alpha\beta} P^\alpha P^\beta$  at the r.h.s of Eq. (A.23):

$$\begin{aligned} \Gamma^0_{\alpha\beta} P^\alpha P^\beta &= \Gamma^0_{00} (P^0)^2 + 2\Gamma^0_{0i} P^0 P^i + \Gamma^0_{ij} P^i P^j \\ &= \frac{E^2}{a^2} (\mathcal{H} + \psi') (1 - 2\psi) + 2\frac{pE}{a^2} \hat{n}^i \partial_i \psi + \frac{p^2}{a^2} (\mathcal{H} - \phi' - 2\mathcal{H}(\phi + \psi)) (1 + 2\phi) \\ &= \frac{E^2}{a^2} (\mathcal{H}(1 - 2\psi) + \psi') + 2\frac{pE}{a^2} \hat{n}^i \partial_i \psi + \frac{p^2}{a^2} (\mathcal{H}(1 - 2\psi) - \phi') \end{aligned} \quad (\text{A.24})$$

We plug this in Eq. (A.23). After using  $(1 - 2\psi)(1 + 2\psi) \simeq 1$ , many terms simplify and we are left with

$$\frac{dp}{d\tau} = -p\mathcal{H} + p\phi' - E\hat{n}^i \partial_i \psi. \quad (\text{A.25})$$

In terms of comoving momentum  $q = ap$  and comoving energy  $\mathcal{E} = aE$ :

$$\frac{dq}{d\tau} = q\phi' - \mathcal{E} \hat{n}^i \partial_i \psi. \quad (\text{A.26})$$

## A.4 Elements of perturbed stress-energy tensor

We want to derive the relations between the elements of the perturbed stress-energy tensor and the Legendre multipoles of the perturbed PSD  $\Psi$ . We remind that

$$\delta T^\mu{}_\nu(\tau, k) = g \int \frac{d^3\vec{P}}{(2\pi)^3} (-\det(g))^{-1/2} \frac{P^\mu P_\nu}{P^0} \bar{f}(\tau, q) \Psi(\tau, q, k, \mu). \quad (\text{A.27})$$

For the newtonian gauge, the determinant gives  $(-\det(g))^{-1/2} = a^{-4}(1 - \psi - 3\phi)$ , but the  $\psi$  and  $\phi$  terms are irrelevant since the integrand in Eq. (A.27) contains  $\Psi$ , which is already first-order. We remind that the integral in Eq. (A.27) is over covariant three-momenta, which is given by

$$P_i = g_{ij} P^j = a^2(1 - 2\phi)(1 + \phi)p\hat{n}_i/a = (1 - \phi)q\hat{n}_i. \quad (\text{A.28})$$

This means that the integral measure can be expressed as

$$\int \int \int d^3\vec{P} = \int_0^{2\pi} d\varphi \int_{-1}^1 d\mu \int_0^\infty dq q^2 (1 - 3\phi), \quad (\text{A.29})$$

where the term with  $\phi$  is again irrelevant for being first-order. Now, the  $\mu$  integrals will select some particular multipole  $\Psi_\ell$  for each of the components of  $\delta T^\mu_\nu$ <sup>1</sup>, which can easily be seen by plugging the expansion of Eq. (1.190) in Eq. (A.27), and using the orthogonality property of the Legendre polynomials

$$\int_{-1}^1 d\mu P_\ell(\mu)P_m(\mu) = \frac{2\delta_{\ell m}}{2\ell + 1}. \quad (\text{A.31})$$

The overdensity  $\bar{\rho}\delta$  picks the  $\ell = 0$  multipole ( $P_0 = 1$ ), since in this case the integrand contains no  $\mu$  terms, just the factor  $P_0 = g_{00}P^0 = -\mathcal{E}(1 + \psi)$ . The same arises for the pressure perturbation  $\delta P$ , whose integrand has

$$\sum_i \frac{P^i P_i}{P^0} = \frac{q^2}{\mathcal{E}}(1 + \psi) \sum_i \hat{n}^i \hat{n}^j \delta_{ij}, \quad (\text{A.32})$$

with  $\sum_i \hat{n}^i \hat{n}^j \delta_{ij} = 1$ . The velocity divergence selects the  $\ell = 1$  multipole ( $P_1 = \mu$ ), given that the integrand includes  $\sum_i \hat{k}_i P_i = (1 - \phi)q\mu$ . Lastly, the anisotropic stress  $\sigma$  picks the  $\ell = 2$  multipole ( $P_2 = \frac{1}{2}(3\mu^2 - 1)$ ), as the integrand contains

$$\sum_{i,j} \left( -\hat{k}_i \hat{k}_j + \frac{\delta_{ij}}{3} \right) \frac{P^i P_j}{P^0} = \frac{q^2}{\mathcal{E}}(1 + \psi) \underbrace{\sum_{i,j} \left( -\hat{k}_i \hat{k}_j + \frac{\delta_{ij}}{3} \right) \hat{n}^i \hat{n}^j}_{-\mu^2 + \frac{1}{3}}. \quad (\text{A.33})$$

In short,

$$\bar{\rho}\delta = \frac{4\pi}{a^4} \int_0^\infty dq q^2 \mathcal{E} \bar{f} \Psi_0, \quad (\text{A.34})$$

$$(\bar{\rho} + \bar{P})\theta = \frac{4\pi k}{a^4} \int_0^\infty dq q^2 q \bar{f} \Psi_1, \quad (\text{A.35})$$

$$\bar{\rho}\Pi = \frac{4\pi}{3a^4} \int_0^\infty dq q^2 \frac{q^2}{\mathcal{E}} \bar{f} \Psi_0, \quad (\text{A.36})$$

$$(\bar{\rho} + \bar{P})\sigma = \frac{8\pi}{3a^4} \int_0^\infty dq q^2 \frac{q^2}{\mathcal{E}} \bar{f} \Psi_2, \quad (\text{A.37})$$

where we have absorbed a factor  $g/(2\pi)^3$  inside  $\bar{f}$ .

## A.5 Collision term for photons

The task is to determine the collision integral  $\mathcal{C}_\gamma$  appearing in the Boltzmann equation for the photon perturbations (c.f. Eq. (1.199)). We'll start assuming totally generic PSD for the particles involved, and perform the decomposition into a background and a linear contribution at the end. In practice, we'll see that the collision integral only contains first-order terms  $\mathcal{C}_\gamma = \mathcal{C}_\gamma^{(1)}$ . The process we want to describe is the Compton scattering off electrons

$$e^-(\vec{q}) + \gamma(\vec{p}) \longleftrightarrow e^-(\vec{q}') + \gamma(\vec{p}'), \quad (\text{A.38})$$

<sup>1</sup>In Fourier space, the elements of the perturbed stress-energy tensor are computed as

$$\bar{\rho}\delta = -\delta T^0_0, \quad (\bar{\rho} + \bar{P})\theta = ik \sum_i \hat{k}_i \delta T^0_i, \quad \bar{\rho}\Pi = \frac{1}{3} \sum_i T^i_i, \quad (\bar{\rho} + \bar{P})\sigma = \sum_{i,j} \left( -\hat{k}_i \hat{k}_j + \frac{\delta_{ij}}{3} \right) \delta T^i_j. \quad (\text{A.30})$$

where we have already labelled the momenta of each particle (beware of notation, we're working with physical and not comoving momenta, even if we use the letter  $q$ ). According to the general expression that we wrote in Eq. (1.63), the collision term reads <sup>2</sup>

$$\begin{aligned} \mathcal{C}_\gamma[f_\gamma(p)] = & \int \frac{d^3\vec{q}}{(2\pi)^3 2E_e(q)} \int \frac{d^3\vec{q}'}{(2\pi)^3 2E_e(q')} \int \frac{d^3\vec{p}'}{(2\pi)^3 2E_\gamma(p')} |\mathcal{M}|^2 (2\pi)^4 \delta^3[\vec{p} + \vec{q} - \vec{p}' - \vec{q}'] \\ & \times \delta[E_\gamma(p) + E_e(q) - E_\gamma(p') - E_e(q')] \{f_e(q')f_\gamma(p') - f_e(q)f_\gamma(p)\}, \end{aligned} \quad (\text{A.39})$$

where  $\mathcal{M} = \mathcal{M}_{e\gamma, e\gamma}$  denotes the invariant amplitude for Compton scattering. In the previous expression, we have neglected  $(1 \pm f)$  factors related to stimulated emission and Pauli blocking, since they play a negligible role in this context. Energies are of the order of relativistic limit for photons and non-relativistic for electrons. Namely,  $E_\gamma(p) = p$  and  $E_e(q) = m_e + \frac{q^2}{2m_e}$ . During the recombination epoch, the kinetic energy of electrons is very small compared to their mass, so we can set  $E_e \simeq m_e$  in the denominator of Eq. (A.39). Performing the  $d^3\vec{q}'$  integral with the 3-dimensional delta distribution yields

$$\begin{aligned} \mathcal{C}_\gamma = & \frac{\pi}{4m_e^2} \int \frac{d^3\vec{q}}{(2\pi)^3} \int \frac{d^3\vec{p}'}{(2\pi)^3 p'} \delta \left[ p + \frac{q^2}{2m_e} - p' - \frac{|\vec{q} + \vec{p} - \vec{p}'|^2}{2m_e} \right] \\ & \times |\mathcal{M}|^2 \{f_e(q + p - p')f_\gamma(p') - f_e(q)f_\gamma(p)\}. \end{aligned} \quad (\text{A.40})$$

We can simplify the scary-looking aspect of the Dirac delta by noticing that, in the non-relativistic Compton scattering process, very few energy is transferred

$$E_e(q) - E_e(q + p - p') = \frac{q^2}{2m_e} - \frac{(\vec{q} + \vec{p} - \vec{p}')^2}{2m_e} \simeq \frac{(\vec{p}' - \vec{p}) \cdot \vec{q}}{m_e}, \quad (\text{A.41})$$

since  $q \gg p, p'$ . That is, we can restrict ourselves to the Thomson limit of Compton scattering. Now, given that  $p \simeq p'$ , the rhs of Eq. (A.41) is roughly  $pq/m_e$ , where  $q/m_e$  is of the order of the baryon velocity  $q/m_e \sim v_b \ll 1$ . Therefore, we can consider the quantity  $E_e(q) - E_e(q + p - p')$  to be a small perturbation around  $(p - p')$  inside the delta distribution, and formally perform an expansion up to first order. With this and using that  $f_e(q + p - p') \simeq f_e(q)$ , we write Eq. (A.40) as

$$\mathcal{C}_\gamma = \frac{\pi}{4m_e^2} \int \frac{d^3\vec{q}}{(2\pi)^3} f_e(q) \int \frac{d^3\vec{p}'}{(2\pi)^3 p'} |\mathcal{M}|^2 \left[ \delta(p - p') + \frac{(\vec{p}' - \vec{p}) \cdot \vec{q}}{m_e} \frac{\partial \delta(p - p')}{\partial p'} \right] \{f_\gamma(p') - f_\gamma(p)\}. \quad (\text{A.42})$$

The expansion of the Dirac delta is obviously very ill-defined, but it will soon find justification when doing integration by parts. What about  $|\mathcal{M}|^2$ ? This amplitude can be computed with the help of the Feynman rules for quantum electrodynamics, as explained for example in PESKIN et al. (1995). It can be written as

$$|\mathcal{M}|^2 = 6\pi\sigma_T m_e^2 (1 + (\hat{p} \cdot \hat{p}')^2) \quad (\text{A.43})$$

where we have introduced the Thomson cross-section  $\sigma_T = \frac{8\pi\alpha^2}{3m_e^2}$ , with  $\alpha = e^2/4\pi$  the fine-structure constant. In reality, the invariant amplitude also depends on polarization ( $\propto |\hat{\epsilon} \cdot \hat{\epsilon}'|^2$ , where  $\hat{\epsilon}$  and  $\hat{\epsilon}'$  are the polarizations of the incoming and outgoing photons), which has been implicitly summed over in Eq. (A.43). This means that Compton scattering induces some level of polarization on the CMB. Since the description of the polarization photon field is beyond the scope of this work, and its impact

<sup>2</sup>To shorten notation, we will omit the dependence of the PSD  $f_i$  on  $\mu, \tau, k$ , and write only the dependency on momenta.

on the evolution of the photon temperature field is very small, we will neglect this effect in the following (however see Sect. 1.6.5 for a short discussion). For the moment, let us consider the angle average of Eq. (A.43)

$$|\mathcal{M}_{\text{iso}}|^2 = 8\pi\sigma_T m_e^2 \quad (\text{A.44})$$

Using Eq. (A.44), Eq. (A.42) can be expressed as

$$\mathcal{C}_\gamma = 2\pi^2 \bar{n}_e \sigma_T \int \frac{d^3 \vec{p}'}{(2\pi)^3 p'} \left[ \delta(p - p') + (\vec{p} - \vec{p}') \cdot \vec{v}_b \frac{\partial \delta(p - p')}{\partial p'} \right] \{f_\gamma(p') - f_\gamma(p)\}. \quad (\text{A.45})$$

The factors with  $\bar{n}_e$  and  $\bar{n}_e \vec{v}_b$  have appeared as a result of two integrals in  $q$ :

$$\int \frac{d^3 \vec{q}}{(2\pi)^3} f_e = \int \frac{d^3 \vec{q}}{(2\pi)^3} \bar{f}_e + \int \frac{d^3 \vec{q}}{(2\pi)^3} \delta f_e = \bar{n}_e, \quad (\text{A.46})$$

$$\int \frac{d^3 \vec{q}}{(2\pi)^3} f_e \vec{q} = \int \frac{d^3 \vec{q}}{(2\pi)^3} \bar{f}_e \vec{q} + \int \frac{d^3 \vec{q}}{(2\pi)^3} \delta f_e \vec{q} = (\bar{\rho}_e + \bar{P}_e) \vec{v}_b \simeq m_e \bar{n}_e \vec{v}_b. \quad (\text{A.47})$$

In Eq. (A.46), we discard the integral over  $\delta f_e$  since we neglect the impact of perturbed recombination on the CMB. In Eq. (A.47), the integral over  $\bar{f}_e \vec{q}$  vanishes by symmetry, and we use  $\bar{P}_e \simeq 0$  and  $\bar{\rho}_e \simeq m_e \bar{n}_e$ , since electrons were non-relativistic by this time. The next step is to plug in Eq. (A.45) the expansion for the photon PSD that we showed already in Eq. (1.197)

$$f_\gamma = \bar{f}_\gamma - p \frac{\partial \bar{f}_\gamma}{\partial p} \Theta. \quad (\text{A.48})$$

This yields:

$$\begin{aligned} \mathcal{C}_\gamma &= \mathcal{C}_\gamma^{(1)} = 2\pi^2 \bar{n}_e \sigma_T \int \frac{d^3 \vec{p}'}{(2\pi)^3 p'} \left[ \delta(p - p') + (\vec{p} - \vec{p}') \cdot \vec{v}_b \frac{\partial \delta(p - p')}{\partial p'} \right] \\ &\quad \times \left\{ \bar{f}(p') - \bar{f}(p) - p' \frac{\partial \bar{f}}{\partial p'} \Theta(\hat{p}') + p \frac{\partial \bar{f}}{\partial p} \Theta(\hat{p}) \right\} \\ &= \frac{\bar{n}_e \sigma_T}{4\pi} \int_0^\infty dp' p' \int d\Omega' \left( \delta(p - p') \left[ -p' \frac{\partial \bar{f}}{\partial p'} \Theta(\hat{p}') + p \frac{\partial \bar{f}}{\partial p} \Theta(\hat{p}) \right] \right. \\ &\quad \left. + (\vec{p} - \vec{p}') \cdot \vec{v}_b \frac{\partial \delta(p - p')}{\partial p'} (\bar{f}(p') - \bar{f}(p)) \right) \end{aligned} \quad (\text{A.49})$$

In Eq. (A.49) there are only two terms that depend on  $\hat{p}'$  and thus must be accounted in the solid angle integral:  $\Theta(\hat{p}')$  and  $\hat{p}' \cdot \vec{v}_b$ . The first one will just give rise to the monopole perturbation  $\Theta_0 = \frac{1}{4\pi} \int d\Omega' \Theta(\hat{p}')$ . The second term will vanish, since we are integrating  $\hat{p}' \cdot \vec{v}_b = v_b \mu'$  over  $d\Omega' = -d\varphi' d\mu'$  (notice that  $\vec{v}_b = v_b \hat{k}$  since we only consider the scalar/ irrotational component of the velocity). Therefore,

$$\mathcal{C}_\gamma^{(1)} = \bar{n}_e \sigma_T \int_0^\infty dp' p' \left( \delta(p - p') \left[ -p' \frac{\partial \bar{f}}{\partial p'} \Theta_0 + p \frac{\partial \bar{f}}{\partial p} \Theta(\hat{p}) \right] + p \mu v_b \frac{\partial \delta(p - p')}{\partial p'} (\bar{f}(p') - \bar{f}(p)) \right). \quad (\text{A.50})$$

It just remains to use integration by parts on the second term inside the integrand, and then apply the Dirac deltas. This leads to

$$\mathcal{C}_\gamma^{(1)} = -p^2 \frac{\partial \bar{f}}{\partial p} \bar{n}_e \sigma_T [\Theta_0 - \Theta + \mu v_b]. \quad (\text{A.51})$$

This is not yet the final expression, since we totally neglected the angular dependence in Eq. (A.43). Taking this dependence into account, leads an extra term in the collision integral which is proportional to the quadrupole  $\Theta_2$ . To see this, let us extract the anisotropic part of the invariant amplitude

$$\delta|\mathcal{M}|^2 = |\mathcal{M}|^2 - |\mathcal{M}_{\text{iso}}|^2 = 2\pi\sigma_T m_e^2 [3(\hat{p} \cdot \hat{p}')^2 - 1]. \quad (\text{A.52})$$

The term in square brackets is equal to  $2P_2(\hat{p} \cdot \hat{p}')$ . It will be convenient to factorize the dependence on  $\hat{p}$  and  $\hat{p}'$  by means on the useful identity

$$P_\ell(\hat{p} \cdot \hat{p}') = \frac{4\pi}{2\ell + 1} \sum_{m=-\ell}^{m=+\ell} Y_{\ell m}(\hat{p}) Y_{\ell m}^*(\hat{p}'). \quad (\text{A.53})$$

Hence,

$$\delta|\mathcal{M}|^2 = \sigma_T m_e^2 \frac{16\pi}{5} \sum_{m=-2}^{m=+2} Y_{2m}(\hat{p}) Y_{2m}^*(\hat{p}') \stackrel{!}{=} \sigma_T m_e^2 \frac{16\pi}{5} Y_{20}(\hat{p}) Y_{20}(\hat{p}'). \quad (\text{A.54})$$

In the last equality, we have taken only the  $m = 0$  part, since the other  $Y_{2m}$  contain factors  $e^{\pm i\varphi}$ ,  $e^{\pm 2i\varphi}$ , which would vanish under the  $\int_0^{2\pi} d\varphi$  integral. The spherical harmonic  $Y_{20}$  is directly related to the second Legendre polynomial,  $Y_{20}(\hat{p}) = -\sqrt{\frac{5}{4\pi}} P_2(\mu)$ , with  $\mu = \hat{p} \cdot \hat{k}$ . Thus, the extra anisotropic contribution to the collision term is

$$\begin{aligned} \delta\mathcal{C}_\gamma^{(1)} &= \frac{\bar{n}_e \sigma_T}{8\pi} P_2(\mu) \int_0^\infty dp' p' \int d\Omega' P_2(\mu') \left( \delta(p - p') \left[ -p' \frac{\partial \bar{f}}{\partial p'} \Theta(\mu') + p \frac{\partial \bar{f}}{\partial p} \Theta(\mu) \right] \right. \\ &\quad \left. + (\vec{p} - \vec{p}') \cdot \vec{v}_b \frac{\partial \delta(p - p')}{\partial p'} (\bar{f}(p') - \bar{f}(p)) \right). \end{aligned} \quad (\text{A.55})$$

In the previous expression, the only term that survives after performing the solid angle integral is the one proportional to  $\Theta(\mu')$ , since  $\int_{-1}^{+1} d\mu' P_2(\mu') = 0$  and  $\int_{-1}^{+1} d\mu' P_2(\mu') \mu' = 0$ . Thus,

$$\delta\mathcal{C}_\gamma^{(1)} = -\frac{\bar{n}_e \sigma_T}{2} P_2(\mu) \int_0^\infty dp' p'^2 \delta(p - p') \frac{\partial \bar{f}}{\partial p'} \int_{-1}^{+1} \frac{d\mu'}{2} P_2(\mu') \Theta(\mu'). \quad (\text{A.56})$$

The  $\mu'$  integral in the previous equation gives rise to  $-\Theta_2$ . After applying the Dirac delta,

$$\delta\mathcal{C}_\gamma^{(1)} = p^2 \frac{\partial \bar{f}}{\partial p} \frac{\bar{n}_e \sigma_T}{2} P_2(\mu) \Theta_2, \quad (\text{A.57})$$

so the full collision term reads

$$\mathcal{C}_\gamma^{(1)} = -p^2 \frac{\partial \bar{f}}{\partial p} \bar{n}_e \sigma_T \left[ \Theta_0 - \Theta + \mu v_b - \frac{P_2(\mu)}{2} \Theta_2 \right]. \quad (\text{A.58})$$

## A.6 Conservation equations from the collisionless Boltzmann equation

Here we derive the two conservation equations, by integrating the collisionless Boltzmann hierarchy over the phase space. This calculation is relevant for massive neutrinos but also for any warm species that decoupled in the very early universe. We'll be using repeatedly the integral expressions for  $\delta$ ,  $\theta$ ,  $\delta P$  and  $\sigma$  shown in

Eq. (1.192)-Eq. (1.195), as well as the integral expressions for  $\bar{\rho}$  and  $\bar{P}$  shown in Eq. (1.55) and Eq. (1.56). We start with the perturbed continuity equation. This can be obtained from the equation for the zeroth multipole (c.f. Eq. (1.211))

$$\frac{\partial \Psi_{\nu,0}}{\partial \tau} = -\frac{kq}{\mathcal{E}} \Psi_{\nu,1} - \frac{d \ln \bar{f}}{d \ln q} \phi', \quad (\text{A.59})$$

The idea is to integrate previous equation over  $4\pi a^{-4} \int dq q^2 \mathcal{E} \bar{f}$ , in order to get a dynamical equation for  $\delta \rho_\nu$ . This yields

$$\underbrace{\frac{4\pi}{a^4} \int dq q^2 \mathcal{E} \frac{\partial (\bar{f} \Psi_{\nu,0})}{\partial \tau}}_{\text{I}} = - \underbrace{\frac{4\pi k}{a^4} \int dq q^3 \bar{f} \Psi_{\nu,1}}_{\text{II}} - \underbrace{\frac{\phi' 4\pi}{a^4} \int dq q^3 \mathcal{E} \frac{d \bar{f}}{dq}}_{\text{III}}. \quad (\text{A.60})$$

Let us focus on each term separately. The term II is the easiest one, since it directly gives  $(\bar{\rho}_\nu + \bar{P}_\nu) \theta_\nu$  by definition. For the term III, we need to perform integration by parts. Using  $\frac{\partial \mathcal{E}}{\partial q} = \frac{q}{\mathcal{E}}$ , we get

$$q^3 \mathcal{E} \frac{d \bar{f}}{dq} = \frac{d}{dq} (q^3 \mathcal{E} \bar{f}) - 3 \left( \bar{f} q^2 \mathcal{E} + \bar{f} \frac{q^4}{3 \mathcal{E}} \right). \quad (\text{A.61})$$

When this is inserted in the integral for the term III, the total derivative term vanishes, and we are left with  $-3(\bar{\rho}_\nu + \bar{P}_\nu) \phi'$ . Moving to the term I, the goal is to take the time derivative out of the integral, which will require to know the time derivative of the energy,  $\mathcal{E}'$ . Since  $\mathcal{E} = \sqrt{q^2 + a^2 m_\nu^2}$ , this gives

$$\mathcal{E}' = \frac{m_\nu^2 a^2}{\mathcal{E}} \mathcal{H} = \frac{\mathcal{E}^2 - q^2}{\mathcal{E}} \mathcal{H} = \mathcal{E} \mathcal{H} - \frac{q^2}{\mathcal{E}} \mathcal{H}. \quad (\text{A.62})$$

We can now proceed to take the time derivative out of the term I in order to make  $\delta \rho'_\nu$  appear, and evaluate the remaining terms:

$$\begin{aligned} \text{I} &= \frac{4\pi}{a^4} \frac{\partial}{\partial \tau} \left( \int dq q^2 \mathcal{E} \bar{f} \Psi_{\nu,0} \right) - \frac{4\pi}{a^4} \int dq q^2 \bar{f} \Psi_{\nu,0} \mathcal{E}' \\ &= (\delta \rho_\nu)' + 4\mathcal{H} \delta \rho_\nu - \mathcal{H} \left( \frac{4\pi}{a^4} \int dq q^2 \mathcal{E} \bar{f} \Psi_{\nu,0} - \frac{4\pi}{a^4} \int dq q^2 \frac{q^2}{\mathcal{E}} \bar{f} \Psi_{\nu,0} \right) \\ &= (\delta \rho_\nu)' + 4\mathcal{H} \delta \rho_\nu - \mathcal{H} (\delta \rho_\nu - 3\delta P_\nu) \\ &= (\delta \rho_\nu)' + 4\mathcal{H} \delta \rho_\nu - \mathcal{H} \delta \rho_\nu (1 - 3c_s^2) \\ &= (\delta \rho_\nu)' + 3\mathcal{H} \delta \rho_\nu (1 + c_s^2). \end{aligned} \quad (\text{A.63})$$

Putting all together,

$$(\delta \rho_\nu)' = \delta'_\nu \bar{\rho}_\nu + \delta_\nu \bar{\rho}'_\nu = -3\mathcal{H} \delta \rho_\nu (1 + c_s^2) - \bar{\rho}_\nu (1 + w_\nu) \theta_\nu + 3\bar{\rho}_\nu (1 + w_\nu) \phi'. \quad (\text{A.64})$$

Dividing by  $\bar{\rho}_\nu$ , it can be equivalently written as:

$$\delta'_\nu = -\frac{\bar{\rho}'_\nu}{\bar{\rho}_\nu} \delta_\nu - 3\mathcal{H} \delta_\nu (1 + c_s^2) - (1 + w_\nu) (\theta_\nu - 3\phi'). \quad (\text{A.65})$$

Using  $\frac{\bar{\rho}'_\nu}{\bar{\rho}_\nu} = -3\mathcal{H}(1 + w_\nu)$ <sup>3</sup>, we arrive at the perturbed continuity equation:

$$\delta'_\nu = -3\mathcal{H}(c_s^2 - w_\nu) \delta_\nu - (1 + w_\nu) (\theta_\nu - 3\phi'). \quad (\text{A.66})$$

<sup>3</sup>The background continuity equation,  $\bar{\rho}'_\nu = -3\mathcal{H}(1 + w_\nu) \bar{\rho}_\nu$ , could be derived in a very similar way by integration of the background Boltzmann equation,  $\frac{\partial \bar{f}}{\partial \tau} = 0$ , over  $4\pi a^{-4} \int dq q^2 \mathcal{E}$ .



Let us now consider the Euler equation. It can be derived from the equation for the first multipole (c.f. Eq. (1.212))

$$\frac{\partial \Psi_{\nu,1}}{\partial \tau} = \frac{kq}{3\mathcal{E}} [\Psi_{\nu,0} - 2\Psi_{\nu,2}] - \frac{\mathcal{E}k}{3q} \frac{d\ln \bar{f}}{d\ln q} \psi, \quad (\text{A.67})$$

To get a dynamical equation for  $\theta_\nu$ , we integrate the former equation over  $4\pi k a^{-4} \int dq q^3 \bar{f}$ , yielding

$$\underbrace{\frac{4\pi}{a^4} \int dq q^3 \frac{\partial(\bar{f}\Psi_{\nu,1})}{\partial \tau}}_{\text{I}} = \underbrace{\frac{4\pi k^2}{3a^4} \int dq \frac{q^4}{\mathcal{E}} \bar{f}\Psi_{\nu,0}}_{\text{II}} - \underbrace{\frac{8\pi k^2}{3a^4} \int dq \frac{q^4}{\mathcal{E}} \bar{f}\Psi_{\nu,2}}_{\text{III}} - \underbrace{\frac{\psi 4\pi k^2}{3a^4} \int dq q^3 \mathcal{E} \frac{d\bar{f}}{dq}}_{\text{IV}}. \quad (\text{A.68})$$

The terms II and III give by definition  $k^2 \delta P_\nu$  and  $k^2(\bar{\rho}_\nu + \bar{P}_\nu)\sigma_\nu$ , respectively. For the term IV we need to integrate by parts on  $q^3 \mathcal{E} \frac{d\bar{f}}{dq}$ , but this is precisely what we already did in Eq. (A.61). Thus, the term IV just gives  $-(\bar{\rho}_\nu + \bar{P}_\nu)k^2\psi$ . Regarding the term I, the goal is again to take the time derivative out of the integral to make  $\theta'_\nu$  appear:

$$\begin{aligned} \text{I} &= \frac{4\pi}{a^4} \frac{\partial}{\partial \tau} \left( \int dq q^3 \bar{f} \Psi_{\nu,1} \right) \\ &= \frac{\partial}{\partial \tau} \left[ (\bar{\rho}_\nu + \bar{P}_\nu) \theta_\nu \right] + 4\mathcal{H}(\bar{\rho}_\nu + \bar{P}_\nu) \theta_\nu \\ &= \bar{\rho}'_\nu (1 + c_g^2) \theta_\nu + \bar{\rho}_\nu (1 + w_\nu) \theta'_\nu + 4\mathcal{H} \bar{\rho}_\nu (1 + w_\nu) \theta_\nu. \end{aligned} \quad (\text{A.69})$$

Putting all together,

$$\bar{\rho}_\nu (1 + w_\nu) \theta'_\nu = -\bar{\rho}'_\nu (1 + c_g^2) \theta_\nu - 4\mathcal{H} \bar{\rho}_\nu (1 + w_\nu) \theta_\nu + k^2 \delta P_\nu - k^2 \rho_\nu (1 + w_\nu) \sigma_\nu + k^2 \rho_\nu (1 + w_\nu) \psi. \quad (\text{A.70})$$

The expression simplifies after dividing by  $\bar{\rho}_\nu (1 + w_\nu)$ ,

$$\theta'_\nu = -\frac{\bar{\rho}'_\nu}{\bar{\rho}_\nu} \frac{(1 + c_g^2)}{(1 + w_\nu)} \theta_\nu - 4\mathcal{H} \theta_\nu + \frac{k^2 c_s^2 \delta \rho_\nu}{\bar{\rho}_\nu (1 + w_\nu)} - k^2 \sigma_\nu + k^2 \psi. \quad (\text{A.71})$$

Finally, using  $\frac{\bar{\rho}'_\nu}{\bar{\rho}_\nu} = -3\mathcal{H}(1 + w_\nu)$ , we arrive at the Euler equation

$$\theta'_\nu = -\mathcal{H}(1 - 3c_g^2) \theta_\nu + k^2 \left( \frac{c_s^2}{1 + w} \delta_\nu + \psi - \sigma_\nu \right). \quad (\text{A.72})$$

## A.7 Perturbed Einstein equations

The goal is to determine Einstein equations in the perturbed FLRW universe, focusing only in the scalar sector. We'll have to compute the Ricci tensor  $R_{\mu\nu}$  and Ricci scalar  $R$  appearing in the Einstein tensor at the l.h.s. of Einstein equations:

$$G_{\mu\nu} \equiv R_{\mu\nu} - \frac{1}{2} g_{\mu\nu} R = 8\pi G T_{\mu\nu}. \quad (\text{A.73})$$

In order to compute the components of the perturbed Ricci tensor, we just need to plug the Christoffels we computed in Eq. (A.11)-Eq. (A.16) into the definition for  $R_{\mu\nu}$ :

$$R_{\mu\nu} \equiv \partial_\lambda \Gamma^\lambda_{\mu\nu} - \partial_\nu \Gamma^\lambda_{\mu\lambda} + \Gamma^\lambda_{\lambda\rho} \Gamma^\rho_{\mu\nu} - \Gamma^\rho_{\mu\lambda} \Gamma^\lambda_{\nu\rho}. \quad (\text{A.74})$$

$R_{00}$ :

$$\begin{aligned}
R_{00} &= \partial_\lambda \Gamma^\lambda_{00} - \partial_0 \Gamma^\lambda_{0\lambda} + \Gamma^\lambda_{\lambda\rho} \Gamma^\rho_{00} - \Gamma^\rho_{0\lambda} \Gamma^\lambda_{0\rho} \\
&= \cancel{\partial_0 \Gamma^0_{00}} + \partial_i \Gamma^i_{00} - \cancel{\partial_0 \Gamma^0_{00}} - \cancel{\partial_0 \Gamma^i_{0i}} + \Gamma^0_{00} \Gamma^0_{00} + \Gamma^0_{0i} \Gamma^i_{00} + \Gamma^i_{i0} \Gamma^0_{00} \\
&\quad + \underbrace{\Gamma^i_{ij} \Gamma^j_{00}}_{\mathcal{O}(2)} - \cancel{\Gamma^0_{00} \Gamma^0_{00}} - \cancel{\Gamma^i_{00} \Gamma^0_{0i}} - \underbrace{\Gamma^0_{0i} \Gamma^i_{00}}_{\mathcal{O}(2)} - \Gamma^i_{0j} \Gamma^j_{0i} \\
&= \nabla^2 \psi - 3\partial_0 (\mathcal{H} - \phi') + 3(\mathcal{H} + \psi')(\mathcal{H} - \phi') - (\mathcal{H} - \phi')^2 \underbrace{\delta^j_i \delta^i_j}_{=3} \\
&= -3\mathcal{H}' + \nabla^2 \psi + 3\mathcal{H}(\phi' + \psi') + 3\phi''. \tag{A.75}
\end{aligned}$$

 $R_{0i}$ :

$$\begin{aligned}
R_{0i} &= \partial_\lambda \Gamma^\lambda_{0i} - \partial_i \Gamma^\lambda_{0\lambda} + \Gamma^\lambda_{\lambda\rho} \Gamma^\rho_{0i} - \Gamma^\rho_{0\lambda} \Gamma^\lambda_{i\rho} \\
&= \partial_0 \Gamma^0_{0i} + \partial_j \Gamma^j_{0i} - \partial_i \Gamma^0_{00} - \partial_i \Gamma^j_{0j} + \Gamma^0_{00} \Gamma^0_{0i} + \Gamma^j_{j0} \Gamma^0_{0i} + \Gamma^0_{0j} \Gamma^j_{0i} \\
&\quad + \Gamma^k_{kj} \Gamma^j_{0i} - \cancel{\Gamma^0_{00} \Gamma^0_{0i}} - \cancel{\Gamma^0_{0j} \Gamma^j_{0i}} - \Gamma^j_{00} \Gamma^0_{ij} - \Gamma^k_{0j} \Gamma^j_{ik} \\
&= \cancel{\partial_i \phi'} - \partial_i \phi' - \cancel{\partial_i \phi'} + 3\partial_i \phi' + 3(\mathcal{H} - \phi') \partial_i \psi - \underbrace{3\delta^j_i (\mathcal{H} - \phi') \partial_j \phi}_{-3\mathcal{H} \partial_i \phi} \\
&\quad - \underbrace{\delta^{jk} \delta_{ij} \partial_k \psi \{ \mathcal{H} - \phi' - 2\mathcal{H}(\phi + \psi) \}}_{\delta_i^k} - \underbrace{(\mathcal{H} - \phi') \delta^k_j \{ -2\delta^j_i \partial_k \phi + \delta_{ik} \delta^{jl} \partial_l \phi \}}_{+3\mathcal{H} \partial_i \phi} \\
&= 2\partial_i \phi' + 3\mathcal{H} \partial_i \psi - \mathcal{H} \partial_i \psi = 2\partial_i \phi' + 2\mathcal{H} \partial_i \psi. \tag{A.76}
\end{aligned}$$

We have of course neglected all higher order terms and used that  $\partial_i \mathcal{H} = 0$ .

 $R_{ij}$ :

$$\begin{aligned}
R_{ij} &= \partial_\lambda \Gamma^\lambda_{ij} - \partial_j \Gamma^\lambda_{i\lambda} + \Gamma^\lambda_{\lambda\rho} \Gamma^\rho_{ij} - \Gamma^\rho_{i\lambda} \Gamma^\lambda_{j\rho} \\
&= \partial_0 \Gamma^0_{ij} + \partial_k \Gamma^k_{ij} - \partial_j \Gamma^0_{i0} - \partial_j \Gamma^k_{ik} + \Gamma^0_{00} \Gamma^0_{ij} + \Gamma^k_{k0} \Gamma^0_{ij} + \underbrace{\Gamma^0_{0k} \Gamma^k_{ij}}_{\mathcal{O}(2)} \\
&\quad + \underbrace{\Gamma^k_{kl} \Gamma^l_{ij}}_{\mathcal{O}(2)} - \underbrace{\Gamma^0_{i0} \Gamma^0_{j0}}_{\mathcal{O}(2)} - \Gamma^k_{i0} \Gamma^0_{jk} - \Gamma^0_{ik} \Gamma^k_{j0} - \underbrace{\Gamma^k_{il} \Gamma^l_{jk}}_{\mathcal{O}(2)} \\
&= [\mathcal{H} - \phi' - 2(\phi + \psi)]' \delta_{ij} + \partial_k \left( -2\delta^k_i \partial_j \phi + \delta_{ij} \delta^{kl} \partial_l \phi \right) \\
&\quad - \partial_j \partial_i \psi + 3\partial_j \partial_i \phi + (\mathcal{H} + \psi') [\mathcal{H} - \phi' - 2\mathcal{H}(\phi + \psi)] \delta_{ij} \\
&\quad + (\mathcal{H} - \phi') [\mathcal{H} - \phi' - 2(\phi + \psi)] (3\delta_{ij} - \delta^k_i \delta_{kj} - \delta^k_j \delta_{ki}) \\
&= \left[ \mathcal{H}' + 2\mathcal{H}^2 - \phi'' + \nabla^2 \phi - 2(\mathcal{H}' + 2\mathcal{H}^2)(\phi + \psi) - \mathcal{H}\psi' - 5\mathcal{H}\phi' \right] \delta_{ij} + \partial_i \partial_j (\phi - \psi). \tag{A.77}
\end{aligned}$$

Let us now compute the Ricci scalar,  $R \equiv g^{\mu\nu} R_{\mu\nu}$ . Its expression gets simplified because of the fact that  $g^{0i} = 0$ , meaning that  $R = g^{00} R_{00} + g^{ij} R_{ij}$ . By collecting the previous results for the Ricci tensor and using  $\delta^{ij} \partial_i \partial_j = \nabla^2$  and  $\delta^{ij} \delta_{ij} = 3$ , we have

$$\begin{aligned}
a^2 R &= -(1 - 2\psi) \left[ -3\mathcal{H}' + \nabla^2 \psi + 3\mathcal{H}(\phi' + \psi') + 3\phi'' \right] + (1 + 2\phi) \nabla^2 (\phi - \psi) \\
&\quad + 3(1 + 2\phi) \left[ \mathcal{H}' + 2\mathcal{H}^2 - \phi'' + \nabla^2 \phi - 2(\mathcal{H}' + 2\mathcal{H}^2)(\phi + \psi) - \mathcal{H}\psi' - 5\mathcal{H}\phi' \right] \\
&= 6(\mathcal{H}' + \mathcal{H}^2) - 2\nabla^2 \psi + 4\nabla^2 \phi - 12(\mathcal{H}' + \mathcal{H}^2)\psi - 6\phi'' - 6\mathcal{H}(\psi' + 3\phi'). \tag{A.78}
\end{aligned}$$

We are now ready to compute each component of  $G_{\mu\nu}$ .

$G_{00}$ :

$$\begin{aligned} G_{00} &= R_{00} - \frac{1}{2}g_{00}R = -3\mathcal{H}' + \nabla^2\psi + 3\mathcal{H}(\phi' + \psi') + 3\phi'' + 3(1 + 2\psi)(\mathcal{H}' + \mathcal{H}^2) \\ &\quad + \frac{1}{2} \left[ -2\nabla^2\psi + 4\nabla^2\phi - 12(\mathcal{H}' + \mathcal{H}^2)\psi - 6\phi'' - 6\mathcal{H}(\psi' + 3\phi') \right] \\ &= 3\mathcal{H}^2 + 2\nabla^2\phi - 6\mathcal{H}\phi'. \end{aligned} \quad (\text{A.79})$$

$G_{0i}$ :

$$G_{0i} = R_{0i} = 2\partial_i(\phi' + \mathcal{H}\psi). \quad (\text{A.80})$$

$G_{ij}$ :

$$\begin{aligned} G_{ij} &= R_{ij} - \frac{1}{2}g_{ij}R = \left[ \mathcal{H}' + 2\mathcal{H}^2 - \phi'' + \nabla^2\phi - 2(\mathcal{H}' + 2\mathcal{H}^2)(\phi + \psi) - \mathcal{H}\psi' - 5\mathcal{H}\phi' \right] \delta_{ij} \\ &\quad + \partial_i\partial_j(\phi - \psi) - 3(1 - 2\phi)(\mathcal{H}' + \mathcal{H}^2)\delta_{ij} \\ &\quad - \frac{1}{2} \left[ -2\nabla^2\psi + 4\nabla^2\phi - 12(\mathcal{H}' + \mathcal{H}^2)\psi - 6\phi'' - 6\mathcal{H}(\psi' + 3\phi') \right] \delta_{ij} \\ &= -(2\mathcal{H}' + \mathcal{H}^2)\delta_{ij} + \left[ \nabla^2(\psi - \phi) + 2\phi'' + 2(2\mathcal{H}' + \mathcal{H}^2)(\phi + \psi) + 2\mathcal{H}\psi' + 4\mathcal{H}\phi' \right] \delta_{ij} \\ &\quad + \partial_i\partial_j(\phi - \psi). \end{aligned} \quad (\text{A.81})$$

It is time to relate the components of the perturbed Einstein tensor we just obtained, to the components of the perturbed stress-energy tensor in Eq. (1.147)-Eq. (1.150), as demanded by Einstein equations. We switch at this point to Fourier space, meaning that we can make the replacements  $\partial_i \rightarrow ik_i$  and  $\nabla^2 \rightarrow -k^2$ .

- We start with the trace-free projection of the  $ij$  equation. That is, we consider  $\tilde{G} = 8\pi G\tilde{T}$ , where  $\tilde{G} \equiv \sum_{i,j} \left( \hat{k}_i\hat{k}_j - \frac{\delta_{ij}}{3} \right) G_{ij}$  and  $\tilde{T} \equiv \sum_{i,j} \left( \hat{k}_i\hat{k}_j - \frac{\delta_{ij}}{3} \right) T_{ij}$ , with  $T_{ij} = g_{ik}T^k_j$ . According to Eq. (A.81),  $\tilde{G} = -\frac{2}{3}k^2(\phi - \psi)$ , whereas  $\tilde{T}$  gives at linear order  $-a^2\sum_I(\bar{\rho}_I + \bar{P}_I)\sigma_I$ , by definition of the anisotropic stress. Hence, we have

$$k^2(\phi - \psi) = 12\pi Ga^2 \sum_I (\bar{\rho}_I + \bar{P}_I)\sigma_I \quad (\text{A.82})$$

The index  $I$  runs over all cosmological species: photons, neutrinos, cold dark matter and baryons.

- We move to the 00 equation. From Eq. (A.79) we get

$$3\mathcal{H}^2 - 2k^2\phi - 6\mathcal{H}\phi' = 8\pi Gg_{0\mu}T^\mu_0 = 8\pi Gg_{00}T^0_0 = 8\pi Ga^2(1 + 2\psi) \sum_I (\bar{\rho}_I + \delta\rho_I). \quad (\text{A.83})$$

The zeroth-order part gives the first Friedmann equation (in conformal time)

$$\mathcal{H}^2 = \frac{8\pi G}{3}a^2 \sum_I \bar{\rho}_I, \quad (\text{A.84})$$

while the first-order part gives  $-k^2\phi - 3\mathcal{H}\phi' = 4\pi Ga^2(\sum_I \delta\rho_I + 2\psi \sum_I \bar{\rho}_I)$ . By using Eq. (A.84) this last equation can be more conveniently expressed as

$$k^2\phi + 3\mathcal{H}(\phi' + \mathcal{H}\psi) = -4\pi Ga^2 \sum_I \delta\rho_I. \quad (\text{A.85})$$

- Next, we consider the  $0i$  equation,  $G_{0i} = 8\pi G T_{0i}$ . By virtue of Eq. (A.80), we find it to be  $ik_i(\phi' + \mathcal{H}\psi) = 4\pi G g_{00} T_i^0 = -4\pi G a^2 \delta T_i^0$ . Contracting each side of the equation with  $i \sum_i k^i$ , we get

$$k^2(\phi' + \mathcal{H}\psi) = 4\pi G a^2 \sum_I (\bar{\rho}_I + \bar{P}_I) \theta_I. \quad (\text{A.86})$$

- At last, we compute the trace of the  $ij$  equation,  $\sum_i G^i_i = 8\pi G \sum_i T^i_i$ . For the r.h.s. we have  $\sum_i T^i_i = 3 \sum_I (\bar{P}_I + \delta P_I)$ , whereas the l.h.s. gives:

$$\begin{aligned} \sum_i G^i_i &= \sum_{i,k} g^{ik} G_{ki} \\ &= 3a^{-2} \left[ -(2\mathcal{H}' + \mathcal{H}^2) + \frac{2k^2}{3}(\phi - \psi) + 2\phi'' + 2\psi(2\mathcal{H}' + \mathcal{H}^2) + 2\mathcal{H}(\psi' + 2\phi') \right] \end{aligned} \quad (\text{A.87})$$

At zeroth order we get the second Friedmann equation

$$2\mathcal{H}' + \mathcal{H}^2 = -8\pi G a^2 \sum_I \bar{P}_I. \quad (\text{A.88})$$

At first order, we obtain

$$\phi'' + \mathcal{H}(\psi' + 2\phi') + (2\mathcal{H}' + \mathcal{H}^2)\psi + \frac{k^2}{3}(\phi - \psi) = 4\pi G a^2 \sum_I \delta P_I. \quad (\text{A.89})$$

## A.8 Conservation of the comoving curvature perturbation

We want to show that the comoving curvature perturbation, whose expression in the Newtonian gauge is given by

$$\mathcal{R} = \phi + \frac{\mathcal{H}(\phi' + \mathcal{H}\psi)}{4\pi G a^2 (\bar{\rho}_{\text{tot}} + \bar{P}_{\text{tot}})}, \quad (\text{A.90})$$

is indeed constant for super-Hubble scales and for adiabatic initial conditions.

Differentiating Eq. (A.90) and multiplying by  $4\pi G a^2 (\bar{\rho}_{\text{tot}} + \bar{P}_{\text{tot}})$ , we get:

$$\begin{aligned} 4\pi G a^2 (\bar{\rho}_{\text{tot}} + \bar{P}_{\text{tot}}) \mathcal{R}' &= 4\pi G a^2 (\bar{\rho}_{\text{tot}} + \bar{P}_{\text{tot}}) \phi' + \mathcal{H}'(\phi' + \mathcal{H}\psi) + \mathcal{H}(\phi'' + \mathcal{H}'\psi + \mathcal{H}\psi') \\ &\quad + \mathcal{H}^2(\phi' + \mathcal{H}\psi) + 3\mathcal{H}^2 \frac{\bar{P}'_{\text{tot}}}{\bar{\rho}'_{\text{tot}}} (\phi' + \mathcal{H}\psi), \end{aligned} \quad (\text{A.91})$$

where we used  $\rho'_{\text{tot}} = -3\mathcal{H}(\bar{\rho}_{\text{tot}} + \bar{P}_{\text{tot}})$ . Let us try to simplify the previous expression. Using the two Friedmann equations Eq. (A.84) and Eq. (A.88) we can replace  $4\pi G a^2 (\bar{\rho}_{\text{tot}} + \bar{P}_{\text{tot}})$  by  $\mathcal{H}^2 - \mathcal{H}'$ . In the last term on the r.h.s., we can use the Poisson equation Eq. (A.85) in order to replace  $3\mathcal{H}(\phi' + \mathcal{H}\psi)$  by  $-4\pi G a^2 \delta\rho_{\text{tot}} - k^2\phi$ . Hence:

$$\begin{aligned} (\mathcal{H}^2 - \mathcal{H}') \mathcal{R}' &= (\mathcal{H}^2 - \mathcal{H}') \phi' + \mathcal{H}'(\phi' + \mathcal{H}\psi) + \mathcal{H}(\phi'' + \mathcal{H}'\psi + \mathcal{H}\psi') \\ &\quad + \mathcal{H}^2(\phi' + \mathcal{H}\psi) - \mathcal{H} \frac{\bar{P}'_{\text{tot}}}{\bar{\rho}'_{\text{tot}}} (k^2\phi + 4\pi G a^2 \delta\rho_{\text{tot}}). \end{aligned} \quad (\text{A.92})$$

We can now add and subtract  $4\pi G a^2 \mathcal{H} \delta P_{\text{tot}} + \frac{k^2 \mathcal{H}}{3} (\psi - \phi)$  on the r.h.s. and simplify, to find

$$\begin{aligned}
 (\mathcal{H}^2 - \mathcal{H}') \mathcal{R}' = & \mathcal{H} \left[ \phi'' + \mathcal{H}(\psi' + 2\phi') + (2\mathcal{H}' + \mathcal{H}^2)\psi + \frac{k^2}{3}(\phi - \psi) - 4\pi G a^2 \delta P_{\text{tot}} \right] \\
 & + 4\pi G a^2 \mathcal{H} \delta P_{\text{nad}} - \mathcal{H} k^2 \left( \phi \frac{\bar{P}'_{\text{tot}}}{\bar{\rho}'_{\text{tot}}} - \frac{(\phi - \psi)}{3} \right), \tag{A.93}
 \end{aligned}$$

where  $\delta P_{\text{nad}}$  is the *non-adiabatic pressure perturbation*

$$\delta P_{\text{nad}} \equiv \delta P_{\text{tot}} - \frac{\bar{P}'_{\text{tot}}}{\bar{\rho}'_{\text{tot}}} \delta \rho_{\text{tot}}. \tag{A.94}$$

This quantity vanishes for adiabatic modes. In addition, we notice that the first term in brackets at the r.h.s. of Eq. (A.93) vanishes by virtue of the *ii* Einstein equation Eq. (A.89). We are thus left with

$$(\mathcal{H}^2 - \mathcal{H}') \mathcal{R}' = -\mathcal{H} k^2 \left( \phi \frac{\bar{P}'_{\text{tot}}}{\bar{\rho}'_{\text{tot}}} - \frac{(\phi - \psi)}{3} \right). \tag{A.95}$$

This equation tells us that the variation of  $\mathcal{R}$  is of the order  $\frac{d\mathcal{R}}{d \ln a} \sim \left(\frac{k}{\mathcal{H}}\right)^2 \phi$ , meaning that the comoving curvature perturbation doesn't evolve on super-Hubble scales.

# B

---

## Complements on parameter inference

---

In this appendix, we explain some basic tools about bayesian statistics and parameter extraction, that are routinely used to test cosmological models (such as the ones considered in this work) against actual data. We mainly follow [VERDE \(2010\)](#), [HEAVENS \(2009\)](#) and [TROTТА \(2008\)](#).

### B.1 Parameter extraction

Statistics has become an essential tool for cosmologists. A minimum knowledge of some sophisticated statistical techniques is required in order to properly extract cosmological information from the current observables, allowing us to test deviations from the standard  $\Lambda$ CDM model, or to better determine the values of a specific set of parameters.

There are two different ways of dealing with statistics: the *frequentist* and the *Bayesian* approach. As the name suggests, the first one is based on the classical thought that probability can be seen as a frequency, that is, the number of times some event occurs over the total number of trials. That is, *for a frequentist, data are repeatable but the model is fixed*. For several reasons, the frequentist approach is not the most preferred in cosmology. In particular, we cannot conduct the same procedure for measuring a particular quantity (let's say,  $H_0$ ), since we only observe one realization of the universe. The predominant method in cosmology is the Bayesian approach, in which probability is seen as a *measurement of the degree of belief about a proposition*. With this notion, one can consider the probability of any event, without necessarily having to repeat many experiments. Thus, *for a Bayesian, what is repeatable is the model, while data are fixed*. Another consequence of this definition is that, unlike in the frequentist case, hypothesis can also be considered as events with a certain probability distribution. The prescription for dealing with states of belief is given by Bayes theorem, that we proceed to describe below.

### B.1.1 Bayes Theorem

The Bayes Theorem is a trivial consequence of the axioms of probability. Let us consider some propositions  $A$  and  $B$ . The probabilities that these propositions have a certain outcome, assuming some information  $I$  is true, are denoted by  $P(A|I)$  and  $P(B|I)$ . These probabilities can be discrete or continuous. The multiplication rule says that the joint probability of  $A$  and  $B$  equals the probability of  $B$ , times the conditional probability of  $A$  given that  $B$  has occurred (both conditional on  $I$ ), *i.e.*

$$P(A, B|I) = P(A|B, I)P(B|I). \quad (\text{B.1})$$

Since we have  $P(A, B|I) = P(B, A|I)$ , one easily arrives at the Bayes theorem

$$P(B|A, I) = \frac{P(A|B, I)P(B|I)}{P(A|I)}. \quad (\text{B.2})$$

What is less obvious is the way we interpret previous formula in order to extract parameter information. Let us suppose that  $I$  is a model  $\mathcal{M}$  we assume to be true (for example, the flat  $\Lambda$ CDM model with gravity described by General Relativity). We now replace  $B$  by some hypothesis  $\theta$  we want to test (here  $\theta = \{\theta_1, \dots, \theta_N\}$  can represent the set of  $N$  parameters of the underlying model  $\mathcal{M}$ ) and  $A$  by the observed data  $d$ . In this manner, we can rewrite the Bayes theorem in a more informative way

$$P(\theta|d, \mathcal{M}) = \frac{P(d|\theta, \mathcal{M})P(\theta|\mathcal{M})}{P(d|\mathcal{M})}. \quad (\text{B.3})$$

Here  $P(\theta|\mathcal{M})$  is the *prior*,  $P(\theta|d, \mathcal{M})$  is the *posterior*,  $P(d|\theta, \mathcal{M})$  is the *likelihood*, and  $P(d|\mathcal{M})$  is the *Bayesian evidence*. Let us describe each of these quantities:

- **The prior.** This represents our state of knowledge before observing the data. It is a key quantity in Bayesian inference, since we can update a posterior probability by using it as a prior on a new application of the Bayes theorem. For example, a prior of the Hubble parameter  $P(H_0|\Lambda\text{CDM})$  can be just a top-hat function on the interval  $[50, 100] \text{ km s}^{-1}\text{Mpc}^{-1}$ .
- **The posterior distribution.** This is what we aim to determine, it gives the probability of observing the parameters of the model, given some data. One is in general interested in the 1-dimensional posterior distribution for the  $i$ th parameter,  $P(\theta_i|d, \mathcal{M})$ . If the parameter space is  $N$ -dimensional, then  $P(\theta_i|d, \mathcal{M})$  is obtained by integrating the posterior over the remaining  $N - 1$  parameters (this is known as *marginalization*). For example, if our model aims to describe the data with only the parameters  $\Omega_M$  and  $H_0$ , we can get the marginal 1D posterior of  $H_0$  by

$$P(H_0|d, \mathcal{M}) = \int d\Omega_M P(\{H_0, \Omega_M\}|d, \mathcal{M}). \quad (\text{B.4})$$

Once the 1D distribution  $P(X|d, \mathcal{M})$  of a certain parameter  $X$  is determined, one can compute the corresponding moments, such as the mean

$$\mu = \bar{X} = \langle X \rangle = \int X P(X|d, \mathcal{M}) dX, \quad (\text{B.5})$$

or the variance (giving the width of the distribution)

$$\sigma^2 = \langle (X - \mu)^2 \rangle = \int (X - \mu)^2 P(X|d, \mathcal{M}) dX. \quad (\text{B.6})$$



For the uncertainty, it's customary to quote the 68.3 % confidence intervals  ${}_{-a}^{+b}$ . This can be obtained with the following prescription: 1) find the value that maximizes the posterior,  $X_{\max}$ , 2) go to smaller and larger values than  $X_{\max}$  until the 68.3 % of the total probability is enclosed, *i.e.* find  $a$  and  $b$  such that  $P(X = a|d, \mathcal{M}) = P(X = b|d, \mathcal{M})$  and

$$\int_a^b P(X|d, \mathcal{M})dX = 0.683 \int_{-\infty}^{\infty} P(X|d, \mathcal{M})dX. \quad (\text{B.7})$$

In a similar way, one can find the 95.4 % confidence intervals <sup>1</sup>.

- **The likelihood.** This represents the probability of observing the data, given the parameters of the model. For a fixed data and model, it is typically written as  $\mathcal{L}(\theta) = P(d|\theta, \mathcal{M})$ , so it describes a surface over the parameter space. One can find the most likely model (or best-fit), by maximizing  $\mathcal{L}(\theta)$ . For normally distributed data consisting in  $\mathcal{N}$  data points  $d_i$  (for example, the distance luminosity curves to several SNIa), and a model  $y_i(\theta)$  for these data, the likelihood is expressed as a multivariate gaussian <sup>2</sup>

$$\mathcal{L}(\theta) = \frac{1}{(2\pi)^{\mathcal{N}/2}(\det[C_{ij}])^{1/2}} e^{-\chi^2/2} \quad (\text{B.8})$$

where  $\chi^2$  is the the chi-squared statistics, given by

$$\chi^2 = \sum_{i,j=1}^{\mathcal{N}} (d_i - y_i(\theta))C_{ij}^{-1}(d_j - y_j(\theta)), \quad (\text{B.9})$$

and  $C_{ij} \equiv \langle (d_i - y_i(\theta))(d_j - y_j(\theta)) \rangle$  is the covariance matrix. The variances are given by the diagonal elements of the correlation matrix,  $\sigma_i^2 = C_{ii}$ . The ubiquity of gaussian likelihoods is motivated by the central limit theorem. This theorem tells us that the joint distribution of a collection of data points (independent and identically distributed, but not necessarily in a gaussian way), approaches that of a gaussian as the sample size increases. For gaussian likelihoods, we see that maximizing the likelihood is equivalent to minimizing the  $\chi^2$ .

In many cases, the distribution of  $\chi^2$  around its minimum follows a  $\chi^2$  distribution with  $n = \mathcal{N} - N$  degrees of freedom, where  $\mathcal{N}$  is the number of independent data points and  $N$  is the number of parameters. The  $\chi^2$  distribution is formally defined as the distribution for the sum of the squares of gaussian variables,  $Y = X_1^2 + X_2^2 + \dots + X_n^2$  (where  $X_i$  are gaussian variables with zero mean and variance of one), and is given by

$$P(Y) = \frac{1}{2^{n/2}\Gamma(n/2)} Y^{n/2-1} e^{-Y/2} \quad (\text{B.10})$$

This distribution has a mean given by  $n$  and a variance of  $2n$ . An alternative way to derive confidence intervals by looking at regions of the  $N$ -dimensional parameter space with constant  $\chi^2$  around the minimum (best-fit)  $\chi_{\min}^2$ . This is

<sup>1</sup>The 68.3 % and 95.4 % confidence interval are often referred as the 1- $\sigma$  and 2- $\sigma$  values, because the nomenclature agrees for gaussian distributions. However, this is an abuse of notation, since in most cases the posterior distribution do not have a gaussian shape.

<sup>2</sup>It's important to note that the likelihood is gaussian in the data, but in general it is not gaussian in the parameters, due to the non-linear relations between the observable and the parameters.

p	1	2	3
68.3%	1.00	2.30	3.53
95.4%	2.71	4.61	6.25
99.73%	9.00	11.8	14.2

**Table B.1** –  $\Delta\chi^2$  values for the conventionals 1, 2 and 3- $\sigma$  as a function of the number of parameters in the joint distribution.

a common approach in frequentist analysis, since one doesn't need to integrate probabilities over prior regions in order to get confidence limits. Using the properties of the  $\chi^2$  distribution, one can find the intervals of  $\Delta\chi^2 = \chi^2 - \chi_{\min}^2$  enclosing regions of 68.3 %, 95.4 % and 99.5% probability, as a function of the number of parameters in the joint distribution. Some of these  $\Delta\chi^2$  values are shown in Tab. (B.1).

Apart from finding the best-fit parameter values (as well as the confidence limits), one might wonder whether the model, evaluated at the best-fit, provides a good fit to the data. A simple rule of thumb to estimate the *goodness-of-fit* is to compute the  $\chi^2$  statistics and compare its minimum value to the number of degrees of freedom  $n$ . If the model provides a good fit to the data, we expect the data to scatter symmetrically around the model by 1- $\sigma$  (on average), which is translated into the requirement  $\chi_{\min}^2 \simeq n = N_{\text{dof}}$ .

- **The Bayesian evidence.** This plays the role of a normalization constant, that can be computed by means of an integral over the parameter space

$$P(d|\mathcal{M}) = \int d^N\theta P(d|\theta, \mathcal{M})P(\theta|\mathcal{M}). \quad (\text{B.11})$$

This quantity is important in model selection, and we shall discuss it in more detail later

Thus, given some data sets (whose likelihood is for example gaussianly distributed) and some choice of priors, we can obtain the 1D posterior distributions of the parameters in which we are interested, by means of the previous formulas. Unfortunately, when the parameter space is big, these analytical recipes are very time consuming. For example, let us suppose we take a model with  $N = 10$  parameters, a typical amount in cosmology. In order to compute the integrals appearing in Eq. (B.4) and Eq. (B.11), we decide to grid each parameter in  $M = 20$  discrete points. In this case, one is forced to carry out  $M^N = 20^{10}$  likelihood evaluations, a huge number that makes the data analysis completely unachievable. In order to overcome these complications, one typically resort to Monte Carlo methods.

## B.2 Monte Carlo Markov chains

Monte Carlo Markov chains (MCMC) are a class of algorithms which allow to *sample* the posterior distribution in an extremely efficient way. Instead of going exponentially with the number of parameters, the MCMC calculation goes linearly with  $N$ . The name "Monte Carlo" indicates that they are based on the generation of random numbers, while the name "Markov process" indicates that we consider processes (or chains) in which the future state depends only on the present state,

and not on the past ones.

The main idea is to explore the parameter space in some intelligent manner, that is, to cover only the regions which are close enough to the best-fit values. For doing so, the MCMC starts from some initial point  $\theta^{(t)}$  in the  $N$ -dimensional parameter space, and evaluates its likelihood,  $\mathcal{L}(\theta^{(t)})$ . Then a new point  $\theta^{(\text{new})}$  is proposed in a random way (but using a specific probability distribution), and the likelihood is computed again. Depending on the value of  $\mathcal{L}(\theta^{(\text{new})})$ , a specific algorithm must decide whether this new point should be accepted or rejected.

### B.2.1 Metropolis-Hastings algorithm

A commonly used MCMC algorithm is the **Metropolis-Hastings** (MH) algorithm, defined by the following iterative steps:

- We propose a random point in the parameter space around the last point in a chain, drawn from a proposal probability distribution  $Q(\theta^{(\text{new})}|\theta^{(t)})$ .
- We compute the likelihood at this point,  $\mathcal{L}(\theta^{(\text{new})})$ , and the ratio  $r = \mathcal{L}(\theta^{(\text{new})})/\mathcal{L}(\theta^{(t)})$ .
- If  $r \geq 1$ , we accept and move to the new point in the chain,  $\theta^{(t+1)} = \theta^{(\text{new})}$ . Otherwise, we select a random number  $\alpha$  from a uniform probability distribution  $U[0, 1]$ :
  - If  $\alpha \geq r$ , we reject the new point and stay where we were:  $\theta^{(t+1)} = \theta^{(t)}$ .
  - If  $\alpha < r$ , we accept and move to the new point,  $\theta^{(t+1)} = \theta^{(\text{new})}$ .

Therefore, the MH algorithm does not accept new points only when the likelihood is higher, in which case it would reach a maximum too rapidly. The algorithm also accepts points with smaller likelihood, at a smaller rate, so that it can explore the parameter space and trace the underlying posterior distribution. To be more precise, we end generating the weights of each point in the parameter space, i.e., the number of times we waited and did not move. If the number of steps  $N_{\text{steps}}$  performed in the chain is big enough (the order of  $10^4 - 10^6$ ), then *these weights are proportional to the posterior distribution that we are looking for*. Obtaining marginal 1D distribution of some parameter  $\theta_i$  is also very easy, we simply have to plot the histogram with the values of  $\theta_i$  versus the corresponding weights. From these histograms, quantities such as the mean, best-fit and  $1-\sigma$  values (the first two do not necessarily agree for asymmetrical distributions) are straightforward to compute. Notice that the MH algorithm does not provide information about the bayesian evidence in Eq. (B.11).

The idea of the algorithm is pretty simple, but there are questions that remain. What is the best starting point for the chain? And which is a good choice for the proposal distribution? A good strategy is the following: for the starting point, use an estimate of the best-fit value, and for a proposal distribution, use a multi-variate gaussian (centered in the current point), with an estimate of the covariance matrix<sup>3</sup>. These estimates can be pre-computed with a short initial run. Using good initial values and a good proposal distribution is important in order to make sure the

<sup>3</sup>Typically the covariance matrix is scaled up by a certain factor, whose optimal value has been shown to be approximately 2.4.

chain converges in a reasonable amount of time. A sign that the chain is efficient is that the acceptance ratio is  $\sim 0.3$ , that is to say, that new points  $\theta^{(\text{new})}$  are accepted about 1/3 of the times. To speed up the MCMC analysis, it is also common to decompose the covariance matrix into *fast* and *slow* parameters, using the so-called Cholesky decomposition (LEWIS 2013). This allows to handle separately the part of the likelihood associated with nuisance parameters, that do not require to re-run the full Boltzmann code.

Another way of decreasing the runtime is to initialize several different chains and then analyze them together. Since the Markov chains often take same time to converge, normally the first  $\sim 1000$  steps of each chain need to be discarded, this is the so called *burn-in* stage. Finally, it is necessary to use some convergence diagnostic to determine if the chains have converged. One of the most used is the *Gelman-Rubin criterium*. It is based on the calculation of a ratio  $R$  (for a given parameter of the model), which compares the variance of means within each chain with the mean of variances among different chains. In practice, one calculates first the mean  $\bar{x}_i$  and the variance  $\sigma_i^2$  from each chain  $i = 1, \dots, n_c$ , as well as the total mean from all chains,  $\bar{x} = \sum_i \bar{x}_i / (n_c - 1)$ . Afterwards, one calculates the variance of the chain means  $\sigma^2(\bar{x}) = \sum_i (\bar{x}_i^2 - \bar{x}^2) / (n_c - 1)$  and the mean of the chain variances  $\bar{\sigma} = \sum_i \sigma_i / (n_c - 1)$ . The ratio  $R \equiv \sigma(\bar{x}) / \bar{\sigma}$  should be close to one if the chains are converged. The threshold for convergence is a matter of taste, but a common criterion to stop the chains is when we have  $R - 1 < 0.01$  for all the parameters of the model.

### B.3 Model selection

We introduced previously the  $\chi^2$  test to quantify the goodness-of-the-fit. However, this method is not adequate to compare the goodness-of-the-fit among different models, since it does not include Occam's razor factors to penalize models with a larger number of free parameters. A tool that is widely used to perform model comparison in the Bayesian framework is the Bayes factor.

Until now we have considered that all probabilities were conditional on some model  $\mathcal{M}$ , that we assume to be true. However, the Bayesian framework also allows to do comparison between models. For example, given CMB data, is there preference for dark energy as a cosmological constant ( $\Lambda$ CDM) or as fluid with a generic equation of state ( $w$ CDM)? For that purpose, let us apply Bayes theorem again, but on a model level

$$P(\mathcal{M}|d) = \frac{P(d|\mathcal{M})P(\mathcal{M})}{P(d)}. \quad (\text{B.12})$$

Here  $P(\mathcal{M})$  is the model prior (irrespective on the data), while  $P(d)$  is the data prior (irrespective of the model). Let us suppose we have two different models  $\mathcal{M}_0$  and  $\mathcal{M}_1$  that we wish to compare. In that case, we can take the ratio between the posteriors on the models, which according to eq. (B.12) gives

$$\frac{P(\mathcal{M}_0|d)}{P(\mathcal{M}_1|d)} = \frac{P(d|\mathcal{M}_0)P(\mathcal{M}_0)}{P(d|\mathcal{M}_1)P(\mathcal{M}_1)} \equiv B_{01} \frac{P(\mathcal{M}_0)}{P(\mathcal{M}_1)}, \quad (\text{B.13})$$

$ \ln B_{01} $	Odds	Probability	Strength of evidence
$< 1.0$	$\lesssim 3 : 1$	$< 0.750$	Inconclusive
$1.0$	$\sim 3 : 1$	$0.750$	Weak evidence
$2.5$	$\sim 12 : 1$	$0.923$	Moderate evidence
$5.0$	$\sim 150 : 1$	$0.993$	Strong evidence

**Table B.2** – Empirical Jeffreys’ scale for evaluating the strength of evidence when comparing two models  $\mathcal{M}_0$  and  $\mathcal{M}_1$ . The probability column refers to the posterior probability of the favored model assuming  $P(\mathcal{M}_0) = P(\mathcal{M}_1)$  and that the two models cover entirely the model space  $P(\mathcal{M}_0|d) + P(\mathcal{M}_1|d) = 1$ .

where  $B_{01}$  is the *Bayes factor*, given by the ratio of the Bayesian evidences in each model,

$$B_{01} \equiv \frac{P(d|\mathcal{M}_0)}{P(d|\mathcal{M}_1)}. \quad (\text{B.14})$$

Given the observed data  $d$ , and assuming the same prior probability for both models  $P(\mathcal{M}_0) = P(\mathcal{M}_1)$ , a value of the Bayes factor that is bigger (smaller) than 1, increases (decreases) the support in favor of model  $\mathcal{M}_1$  with respect to model  $\mathcal{M}_2$ . Bayes factor are usually interpreted against the empirical “Jeffreys’ scale” for the strength of evidence (JEFFREYS 1961), that we report in Tab. (B.2).

From the definition of Bayes factor, it’s clear that we need to integrate the likelihood over the prior volume for each model. In general, this is something not easy to achieve with MCMC, so one needs to use Nested sampling algorithms such as **MultiNest** (FEROZ et al. 2009). For brevity we don’t describe this algorithm in details, but the main idea is the following: one samples from the prior volume, and gradually concentrates more points near the maximum of the likelihood, by repeatedly replacing the point with the lowest target density by one drawn from the prior volume with higher target density. Nested sampling methods are also more adequate for handling complicated multi-modal posteriors, for which the MH algorithm could easily get stuck in local minima.

Bayes factors correctly account for the increased complexity of a model, but they are very sensitive to the choice of priors, which can be problematic when a parameter is not well constrained. There are frequentist tools for model comparison that do not suffer from this problem, such as the Akaike Information Criterium (AIC) that we introduced in Chapter 2. In this work, we have made use of the **MontePython-v3** code (AUDREN et al. 2013; BRINCKMANN et al. 2019a), which incorporates both the **Metropolis-Hastings** and the **MultiNest** algorithms.



# C

## Complements on Early Dark Energy

In this appendix we provide some complements on [Chapter 2](#), concerning the  $\chi^2$  information and the details about our  $N$ -body simulations.

### C.1 $\chi^2$ Tables

We report all  $\chi^2_{\min}$ 's obtained with the MINUIT algorithm ([JAMES et al. 1975](#)) through the `iMinuit` python package for the various model and data-set combination considered in this work.

$\Lambda$ CDM cosmology									
Planck18 high- $\ell$ TT,TE,EE	2347.86	2351.81	2347.02	2349.78	–	2351.53	2349.68	2351.24	2352.88
Planck18 low- $\ell$ EE	396.03	395.8	399.60	395.71	–	395.78	396.94	395.88	397.21
Planck18 low- $\ell$ TT	23.18	22.25	22.74	22.62	–	22.99	22.83	22.34	22.09
Planck18 lensing	–	–	8.65	9.56	–	9.49	9.05	9.93	10.05
PANTHEON	–	–	1026.83	1026.82	–	1026.84	1026.69	1026.72	1026.67
BAO FS BOSS DR12	–	–	6.25	6.11	–	6.23	5.88	5.86	6.18
BAO BOSS low- $z$	–	–	1.38	1.39	–	1.34	1.82	1.65	2.22
SHOES	–	16.57	–	18.57	–	–	16.05	–	14.23
KIDS/VIKING	–	–	–	–	177.9	182.62	182.21	–	–
COSEBI	–	–	–	–	–	–	–	8.30	6.44
total	2767.07	2786.43	3812.47	3830.57	177.9	3996.82	4011.16	3821.93	3837.98

**Table C.1** – Best-fit  $\chi^2$  per experiment (and total) in the  $\Lambda$ CDM model.

3-parameter EDE cosmology				
Planck18 high- $\ell$ TT,TE,EE	2343.07	2350.24	2349.30	2347.73
Planck18 low- $\ell$ EE	397.47	396.20	398.19	395.88
Planck18 low- $\ell$ TT	21.54	20.80	20.56	21.09
Planck18 lensing	–	–	10.12	9.85
PANTHEON	–	–	1026.72	1026.68
BAO BOSS DR12	–	–	3.46	–
BAO BOSS low- $z$	–	–	2.06	1.81
BAO/FS BOSS DR12	–	–	–	6.73
SHOES	–	0.47	1.38	2.13
total	2762.08	2767.72	2786.43	3811.89

**Table C.2** – Best-fit  $\chi^2$  per experiment (and total) in the 3-parameter EDE model.



1-parameter EDE cosmology									
Planck18 high- $\ell$ TT,TE,EE	2345.02	2347.63	2344.98	2347.42	–	2345.16	2349.15	2350.22	2349.82
Planck18 low- $\ell$ EE	395.80	395.97	395.82	395.90	–	396.33	395.88	396.10	395.79
Planck18 low- $\ell$ TT	21.49	20.82	21.89	20.85	–	22.38	20.97	21.54	20.84
Planck18 lensing	–	–	9.39	10.00	–	9.07	10.04	10.22	10.91
PANTHEON	–	–	1026.80	1026.69	–	1026.84	1026.7	1026.69	1026.80
BAO FS BOSS DR12	–	–	6.44	7.18	–	6.43	7.08	6.47	7.70
BAO BOSS low- $z$	–	–	1.41	2.33	–	1.33	2.33	2.38	2.83
SHOES	–	1.07	–	1.64	–	–	1.62	–	2.43
KiDS/VIKING	–	–	–	–	178.0	184.57	183.88	–	–
COSEBI	–	–	–	–	–	–	–	6.83	9.22
total	2762.31	2765.49	3806.74	3812.01	178.0	3992.11	3997.67	3820.46	3826.35

**Table C.3** – Best-fit  $\chi^2$  per experiment (and total) in the 1-parameter EDE model.

Model	$\Lambda$ CDM		EDE cosmology	
Planck18 high- $\ell$ TT,TE,EE	2339.92	2340.96	2335.71	2336.12
Planck18 low- $\ell$ EE	395.67	395.87	395.80	397.01
Planck18 low- $\ell$ TT	21.93	21.03	20.65	20.44
Planck18 lensing	8.47	8.35	9.82	9.36
PANTHEON	–	1026.88	–	1026.99
BAO FS BOSS DR12	–	8.04	–	9.02
BAO BOSS low- $z$	–	3.20	–	3.48
SHOES	–	10.67	–	1.91
COSEBI	–	1.2	–	4.07
total	2765.99	3816.23	2761.98	3808.40

**Table C.4** – Best-fit  $\chi^2$  per experiment (and total) in  $\Lambda$ CDM and the 1-parameter EDE model when marginalizing over the lensing information in Planck.

## C.2 A closer look to $N$ -body simulations

The main systematical uncertainties in numerical simulations come from their limited box size and resolution, as it has been thoroughly discussed in past literature (see, *e.g.* HEITMANN et al. (2010), RASERA et al. (2014), SCHNEIDER et al. (2016), and KLYPIN et al. (2019)). In order to minimize the missing large-scale modes, potentially affecting small-box simulations, and to overcome the impossibility of capturing the very non-linear scales in our large-box simulations, we adopted a splicing technique to bind together the matter power spectra extracted from simulations with different resolutions, for each redshift and model, as in MCDONALD (2003) and BORDE et al. (2014).

For both the  $\Lambda$ CDM model and the EDE best fit model from T. L. SMITH et al. (2020), we indeed performed: i) one Large Box (LB hereafter) simulation with  $N = 1024^3$  DM particles and box size  $L = 250 h^{-1}\text{Mpc}$ ; ii) one High Resolution (HR hereafter) simulation with  $N = 1024^3$  DM particles and box size  $L = 1000 h^{-1}\text{Mpc}$ ; iii) one Low Resolution (LR hereafter) simulation with the same box size of the HR one and the same resolution of the LB, namely  $N = 256^3$  and  $L = 250 h^{-1}\text{Mpc}$ , to be used as a transition simulation. The spliced non-linear matter power spectrum  $P(k)$  is given by (BORDE et al. 2014)

$$P(k) = \begin{cases} P_{\text{LB}}(k) \cdot \frac{P_{\text{HR}}(k_{\text{MIN}}^{250})}{P_{\text{LR}}(k_{\text{MIN}}^{250})}, & \text{if } k \leq k_{\text{MIN}}^{250} \\ P_{\text{LB}}(k) \cdot \frac{P_{\text{HR}}(k)}{P_{\text{LR}}(k)}, & \text{if } k_{\text{MIN}}^{250} < k < \frac{1}{2} k_{\text{Nyq}}^{\text{LB}} \\ P_{\text{HR}}(k) \cdot \frac{P_{\text{LB}}(0.5 \cdot k_{\text{Nyq}}^{\text{LB}})}{P_{\text{LR}}(0.5 \cdot k_{\text{Nyq}}^{\text{LB}})}, & \text{if } k \geq 0.5 \cdot k_{\text{Nyq}}^{\text{LB}} \end{cases} \quad (\text{C.1})$$

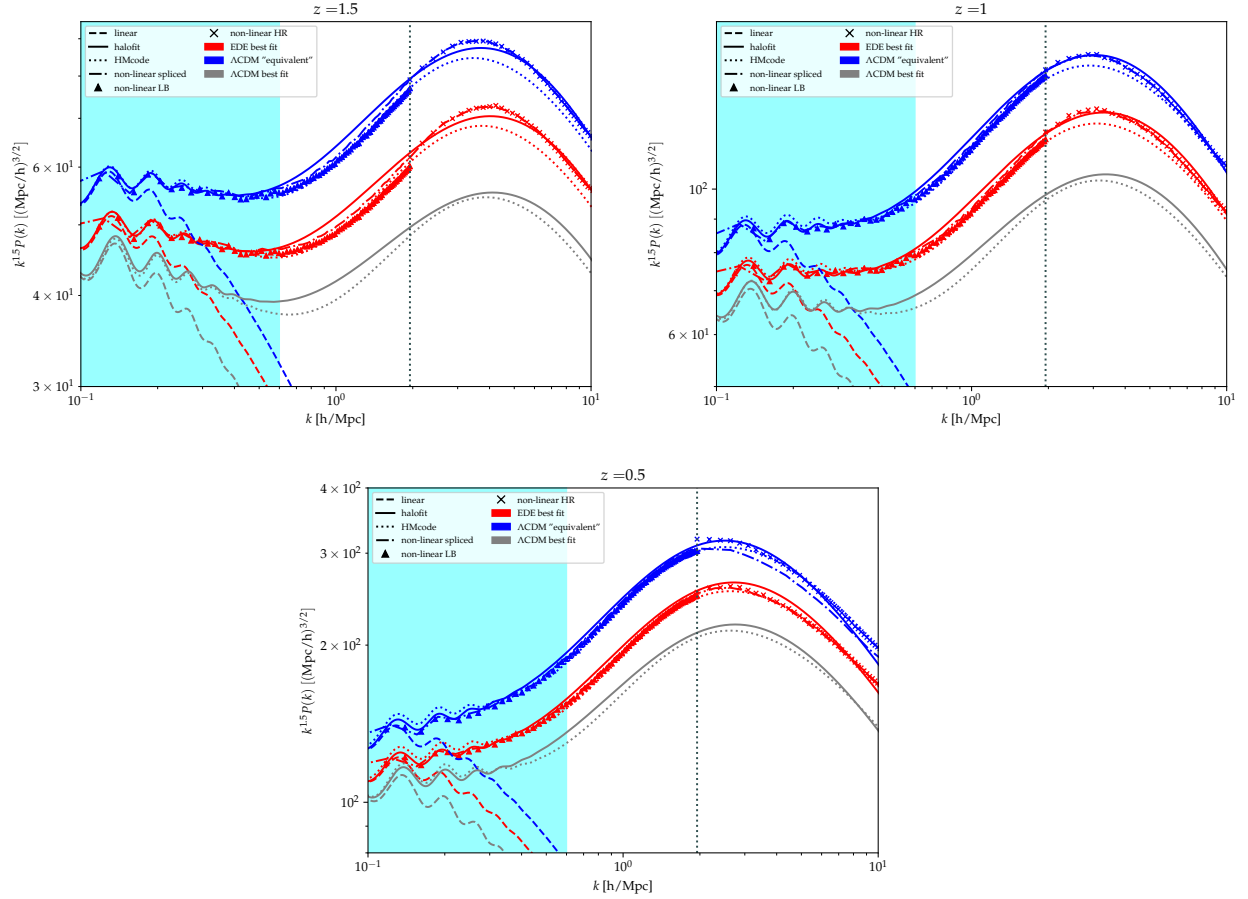


**Figure C.1** – Here we compare the matter power spectra extracted from our simulations, with the ones computed with **HALOFIT** /**HMCODE**, in three different redshift bins from  $z = 1.5$  to  $z = 0.5$ . The blue curves refer to the  $\Lambda$ CDM scenario, whereas the red ones refer to the EDE best fit model. As a reference, we also report the best fit  $\Lambda$ CDM case from Planck 2018. The spliced power spectra are denoted by thick dot-dashed lines. Symbols stand for the output power spectra of the “non-spliced” LB and HR simulations. The solid/dotted lines are the non-linear power spectra from **HALOFIT** /**HMCODE**, while the dashed lines are the corresponding linear power spectra used to set the initial conditions for the simulations. The cyan shaded band approximately corresponds to the scales probed by DES-Y1.

where  $k_{\text{MIN}}^{250}$  is the minimum  $k$ -mode in our small-box simulations (HR and LR), while  $k_{\text{Nyq}}^{\text{LB}}$  is the Nyquist wave-number of the LB one.

Besides the aforementioned systematical uncertainties, numerical simulations are also affected by two primary sources of statistical errors: the cosmic variance, affecting the large-scale part of the spectra, and the shot noise due to the discreteness of the DM particles, thereby affecting the smallest scales.

Concerning the shot noise term, its contribution to the power spectrum is simply given by  $P_{\text{SN}} = (L/N)^3$ . It is straightforward to see that it is largely subdominant at the scales and redshifts considered in this work, from Fig. C.1, where we compare the matter power spectra extracted from our simulations with the ones computed with **HALOFIT** /**HMCODE**, in three different redshift bins from  $z = 1.5$  to  $z = 0.5$  – given that we have already discussed the  $z = 0$  case in Sect. 2.4.3. In Fig. C.2 we plot the

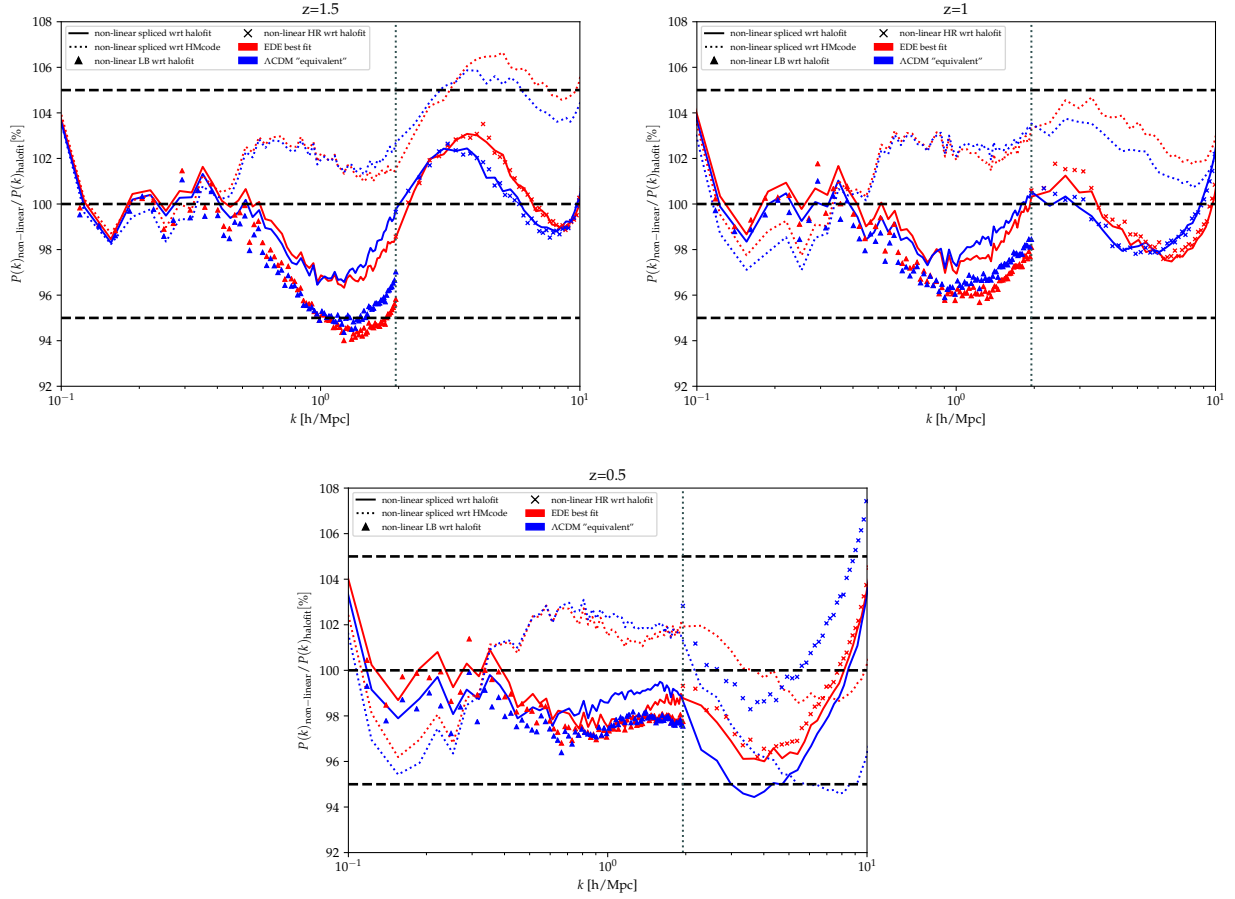


**Figure C.2** – Here we show the ratio between the non-linear matter power spectra from our simulations and the ones computed with **HALOFIT** /**HMCODE** , for both the  $\Lambda$ CDM equivalent and the EDE best-fit models. We have adopted the same linestyle-code and color-code of Fig. C.1.

ratio between the power spectrum predicted by **HALOFIT** /**HMCODE** and that extracted from the numerical simulation in order to explicitly demonstrate that the differences are below 5% level, for scales  $10^{-2} \lesssim k \lesssim 10$  h/Mpc, at redshifts  $0.5 \leq z \leq 2$ , for both  $\Lambda$ CDM and EDE models. This extends the  $z = 0$  result presented in the main text to cover the full redshift range from KIDS-VIKING.

It is also informative to compare the prediction from algorithms with  $N$ -body at larger scales than that depicted in Fig. C.1 and Fig. C.2. Indeed, these are affected by higher statistical noise, due to cosmic variance, as one might already guess from the lower- $k$  part of both figures. To beat down cosmic variance, one should run several statistical realizations of the same simulation, by producing initial conditions starting from different random seeds. To circumvent this issue and save computational time, we adopted the simple solution to run the two sets of simulations (EDE and  $\Lambda$ CDM) with identical random seeds for the realization of their initial conditions, and to present our results in terms of ratios in the matter power spectra between the EDE and the  $\Lambda$ CDM models, in Fig. C.3 and Fig. C.4. Any scatter related to the cosmic variance is now removed, allowing us to go down one order of magnitude in terms of wave-numbers  $k$ 's. We show in both figures by vertical dashed lines the scales corresponding to  $k_{\text{MIN}}^{250}$  and  $k_{\text{Nyq}}^{\text{LB}}/2$ . One can clearly see again that the EDE by itself

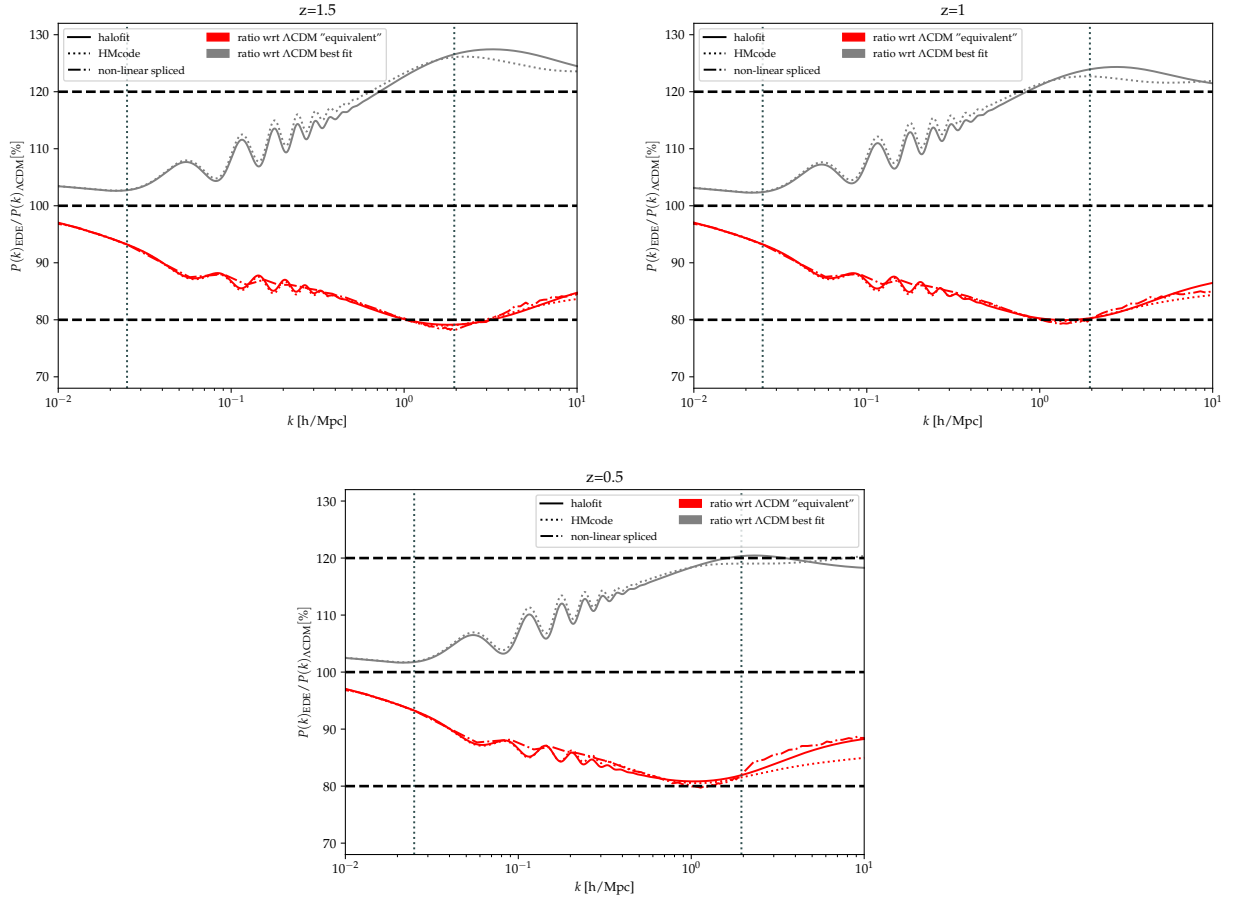


**Figure C.3** – Here we compare departures from the  $\Lambda$ CDM “equivalent” model in terms of ratios of non-linear matter power spectra. The EDE best-fit case is shown in red, while the gray lines refer to the  $\Lambda$ CDM best-fit model. Solid and dotted lines stand for the non-linear power spectra from **HALOFIT** and **HMCODE**, respectively. Dot-dashed lines refer to the outputs of our simulations. The cyan shaded band approximately corresponds to the scales probed by DES-Y1.

lead to a decrease in power. However, the increase in  $\omega_{\text{cdm}}$ , leads the EDE best-fit model to predict  $\mathcal{O}(20\%)$  increase in power, when compared to the best-fit  $\Lambda$ CDM model. Note how the differences become even more manifest at higher redshift. This illustrates that high- $z$  LSS measurements have the potential to put EDE under crucial tests (KLYPIN et al. 2021).

Another way of presenting our results is in terms of the accuracy at which **HALOFIT** /**HMCODE** can predict *deviations* in the non-linear power spectrum of EDE models with respect to the  $\Lambda$ CDM ‘equivalent’ case (as opposed to predicting the absolute power spectrum). This is what we show in Fig. C.4, where we now compare the ratio between the EDE and  $\Lambda$ CDM power spectra from **HALOFIT** /**HMCODE** against the same ratio extracted from simulations. The thick horizontal lines highlight  $\pm 5\%$  deviations. In light of all of this, we conclude that, in the EDE framework, **HALOFIT** /**HMCODE** predictions on  $\Lambda$ CDM departures are reliable at  $\leq 5\%$  level with respect to the outputs of  $N$ -Body simulations, for scales  $10^{-2} \lesssim k \lesssim 10 \text{ h/Mpc}$ , at redshifts  $0 \leq z \leq 2$ .

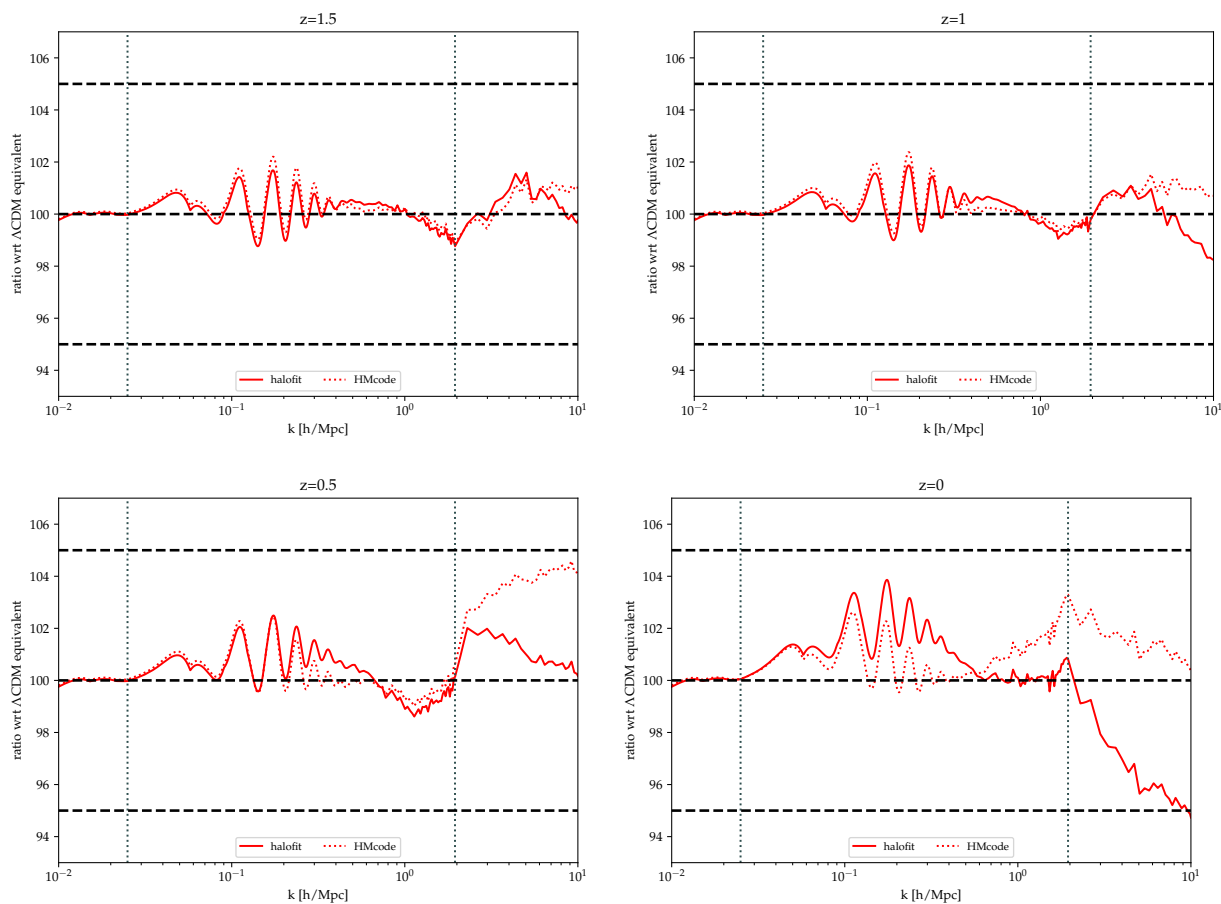


**Figure C.4** – Here we compare the outputs of our simulations with the **HALOFIT** /**HMcode** predictions, in terms of deviations in the ratios of the EDE best-fit power spectra over the  $\Lambda$ CDM “equivalent” ones, in four redshift bins from  $z = 2$  to  $z = 0$ . Solid and dotted lines stand for **HALOFIT** and **HMcode**, respectively.

# D

---

## Complements on decaying dark matter

---

In this appendix we detail some important calculations concerning the dynamics of decaying dark matter with warm decay products, that were too long to be included in the main text of [Chapter 3](#). We also describe our numerical implementation, and include some extra tables and plots.

### D.1 Boltzmann equation for decaying dark matter in the synchronous gauge

The goal is to derive the generic Boltzmann equation for decaying dark matter models with arbitrary decay mass products. We'll work with the synchronous gauge comoving with the mother particles, following [AOYAMA et al. \(2014\)](#). The metric is thus written as

$$ds^2 = a^2(\tau) \left[ -d\tau^2 + (\delta_{ij} + H_{ij}) dx^i dx^j \right], \quad (\text{D.1})$$

where  $H_{ij}$  reads in Fourier space

$$H_{ij} = \hat{k}_i \hat{k}_j h + \left( \hat{k}_i \hat{k}_j - \frac{\delta_{ij}}{3} \right) 6\eta. \quad (\text{D.2})$$

Let us denote the PSD distribution of the  $I$ -th dark component as  $f_I(k, q, \mu, \tau)$ , where  $I = \{\text{cdm}, \text{dr}, \text{wdm}\}$ . The starting point is the same as in [Eq. \(1.185\)](#)

$$\frac{\partial f_I}{\partial \tau} + \frac{\partial f_I}{\partial x^i} \frac{dx^i}{d\tau} + \frac{\partial f_I}{\partial q} \frac{dq}{d\tau} + \frac{\partial f_I}{\partial \hat{n}^i} \frac{d\hat{n}^i}{d\tau} = \left( \frac{\partial f_I}{\partial \tau} \right)_C = \frac{\mathcal{C}[f_I]}{P^0}. \quad (\text{D.3})$$

We focus first on the l.h.s. of previous equation. The last term at the l.h.s. can be neglected as usual because it's second order in perturbations. For the second term, we note that

$$\frac{dx^i}{d\tau} = \frac{dx^i}{d\sigma} \frac{d\sigma}{d\tau} = \frac{P^i}{P^0}. \quad (\text{D.4})$$

Let us obtain  $P^0$  and  $P^i$ <sup>1</sup>. To get  $P^0$ , we simply use the closure relation  $g_{\mu\nu}P^\mu P^\nu = g_{00}(P^0)^2 + p^2 = -m^2$  and the fact that  $g_{00} = -a^2(\tau)$ . To get  $P^i$ , we write  $P^i = C\hat{n}^i$  (where  $\hat{n}^i$  is some unit vector), and obtain the constant  $C$  from the definition of  $p$

$$p^2 = g_{ij}P^iP^j = a^2 \left[ 1 + H_{ij}\hat{n}^i\hat{n}^j \right] C^2 \quad \longrightarrow \quad C \simeq \frac{p}{a} \left[ 1 - \frac{1}{2}H_{ij}\hat{n}^i\hat{n}^j \right]. \quad (\text{D.5})$$

Therefore, the elements of the 4-momentum in synchronous gauge are

$$P^0 = \frac{\mathcal{E}}{a^2}, \quad P^i = \frac{q\hat{n}^j}{a^2} \left[ \delta_{ij} - \frac{1}{2}H_{ij} \right], \quad (\text{D.6})$$

so that

$$\frac{dx^i}{d\tau} = \frac{q\hat{n}^j}{\mathcal{E}} \left[ \delta_{ij} - \frac{1}{2}H_{ij} \right]. \quad (\text{D.7})$$

### D.1.1 Geodesic equation

For the factor  $\frac{dq}{d\tau}$  in Eq. (D.3), we need to use the 0 component of the geodesic equation:

$$P^0 \frac{dP^0}{d\tau} = -\Gamma^0_{\alpha\beta} P^\alpha P^\beta. \quad (\text{D.8})$$

The calculation is similar to the one we did in App. A.3, except that now we're working in a different gauge. Firstly, we need to know  $\Gamma^0_{00}, \Gamma^0_{i0}$  and  $\Gamma^0_{ij}$ . Using the definition of the Christoffel symbols given in Eq. (A.10), we get

$\Gamma^0_{00}$  :

$$\Gamma^0_{00} = \frac{g^{0\lambda}}{2} (2\partial_0 g_{\lambda 0} - \partial_\lambda g_{00}) = \frac{g^{00}}{2} \partial_0 g_{00} = \mathcal{H}. \quad (\text{D.9})$$

$\Gamma^0_{i0}$  :

$$\Gamma^0_{i0} = \frac{g^{0\lambda}}{2} (\partial_0 g_{\lambda i} + \partial_i g_{\lambda 0} - \partial_\lambda g_{i0}) = \frac{g^{00}}{2} \partial_i g_{00} = 0. \quad (\text{D.10})$$

$\Gamma^0_{ij}$  :

$$\Gamma^0_{ij} = \frac{g^{0\lambda}}{2} (\partial_i g_{\lambda j} + \partial_j g_{\lambda i} - \partial_\lambda g_{ij}) = -\frac{g^{00}}{2} \partial_0 g_{ij} = \frac{1}{2} H'_{ij} + \mathcal{H}(\delta_{ij} + H_{ij}). \quad (\text{D.11})$$

Now, we want to express the l.h.s. of Eq. (D.8) in terms of  $q$ . This can be straightforwardly achieved by differentiating the relation  $a^4(P^0)^2 = q^2 + a^2m^2$ . After a little bit of algebra, this yields

$$P^0 \frac{dP^0}{d\tau} = -\frac{2}{a^4} \mathcal{H} q^2 - \frac{m^2}{a^2} \mathcal{H} + \frac{q}{a^4} \frac{dq}{d\tau}. \quad (\text{D.12})$$

Using the expression for the Christoffels that we computed in Eq. (D.9)-Eq. (D.11), we can compute the r.h.s. of Eq. (D.8)

<sup>1</sup>We omit the label  $I$  in  $P^0$  and  $P^i$  to shorten notation.



$$\begin{aligned}
 -\Gamma^0_{\alpha\beta} P^\alpha P^\beta &= -\Gamma^0_{00} (P^0)^2 - \Gamma^0_{ij} P^i P^j \\
 &= -\frac{\mathcal{H}}{a^4} (q^2 + m^2 a^2) - \left[ \frac{H'_{ij}}{2} + \mathcal{H}(\delta_{ij} + H_{ij}) \right] \frac{q^k}{a^2} \left[ \delta_{ik} - \frac{H_{ik}}{2} \right] \frac{q^l}{a^2} \left[ \delta_{jl} - \frac{H_{jl}}{2} \right] \\
 &= -\frac{\mathcal{H}}{a^4} (q^2 + m^2 a^2) - \frac{1}{a^4} \left[ \frac{H'_{ij}}{2} + \mathcal{H}(\delta_{ij} + H_{ij}) \right] \left[ q^i q^j - \frac{q^j q^k}{2} H_{ik} - \frac{q^i q^l}{2} H_{jl} \right] \\
 &= -\frac{2\mathcal{H}}{a^4} q^2 - \frac{\mathcal{H}}{a^4} m^2 a^2 - \frac{1}{2a^4} H'_{ij} q^i q^j. \tag{D.13}
 \end{aligned}$$

Equating Eq. (D.12) with Eq. (D.13), as demanded by the geodesic equation, some terms cancel out and we are left with

$$\begin{aligned}
 \frac{1}{q} \frac{dq}{d\tau} &= -\frac{1}{2} H'_{ij} \hat{n}^i \hat{n}^j \\
 &= -\frac{1}{2} \left[ \hat{k}_i \hat{k}_j h' + \left( \hat{k}_i \hat{k}_j - \frac{\delta_{ij}}{3} \right) 6\eta' \right] \hat{n}^i \hat{n}^j \\
 &= \eta' - \frac{h' + 6\eta'}{2} \mu^2. \tag{D.14}
 \end{aligned}$$

In summary, we write the Boltzmann equation in Fourier space as

$$\frac{\partial f_I}{\partial \tau} + i\mu \frac{kq}{\mathcal{E}_I} f_I + \frac{df_I}{d \ln q} \left( \eta' - \frac{h' + 6\eta'}{2} \mu^2 \right) = \left( \frac{\partial f_I}{\partial \tau} \right)_C, \tag{D.15}$$

where it is understood that the second term at the l.h.s is first order.

### D.1.2 Collision integrals

Let us now move to describe the collision term for the decay process

$$\text{DCDM} (Q_1) \longrightarrow \text{WDM} (Q_2) + \text{DR} (Q_3), \tag{D.16}$$

where we labelled already the comoving four-momentum of each species,  $Q_I = (\mathcal{E}_I, \vec{q}_I)$ . Notice that  $\mathcal{E}_1 = am_{\text{dcdm}}$  and  $\mathcal{E}_3 = q_3$ . Neglecting quantum statistics and inverse decays, the collision integrals for the mother and daughter particles can be written as

$$\left( \frac{\partial f_{\text{dcdm}}}{\partial \tau} \right)_C = -\frac{a^2}{2\mathcal{E}_1} \int \frac{d^3 \vec{q}_3}{(2\pi)^3 2\mathcal{E}_3} \frac{d^3 \vec{q}_2}{(2\pi)^3 2\mathcal{E}_2} |\mathcal{M}|^2 (2\pi)^4 \delta^{(4)}(Q_1 - Q_2 - Q_3) f_{\text{dcdm}}(q_1), \tag{D.17}$$

$$\left( \frac{\partial f_{\text{wdm}}}{\partial \tau} \right)_C = +\frac{a^2}{2\mathcal{E}_2} \int \frac{d^3 \vec{q}_1}{(2\pi)^3 2\mathcal{E}_1} \frac{d^3 \vec{q}_3}{(2\pi)^3 2\mathcal{E}_3} |\mathcal{M}|^2 (2\pi)^4 \delta^{(4)}(Q_1 - Q_2 - Q_3) f_{\text{dcdm}}(q_1), \tag{D.18}$$

$$\left( \frac{\partial f_{\text{dr}}}{\partial \tau} \right)_C = +\frac{a^2}{2\mathcal{E}_3} \int \frac{d^3 \vec{q}_1}{(2\pi)^3 2\mathcal{E}_1} \frac{d^3 \vec{q}_2}{(2\pi)^3 2\mathcal{E}_2} |\mathcal{M}|^2 (2\pi)^4 \delta^{(4)}(Q_1 - Q_2 - Q_3) f_{\text{dcdm}}(q_1). \tag{D.19}$$

These integrals are performed over comoving three-momenta. As we already discussed in Sect. 3.2, because of our gauge choice and the assumption that mother particles are fully non-relativistic, we can take the following ansatz for the PSD of the DCDM species:

$$f_{\text{dcdm}}(k, q, \tau) = N_{\text{dcdm}}(k, \tau) \frac{\delta(q)}{4\pi q^2}, \tag{D.20}$$

with  $N_{\text{dcdm}}$  the comoving number density of the DCDM. This will allow to simplify the collision integrals written above. In the context of two-body decays to massive and massless particles, the invariant amplitude squared  $|\mathcal{M}|^2$  is simply related to the rest-frame decay width of the DCDM as  $|\mathcal{M}|^2 = 8\pi\Gamma m_{\text{dcdm}}/\varepsilon$ , with  $\varepsilon = 0.5(1 - m_{\text{wdm}}^2/m_{\text{dcdm}}^2)$  the fraction of DCDM rest mass energy converted into DR (BARNETT et al. 1996). In addition, we will be using two useful mathematical relations associated with the Dirac delta function:

$$\int \frac{d^3\vec{q}_I}{2\mathcal{E}_I} = \int d^4Q_I \delta(\mathcal{E}_I^2 - q_I^2 - a^2m_I^2)\Theta(\mathcal{E}_I), \quad (\text{D.21})$$

$$\delta(f(x)) = \sum_i \frac{\delta(x - x_0)}{|f'(x_0)|}, \quad \text{with } x_0 \text{ such that } f(x_0) = 0. \quad (\text{D.22})$$

Let us start with Eq. (D.17):

$$\begin{aligned} \left(\frac{\partial f_{\text{dcdm}}}{\partial\tau}\right)_{\text{C}} &= -\frac{a|\mathcal{M}|^2 f_{\text{dcdm}}(q_1)}{2m_{\text{dcdm}}(2\pi)^2} \int \frac{d^3\vec{q}_3}{2\mathcal{E}_3} \delta\left((\mathcal{E}_1 - \mathcal{E}_3)^2 - |\vec{q}_1 - \vec{q}_3|^2 - a^2m_{\text{wdm}}^2\right) \Theta(\mathcal{E}_1 - \mathcal{E}_3) \\ &= -a\Gamma f_{\text{dcdm}}(q_1) \frac{2}{\varepsilon} \int dq_3 q_3 \delta\left(2am_{\text{dcdm}}q_3 - a^2(m_{\text{dcdm}}^2 - m_{\text{wdm}}^2)\right) \Theta(am_{\text{dcdm}} - q_3) \\ &= -a\Gamma f_{\text{dcdm}}(q_1) \frac{2}{\varepsilon} \int dq_3 q_3 \frac{\delta(q_3 - \varepsilon am_{\text{dcdm}})}{2am_{\text{dcdm}}} \Theta(am_{\text{dcdm}} - q_3) \\ &= -a\Gamma f_{\text{dcdm}}(q_1). \end{aligned} \quad (\text{D.23})$$

We proceed in a similar fashion for Eq. (D.18):

$$\begin{aligned} \left(\frac{\partial f_{\text{wdm}}}{\partial\tau}\right)_{\text{C}} &= \frac{a^2|\mathcal{M}|^2}{2\mathcal{E}_2(2\pi)^2} \int \frac{d^3\vec{q}_1}{2\mathcal{E}_1} \delta\left((\mathcal{E}_1 - \mathcal{E}_2)^2 - |\vec{q}_1 - \vec{q}_2|^2\right) \Theta(\mathcal{E}_1 - \mathcal{E}_2) f_{\text{dcdm}}(q_1) \\ &= \frac{a^2\Gamma m_{\text{dcdm}}}{\mathcal{E}_2 2\pi\varepsilon} \int \frac{d^3\vec{q}_1}{\mathcal{E}_1} \delta\left(2\mathcal{E}_1\mathcal{E}_2 + 2\vec{q}_1 \cdot \vec{q}_2 - a^2(m_{\text{dcdm}}^2 + m_{\text{wdm}}^2)\right) \Theta(\mathcal{E}_1 - \mathcal{E}_2) f_{\text{dcdm}}(q_1) \\ &= \frac{a\Gamma N_{\text{dcdm}}}{\mathcal{E}_2 2\pi\varepsilon} \delta\left(2am_{\text{dcdm}}\sqrt{q_2^2 + a^2m_{\text{wdm}}^2} - a^2(m_{\text{dcdm}}^2 + m_{\text{wdm}}^2)\right) \\ &= \frac{a\Gamma N_{\text{dcdm}}}{\mathcal{E}_2 2\pi\varepsilon} \frac{\delta(q_2 - am_{\text{dcdm}}\varepsilon)\mathcal{E}_2}{2am_{\text{dcdm}}q_2} \\ &= \frac{a\Gamma N_{\text{dcdm}}}{4\pi q_2^2} \delta(q_2 - ap_{\text{max}}). \end{aligned} \quad (\text{D.24})$$

A similar procedure could be carried out for Eq. (D.19) and the result would be the same as in Eq. (D.24).

## D.2 Background continuity equation for the WDM species

We seek to obtain the background continuity equation for the WDM species, by integrating the corresponding Boltzmann equation over the phase space. The starting point is (c.f. Eq. (3.17))

$$\frac{\partial \bar{f}_{\text{wdm}}}{\partial\tau} = \frac{a\Gamma \bar{N}_{\text{dcdm}}(\tau)}{4\pi q^2} \delta(q - ap_{\text{max}}), \quad (\text{D.25})$$

with  $p_{\text{max}} = m_{\text{dcdm}}\varepsilon = m_{\text{wdm}}\varepsilon/\sqrt{1-2\varepsilon}$ . We integrate the previous equation over  $4\pi a^{-4} \int dq q^2 \mathcal{E}_2$ :

$$\frac{4\pi}{a^4} \int dq q^2 \mathcal{E}_2(q) \frac{\partial \bar{f}_{\text{wdm}}(q)}{\partial\tau} = \frac{\Gamma \bar{N}_{\text{dcdm}}(\tau)}{a^3} \int dq \mathcal{E}_2(q) \delta(q - ap_{\text{max}}). \quad (\text{D.26})$$

Let us focus first on the l.h.s. of the equation. To get an equation for  $\bar{\rho}_{\text{wdm}}$ , we have to move the time derivative out of the integral. This is easily achieved using that  $\mathcal{E}'_2 = \mathcal{E}_2 \mathcal{H} - \frac{q^2}{\mathcal{E}_2} \mathcal{H}$ . Hence:

$$\begin{aligned}
\frac{4\pi}{a^4} \int dq q^2 \mathcal{E}_2(q) \frac{\partial \bar{f}_{\text{wdm}}(q)}{\partial \tau} &= \frac{4\pi}{a^4} \frac{\partial}{\partial \tau} \left( \int dq q^2 \mathcal{E}_2 \bar{f}_{\text{wdm}} \right) - \frac{4\pi}{a^4} \int dq q^2 \bar{f}_{\text{wdm}} \mathcal{E}'_2 \\
&= \bar{\rho}'_{\text{wdm}} + 4\mathcal{H} \bar{\rho}_{\text{wdm}} - \mathcal{H} \left( \frac{4\pi}{a^4} \int dq q^2 \mathcal{E}_2 \bar{f}_{\text{wdm}} - \frac{4\pi}{a^4} \int dq q^2 \frac{q^2}{\mathcal{E}_2} \bar{f}_{\text{wdm}} \right) \\
&= \bar{\rho}'_{\text{wdm}} + 4\mathcal{H} \bar{\rho}_{\text{wdm}} - \mathcal{H} (\bar{\rho}_{\text{wdm}} - 3\bar{P}_{\text{wdm}}) \\
&= \bar{\rho}'_{\text{wdm}} + 4\mathcal{H} \bar{\rho}_{\text{wdm}} - \mathcal{H} \bar{\rho}_{\text{wdm}} (1 - 3w) \\
&= \bar{\rho}'_{\text{wdm}} + 3\mathcal{H} \bar{\rho}_{\text{wdm}} (1 + w).
\end{aligned} \tag{D.27}$$

We move now to compute the r.h.s. of Eq. (D.26). It's just a matter of applying the Dirac delta and simplify

$$\begin{aligned}
\frac{\Gamma \bar{N}_{\text{dcdm}}}{a^3} \int dq \mathcal{E}_2(q) \delta(q - ap_{\text{max}}) &= \frac{\Gamma \bar{N}_{\text{dcdm}}}{a^3} \sqrt{a^2 m_{\text{wdm}}^2 + a^2 p_{\text{max}}^2} \\
&= \frac{a \Gamma \bar{N}_{\text{dcdm}} m_{\text{dcdm}}}{a^3} \sqrt{1 - 2\varepsilon + \varepsilon^2} \\
&= a \Gamma \bar{\rho}_{\text{dcdm}} (1 - \varepsilon).
\end{aligned} \tag{D.28}$$

In summary, the continuity equation for the WDM reads:

$$\bar{\rho}'_{\text{wdm}} = -3(1 + w) \mathcal{H} \bar{\rho}_{\text{wdm}} + (1 - \varepsilon) a \Gamma \bar{\rho}_{\text{dcdm}}. \tag{D.29}$$

### D.3 Linear fluid equations for the WDM species

In this section we proceed to derive the fluid equations for the WDM daughter particles that we wrote in Eq. (3.41)-Eq. (3.44). We start considering the Boltzmann hierarchy for the WDM linear multipoles (c.f. Eq. (3.28)-Eq. (3.31)):

$$\frac{\partial (\Delta f_{\text{wdm},0})}{\partial \tau} = -\frac{qk}{\mathcal{E}_2} \Delta f_{\text{wdm},1} + q \frac{\partial \bar{f}_{\text{wdm}}}{\partial q} \frac{h'}{6} + \frac{a \Gamma \bar{N}_{\text{dcdm}}}{4\pi q^2} \delta(q - ap_{\text{max}}) \delta_{\text{dcdm}}, \tag{D.30}$$

$$\frac{\partial (\Delta f_{\text{wdm},1})}{\partial \tau} = \frac{qk}{3\mathcal{E}_2} [\Delta f_{\text{wdm},0} - 2\Delta f_{\text{wdm},2}], \tag{D.31}$$

$$\frac{\partial (\Delta f_{\text{wdm},2})}{\partial \tau} = \frac{qk}{5\mathcal{E}_2} [2\Delta f_{\text{wdm},1} - 3\Delta f_{\text{wdm},3}] - q \frac{\partial \bar{f}_{\text{wdm}}}{\partial q} \frac{(h' + 6\eta')}{15}, \tag{D.32}$$

$$\frac{\partial (\Delta f_{\text{wdm},\ell})}{\partial \tau} = \frac{qk}{(2\ell + 1)\mathcal{E}_2} [\ell \Delta f_{\text{wdm},\ell-1} - (\ell + 1) \Delta f_{\text{wdm},\ell+1}] \quad (\ell \geq 3). \tag{D.33}$$

The continuity and Euler equations are obtained by multiplying both sides of Eq. (D.30) and Eq. (D.31) by  $4\pi q^2 \mathcal{E}_2 a^{-4}$  and  $4\pi q^3 k a^{-4}$ , respectively, and integrating over  $q$ . We already did most of the job in App. A.6, when writing the conservation equations for massive neutrinos, so there is no need to repeat all the steps. However, we have to take into account three important differences. Firstly, these equations were written in the Newtonian gauge, and not the synchronous one. This simply amounts to replacing  $-3\phi'$  by  $h'/2$  in the continuity equation, and removing the  $\psi$  term in the Euler equation. Secondly, the background density has a more complicated evolution,  $\bar{\rho}'_{\text{wdm}}/\bar{\rho}_{\text{wdm}} \neq -3\mathcal{H}(1 + w)$ . And thirdly, there is an extra term associated to the decay at the l.h.s. of Eq. (D.30).

### D.3.1 Continuity equation

Having all of this in mind, after integrating  $4\pi q^2 \mathcal{E}_2 a^{-4} \times \text{Eq. (D.30)}$  over momenta and dividing by  $\bar{\rho}_{\text{wdm}}$ , we get:

$$\delta'_{\text{wdm}} = -\frac{\bar{\rho}'_{\text{wdm}}}{\bar{\rho}_{\text{wdm}}} \delta_{\text{wdm}} - 3\mathcal{H} \delta_{\text{wdm}} (1 + c_s^2) - (1 + w) \left( \theta_{\text{wdm}} + \frac{h'}{2} \right) + \frac{\Gamma \bar{N}_{\text{dcdm}} \delta_{\text{dcdm}}}{a^3 \bar{\rho}_{\text{wdm}}} \int dq \mathcal{E}_2 \delta(q - ap_{\text{max}}). \quad (\text{D.34})$$

For the last term, we apply the Dirac delta as in [Eq. \(D.28\)](#), to get

$$\frac{\Gamma \bar{N}_{\text{dcdm}} \delta_{\text{dcdm}}}{a^3 \bar{\rho}_{\text{wdm}}} \int dq \mathcal{E}_2 \delta(q - ap_{\text{max}}) = a \Gamma \frac{\bar{\rho}_{\text{dcdm}}}{\bar{\rho}_{\text{wdm}}} \delta_{\text{dcdm}} (1 - \varepsilon). \quad (\text{D.35})$$

Using  $\bar{\rho}'_{\text{wdm}}/\bar{\rho}_{\text{wdm}} = -3\mathcal{H}(1 + w) + (1 - \varepsilon)a\Gamma\bar{\rho}_{\text{dcdm}}/\bar{\rho}_{\text{wdm}}$  (by virtue of [Eq. \(D.29\)](#)), we arrive at the continuity equation

$$\delta'_{\text{wdm}} = -3\mathcal{H}(c_s^2 - w) \delta_{\text{wdm}} - (1 + w) \left( \theta_{\text{wdm}} + \frac{h'}{2} \right) + (1 - \varepsilon)a\Gamma \frac{\bar{\rho}_{\text{dcdm}}}{\bar{\rho}_{\text{wdm}}} (\delta_{\text{dcdm}} - \delta_{\text{wdm}}), \quad (\text{D.36})$$

where  $c_s^2 = \delta P_{\text{wdm}}/\delta \rho_{\text{wdm}}$ .

### D.3.2 Euler equation

In a similar way, we can integrate  $4\pi q^3 k a^{-4} \times \text{Eq. (D.31)}$  over momenta and divide by  $\bar{\rho}_{\text{wdm}}(1 + w)$ , to get:

$$\theta'_{\text{wdm}} = -\frac{\bar{\rho}'_{\text{wdm}}}{\bar{\rho}_{\text{wdm}}} \frac{(1 + c_g^2)}{(1 + w)} \theta_{\text{wdm}} - 4\mathcal{H} \theta_{\text{wdm}} + \frac{k^2 c_s^2 \delta_{\text{wdm}}}{(1 + w)} - k^2 \sigma_{\text{wdm}}, \quad (\text{D.37})$$

where  $c_g^2 = \bar{P}'_{\text{wdm}}/\bar{\rho}'_{\text{wdm}}$ . Using again that  $\bar{\rho}'_{\text{wdm}}/\bar{\rho}_{\text{wdm}} = -3\mathcal{H}(1 + w) + (1 - \varepsilon)a\Gamma\bar{\rho}_{\text{dcdm}}/\bar{\rho}_{\text{wdm}}$ , we arrive at the Euler equation

$$\theta'_{\text{wdm}} = -\mathcal{H}(1 - 3c_g^2) \theta_{\text{wdm}} + \frac{c_s^2}{1 + w} k^2 \delta_{\text{wdm}} - k^2 \sigma_{\text{wdm}} - (1 - \varepsilon)a\Gamma \frac{1 + c_g^2}{1 + w} \frac{\bar{\rho}_{\text{dcdm}}}{\bar{\rho}_{\text{wdm}}} \theta_{\text{wdm}}. \quad (\text{D.38})$$

### D.3.3 Adiabatic sound speed

We still need to compute the adiabatic sound speed  $c_g^2$ . As we mentioned in [Sect. 3.2.3](#), we can write  $c_g^2$  as

$$c_g^2 = w \frac{\bar{P}'_{\text{wdm}}}{\bar{P}_{\text{wdm}}} \left( \frac{\bar{\rho}'_{\text{wdm}}}{\bar{\rho}_{\text{wdm}}} \right)^{-1}. \quad (\text{D.39})$$

The factor  $(\bar{\rho}'_{\text{wdm}}/\bar{\rho}_{\text{wdm}})^{-1}$  is just given by the background continuity equation. To get  $\bar{P}'_{\text{wdm}}$ , we have to take the time derivative of the general expression for the background pressure:

$$\bar{P}_{\text{wdm}} = \frac{4\pi}{3a^4} \int_0^\infty dq \frac{q^4}{\mathcal{E}_2} \bar{f}_{\text{wdm}} \quad (\text{D.40})$$

Thus,

$$\begin{aligned} \bar{P}'_{\text{wdm}} &= -4\mathcal{H} \bar{P}_{\text{wdm}} - \frac{4\pi}{3a^4} \int_0^\infty dq \frac{q^4}{\mathcal{E}_2^2} \mathcal{E}'_2 \bar{f}_{\text{wdm}} + \frac{4\pi}{3a^4} \int_0^\infty dq \frac{q^4}{\mathcal{E}_2} \bar{f}'_{\text{wdm}} \\ &= -4\mathcal{H} \bar{P}_{\text{wdm}} - \mathcal{H} \bar{P}_{\text{wdm}} + \mathcal{H} \frac{4\pi}{3a^4} \int_0^\infty dq \frac{q^6}{\mathcal{E}_2^3} \bar{f}_{\text{wdm}} + \frac{4\pi}{3a^4} \int_0^\infty dq \frac{q^4}{\mathcal{E}_2} \bar{f}'_{\text{wdm}}, \end{aligned} \quad (\text{D.41})$$

where we used once more time that  $\mathcal{E}'_2 = \mathcal{E}_2 \mathcal{H} - \frac{q^2}{\mathcal{E}_2} \mathcal{H}$ . We see that  $\bar{P}'_{\text{wdm}}$  involves a new higher momenta integral of  $\bar{f}'_{\text{wdm}}$ , called the *pseudo-pressure*

$$\mathfrak{p}_{\text{wdm}} \equiv \frac{4\pi}{3a^4} \int_0^\infty dq \frac{q^6}{\mathcal{E}_2^3} \bar{f}'_{\text{wdm}}. \quad (\text{D.42})$$

For the last term in Eq. (D.41), we just have to insert the background Boltzmann equation Eq. (D.25) and again apply the Dirac delta:

$$\begin{aligned} \frac{4\pi}{3a^4} \int_0^\infty dq \frac{q^4}{\mathcal{E}_2} \bar{f}'_{\text{wdm}} &= \frac{\Gamma \bar{N}_{\text{dcdm}}}{3a^3} \int_0^\infty dq \frac{q^2}{\mathcal{E}_2} \delta(q - ap_{\text{max}}) \\ &= \frac{\Gamma \bar{N}_{\text{dcdm}}}{3a^3} \frac{a^2 p_{\text{max}}^2}{\sqrt{a^2 m_{\text{wdm}}^2 + a^2 p_{\text{max}}^2}} \\ &= \frac{\Gamma \bar{N}_{\text{dcdm}}}{3a^3} \frac{am_{\text{dcdm}} \varepsilon^2}{\sqrt{1 - 2\varepsilon + \varepsilon^2}} \\ &= \frac{a\Gamma \bar{\rho}_{\text{dcdm}}}{3} \frac{\varepsilon^2}{1 - \varepsilon}. \end{aligned} \quad (\text{D.43})$$

To summarize, the time derivative of the pressure is

$$\bar{P}'_{\text{wdm}} = \mathcal{H}(\mathfrak{p}_{\text{wdm}} - 5\bar{P}_{\text{wdm}}) + \frac{a\Gamma \bar{\rho}_{\text{dcdm}}}{3} \frac{\varepsilon^2}{1 - \varepsilon} \quad (\text{D.44})$$

so that the adiabatic sound speed reads

$$c_g^2 = w \left( 5 - \frac{\mathfrak{p}_{\text{wdm}}}{\bar{P}_{\text{wdm}}} - \frac{\bar{\rho}_{\text{dcdm}}}{\bar{\rho}_{\text{wdm}}} \frac{a\Gamma}{3w\mathcal{H}} \frac{\varepsilon^2}{1 - \varepsilon} \right) \left( 3(1 + w) - \frac{\bar{\rho}_{\text{dcdm}}}{\bar{\rho}_{\text{wdm}}} \frac{a\Gamma}{\mathcal{H}} (1 - \varepsilon) \right)^{-1}. \quad (\text{D.45})$$

When  $\Gamma \rightarrow 0$ , this expression reduces to the adiabatic sound speed for massive neutrinos (LESGOURGUES et al. 2011). In addition, it yields  $c_g^2 \rightarrow 1/3$  in the relativistic limit, as it should.

### D.3.4 Anisotropic stress

To close the system of equations Eq. (D.36) and Eq. (D.38), we need to select an appropriate truncation formula for  $\Delta f_{\text{wdm},2}$ . One might naively apply Eq. (3.40) with  $\ell_{\text{max}} = 2$ . However, Eq. (3.40) relies on the fact that the formal solution for the PSD multipoles are approximately proportional the spherical Bessel functions,  $j_\ell(k\tau)$ , and thus they inherit the same recurrence relation (MA et al. 1995). This is only true when the source term  $S$  (which in the collisionless DM case only depends on  $h'$  and  $\eta'$ ) can be neglected. If  $S \neq 0$ , the the PSD multipole solution contains an additional non-trivial integral (convoluted with a Bessel function), involving derivatives of terms in  $S$  (BLAS et al. 2011). To circumvent this problem, publicly available Boltzmann codes generally consider  $\ell_{\text{max}} \gg 1$ .

Alternatively, it is possible to limit the analysis to sub-Hubble scales ( $k\tau \gg 1$ ), truncate at a lower  $\ell_{\text{max}}$  ( $= 2$  for a viscous fluid), and obtain an approximated analytical result for the aforementioned convolution integral. This is what is done in BLAS et al. (2011) in order to derive fluid equations for the massless neutrinos, and is further generalized in LESGOURGUES et al. (2011) to the case of massive neutrinos. We apply the same philosophy of those two works to the WDM case, where the source

function  $S$  now also includes a term related to the decay. Inspired by those works, we write the truncation formula as

$$\Delta f'_{\text{wdm},2} = \frac{qk}{\mathcal{E}_2} \Delta f_{\text{wdm},1} - \frac{3}{\tau} \Delta f_{\text{wdm},2} - q \frac{\partial \bar{f}_{\text{wdm}}}{\partial q} \frac{h'}{6} - \bar{f}'_{\text{wdm}} \delta_{\text{dcdm}}. \quad (\text{D.46})$$

Now, in a similar way as we did before for the  $\delta'_{\text{wdm}}$  and  $\theta'_{\text{wdm}}$  equations, we multiply at each side of Eq. (D.46) by  $(8\pi/3)[\bar{\rho}_{\text{wdm}}(1+w)a^4]^{-1}(q^4/\mathcal{E}_2)$ , and then integrate over  $q$ . After some algebra, we find

$$\begin{aligned} \sigma'_{\text{wdm}} = & -3 \left( \frac{1}{\tau} + \mathcal{H} \left[ \frac{2}{3} - c_g^2 - \frac{1}{3} \frac{\Sigma_{\text{wdm}}}{\sigma_{\text{wdm}}} \right] + a\Gamma \frac{\bar{\rho}_{\text{dcdm}}}{\bar{\rho}_{\text{wdm}}} (1-\varepsilon) \frac{1+c_g^2}{3(1+w)} \right) \sigma_{\text{wdm}} \\ & + \frac{2}{3} \left[ \Theta_{\text{wdm}} + \frac{h'}{2} \frac{w}{(1+w)} \left( 5 - \frac{\mathfrak{p}_{\text{wdm}}}{\bar{P}_{\text{wdm}}} \right) - a\Gamma \frac{\bar{\rho}_{\text{dcdm}}}{\bar{\rho}_{\text{wdm}}} \frac{\varepsilon^2}{(1-\varepsilon)} \frac{\delta_{\text{dcdm}}}{(1+w)} \right]. \end{aligned} \quad (\text{D.47})$$

We have introduced two higher momenta variables, defined as

$$(\bar{\rho}_{\text{wdm}} + \bar{P}_{\text{wdm}}) \Theta_{\text{wdm}} \equiv \frac{4\pi k}{a^4} \int_0^\infty dq q^2 \frac{q^3}{\mathcal{E}_2^2} \Delta f_{\text{wdm},1}, \quad (\text{D.48})$$

$$(\bar{\rho}_{\text{wdm}} + \bar{P}_{\text{wdm}}) \Sigma_{\text{wdm}} \equiv \frac{8\pi}{3a^4} \int_0^\infty dq q^2 \frac{q^4}{\mathcal{E}_2^3} \Delta f_{\text{wdm},2}. \quad (\text{D.49})$$

As we see from above definitions, it's clear that  $\Theta_{\text{wdm}} \rightarrow \theta_{\text{wdm}}$  and  $\Sigma_{\text{wdm}} \rightarrow \sigma_{\text{wdm}}$  in the relativistic limit, and that  $\Theta_{\text{wdm}}/\theta_{\text{wdm}} \ll 1$  and  $\Sigma_{\text{wdm}}/\sigma_{\text{wdm}} \ll 1$  in the non-relativist regime. Thus, one way of closing the system of fluid equations is to replace  $\Theta_{\text{wdm}}$  and  $\Sigma_{\text{wdm}}$  by the usual  $\theta_{\text{wdm}}$  and  $\sigma_{\text{wdm}}$  multiplied by functions depending only on background quantities. Following LESGOURGUES et al. (2011), we write <sup>2</sup>

$$\Sigma_{\text{wdm}} = 3w_\sigma \sigma_{\text{wdm}}, \quad (\text{D.50})$$

$$\Theta_{\text{wdm}} + \frac{h'}{2} \frac{w}{(1+w)} \left( 5 - \frac{\mathfrak{p}_{\text{wdm}}}{\bar{P}_{\text{wdm}}} \right) = 3w_\theta \left[ \theta_{\text{wdm}} + \frac{h'}{2} \right], \quad (\text{D.51})$$

where  $w_\sigma$  and  $w_\theta$  can be any function of time going from 1/3 in the relativistic limit to 0 in the non-relativistic one. We set  $w_\sigma = \mathfrak{p}_{\text{wdm}}/3\bar{P}_{\text{wdm}}$  and  $w_\theta = 4wc_g^2/(1+w)$ , which were found to be good choices in LESGOURGUES et al. (2011). With this in mind, Eq. (D.47) can be rewritten as

$$\begin{aligned} \sigma'_{\text{wdm}} = & -3 \left( \frac{1}{\tau} + \mathcal{H}\xi + (1-\varepsilon)a\Gamma \frac{\bar{\rho}_{\text{dcdm}}}{\bar{\rho}_{\text{wdm}}} \frac{1+c_g^2}{3(1+w)} \right) \sigma_{\text{wdm}} \\ & + \frac{8wc_g^2}{1+w} \left[ \theta_{\text{wdm}} + \frac{h'}{2} \right] - \frac{2}{3} \frac{\varepsilon^2 a\Gamma}{(1-\varepsilon)} \frac{\bar{\rho}_{\text{dcdm}}}{\bar{\rho}_{\text{wdm}}} \frac{\delta_{\text{dcdm}}}{(1+w)}, \end{aligned} \quad (\text{D.52})$$

<sup>2</sup>The extra terms proportional to  $h'$  in Eq. (D.51) arise due to the gauge dependence of  $\theta$ ,  $\theta^{\text{new}} = \theta^{\text{syn}} + \alpha k^2$ , with  $\alpha = (6\eta' + h')/2k^2$ . At the level of the phase space variable  $\Delta f_{\text{wdm},1}$ , this corresponds to a relation

$$\Delta f_{\text{wdm},1}^{\text{new}} = \Delta f_{\text{wdm},1}^{\text{syn}} - \alpha k \frac{\mathcal{E}_2}{3} \frac{d\bar{f}_{\text{wdm}}}{dq}.$$

When integrating this relation to find  $\Theta_{\text{wdm}}$ , we thus get a term proportional to

$$\frac{4\pi}{a^4} \int dq q^5 \frac{d\bar{f}_{\text{wdm}}}{dq} = -w\bar{\rho}_{\text{wdm}} \left( 5 - \frac{\mathfrak{p}_{\text{wdm}}}{\bar{P}_{\text{wdm}}} \right).$$

However, it was found in BLAS et al. (2011) that removing the  $\eta'$  term leads to better results for the matter power spectrum, as can be justified by an analytic approximation of the full solution. That's why we simply replace  $\alpha k^2$  by  $h'/2$ .

where  $\xi \equiv 2/3 - c_g^2 - \mathbf{p}_{\text{wdm}}/3\bar{P}_{\text{wdm}}$  is a function that vanishes in the relativistic limit. Let us now consider the relativistic limit of Eq. (D.52), and multiply the decay terms by a factor of 2. Such an expression, corresponding to a CDM decay into 2 massless components, reads

$$\sigma'_{\text{dr}} = - \left( \frac{3}{\tau} + a\Gamma \frac{\bar{\rho}_{\text{dcdm}}}{\bar{\rho}_{\text{dr}}} \right) \sigma_{\text{dr}} + \frac{2}{3} \theta_{\text{dr}} + \frac{h'}{3} - a\Gamma \frac{\bar{\rho}_{\text{dcdm}}}{\bar{\rho}_{\text{dr}}} \frac{\delta_{\text{dcdm}}}{2} \quad (\text{D.53})$$

In ENGVIST et al. (2015), the authors derived an equation for the shear of the dark radiation daughters. It turns out that their equation is formally incorrect<sup>3</sup>, but if one places all numerical factors fairly, their equation is identical to Eq. (D.53).

### D.3.5 Semi-analytic understanding of the WDM sound speed

Here we obtain a formal equation that dictates the evolution of the WDM sound speed in the synchronous gauge,  $c_s^2$ . The first natural step is to write a dynamical equation for the normalized pressure perturbation,  $\Pi_{\text{wdm}} = \delta P_{\text{wdm}}/\bar{\rho}_{\text{wdm}}$ . This can be achieved by multiplying Eq. (D.30) by  $4\pi q^2 \frac{q^2}{3\varepsilon^2} a^{-4}$ , integrating over  $q$  and then using Eq. (D.29). By doing so, two higher velocity-weight integrals appear. One of them is  $\Theta_{\text{wdm}}$ , that we already wrote in Eq. (D.48), and the other is

$$\delta\mathcal{P}_{\text{wdm}} \equiv \frac{4\pi}{3a^4} \int_0^\infty dq \frac{q^6}{\varepsilon_{\text{wdm}}^3} \Delta f_{\text{wdm},0}. \quad (\text{D.54})$$

Similarly to what happens with  $\Theta_{\text{wdm}}$ , we see that  $\delta\mathcal{P}_{\text{wdm}} \rightarrow \delta P_{\text{wdm}}$  in the relativistic limit, while  $\delta\mathcal{P}_{\text{wdm}}/\delta P_{\text{wdm}} \ll 1$  in the non-relativistic one. This means that one can write  $\delta\mathcal{P}_{\text{wdm}} = \delta P_{\text{wdm}} 3\omega_p$  and  $\Theta_{\text{wdm}} = \theta_{\text{wdm}} 3\omega_\theta$ <sup>4</sup>, where  $\omega_p$  and  $\omega_\theta$  are arbitrary functions, going from 1/3 in the relativistic limit, to 0 in the non-relativistic case. In terms of these functions, the equation for  $\Pi_{\text{wdm}}$  becomes

$$\begin{aligned} \Pi'_{\text{wdm}} = & -3\mathcal{H}\Pi_{\text{wdm}} \left( \frac{2}{3} - \omega_p - \omega \right) - \omega_\theta (1 + \omega) \theta_{\text{wdm}} - \frac{h'\omega}{6} \left[ 5 - \frac{\mathbf{p}_{\text{wdm}}}{p_{\text{wdm}}} \right] \\ & + a\Gamma \frac{\bar{\rho}_{\text{dcdm}}}{\bar{\rho}_{\text{wdm}}} \left[ \frac{\varepsilon^2}{(1-\varepsilon)} \frac{\delta_{\text{dcdm}}}{3} - (1-\varepsilon)\Pi_{\text{wdm}} \right] \end{aligned} \quad (\text{D.55})$$

One can convert this into an equation for the sound speed by noting that  $\Pi_{\text{wdm}} = c_s^2 \delta_{\text{wdm}}$ , and using the background continuity equation Eq. (D.29). The final result reads:

$$\begin{aligned} \frac{\partial c_s^2}{\partial \tau} = & -3\mathcal{H}c_s^2 \left( \frac{2}{3} - \omega_p - c_s^2 \right) - (1 + \omega) \frac{\theta_{\text{wdm}}}{\delta_{\text{wdm}}} (\omega_\theta - c_s^2) - \frac{h'}{2\delta_{\text{wdm}}} \left[ \frac{\omega}{3} \left( 5 - \frac{\mathbf{p}_{\text{wdm}}}{\bar{P}_{\text{wdm}}} \right) - c_s^2 (1 + \omega) \right] \\ & + a\Gamma \frac{\bar{\rho}_{\text{dcdm}}}{\bar{\rho}_{\text{wdm}}} \frac{\delta_{\text{dcdm}}}{\delta_{\text{wdm}}} \left[ \frac{\varepsilon^2}{3(1-\varepsilon)} - (1-\varepsilon)c_s^2 \right]. \end{aligned} \quad (\text{D.56})$$

We remark that the previous equation is highly non-linear in the perturbed quantities, so it can easily give rise to numerical instabilities. In addition, there is no closed expression for computing  $\omega_p$  and  $\omega_\theta$ . If these functions were scale independent, one possible approximation would be to trade them for some background functions,

<sup>3</sup>In particular, in their derivation they used that the value of the integral  $\int_0^\infty \frac{j_2(x)}{x}$  is  $-1/3$ , while the correct value is  $1/3$ .

<sup>4</sup>We forget about the issue of the gauge dependence of  $\Delta f_{\text{wdm},0}$  and  $\Delta f_{\text{wdm},1}$ , since we will be restricting to sub-Hubble scales later on.



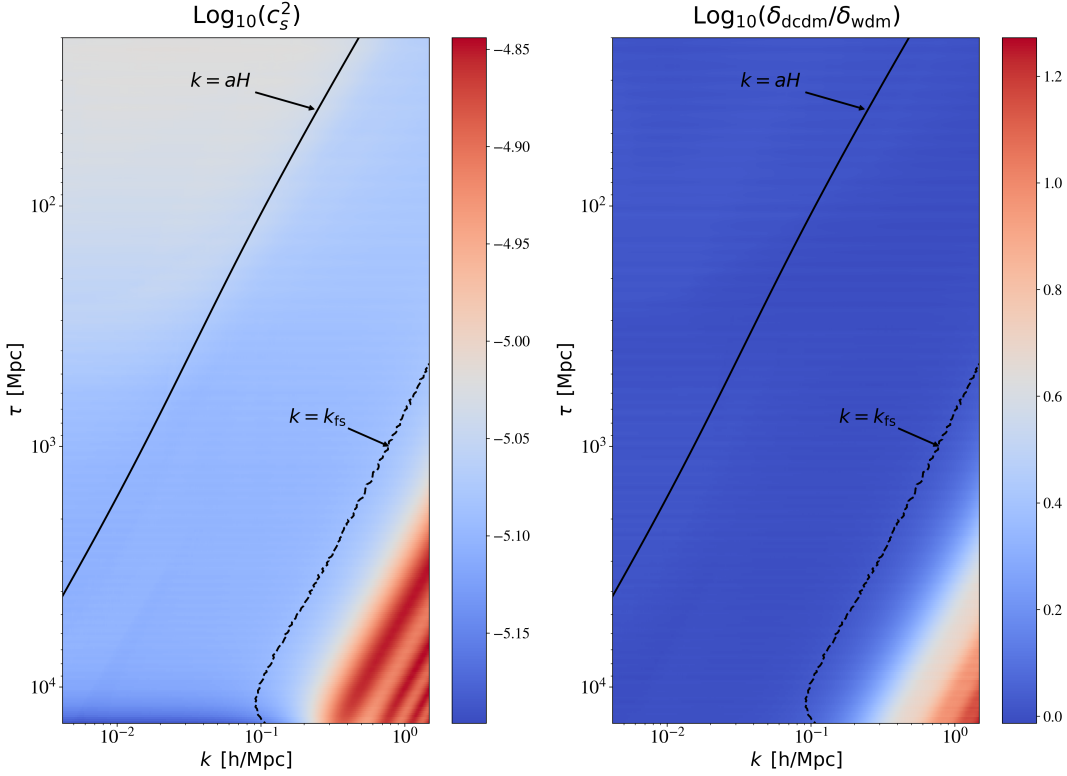


**Figure D.1 – Left panel:** The sound speed of the WDM species in the synchronous gauge, as a function of conformal time and wavenumber. **Right panel:** The ratio between the perturbed densities of the DCDM and the WDM components, as a function of conformal time and wavenumber. The black solid and dashed lines indicate the horizon and free-streaming crossing scales, respectively. We have set  $\varepsilon = 0.007$  and  $\Gamma^{-1} = 55$  Gyrs.

such as  $w$  or  $c_g^2$ . However, calculations using the full hierarchy show that  $\omega_p$  and  $\omega_\theta$  exhibit a  $k$ -dependence similar to that of  $c_s^2$ . For these reasons, we do not implement Eq. (D.56) in our code.

Nonetheless, by making some simplifying assumptions, Eq. (D.56) allows to qualitatively understand why there is a particular  $k$ -dependence of  $c_s^2$  in the decaying scenario, that is not present in the case of massive neutrinos. Let us consider the non-relativistic limit of Eq. (D.56), since data favors in general very small DR energy fractions,  $\varepsilon \ll 1$ . This also implies that  $w_p, c_s^2, w \ll 1$ . Let us further assume that  $\omega_\theta$  and  $c_s^2$  behave similarly, so that the difference  $\omega_\theta - c_s^2$  can be neglected. Finally, let us also restrict to sub-Hubble scales, for which the term  $h'/\delta_{\text{wdm}}$  is very small and can be also neglected. In this case, Eq. (D.56) reduces to

$$\frac{\partial c_s^2}{\partial \tau} = -2\mathcal{H}c_s^2 - a\Gamma \frac{\bar{\rho}_{\text{dcdm}}}{\bar{\rho}_{\text{wdm}}} \frac{\delta_{\text{dcdm}}}{\delta_{\text{wdm}}} c_s^2. \quad (\text{D.57})$$

In absence of the decay term, we see that the sound speed dilutes as  $c_s^2 \propto a^{-2}$ , which is a well-known result for massive neutrinos. This dilution can be compensated by the presence of the decay term, leading to a  $c_s^2 \sim \text{cte}$ , as long as the ratio  $\delta_{\text{dcdm}}/\delta_{\text{wdm}}$  doesn't change. In practice, for scales and times such that  $k < k_{\text{fs}}(\tau)$ , we have  $\delta_{\text{dcdm}}/\delta_{\text{wdm}} = 1$ . In this regime, the sound speed  $c_s^2$  is well approximated by the adiabatic sound speed  $c_g^2$ . However, when  $k > k_{\text{fs}}(\tau)$ ,  $\delta_{\text{wdm}}$  oscillates and starts to become suppressed with

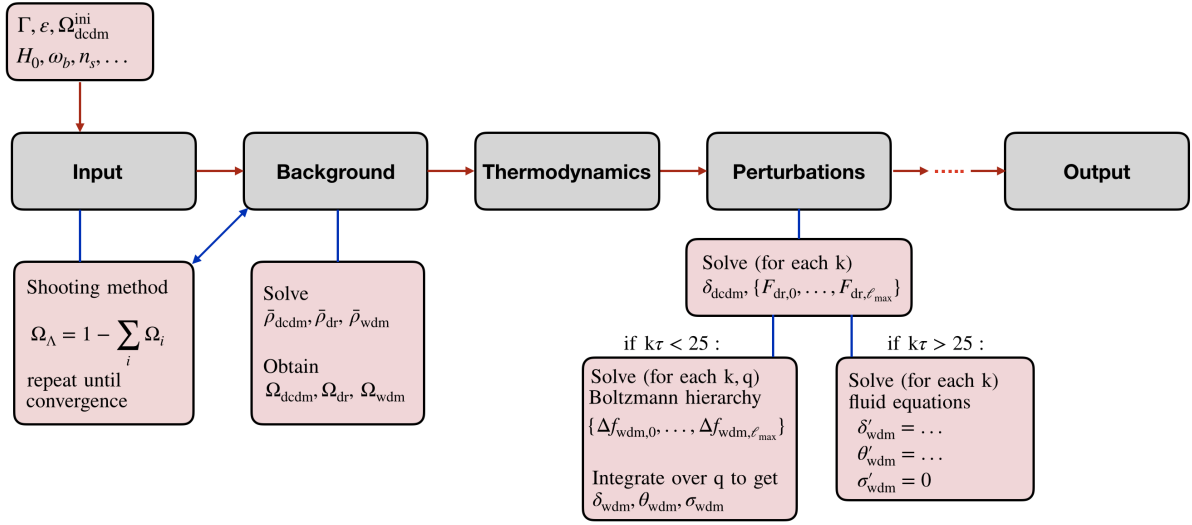


**Figure D.2** – Schematic view of the implementation of the  $\Lambda$ DDM model in the public Boltzmann solver **CLASS**. The grey boxes denote the standard modules of **CLASS**, while the pink boxes indicate which parts of these modules have been modified in order to describe the new species.

respect to  $\delta_{\text{dcdm}}$ , which leads to oscillatory features and a small enhancement in the evolution of  $c_s^2$ . This is visible in Fig. D.1, where we have plotted  $c_s^2$  and  $\delta_{\text{dcdm}}/\delta_{\text{wdm}}$  in the  $k-\tau$  plane using the full Boltzmann hierarchy, and setting  $\varepsilon = 0.007$ ,  $\Gamma^{-1} = 55$  Gyrs.

One can see that this  $k$ -dependent effect appears only because of the coupling term in Eq. (D.57), which is not present for massive neutrinos. This also justifies why the sound speed  $c_s^2$  is well approximated by a background function such as  $c_g^2$  in the case of massive neutrinos. In the case of the WDM daughter species, the approximation  $c_s^2 \simeq c_g^2$  will only work when  $k < k_{\text{fs}}(\tau)$ . This motivates the use of the fitting formula introduced in Eq. (3.46), that accounts for the small enhancement at scales smaller than the free-streaming scale. While this simple fitting formula is not able to capture the oscillatory features described previously, it leads to results that are accurate enough for all the observables analyzed in this work.

## D.4 Numerical implementation and accuracy of the fluid approximation

In order to solve the cosmic evolution equations discussed in Sect. 3.2, we modified the publicly available numerical Boltzmann solver **CLASS** (BLAS et al. 2011; LESGOURGUES et al. 2011). We now briefly illustrate our implementation of the  $\Lambda$ DDM model.

First let us notice that, when solving the background equations for all cosmological species, the dark energy abundance is iteratively derived through the budget equation,  $\Omega_\Lambda = 1 - \sum_i \Omega_i$ , where the sum includes the current abundance of all other components, which are not known a priori. We thus applied a *shooting method* for the aforementioned parameter, *i.e.* we guess an initial  $\Omega_\Lambda$ , we solve the system

of background equations to obtain  $\sum_i \Omega_i$ , and re-compute  $\Omega_\Lambda$ <sup>5</sup>. The procedure is iterated until convergence is achieved. The WDM density is computed by solving Eq. (3.22) in 2800 momentum bins, approximately as many as the time-steps used to describe its background evolution.

At the linear perturbation level, we truncate the hierarchy of the PSD multipole equations for both the daughter particles at a  $\ell_{\max} = 17$  (see Eq. (3.39) and Eq. (3.40)). We set the initial conditions for the WDM species following the same procedure of AOYAMA et al. (2014). On conformal times  $\tau < \tau_q$ , we set all  $\Delta f_{\text{wdm},\ell} = 0$ , since no daughter particle with comoving momentum  $q$  could have been produced. On the crossing time  $\tau = \tau_q$ , one should be more careful, as the terms with  $f_{\text{wdm}}$  in Eq. (D.30) and Eq. (D.32) contain a Dirac delta and, when integrated, a Heaviside function. Thus, the corresponding initial conditions for  $\Delta f_{\text{wdm},0}(\tau_q)$  and  $\Delta f_{\text{wdm},2}(\tau_q)$  are not-vanishing. We set them according to the analytical formulas (A.5) and (A.7) from AOYAMA et al. (2014):

$$\Delta f_{\text{wdm},0}(q, \tau_q) = \left[ \frac{-h'(\tau_q)}{6\mathcal{H}_q} + \delta_{\text{dcdm}}(\tau_q) \right] \frac{a_q \Gamma \bar{N}_{\text{dcdm}}(\tau_q)}{4\pi q^3 \mathcal{H}_q}, \quad (\text{D.58})$$

$$\Delta f_{\text{wdm},2}(q, \tau_q) = \frac{1}{\mathcal{H}_q} \left[ \frac{h'(\tau_q)}{15} + \frac{2\eta'(\tau_q)}{5} \right] \frac{a_q \Gamma \bar{N}_{\text{dcdm}}(\tau_q)}{4\pi q^3 \mathcal{H}_q}. \quad (\text{D.59})$$

Finally, on times  $\tau > \tau_q$ , we treat the WDM component as a massive neutrino species, and we solve the corresponding hierarchy of equations in 300 momentum-bins. This number of bins is chosen simply because it gives a good compromise between speed and accuracy: it is large enough to accurately describe the super-Hubble and Hubble-crossing scales, where the dynamics is relatively simple, and small enough to not become too computationally expensive<sup>6</sup>. On sub-Hubble scales, when  $k\tau$  is larger than a threshold value  $(k\tau)_{\text{fluid}}$ , we switch-on the fluid approximation described in section Sect. 3.2.3. The WDM dynamics is now described by Eq. (3.41)-Eq. (3.44) and Eq. (3.46). After trying several values of  $(k\tau)_{\text{fluid}}$ , we found  $(k\tau)_{\text{fluid}} = 25$  to provide the speed yet accurate enough for the purposes of the current analyses. Our implementation is summarized in Fig. D.2.

In Fig. D.3 and Fig. D.4 we explicitly compare the novel approximation scheme with the results of the “exact” computation for the WDM species. For the latter, we solve the full Boltzmann hierarchy using  $10^4$  momentum-bins and  $\ell_{\max} = 17$ . In Fig. D.3 we show the residuals of the lensed CMB TT and EE power spectra in the WDM fluid approximation, with respect to the full computation, for a grid of parameter values given by  $\Gamma/H_0 = 0.1, 1, 10$  and  $\varepsilon = 0.5, 0.1, 0.01, 0.001$ . These values span most of the parameter space in the  $\Lambda$ DDM framework, and for none of them the residuals exceed the *Planck*  $1\sigma$  uncertainties, which are indicated by the gray shaded regions, nor the error bars for a cosmic-variance-limited experiment (close to CMB-S4 errors), indicated by the pink shaded regions.

<sup>5</sup>This procedure corresponds to the case in which  $\Omega_{\text{dcdm}}^{\text{ini}}$  is passed as an input parameter. Alternatively, the user can pass as input the present abundance of DCDM, WDM and DR,  $\Omega_{\text{dcdm}+\text{dr}+\text{wdm}}$ , in which case a shooting method is also performed in order to find the corresponding  $\Omega_{\text{dcdm}}^{\text{ini}}$ .

<sup>6</sup>Note that the number of bins used at both the background and perturbation level is much larger than the one typically used in standard CLASS analysis for massive active neutrinos, given that the time-dependence of the background PSD of the WDM requires a finer momentum resolution. Regarding the momentum spacing, we have considered a logarithmic Simpson quadrature instead of the Gauss-Laguerre quadrature typically used in standard CLASS analysis.

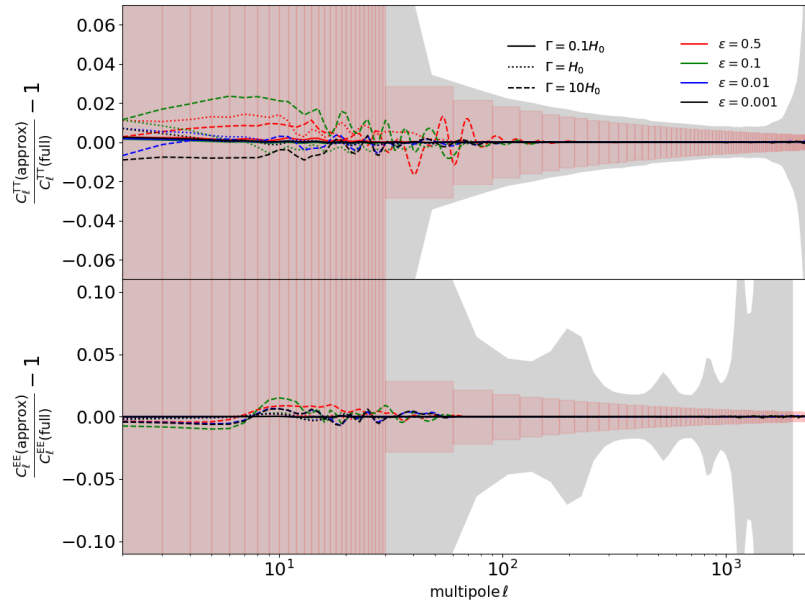


**Figure D.3** – Residuals of the lensed CMB TT power spectrum (upper) and EE power spectrum (lower) in the WDM fluid approximation, with respect to the full hierarchy calculation, for a grid of values covering most of the parameter space:  $\Gamma/H_0 = 0.1, 1, 10$  and  $\varepsilon = 0.5, 0.1, 0.01, 0.001$ . The gray shaded regions indicate *Planck*  $1\sigma$  errors, while the pink shaded areas indicate cosmic variance up to  $\ell = 3000$ .

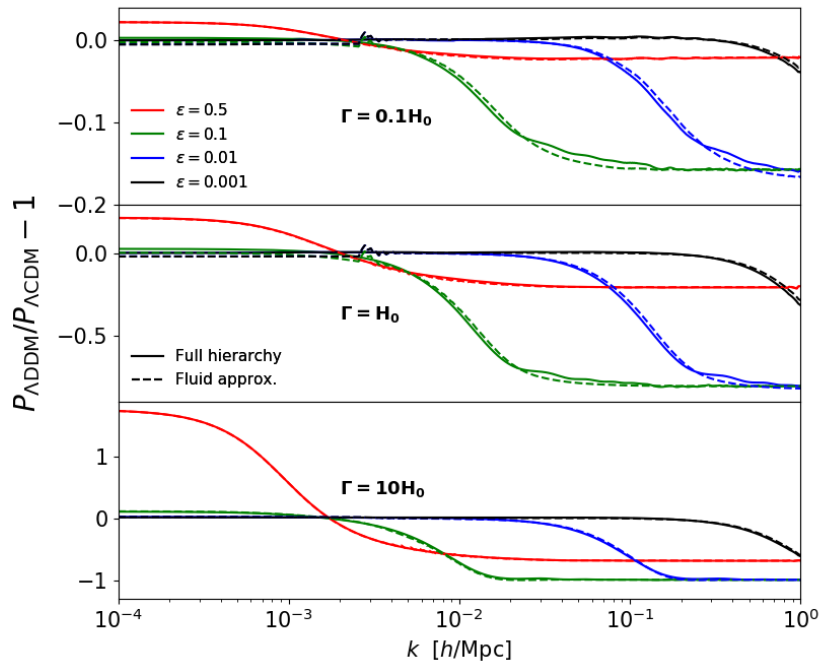


**Figure D.4** – Residuals of the linear matter power spectrum (at  $z = 0$ ), with respect to the baseline  $\Lambda$ CDM model, for the same grid of parameter values considered in Fig. D.3, both from the full hierarchy calculation (solid lines) and the WDM fluid approximation (dashed lines).

The predictions for the linear matter power spectrum  $P(k)$  are less accurate than for the anisotropy spectra, because the former is more sensitive to the dynamics of

the daughter particles. Close to the best-fit parameter values, and in general close to  $\Lambda$ CDM, the residual errors between the full and the fluid calculations in  $P(k)$  are  $\mathcal{O}(1\%)$ , but they can become higher far away from the best-fit. In particular, we have verified that inside the parameter region delimited by  $\text{Log}_{10}\varepsilon \in [-2.3, -0.7]$  and  $\text{Log}_{10}(\Gamma/\text{Gyrs}^{-1}) \in [-1.3, 1]$ , the residual errors are typically larger than 10%, so the fluid approximation should be used with caution in this region. However, this portion of the parameter space is deeply inside the  $2\sigma$  exclusion region, as one can check by looking at Fig. 3.7. In addition, given that current data are mostly sensitive to integrals over  $P(k)$  (e.g.  $S_8$ , CMB lensing), we are mainly interested in getting accurate predictions for the departures from  $\Lambda$ CDM (rather than the exact shape of the matter spectrum itself). To illustrate that, we have computed the residuals of the linear matter power spectrum (at  $z = 0$ ) with respect to our baseline  $\Lambda$ CDM model, for both the fluid and the full hierarchy calculations. The results are shown in Fig. D.4, where we have spanned the same parameter values as in Fig. D.3. We can see that, for all the  $\Lambda$ DDM models, the shape of the power suppression (that is, the depth and the cut-off scale) is excellently well-captured by our fluid prescription. Furthermore, we verified that the residuals in the structure growth parameter  $S_8 \equiv \sigma_8(\Omega_m/0.3)^{0.5}$  are always smaller than the  $\sim 1.8\%$  relative error of the  $S_8$  measurement from HEYMANS et al. (2021). We thus conclude that the new WDM viscous fluid approximation is accurate enough for our analyses.

## D.5 Best-fit $\chi^2$ per experiment

In Tab. (D.1) and Tab. (D.2) we report all  $\chi_{\text{min}}^2$ 's obtained with the MINUIT algorithm (JAMES et al. 1975) through the `iMinuit` python package for the various model and data-set combinations considered in this work.

	BAO+SNIa	+Planck w/o $S_8$	+Planck w/ $S_8$					+SPTpol		+ACTPol	
			w/ $A_{\text{lens}}$	$\varepsilon = 0.05$	w/o $S_8$	w/ $S_8$	w/o $S_8$	w/ $S_8$			
Pantheon SNIa	1026.9	1028.2	1027.5	1026.8	1029.2	1028.0	1027.1	1027.0	1026.9	1027.0	1026.84
BAO+FS BOSS DR12	-	6.63	7.06	6.93	7.11	6.14	6.59	5.94	6.17	6.78	6.66
BAO BOSS DR12	3.52	-	-	-	-	-	-	-	-	-	-
BAO BOSS low- $z$	1.84	1.20	1.22	1.18	1.24	1.83	1.28	1.58	1.79	1.17	1.34
BAO eBOSS DR14	4.29	4.94	4.91	4.94	4.83	4.52	4.88	4.68	4.53	4.97	4.77
Planck high- $\ell$ TT,TE,EE 'lite'	-	584.8	585.9	585.3	586.9	577.7	587.5	-	-	589.216	590.545
Planck high- $\ell$ TT 'lite'	-	-	-	-	-	-	-	207.8	207.8	-	-
Planck low- $\ell$ EE	-	396.9	396.9	397.2	396.3	395.7	396.3	395.8	396.1	396.2	397.15
Planck low- $\ell$ TT	-	23.1	23.1	23.2	23.0	22.1	23.0	22.3	22.1	22.6	22.46
Planck lensing	-	8.78	9.12	8.88	9.47	8.53	9.83	-	-	8.8	8.94
SPTpol high- $\ell$ TE,EE	-	-	-	-	-	-	-	145.9	145.6	-	-
SPTpol lensing	-	-	-	-	-	-	-	5.43	5.93	-	-
ACTPol	-	-	-	-	-	-	-	-	-	238.235	237.359
KiDS+BOSS+2dFLens	-	-	0.0003	-	-	0.0097	0.98	-	0.0015	-	-
DES	-	-	-	0.19	-	-	-	-	-	-	-
KiDS+Viking+DES	-	-	-	-	0.20	-	-	-	-	-	-
total $\chi^2$	1036.6	2053.4	2055.0	2054.8	2055.9	2043.2	2057.6	1816.3	1816.8	2294.8	2296.2

**Table D.1** – Best-fit  $\chi^2$  per experiment (and total) for the different  $\Lambda$ DDM analyses performed in this work.

## D.6 Comparison with the *Planck* constraints from CLARK et al. (2021a)

Here we carry out an explicit comparison of our constraints with those of CLARK et al. (2021a), which performed an analysis of the  $\Lambda$ DDM model against *Planck* data, neglecting the perturbations of the warm daughter particles. As shown in Fig. D.5,

Model	$\nu\Lambda$ CDM		$\Lambda$ DDM	
Experiment	w/o $S_8$	w/ $S_8$	w/o $S_8$	w/ $S_8$
Planck high- $\ell$ TT,TE,EE	586.67	587.57	584.82	585.74
Planck low- $\ell$ EE	396.06	396.05	396.92	396.92
Planck low- $\ell$ TT	23.18	22.66	23.12	23.09
Planck lensing	8.93	9.60	8.78	9.07
Pantheon	1026.93	1026.73	1026.94	1026.93
BAO BOSS low- $z$	1.23	1.62	1.20	1.21
BAO FS BOSS DR12	6.51	5.88	6.63	6.95
eBOSS DR14 Ly- $\alpha$	4.93	4.68	4.94	4.91
KIDS1000+BOSS+2dfLenS	–	5.64	–	0.15
total	2053.4	2060.5	2053.4	2055.0

**Table D.2** – Best-fit  $\chi^2$  per experiment (and total) in  $\nu\Lambda$ CDM and  $\Lambda$ DDM, with and without a split-normal likelihood on  $S_8$  from KiDS-1000+BOSS+2dFLens.

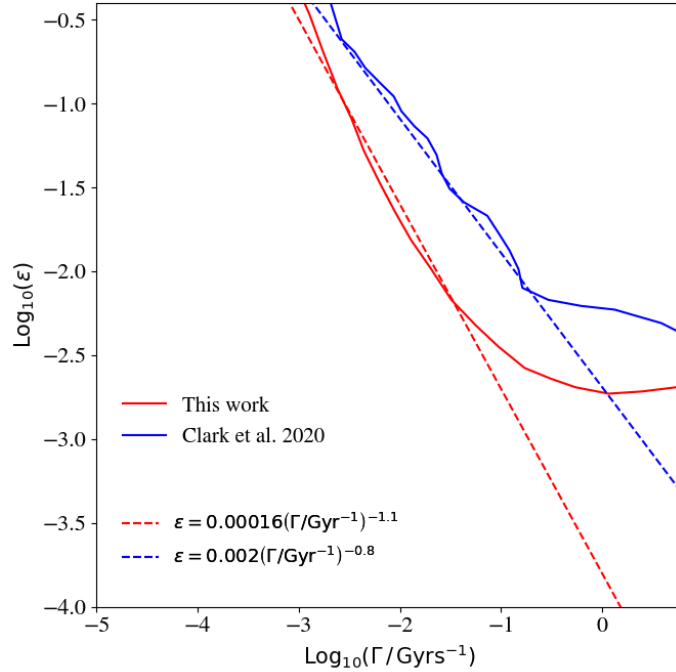


**Figure D.5** – Comparison between the  $2\sigma$  exclusion bounds (solid lines) from the *Planck* analysis of CLARK et al. (2021a) and our *Planck*+BAO+SNIa analysis. In each case, the dashed line indicates a fit that roughly describes the  $2\sigma$  limit in the range  $\Gamma \sim 10^{-3} - 10^{-1} \text{ Gyrs}^{-1}$ .

we find that the constraints on the  $\Lambda$ DDM models are up to (roughly) one order of magnitude stronger when our improved treatment is considered.

## D.7 Results with a linear prior on $\Gamma$ and $\varepsilon$

In our baseline analysis we have made use of log-prior on  $\varepsilon$  and  $\Gamma$ , to ease comparison with earlier works (VATTIS et al. 2019; CLARK et al. 2021a) who adopted the same choice. Here we present results using linear priors on the DDM parameters.

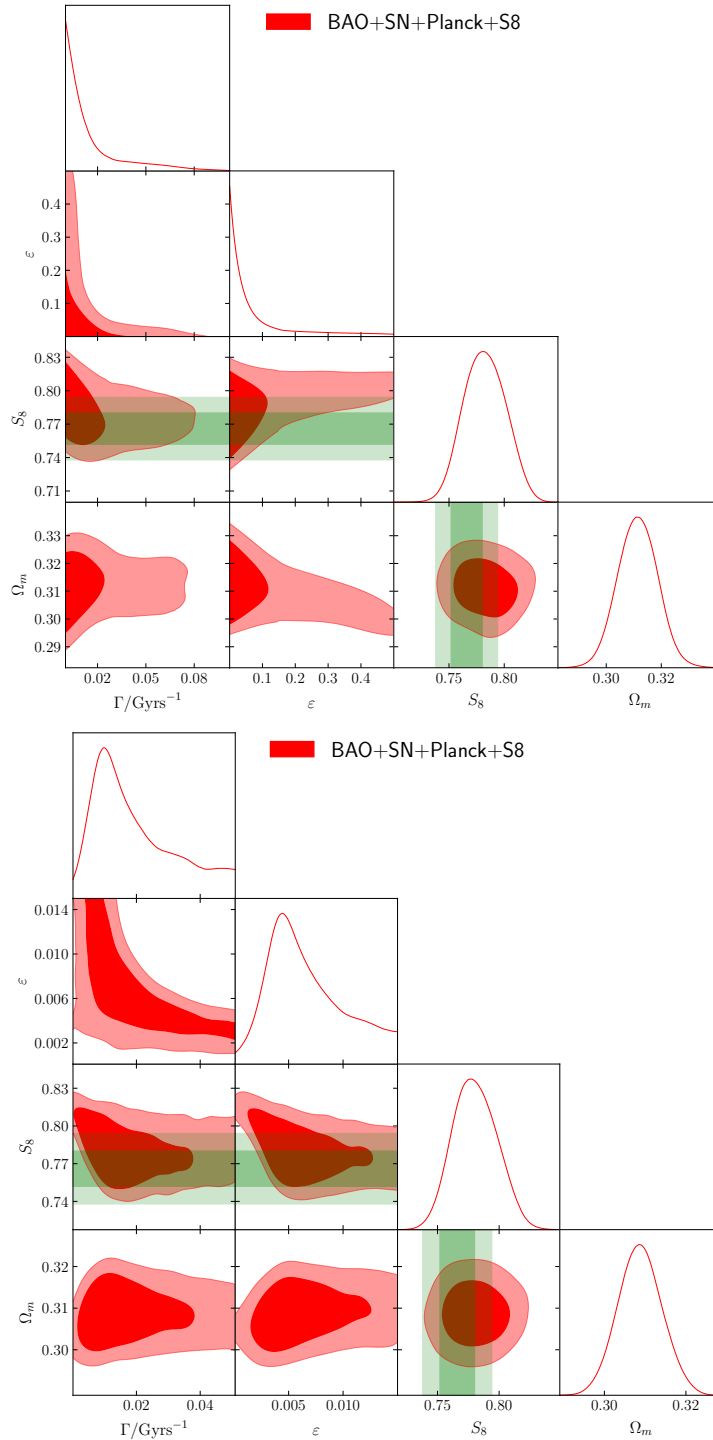


**Figure D.6** – Reconstructed 2D posteriors of a BAO + SNIa + *Planck* +  $S_8$  (from KiDS+BOSS+2dFLens) analysis, with linear priors and sampling either with the original prior range (**upper panel**) or within a restricted prior range (**lower panel**).

Let us however stress that the use of a linear prior is less informative than adopting a logarithmic one. That is because a linear prior carries a scale (due to the large error bars used in the proposal distribution of the MCMC sampler), so that it is hard for the sampler to detect fine structure over 4 orders of magnitude by using a linear scale, in particular at very small values. In other words, given the difference



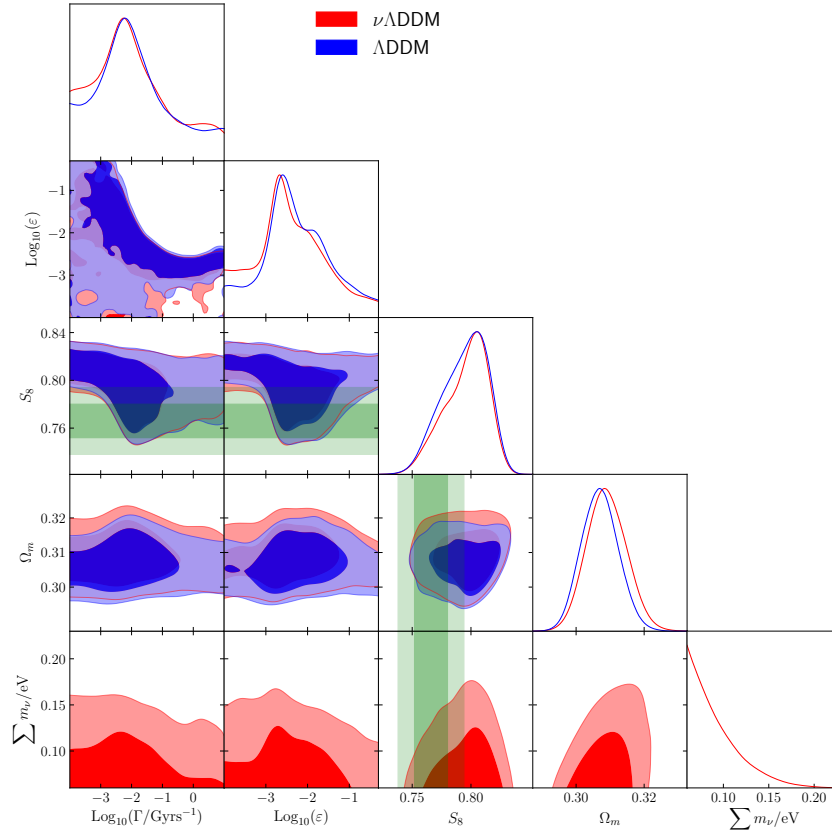


**Figure D.7** – Reconstructed 2D posterior distributions of  $\{S_8, \Omega_m, \text{Log}_{10}(\Gamma/\text{Gyrs}^{-1}), \text{Log}_{10}(\varepsilon), \sum m_\nu/\text{eV}\}$  with the neutrino mass fixed to 0.06 eV (blue) or let free to vary (red).

between the scale of the upper limit on  $\Gamma/\text{Gyrs}^{-1}$  and  $\varepsilon$  ( $\sim 10^{-1}$ ) and that of the lower limit ( $\sim 10^{-3}$ ), it is very difficult to accurately reconstruct the parameter space with a linear prior. Such a difficulty is illustrated in Fig. D.6, where we provide the results of two linear-prior analyses: the upper panel corresponding to the original prior range, the lower panel corresponding to a more restricted range:  $\varepsilon \in [0.0001, 0.015]$  and  $\Gamma/\text{Gyrs}^{-1} \in [0.0001, 0.05]$ . While in the latter case  $\varepsilon$  and  $\Gamma$  are detected at the  $2\sigma$  level – similarly to the log-prior results – the former case weighs in favor of larger  $\varepsilon$  values, so that one would incorrectly deduce an upper limit only.

## D.8 Results with the neutrino mass free in the $\Lambda$ DDM cosmology

We show in Fig. D.7 the 2D posteriors of  $\{S_8, \Omega_m, \text{Log}_{10}(\Gamma/\text{Gyrs}^{-1}), \text{Log}_{10}(\varepsilon), \sum m_\nu/\text{eV}\}$  with the (individual) neutrino mass fixed to 0.06 eV (red) or let free to vary (blue). When considering the neutrino mass a free parameter, we model neutrinos as three degenerate state, while when the neutrino mass is fixed to 0.06 eV we consider one massive, two massless neutrinos. One can see that the results are unaffected by our choice of keeping the neutrino mass fixed to 0.06 eV in our fiducial analysis.



# E

---

## Complements on decaying neutrinos

---

In this appendix we detail some important calculations concerning the dynamics of decaying neutrinos to dark radiation, that were too long to be included in the main text of [Chapter 4](#). We also include an extra run to show the effects of imposing the non-relativistic limit as a prior on the MCMC.

### E.1 Collision term for decaying neutrinos

The goal is to simplify as much as possible the general expression for the decaying neutrino collision term (*c.f.* [Eq. \(4.12\)](#)):

$$\left(\frac{\partial f_\nu}{\partial \tau}\right)_C = -\frac{a^2 f_\nu(q)}{2\mathcal{E}_\nu(2\pi)^2} \int \frac{d^3\vec{q}_1}{2\mathcal{E}_1} \frac{d^3\vec{q}_2}{2\mathcal{E}_2} |\mathcal{M}|^2 \delta^{(4)}(Q - Q_1 - Q_2). \quad (\text{E.1})$$

In the context of two-body decays to massless particles, the invariant amplitude squared  $|\mathcal{M}|^2$  is simply related to the rest-frame decay width of the neutrinos as  $|\mathcal{M}|^2 = 16\pi\Gamma_\nu m_\nu$  ([BARNETT et al. 1996](#)). As in [App. D.1](#), we will be using the following relations associated with the Dirac delta function:

$$\int \frac{d^3\vec{q}_I}{2\mathcal{E}_I} = \int d^4Q_I \delta(\mathcal{E}_I^2 - q_I^2 - a^2 m_I^2) \Theta(\mathcal{E}_I), \quad (\text{E.2})$$

$$\delta(f(x)) = \sum_i \frac{\delta(x - x_0)}{|f'(x_0)|}, \quad \text{with } x_0 \text{ such that } f(x_0) = 0. \quad (\text{E.3})$$

The calculation is very similar to the one we performed for decaying dark matter in [App. D.1](#). However, there are two important differences we have to take into account: 1) the momentum of mother particles is not negligible anymore,  $\vec{q}_\nu = \vec{q} \neq 0$ , and 2) both daughter particles are massless,  $\mathcal{E}_1 = q_1$ ,  $\mathcal{E}_2 = q_2$ . The former implies that now

we'll have to take care of the angular integral over  $\hat{q} \cdot \hat{q}_1 = \cos \theta$ . Hence:

$$\begin{aligned} \left( \frac{\partial f_\nu}{\partial \tau} \right)_C &= -\frac{2a^2 \Gamma_\nu m_\nu f_\nu}{\pi \mathcal{E}_\nu} \int \frac{d^3 \vec{q}_1}{2\mathcal{E}_1} \delta \left( (\mathcal{E}_\nu - \mathcal{E}_1)^2 - |\vec{q} - \vec{q}_1|^2 \right) \Theta(\mathcal{E}_\nu - \mathcal{E}_1) \\ &= -\frac{2a^2 \Gamma_\nu m_\nu f_\nu}{\mathcal{E}_\nu} \int_0^\infty dq_1 q_1 \int_{-1}^{+1} d \cos \theta \delta \left( 2\mathcal{E}_\nu q_1 - 2q q_1 \cos \theta - a^2 m_\nu^2 \right) \Theta(\mathcal{E}_\nu - q_1). \\ &= -\frac{2a^2 \Gamma_\nu m_\nu f_\nu}{\mathcal{E}_\nu} \int_0^\infty dq_1 q_1 \int_{-1}^{+1} d \cos \theta \frac{\delta(\cos \theta - \cos \theta_*)}{2q q_1} \Theta(\mathcal{E}_\nu - q_1), \end{aligned} \quad (\text{E.4})$$

where  $\cos \theta_*$  is given by

$$\cos \theta_* = \frac{2\mathcal{E}_\nu q_1 + a^2 m_\nu^2}{2q q_1}. \quad (\text{E.5})$$

The integral over  $\cos \theta$  is performed trivially thanks to the Dirac delta. However, this will introduce a step function  $\Theta(1 - \cos^2 \theta_*)$ , in order to enforce the condition  $\cos \theta_* \in [-1, 1]$ . This will in turn restrict the integration limits for the remaining momentum integral to  $q_1^\pm = \frac{1}{2}(\mathcal{E}_\nu \pm q)$ , which are nothing but the roots of  $1 - \cos^2 \theta_*$ . Thus, we arrive at

$$\left( \frac{\partial f_\nu}{\partial \tau} \right)_C = -\frac{a^2 \Gamma_\nu m_\nu f_\nu}{\mathcal{E}_\nu q} \int_{q_1^-}^{q_1^+} dq_1 = -\frac{a^2 \Gamma_\nu m_\nu f_\nu}{\mathcal{E}_\nu}. \quad (\text{E.6})$$

## E.2 Collision term for dark radiation daughters

The starting point is the collision term appearing in the equations for the perturbed PSD multipoles of the dark radiation,  $F_{\text{dr},\ell}$ . It is given by (c.f. Eq. (4.32))

$$\begin{aligned} C_\ell &= 2i^\ell \int \frac{d\Omega_k}{4\pi} P_\ell(\hat{k} \cdot q_1) \left( \frac{4\pi}{\rho_c} \int dq_1 q_1^3 \left( \frac{\partial f_{\text{dr}}}{\partial \tau} \right)_C [q_1, \hat{k} \cdot q_1] \right) \\ &= i^\ell \left( \frac{8a^2 \Gamma_\nu m_\nu}{\pi \rho_c} \right) \int d\Omega_k P_\ell(\hat{k} \cdot q_1) \int \frac{dq_1}{2\mathcal{E}_1} q_1^3 \int \frac{d^3 q_2}{2\mathcal{E}_2} \frac{d^3 q}{2\mathcal{E}_\nu} \Delta f_\nu(q, \hat{k} \cdot q) \delta^{(4)}(Q - Q_1 - Q_2). \end{aligned} \quad (\text{E.7})$$

where in the second line we inserted the expression for  $\left( \frac{\partial f_{\text{dr}}}{\partial \tau} \right)_C$  in Eq. (4.13) and used that  $|\mathcal{M}|^2 = 16\pi \Gamma_\nu m_\nu$ . In this expression  $d\Omega_k$  represents the differential solid angle along the direction  $\hat{k}$ , while  $q_{1,2}$  are the momenta of daughter particles. The  $d^3 q_2$  integral can be easily evaluated using the delta function corresponding to momentum conservation. In order to perform the integral over  $d\Omega_k$ , we notice that the direction of  $\hat{k}$  enters only via  $P_\ell(\hat{k} \cdot \hat{q}_1)$  and  $\Delta f_\nu(q, \hat{k} \cdot \hat{q})$ . Now, using the Legendre expansion of  $\Delta f_\nu(q, \hat{k} \cdot \hat{q})$  in Eq. (4.22) and employing the identity

$$\int d\Omega_k P_\ell(\hat{k} \cdot \hat{q}) P_{\ell'}(\hat{k} \cdot \hat{q}_1) = \left( \frac{4\pi}{2\ell + 1} \right) P_\ell(\hat{q} \cdot \hat{q}_1) \delta_{\ell\ell'}, \quad (\text{E.8})$$

we can evaluate the  $d\Omega_k$  integral to obtain

$$C_\ell = \left( \frac{32m_\nu \Gamma_\nu a^2}{\rho_c} \right) \int \frac{d^3 q dq_1}{8\mathcal{E}_\nu \mathcal{E}_1 \mathcal{E}_2} q_1^3 P_\ell(\hat{q}_1 \cdot \hat{q}) \Delta f_{\nu,\ell}(q) \delta(\mathcal{E}_\nu - \mathcal{E}_1 - \mathcal{E}_2). \quad (\text{E.9})$$

Now, notice that the direction of the neutrino momentum only enters the integrand via the angle between the neutrino momentum  $q$  and the daughter momentum  $q_1$ ,  $\cos \theta \equiv \hat{q} \cdot \hat{q}_1$ . The energy conserving delta function can be expressed in terms of this angle as

$$\delta(\mathcal{E}_\nu - \mathcal{E}_1 - \mathcal{E}_2) = \frac{\mathcal{E}_2}{q q_1} \delta(\cos \theta - \cos \theta_*), \quad (\text{E.10})$$

where  $\cos \theta_*$  is given by Eq. (E.5). As before, The energy conservation restricts the daughter momentum to a range of values  $(q_1^+, q_1^-)$ . The edges of this range occur when the extreme values,  $\cos \theta_1^* = \pm 1$ , are reached. These values correspond to  $q_1^\pm = \frac{1}{2}(\mathcal{E}_\nu \pm q)$ . After integrating over the delta function corresponding to energy conservation, this reduces to

$$C_\ell = \left( \frac{8\pi m_\nu \Gamma_\nu a^2}{\rho_c} \right) \int \frac{dq}{\mathcal{E}_\nu} q \Delta f_{\nu,\ell} \int_{q_1^-}^{q_1^+} dq_1 q_1 P_\ell \left( \frac{2\mathcal{E}_\nu q_1 - a^2 m_\nu^2}{2qq_1} \right). \quad (\text{E.11})$$

### E.3 Fluid equations for decaying neutrinos

We seek to derive viscous fluid equations for decaying neutrinos, in order to simplify the dynamics dictated by the following Boltzmann hierarchy of equations:

$$\Delta f'_{\nu,0} = -\frac{qk}{\mathcal{E}_\nu} \Delta f_{\nu,1} + q \frac{\partial \bar{f}_\nu}{\partial q} \frac{h'}{6} - \frac{a^2 \Gamma_\nu m_\nu}{\mathcal{E}_\nu} \Delta f_{\nu,0}, \quad (\text{E.12})$$

$$\Delta f'_{\nu,1} = \frac{qk}{3\mathcal{E}_\nu} [\Delta f_{\nu,0} - 2\Delta f_{\nu,2}] - \frac{a^2 \Gamma_\nu m_\nu}{\mathcal{E}_\nu} \Delta f_{\nu,1}, \quad (\text{E.13})$$

$$\Delta f'_{\nu,2} = \frac{qk}{5\mathcal{E}_\nu} [2\Delta f_{\nu,1} - 3\Delta f_{\nu,3}] - q \frac{\partial \bar{f}_\nu}{\partial q} \frac{(h' + 6\eta')}{15} - \frac{a^2 \Gamma_\nu m_\nu}{\mathcal{E}_\nu} \Delta f_{\nu,2}, \quad (\text{E.14})$$

$$\Delta f'_{\nu,\ell>2} = \frac{qk}{(2\ell+1)\mathcal{E}_\nu} [\ell \Delta f_{\nu,\ell-1} - (\ell+1) \Delta f_{\nu,\ell+1}] - \frac{a^2 \Gamma_\nu m_\nu}{\mathcal{E}_\nu} \Delta f_{\nu,\ell}. \quad (\text{E.15})$$

The fluid viscous equations are obtained by truncating Eq. (E.12)-Eq. (E.15) at  $\ell = 2$  and integrating over  $q$  as discussed in BLAS et al. (2011) and LESGOURGUES et al. (2011). As already mentioned in Chapter 3, the fluid description is only valid at scales deeply inside the Hubble radius, where high- $\ell$  and low- $\ell$  modes are effectively decoupled. The calculations are totally analogous to the ones carried out for the warm dark daughter in App. D.3, except that the decay terms are slightly different. The continuity and Euler equation are:

$$\delta'_\nu = -3\mathcal{H}(c_{\text{syn}}^2 - w_\nu)\delta_\nu - (1 + w_\nu) \left( \theta_\nu + \frac{h'}{2} \right) - a\Gamma_\nu \delta_\nu \left( 1 - 3w_\delta - \frac{\bar{n}_\nu m_\nu}{\bar{\rho}_\nu} \right), \quad (\text{E.16})$$

$$\theta'_\nu = -\mathcal{H}(1 - 3c_g^2)\theta_\nu + \frac{c_{\text{syn}}^2}{1 + w_\nu} k^2 \delta_\nu - k^2 \sigma_\nu - a\Gamma_\nu \theta_\nu \left( 1 - 3w_\theta - \frac{1 + c_g^2}{1 + w_\nu} \frac{\bar{n}_\nu m_\nu}{\bar{\rho}_\nu} \right), \quad (\text{E.17})$$

while the dynamical equation for the shear stress is written as

$$\sigma'_\nu = -3 \left( \frac{1}{\tau} + \mathcal{H}\xi \right) \sigma_\nu + \frac{8w_\nu c_g^2}{1 + w_\nu} \left[ \theta_\nu + \frac{h'}{2} \right] - a\Gamma_\nu \sigma_\nu \left( 1 - 3w_\sigma - \frac{1 + c_g^2}{1 + w_\nu} \frac{\bar{n}_\nu m_\nu}{\bar{\rho}_\nu} \right), \quad (\text{E.18})$$

where  $\xi \equiv 2/3 - c_g^2 - \mathfrak{p}_\nu/(3\bar{P}_\nu)$ . As usual, we have introduced the adiabatic sound speed,  $c_g^2 \equiv \bar{P}'_\nu/\bar{\rho}'_\nu$ , and the sound speed in the synchronous gauge,  $c_{\text{syn}}^2 \equiv \delta P_\nu/\delta \rho_\nu$ . For the latter, one can follow the same approximation as for stable massive neutrinos (LESGOURGUES et al. 2011)

$$c_{\text{syn}}^2 \simeq c_g^2. \quad (\text{E.19})$$

The adiabatic sound speed can straightforwardly be computed using the following expression

$$c_g^2 = w_\nu \left( 5 - \frac{\mathfrak{p}_\nu}{\bar{P}_\nu} + \frac{a\Gamma_\nu}{3w_\nu \mathcal{H}} \frac{\mathfrak{n}_\nu m_\nu}{\bar{\rho}_\nu} \right) \left[ 3(1 + w_\nu) + \frac{a\Gamma_\nu}{\mathcal{H}} \frac{\bar{n}_\nu m_\nu}{\bar{\rho}_\nu} \right]^{-1}. \quad (\text{E.20})$$

When setting  $\Gamma_\nu$  to 0, Eq. (E.16)-Eq. (E.20) reduce to the fluid equations for massive stable neutrinos considered in LESGOURGUES et al. (2011). In Eq. (E.20), the quantities  $\mathfrak{p}_\nu$  and  $\mathfrak{n}_\nu$  denote the pseudo-pressure and pseudo-number density, respectively. These are higher momenta integrals of the background p.s.d.,  $\bar{f}_\nu(q, \tau)$ , that reduce to the standard pressure  $\bar{P}_\nu$  and number density  $\bar{n}_\nu$  in the relativistic limit. They can be computed as:

$$\mathfrak{p}_\nu = \frac{4\pi}{3a^4} \int dq \frac{q^6}{\mathcal{E}_\nu^3} \bar{f}_\nu, \quad \mathfrak{n}_\nu = \frac{4\pi}{a^3} \int dq \frac{q^4}{\mathcal{E}_\nu^2} \bar{f}_\nu. \quad (\text{E.21})$$

In Eq. (E.16)-Eq. (E.18), the quantities  $w_i$  (for  $i = \delta, \theta, \sigma$ ) are determined through the following expressions:

$$1 - 3\omega_\delta \equiv \frac{m_\nu \delta n_\nu}{\delta \rho_\nu} = \frac{\frac{4\pi}{a^4} \int dq q^2 a m_\nu \Delta f_{\nu,0}}{\frac{4\pi}{a^4} \int dq q^2 \mathcal{E}_\nu \Delta f_{\nu,0}}, \quad (\text{E.22})$$

$$1 - 3\omega_\theta \equiv \frac{(\bar{\rho}_\nu + \bar{P}_\nu)\Theta_\nu}{(\bar{\rho}_\nu + \bar{P}_\nu)\theta_\nu} = \frac{\frac{4\pi k}{a^4} \int dq q^3 \frac{a m_\nu}{\mathcal{E}_\nu} \Delta f_{\nu,1}}{\frac{4\pi k}{a^4} \int dq q^3 \Delta f_{\nu,1}}, \quad (\text{E.23})$$

$$1 - 3\omega_\sigma \equiv \frac{(\bar{\rho}_\nu + \bar{P}_\nu)\Sigma_\nu}{(\bar{\rho}_\nu + \bar{P}_\nu)\sigma_\nu} = \frac{\frac{8\pi}{3a^4} \int dq q^4 \frac{a m_\nu}{\mathcal{E}_\nu^2} \Delta f_{\nu,2}}{\frac{8\pi}{3a^4} \int dq \frac{q^4}{\mathcal{E}_\nu} \Delta f_{\nu,2}}. \quad (\text{E.24})$$

The variables  $\Theta_\nu$  and  $\Sigma_\nu$  were already discussed in App. D.3 when writing fluid equations for the warm daughter particles. In order to close the system of Eq. (E.16)-Eq. (E.18) we need some prescription for computing the quantities  $\omega_\delta$ ,  $\omega_\theta$  and  $\omega_\sigma$  without having to solve the full Boltzmann hierarchy for each momentum bin. By having a look at Eq. (E.22)-Eq. (E.24), we realize that  $m_\nu \delta n_\nu / \delta \rho_\nu \rightarrow 1$ ,  $\Theta_\nu / \theta_\nu \rightarrow 1$  and  $\Sigma_\nu / \sigma_\nu \rightarrow 1$  in the non-relativistic limit, while  $m_\nu \delta n_\nu / \delta \rho_\nu \rightarrow 0$ ,  $\Theta_\nu / \theta_\nu \rightarrow 0$  and  $\Sigma_\nu / \sigma_\nu \rightarrow 0$  in the relativistic limit (by a factor  $a m_\nu / q \ll 1$ ). Therefore, we could approximate  $\omega_\delta$ ,  $\omega_\theta$  and  $\omega_\sigma$  by some background functions that go from 0 in the non-relativistic limit to 1/3 in the relativistic limit. An obvious guess would be the following

$$w_\delta \simeq w_\theta \simeq w_\sigma \simeq w_\nu, \quad (\text{E.25})$$

where  $w_\nu \equiv \bar{P}_\nu / \bar{\rho}_\nu$  is the EoS of the neutrino species. However, there are many other possible choices, such as  $c_g^2$ ,  $3w_\nu c_g^2$ ,  $3w_\nu(1 + w_\nu)/4$ ,  $\mathfrak{p}_\nu / 3\bar{P}_\nu$ ,  $\mathfrak{n}_\nu / 3\bar{n}_\nu$ , etc. In order to get the best candidates, one should compare these background functions with the exact formulas Eq. (E.22)-Eq. (E.24) computed with the full hierarchy, to see which one reproduces better the transition regime. For all the choices we tried, we verified that the decay terms in Eq. (E.16)-Eq. (E.18) play a very minor role, *i.e.* they give almost the same results as the fluid equations for stable massive neutrinos. This is not so surprising, given that these decay terms vanish both in the relativistic limit (for which  $w_i \simeq w_\nu \simeq c_g^2 \simeq 1/3$  and  $\bar{n}_\nu m_\nu \ll \bar{\rho}_\nu$ ) and in the non-relativistic one (for which  $w_i \simeq w_\nu \simeq c_g^2 \simeq 0$  and  $\bar{n}_\nu m_\nu \simeq \bar{\rho}_\nu$ ).

We would still need to relate the collision terms up to  $\ell_{\max} = 2$  in the Boltzmann hierarchy for the dark radiation daughter with  $\delta_\nu$ ,  $\theta_\nu$  and  $\sigma_\nu$ , and then set  $C_{\ell > \ell_{\max}} = 0$ .

The first three collision terms are (c.f. Eq. (4.34)-Eq. (4.37))

$$C_0 = \frac{4\pi a^2 \Gamma_\nu m_\nu}{\rho_c} \int dq q^2 \Delta f_{\nu,0}, \quad (\text{E.26})$$

$$C_1 = \frac{4\pi a^2 \Gamma_\nu m_\nu}{\rho_c} \int dq q^2 \frac{q}{\mathcal{E}_\nu} \Delta f_{\nu,1}, \quad (\text{E.27})$$

$$C_2 = \frac{4\pi a^2 \Gamma_\nu m_\nu}{\rho_c} \int dq q^2 \left[ \frac{5}{2} - \frac{3}{2} \frac{\mathcal{E}_\nu^2}{q^2} + \frac{3}{4} \frac{(\mathcal{E}_\nu^2 - q^2)^2}{\mathcal{E}_\nu q^3} \ln \left( \frac{\mathcal{E}_\nu + q}{\mathcal{E}_\nu - q} \right) \right] \Delta f_{\nu,2}. \quad (\text{E.28})$$

By looking at the asymptotic limits of Eq. (E.26) and Eq. (E.27), it's easy to see that they can be interpolated in the following manner:

$$C_0 = \frac{\alpha^5 \Gamma_\nu}{\rho_c} (1 - 3w_\delta) \bar{\rho}_\nu \delta_\nu, \quad (\text{E.29})$$

$$C_1 = \frac{\alpha^5 \Gamma_\nu}{\rho_c} (1 - 3w_\theta) \bar{\rho}_\nu (1 + w_\nu) \frac{\theta_\nu}{k}. \quad (\text{E.30})$$

Unfortunately, it's not so easy to relate  $C_2$  with the neutrino shear  $\sigma_\nu$ , given the complicated integrand appearing in Eq. (E.28). In addition, the fluid equations do not provide such a high gain in speed as compared to the decaying dark matter scenario, because **CLASS** implements an optimal momentum sampling that makes the resolution of the neutrino Boltzmann hierarchy in Eq. (E.12)-Eq. (E.13) very manageable. For these reasons, we don't use the fluid equations in our analysis. Nevertheless, Eq. (E.16)-Eq. (E.18) provide a first step to achieve a fluid description of the relativistic neutrino decay, for which the inverse decay terms cannot be neglected and would likely make the resolution of the full Boltzmann hierarchy computationally prohibitive.

## E.4 Excluding the relativistic decay regime from the MCMC analysis

In our baseline analysis, we have extrapolated our scans to the (mildly-)relativistic decay regime, despite the fact that the equations do not include inverse decays. We have then interpreted the bound on the sum of neutrino masses when considering non-relativistic decays as the intersect between the non-relativistic decay condition  $\Gamma_\nu > H(T_\nu = m_\nu/3)$  and the  $2\sigma$  limit derived from our analysis.

In this appendix, we investigate how excluding the relativistic decay regime of parameter space from the scan can affect the bounds on  $\sum m_\nu/\text{eV}$  and  $\text{Log}_{10}(\Gamma_\nu/[\text{km/s/Mpc}])$ . As we are interested in (semi-)relativistic decays, we focus on the parameter space  $\text{Log}_{10}(\Gamma_\nu/[\text{km/s/Mpc}]) \in [3, 6.5]$ . Our results are presented in Fig. E.1. In the 2D plane  $\{\text{Log}_{10}\Gamma_\nu, \sum m_\nu\}$  and below the non-relativistic line  $\Gamma_\nu = H(T_\nu = m_\nu/3)$ , we find that imposing the condition directly within the MCMC prior relaxes the bound by  $\sim 10 - 20\%$ . Nevertheless, after marginalizing over  $\text{Log}_{10}(\Gamma_\nu)$ , we find that the 'naive' bound coming from the intersect between the non-relativistic line ( $\Gamma_\nu > H(T_\nu = m_\nu/3)$ ) and the  $2\sigma$  limit without priors is in excellent agreement with that coming from imposing this condition as a prior in the analysis, both yielding  $\sum m_\nu < 0.42 \text{ eV}$ .



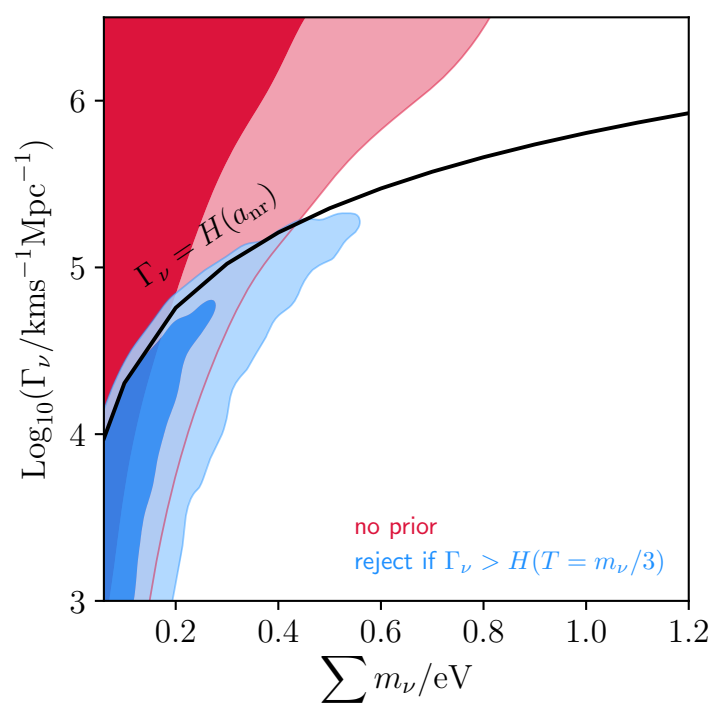


**Figure E.1** – Posterior distribution of  $\sum m_\nu$  and  $\text{Log}_{10}(\Gamma_\nu / [\text{km/s/Mpc}])$  when confronted to *Planck* 2018 + BAO + FS + Pantheon for two different choices of priors on  $\Gamma_\nu$  (see legend).

# F

---

## Résumé détaillé en français

---

### F.1 L'ère de la cosmologie de précision

La cosmologie est l'étude de l'évolution et des propriétés de l'univers dans son ensemble. Cette discipline scientifique aborde des questions aussi anciennes que l'humanité elle-même (c'est-à-dire "l'univers tel que nous le connaissons a-t-il existé depuis toujours ?" "quel est le destin ultime du cosmos ?"). Cependant, ce n'est qu'au début du 20<sup>e</sup> siècle qu'elle est devenue une science prédictive, lorsque la théorie de la relativité générale (RG) s'est imposée comme un cadre théorique solide pour décrire l'univers. Depuis lors, le domaine de la cosmologie n'a cessé d'évoluer, grâce à l'augmentation rapide de la quantité et de la précision des observations.

Au cours des deux dernières décennies, le modèle de cosmologie appelé  $\Lambda$  Cold Dark Matter ( $\Lambda$ CDM) est devenu un paradigme réussi pour expliquer plusieurs sondes indépendantes avec un degré de précision étonnant. Ce modèle suppose que l'univers est bien décrit par une métrique plate de Friedman-Lemaître-Robertson-Walker, et qu'il est principalement composé d'environ 5 % de matière ordinaire, 26 % de matière noire froide et 69 % d'énergie noire sous forme de une constante cosmologique  $\Lambda$ . Malheureusement, la nature de ses principaux constituants, la matière noire et l'énergie noire, reste encore un mystère. De plus, l'augmentation de la précision des données cosmologiques a récemment conduit à l'apparition de plusieurs divergences expérimentales entre les sondes de l'univers primordial et tardif. En particulier, il existe une tension de  $5\sigma$  dans la détermination du taux d'expansion actuel de l'univers (la constante de Hubble), et une tension de  $2 - 3\sigma$  dans la détermination de l'amplitude d'agglutination dans l'univers (décrite par le paramètre  $S_8$ ). Pour ces raisons, ces dernières années, il y a eu un intérêt croissant pour l'exploration de différentes extensions du modèle  $\Lambda$ CDM, qui pourraient donner des indices sur les composants sombres très mystérieux, et éventuellement offrir une explication aux divergences expérimentales susmentionnés.

D'autre part, la découverte des oscillations des neutrinos fournit des preuves solides de l'existence de masses de neutrinos minuscules mais non nulles, un phénomène qui ne peut pas être expliqué dans le cadre du modèle standard de la physique des particules. La cosmologie est actuellement la sonde la plus puissante des masses de neutrinos, et elle peut offrir des indices très précieux sur ses

propriétés.

Dans cette thèse, nous avons étudié en détail les implications cosmologiques de plusieurs extensions du paradigme  $\Lambda$ CDM. Dans la première partie, nous avons étudié deux modèles, l'énergie sombre précoce (EDE) et la matière noire instable (DDM), qui sont directement ciblés à expliquer les tensions de Hubble et  $S_8$ , respectivement. Dans la deuxième partie, nous avons analysé un autre scénario exotique motivé par le mystère de la masse des neutrinos, la désintégration des neutrinos, dont le formalisme est très similaire à celui de la matière noire instable.

Nous avons expliqué comment les mesures très précises des anisotropies du fond diffus cosmologique (CMB) jouent toujours un rôle central dans la définition de nouvelles contraintes robustes pour chacun de ces modèles. Pour rendre ce travail aussi autonome que possible, tout d'abord nous avons décrit les outils mathématiques et les observables les plus pertinents en cosmologie. Nous avons commencé par une courte introduction historique de la cosmologie moderne et une esquisse de les événements majeurs de l'histoire de l'univers. Ensuite, nous avons passé à la récapitulation du formalisme nécessaire pour comprendre les observables cosmologiques telles que l'anisotropie du fond diffus cosmologique et le spectre de puissance de la matière. Nous avons commencé par la description de l'univers homogène, et avons expliqué quelques concepts essentiels sur l'inflation. Plus tard, nous avons procédé à l'étude des écarts à l'équilibre en introduisant le formalisme de Boltzmann. Nous avons continué avec une présentation très détaillée de la théorie des perturbations linéaires. Dans la partie finale, nous avons discuté des défis les plus importants du modèle  $\Lambda$ CDM: la nature du secteur sombre et les tensions cosmologiques.

## F.2 Energie noire précoce et la tension $H_0$

Une composante constante d'énergie sombre précoce (EDE) contribuant à une fraction  $f_{\text{EDE}}(z_c) \sim 10\%$  de la densité d'énergie de l'univers autour de  $z_c \simeq 3500$  et se diluant au même rythme ou plus rapidement que le rayonnement par la suite, peut fournir une résolution simple à la tension de Hubble. Cependant, il a été souligné que l'inclusion de données de structure à grande échelle (LSS), qui sont en tension  $\sim 3\sigma$  avec les cosmologies  $\Lambda$ CDM et EDE, pourrait briser une certaine dégénérescence des paramètres et modifier ces conclusions. Nous réévaluons la viabilité de l'EDE en combinant les observations LSS des récentes enquêtes à faible lentille (WL) avec les données CMB, BAO, fonction de croissance (FS) et SNIa. Nos résultats peuvent être résumés comme suit :

1. Dans un modèle EDE phénoménologique à 3 paramètres (3pEDE), nous confirmons que [Planck18](#)+ BAO+FS+PANTHEON+SHOES favorisent  $f_{\text{EDE}}(z_c) \simeq 0.1 \pm 0.03$ ,  $z_c \simeq 4000_{-500}^{+1400}$  et  $\Theta_i = 2,6_{-0,03}^{+0,4}$ , avec un  $\Delta\chi^2 = -18,7$  par rapport à  $\Lambda$ CDM ajusté sur le même ensemble de données. L'inclusion des dernières données [Planck18](#) (et en particulier les mesures de polarisation plus précises) ne gêne pas le succès de la résolution EDE à la tension de Hubble.
2. Nous avons alors montré que *réduisant* l'espace des paramètres à un modèle EDE à 1 paramètre (1pEDE) en fixant  $\text{Log}_{10}(z_c)$  et  $\Theta_i$  à leurs meilleures valeurs d'ajustement tel qu'obtenu à partir d'une analyse de [Planck18](#) données

uniquement – qui coïncide de manière frappante avec celles de l’analyse combinée avec SHOES – conduit à une préférence  $\sim 2\sigma$  pour l’EDE non nul, à savoir  $f_{\text{EDE}}(z_c) \simeq 0.08 \pm 0.04$  à partir des données [Planck18](#) CMB seules. Dans cette cosmologie, le  $H_0 \simeq 70 \pm 1.5$  km/s/Mpc inféré est en accord à mieux que  $2\sigma$  avec sa mesure locale de SHOES. L’ajout des données BAO, FS et PANTHEON n’a pas d’impact significatif sur le résultat.

3. Pour justifier l’inclusion des données LSS dans nos analyses, nous avons confronté le spectre de puissance de la matière non linéaire EDE tel que prédit par des algorithmes semi-analytiques standard à un ensemble dédié de simulations  $N$ -corps. Nous avons ensuite testé la cosmologie 1pEDE par rapport aux données WL, constatant qu’elle n’aggrave pas de manière significative l’ajustement aux mesures  $S_8$  par rapport à  $\Lambda$ CDM, et que les observations WL actuelles n’excluent pas la résolution EDE à la tension de Hubble.
4. Nous mettons également en garde contre l’interprétation des contraintes obtenues en combinant [Planck18](#) avec KiDS-VIKING+DES. Comme nous l’avons montré, la cosmologie de « compromis » obtenue est un mauvais ajustement à KiDS-VIKING+DES et dégrade l’ajustement aux données de [Planck18](#), même en  $\Lambda$ CDM. Cela illustre que ces ensembles de données sont statistiquement incohérents dans un cadre  $\Lambda$ CDM, et il est facilement concevable que la résolution de cette tension se situe ailleurs (qu’il s’agisse d’un effet systématique ou d’une nouvelle physique).
5. À la lumière de l’anomalie  $A_{\text{lens}}$  du CMB, nous avons montré que les données CMB marginalisées par  $A_{\text{lens}}$  favorisent l’EDE non nul à  $\sim 2\sigma$ , prédisent  $H_0$  en accord  $1,4\sigma$  avec SHOES et  $S_8$  en  $1.5\sigma$  et  $0.8\sigma$  concordent respectivement avec KiDS-VIKING et DES. Il existe cependant toujours une tension  $\sim 2.5\sigma$  avec les résultats conjoints de KiDS-VIKING et DES. De plus, la présence d’EDE n’affecte pas la quantité de lentilles anormales.

Dans la deuxième partie de ce travail, nous avons utilisé une méthodologie commune pour comparer et contraster le succès relatif de dix-sept modèles (y compris EDE) proposés pour atténuer la tension de Hubble; cette approche se veut donc une juste comparaison entre les solutions proposées, et fournit un repère utile pour ceux qui souhaitent proposer des idéaux nouveaux. Nous avons réparti les différents modèles en trois catégories génériques: ceux qui modifient l’horizon sonore en incluant une composante de rayonnement sombre (DR) impactant l’histoire de l’expansion précoce, les solutions qui modifient l’horizon sonore par un autre mécanisme (tel qu’un retard de recombinaison ou une certaine contribution à l’expansion avant la recombinaison), et des solutions qui tentent de modifier l’histoire de l’expansion tardive.

Pour chaque modèle et ensemble de données, nous quantifions la tension résiduelle à l’aide d’une série de mesures, chacune présentant à la fois des avantages et des inconvénients, et en essayant de répondre à des questions légèrement différentes, à savoir : étant donné un modèle, (i) dans quelle mesure la confrontation avec des données (autres que SHOES) génèrent des distributions a posteriori compatibles avec des valeurs élevées de  $H_0$ , (ii) dans quelle mesure peut-on obtenir un bon ajustement combiné à toutes les données, et (iii) dans quelle mesure ce modèle est-il préféré à  $\Lambda$ CDM ? Le résumé de nos conclusions est qu’aucun modèle ne fonctionne parfaitement bien dans tous nos tests – tous les modèles se retrouvent avec une

tension résiduelle, le plus prometteur réduisant la tension au niveau  $\sim 1,6\sigma$ , et avec très peu modèles réduisant réellement la tension en dessous de  $3\sigma$ . De même, seul un petit sous-ensemble de modèles est capable d'améliorer suffisamment l'ajustement pour réussir le test AIC. Six modèles, EDE, NEDE, EMG, varying  $m_e$  (avec et sans courbure), et le Majoron, sont capables de satisfaire simultanément les critères  $Q_{\text{DMAP}}$  et  $\Delta\text{AIC}$ . De plus, seul le varying  $m_e$  (avec et sans courbure) passe le critère gaussien et permet un haut  $H_0$  (ou  $M_B$ ) sans SHOES préalable, recevant la seule "médaille d'or" de notre tournoi.

De plus, nous notons qu'en dehors de l'EDE, aucun des modèles d'intérêt n'atténue (ni n'exacerbe) la tension  $S_8$ . Certains modèles qui avaient précédemment montré un certain succès dans la réduction de la tension  $S_8$ , à savoir DM-DR et les neutrinos à forte interaction, sont maintenant défavorisés par les données. Trouver une résolution commune aux deux tensions renforcerait certainement le degré de croyance dans la nouvelle cosmologie de la concordance; cependant, nous réitérons que la résolution de ces tensions pourrait provenir de secteurs indépendants - soit de la nouvelle physique, soit des erreurs systématiques. Nous concluons que certains des modèles présentés dans ce travail peuvent fournir un bon ajustement combiné à toutes les données considérées (y compris SHOES), démontrant qu'il existe au moins des solutions potentielles à la tension  $H_0$ , mais il reste encore de nombreuses difficultés à surmonter dans la construction du modèle et dans l'explication de la tension  $S_8$  croissante. Des travaux supplémentaires doivent être effectués pour établir si ces problèmes théoriques et observationnels restants peuvent être surmontés dans une nouvelle cosmologie concordante, qui peut soit s'appuyer sur les modèles étudiés ici, soit peut-être se situer dans une direction encore inexplorée.

### F.3 Matière noire instable et la tension $S_8$

Dans ce travail, nous avons réalisé une étude cosmologique complète du scénario de désintégration de la matière noire froide (CDM) à 2 corps appelé 'ADDM', dans lequel les désintégrations sont caractérisées à la fois par le taux de désintégration  $\Gamma$  et la fraction d'énergie convertie en rayonnement  $\varepsilon$ , incluant pour la première fois un traitement totalement cohérent des perturbations linéaires de la composante fille tiède (WDM). À cette fin, nous avons utilisé un nouveau schéma d'approximation, qui permet de calculer avec précision et rapidité la dynamique des perturbations linéaires de la WDM en traitant l'espèce WDM comme un fluide visqueux. Proche des valeurs les mieux ajustées, notre schéma d'approximation est précis au niveau  $\mathcal{O}(0,1\%)$  dans les spectres de puissance de CMB et  $\mathcal{O}(1\%)$  dans le spectre linéaire de puissance de la matière. Nous avons ensuite discuté en détail la dynamique des perturbations linéaires des particules mères et filles, ainsi que les effets physiques du modèle ADDM sur les spectres de puissance du CMB et de la matière.

Dans une deuxième partie, nous avons effectué un ensemble d'analyses MCMC du modèle ADDM par rapport à une suite d'ensembles de données à jour à faible et à haut décalage vers le rouge. Nous avons comparé les contraintes obtenues à partir des données BAO et SNIa, donc uniquement basées sur les effets de fond, à celles obtenues à partir du jeu de données complet *Planck*, qui nécessite plutôt une description précise des perturbations linéaires WDM. Nous constatons que les données CMB *Planck* contraignent le modèle ADDM  $\sim 1$  ordre de grandeur mieux que

les données BAO+SNIa actuelles. Cependant, nous montrons également que malgré ces contraintes, le modèle  $\Lambda$ DDM offre une possibilité prometteuse pour résoudre la tension  $S_8$ .

Nous avons ensuite testé la robustesse de la résolution de  $\Lambda$ DDM à la tension  $S_8$  à un certain nombre de changements dans l'analyse. Nous montrons que la légère préférence pour le modèle  $\Lambda$ DDM par rapport à  $\Lambda$ CDM est liée à la valeur  $S_8$  choisie dans l'analyse. Concrètement, la valeur  $S_8$  de l'analyse KiDS+Viking+DES, qui a un niveau de tension plus élevé avec la prédiction *Planck*  $\Lambda$ CDM que la valeur de référence KiDS+BOSS+2dFLens, conduit à une préférence plus forte en faveur du modèle  $\Lambda$ DDM. Cependant, le résultat DES uniquement, qui est raisonnablement en accord avec *Planck*, conduit à une préférence plus faible pour le modèle  $\Lambda$ DDM. De même, une fois marginalisé sur les informations de lentille dans *Planck* via le paramètre  $A_{\text{lens}}$ , ou lors de l'échange des spectres de puissance TE,EE  $\ell$  élevés *Planck* contre les spectres SPTpol, la préférence pour le modèle  $\Lambda$ DDM diminue. En effet, dans ces deux cas, le modèle inféré  $\Lambda$ CDM a une valeur  $S_8$  plus petite, montrant moins de tension avec les enquêtes à faible lentille. Cela indique que si la tension  $S_8$  finit par provenir d'une systématique inconnue dans les enquêtes à faible lentille ou dans les données *Planck*, la préférence pour le modèle  $\Lambda$ DDM disparaîtra probablement. D'un autre côté, en combinant *Planck* avec ACTPol, la légère préférence pour  $\Lambda$ DDM augmente, et la 'tension' restante avec  $S_8$  n'est plus que  $\sim 1.3\sigma$ .

Nous avons également testé la possibilité intrigante que le récent excès de Xenon1T soit dû au modèle  $\Lambda$ DDM. À cette fin, nous avons effectué une analyse MCMC supplémentaire fixant  $\varepsilon = 0.05$  comme requis par Xenon1T. Nous constatons qu'il est facile de résoudre la tension  $S_8$  dans ce cas, indiquant une durée de vie DCDM de  $\text{Log}_{10}(\Gamma/[\text{Gyr}^{-1}]) = -2.72^{+0.61}_{-0.21}$ . Fait intéressant, cela se fait au prix d'une dégradation très mineure de l'ajustement *Planck* ( $\Delta\chi^2 \simeq +1.7$ ), indiquant que les données *Planck*, BAO et SNIa sont en bon accord avec ce modèle. Enfin, en effectuant une analyse où nous introduisons artificiellement un signal DDM dans un ensemble de données CMB fictives, nous démontrons explicitement que, même si les données CMB actuelles ne sont pas suffisamment sensibles pour faire la distinction entre CDM standard et DDM, les expériences CMB de nouvelle génération (CMB-S4) pourront détecter sans ambiguïté sa signature.

## F.4 Nouvelles contraintes sur la masse et la durée de vie des neutrinos

Les observations cosmologiques sont connues pour imposer les contraintes les plus fortes sur la somme des masses des neutrinos. Pourtant, les contraintes liées aux mesures CMB et LSS, qui supposent que les neutrinos sont stables, est considérablement affaiblie si les neutrinos se désintègrent. Dans ce travail, nous fournissons des limites à jour sur la durée de vie des neutrinos massifs qui se désintègrent en rayonnement sombre après être devenus non-relativistes, à partir d'une combinaison de mesures de CMB, BAO, de facteurs de croissance et de données Pantheon SNIa.

Par rapport à l'analyse précédente dans C19, nous avons incorporé des corrections d'ordre supérieur jusqu'à  $\mathcal{O}((T_{\text{dec}}/m_\nu)^3)$  lors de la résolution des perturbations

de rayonnement sombre, et a également effectué le calcul complet de la densité d'énergie moyenne du neutrino instable. Le traitement plus précis des équations de Boltzmann et de l'évolution de l'énergie moyenne dans notre étude MCMC améliore la couverture du cas où les neutrinos se désintègrent tôt de sorte que leurs impulsions moyennes sont proches de leurs masses. Si les neutrinos se désintègrent lorsqu'ils ont  $T_\nu \ll m_\nu/3$ , l'inclusion de perturbations de moment plus élevées  $C_{\ell \geq 2}$  donne un changement négligeable au spectre de puissance par rapport aux incertitudes expérimentales. Cependant, le calcul complet de l'énergie du neutrino améliore considérablement la prédiction du spectre de puissance à partir du résultat approximatif lorsque les désintégrations se produisent de manière semi-relativiste. Néanmoins, nous avons trouvé que les contraintes de [Planck15](#), étant donné leur précision limitée, ne sont pas affectées par ces considérations. Cependant, nous prévoyons que ces effets seront pertinents pour les expériences futures (ainsi qu'une contribution essentielle dans le cas relativiste, à considérer dans le futur).

En fait, nous avons montré que l'essentiel de l'amélioration du pouvoir contraignant par rapport à [C19](#) provient de l'utilisation des données de [Planck18](#). En effet, nous avons démontré que la mesure améliorée de  $\tau_{\text{reio}}$  à partir des données de polarisation à faible  $\ell$  aide à briser la dégénérescence de l'amplitude du spectre de puissance CMB et renforce la limite sur la masse et la durée de vie des neutrinos. En conséquence, nous avons constaté que les neutrinos avec  $\sum m_\nu > 0,42$  eV ( $2\sigma$ ) ne peuvent pas être rendus cohérents avec les données cosmologiques s'ils se désintègrent alors qu'ils ne sont pas relativistes, une amélioration significative par rapport AUX données de [Planck15](#) pour lesquelles des masses aussi élevées que  $\sum m_\nu \sim 0,9$  eV étaient cohérentes avec le scénario de désintégration non-relativiste ([C19](#)).

Nous avons soutenu qu'une application notable de ce résultat est que, si l'expérience KATRIN détecte un neutrino électronique avec  $m_\nu 0,2$  eV (la sensibilité prédite), notre résultat contraindra  $\Gamma_\nu \gtrsim 10^{5.5}$  km/s/Mpc, *i.e.* les neutrinos auraient besoin de se désintégrer entre  $z \approx 2 \times 10^2 - 4 \times 10^3$ , alors qu'ils sont encore relativistes, de sorte que nos bornes et les bornes étudiées dans [B20](#) ne s'appliqueraient pas. Dans le cas d'une découverte massive de neutrinos à KATRIN, une analyse plus complexe comprenant des désintégrations inverses serait nécessaire pour confirmer fermement que le scénario de désintégration peut concilier les mesures de laboratoire et cosmologiques.



# Bibliography

- [1] H. S. LEAVITT y E. C. PICKERING. "Periods of 25 Variable Stars in the Small Magellanic Cloud". *Harvard Obs. Circ.* 173 (1912), pp. 1–3 [p. 103].
- [2] V. M. SLIPHER. "Spectrographic Observations of Nebulae". *Popular Astronomy* 23 (1915), pp. 21–24 [p. 3].
- [3] A. EINSTEIN. "Cosmological Considerations in the General Theory of Relativity". *Sitzungsber. Preuss. Akad. Wiss. Berlin (Math. Phys. )* (1917), pp. 142–152 [p. 3].
- [4] T. KALUZA. "Zum Unitätsproblem der Physik". *Sitzungsber. Preuss. Akad. Wiss. Berlin (Math. Phys. )* 1921 (1921), pp. 966–972. DOI: [10.1142/S0218271818700017](https://doi.org/10.1142/S0218271818700017). arXiv: [1803.08616](https://arxiv.org/abs/1803.08616) [physics.hist-ph] [p. 88].
- [5] A. FRIEDMANN. "Über die Krümmung des Raumes". *Zeitschrift für Physik* 10 (1922), pp. 377–386 [p. 3].
- [6] O. KLEIN. "Quantum Theory and Five-Dimensional Theory of Relativity. (In German and English)". *Z. Phys.* 37 (1926). Ed. by J. C. TAYLOR, pp. 895–906. DOI: [10.1007/BF01397481](https://doi.org/10.1007/BF01397481) [p. 88].
- [7] G. LEMAÎTRE. "Un univers homogène de masse constante et de rayon croissant rendant compte de la vitesse radiale des nébuleuses extra-galactiques". *Annales de la Société scientifique de Bruxelles* 47 (1927), pp. 49–59 [p. 3].
- [8] E. HUBBLE. "A relation between distance and radial velocity among extra-galactic nebulae". *Proceedings of the National Academy of Sciences* 15 (1929), pp. 168–173. DOI: [10.1073/pnas.15.3.168](https://doi.org/10.1073/pnas.15.3.168) [pp. 3, 4].
- [9] A. S. EDDINGTON. "On the Instability of Einstein's Spherical World". *Monthly Notices of the Royal Astronomical Society* 90 (1930), pp. 668–678 [p. 4].
- [10] A. EINSTEIN y W. de SITTER. "On the Relation between the Expansion and the Mean Density of the Universe". *Proceedings of the National Academy of Sciences* 18 (1932), pp. 213–214. DOI: [10.1073/pnas.18.3.213](https://doi.org/10.1073/pnas.18.3.213) [p. 5].
- [11] F. ZWICKY. "Die Rotverschiebung von extragalaktischen Nebeln". *Helvetica Physica Acta* 6 (1933), pp. 110–127 [p. 5].
- [12] E. LIFSHITZ. "Republication of: On the gravitational stability of the expanding universe". *J. Phys. (USSR)* 10.2 (1946), p. 116. DOI: [10.1007/s10714-016-2165-8](https://doi.org/10.1007/s10714-016-2165-8) [p. 48].
- [13] R. A. ALPHER, H. BETHE y G. GAMOW. "The origin of chemical elements". *Physical Review* 73 (1948), pp. 803–804. DOI: [10.1103/PhysRev.73.803](https://doi.org/10.1103/PhysRev.73.803) [p. 4].
- [14] B. PONTECORVO. "Inverse beta processes and nonconservation of lepton charge". *Zh. Eksp. Teor. Fiz.* 34 (1957), p. 247 [p. 178].
- [15] C. BRANS y R. H. DICKE. "Mach's principle and a relativistic theory of gravitation". *Phys. Rev.* 124 (1961). Ed. by J.-P. HSU y D. FINE, pp. 925–935. DOI: [10.1103/PhysRev.124.925](https://doi.org/10.1103/PhysRev.124.925) [p. 91].
- [16] H. JEFFREYS. *Theory of Probability*. Third. Oxford, 1961 [pp. 130, 160, 225].
- [17] J. E. GUNN y B. A. PETERSON. "On the Density of Neutral Hydrogen in Intergalactic Space". *Astrophys. J.* 142 (1965), p. 1633. DOI: [10.1086/148444](https://doi.org/10.1086/148444) [p. 41].
- [18] R. K. SACHS y A. M. WOLFE. "Perturbations of a cosmological model and angular variations of the microwave background". *Astrophys. J.* 147 (1967), pp. 73–90. DOI: [10.1007/s10714-007-0448-9](https://doi.org/10.1007/s10714-007-0448-9) [p. 72].
- [19] R. V. WAGONER, W. A. FOWLER y F. HOYLE. "On the Synthesis of elements at very high temperatures". *Astrophys. J.* 148 (1967), pp. 3–49. DOI: [10.1086/149126](https://doi.org/10.1086/149126) [p. 33].

- [20] Y. B. ZEL'DOVICH e I. D. NOVIKOV. "The Hypothesis of Cores Retarded during Expansion and the Hot Cosmological Model". *Soviet Astron. AJ (Engl. Transl. )*, 10 (1967), p. 602 [p. 90].
- [21] P. J. E. PEEBLES. "Recombination of the Primeval Plasma". *Astrophysical Journal* 153 (1968), p. 1 [p. 38].
- [22] J. SILK. "Cosmic black body radiation and galaxy formation". *Astrophys. J.* 151 (1968), pp. 459–471. DOI: [10.1086/149449](https://doi.org/10.1086/149449) [p. 65].
- [23] Y. B. ZELDOVICH, V. G. KURT y R. A. SYUNYAEV. "Recombination of Hydrogen in the Hot Model of the Universe". *Zhurnal Eksperimentalnoi i Teoreticheskoi Fiziki* 55 (1968), pp. 278–286 [p. 38].
- [24] V. C. RUBIN y J. FORD W. Kent. "Rotation of the Andromeda Nebula from a Spectroscopic Survey of Emission Regions". *Astrophysical Journal* 159 (1970), p. 379. DOI: [10.1086/150317](https://doi.org/10.1086/150317) [p. 5].
- [25] S. HAWKING. "Gravitationally collapsed objects of very low mass". *Mon. Not. Roy. Astron. Soc.* 152 (1971), p. 75 [p. 90].
- [26] D. LOVELOCK. "The Einstein tensor and its generalizations". *J. Math. Phys.* 12 (1971), pp. 498–501. DOI: [10.1063/1.1665613](https://doi.org/10.1063/1.1665613) [p. 90].
- [27] B. J. CARR y S. W. HAWKING. "Black holes in the early Universe". *Mon. Not. Roy. Astron. Soc.* 168 (1974), pp. 399–415 [p. 90].
- [28] G. W. HORNDESKI. "Second-order scalar-tensor field equations in a four-dimensional space". *Int. J. Theor. Phys.* 10 (1974), pp. 363–384. DOI: [10.1007/BF01807638](https://doi.org/10.1007/BF01807638) [p. 91].
- [29] P. MESZAROS. "The behaviour of point masses in an expanding cosmological substratum". *Astron. Astrophys.* 37 (1974), pp. 225–228 [p. 80].
- [30] F. JAMES y M. ROOS. "Minuit: A System for Function Minimization and Analysis of the Parameter Errors and Correlations". *Comput. Phys. Commun.* 10 (1975), pp. 343–367. DOI: [10.1016/0010-4655\(75\)90039-9](https://doi.org/10.1016/0010-4655(75)90039-9) [pp. 110, 156, 227, 246].
- [31] B. W. LEE y S. WEINBERG. "Cosmological Lower Bound on Heavy Neutrino Masses". *Phys. Rev. Lett.* 39 (1977). Ed. by M. A. SREDNICKI, pp. 165–168. DOI: [10.1103/PhysRevLett.39.165](https://doi.org/10.1103/PhysRevLett.39.165) [p. 88].
- [32] R. D. PECCEI y H. R. QUINN. "CP Conservation in the Presence of Instantons". *Phys. Rev. Lett.* 38 (1977), pp. 1440–1443. DOI: [10.1103/PhysRevLett.38.1440](https://doi.org/10.1103/PhysRevLett.38.1440) [p. 89].
- [33] S. WEINBERG. "A New Light Boson?" *Phys. Rev. Lett.* 40 (1978), pp. 223–226. DOI: [10.1103/PhysRevLett.40.223](https://doi.org/10.1103/PhysRevLett.40.223) [p. 89].
- [34] F. WILCZEK. "Problem of Strong  $P$  and  $T$  Invariance in the Presence of Instantons". *Phys. Rev. Lett.* 40 (1978), pp. 279–282. DOI: [10.1103/PhysRevLett.40.279](https://doi.org/10.1103/PhysRevLett.40.279) [p. 89].
- [35] L. WOLFENSTEIN. "Neutrino Oscillations in Matter". *Phys. Rev. D* 17 (1978), pp. 2369–2374. DOI: [10.1103/PhysRevD.17.2369](https://doi.org/10.1103/PhysRevD.17.2369) [p. 180].
- [36] A. A. STAROBINSKY. "Spectrum of relict gravitational radiation and the early state of the universe". *JETP Lett.* 30 (1979). Ed. by I. M. KHALATNIKOV y V. P. MINEEV, pp. 682–685 [p. 76].
- [37] J. M. BARDEEN. "Gauge-invariant cosmological perturbations". *Physical Review D* 22 (1980), pp. 1882–1905 [p. 44].
- [38] J. R. BOND, G. EFSTATHIOU y J. SILK. "Massive Neutrinos and the Large Scale Structure of the Universe". *Phys. Rev. Lett.* 45 (1980). Ed. by M. A. SREDNICKI, pp. 1980–1984. DOI: [10.1103/PhysRevLett.45.1980](https://doi.org/10.1103/PhysRevLett.45.1980) [p. 176].
- [39] A. H. GUTH. "The Inflationary Universe: A Possible Solution to the Horizon and Flatness Problems". *Phys. Rev. D* 23 (1981). Ed. by L.-Z. FANG y R. RUFFINI, pp. 347–356. DOI: [10.1103/PhysRevD.23.347](https://doi.org/10.1103/PhysRevD.23.347) [p. 20].
- [40] S. P. MIKHEYEV y A. Y. SMIRNOV. "Resonance Amplification of Oscillations in Matter and Spectroscopy of Solar Neutrinos". *Sov. J. Nucl. Phys.* 42 (1985), pp. 913–917 [p. 180].
- [41] N. KAISER. "Clustering in real space and in redshift space". *Mon. Not. Roy. Astron. Soc.* 227 (1987), pp. 1–27 [p. 87].
- [42] J. BERNSTEIN. *Kinetic Theory in the Expanding Universe*. Cambridge University Press, 1988 [p. 25].
- [43] J. A. FRIEMAN, H. E. HABER y K. FREESE. "Neutrino Mixing, Decays and Supernova Sn1987a". *Phys. Lett. B* 200 (1988), pp. 115–121. DOI: [10.1016/0370-2693\(88\)91120-3](https://doi.org/10.1016/0370-2693(88)91120-3) [p. 177].

- 
- [44] B. RATRA y P. J. E. PEEBLES. "Cosmological Consequences of a Rolling Homogeneous Scalar Field". *Phys. Rev. D* 37 (1988), p. 3406. DOI: [10.1103/PhysRevD.37.3406](https://doi.org/10.1103/PhysRevD.37.3406) [p. 90].
- [45] J. M. STEWART. "Perturbations of Friedmann-Robertson-Walker cosmological models". *Class. Quant. Grav.* 7 (1990), pp. 1169–1180. DOI: [10.1088/0264-9381/7/7/013](https://doi.org/10.1088/0264-9381/7/7/013) [p. 44].
- [46] V. BEREZINSKY, A. MASIERO y J. W. F. VALLE. "Cosmological signatures of supersymmetry with spontaneously broken R-parity". *Phys. Lett. B* 266 (1991), pp. 382–388. DOI: [10.1016/0370-2693\(91\)91055-z](https://doi.org/10.1016/0370-2693(91)91055-z) [p. 140].
- [47] A. GELMAN y D. B. RUBIN. "Inference from Iterative Simulation Using Multiple Sequences". *Statist. Sci.* 7 (1992), pp. 457–472. DOI: [10.1214/ss/1177011136](https://doi.org/10.1214/ss/1177011136) [pp. 110, 156, 193].
- [48] V. BEREZINSKY y J. W. F. VALLE. "The KeV majoron as a dark matter particle". *Phys. Lett. B* 318 (1993), pp. 360–366. DOI: [10.1016/0370-2693\(93\)90140-D](https://doi.org/10.1016/0370-2693(93)90140-D). arXiv: [hep-ph/9309214](https://arxiv.org/abs/hep-ph/9309214) [p. 140].
- [49] M. S. SMITH, L. H. KAWANO y R. A. MALANEY. "Experimental, computational, and observational analysis of primordial nucleosynthesis". *Astrophys. J. Suppl.* 85 (1993), pp. 219–247. DOI: [10.1086/191763](https://doi.org/10.1086/191763) [p. 33].
- [50] R. E. KASS y A. E. RAFTERY. "Bayes Factors". *J. Am. Statist. Assoc.* 90.430 (1995), pp. 773–795. DOI: [10.1080/01621459.1995.10476572](https://doi.org/10.1080/01621459.1995.10476572) [p. 130].
- [51] C.-P. MA y E. BERTSCHINGER. "Cosmological perturbation theory in the synchronous and conformal Newtonian gauges". *Astrophys. J.* 455 (1995), pp. 7–25. DOI: [10.1086/176550](https://doi.org/10.1086/176550). arXiv: [astro-ph/9506072](https://arxiv.org/abs/astro-ph/9506072) [pp. 53, 54, 147, 239].
- [52] M. E. PESKIN y D. V. SCHROEDER. *An Introduction to quantum field theory*. Addison-Wesley, 1995. ISBN: 978-0-201-50397-5 [p. 210].
- [53] M. ZALDARRIAGA y D. D. HARARI. "Analytic approach to the polarization of the cosmic microwave background in flat and open universes". *Phys. Rev. D* 52 (1995), pp. 3276–3287. DOI: [10.1103/PhysRevD.52.3276](https://doi.org/10.1103/PhysRevD.52.3276). arXiv: [astro-ph/9504085](https://arxiv.org/abs/astro-ph/9504085) [p. 70].
- [54] R. M. BARNETT et al. "Review of particle physics. Particle Data Group". *Phys. Rev. D* 54 (1996), pp. 1–720. DOI: [10.1103/PhysRevD.54.1](https://doi.org/10.1103/PhysRevD.54.1) [pp. 236, 251].
- [55] G. JUNGMAN, M. KAMIONKOWSKI y K. GRIEST. "Supersymmetric dark matter". *Phys. Rept.* 267 (1996), pp. 195–373. DOI: [10.1016/0370-1573\(95\)00058-5](https://doi.org/10.1016/0370-1573(95)00058-5). arXiv: [hep-ph/9506380](https://arxiv.org/abs/hep-ph/9506380) [p. 88].
- [56] W. HU y M. J. WHITE. "The Damping tail of CMB anisotropies". *Astrophys. J.* 479 (1997), p. 568. DOI: [10.1086/303928](https://doi.org/10.1086/303928). arXiv: [astro-ph/9609079](https://arxiv.org/abs/astro-ph/9609079) [p. 65].
- [57] D. J. EISENSTEIN y W. HU. "Baryonic features in the matter transfer function". *Astrophys. J.* 496 (1998), p. 605. DOI: [10.1086/305424](https://doi.org/10.1086/305424). arXiv: [astro-ph/9709112](https://arxiv.org/abs/astro-ph/9709112) [pp. 81, 83].
- [58] W. HU, D. J. EISENSTEIN y M. TEGMARK. "Weighing neutrinos with galaxy surveys". *Phys. Rev. Lett.* 80 (1998), pp. 5255–5258. DOI: [10.1103/PhysRevLett.80.5255](https://doi.org/10.1103/PhysRevLett.80.5255). arXiv: [astro-ph/9712057](https://arxiv.org/abs/astro-ph/9712057) [pp. 176, 191].
- [59] A. G. RIESS et al. "Observational evidence from supernovae for an accelerating universe and a cosmological constant". *The Astronomical Journal* 116 (1998), pp. 1009–1038. DOI: [10.1086/300499](https://doi.org/10.1086/300499). arXiv: [astro-ph/9805201](https://arxiv.org/abs/astro-ph/9805201) [pp. 6, 7].
- [60] L. COVI, J. E. KIM y L. ROSZKOWSKI. "Axinos as cold dark matter". *Phys. Rev. Lett.* 82 (1999), pp. 4180–4183. DOI: [10.1103/PhysRevLett.82.4180](https://doi.org/10.1103/PhysRevLett.82.4180). arXiv: [hep-ph/9905212](https://arxiv.org/abs/hep-ph/9905212) [p. 140].
- [61] S. PERLMUTTER et al. "Measurements of  $\Omega$  and  $\Lambda$  from 42 high redshift supernovae". *Astrophysical Journal* 517 (1999), pp. 565–586. DOI: [10.1086/307221](https://doi.org/10.1086/307221). arXiv: [astro-ph/9812133](https://arxiv.org/abs/astro-ph/9812133) [p. 6].
- [62] L. RANDALL y R. SUNDRUM. "A Large mass hierarchy from a small extra dimension". *Phys. Rev. Lett.* 83 (1999), pp. 3370–3373. DOI: [10.1103/PhysRevLett.83.3370](https://doi.org/10.1103/PhysRevLett.83.3370). arXiv: [hep-ph/9905221](https://arxiv.org/abs/hep-ph/9905221) [p. 88].
- [63] S. SEAGER, D. D. SASSELOV y D. SCOTT. "A new calculation of the recombination epoch". *Astrophys. J. Lett.* 523 (1999), pp. L1–L5. DOI: [10.1086/312250](https://doi.org/10.1086/312250). arXiv: [astro-ph/9909275](https://arxiv.org/abs/astro-ph/9909275) [p. 40].
- [64] G. R. DVALI, G. GABADADZE y M. PORRATI. "4-D gravity on a brane in 5-D Minkowski space". *Phys. Lett. B* 485 (2000), pp. 208–214. DOI: [10.1016/S0370-2693\(00\)00669-9](https://doi.org/10.1016/S0370-2693(00)00669-9). arXiv: [hep-th/0005016](https://arxiv.org/abs/hep-th/0005016) [p. 91].
- [65] A. LEWIS, A. CHALLINOR y A. LASENBY. "Efficient computation of CMB anisotropies in closed FRW models". *Astrophys. J.* 538 (2000), pp. 473–476. DOI: [10.1086/309179](https://doi.org/10.1086/309179). arXiv: [astro-ph/9911177](https://arxiv.org/abs/astro-ph/9911177) [p. 101].

- [66] T. APPELQUIST, H.-C. CHENG y B. A. DOBRESU. "Bounds on universal extra dimensions". *Phys. Rev. D* 64 (2001), p. 035002. DOI: [10.1103/PhysRevD.64.035002](https://doi.org/10.1103/PhysRevD.64.035002). arXiv: [hep-ph/0012100](https://arxiv.org/abs/hep-ph/0012100) [p. 89].
- [67] M. CHEVALLIER y D. POLARSKI. "Accelerating universes with scaling dark matter". *Int. J. Mod. Phys. D* 10 (2001), pp. 213–224. DOI: [10.1142/S0218271801000822](https://doi.org/10.1142/S0218271801000822). arXiv: [gr-qc/0009008](https://arxiv.org/abs/gr-qc/0009008) [p. 128].
- [68] S. HANNESTAD. "On the Coupling between different species during recombination". *New Astron.* 6 (2001), p. 17. DOI: [10.1016/S1384-1076\(01\)00038-0](https://doi.org/10.1016/S1384-1076(01)00038-0). arXiv: [astro-ph/0008452](https://arxiv.org/abs/astro-ph/0008452) [p. 55].
- [69] W. B. LIN et al. "Nonthermal production of WIMPs and the subgalactic structure of the universe". *Phys. Rev. Lett.* 86 (2001), p. 954. DOI: [10.1103/PhysRevLett.86.954](https://doi.org/10.1103/PhysRevLett.86.954). arXiv: [astro-ph/0009003](https://arxiv.org/abs/astro-ph/0009003) [p. 140].
- [70] V. SPRINGEL et al. "Populating a cluster of galaxies. 1. Results at  $z = 0$ ". *Mon. Not. Roy. Astron. Soc.* 328 (2001), p. 726. DOI: [10.1046/j.1365-8711.2001.04912.x](https://doi.org/10.1046/j.1365-8711.2001.04912.x). arXiv: [astro-ph/0012055](https://arxiv.org/abs/astro-ph/0012055) [pp. 85, 116].
- [71] J. F. BEACOM y N. F. BELL. "Do Solar Neutrinos Decay?" *Phys. Rev. D* 65 (2002), p. 113009. DOI: [10.1103/PhysRevD.65.113009](https://doi.org/10.1103/PhysRevD.65.113009). arXiv: [hep-ph/0204111](https://arxiv.org/abs/hep-ph/0204111) [p. 177].
- [72] R. R. CALDWELL. "A Phantom menace?" *Phys. Lett. B* 545 (2002), pp. 23–29. DOI: [10.1016/S0370-2693\(02\)02589-3](https://doi.org/10.1016/S0370-2693(02)02589-3). arXiv: [astro-ph/9908168](https://arxiv.org/abs/astro-ph/9908168) [p. 91].
- [73] A. S. JOSHIPURA, E. MASSO y S. MOHANTY. "Constraints on decay plus oscillation solutions of the solar neutrino problem". *Phys. Rev. D* 66 (2002), p. 113008. DOI: [10.1103/PhysRevD.66.113008](https://doi.org/10.1103/PhysRevD.66.113008). arXiv: [hep-ph/0203181](https://arxiv.org/abs/hep-ph/0203181) [p. 177].
- [74] H.-B. KIM y J. E. KIM. "Late decaying axino as CDM and its lifetime bound". *Phys. Lett. B* 527 (2002), pp. 18–22. DOI: [10.1016/S0370-2693\(01\)01507-6](https://doi.org/10.1016/S0370-2693(01)01507-6). arXiv: [hep-ph/0108101](https://arxiv.org/abs/hep-ph/0108101) [p. 140].
- [75] S. WEINBERG. "Cosmological fluctuations of short wavelength". *Astrophys. J.* 581 (2002), pp. 810–816. DOI: [10.1086/344441](https://doi.org/10.1086/344441). arXiv: [astro-ph/0207375](https://arxiv.org/abs/astro-ph/0207375) [p. 80].
- [76] A. BANDYOPADHYAY, S. CHOUBEY y S. GOSWAMI. "Neutrino decay confronts the SNO data". *Phys. Lett. B* 555 (2003), pp. 33–42. DOI: [10.1016/S0370-2693\(03\)00044-3](https://doi.org/10.1016/S0370-2693(03)00044-3). arXiv: [hep-ph/0204173](https://arxiv.org/abs/hep-ph/0204173) [p. 177].
- [77] R. R. CALDWELL, M. KAMIONKOWSKI y N. N. WEINBERG. "Phantom energy and cosmic doomsday". *Phys. Rev. Lett.* 91 (2003), p. 071301. DOI: [10.1103/PhysRevLett.91.071301](https://doi.org/10.1103/PhysRevLett.91.071301). arXiv: [astro-ph/0302506](https://arxiv.org/abs/astro-ph/0302506) [p. 91].
- [78] S. DODELSON. *Modern Cosmology*. Academic Press, 2003 [pp. 10, 33, 65, 78].
- [79] J. L. FENG, A. RAJARAMAN y F. TAKAYAMA. "SuperWIMP dark matter signals from the early universe". *Phys. Rev. D* 68 (2003), p. 063504. DOI: [10.1103/PhysRevD.68.063504](https://doi.org/10.1103/PhysRevD.68.063504). arXiv: [hep-ph/0306024](https://arxiv.org/abs/hep-ph/0306024) [p. 140].
- [80] L. M. KRAUSS y B. CHABOYER. "Age Estimates of Globular Clusters in the Milky Way: Constraints on Cosmology". *Science* 299 (2003), pp. 65–70. DOI: [10.1126/science.1075631](https://doi.org/10.1126/science.1075631) [p. 7].
- [81] D. LANGLOIS. "Isocurvature cosmological perturbations and the CMB". *Comptes Rendus Physique* 4 (2003), pp. 953–959. DOI: [10.1016/j.crhy.2003.09.004](https://doi.org/10.1016/j.crhy.2003.09.004) [p. 61].
- [82] E. V. LINDER. "Exploring the expansion history of the universe". *Phys. Rev. Lett.* 90 (2003), p. 091301. DOI: [10.1103/PhysRevLett.90.091301](https://doi.org/10.1103/PhysRevLett.90.091301). arXiv: [astro-ph/0208512](https://arxiv.org/abs/astro-ph/0208512) [p. 128].
- [83] P. McDONALD. "Toward a measurement of the cosmological geometry at  $Z$  2: predicting lyman-alpha forest correlation in three dimensions, and the potential of future data sets". *Astrophys. J.* 585 (2003), pp. 34–51. DOI: [10.1086/345945](https://doi.org/10.1086/345945). arXiv: [astro-ph/0108064](https://arxiv.org/abs/astro-ph/0108064) [p. 228].
- [84] T. OKAMOTO y W. HU. "CMB lensing reconstruction on the full sky". *Phys. Rev. D* 67 (2003), p. 083002. DOI: [10.1103/PhysRevD.67.083002](https://doi.org/10.1103/PhysRevD.67.083002). arXiv: [astro-ph/0301031](https://arxiv.org/abs/astro-ph/0301031) [p. 79].
- [85] R. E. SMITH et al. "Stable clustering, the halo model and nonlinear cosmological power spectra". *Mon. Not. Roy. Astron. Soc.* 341 (2003), p. 1311. DOI: [10.1046/j.1365-8711.2003.06503.x](https://doi.org/10.1046/j.1365-8711.2003.06503.x). arXiv: [astro-ph/0207664](https://arxiv.org/abs/astro-ph/0207664) [pp. 83, 85, 101, 115].
- [86] D. N. SPERGEL et al. "First-Year Wilkinson Microwave Anisotropy Probe (WMAP) Observations: Determination of Cosmological Parameters". *The Astrophysical Journal Supplement Series* 148.1 (Sept. 2003), pp. 175–194. ISSN: 1538-4365. DOI: [10.1086/377226](https://doi.org/10.1086/377226) [p. 5].



- 
- [87] S. BASHINSKY y U. SELJAK. “Neutrino perturbations in CMB anisotropy and matter clustering”. *Phys. Rev. D* 69 (2004), p. 083002. DOI: 10.1103/PhysRevD.69.083002. arXiv: astro-ph/0310198 [p. 182].
- [88] J. F. BEACOM, N. F. BELL y S. DODELSON. “Neutrinoless universe”. *Phys. Rev. Lett.* 93 (2004), p. 121302. DOI: 10.1103/PhysRevLett.93.121302. arXiv: astro-ph/0404585 [p. 176].
- [89] J. ANGRİK et al. “KATRIN design report 2004” (Feb. 2005) [p. 183].
- [90] J. A. R. CEMBRANOS et al. “SuperWIMP solutions to small scale structure problems”. *Phys. Rev. Lett.* 95 (2005), p. 181301. DOI: 10.1103/PhysRevLett.95.181301. arXiv: hep-ph/0507150 [p. 140].
- [91] D. J. EISENSTEIN et al. “Detection of the Baryon Acoustic Peak in the Large-Scale Correlation Function of SDSS Luminous Red Galaxies”. *Astrophys. J.* 633 (2005), pp. 560–574. DOI: 10.1086/466512. arXiv: astro-ph/0501171 [p. 84].
- [92] A. M. GREEN, S. HOFMANN y D. J. SCHWARZ. “The First wimpy halos”. *JCAP* 08 (2005), p. 003. DOI: 10.1088/1475-7516/2005/08/003. arXiv: astro-ph/0503387 [p. 81].
- [93] S. HANNESTAD y G. RAFFELT. “Constraining invisible neutrino decays with the cosmic microwave background”. *Phys. Rev. D* 72 (2005), p. 103514. DOI: 10.1103/PhysRevD.72.103514. arXiv: hep-ph/0509278 [p. 177].
- [94] M. KAPLINGHAT. “Dark matter from early decays”. *Phys. Rev. D* 72 (2005), p. 063510. DOI: 10.1103/PhysRevD.72.063510. arXiv: astro-ph/0507300 [p. 140].
- [95] V. SPRINGEL. “The Cosmological simulation code GADGET-2”. *Mon. Not. Roy. Astron. Soc.* 364 (2005), pp. 1105–1134. DOI: 10.1111/j.1365-2966.2005.09655.x. arXiv: astro-ph/0505010 [pp. 85, 116].
- [96] E. J. COPELAND, M. SAMI y S. TSUJIKAWA. “Dynamics of dark energy”. *Int. J. Mod. Phys. D* 15 (2006), pp. 1753–1936. DOI: 10.1142/S021827180600942X. arXiv: hep-th/0603057 [p. 90].
- [97] M. CROCCE, S. PUEBLAS y R. SCOCCIMARRO. “Transients from Initial Conditions in Cosmological Simulations”. *Mon. Not. Roy. Astron. Soc.* 373 (2006), pp. 369–381. DOI: 10.1111/j.1365-2966.2006.11040.x. arXiv: astro-ph/0606505 [p. 116].
- [98] C. HIRATA. *Recombination lecture notes*. 2006 [pp. 38–40].
- [99] D. HUTERER et al. “Systematic errors in future weak lensing surveys: Requirements and prospects for self-calibration”. *Mon. Not. Roy. Astron. Soc.* 366 (2006), pp. 101–114. DOI: 10.1111/j.1365-2966.2005.09782.x. arXiv: astro-ph/0506030 [p. 95].
- [100] J. LESGOURGUES y S. PASTOR. “Massive neutrinos and cosmology”. *Phys. Rept.* 429 (2006), pp. 307–379. DOI: 10.1016/j.physrep.2006.04.001. arXiv: astro-ph/0603494 [pp. 153, 162].
- [101] A. LEWIS y A. CHALLINOR. “Weak gravitational lensing of the CMB”. *Phys. Rept.* 429 (2006), pp. 1–65. DOI: 10.1016/j.physrep.2006.03.002. arXiv: astro-ph/0601594 [p. 78].
- [102] P. SVRCEK y E. WITTEN. “Axions In String Theory”. *JHEP* 06 (2006), p. 051. DOI: 10.1088/1126-6708/2006/06/051. arXiv: hep-th/0605206 [p. 107].
- [103] S. BRIDLE y L. KING. “Dark energy constraints from cosmic shear power spectra: impact of intrinsic alignments on photometric redshift requirements”. *New J. Phys.* 9 (2007), p. 444. DOI: 10.1088/1367-2630/9/12/444. arXiv: 0705.0166 [astro-ph] [p. 95].
- [104] M. R. DOUGLAS y S. KACHRU. “Flux compactification”. *Rev. Mod. Phys.* 79 (2007), pp. 733–796. DOI: 10.1103/RevModPhys.79.733. arXiv: hep-th/0610102 [p. 107].
- [105] C. GIUNTI y C. W. KIM. *Fundamentals of Neutrino Physics and Astrophysics*. 2007. ISBN: 978-0-19-850871-7 [pp. 179, 181].
- [106] P. D. SERPICO. “Cosmological Neutrino Mass Detection: The Best Probe of Neutrino Lifetime”. *Phys. Rev. Lett.* 98 (2007), p. 171301. DOI: 10.1103/PhysRevLett.98.171301. arXiv: astro-ph/0701699 [p. 176].
- [107] E. CALABRESE et al. “Cosmic Microwave Weak lensing data as a test for the dark universe”. *Phys. Rev. D* 77 (2008), p. 123531. DOI: 10.1103/PhysRevD.77.123531. arXiv: 0803.2309 [astro-ph] [p. 96].
- [108] M. C. GONZALEZ-GARCIA y M. MALTONI. “Status of Oscillation plus Decay of Atmospheric and Long-Baseline Neutrinos”. *Phys. Lett. B* 663 (2008), pp. 405–409. DOI: 10.1016/j.physletb.2008.04.041. arXiv: 0802.3699 [hep-ph] [p. 177].

- [109] D. HOOPER. *TASI 2008 lectures on dark matter*. 2008 [p. 32].
- [110] M. LATTANZI. “Decaying Majoron Dark Matter and Neutrino Masses”. *AIP Conf. Proc.* 966.1 (2008). Ed. by C. L. BIANCO y S.-S. XUE, pp. 163–169. DOI: [10.1063/1.2836988](https://doi.org/10.1063/1.2836988). arXiv: [0802.3155](https://arxiv.org/abs/0802.3155) [astro-ph] [p. 140].
- [111] O. PISANTI et al. “PARthENoPE: Public Algorithm Evaluating the Nucleosynthesis of Primordial Elements”. *Comput. Phys. Commun.* 178 (2008), pp. 956–971. DOI: [10.1016/j.cpc.2008.02.015](https://doi.org/10.1016/j.cpc.2008.02.015). arXiv: [0705.0290](https://arxiv.org/abs/0705.0290) [astro-ph] [p. 35].
- [112] R. TROTTA. “Bayes in the sky: Bayesian inference and model selection in cosmology”. *Contemp. Phys.* 49 (2008), pp. 71–104. DOI: [10.1080/00107510802066753](https://doi.org/10.1080/00107510802066753). arXiv: [0803.4089](https://arxiv.org/abs/0803.4089) [astro-ph] [pp. 160, 219].
- [113] A. BASBOLL et al. “Are cosmological neutrinos free-streaming?” *Phys. Rev. D* 79 (2009), p. 043512. DOI: [10.1103/PhysRevD.79.043512](https://doi.org/10.1103/PhysRevD.79.043512). arXiv: [0806.1735](https://arxiv.org/abs/0806.1735) [astro-ph] [p. 177].
- [114] C.-R. CHEN, F. TAKAHASHI y T. T. YANAGIDA. “Gamma rays and positrons from a decaying hidden gauge boson”. *Phys. Lett. B* 671 (2009), pp. 71–76. DOI: [10.1016/j.physletb.2008.11.048](https://doi.org/10.1016/j.physletb.2008.11.048). arXiv: [0809.0792](https://arxiv.org/abs/0809.0792) [hep-ph] [p. 140].
- [115] F. FERROZ, M. P. HOBSON y M. BRIDGES. “MultiNest: an efficient and robust Bayesian inference tool for cosmology and particle physics”. *Mon. Not. Roy. Astron. Soc.* 398 (2009), pp. 1601–1614. DOI: [10.1111/j.1365-2966.2009.14548.x](https://doi.org/10.1111/j.1365-2966.2009.14548.x). arXiv: [0809.3437](https://arxiv.org/abs/0809.3437) [astro-ph] [pp. 159, 225].
- [116] A. HEAVENS. “Statistical techniques in cosmology” (June 2009). arXiv: [0906.0664](https://arxiv.org/abs/0906.0664) [astro-ph.CO] [p. 219].
- [117] C. M. HIRATA. “Tidal alignments as a contaminant of redshift space distortions”. *Mon. Not. Roy. Astron. Soc.* 399 (2009), p. 1074. DOI: [10.1111/j.1365-2966.2009.15353.x](https://doi.org/10.1111/j.1365-2966.2009.15353.x). arXiv: [0903.4929](https://arxiv.org/abs/0903.4929) [astro-ph.CO] [p. 95].
- [118] P. D. SERPICO. “Neutrinos and cosmology: a lifetime relationship”. *J. Phys. Conf. Ser.* 173 (2009). Ed. by F. AVIGNONE, R. CRESWICK y K. KUBODERA, p. 012018. DOI: [10.1088/1742-6596/173/1/012018](https://doi.org/10.1088/1742-6596/173/1/012018) [p. 176].
- [119] A. ARVANITAKI et al. “String Axiverse”. *Phys. Rev. D* 81 (2010), p. 123530. DOI: [10.1103/PhysRevD.81.123530](https://doi.org/10.1103/PhysRevD.81.123530). arXiv: [0905.4720](https://arxiv.org/abs/0905.4720) [hep-th] [p. 107].
- [120] X. CHEN. “Primordial Non-Gaussianities from Inflation Models”. *Adv. Astron.* 2010 (2010), p. 638979. DOI: [10.1155/2010/638979](https://doi.org/10.1155/2010/638979). arXiv: [1002.1416](https://arxiv.org/abs/1002.1416) [astro-ph.CO] [p. 96].
- [121] K. HEITMANN et al. “The Coyote Universe I: Precision Determination of the Nonlinear Matter Power Spectrum”. *Astrophys. J.* 715 (2010), pp. 104–121. DOI: [10.1088/0004-637X/715/1/104](https://doi.org/10.1088/0004-637X/715/1/104). arXiv: [0812.1052](https://arxiv.org/abs/0812.1052) [astro-ph] [p. 228].
- [122] A. H. G. PETER y A. J. BENSON. “Dark-matter decays and Milky Way satellite galaxies”. *Phys. Rev. D* 82 (2010), p. 123521. DOI: [10.1103/PhysRevD.82.123521](https://doi.org/10.1103/PhysRevD.82.123521). arXiv: [1009.1912](https://arxiv.org/abs/1009.1912) [astro-ph.GA] [p. 140].
- [123] A. H. G. PETER, C. E. MOODY y M. KAMIONKOWSKI. “Dark-Matter Decays and Self-Gravitating Halos”. *Phys. Rev. D* 81 (2010), p. 103501. DOI: [10.1103/PhysRevD.81.103501](https://doi.org/10.1103/PhysRevD.81.103501). arXiv: [1003.0419](https://arxiv.org/abs/1003.0419) [astro-ph.CO] [p. 140].
- [124] M. POSPELOV y J. PRADLER. “Big Bang Nucleosynthesis as a Probe of New Physics”. *Ann. Rev. Nucl. Part. Sci.* 60 (2010), pp. 539–568. DOI: [10.1146/annurev.nucl.012809.104521](https://doi.org/10.1146/annurev.nucl.012809.104521). arXiv: [1011.1054](https://arxiv.org/abs/1011.1054) [hep-ph] [p. 35].
- [125] M. SHOJI y E. KOMATSU. “Massive Neutrinos in Cosmology: Analytic Solutions and Fluid Approximation”. *Phys. Rev. D* 81 (2010). [Erratum: *Phys.Rev.D* 82, 089901 (2010)], p. 123516. DOI: [10.1103/PhysRevD.81.123516](https://doi.org/10.1103/PhysRevD.81.123516). arXiv: [1003.0942](https://arxiv.org/abs/1003.0942) [astro-ph.CO] [pp. 30, 54].
- [126] L. VERDE. “Statistical methods in cosmology”. *Lect. Notes Phys.* 800 (2010), pp. 147–177. DOI: [10.1007/978-3-642-10598-2\\_4](https://doi.org/10.1007/978-3-642-10598-2_4). arXiv: [0911.3105](https://arxiv.org/abs/0911.3105) [astro-ph.CO] [p. 219].
- [127] Y. ALI-HAIMOUD y C. M. HIRATA. “HyRec: A fast and highly accurate primordial hydrogen and helium recombination code”. *Physical Review D* 83 (2011), p. 043513. DOI: [10.1103/PhysRevD.83.043513](https://doi.org/10.1103/PhysRevD.83.043513). arXiv: [1011.3758](https://arxiv.org/abs/1011.3758) [astro-ph.CO] [p. 40].
- [128] S. AOYAMA et al. “Formulation and constraints on decaying dark matter with finite mass daughter particles”. *JCAP* 09 (2011), p. 025. DOI: [10.1088/1475-7516/2011/09/025](https://doi.org/10.1088/1475-7516/2011/09/025). arXiv: [1106.1984](https://arxiv.org/abs/1106.1984) [astro-ph.CO] [p. 140].

- 
- [129] F. BEUTLER et al. “The 6dF Galaxy Survey: Baryon Acoustic Oscillations and the Local Hubble Constant”. *Mon. Not. Roy. Astron. Soc.* 416 (2011), pp. 3017–3032. DOI: 10.1111/j.1365-2966.2011.19250.x. arXiv: 1106.3366 [astro-ph.CO] [pp. 110, 131, 134, 155, 192].
- [130] D. BLAS, J. LESGOURGUES y T. TRAM. “The Cosmic Linear Anisotropy Solving System (CLASS) II: Approximation schemes”. *Journal of Cosmology and Astroparticle Physics* 2011.7 (July 22, 2011), pp. 034–034. ISSN: 1475-7516. DOI: 10.1088/1475-7516/2011/07/034. arXiv: 1104.2933 [pp. 10, 116, 144, 146, 239, 240, 243, 253].
- [131] J. CHLUBA y R. M. THOMAS. “Towards a complete treatment of the cosmological recombination problem”. *Mon. Not. Roy. Astron. Soc.* 412 (2011), p. 748. DOI: 10.1111/j.1365-2966.2010.17940.x. arXiv: 1010.3631 [astro-ph.CO] [p. 40].
- [132] T. HAMBYE. “On the stability of particle dark matter”. *PoS IDM2010* (2011), p. 098. DOI: 10.22323/1.110.0098. arXiv: 1012.4587 [hep-ph] [p. 140].
- [133] K. JEDAMZIK y T. ABEL. “Weak Primordial Magnetic Fields and Anisotropies in the Cosmic Microwave Background Radiation” (Aug. 2011). arXiv: 1108.2517 [astro-ph.CO] [p. 128].
- [134] J. LESGOURGUES. “The Cosmic Linear Anisotropy Solving System (CLASS) I: Overview” (Apr. 2011). arXiv: 1104.2932 [astro-ph.IM] [p. 101].
- [135] J. LESGOURGUES y T. TRAM. “The Cosmic Linear Anisotropy Solving System (CLASS) IV: efficient implementation of non-cold relics”. *JCAP* 09 (2011), p. 032. DOI: 10.1088/1475-7516/2011/09/032. arXiv: 1104.2935 [astro-ph.CO] [pp. 54, 144, 148, 149, 239, 240, 243, 253, 254].
- [136] Y. Y. Y. WONG. “Neutrino mass in cosmology: status and prospects”. *Ann. Rev. Nucl. Part. Sci.* 61 (2011), pp. 69–98. DOI: 10.1146/annurev-nucl-102010-130252. arXiv: 1111.1436 [astro-ph.CO] [p. 176].
- [137] K. N. ABAZAJIAN et al. “Light Sterile Neutrinos: A White Paper” (Apr. 2012). arXiv: 1204.5379 [hep-ph] [p. 140].
- [138] P. BAERWALD, M. BUSTAMANTE y W. WINTER. “Neutrino Decays over Cosmological Distances and the Implications for Neutrino Telescopes”. *JCAP* 10 (2012), p. 020. DOI: 10.1088/1475-7516/2012/10/020. arXiv: 1208.4600 [astro-ph.CO] [p. 177].
- [139] S. BIRD, M. VIEL y M. G. HAEHNELT. “Massive Neutrinos and the Non-linear Matter Power Spectrum”. *Mon. Not. Roy. Astron. Soc.* 420 (2012), pp. 2551–2561. DOI: 10.1111/j.1365-2966.2011.20222.x. arXiv: 1109.4416 [astro-ph.CO] [p. 85].
- [140] M. CIRELLI et al. “Gamma ray constraints on Decaying Dark Matter”. *Phys. Rev. D* 86 (2012), p. 083506. DOI: 10.1103/PhysRevD.86.083506. arXiv: 1205.5283 [astro-ph.CO] [p. 140].
- [141] T. CLIFTON et al. “Modified Gravity and Cosmology”. *Phys. Rept.* 513 (2012), pp. 1–189. DOI: 10.1016/j.physrep.2012.01.001. arXiv: 1106.2476 [astro-ph.CO] [p. 91].
- [142] C. KNOBEL. “An introduction into the theory of cosmological structure formation” (Aug. 2012). arXiv: 1208.5931 [astro-ph.CO] [p. 44].
- [143] P. MELCHIOR y M. VIOLA. “Means of confusion: how pixel noise affects shear estimates for weak gravitational lensing”. *Mon. Not. Roy. Astron. Soc.* 424 (2012), p. 2757. DOI: 10.1111/j.1365-2966.2012.21381.x. arXiv: 1204.5147 [astro-ph.IM] [p. 95].
- [144] A. J. ROSS et al. “The clustering of galaxies in the SDSS-III Baryon Oscillation Spectroscopic Survey: Analysis of potential systematics”. *Mon. Not. Roy. Astron. Soc.* 424 (2012), p. 564. DOI: 10.1111/j.1365-2966.2012.21235.x. arXiv: 1203.6499 [astro-ph.CO] [p. 95].
- [145] R. TAKAHASHI et al. “Revising the Halofit Model for the Nonlinear Matter Power Spectrum”. *Astrophys. J.* 761 (2012), p. 152. DOI: 10.1088/0004-637X/761/2/152. arXiv: 1208.2701 [astro-ph.CO] [pp. 83, 85, 101, 115].
- [146] M.-Y. WANG y A. R. ZENTNER. “Effects of Unstable Dark Matter on Large-Scale Structure and Constraints from Future Surveys”. *Phys. Rev. D* 85 (2012), p. 043514. DOI: 10.1103/PhysRevD.85.043514. arXiv: 1201.2426 [astro-ph.CO] [p. 172].
- [147] B. AUDREN et al. “Conservative Constraints on Early Cosmology: an illustration of the Monte Python cosmological parameter inference code”. *JCAP* 02 (2013), p. 001. DOI: 10.1088/1475-7516/2013/02/001. arXiv: 1210.7183 [astro-ph.CO] [pp. 110, 155, 192, 225].
- [148] C. L. BENNETT et al. “Nine-Year Wilkinson Microwave Anisotropy Probe (WMAP) Observations: Final Maps and Results”. *Astrophys. J. Suppl.* 208 (2013), p. 20. DOI: 10.1088/0067-0049/208/2/20. arXiv: 1212.5225 [astro-ph.CO] [pp. 92, 94, 136].



- [149] R. ESSIG et al. “Constraining Light Dark Matter with Diffuse X-Ray and Gamma-Ray Observations”. *JHEP* 11 (2013), p. 193. DOI: [10.1007/JHEP11\(2013\)193](https://doi.org/10.1007/JHEP11(2013)193). arXiv: [1309.4091](https://arxiv.org/abs/1309.4091) [hep-ph] [p. 140].
- [150] K. HELGE. *Conceptions of Cosmos: From Myths To The Accelerating Universe: A History Of Cosmology*. Oxford University Press, 2013 [p. 3].
- [151] C. HEYMANS et al. “CFHTLenS tomographic weak lensing cosmological parameter constraints: Mitigating the impact of intrinsic galaxy alignments”. *Mon. Not. Roy. Astron. Soc.* 432 (2013), p. 2433. DOI: [10.1093/mnras/stt601](https://doi.org/10.1093/mnras/stt601). arXiv: [1303.1808](https://arxiv.org/abs/1303.1808) [astro-ph.CO] [pp. 95, 101].
- [152] H.-B. JIN, Y.-L. WU e Y.-F. ZHOU. “Implications of the first AMS-02 measurement for dark matter annihilation and decay”. *JCAP* 11 (2013), p. 026. DOI: [10.1088/1475-7516/2013/11/026](https://doi.org/10.1088/1475-7516/2013/11/026). arXiv: [1304.1997](https://arxiv.org/abs/1304.1997) [hep-ph] [p. 140].
- [153] J. LESGOURGUES. “Cosmological Perturbations”. *Theoretical Advanced Study Institute in Elementary Particle Physics: Searching for New Physics at Small and Large Scales*. 2013, pp. 29–97. DOI: [10.1142/9789814525220\\_0002](https://doi.org/10.1142/9789814525220_0002). arXiv: [1302.4640](https://arxiv.org/abs/1302.4640) [astro-ph.CO] [p. 70].
- [154] A. LEWIS. “Efficient sampling of fast and slow cosmological parameters”. *Phys. Rev. D* 87.10 (2013), p. 103529. DOI: [10.1103/PhysRevD.87.103529](https://doi.org/10.1103/PhysRevD.87.103529). arXiv: [1304.4473](https://arxiv.org/abs/1304.4473) [astro-ph.CO] [pp. 109, 224].
- [155] S. NESSERIS y J. GARCIA-BELLIDO. “Is the Jeffreys’ scale a reliable tool for Bayesian model comparison in cosmology?” *JCAP* 08 (2013), p. 036. DOI: [10.1088/1475-7516/2013/08/036](https://doi.org/10.1088/1475-7516/2013/08/036). arXiv: [1210.7652](https://arxiv.org/abs/1210.7652) [astro-ph.CO] [pp. 130, 160].
- [156] L. VERDE, P. PROTOPAPAS y R. JIMENEZ. “Planck and the local Universe: Quantifying the tension”. *Phys. Dark Univ.* 2 (2013), pp. 166–175. DOI: [10.1016/j.dark.2013.09.002](https://doi.org/10.1016/j.dark.2013.09.002). arXiv: [1306.6766](https://arxiv.org/abs/1306.6766) [astro-ph.CO] [p. 130].
- [157] M.-Y. WANG et al. “Lyman- $\alpha$  forest constraints on decaying dark matter”. *Phys. Rev. D* 88.12 (2013), p. 123515. DOI: [10.1103/PhysRevD.88.123515](https://doi.org/10.1103/PhysRevD.88.123515). arXiv: [1309.7354](https://arxiv.org/abs/1309.7354) [astro-ph.CO] [p. 173].
- [158] P. A. R. ADE et al. “Planck2013 results. XVI. Cosmological parameters”. *Astronomy Astrophysics* 571 (Oct. 2014), A16. ISSN: 1432-0746. DOI: [10.1051/0004-6361/201321591](https://doi.org/10.1051/0004-6361/201321591) [pp. 5, 95].
- [159] S. AOYAMA et al. “Evolution of perturbations and cosmological constraints in decaying dark matter models with arbitrary decay mass products”. *JCAP* 07 (2014), p. 021. DOI: [10.1088/1475-7516/2014/07/021](https://doi.org/10.1088/1475-7516/2014/07/021). arXiv: [1402.2972](https://arxiv.org/abs/1402.2972) [astro-ph.CO] [pp. 140–142, 144, 233, 244].
- [160] M. ARCHIDIACONO y S. HANNESTAD. “Updated constraints on non-standard neutrino interactions from Planck”. *JCAP* 07 (2014), p. 046. DOI: [10.1088/1475-7516/2014/07/046](https://doi.org/10.1088/1475-7516/2014/07/046). arXiv: [1311.3873](https://arxiv.org/abs/1311.3873) [astro-ph.CO] [p. 177].
- [161] B. AUDREN et al. “Strongest model-independent bound on the lifetime of Dark Matter”. *JCAP* 12 (2014), p. 028. DOI: [10.1088/1475-7516/2014/12/028](https://doi.org/10.1088/1475-7516/2014/12/028). arXiv: [1407.2418](https://arxiv.org/abs/1407.2418) [astro-ph.CO] [pp. 129, 140, 142, 146, 158].
- [162] G. BLACKADDER y S. M. KOUSHIAPPAS. “Dark matter with two- and many-body decays and supernovae type Ia”. *Phys. Rev. D* 90.10 (2014), p. 103527. DOI: [10.1103/PhysRevD.90.103527](https://doi.org/10.1103/PhysRevD.90.103527). arXiv: [1410.0683](https://arxiv.org/abs/1410.0683) [astro-ph.CO] [pp. 141, 142, 144].
- [163] A. BORDE et al. “New approach for precise computation of Lyman- $\alpha$  forest power spectrum with hydrodynamical simulations”. *JCAP* 07 (2014), p. 005. DOI: [10.1088/1475-7516/2014/07/005](https://doi.org/10.1088/1475-7516/2014/07/005). arXiv: [1401.6472](https://arxiv.org/abs/1401.6472) [astro-ph.CO] [p. 228].
- [164] A. FONT-RIBERA et al. “DESI and other dark energy experiments in the era of neutrino mass measurements”. *JCAP* 05 (2014), p. 023. DOI: [10.1088/1475-7516/2014/05/023](https://doi.org/10.1088/1475-7516/2014/05/023). arXiv: [1308.4164](https://arxiv.org/abs/1308.4164) [astro-ph.CO] [p. 195].
- [165] M. KAMIONKOWSKI, J. PRADLER y D. G. E. WALKER. “Dark energy from the string axiverse”. *Phys. Rev. Lett.* 113.25 (2014), p. 251302. DOI: [10.1103/PhysRevLett.113.251302](https://doi.org/10.1103/PhysRevLett.113.251302). arXiv: [1409.0549](https://arxiv.org/abs/1409.0549) [hep-ph] [p. 107].
- [166] Y. RASERA et al. “Cosmic variance limited Baryon Acoustic Oscillations from the DEUS-FUR  $\Lambda$ CDM simulation”. *Mon. Not. Roy. Astron. Soc.* 440.2 (2014), pp. 1420–1434. DOI: [10.1093/mnras/stu295](https://doi.org/10.1093/mnras/stu295). arXiv: [1311.5662](https://arxiv.org/abs/1311.5662) [astro-ph.CO] [p. 228].
- [167] C. de RHAM. “Massive Gravity”. *Living Rev. Rel.* 17 (2014), p. 7. DOI: [10.12942/lrr-2014-7](https://doi.org/10.12942/lrr-2014-7). arXiv: [1401.4173](https://arxiv.org/abs/1401.4173) [hep-th] [p. 91].

- 
- [168] M.-Y. WANG et al. “Cosmological simulations of decaying dark matter: implications for small-scale structure of dark matter haloes”. *Mon. Not. Roy. Astron. Soc.* 445.1 (2014), pp. 614–629. DOI: 10.1093/mnras/stu1747. arXiv: 1406.0527 [astro-ph.CO] [p. 172].
- [169] R. ALLAHVERDI et al. “Dark Matter from Late Invisible Decays to/of Gravitinos”. *Phys. Rev. D* 91.5 (2015), p. 055033. DOI: 10.1103/PhysRevD.91.055033. arXiv: 1412.4391 [hep-ph] [p. 140].
- [170] É. AUBOURG et al. “Cosmological implications of baryon acoustic oscillation measurements”. *Phys. Rev. D* 92.12 (2015), p. 123516. DOI: 10.1103/PhysRevD.92.123516. arXiv: 1411.1074 [astro-ph.CO] [p. 92].
- [171] B. AUDREN et al. “Robustness of cosmic neutrino background detection in the cosmic microwave background”. *JCAP* 03 (2015), p. 036. DOI: 10.1088/1475-7516/2015/03/036. arXiv: 1412.5948 [astro-ph.CO] [p. 182].
- [172] G. D. BECKER, J. S. BOLTON y A. LIDZ. “Reionisation and High-Redshift Galaxies: The View from Quasar Absorption Lines”. *Publ. Astron. Soc. Austral.* 32 (2015), e045. DOI: 10.1017/pasa.2015.45. arXiv: 1510.03368 [astro-ph.CO] [pp. 41, 42].
- [173] Z. BEREZHIANI, A. D. DOLGOV e I. I. TKACHEV. “Reconciling Planck results with low redshift astronomical measurements”. *Phys. Rev. D* 92.6 (2015), p. 061303. DOI: 10.1103/PhysRevD.92.061303. arXiv: 1505.03644 [astro-ph.CO] [p. 140].
- [174] J. M. BERRYMAN, A. de GOUVEA y D. HERNANDEZ. “Solar Neutrinos and the Decaying Neutrino Hypothesis”. *Phys. Rev. D* 92.7 (2015), p. 073003. DOI: 10.1103/PhysRevD.92.073003. arXiv: 1411.0308 [hep-ph] [p. 177].
- [175] M. A. BUEN-ABAD, G. MARQUES-TAVARES y M. SCHMALTZ. “Non-Abelian dark matter and dark radiation”. *Phys. Rev. D* 92.2 (2015), p. 023531. DOI: 10.1103/PhysRevD.92.023531. arXiv: 1505.03542 [hep-ph] [pp. 134, 135].
- [176] J. CHLUBA, J. HAMANN y S. P. PATIL. “Features and New Physical Scales in Primordial Observables: Theory and Observation”. *Int. J. Mod. Phys. D* 24.10 (2015), p. 1530023. DOI: 10.1142/S0218271815300232. arXiv: 1505.01834 [astro-ph.CO] [p. 96].
- [177] K. ENQVIST et al. “Decaying dark matter and the tension in  $\sigma_8$ ”. *JCAP* 09 (2015), p. 067. DOI: 10.1088/1475-7516/2015/09/067. arXiv: 1505.05511 [astro-ph.CO] [pp. 140, 149, 241].
- [178] J. FERGUSSON. *Cosmology lecture notes*. 2015 [p. 62].
- [179] B. FOLLIN et al. “First Detection of the Acoustic Oscillation Phase Shift Expected from the Cosmic Neutrino Background”. *Phys. Rev. Lett.* 115.9 (2015), p. 091301. DOI: 10.1103/PhysRevLett.115.091301. arXiv: 1503.07863 [astro-ph.CO] [p. 182].
- [180] G. GIESEN et al. “AMS-02 antiprotons, at last! Secondary astrophysical component and immediate implications for Dark Matter”. *JCAP* 09 (2015), p. 023. DOI: 10.1088/1475-7516/2015/9/023. arXiv: 1504.04276 [astro-ph.HE] [p. 140].
- [181] R. A. GOMES, A. L. G. GOMES y O. L. G. PERES. “Constraints on neutrino decay lifetime using long-baseline charged and neutral current data”. *Phys. Lett. B* 740 (2015), pp. 345–352. DOI: 10.1016/j.physletb.2014.12.014. arXiv: 1407.5640 [hep-ph] [p. 177].
- [182] R. MAARTENS et al. “Overview of Cosmology with the SKA”. *PoS AASKA14* (2015). Ed. by T. L. BOURKE et al., p. 016. DOI: 10.22323/1.215.0016. arXiv: 1501.04076 [astro-ph.CO] [p. 195].
- [183] A. MEAD et al. “An accurate halo model for fitting non-linear cosmological power spectra and baryonic feedback models”. *Mon. Not. Roy. Astron. Soc.* 454.2 (2015), pp. 1958–1975. DOI: 10.1093/mnras/stv2036. arXiv: 1505.07833 [astro-ph.CO] [pp. 101, 115, 118].
- [184] G. PAGLIAROLI et al. “Testing nonradiative neutrino decay scenarios with IceCube data”. *Phys. Rev. D* 92.11 (2015), p. 113008. DOI: 10.1103/PhysRevD.92.113008. arXiv: 1506.02624 [hep-ph] [p. 177].
- [185] M. RIGAULT et al. “Confirmation of a Star Formation Bias in Type Ia Supernova Distances and its Effect on Measurement of the Hubble Constant”. *Astrophys. J.* 802.1 (2015), p. 20. DOI: 10.1088/0004-637X/802/1/20. arXiv: 1412.6501 [astro-ph.CO] [p. 92].
- [186] A. J. ROSS et al. “The clustering of the SDSS DR7 main Galaxy sample – I. A 4 per cent distance measure at  $z = 0.15$ ”. *Mon. Not. Roy. Astron. Soc.* 449.1 (2015), pp. 835–847. DOI: 10.1093/mnras/stv154. arXiv: 1409.3242 [astro-ph.CO] [pp. 110, 131, 134, 155, 192].

- [187] B. P. ABBOTT et al. “Observation of Gravitational Waves from a Binary Black Hole Merger”. *Phys. Rev. Lett.* 116.6 (2016), p. 061102. DOI: 10.1103/PhysRevLett.116.061102. arXiv: 1602.03837 [gr-qc] [p. 90].
- [188] P. A. R. ADE et al. “Planck 2015 results. XIII. Cosmological parameters”. *Astron. Astrophys.* 594 (2016), A13. DOI: 10.1051/0004-6361/201525830. arXiv: 1502.01589 [astro-ph.CO] [pp. 36, 95].
- [189] P. A. R. ADE et al. “Planck 2015 results. XXIV. Cosmology from Sunyaev-Zeldovich cluster counts”. *Astron. Astrophys.* 594 (2016), A24. DOI: 10.1051/0004-6361/201525833. arXiv: 1502.01597 [astro-ph.CO] [p. 95].
- [190] A. AGHAMOUSA et al. “The DESI Experiment Part I: Science, Targeting, and Survey Design” (Oct. 2016). arXiv: 1611.00036 [astro-ph.IM] [p. 172].
- [191] D. BAUMANN et al. “Phases of New Physics in the CMB”. *JCAP* 01 (2016), p. 007. DOI: 10.1088/1475-7516/2016/01/007. arXiv: 1508.06342 [astro-ph.CO] [p. 182].
- [192] J. L. BERNAL, L. VERDE y A. G. RIESS. “The trouble with  $H_0$ ”. *JCAP* 10 (2016), p. 019. DOI: 10.1088/1475-7516/2016/10/019. arXiv: 1607.05617 [astro-ph.CO] [pp. 106, 113, 128].
- [193] S. BIRD et al. “Did LIGO detect dark matter?” *Phys. Rev. Lett.* 116.20 (2016), p. 201301. DOI: 10.1103/PhysRevLett.116.201301. arXiv: 1603.00464 [astro-ph.CO] [p. 90].
- [194] C. BURGESS. *An Introduction to Big Bang Cosmology*. 2016 [p. 10].
- [195] Z. CHACKO et al. “Partially Acoustic Dark Matter, Interacting Dark Radiation, and Large Scale Structure”. *JHEP* 12 (2016), p. 108. DOI: 10.1007/JHEP12(2016)108. arXiv: 1609.03569 [astro-ph.CO] [pp. 134, 135].
- [196] A. CHUDAYKIN, D. GORBUNOV e I. TKACHEV. “Dark matter component decaying after recombination: Lensing constraints with Planck data”. *Phys. Rev. D* 94 (2016), p. 023528. DOI: 10.1103/PhysRevD.94.023528. arXiv: 1602.08121 [astro-ph.CO] [p. 140].
- [197] Y. FARZAN y S. HANNESTAD. “Neutrinos secretly converting to lighter particles to please both KATRIN and the cosmos”. *JCAP* 02 (2016), p. 058. DOI: 10.1088/1475-7516/2016/02/058. arXiv: 1510.02201 [hep-ph] [p. 176].
- [198] E. GIUSARMA et al. “Improvement of cosmological neutrino mass bounds”. *Phys. Rev. D* 94.8 (2016), p. 083522. DOI: 10.1103/PhysRevD.94.083522. arXiv: 1605.04320 [astro-ph.CO] [p. 153].
- [199] R. KAPPL, H. P. NILLES y M. W. WINKLER. “Modulated Natural Inflation”. *Phys. Lett. B* 753 (2016), pp. 653–659. DOI: 10.1016/j.physletb.2015.12.073. arXiv: 1511.05560 [hep-th] [p. 107].
- [200] T. KARWAL y M. KAMIONKOWSKI. “Dark energy at early times, the Hubble parameter, and the string axiverse”. *Phys. Rev. D* 94.10 (2016), p. 103523. DOI: 10.1103/PhysRevD.94.103523. arXiv: 1608.01309 [astro-ph.CO] [p. 107].
- [201] J. LESGOURGUES, G. MARQUES-TAVARES y M. SCHMALTZ. “Evidence for dark matter interactions in cosmological precision data?” *JCAP* 02 (2016), p. 037. DOI: 10.1088/1475-7516/2016/02/037. arXiv: 1507.04351 [astro-ph.CO] [p. 127].
- [202] A. LIU et al. “Eliminating the optical depth nuisance from the CMB with 21 cm cosmology”. *Phys. Rev. D* 93.4 (2016), p. 043013. DOI: 10.1103/PhysRevD.93.043013. arXiv: 1509.08463 [astro-ph.CO] [p. 195].
- [203] D. J. E. MARSH. “Axion Cosmology”. *Phys. Rept.* 643 (2016), pp. 1–79. DOI: 10.1016/j.physrep.2016.06.005. arXiv: 1510.07633 [astro-ph.CO] [pp. 89, 107].
- [204] V. POULIN, P. D. SERPICO y J. LESGOURGUES. “A fresh look at linear cosmological constraints on a decaying dark matter component”. *JCAP* 08 (2016), p. 036. DOI: 10.1088/1475-7516/2016/08/036. arXiv: 1606.02073 [astro-ph.CO] [pp. 129, 140, 147, 148, 158].
- [205] A. SCHNEIDER et al. “Matter power spectrum and the challenge of percent accuracy”. *JCAP* 04 (2016), p. 047. DOI: 10.1088/1475-7516/2016/04/047. arXiv: 1503.05920 [astro-ph.CO] [p. 228].
- [206] N. AGHANIM et al. “Planck intermediate results. LI. Features in the cosmic microwave background temperature power spectrum and shifts in cosmological parameters”. *Astron. Astrophys.* 607 (2017), A95. DOI: 10.1051/0004-6361/201629504. arXiv: 1608.02487 [astro-ph.CO] [pp. 96, 123, 124].

- 
- [207] S. ALAM et al. “The clustering of galaxies in the completed SDSS-III Baryon Oscillation Spectroscopic Survey: cosmological analysis of the DR12 galaxy sample”. *Mon. Not. Roy. Astron. Soc.* 470.3 (2017), pp. 2617–2652. DOI: 10.1093/mnras/stx721. arXiv: 1607.03155 [astro-ph.CO] [pp. 105, 110, 131, 134, 155, 192].
- [208] M. ARCHIDIACONO et al. “Physical effects involved in the measurements of neutrino masses with future cosmological data”. *JCAP* 02 (2017), p. 052. DOI: 10.1088/1475-7516/2017/02/052. arXiv: 1610.09852 [astro-ph.CO] [pp. 194, 195].
- [209] C. BRUST, Y. CUI y K. SIGURDSON. “Cosmological Constraints on Interacting Light Particles”. *JCAP* 08 (2017), p. 020. DOI: 10.1088/1475-7516/2017/08/020. arXiv: 1703.10732 [astro-ph.CO] [p. 127].
- [210] J. S. BULLOCK y M. BOYLAN-KOLCHIN. “Small-Scale Challenges to the  $\Lambda$ CDM Paradigm”. *Ann. Rev. Astron. Astrophys.* 55 (2017), pp. 343–387. DOI: 10.1146/annurev-astro-091916-055313. arXiv: 1707.04256 [astro-ph.CO] [p. 96].
- [211] M. BUSTAMANTE, J. F. BEACOM y K. MURASE. “Testing decay of astrophysical neutrinos with incomplete information”. *Phys. Rev. D* 95.6 (2017), p. 063013. DOI: 10.1103/PhysRevD.95.063013. arXiv: 1610.02096 [astro-ph.HE] [p. 177].
- [212] A. CALDWELL et al. “Global Bayesian analysis of neutrino mass data”. *Phys. Rev. D* 96.7 (2017), p. 073001. DOI: 10.1103/PhysRevD.96.073001. arXiv: 1705.01945 [hep-ph] [p. 184].
- [213] P. CREMINELLI y F. VERNIZZI. “Dark Energy after GW170817 and GRB170817A”. *Phys. Rev. Lett.* 119.25 (2017), p. 251302. DOI: 10.1103/PhysRevLett.119.251302. arXiv: 1710.05877 [astro-ph.CO] [p. 91].
- [214] E. DI VALENTINO, A. MELCHIORRI y O. MENA. “Can interacting dark energy solve the  $H_0$  tension?” *Phys. Rev. D* 96.4 (2017), p. 043503. DOI: 10.1103/PhysRevD.96.043503. arXiv: 1704.08342 [astro-ph.CO] [p. 113].
- [215] E. DI VALENTINO et al. “Constraining Dark Energy Dynamics in Extended Parameter Space”. *Phys. Rev. D* 96.2 (2017), p. 023523. DOI: 10.1103/PhysRevD.96.023523. arXiv: 1704.00762 [astro-ph.CO] [p. 113].
- [216] M. DREWES et al. “A White Paper on keV Sterile Neutrino Dark Matter”. *JCAP* 01 (2017), p. 025. DOI: 10.1088/1475-7516/2017/01/025. arXiv: 1602.04816 [hep-ph] [p. 89].
- [217] M. GERBINO et al. “A novel approach to quantifying the sensitivity of current and future cosmological datasets to the neutrino mass ordering through Bayesian hierarchical modeling”. *Phys. Lett. B* 775 (2017), pp. 239–250. DOI: 10.1016/j.physletb.2017.10.052. arXiv: 1611.07847 [astro-ph.CO] [p. 184].
- [218] H. GIL-MARIN et al. “The clustering of galaxies in the SDSS-III Baryon Oscillation Spectroscopic Survey: RSD measurement from the power spectrum and bispectrum of the DR12 BOSS galaxies”. *Mon. Not. Roy. Astron. Soc.* 465.2 (2017), pp. 1757–1788. DOI: 10.1093/mnras/stw2679. arXiv: 1606.00439 [astro-ph.CO] [p. 94].
- [219] C. HAHN et al. “The effect of fibre collisions on the galaxy power spectrum multipoles”. *Mon. Not. Roy. Astron. Soc.* 467.2 (2017), pp. 1940–1956. DOI: 10.1093/mnras/stx185. arXiv: 1609.01714 [astro-ph.CO] [p. 95].
- [220] H. HILDEBRANDT et al. “KiDS-450: Cosmological parameter constraints from tomographic weak gravitational lensing”. *Mon. Not. Roy. Astron. Soc.* 465 (2017), p. 1454. DOI: 10.1093/mnras/stw2805. arXiv: 1606.05338 [astro-ph.CO] [p. 95].
- [221] S. JOUDAKI et al. “CFHTLenS revisited: assessing concordance with Planck including astrophysical systematics”. *Mon. Not. Roy. Astron. Soc.* 465.2 (2017), pp. 2033–2052. DOI: 10.1093/mnras/stw2665. arXiv: 1601.05786 [astro-ph.CO] [p. 95].
- [222] S. JOUDAKI et al. “KiDS-450: Testing extensions to the standard cosmological model”. *Mon. Not. Roy. Astron. Soc.* 471.2 (2017), pp. 1259–1279. DOI: 10.1093/mnras/stx998. arXiv: 1610.04606 [astro-ph.CO] [p. 116].
- [223] T. D. KITCHING et al. “The Limits of Cosmic Shear”. *Mon. Not. Roy. Astron. Soc.* 469.3 (2017), pp. 2737–2749. DOI: 10.1093/mnras/stx1039. arXiv: 1611.04954 [astro-ph.CO] [p. 95].
- [224] K. S. MANDEL et al. “The Type Ia Supernova Color–Magnitude Relation and Host Galaxy Dust: A Simple Hierarchical Bayesian Model”. *Astrophys. J.* 842.2 (2017), p. 93. DOI: 10.3847/1538-4357/aa6038. arXiv: 1609.04470 [astro-ph.CO] [p. 18].



- [225] R. MURGIA et al. ““Non-cold” dark matter at small scales: a general approach”. *JCAP* 11 (2017), p. 046. DOI: [10.1088/1475-7516/2017/11/046](https://doi.org/10.1088/1475-7516/2017/11/046). arXiv: [1704.07838](https://arxiv.org/abs/1704.07838) [astro-ph.CO] [pp. [87](#), [118](#), [152](#), [173](#)].
- [226] V. POULIN. “Gravitative und elektromagnetische Signaturen von massiven Relikten in Kosmologie”. PhD thesis. RWTH Aachen U., 2017. DOI: [10.18154/RWTH-2018-225652](https://doi.org/10.18154/RWTH-2018-225652) [pp. [42](#), [66](#)].
- [227] V. POULIN, J. LESGOURGUES y P. D. SERPICO. “Cosmological constraints on exotic injection of electromagnetic energy”. *JCAP* 03 (2017), p. 043. DOI: [10.1088/1475-7516/2017/03/043](https://doi.org/10.1088/1475-7516/2017/03/043). arXiv: [1610.10051](https://arxiv.org/abs/1610.10051) [astro-ph.CO] [p. [140](#)].
- [228] T. SCHWETZ et al. “Comment on “Strong Evidence for the Normal Neutrino Hierarchy”” (Mar. 2017). arXiv: [1703.04585](https://arxiv.org/abs/1703.04585) [astro-ph.CO] [p. [184](#)].
- [229] F. SIMPSON et al. “Strong Bayesian Evidence for the Normal Neutrino Hierarchy”. *JCAP* 06 (2017), p. 029. DOI: [10.1088/1475-7516/2017/06/029](https://doi.org/10.1088/1475-7516/2017/06/029). arXiv: [1703.03425](https://arxiv.org/abs/1703.03425) [astro-ph.CO] [pp. [184](#), [196](#)].
- [230] T. R. SLATYER y C.-L. WU. “General Constraints on Dark Matter Decay from the Cosmic Microwave Background”. *Phys. Rev. D* 95.2 (2017), p. 023010. DOI: [10.1103/PhysRevD.95.023010](https://doi.org/10.1103/PhysRevD.95.023010). arXiv: [1610.06933](https://arxiv.org/abs/1610.06933) [astro-ph.CO] [p. [140](#)].
- [231] S. VAGNOZZI et al. “Unveiling  $\nu$  secrets with cosmological data: neutrino masses and mass hierarchy”. *Phys. Rev. D* 96.12 (2017), p. 123503. DOI: [10.1103/PhysRevD.96.123503](https://doi.org/10.1103/PhysRevD.96.123503). arXiv: [1701.08172](https://arxiv.org/abs/1701.08172) [astro-ph.CO] [pp. [184](#), [196](#)].
- [232] L. VERDE et al. “The length of the low-redshift standard ruler”. *Mon. Not. Roy. Astron. Soc.* 467.1 (2017), pp. 731–736. DOI: [10.1093/mnras/stx116](https://doi.org/10.1093/mnras/stx116). arXiv: [1607.05297](https://arxiv.org/abs/1607.05297) [astro-ph.CO] [p. [92](#)].
- [233] G.-B. ZHAO et al. “Dynamical dark energy in light of the latest observations”. *Nature Astron.* 1.9 (2017), pp. 627–632. DOI: [10.1038/s41550-017-0216-z](https://doi.org/10.1038/s41550-017-0216-z). arXiv: [1701.08165](https://arxiv.org/abs/1701.08165) [astro-ph.CO] [p. [113](#)].
- [234] J. L. AALBERTS et al. “Precision constraints on radiative neutrino decay with CMB spectral distortion”. *Phys. Rev. D* 98 (2018), p. 023001. DOI: [10.1103/PhysRevD.98.023001](https://doi.org/10.1103/PhysRevD.98.023001). arXiv: [1803.00588](https://arxiv.org/abs/1803.00588) [astro-ph.CO] [p. [176](#)].
- [235] T. M. C. ABBOTT et al. “Dark Energy Survey year 1 results: Cosmological constraints from galaxy clustering and weak lensing”. *Phys. Rev. D* 98.4 (2018), p. 043526. DOI: [10.1103/PhysRevD.98.043526](https://doi.org/10.1103/PhysRevD.98.043526). arXiv: [1708.01530](https://arxiv.org/abs/1708.01530) [astro-ph.CO] [pp. [101](#), [155](#), [162](#)].
- [236] G. E. ADDISON et al. “Elucidating  $\Lambda$ CDM: Impact of Baryon Acoustic Oscillation Measurements on the Hubble Constant Discrepancy”. *Astrophys. J.* 853.2 (2018), p. 119. DOI: [10.3847/1538-4357/aaa1ed](https://doi.org/10.3847/1538-4357/aaa1ed). arXiv: [1707.06547](https://arxiv.org/abs/1707.06547) [astro-ph.CO] [p. [113](#)].
- [237] L. AMENDOLA et al. “Cosmology and fundamental physics with the Euclid satellite”. *Living Rev. Rel.* 21.1 (2018), p. 2. DOI: [10.1007/s41114-017-0010-3](https://doi.org/10.1007/s41114-017-0010-3). arXiv: [1606.00180](https://arxiv.org/abs/1606.00180) [astro-ph.CO] [pp. [118](#), [172](#), [181](#), [195](#)].
- [238] G. BERTONE y D. HOOPER. “History of dark matter”. *Rev. Mod. Phys.* 90.4 (2018), p. 045002. DOI: [10.1103/RevModPhys.90.045002](https://doi.org/10.1103/RevModPhys.90.045002). arXiv: [1605.04909](https://arxiv.org/abs/1605.04909) [astro-ph.CO] [p. [6](#)].
- [239] T. BRINGMANN et al. “Converting nonrelativistic dark matter to radiation”. *Phys. Rev. D* 98.2 (2018), p. 023543. DOI: [10.1103/PhysRevD.98.023543](https://doi.org/10.1103/PhysRevD.98.023543). arXiv: [1803.03644](https://arxiv.org/abs/1803.03644) [astro-ph.CO] [p. [140](#)].
- [240] M. A. BUEN-ABAD et al. “Interacting Dark Sector and Precision Cosmology”. *JCAP* 01 (2018), p. 008. DOI: [10.1088/1475-7516/2018/01/008](https://doi.org/10.1088/1475-7516/2018/01/008). arXiv: [1708.09406](https://arxiv.org/abs/1708.09406) [astro-ph.CO] [pp. [127](#), [134](#)].
- [241] S. CHOUBEY, D. DUTTA y D. PRAMANIK. “Invisible neutrino decay in the light of NOvA and T2K data”. *JHEP* 08 (2018), p. 141. DOI: [10.1007/JHEP08\(2018\)141](https://doi.org/10.1007/JHEP08(2018)141). arXiv: [1805.01848](https://arxiv.org/abs/1805.01848) [hep-ph] [p. [177](#)].
- [242] P. B. DENTON e I. TAMBORRA. “Invisible Neutrino Decay Could Resolve IceCube’s Track and Cascade Tension”. *Phys. Rev. Lett.* 121.12 (2018), p. 121802. DOI: [10.1103/PhysRevLett.121.121802](https://doi.org/10.1103/PhysRevLett.121.121802). arXiv: [1805.05950](https://arxiv.org/abs/1805.05950) [hep-ph] [p. [177](#)].
- [243] E. DI VALENTINO y S. BRIDLE. “Exploring the Tension between Current Cosmic Microwave Background and Cosmic Shear Data”. *Symmetry* 10.11 (2018), p. 585. DOI: [10.3390/sym10110585](https://doi.org/10.3390/sym10110585) [p. [96](#)].

- 
- [244] E. DI VALENTINO et al. “Reducing the  $H_0$  and  $\sigma_8$  tensions with Dark Matter-neutrino interactions”. *Phys. Rev. D* 97.4 (2018), p. 043513. DOI: [10.1103/PhysRevD.97.043513](https://doi.org/10.1103/PhysRevD.97.043513). arXiv: [1710.02559](https://arxiv.org/abs/1710.02559) [astro-ph.CO] [p. 135].
- [245] S. GARIAZZO et al. “Neutrino masses and their ordering: Global Data, Priors and Models”. *JCAP* 03 (2018), p. 011. DOI: [10.1088/1475-7516/2018/03/011](https://doi.org/10.1088/1475-7516/2018/03/011). arXiv: [1801.04946](https://arxiv.org/abs/1801.04946) [hep-ph] [p. 184].
- [246] L. HART y J. CHLUBA. “New constraints on time-dependent variations of fundamental constants using Planck data”. *Mon. Not. Roy. Astron. Soc.* 474.2 (2018), pp. 1850–1861. DOI: [10.1093/mnras/stx2783](https://doi.org/10.1093/mnras/stx2783). arXiv: [1705.03925](https://arxiv.org/abs/1705.03925) [astro-ph.CO] [p. 128].
- [247] J. W. HENNING et al. “Measurements of the Temperature and E-Mode Polarization of the CMB from 500 Square Degrees of SPTpol Data”. *Astrophys. J.* 852.2 (2018), p. 97. DOI: [10.3847/1538-4357/aa9ff4](https://doi.org/10.3847/1538-4357/aa9ff4). arXiv: [1707.09353](https://arxiv.org/abs/1707.09353) [astro-ph.CO] [pp. 96, 125, 156, 165].
- [248] D. O. JONES et al. “Should Type Ia Supernova Distances be Corrected for their Local Environments?” *Astrophys. J.* 867.2 (2018), p. 108. DOI: [10.3847/1538-4357/aae2b9](https://doi.org/10.3847/1538-4357/aae2b9). arXiv: [1805.05911](https://arxiv.org/abs/1805.05911) [astro-ph.CO] [p. 92].
- [249] M. LATTANZI y M. GERBINO. “Status of neutrino properties and future prospects - Cosmological and astrophysical constraints”. *Front. in Phys.* 5 (2018), p. 70. DOI: [10.3389/fphy.2017.00070](https://doi.org/10.3389/fphy.2017.00070). arXiv: [1712.07109](https://arxiv.org/abs/1712.07109) [astro-ph.CO] [p. 176].
- [250] J. LESGOURGUES et al. *Neutrino Cosmology*. Cambridge University Press, 2018 [pp. 10, 60, 74, 84, 176, 178, 191].
- [251] R. MANDELBAUM et al. “The LSST Dark Energy Science Collaboration (DESC) Science Requirements Document” (Sept. 2018). arXiv: [1809.01669](https://arxiv.org/abs/1809.01669) [astro-ph.CO] [p. 172].
- [252] A. MANZOTTI. “Future cosmic microwave background delensing with galaxy surveys”. *Phys. Rev. D* 97.4 (2018), p. 043527. DOI: [10.1103/PhysRevD.97.043527](https://doi.org/10.1103/PhysRevD.97.043527). arXiv: [1710.11038](https://arxiv.org/abs/1710.11038) [astro-ph.CO] [pp. 154, 162].
- [253] P. MOTLOCH y W. HU. “Tensions between direct measurements of the lens power spectrum from Planck data”. *Phys. Rev. D* 97.10 (2018), p. 103536. DOI: [10.1103/PhysRevD.97.103536](https://doi.org/10.1103/PhysRevD.97.103536). arXiv: [1803.11526](https://arxiv.org/abs/1803.11526) [astro-ph.CO] [pp. 96, 124, 125].
- [254] R. MURGIA, V. IRŠIČ y M. VIEL. “Novel constraints on noncold, nonthermal dark matter from Lyman- $\alpha$  forest data”. *Phys. Rev. D* 98.8 (2018), p. 083540. DOI: [10.1103/PhysRevD.98.083540](https://doi.org/10.1103/PhysRevD.98.083540). arXiv: [1806.08371](https://arxiv.org/abs/1806.08371) [astro-ph.CO] [pp. 118, 152].
- [255] V. POULIN et al. “Cosmological implications of ultralight axionlike fields”. *Phys. Rev. D* 98.8 (2018), p. 083525. DOI: [10.1103/PhysRevD.98.083525](https://doi.org/10.1103/PhysRevD.98.083525). arXiv: [1806.10608](https://arxiv.org/abs/1806.10608) [astro-ph.CO] [pp. 107, 108].
- [256] V. POULIN et al. “Implications of an extended dark energy cosmology with massive neutrinos for cosmological tensions”. *Phys. Rev. D* 97.12 (2018), p. 123504. DOI: [10.1103/PhysRevD.97.123504](https://doi.org/10.1103/PhysRevD.97.123504). arXiv: [1803.02474](https://arxiv.org/abs/1803.02474) [astro-ph.CO] [pp. 106, 113].
- [257] P. F. de SALAS et al. “Status of neutrino oscillations 2018:  $3\sigma$  hint for normal mass ordering and improved CP sensitivity”. *Phys. Lett. B* 782 (2018), pp. 633–640. DOI: [10.1016/j.physletb.2018.06.019](https://doi.org/10.1016/j.physletb.2018.06.019). arXiv: [1708.01186](https://arxiv.org/abs/1708.01186) [hep-ph] [p. 180].
- [258] D. M. SCOLNIC et al. “The Complete Light-curve Sample of Spectroscopically Confirmed SNe Ia from Pan-STARRS1 and Cosmological Constraints from the Combined Pantheon Sample”. *Astrophys. J.* 859.2 (2018), p. 101. DOI: [10.3847/1538-4357/aab9bb](https://doi.org/10.3847/1538-4357/aab9bb). arXiv: [1710.00845](https://arxiv.org/abs/1710.00845) [astro-ph.CO] [pp. 104, 105, 110, 131, 135, 155, 192].
- [259] G. SIMARD et al. “Constraints on Cosmological Parameters from the Angular Power Spectrum of a Combined 2500 deg<sup>2</sup> SPT-SZ and Planck Gravitational Lensing Map”. *Astrophys. J.* 860.2 (2018), p. 137. DOI: [10.3847/1538-4357/aac264](https://doi.org/10.3847/1538-4357/aac264). arXiv: [1712.07541](https://arxiv.org/abs/1712.07541) [astro-ph.CO] [p. 125].
- [260] M. TANABASHI et al. “Review of Particle Physics”. *Phys. Rev. D* 98 (3 Aug. 2018), p. 030001. DOI: [10.1103/PhysRevD.98.030001](https://doi.org/10.1103/PhysRevD.98.030001) [p. 36].
- [261] M. A. TROXEL et al. “Dark Energy Survey Year 1 results: Cosmological constraints from cosmic shear”. *Phys. Rev. D* 98.4 (2018), p. 043528. DOI: [10.1103/PhysRevD.98.043528](https://doi.org/10.1103/PhysRevD.98.043528). arXiv: [1708.01538](https://arxiv.org/abs/1708.01538) [astro-ph.CO] [p. 95].
- [262] P. ZARROUK et al. “The clustering of the SDSS-IV extended Baryon Oscillation Spectroscopic Survey DR14 quasar sample: measurement of the growth rate of structure from the anisotropic correlation function between redshift 0.8 and 2.2”. *Mon. Not. Roy. Astron. Soc.* 477.2 (2018), pp. 1639–1663. DOI: [10.1093/mnras/sty506](https://doi.org/10.1093/mnras/sty506). arXiv: [1801.03062](https://arxiv.org/abs/1801.03062) [astro-ph.CO] [p. 134].

- [263] P. AGRAWAL et al. “Rock ‘n’ Roll Solutions to the Hubble Tension” (Apr. 2019). arXiv: 1904.01016 [astro-ph.CO] [p. 108].
- [264] B. AHARMIM et al. “Constraints on Neutrino Lifetime from the Sudbury Neutrino Observatory”. *Phys. Rev. D* 99.3 (2019), p. 032013. DOI: 10.1103/PhysRevD.99.032013. arXiv: 1812.01088 [hep-ex] [p. 177].
- [265] S. ALEXANDER y E. MCDONOUGH. “Axion-Dilaton Destabilization and the Hubble Tension”. *Phys. Lett. B* 797 (2019), p. 134830. DOI: 10.1016/j.physletb.2019.134830. arXiv: 1904.08912 [astro-ph.CO] [p. 100].
- [266] M. ARCHIDIACONO et al. “Constraining Dark Matter-Dark Radiation interactions with CMB, BAO, and Lyman- $\alpha$ ”. *JCAP* 10 (2019), p. 055. DOI: 10.1088/1475-7516/2019/10/055. arXiv: 1907.01496 [astro-ph.CO] [pp. 118, 127, 173].
- [267] K. AYLOR et al. “Sounds Discordant: Classical Distance Ladder &  $\Lambda$ CDM -based Determinations of the Cosmological Sound Horizon”. *Astrophys. J.* 874.1 (2019), p. 4. DOI: 10.3847/1538-4357/ab0898. arXiv: 1811.00537 [astro-ph.CO] [pp. 106, 113].
- [268] M. BLOMQUIST et al. “Baryon acoustic oscillations from the cross-correlation of Ly $\alpha$  absorption and quasars in eBOSS DR14”. *Astron. Astrophys.* 629 (2019), A86. DOI: 10.1051/0004-6361/201935641. arXiv: 1904.03430 [astro-ph.CO] [pp. 92, 105, 134, 155, 192].
- [269] A. BOYARSKY et al. “Sterile neutrino Dark Matter”. *Prog. Part. Nucl. Phys.* 104 (2019), pp. 1–45. DOI: 10.1016/j.pnpnp.2018.07.004. arXiv: 1807.07938 [hep-ph] [p. 89].
- [270] T. BRINCKMANN y J. LESGOURGUES. “MontePython 3: boosted MCMC sampler and other features”. *Phys. Dark Univ.* 24 (2019), p. 100260. DOI: 10.1016/j.dark.2018.100260. arXiv: 1804.07261 [astro-ph.CO] [pp. 110, 155, 192, 225].
- [271] T. BRINCKMANN et al. “The promising future of a robust cosmological neutrino mass measurement”. *JCAP* 01 (2019), p. 059. DOI: 10.1088/1475-7516/2019/01/059. arXiv: 1808.05955 [astro-ph.CO] [p. 170].
- [272] A. CUCEU et al. “Baryon Acoustic Oscillations and the Hubble Constant: Past, Present and Future”. *JCAP* 10 (2019), p. 044. DOI: 10.1088/1475-7516/2019/10/044. arXiv: 1906.11628 [astro-ph.CO] [p. 92].
- [273] E. DI VALENTINO, A. MELCHIORRI y J. SILK. “Planck evidence for a closed Universe and a possible crisis for cosmology”. *Nature Astron.* 4.2 (2019), pp. 196–203. DOI: 10.1038/s41550-019-0906-9. arXiv: 1911.02087 [astro-ph.CO] [p. 96].
- [274] G. EFSTATHIOU y S. GRATTON. “A Detailed Description of the CamSpec Likelihood Pipeline and a Reanalysis of the Planck High Frequency Maps” (Oct. 2019). DOI: 10.21105/astro.1910.00483. arXiv: 1910.00483 [astro-ph.CO] [p. 96].
- [275] M. ESCUDERO y M. FAIRBAIRN. “Cosmological Constraints on Invisible Neutrino Decays Revisited”. *Phys. Rev. D* 100.10 (2019), p. 103531. DOI: 10.1103/PhysRevD.100.103531. arXiv: 1907.05425 [hep-ph] [p. 177].
- [276] W. L. FREEDMAN et al. “The Carnegie-Chicago Hubble Program. VIII. An Independent Determination of the Hubble Constant Based on the Tip of the Red Giant Branch” (July 2019). DOI: 10.3847/1538-4357/ab2f73. arXiv: 1907.05922 [astro-ph.CO] [p. 92].
- [277] W. HANDLEY y P. LEMOS. “Quantifying tensions in cosmological parameters: Interpreting the DES evidence ratio”. *Phys. Rev. D* 100.4 (2019), p. 043504. DOI: 10.1103/PhysRevD.100.043504. arXiv: 1902.04029 [astro-ph.CO] [pp. 122, 130].
- [278] C. HIKAGE et al. “Cosmology from cosmic shear power spectra with Subaru Hyper Suprime-Cam first-year data”. *Publ. Astron. Soc. Jap.* 71.2 (2019), p. 43. DOI: 10.1093/pasj/psz010. arXiv: 1809.09148 [astro-ph.CO] [pp. 95, 101].
- [279] C. D. HUANG et al. “Hubble Space Telescope Observations of Mira Variables in the Type Ia Supernova Host NGC 1559: An Alternative Candle to Measure the Hubble Constant” (Aug. 2019). DOI: 10.3847/1538-4357/ab5dbd. arXiv: 1908.10883 [astro-ph.CO] [p. 92].
- [280] N. KALOPEP. “Dark energy,  $H_0$  and weak gravity conjecture”. *Int. J. Mod. Phys. D* 28.14 (2019), p. 1944017. DOI: 10.1142/S0218271819440176. arXiv: 1903.11676 [hep-th] [p. 100].
- [281] W. D. KENWORTHY, D. SCOLNIC y A. RIESS. “The Local Perspective on the Hubble Tension: Local Structure Does Not Impact Measurement of the Hubble Constant”. *Astrophys. J.* 875.2 (2019), p. 145. DOI: 10.3847/1538-4357/ab0ebf. arXiv: 1901.08681 [astro-ph.CO] [p. 92].



- 
- [282] A. KLYPIN y F. PRADA. “Effects of long-wavelength fluctuations in large galaxy surveys”. *Mon. Not. Roy. Astron. Soc.* 489.2 (2019), pp. 1684–1696. DOI: 10.1093/mnras/stz2194. arXiv: 1809.03637 [astro-ph.CO] [p. 228].
- [283] P. LEMOS et al. “Model independent  $H(z)$  reconstruction using the cosmic inverse distance ladder”. *Mon. Not. Roy. Astron. Soc.* 483.4 (2019), pp. 4803–4810. DOI: 10.1093/mnras/sty3082. arXiv: 1806.06781 [astro-ph.CO] [p. 106].
- [284] X. LI y A. SHAFIELOO. “A Simple Phenomenological Emergent Dark Energy Model can Resolve the Hubble Tension”. *Astrophys. J. Lett.* 883.1 (2019), p. L3. DOI: 10.3847/2041-8213/ab3e09. arXiv: 1906.08275 [astro-ph.CO] [p. 128].
- [285] M.-X. LIN et al. “Acoustic Dark Energy: Potential Conversion of the Hubble Tension”. *Phys. Rev. D* 100.6 (2019), p. 063542. DOI: 10.1103/PhysRevD.100.063542. arXiv: 1905.12618 [astro-ph.CO] [pp. 107, 111].
- [286] C. MILLER, A. L. ERICKCEK y R. MURGIA. “Constraining nonthermal dark matter’s impact on the matter power spectrum”. *Phys. Rev. D* 100.12 (2019), p. 123520. DOI: 10.1103/PhysRevD.100.123520. arXiv: 1908.10369 [astro-ph.CO] [pp. 118, 152].
- [287] G. PARIMBELLI, M. VIEL y E. SEFUSATTI. “On the degeneracy between baryon feedback and massive neutrinos as probed by matter clustering and weak lensing”. *JCAP* 01 (2019), p. 010. DOI: 10.1088/1475-7516/2019/01/010. arXiv: 1809.06634 [astro-ph.CO] [p. 153].
- [288] M. PARK et al. “ $\Lambda$ CDM or self-interacting neutrinos: How CMB data can tell the two models apart”. *Phys. Rev. D* 100.6 (2019), p. 063524. DOI: 10.1103/PhysRevD.100.063524. arXiv: 1904.02625 [astro-ph.CO] [p. 127].
- [289] V. POULIN et al. “Early Dark Energy Can Resolve The Hubble Tension”. *Phys. Rev. Lett.* 122.22 (2019), p. 221301. DOI: 10.1103/PhysRevLett.122.221301. arXiv: 1811.04083 [astro-ph.CO] [pp. 101, 107, 111, 113, 128, 129].
- [290] G. W. PRATT et al. “The galaxy cluster mass scale and its impact on cosmological constraints from the cluster population”. *Space Sci. Rev.* 215.2 (2019), p. 25. DOI: 10.1007/s11214-019-0591-0. arXiv: 1902.10837 [astro-ph.CO] [p. 95].
- [291] M. RAVERI y W. HU. “Concordance and Discordance in Cosmology”. *Phys. Rev. D* 99.4 (2019), p. 043506. DOI: 10.1103/PhysRevD.99.043506. arXiv: 1806.04649 [astro-ph.CO] [pp. 115, 122, 130, 159, 160].
- [292] A. G. RIESS et al. “Large Magellanic Cloud Cepheid Standards Provide a 1% Foundation for the Determination of the Hubble Constant and Stronger Evidence for Physics beyond  $\Lambda$ CDM”. *Astrophys. J.* 876.1 (2019), p. 85. DOI: 10.3847/1538-4357/ab1422. arXiv: 1903.07603 [astro-ph.CO] [pp. 110, 155, 163].
- [293] V. de SAINTE AGATHE et al. “Baryon acoustic oscillations at  $z = 2.34$  from the correlations of  $\text{Ly}\alpha$  absorption in eBOSS DR14”. *Astron. Astrophys.* 629 (2019), A85. DOI: 10.1051/0004-6361/201935638. arXiv: 1904.03400 [astro-ph.CO] [pp. 134, 155, 192].
- [294] N. SCHÖNEBERG, J. LESGOURGUES y D. C. HOOPER. “The BAO+BBN take on the Hubble tension”. *JCAP* 10 (2019), p. 029. DOI: 10.1088/1475-7516/2019/10/029. arXiv: 1907.11594 [astro-ph.CO] [p. 92].
- [295] A. SLOSAR et al. “Scratches from the Past: Inflationary Archaeology through Features in the Power Spectrum of Primordial Fluctuations”. *Bull. Am. Astron. Soc.* 51.3 (2019), p. 98. arXiv: 1903.09883 [astro-ph.CO] [p. 96].
- [296] K. VATTIS, S. M. KOUSHIAPPAS y A. LOEB. “Dark matter decaying in the late Universe can relieve the  $H_0$  tension”. *Phys. Rev. D* 99.12 (2019), p. 121302. DOI: 10.1103/PhysRevD.99.121302. arXiv: 1903.06220 [astro-ph.CO] [pp. 140, 141, 158, 247].
- [297] W. L. K. WU et al. “A Measurement of the Cosmic Microwave Background Lensing Potential and Power Spectrum from 500  $\text{deg}^2$  of SPTpol Temperature and Polarization Data”. *Astrophys. J.* 884 (2019), p. 70. DOI: 10.3847/1538-4357/ab4186. arXiv: 1905.05777 [astro-ph.CO] [p. 125].
- [298] W. YUAN et al. “Consistent Calibration of the Tip of the Red Giant Branch in the Large Magellanic Cloud on the Hubble Space Telescope Photometric System and a Re-determination of the Hubble Constant”. *Astrophys. J.* 886 (2019), p. 61. DOI: 10.3847/1538-4357/ab4bc9. arXiv: 1908.00993 [astro-ph.GA] [p. 92].

- [299] A. ABDULLAHI y P. B. DENTON. “Visible Decay of Astrophysical Neutrinos at IceCube”. *Phys. Rev. D* 102.2 (2020), p. 023018. DOI: [10.1103/PhysRevD.102.023018](https://doi.org/10.1103/PhysRevD.102.023018). arXiv: 2005.07200 [hep-ph] [p. 177].
- [300] N. AGHANIM et al. “Planck 2018 results. V. CMB power spectra and likelihoods”. *Astron. Astrophys.* 641 (2020), A5. DOI: [10.1051/0004-6361/201936386](https://doi.org/10.1051/0004-6361/201936386). arXiv: 1907.12875 [astro-ph.CO] [p. 109].
- [301] N. AGHANIM et al. “Planck 2018 results. VI. Cosmological parameters”. *Astron. Astrophys.* 641 (2020). [Erratum: *Astron. Astrophys.* 652, C4 (2021)], A6. DOI: [10.1051/0004-6361/201833910](https://doi.org/10.1051/0004-6361/201833910). arXiv: 1807.06209 [astro-ph.CO] [pp. 10, 30, 91, 93, 94, 96, 105, 123, 126, 172, 176, 181, 193].
- [302] N. AGHANIM et al. “Planck 2018 results. VIII. Gravitational lensing”. *Astron. Astrophys.* 641 (2020), A8. DOI: [10.1051/0004-6361/201833886](https://doi.org/10.1051/0004-6361/201833886). arXiv: 1807.06210 [astro-ph.CO] [p. 109].
- [303] S. AIOLA et al. “The Atacama Cosmology Telescope: DR4 Maps and Cosmological Parameters”. *JCAP* 12 (2020), p. 047. DOI: [10.1088/1475-7516/2020/12/047](https://doi.org/10.1088/1475-7516/2020/12/047). arXiv: 2007.07288 [astro-ph.CO] [pp. 156, 165, 168].
- [304] E. APRILE et al. “Excess electronic recoil events in XENON1T”. *Phys. Rev. D* 102.7 (2020), p. 072004. DOI: [10.1103/PhysRevD.102.072004](https://doi.org/10.1103/PhysRevD.102.072004). arXiv: 2006.09721 [hep-ex] [pp. 140, 156, 164].
- [305] M. ASGARI et al. “KiDS+VIKING-450 and DES-Y1 combined: Mitigating baryon feedback uncertainty with COSEBIs”. *Astron. Astrophys.* 634 (2020), A127. DOI: [10.1051/0004-6361/201936512](https://doi.org/10.1051/0004-6361/201936512). arXiv: 1910.05336 [astro-ph.CO] [pp. 95, 101, 119].
- [306] I. BALDES et al. “Non-Cold Dark Matter from Primordial Black Hole Evaporation”. *JCAP* 08 (2020), p. 045. DOI: [10.1088/1475-7516/2020/08/045](https://doi.org/10.1088/1475-7516/2020/08/045). arXiv: 2004.14773 [astro-ph.CO] [p. 118].
- [307] G. BENEVENTO, W. HU y M. RAVERI. “Can Late Dark Energy Transitions Raise the Hubble constant?” *Phys. Rev. D* 101.10 (2020), p. 103517. DOI: [10.1103/PhysRevD.101.103517](https://doi.org/10.1103/PhysRevD.101.103517). arXiv: 2002.11707 [astro-ph.CO] [pp. 106, 132].
- [308] J. J. BENNETT et al. “Towards a precision calculation of the effective number of neutrinos  $N_{\text{eff}}$  in the Standard Model I: the QED equation of state”. *JCAP* 03 (2020). [Addendum: *JCAP* 03, A01 (2021)], p. 003. DOI: [10.1088/1475-7516/2020/03/003](https://doi.org/10.1088/1475-7516/2020/03/003). arXiv: 1911.04504 [hep-ph] [p. 29].
- [309] K. V. BERGHAUS y T. KARWAL. “Thermal Friction as a Solution to the Hubble Tension”. *Phys. Rev. D* 101.8 (2020), p. 083537. DOI: [10.1103/PhysRevD.101.083537](https://doi.org/10.1103/PhysRevD.101.083537). arXiv: 1911.06281 [astro-ph.CO] [pp. 100, 115].
- [310] J. L. BERNAL et al. “Robustness of baryon acoustic oscillation constraints for early-Universe modifications of  $\Lambda$ CDM cosmology”. *Phys. Rev. D* 102.12 (2020), p. 123515. DOI: [10.1103/PhysRevD.102.123515](https://doi.org/10.1103/PhysRevD.102.123515). arXiv: 2004.07263 [astro-ph.CO] [p. 92].
- [311] F. BIANCHINI et al. “Constraints on Cosmological Parameters from the 500 deg<sup>2</sup> SPTpol Lensing Power Spectrum”. *Astrophys. J.* 888 (2020), p. 119. DOI: [10.3847/1538-4357/ab6082](https://doi.org/10.3847/1538-4357/ab6082). arXiv: 1910.07157 [astro-ph.CO] [p. 165].
- [312] S. BIRRER et al. “TDCOSMO - IV. Hierarchical time-delay cosmography – joint inference of the Hubble constant and galaxy density profiles”. *Astron. Astrophys.* 643 (2020), A165. DOI: [10.1051/0004-6361/202038861](https://doi.org/10.1051/0004-6361/202038861). arXiv: 2007.02941 [astro-ph.CO] [p. 92].
- [313] N. BLINOV, C. KEITH y D. HOOPER. “Warm Decaying Dark Matter and the Hubble Tension”. *JCAP* 06 (2020), p. 005. DOI: [10.1088/1475-7516/2020/06/005](https://doi.org/10.1088/1475-7516/2020/06/005). arXiv: 2004.06114 [astro-ph.CO] [p. 186].
- [314] N. BLINOV y G. MARQUES-TAVARES. “Interacting radiation after Planck and its implications for the Hubble Tension”. *JCAP* 09 (2020), p. 029. DOI: [10.1088/1475-7516/2020/09/029](https://doi.org/10.1088/1475-7516/2020/09/029). arXiv: 2003.08387 [astro-ph.CO] [p. 127].
- [315] S. BOHR et al. “ETHOS – an effective parametrization and classification for structure formation: the non-linear regime at  $z \gtrsim 5$ ”. *Mon. Not. Roy. Astron. Soc.* 498.3 (2020), pp. 3403–3419. DOI: [10.1093/mnras/staa2579](https://doi.org/10.1093/mnras/staa2579). arXiv: 2006.01842 [astro-ph.CO] [p. 152].
- [316] M. BRAGLIA et al. “Larger value for  $H_0$  by an evolving gravitational constant”. *Phys. Rev. D* 102.2 (2020), p. 023529. DOI: [10.1103/PhysRevD.102.023529](https://doi.org/10.1103/PhysRevD.102.023529). arXiv: 2004.11161 [astro-ph.CO] [pp. 100, 115].

- 
- [317] M. BRAGLIA et al. “Unified framework for early dark energy from  $\alpha$ -attractors”. *Phys. Rev. D* 102.8 (2020), p. 083513. DOI: 10.1103/PhysRevD.102.083513. arXiv: 2005.14053 [astro-ph.CO] [p. 100].
- [318] M. BUSTAMANTE. “New limits on neutrino decay from the Glashow resonance of high-energy cosmic neutrinos” (Apr. 2020). arXiv: 2004.06844 [astro-ph.HE] [p. 177].
- [319] P. CARTER et al. “The impact of the fiducial cosmology assumption on BAO distance scale measurements”. *Mon. Not. Roy. Astron. Soc.* 494.2 (2020), pp. 2076–2089. DOI: 10.1093/mnras/staa761. arXiv: 1906.03035 [astro-ph.CO] [p. 92].
- [320] W. CERNY et al. “Multi-Wavelength, Optical (VI) and Near-Infrared (JHK) Calibration of the Tip of the Red Giant Branch Method based on Milky Way Globular Clusters” (Dec. 2020). arXiv: 2012.09701 [astro-ph.GA] [p. 92].
- [321] Z. CHACKO et al. “Cosmological Limits on the Neutrino Mass and Lifetime”. *JHEP* 04 (2020), p. 020. DOI: 10.1007/JHEP04(2020)020. arXiv: 1909.05275 [hep-ph] [pp. 177, 178].
- [322] G. CHOI, M. SUZUKI y T. T. YANAGIDA. “Degenerate Sub-keV Fermion Dark Matter from a Solution to the Hubble Tension”. *Phys. Rev. D* 101.7 (2020), p. 075031. DOI: 10.1103/PhysRevD.101.075031. arXiv: 2002.00036 [hep-ph] [p. 140].
- [323] G. CHOI, M. SUZUKI y T. T. YANAGIDA. “XENON1T Anomaly and its Implication for Decaying Warm Dark Matter”. *Phys. Lett. B* 811 (2020), p. 135976. DOI: 10.1016/j.physletb.2020.135976. arXiv: 2006.12348 [hep-ph] [pp. 140, 165].
- [324] G. CHOI, M. SUZUKI y T. T. YANAGIDA. “Degenerate fermion dark matter from a broken  $U(1)_{B-L}$  gauge symmetry”. *Phys. Rev. D* 102.3 (2020), p. 035022. DOI: 10.1103/PhysRevD.102.035022. arXiv: 2004.07863 [hep-ph] [p. 140].
- [325] S. K. CHOI et al. “The Atacama Cosmology Telescope: a measurement of the Cosmic Microwave Background power spectra at 98 and 150 GHz”. *JCAP* 12 (2020), p. 045. DOI: 10.1088/1475-7516/2020/12/045. arXiv: 2007.07289 [astro-ph.CO] [pp. 92, 94, 136, 165].
- [326] A. CHUDAYKIN, D. GORBUNOV y N. NEDELKO. “Combined analysis of Planck and SPTPol data favors the early dark energy models”. *JCAP* 08 (2020), p. 013. DOI: 10.1088/1475-7516/2020/08/013. arXiv: 2004.13046 [astro-ph.CO] [pp. 96, 125, 165, 166].
- [327] A. CHUDAYKIN et al. “Nonlinear perturbation theory extension of the Boltzmann code CLASS”. *Phys. Rev. D* 102.6 (2020), p. 063533. DOI: 10.1103/PhysRevD.102.063533. arXiv: 2004.10607 [astro-ph.CO] [pp. 118, 173].
- [328] S. DHAWAN et al. “Cosmological Model Insensitivity of Local  $H_0$  from the Cepheid Distance Ladder”. *Astrophys. J.* 894.1 (2020), p. 54. DOI: 10.3847/1538-4357/ab7fb0. arXiv: 2001.09260 [astro-ph.CO] [p. 106].
- [329] E. DI VALENTINO, A. MELCHIORRI y J. SILK. “Cosmological constraints in extended parameter space from the Planck 2018 Legacy release”. *JCAP* 01 (2020), p. 013. DOI: 10.1088/1475-7516/2020/01/013. arXiv: 1908.01391 [astro-ph.CO] [pp. 128, 129].
- [330] E. DI VALENTINO et al. “Interacting dark energy in the early 2020s: A promising solution to the  $H_0$  and cosmic shear tensions”. *Phys. Dark Univ.* 30 (2020), p. 100666. DOI: 10.1016/j.dark.2020.100666. arXiv: 1908.04281 [astro-ph.CO] [p. 135].
- [331] G. DOMÈNECH et al. “Planck residuals anomaly as a fingerprint of alternative scenarios to inflation”. *JCAP* 10 (2020), p. 005. DOI: 10.1088/1475-7516/2020/10/005. arXiv: 2005.08998 [astro-ph.CO] [p. 96].
- [332] R. DURRER. *The Cosmic Microwave Background*. Cambridge University Press, Dec. 2020. ISBN: 978-1-316-47152-4, 978-1-107-13522-2. DOI: 10.1017/9781316471524 [p. 77].
- [333] G. EFSTATHIOU. “A Lockdown Perspective on the Hubble Tension (with comments from the SH0ES team)” (July 2020). arXiv: 2007.10716 [astro-ph.CO] [p. 92].
- [334] G. EFSTATHIOU y S. GRATTON. “The evidence for a spatially flat Universe”. *Mon. Not. Roy. Astron. Soc.* 496.1 (2020), pp. L91–L95. DOI: 10.1093/mnras/1/slaa093. arXiv: 2002.06892 [astro-ph.CO] [p. 96].
- [335] M. ESCUDERO y S. J. WITTE. “A CMB search for the neutrino mass mechanism and its relation to the Hubble tension”. *Eur. Phys. J. C* 80.4 (2020), p. 294. DOI: 10.1140/epjc/s10052-020-7854-5. arXiv: 1909.04044 [astro-ph.CO] [p. 128].

- [336] M. ESCUDERO et al. “Relaxing Cosmological Neutrino Mass Bounds with Unstable Neutrinos”. *JHEP* 12 (2020), p. 119. DOI: [10.1007/JHEP12\(2020\)119](https://doi.org/10.1007/JHEP12(2020)119). arXiv: 2007.04994 [hep-ph] [p. 182].
- [337] W. L. FREEDMAN et al. “Calibration of the Tip of the Red Giant Branch (TRGB)” (Feb. 2020). DOI: [10.3847/1538-4357/ab7339](https://doi.org/10.3847/1538-4357/ab7339). arXiv: 2002.01550 [astro-ph.GA] [p. 92].
- [338] M. GONZALEZ, M. P. HERTZBERG y F. ROMPINEVE. “Ultralight Scalar Decay and the Hubble Tension”. *JCAP* 10 (2020), p. 028. DOI: [10.1088/1475-7516/2020/10/028](https://doi.org/10.1088/1475-7516/2020/10/028). arXiv: 2006.13959 [astro-ph.CO] [pp. 100, 115].
- [339] B. S. HARIDASU y M. VIEL. “Late-time decaying dark matter: constraints and implications for the  $H_0$ -tension”. *Mon. Not. Roy. Astron. Soc.* 497.2 (2020), pp. 1757–1764. DOI: [10.1093/mnras/staa1991](https://doi.org/10.1093/mnras/staa1991). arXiv: 2004.07709 [astro-ph.CO] [pp. 140, 141, 158].
- [340] L. HART y J. CHLUBA. “Updated fundamental constant constraints from Planck 2018 data and possible relations to the Hubble tension”. *Mon. Not. Roy. Astron. Soc.* 493.3 (2020), pp. 3255–3263. DOI: [10.1093/mnras/staa412](https://doi.org/10.1093/mnras/staa412). arXiv: 1912.03986 [astro-ph.CO] [p. 128].
- [341] S. HEIMERSHEIM et al. “Cannibalism hinders growth: Cannibal Dark Matter and the  $S_8$  tension”. *JCAP* 12 (2020), p. 016. DOI: [10.1088/1475-7516/2020/12/016](https://doi.org/10.1088/1475-7516/2020/12/016). arXiv: 2008.08486 [astro-ph.CO] [p. 135].
- [342] H. HILDEBRANDT et al. “KiDS+VIKING-450: Cosmic shear tomography with optical and infrared data”. *Astron. Astrophys.* 633 (2020), A69. DOI: [10.1051/0004-6361/201834878](https://doi.org/10.1051/0004-6361/201834878). arXiv: 1812.06076 [astro-ph.CO] [pp. 95, 101, 118, 120, 121, 162].
- [343] J. C. HILL et al. “Early dark energy does not restore cosmological concordance”. *Phys. Rev. D* 102.4 (2020), p. 043507. DOI: [10.1103/PhysRevD.102.043507](https://doi.org/10.1103/PhysRevD.102.043507). arXiv: 2003.07355 [astro-ph.CO] [pp. 100, 101, 110, 113, 115, 122, 134].
- [344] J. HOU et al. “The Completed SDSS-IV extended Baryon Oscillation Spectroscopic Survey: BAO and RSD measurements from anisotropic clustering analysis of the Quasar Sample in configuration space between redshift 0.8 and 2.2”. *Mon. Not. Roy. Astron. Soc.* 500.1 (2020), pp. 1201–1221. DOI: [10.1093/mnras/staa3234](https://doi.org/10.1093/mnras/staa3234). arXiv: 2007.08998 [astro-ph.CO] [p. 105].
- [345] M. M. IVANOV et al. “Constraining Early Dark Energy with Large-Scale Structure”. *Phys. Rev. D* 102.10 (2020), p. 103502. DOI: [10.1103/PhysRevD.102.103502](https://doi.org/10.1103/PhysRevD.102.103502). arXiv: 2006.11235 [astro-ph.CO] [pp. 101, 111, 113, 115, 118, 134].
- [346] K. JEDAMZIK y L. POGOSIAN. “Relieving the Hubble tension with primordial magnetic fields”. *Phys. Rev. Lett.* 125.18 (2020), p. 181302. DOI: [10.1103/PhysRevLett.125.181302](https://doi.org/10.1103/PhysRevLett.125.181302). arXiv: 2004.09487 [astro-ph.CO] [pp. 128, 134].
- [347] S. JOUDAKI et al. “KiDS+VIKING-450 and DES-Y1 combined: Cosmology with cosmic shear”. *Astron. Astrophys.* 638 (2020), p. L1. DOI: [10.1051/0004-6361/201936154](https://doi.org/10.1051/0004-6361/201936154). arXiv: 1906.09262 [astro-ph.CO] [pp. 101, 155, 162].
- [348] K. KANNIKE et al. “Dark Matter and the XENON1T electron recoil excess”. *Phys. Rev. D* 102.9 (2020), p. 095002. DOI: [10.1103/PhysRevD.102.095002](https://doi.org/10.1103/PhysRevD.102.095002). arXiv: 2006.10735 [hep-ph] [p. 165].
- [349] L. KNOX y M. MILLEA. “Hubble constant hunter’s guide”. *Phys. Rev. D* 101.4 (2020), p. 043533. DOI: [10.1103/PhysRevD.101.043533](https://doi.org/10.1103/PhysRevD.101.043533). arXiv: 1908.03663 [astro-ph.CO] [p. 106].
- [350] C. D. KREISCH, F.-Y. CYR-RACINE y O. DORÉ. “Neutrino puzzle: Anomalies, interactions, and cosmological tensions”. *Phys. Rev. D* 101.12 (2020), p. 123505. DOI: [10.1103/PhysRevD.101.123505](https://doi.org/10.1103/PhysRevD.101.123505). arXiv: 1902.00534 [astro-ph.CO] [pp. 127, 135].
- [351] L. LOMBRISER. “Consistency of the local Hubble constant with the cosmic microwave background”. *Phys. Lett. B* 803 (2020), p. 135303. DOI: [10.1016/j.physletb.2020.135303](https://doi.org/10.1016/j.physletb.2020.135303). arXiv: 1906.12347 [astro-ph.CO] [p. 93].
- [352] G. J. MATHEWS et al. “Cosmological Solutions to the Lithium Problem”. *JPS Conf. Proc.* 31 (2020). Ed. by T. KAWABATA et al., p. 011033. DOI: [10.7566/JPSCP.31.011033](https://doi.org/10.7566/JPSCP.31.011033). arXiv: 1909.01245 [astro-ph.CO] [p. 96].
- [353] A. MEAD et al. “HMcode-2020: Improved modelling of non-linear cosmological power spectra with baryonic feedback” (Sept. 2020). DOI: [10.1093/mnras/stab082](https://doi.org/10.1093/mnras/stab082). arXiv: 2009.01858 [astro-ph.CO] [p. 95].



- 
- [354] P. MOTLOCH y W. HU. “Lensinglike tensions in the *Planck* legacy release”. *Phys. Rev. D* 101.8 (2020), p. 083515. DOI: 10.1103/PhysRevD.101.083515. arXiv: 1912.06601 [astro-ph.CO] [pp. 96, 124–126].
- [355] F. NIEDERMANN y M. S. SLOTH. “Resolving the Hubble tension with new early dark energy”. *Phys. Rev. D* 102.6 (2020), p. 063527. DOI: 10.1103/PhysRevD.102.063527. arXiv: 2006.06686 [astro-ph.CO] [pp. 100, 110–113, 115, 128, 135].
- [356] N. PALANQUE-DELABROUILLE et al. “Hints, neutrino bounds and WDM constraints from SDSS DR14 Lyman- $\alpha$  and Planck full-survey data”. *JCAP* 04 (2020), p. 038. DOI: 10.1088/1475-7516/2020/04/038. arXiv: 1911.09073 [astro-ph.CO] [pp. 96, 181, 184, 196].
- [357] S. PAN et al. “Reconciling  $H_0$  tension in a six parameter space?” *JCAP* 06.06 (2020), p. 062. DOI: 10.1088/1475-7516/2020/06/062. arXiv: 1907.12551 [astro-ph.CO] [p. 128].
- [358] D. W. PESCE et al. “The Megamaser Cosmology Project. XIII. Combined Hubble constant constraints”. *Astrophys. J. Lett.* 891.1 (2020), p. L1. DOI: 10.3847/2041-8213/ab75f0. arXiv: 2001.09213 [astro-ph.CO] [p. 92].
- [359] M. RAVERI. “Reconstructing Gravity on Cosmological Scales”. *Phys. Rev. D* 101.8 (2020), p. 083524. DOI: 10.1103/PhysRevD.101.083524. arXiv: 1902.01366 [astro-ph.CO] [p. 113].
- [360] M. RIGAULT et al. “Strong Dependence of Type Ia Supernova Standardization on the Local Specific Star Formation Rate”. *Astron. Astrophys.* 644 (2020), A176. DOI: 10.1051/0004-6361/201730404. arXiv: 1806.03849 [astro-ph.CO] [p. 92].
- [361] J. SAKSTEIN y M. TRODDEN. “Early Dark Energy from Massive Neutrinos as a Natural Resolution of the Hubble Tension”. *Phys. Rev. Lett.* 124.16 (2020), p. 161301. DOI: 10.1103/PhysRevLett.124.161301. arXiv: 1911.11760 [astro-ph.CO] [pp. 100, 114].
- [362] J. SCHOMBERT, S. MCGAUGH y F. LELLI. “Using the Baryonic Tully–Fisher Relation to Measure  $H_0$ ”. *Astron. J.* 160.2 (2020), p. 71. DOI: 10.3847/1538-3881/ab9d88. arXiv: 2006.08615 [astro-ph.CO] [p. 92].
- [363] T. L. SMITH, V. POULIN y M. A. AMIN. “Oscillating scalar fields and the Hubble tension: a resolution with novel signatures”. *Phys. Rev. D* 101.6 (2020), p. 063523. DOI: 10.1103/PhysRevD.101.063523. arXiv: 1908.06995 [astro-ph.CO] [pp. 100, 107, 108, 111, 113, 116, 228].
- [364] D. VALCIN et al. “Inferring the Age of the Universe with Globular Clusters”. *JCAP* 12 (2020), p. 002. DOI: 10.1088/1475-7516/2020/12/002. arXiv: 2007.06594 [astro-ph.CO] [p. 100].
- [365] K. C. WONG et al. “HOLICOW – XIII. A 2.4 per cent measurement of  $H_0$  from lensed quasars:  $5.3\sigma$  tension between early- and late-Universe probes”. *Mon. Not. Roy. Astron. Soc.* 498.1 (2020), pp. 1420–1439. DOI: 10.1093/mnras/stz3094. arXiv: 1907.04869 [astro-ph.CO] [p. 92].
- [366] B. P. ABBOTT et al. “A Gravitational-wave Measurement of the Hubble Constant Following the Second Observing Run of Advanced LIGO and Virgo”. *Astrophys. J.* 909.2 (2021). [Erratum: *Astrophys. J.* 923, 279 (2021)], p. 218. DOI: 10.3847/1538-4357/abdcb7. arXiv: 1908.06060 [astro-ph.CO] [p. 92].
- [367] S. ALAM et al. “Completed SDSS-IV extended Baryon Oscillation Spectroscopic Survey: Cosmological implications from two decades of spectroscopic surveys at the Apache Point Observatory”. *Phys. Rev. D* 103.8 (2021), p. 083533. DOI: 10.1103/PhysRevD.103.083533. arXiv: 2007.08991 [astro-ph.CO] [p. 181].
- [368] I. J. ALLALI, M. P. HERTZBERG y F. ROMPINEVE. “Dark sector to restore cosmological concordance”. *Phys. Rev. D* 104.8 (2021), p. L081303. DOI: 10.1103/PhysRevD.104.L081303. arXiv: 2104.12798 [astro-ph.CO] [pp. 100, 135].
- [369] M. ASGARI et al. “KiDS-1000 Cosmology: Cosmic shear constraints and comparison between two point statistics”. *Astron. Astrophys.* 645 (2021), A104. DOI: 10.1051/0004-6361/202039070. arXiv: 2007.15633 [astro-ph.CO] [pp. 95, 134].
- [370] G. BARENBOIM et al. “Invisible neutrino decay in precision cosmology”. *JCAP* 03 (2021), p. 087. DOI: 10.1088/1475-7516/2021/03/087. arXiv: 2011.01502 [astro-ph.CO] [pp. 177, 178].
- [371] N. BARRY et al. “SKA-low intensity mapping pathfinder updates: deeper 21 cm power spectrum limits from improved analysis frameworks”. *J. Astron. Telesc. Instrum. Syst.* 8.1 (2021), p. 011007. DOI: 10.1117/1.JATIS.8.1.011007. arXiv: 2110.06173 [astro-ph.CO] [p. 42].
- [372] D. BAUMANN. *Cosmology lecture notes*. 2021 [pp. 10, 21, 28, 62, 63].

- [373] J. L. BERNAL et al. “The trouble beyond  $H_0$  and the new cosmic triangles”. *Phys. Rev. D* 103.10 (2021), p. 103533. DOI: 10.1103/PhysRevD.103.103533. arXiv: 2102.05066 [astro-ph.CO] [pp. 92, 101].
- [374] A. BLANCHARD y S. ILIĆ. “Closing up the cluster tension?” *Astron. Astrophys.* 656 (2021), A75. DOI: 10.1051/0004-6361/202140974. arXiv: 2104.00756 [astro-ph.CO] [p. 95].
- [375] M. BOYLAN-KOLCHIN y D. R. WEISZ. “Uncertain times: the redshift–time relation from cosmology and stars”. *Mon. Not. Roy. Astron. Soc.* 505.2 (2021), pp. 2764–2783. DOI: 10.1093/mnras/stab1521. arXiv: 2103.15825 [astro-ph.CO] [p. 101].
- [376] M. BRAGLIA et al. “Early modified gravity in light of the  $H_0$  tension and LSS data”. *Phys. Rev. D* 103.4 (2021), p. 043528. DOI: 10.1103/PhysRevD.103.043528. arXiv: 2011.12934 [astro-ph.CO] [p. 128].
- [377] D. BROUT y D. SCOLNIC. “It’s Dust: Solving the Mysteries of the Intrinsic Scatter and Host-galaxy Dependence of Standardized Type Ia Supernova Brightnesses”. *Astrophys. J.* 909.1 (2021), p. 26. DOI: 10.3847/1538-4357/abd69b. arXiv: 2004.10206 [astro-ph.CO] [p. 92].
- [378] D. CAMARENA y V. MARRA. “On the use of the local prior on the absolute magnitude of Type Ia supernovae in cosmological inference”. *Mon. Not. Roy. Astron. Soc.* 504 (2021), pp. 5164–5171. DOI: 10.1093/mnras/stab1200. arXiv: 2101.08641 [astro-ph.CO] [pp. 106, 132].
- [379] Z. CHACKO et al. “Determining the Neutrino Lifetime from Cosmology”. *Phys. Rev. D* 103.4 (2021), p. 043519. DOI: 10.1103/PhysRevD.103.043519. arXiv: 2002.08401 [astro-ph.CO] [pp. 177, 195, 196].
- [380] S. J. CLARK, K. VATTIS y S. M. KOUSHIAPPAS. “Cosmological constraints on late-universe decaying dark matter as a solution to the  $H_0$  tension”. *Phys. Rev. D* 103.4 (2021), p. 043014. DOI: 10.1103/PhysRevD.103.043014. arXiv: 2006.03678 [astro-ph.CO] [pp. 140, 141, 158, 246, 247].
- [381] S. J. CLARK et al. “The  $H_0$  and  $S_8$  tensions necessitate early and late time changes to  $\Lambda$ CDM” (Oct. 2021). arXiv: 2110.09562 [astro-ph.CO] [p. 135].
- [382] G. D’AMICO, L. SENATORE y P. ZHANG. “Limits on  $w$ CDM from the EFTofLSS with the PyBird code”. *JCAP* 01 (2021), p. 006. DOI: 10.1088/1475-7516/2021/01/006. arXiv: 2003.07956 [astro-ph.CO] [p. 173].
- [383] G. D’AMICO et al. “The Hubble Tension in Light of the Full-Shape Analysis of Large-Scale Structure Data”. *JCAP* 05 (2021), p. 072. DOI: 10.1088/1475-7516/2021/05/072. arXiv: 2006.12420 [astro-ph.CO] [pp. 101, 113, 115, 118, 134].
- [384] E. DI VALENTINO, S. GARIAZZO y O. MENA. “Most constraining cosmological neutrino mass bounds”. *Phys. Rev. D* 104.8 (2021), p. 083504. DOI: 10.1103/PhysRevD.104.083504. arXiv: 2106.15267 [astro-ph.CO] [pp. 184, 196].
- [385] E. DI VALENTINO et al. “In the realm of the Hubble tension—a review of solutions”. *Class. Quant. Grav.* 38.15 (2021), p. 153001. DOI: 10.1088/1361-6382/ac086d. arXiv: 2103.01183 [astro-ph.CO] [pp. 92, 93, 127].
- [386] D. DUTCHER et al. “Measurements of the E-mode polarization and temperature-E-mode correlation of the CMB from SPT-3G 2018 data”. *Phys. Rev. D* 104.2 (2021), p. 022003. DOI: 10.1103/PhysRevD.104.022003. arXiv: 2101.01684 [astro-ph.CO] [pp. 92, 96, 136].
- [387] G. EFSTATHIOU. “To  $H_0$  or not to  $H_0$ ?” *Mon. Not. Roy. Astron. Soc.* 505.3 (2021), pp. 3866–3872. DOI: 10.1093/mnras/stab1588. arXiv: 2103.08723 [astro-ph.CO] [pp. 106, 132].
- [388] W. ENZI et al. “Joint constraints on thermal relic dark matter from strong gravitational lensing, the  $\text{Ly}\alpha$  forest, and Milky Way satellites”. *Mon. Not. Roy. Astron. Soc.* 506.4 (2021), pp. 5848–5862. DOI: 10.1093/mnras/stab1960. arXiv: 2010.13802 [astro-ph.CO] [p. 173].
- [389] M. ESCUDERO y S. J. WITTE. “The hubble tension as a hint of leptogenesis and neutrino mass generation”. *Eur. Phys. J. C* 81.6 (2021), p. 515. DOI: 10.1140/epjc/s10052-021-09276-5. arXiv: 2103.03249 [hep-ph] [p. 128].
- [390] W. L. FREEDMAN. “Measurements of the Hubble Constant: Tensions in Perspective”. *Astrophys. J.* 919.1 (2021), p. 16. DOI: 10.3847/1538-4357/ac0e95. arXiv: 2106.15656 [astro-ph.CO] [p. 92].
- [391] K. FREESE y M. W. WINKLER. “Chain early dark energy: A Proposal for solving the Hubble tension and explaining today’s dark energy”. *Phys. Rev. D* 104.8 (2021), p. 083533. DOI: 10.1103/PhysRevD.104.083533. arXiv: 2102.13655 [astro-ph.CO] [p. 100].

- 
- [392] A. GOGOI et al. “Early Mass-varying Neutrino Dark Energy: Nugget Formation and Hubble Anomaly”. *Astrophys. J.* 915.2 (2021), p. 132. DOI: [10.3847/1538-4357/abfe5b](https://doi.org/10.3847/1538-4357/abfe5b). arXiv: [2005.11889](https://arxiv.org/abs/2005.11889) [astro-ph.CO] [p. 100].
- [393] A. M. GREEN y B. J. KAVANAGH. “Primordial Black Holes as a dark matter candidate”. *J. Phys. G* 48.4 (2021), p. 043001. DOI: [10.1088/1361-6471/abc534](https://doi.org/10.1088/1361-6471/abc534). arXiv: [2007.10722](https://arxiv.org/abs/2007.10722) [astro-ph.CO] [p. 90].
- [394] W. HANDLEY. “Curvature tension: evidence for a closed universe”. *Phys. Rev. D* 103.4 (2021), p. L041301. DOI: [10.1103/PhysRevD.103.L041301](https://doi.org/10.1103/PhysRevD.103.L041301). arXiv: [1908.09139](https://arxiv.org/abs/1908.09139) [astro-ph.CO] [p. 96].
- [395] L. T. HERGT et al. “Bayesian evidence for the tensor-to-scalar ratio  $r$  and neutrino masses  $m_\nu$ : Effects of uniform vs logarithmic priors”. *Phys. Rev. D* 103 (2021), p. 123511. DOI: [10.1103/PhysRevD.103.123511](https://doi.org/10.1103/PhysRevD.103.123511). arXiv: [2102.11511](https://arxiv.org/abs/2102.11511) [astro-ph.CO] [p. 184].
- [396] C. HEYMANS et al. “KiDS-1000 Cosmology: Multi-probe weak gravitational lensing and spectroscopic galaxy clustering constraints”. *Astron. Astrophys.* 646 (2021), A140. DOI: [10.1051/0004-6361/202039063](https://doi.org/10.1051/0004-6361/202039063). arXiv: [2007.15632](https://arxiv.org/abs/2007.15632) [astro-ph.CO] [pp. 87, 94, 102, 135, 155, 161, 246].
- [397] J. C. HILL et al. “The Atacama Cosmology Telescope: Constraints on Pre-Recombination Early Dark Energy” (Sept. 2021). arXiv: [2109.04451](https://arxiv.org/abs/2109.04451) [astro-ph.CO] [p. 136].
- [398] K. JEDAMZIK, L. POGOSIAN y G.-B. ZHAO. “Why reducing the cosmic sound horizon alone can not fully resolve the Hubble tension”. *Commun. in Phys.* 4 (2021), p. 123. DOI: [10.1038/s42005-021-00628-x](https://doi.org/10.1038/s42005-021-00628-x). arXiv: [2010.04158](https://arxiv.org/abs/2010.04158) [astro-ph.CO] [p. 101].
- [399] N. KHETAN et al. “A new measurement of the Hubble constant using Type Ia supernovae calibrated with surface brightness fluctuations”. *Astron. Astrophys.* 647 (2021), A72. DOI: [10.1051/0004-6361/202039196](https://doi.org/10.1051/0004-6361/202039196). arXiv: [2008.07754](https://arxiv.org/abs/2008.07754) [astro-ph.CO] [p. 92].
- [400] A. KLYPIN et al. “Clustering and Halo Abundances in Early Dark Energy Cosmological Models”. *Mon. Not. Roy. Astron. Soc.* 504.1 (2021), pp. 769–781. DOI: [10.1093/mnras/stab769](https://doi.org/10.1093/mnras/stab769). arXiv: [2006.14910](https://arxiv.org/abs/2006.14910) [astro-ph.CO] [pp. 118, 231].
- [401] N. LEE e Y. ALI-HAIMOUD. “Probing small-scale baryon and dark matter isocurvature perturbations with cosmic microwave background anisotropies”. *Phys. Rev. D* 104.10 (2021), p. 103509. DOI: [10.1103/PhysRevD.104.103509](https://doi.org/10.1103/PhysRevD.104.103509). arXiv: [2108.07798](https://arxiv.org/abs/2108.07798) [astro-ph.CO] [p. 61].
- [402] C. S. LORENZ et al. “Reconstruction of the neutrino mass as a function of redshift”. *Phys. Rev. D* 104.12 (2021), p. 123518. DOI: [10.1103/PhysRevD.104.123518](https://doi.org/10.1103/PhysRevD.104.123518). arXiv: [2102.13618](https://arxiv.org/abs/2102.13618) [astro-ph.CO] [pp. 177, 195].
- [403] M. LUCCA. “Dark energy–dark matter interactions as a solution to the S8 tension”. *Phys. Dark Univ.* 34 (2021), p. 100899. DOI: [10.1016/j.dark.2021.100899](https://doi.org/10.1016/j.dark.2021.100899). arXiv: [2105.09249](https://arxiv.org/abs/2105.09249) [astro-ph.CO] [p. 135].
- [404] E. McDONOUGH et al. “The Early Dark Sector, the Hubble Tension, and the Swampland” (Dec. 2021). arXiv: [2112.09128](https://arxiv.org/abs/2112.09128) [astro-ph.CO] [p. 100].
- [405] E. MORTSELL et al. “The Hubble Tension Bites the Dust: Sensitivity of the Hubble Constant Determination to Cepheid Color Calibration” (May 2021). arXiv: [2105.11461](https://arxiv.org/abs/2105.11461) [astro-ph.CO] [p. 92].
- [406] E. MORTSELL et al. “The Hubble Tension Revisited: Additional Local Distance Ladder Uncertainties” (June 2021). arXiv: [2106.09400](https://arxiv.org/abs/2106.09400) [astro-ph.CO] [p. 92].
- [407] M. R. MOSBECH et al. “The full Boltzmann hierarchy for dark matter-massive neutrino interactions”. *JCAP* 03 (2021), p. 066. DOI: [10.1088/1475-7516/2021/03/066](https://doi.org/10.1088/1475-7516/2021/03/066). arXiv: [2011.04206](https://arxiv.org/abs/2011.04206) [astro-ph.CO] [p. 135].
- [408] H. MOSHAFI, S. BAGHRAM y N. KHOSRAVI. “CMB lensing in a modified  $\Lambda$ CDM model in light of the H0 tension”. *Phys. Rev. D* 104.6 (2021), p. 063506. DOI: [10.1103/PhysRevD.104.063506](https://doi.org/10.1103/PhysRevD.104.063506). arXiv: [2012.14377](https://arxiv.org/abs/2012.14377) [astro-ph.CO] [p. 96].
- [409] F. NIEDERMANN y M. S. SLOTH. “New early dark energy”. *Phys. Rev. D* 103.4 (2021), p. L041303. DOI: [10.1103/PhysRevD.103.L041303](https://doi.org/10.1103/PhysRevD.103.L041303). arXiv: [1910.10739](https://arxiv.org/abs/1910.10739) [astro-ph.CO] [pp. 100, 128].
- [410] F. NIEDERMANN y M. S. SLOTH. “New Early Dark Energy is compatible with current LSS data”. *Phys. Rev. D* 103.10 (2021), p. 103537. DOI: [10.1103/PhysRevD.103.103537](https://doi.org/10.1103/PhysRevD.103.103537). arXiv: [2009.00006](https://arxiv.org/abs/2009.00006) [astro-ph.CO] [p. 134].



- [411] A. NYGAARD, T. TRAM y S. HANNESTAD. “Updated constraints on decaying cold dark matter”. *JCAP* 05 (2021), p. 017. DOI: [10.1088/1475-7516/2021/05/017](https://doi.org/10.1088/1475-7516/2021/05/017). arXiv: [2011.01632](https://arxiv.org/abs/2011.01632) [astro-ph.CO] [pp. 129, 140, 158].
- [412] V. POULIN, T. L. SMITH y A. BARTLETT. “Dark energy at early times and ACT data: A larger Hubble constant without late-time priors”. *Phys. Rev. D* 104.12 (2021), p. 123550. DOI: [10.1103/PhysRevD.104.123550](https://doi.org/10.1103/PhysRevD.104.123550). arXiv: [2109.06229](https://arxiv.org/abs/2109.06229) [astro-ph.CO] [p. 136].
- [413] M. RAVERI y C. DOUX. “Non-Gaussian estimates of tensions in cosmological parameters”. *Phys. Rev. D* 104.4 (2021), p. 043504. DOI: [10.1103/PhysRevD.104.043504](https://doi.org/10.1103/PhysRevD.104.043504). arXiv: [2105.03324](https://arxiv.org/abs/2105.03324) [astro-ph.CO] [p. 130].
- [414] A. G. RIESS et al. “A Comprehensive Measurement of the Local Value of the Hubble Constant with 1 km/s/Mpc Uncertainty from the Hubble Space Telescope and the SH0ES Team” (Dec. 2021). arXiv: [2112.04510](https://arxiv.org/abs/2112.04510) [astro-ph.CO] [pp. 91, 93, 155].
- [415] A. G. RIESS et al. “Cosmic Distances Calibrated to 1% Precision with Gaia EDR3 Parallaxes and Hubble Space Telescope Photometry of 75 Milky Way Cepheids Confirm Tension with  $\Lambda$ CDM”. *Astrophys. J. Lett.* 908.1 (2021), p. L6. DOI: [10.3847/2041-8213/abdbaf](https://doi.org/10.3847/2041-8213/abdbaf). arXiv: [2012.08534](https://arxiv.org/abs/2012.08534) [astro-ph.CO] [pp. 104, 105, 129].
- [416] N. J. SECREST et al. “A Test of the Cosmological Principle with Quasars”. *Astrophys. J. Lett.* 908.2 (2021), p. L51. DOI: [10.3847/2041-8213/abdd40](https://doi.org/10.3847/2041-8213/abdd40). arXiv: [2009.14826](https://arxiv.org/abs/2009.14826) [astro-ph.CO] [p. 96].
- [417] T. SEKIGUCHI y T. TAKAHASHI. “Early recombination as a solution to the  $H_0$  tension”. *Phys. Rev. D* 103.8 (2021), p. 083507. DOI: [10.1103/PhysRevD.103.083507](https://doi.org/10.1103/PhysRevD.103.083507). arXiv: [2007.03381](https://arxiv.org/abs/2007.03381) [astro-ph.CO] [p. 128].
- [418] T. L. SMITH et al. “Early dark energy is not excluded by current large-scale structure data”. *Phys. Rev. D* 103.12 (2021), p. 123542. DOI: [10.1103/PhysRevD.103.123542](https://doi.org/10.1103/PhysRevD.103.123542). arXiv: [2009.10740](https://arxiv.org/abs/2009.10740) [astro-ph.CO] [pp. 101, 112, 134].
- [419] J. SOLTIS, S. CASERTANO y A. G. RIESS. “The Parallax of  $\omega$  Centauri Measured from Gaia EDR3 and a Direct, Geometric Calibration of the Tip of the Red Giant Branch and the Hubble Constant”. *Astrophys. J. Lett.* 908.1 (2021), p. L5. DOI: [10.3847/2041-8213/abdbad](https://doi.org/10.3847/2041-8213/abdbad). arXiv: [2012.09196](https://arxiv.org/abs/2012.09196) [astro-ph.GA] [p. 92].
- [420] F. TAKAHASHI y W. YIN. “Cosmological implications of  $n_s \approx 1$  in light of the Hubble tension” (Dec. 2021). arXiv: [2112.06710](https://arxiv.org/abs/2112.06710) [astro-ph.CO] [p. 100].
- [421] S. VAGNOZZI. “Consistency tests of  $\Lambda$ CDM from the early integrated Sachs-Wolfe effect: Implications for early-time new physics and the Hubble tension”. *Phys. Rev. D* 104.6 (2021), p. 063524. DOI: [10.1103/PhysRevD.104.063524](https://doi.org/10.1103/PhysRevD.104.063524). arXiv: [2105.10425](https://arxiv.org/abs/2105.10425) [astro-ph.CO] [p. 101].
- [422] S. VAGNOZZI, A. LOEB y M. MORESCO. “Eppur è piatto? The Cosmic Chronometers Take on Spatial Curvature and Cosmic Concordance”. *Astrophys. J.* 908.1 (2021), p. 84. DOI: [10.3847/1538-4357/abd4df](https://doi.org/10.3847/1538-4357/abd4df). arXiv: [2011.11645](https://arxiv.org/abs/2011.11645) [astro-ph.CO] [p. 134].
- [423] S. VAGNOZZI, F. PACUCCI y A. LOEB. “Implications for the Hubble tension from the ages of the oldest astrophysical objects” (May 2021). arXiv: [2105.10421](https://arxiv.org/abs/2105.10421) [astro-ph.CO] [p. 101].
- [424] D. VALCIN et al. “The age of the Universe with globular clusters: reducing systematic uncertainties”. *JCAP* 08 (2021), p. 017. DOI: [10.1088/1475-7516/2021/08/017](https://doi.org/10.1088/1475-7516/2021/08/017). arXiv: [2102.04486](https://arxiv.org/abs/2102.04486) [astro-ph.GA] [p. 100].
- [425] S. XU y S. ZHENG. “Resolving XENON Excess With Decaying Cold Dark Matter”. *Eur. Phys. J. C* 81.5 (2021), p. 446. DOI: [10.1140/epjc/s10052-021-09262-x](https://doi.org/10.1140/epjc/s10052-021-09262-x). arXiv: [2012.10827](https://arxiv.org/abs/2012.10827) [hep-ph] [pp. 140, 165].
- [426] W. YANG et al. “Emergent Dark Energy, neutrinos and cosmological tensions”. *Phys. Dark Univ.* 31 (2021), p. 100762. DOI: [10.1016/j.dark.2020.100762](https://doi.org/10.1016/j.dark.2020.100762). arXiv: [2007.02927](https://arxiv.org/abs/2007.02927) [astro-ph.CO] [p. 128].
- [427] W. YANG et al. “Generalized emergent dark energy model and the Hubble constant tension”. *Phys. Rev. D* 104.6 (2021), p. 063521. DOI: [10.1103/PhysRevD.104.063521](https://doi.org/10.1103/PhysRevD.104.063521). arXiv: [2103.03815](https://arxiv.org/abs/2103.03815) [astro-ph.CO] [p. 129].
- [428] E. ABDALLA et al. “Cosmology intertwined: A review of the particle physics, astrophysics, and cosmology associated with the cosmological tensions and anomalies”. *JHEAp* 34 (2022), pp. 49–211. DOI: [10.1016/j.jheap.2022.04.002](https://doi.org/10.1016/j.jheap.2022.04.002). arXiv: [2203.06142](https://arxiv.org/abs/2203.06142) [astro-ph.CO] [pp. 94, 96].

- 
- [429] Z. ABDURASHIDOVA et al. “HERA Phase I Limits on the Cosmic 21 cm Signal: Constraints on Astrophysics and Cosmology during the Epoch of Reionization”. *Astrophys. J.* 924.2 (2022), p. 51. DOI: [10.3847/1538-4357/ac2ffc](https://doi.org/10.3847/1538-4357/ac2ffc). arXiv: [2108.07282](https://arxiv.org/abs/2108.07282) [astro-ph.CO] [p. 42].
- [430] M. AKER et al. “Direct neutrino-mass measurement with sub-electronvolt sensitivity”. *Nature Phys.* 18.2 (2022), pp. 160–166. DOI: [10.1038/s41567-021-01463-1](https://doi.org/10.1038/s41567-021-01463-1). arXiv: [2105.08533](https://arxiv.org/abs/2105.08533) [hep-ex] [p. 181].
- [431] K. K. BODDY et al. “Astrophysical and Cosmological Probes of Dark Matter”. *2022 Snowmass Summer Study*, Mar. 2022. arXiv: [2203.06380](https://arxiv.org/abs/2203.06380) [hep-ph] [p. 88].
- [432] J. Z. CHEN et al. “Weaker yet again: mass spectrum-consistent cosmological constraints on the neutrino lifetime” (Mar. 2022). arXiv: [2203.09075](https://arxiv.org/abs/2203.09075) [hep-ph] [p. 177].
- [433] G. CHOI y T. T. YANAGIDA. “Gravitino cosmology helped by a right handed (s)neutrino”. *Phys. Lett. B* 827 (2022), p. 136954. DOI: [10.1016/j.physletb.2022.136954](https://doi.org/10.1016/j.physletb.2022.136954). arXiv: [2104.02958](https://arxiv.org/abs/2104.02958) [hep-ph] [p. 140].
- [434] C. DALANG y C. BONVIN. “On the kinematic cosmic dipole tension”. *Mon. Not. Roy. Astron. Soc.* 512.3 (2022), pp. 3895–3905. DOI: [10.1093/mnras/stac726](https://doi.org/10.1093/mnras/stac726). arXiv: [2111.03616](https://arxiv.org/abs/2111.03616) [astro-ph.CO] [p. 96].
- [435] S. DAS et al. “Nonthermal neutrino-like hot dark matter in light of the S8 tension”. *Phys. Rev. D* 105.10 (2022), p. 103503. DOI: [10.1103/PhysRevD.105.103503](https://doi.org/10.1103/PhysRevD.105.103503). arXiv: [2104.03329](https://arxiv.org/abs/2104.03329) [astro-ph.CO] [p. 135].
- [436] S. GARIAZZO et al. “Neutrino mass and mass ordering: No conclusive evidence for normal ordering” (May 2022). arXiv: [2205.02195](https://arxiv.org/abs/2205.02195) [hep-ph] [p. 184].
- [437] L. HEROLD, E. G. M. FERREIRA y E. KOMATSU. “New Constraint on Early Dark Energy from Planck and BOSS Data Using the Profile Likelihood”. *Astrophys. J. Lett.* 929.1 (2022), p. L16. DOI: [10.3847/2041-8213/ac63a3](https://doi.org/10.3847/2041-8213/ac63a3). arXiv: [2112.12140](https://arxiv.org/abs/2112.12140) [astro-ph.CO] [p. 112].
- [438] D. C. HOOPER y M. LUCCA. “Hints of dark matter-neutrino interactions in Lyman- $\alpha$  data”. *Phys. Rev. D* 105.10 (2022), p. 103504. DOI: [10.1103/PhysRevD.105.103504](https://doi.org/10.1103/PhysRevD.105.103504). arXiv: [2110.04024](https://arxiv.org/abs/2110.04024) [astro-ph.CO] [p. 96].
- [439] R. JIMENEZ et al. “Neutrino Masses and Mass Hierarchy: Evidence for the Normal Hierarchy” (Mar. 2022). arXiv: [2203.14247](https://arxiv.org/abs/2203.14247) [hep-ph] [pp. 180, 184].
- [440] T. KARWAL et al. “Chameleon early dark energy and the Hubble tension”. *Phys. Rev. D* 105.6 (2022), p. 063535. DOI: [10.1103/PhysRevD.105.063535](https://doi.org/10.1103/PhysRevD.105.063535). arXiv: [2106.13290](https://arxiv.org/abs/2106.13290) [astro-ph.CO] [p. 100].
- [441] A. LA POSTA et al. “Constraints on prerecombination early dark energy from SPT-3G public data”. *Phys. Rev. D* 105.8 (2022), p. 083519. DOI: [10.1103/PhysRevD.105.083519](https://doi.org/10.1103/PhysRevD.105.083519). arXiv: [2112.10754](https://arxiv.org/abs/2112.10754) [astro-ph.CO] [p. 136].
- [442] S. MAU et al. “Milky Way Satellite Census. IV. Constraints on Decaying Dark Matter from Observations of Milky Way Satellite Galaxies” (Jan. 2022). arXiv: [2201.11740](https://arxiv.org/abs/2201.11740) [astro-ph.CO] [p. 173].
- [443] L. PERIVOLAROPOULOS y F. SKARA. “A reanalysis of the latest SH0ES data for  $H_0$ : Effects of new degrees of freedom on the Hubble tension” (Aug. 2022). arXiv: [2208.11169](https://arxiv.org/abs/2208.11169) [astro-ph.CO] [p. 103].
- [444] O. H. E. PHILCOX y M. M. IVANOV. “BOSS DR12 full-shape cosmology:  $\Lambda$ CDM constraints from the large-scale galaxy power spectrum and bispectrum monopole”. *Phys. Rev. D* 105.4 (2022), p. 043517. DOI: [10.1103/PhysRevD.105.043517](https://doi.org/10.1103/PhysRevD.105.043517). arXiv: [2112.04515](https://arxiv.org/abs/2112.04515) [astro-ph.CO] [p. 95].
- [445] V. I. SABLÁ y R. R. CALDWELL. “The Microphysics of Early Dark Energy” (Feb. 2022). arXiv: [2202.08291](https://arxiv.org/abs/2202.08291) [astro-ph.CO] [p. 100].
- [446] N. SABTI, J. B. MUÑOZ y D. BLAS. “New Roads to the Small-scale Universe: Measurements of the Clustering of Matter with the High-redshift UV Galaxy Luminosity Function”. *Astrophys. J. Lett.* 928.2 (2022), p. L20. DOI: [10.3847/2041-8213/ac5e9c](https://doi.org/10.3847/2041-8213/ac5e9c). arXiv: [2110.13161](https://arxiv.org/abs/2110.13161) [astro-ph.CO] [p. 88].
- [447] L. F. SECCO et al. “Dark Energy Survey Year 3 results: Cosmology from cosmic shear and robustness to modeling uncertainty”. *Phys. Rev. D* 105.2 (2022), p. 023515. DOI: [10.1103/PhysRevD.105.023515](https://doi.org/10.1103/PhysRevD.105.023515). arXiv: [2105.13544](https://arxiv.org/abs/2105.13544) [astro-ph.CO] [p. 95].
- [448] T. SIMON et al. “Constraining decaying dark matter with BOSS data and the effective field theory of large-scale structures” (Mar. 2022). arXiv: [2203.07440](https://arxiv.org/abs/2203.07440) [astro-ph.CO] [p. 173].

- [449] T. L. SMITH et al. “Hints of Early Dark Energy in Planck, SPT, and ACT data: new physics or systematics?” (Feb. 2022). arXiv: [2202.09379](#) [[astro-ph.CO](#)] [p. [136](#)].
- [450] R. SOLOMON, G. AGARWAL y D. STOJKOVIC. “Environment Dependent Electron Mass and the  $H_0$ -Tension” (Jan. 2022). arXiv: [2201.03127](#) [[hep-ph](#)] [p. [128](#)].



---

## Abstract

With the advent of large astronomical surveys coming from ground- and space- based telescopes, the field of cosmology has undergone a scientific revolution in the last decades. It is said that we have entered in the era of precision cosmology: not only do we have plenty of measurements from the early and late universe, but also we can use them to test theoretical models with astonishing accuracy. One of such models, describing the universe with a flat Friedman-Lemaître metric and containing around 5 % baryons, 25 % Cold Dark Matter (CDM) and 70 % dark energy in the form of a cosmological constant ( $\Lambda$ ), has shown to provide a remarkable fit to a wide variety of observables. Unfortunately, the nature of its main constituents -dark matter and dark energy - lacks identification. In addition, several experimental discrepancies have emerged in recent years, possibly shedding light on the properties of these mysterious components. On the other hand, the discovery of neutrino oscillations has provided convincing evidence that neutrinos possess non-zero masses, a phenomenon that cannot be explained within the Standard Model of Particle Physics. In my work, I have put new and robust constraints on many different extensions of the  $\Lambda$ CDM paradigm, aiming at explaining some of the present anomalies in cosmology, or to better characterize the properties of the elusive neutrinos. I start confronting a 1-parameter model of Early Dark Energy against a wide variety of data sets, showing that it can resolve the  $H_0$  tension, and that the addition of weak-lensing data doesn't affect this conclusion. In addition, I have made a systematic comparison of seventeen different models which have been proposed to resolve the  $H_0$  tension (including Early Dark Energy), and quantified the relative success of each model using a series of metrics and a wide array of data combinations. Secondly, I have performed a detailed cosmological analysis of a scenario in which dark matter can decay into dark radiation and warm dark matter species, including for the first time a full treatment of perturbations. This study has shown that this model, while unable to ease the Hubble tension, can fully explain the low- $S_8$  measurement from recent weak lensing surveys. I end discussing updated cosmic constraints on a scenario in which neutrinos can decay into dark radiation while being non-relativistic. I show that this allows to significantly relax the bounds on the neutrino masses, making a potential detection in the laboratory compatible with cosmological constraints.

---

## Résumé

Avec l'avènement de grands relevés astronomiques provenant de télescopes terrestres et spatiaux, le domaine de la cosmologie a connu une révolution scientifique au cours des dernières décennies. On dit que nous sommes entrés dans l'ère de la cosmologie de précision : non seulement nous disposons de nombreuses mesures de l'univers ancien et tardif, mais nous pouvons également les utiliser pour tester des modèles théoriques avec une très grande précision. L'un de ces modèles, décrivant l'univers avec une métrique de Friedman-Lemaître plate et contenant environ 5 % baryons, 25 % Matière Noire Froide (acronyme anglais CDM) et 70 % d'énergie noire sous la forme d'une constante cosmologique ( $\Lambda$ ), s'est avérée fournir un ajustement remarquable à une grande variété d'observables. Malheureusement, la nature de ses principaux constituants - la matière noire et l'énergie noire - n'est pas encore identifiée. De plus, plusieurs divergences expérimentales sont apparues ces dernières années, qui pourraient révéler les propriétés de ces composants mystérieux. D'autre part, la découverte des oscillations des neutrinos a fourni des preuves convaincantes que les neutrinos possèdent des masses non nulles, un phénomène qui ne peut pas être expliqué dans le modèle standard de la physique des particules. Dans mon travail, j'ai mis de nouvelles contraintes robustes sur de nombreuses extensions différentes du paradigme  $\Lambda$ CDM, visant à expliquer certaines des anomalies actuelles en cosmologie, ou à mieux caractériser les propriétés des neutrinos insaisissables. Je commence par confronter un modèle à 1 paramètre supplémentaire d'énergie noire précoce à une grande variété d'ensembles de données, montrant qu'il peut résoudre la tension  $H_0$ , et que l'ajout de données du lentillage gravitationnelle faible des galaxies n'affecte pas cette conclusion. De plus, j'ai fait une comparaison systématique de dix-sept modèles différents qui ont été proposés pour résoudre la tension  $H_0$  (y compris l'énergie noire précoce), et quantifié le succès relatif de chaque modèle en utilisant une série de métriques et un large éventail de combinaisons des données. Deuxièmement, j'ai effectué une analyse cosmologique détaillée d'un scénario dans lequel la matière noire peut se désintégrer en un rayonnement sombre et une particule de matière noire "chaude", incluant pour la première fois un traitement complet des perturbations. Cette étude a montré que ce modèle, bien qu'incapable d'atténuer la tension de Hubble, peut pleinement expliquer la mesure de  $S_8$  par des récentes enquêtes à lentillage gravitationnelle faible des galaxies. Je termine en discutant des nouvelles contraintes cosmologiques sur un scénario dans lequel les neutrinos massifs non-relativistes se désintègrent en rayonnement noir. Je montre que cela permet de réduire significativement les limites de masse des neutrinos, rendant compatible une possible détection en laboratoire avec les contraintes cosmologiques.

---